PB89-166615

Proceedings: Advances in Particle Sampling and Measurement. Held in Daytona Beach, Florida in October 1981

Southern Research Inst., Birmingham, AL

Prepared for

Environmental Protection Agency
Research Triangle Park, NC

Feb 89

U.S. Department of Commerce
National Technical Information Service
NTIS

PB89-166615

EPA/600/9-89/004
February 1989

Proceedings:
Advances in Particle Sampling and Measurement
(Daytona Beach, FL, October 1981)

Wallace B. Smith
Ashley D. Williamson
Editors

Southern Research Institute
2000 Ninth Avenue South
Birmingham, Alabama 35255

Contract No. 68-02-3118
Program Element No. EHE624

EPA Project Officer: D. Bruce Harris

Industrial Environmental Research Laboratory
(Air and Energy Engineering Research Laboratory)
Research Triangle Park, NC 27711

AIR AND ENERGY ENGINEERING RESEARCH LABORATORY
OFFICE OF RESEARCH AND DEVELOPMENT
U.S. ENVIRONMENTAL PROTECTION AGENCY
RESEARCH TRIANGLE PARK, NC 27711

REPRODUCED BY
U.S. DEPARTMENT OF COMMERCE
NATIONAL TECHNICAL INFORMATION SERVICE
SPRINGFIELD, VA. 22161

TECHNICAL REPORT DATA

(Please read Instructions on the reverse before completing)

1. REPORT NO. EPA/600/9-89/004	2.	3. RECIPIENT'S ACCESSION NO. PB89 166615/AS
4. TITLE AND SUBTITLE Proceedings: Advances in Particle Sampling and Measurement (Daytona Beach, FL, October 1981)		5. REPORT DATE February 1989
		6. PERFORMING ORGANIZATION CODE
7. AUTHOR(S) W. B. Smith and A. D. Williamson (Editors)		8. PERFORMING ORGANIZATION REPORT NO.
9. PERFORMING ORGANIZATION NAME AND ADDRESS Southern Research Institute 2000 Ninth Avenue, South Birmingham, Alabama 35255		10. PROGRAM ELEMENT NO.
		11. CONTRACT/GRANT NO. 68-02-3118
12. SPONSORING AGENCY NAME AND ADDRESS EPA, Office of Research and Development Air and Energy Engineering Research Laboratory* Research Triangle Park, NC 27711		13. TYPE OF REPORT AND PERIOD COVERED Proceedings; 10/81
		14. SPONSORING AGENCY CODE EPA/600/13

15. SUPPLEMENTARY NOTES AEERL project officer is D. Bruce Harris, Mail Drop 62; 919/541-7807. (*) The former Industrial Environmental Research Laboratory-RTP.

16. ABSTRACT The proceedings consist of reports of research on equipment and techniques for sampling and characterizing particulate emissions from industrial sources (e.g., nickel smelters and a power plant burning low-sulfur coal) and other aerosols (e.g., uranium oxide in high-energy environments, the launch exhaust of the NASA shuttle). Equipment included samplers designed for: collection of particles in the inhalable size range; collection of samples for wave-dispersive x-ray fluorescence; condensation and collection of vapors by dilution; and isokinetic sampling by gas recirculation. Other equipment included piezoelectric microbalances for monitoring mass emissions, a velocimeter for measuring aerodynamic particle sizes, a remote passive opacity meter, and an optical particle counter using coherent detection of phase-shifted light. Techniques included methods for impactor data reduction and prediction of sampler collection efficiency, and comparisons of methods: the EPA source assessment sampling system vs a dilution tunnel for collecting combustion emissions containing organic matter, non-intrusive optical probes vs extractive probes for measuring soot from a swirl-stabilized combustor, plume opacity vs mass concentration, and particle-sizing methods for measuring collection efficiency of fabric filters.

17. KEY WORDS AND DOCUMENT ANALYSIS

a. DESCRIPTORS	b. IDENTIFIERS/OPEN ENDED TERMS	c. COSATI Field/Group
Pollution Particles Dust Aerosols Sampling Measurement	Pollution Control Stationary Sources Particulate	13B 14G 11G 07D 14B

18. DISTRIBUTION STATEMENT Release to Public	19. SECURITY CLASS *(This Report)* Unclassified	21. NO. OF PAGES 403
	20. SECURITY CLASS *(This page)* Unclassified	22. PRICE

EPA Form 2220-1 (9-73)

NOTICE

This document has been reviewed in accordance with U.S. Environmental Protection Agency policy and approved for publication. Mention of trade names or commercial products does not constitute endorsement or recommendation for use.

PREFACE

The symposium was sponsored by the Technical Support Staff, Industrial Environmental Research Laboratory, U.S. Environmental Protection Agency.* D. Bruce Harris (EPA) served as chairman. Session chairmen were Heinz Fissan (University of Duisburg), Michael McElroy (Electric Power Research Institute), Marvin Tillery (Los Alamos Scientific Laboratory), and Wallace B. Smith and Ashley D. Williamson, both of Southern Research Institute. A. B. Craig (EPA) delivered a welcoming address.

(*) On January 1, 1985, the Laboratory was renamed the Air and Energy Engineering Research Laboratory.

CONTENTS

Preface iii
Principal Authors and Chairmen. viii

Paper 1. Aerosol Size and Chemistry at a Coal-Fired Power Plant
J. D. McCain, W. G. Kistler, J. W. Ragland, and R. L. Merritt 1

Paper 2. Airborne Particulate Size Distribution Measurements in Smelter Plumes
Walter H. Chan, Robert J. Vet, Maris A. Lusis, and Gregory B. Skelton . . 27

Paper 3. Characterization of Uranium Oxide Aerosols Produced by High Energy Environments
R. P. Sandoval, G. J. Newton, and B. A. Wong. 42

Paper 4. Characterization of Suspended Particles in the Space Shuttle Exhaust Cloud
David C. Woods and Raymond L. Chuan 52

Paper 5. Recent Research in the Field of Aerosol Sampling, Measurement, and Characterization in European Countries
K. R. Spurny and H. Fissan 65

Paper 6. An Instack Cascade Impactor to Collect Samples for WDXRF Analysis
L. G. Felix, J. D. McCain, D. H. Hussey, R. Smith, and K. Knapp 87

Paper 7. Source Assessment Sampling System (SASS) Versus Dilution Tunnel Sampling
Raymond G. Merrill, Jr., Joellen Lewtas, and Robert E. Hall 112

Paper 8. A Stack Dilution Sampling System for the Measurement of Condensible Vapors in Process Emissions
A. D. Williamson, J. D. McCain, W. B. Smith, and D.B. Harris 120

Paper 9. Passive Remote Smoke Plume Opacity Monitor
Pedro Lilienfeld, Paul Elterman, Roger Stern, and Gary Woker 134

Paper 10. Ultra-Fine Cascade Impactor Particle Size Data Relationships to Opacity: Case Histories
Phillip A. Nelson, David S. Mummey, and Wesley D. Snowden 145

Paper 11. Parameters for Ambient Sampling of Inhalable Particulate Matter
Charles W. Lewis and Robert K. Stevens. 154

Preceding page blank

Paper 12. An Ambient Air Inlet for Collection of TTP and RSP Aerosol Fractions
Andrew R. McFarland, Carlos A. Ortiz, and Clayton M. Rue 162

Paper 13. A 10 Micron Cutpoint Inlet for the Dichotomous Sampler
James B. Wedding, Michael A. Weigand, Theodore C. Carney, and Ralph E. Baumgardner 174

Paper 14. Applications of the "Apparent Diameter" Method for Unimodal and Bimodal Distributions
James W. Gentry, J. San, F. Farzaneh, and P. K. Yu 185

Paper 15. Recent Activities of the National Bureau of Standards and the American Society for Testing and Materials in Developing Particulate Standard Reference Materials
R. Keith Kirby 195

Paper 16. Recent Developments in the Application of Finite Difference Solutions to the Study of Flow Fields and Particle Trajectories
V. A. Marple and D. J. Rader 200

Paper 17. An Industry Response to Meeting its Particle Sizing Information Needs
Timothy J. Abbrott and Jerry E. Whyte 216

Paper 18. A New Piezoelectric Quartz Crystal for Particle Mass Determination
H. Fissan and D. F. Schulze-Froehlich 229

Paper 19. Rapid Testing of Filter Efficiency with a Computerized QCM Cascade Impactor
Raymond L. Chuan and Cam de Pierre 246

Paper 20. New Automatic Piezoelectric Aerosol Mass Monitor
Frederick R. Quant and Gilmore J. Sem. 258

Paper 21. A New Practical Technique for Real-Time Particulate Mass Monitoring
Hiroshi Noguchi, Nobuhisa Mori, and Tokuta Inoue 264

Paper 22. Coherent Detection of Phase-Shifted Light from Submicron Particles
Donald R. Pettit and Thomas W. Peterson 272

Paper 23. Development of an Aerodynamic Particle Sizer
Jugal K. Agarwal and Richard J. Remiarz 303

Paper 24. A High Flow Rate, High Sensitivity Optical Particle Counter: Design and Performance
A. Lieberman 318

Paper 25. A Comparison of Soot Size and Number Density Measured Simultaneously in a Swirl-Stabilized Combustor by Extractive and Non-Intrusive Optical Probes
G. S. Samuelsen, R. L. Hack, C. C. Poon, W. D. Bachalo, and H. J. Clewell . . . 330

Paper 26. A Sensitive Particulate Monitor for Measuring the Approximate Opacity for Fabric Filter Systems
William J. Steele, Wallace B. Smith, William E. Farthing, and Robert C. Carr. . 343

Paper 27. A Comparison of Several Particle-Sizing Techniques
Kenneth M. Cushing, R. Ray Wilson, William E. Farthing, D. Bruce Harris, and Robert C. Carr 357

Paper 28. Interactive Particle Data Reduction for Fine Particles Testing
C. E. Tatsch, W. M. Yeager, and G. L. Johnson 379

Paper 29. Isokinetic Sampling with Fixed Flow Rate Devices Using Exhaust Gas Recirculation
D. B. Harris and L. Beddingfield 388

Metric Conversion Factors 393

Principal Authors and Chairmen

Mr. D. Bruce Harris
Environmental Protection Agency
Industrial Environmental Research Laboratory
Mail Stop MD-62
Research Triangle Park, NC 27711
Phone: 919/541-7807

Mr. A.B. Craig
Environmental Protection Agency
Industrial Environmental Research Laboratory
Mail Stop MD-62
Research Triangle Park, NC 27711
Phone: 919/541-2509

Dr. Wallace B. Smith
Southern Research Institute
Environmental Sciences Research Department
2000 Ninth Avenue, South
Birmingham, AL 35255
Phone: 205/323-6592

Dr. Ashley D. Williamson
Southern Research Institute
Environmental Sciences Research Department
2000 Ninth Avenue, South
Birmingham, AL 35255
Phone: 205/323-6592

Dr. Pedro Lilienfeld
Environmental Instruments
Department
GCA Corporation
Technology Division
213 Burlington Road
Bedford, MA 01730
Phone: 617-275-5444

Dr. Clinton E. Tatsch
Research Triangle Institute
P.O. Box 12194
Research Triangle Park, NC 27709
Phone: 919/541-6000

Dr. Heinz Fissan
Gesamthochschule Duisburg
- Aerosolmesstechnik -
4100 Duisburg
Bismarckstr. 81
WEST GERMANY
Phone: 0203 392 202

Dr. Andrew R. McFarland
Civil Engineering Department
Texas A&M University
College Station, TX 77843
Phone: 713/845-7435

Dr. James B. Wedding
Aerosol Science Laboratory
Colorado State University
Civil Engineering Department
Engineering Research Center
Fort Collins, CO 80523
Phone: 303/491-8571, 8648

Dr. K.R. Spurny
Fraunhofer-Institut für Toxikologie
und Aerosolforschung
D-5948 Schmallenberg-Grafschaft
WEST GERMANY

Dr. R. Keith Kirby
U.S. Department of Commerce
National Bureau of Standards
Washington, DC 20234
Phone: 301/921-2536

Mr. Timothy J. Abrott
Air Quality Section
Environmental Technology Department
Weyerhaeuser Company
Tacoma, WA 98477
Phone: 206/924-2345

Mr. Donald R. Pettit
Department of Chemical Engineering
University of Arizona
Tucson, AZ 85721
Phone: 602/626-1224

Mr. Marvin I. Tillery
Industrial Hygiene Group
Health Division
Los Alamos Scientific Laboratory
University of California
Los Alamos, NM 87545
Phone: 505/667-5722

Mr. H. Noguchi
c/o K. Okabayashi
Manager, Engines & Emission
U.S. Representative Office
Toyota Motor Co., Ltd.
One Harmon Plaza
Secaucus, NJ 07094
Phone: 201/865-5656

Dr. Virgil Marple
University of Minnesota
Mechanical Engineering Department
111 Church Street S.E.
Minneapolis, MN 55455
Phone: 612/373-9984

Mr. Michael McElroy
Electric Power Research Institute
P.O. Box 10412
3412 Hillview Avenue
Palo Alto, CA 94303
Phone: 415/855-2471

Mr. Larry G. Felix
Southern Research Institute
Environmental Sciences Research Department
2000 Ninth Avenue, South
Birmingham, AL 35255
Phone: 205/323-6592

Dr. G.S. Samuelson
Mechanical Engineering
University of California, Irvine
Irvine, CA 92717
Phone: 714-833-6749

Mr. Joseph D. McCain
Southern Research Institute
Environmental Sciences Research Department
2000 Ninth Avenue, South
Birmingham, AL 35255
Phone: 205/323-6592

Dr. Walter H. Chan
Air Resources Branch
Ministry of the Environment
880 Bay St., 4th Floor
Toronto, Ontario
M5S 1Z8
CANADA

J. San
University of Maryland
Institute for Physical Science and
Technology
College Park, MD 20742
Phone: 301/454-2636

Mr. William J. Steele
Southern Research Institute
Environmental Sciences Research Department
2000 Ninth Avenue, South
Birmingham, AL 35255
Phone: 205/323-6592

Mr. Kenneth M. Cushing
Southern Research Institute - West
Environmental Sciences Research Department
P.O. Box 10155
University Park Station
Denver, CO 80210
Phone: 303/922-9765

Mr. Wesley D. Snowden
Alsid, Snowden & Associates
104 Earth Building
1805 - 136th Place N.E.
Bellevue, WA 98005
Phone: 206/641-5130

Dr. Raymond L. Chuan
Defense Division
Brunswick Corporation
3333 Harbor Boulevard
Costa Mesa, CA 92626
Phone: 714/546-8030

Dr. Raymond G. Merrill
Environmental Protection Agency
Industrial Environmental Research
Laboratory
Mail Stop MD-62
Research Triangle Park, NC 27711
Phone: 919/541-2558

Dr. R.P. Sandoval
Transportation Analysis & Information
Division 4551
Transportation Technology Center
Sandia National Laboratories
Albuquerque, NM 87185

Mr. Fred Quant
Aerosol Instruments
TSI Incorporated
500 Cardigan Road
P.O. Box 43394
St. Paul, MN 55164
Phone: 612/483-0900

Mr. Charles W. Lewis
Environmental Protection Agency
Environmental Sciences Research Laboratory
Research Triangle Park, NC 27709

Mr. A. Lieberman
Hiac/Royco Instruments Division
Pacific Scientific
141 Jefferson Drive
Menlo Park, CA 94025
Phone: 415/325-7811

Dr. Jugal Agarwal
Research and Development
TSI Incorporated
500 Cardigan Road
P.O. Box 43394
St. Paul, MN 55164
Phone: 612/483-0900

Although the research described in this paper has been funded (wholly or in part) by the United States Environmental Protection Agency, it has not been subjected to Agency review and, therefore, does not necessarily reflect the views of the Agency and no official endorsement should be inferred.

Paper 1

AEROSOL SIZE AND CHEMISTRY AT A COAL-FIRED POWER PLANT

J.D. McCain, W.G. Kistler, J.W. Ragland, R.L. Merritt
Southern Research Institute

ABSTRACT

Determinations of particle size distributions and chemical composition by particle size of the emissions from a coal fired power station are presented. In order to characterize both supermicron and submicron modes in the effluent aerosol size distribution, data were obtained using cascade impactors and electrical mobility techniques. Samples for the determination of elemental composition by particle size were obtained using an in situ series cyclone sampling system and an extractive diffusional sampling system. The latter system was operated on a trial basis during an extended sampling program in order to determine the feasibility of a method for determining the elemental composition by particle size in the submicron mode of the combustion aerosol. Elemental compositions of all samples were determined by x-ray fluorescence and neutron activation analyses. The size distributions of individual elements in the submicron mode as determined from diffusion battery samples were found, within the uncertainties in the data, to follow the gross submicron mode distribution as measured with Electrical Aerosol Size Analyzers. The bulk composition of the submicron mode was found to be similar to that of the supermicron particles. However, the submicron mode was found to be enriched significantly in a number of elements as compared to the supermicron mode. Further enrichment of some of these elements appears to have occurred during cooling of the aerosol by dilution with ambient temperature filtered air.

INTRODUCTION

Particle formation in coal combustion takes place by several mechanisms, each of which may produce a distinct mode in the resulting aerosol size distribution. Typically the emissions from pulverized coal boilers contain a minimum of three such modes which will vary with the coal properties and changes in the combustion process. A large particle mode will be present, resulting from unburned fuel particles, although it will be of relatively low concentration for a well operated boiler. A second generally dominant, mode will consist of the residue from mineral inclusions in the coal, and a third submicron mode will be produced by the evaporation of some of the more volatile metals and metal oxides during combustion and subsequent condensation as the combustion gasses are cooled The elemental compositions of each of these modes may differ substantially.

In order to assess the potential environmental significance of each mode and the effectiveness of possible control strategies detailed information is needed on the morphology, composition, and size distribution parameters of each mode. This paper describes the results of a series of experiments performed to explore the feasibility of using diffusional particle sizing techniques for investigating elemental composition versus particle size of the submicron mode in the emissions from a pulverized coal boiler. The study was conducted in conjunction with an ambient air visibility study in the vicinity of a large coal fired electric generating station in the Southwestern U.S.

One part of the visibility study involved determination of emission rates, particle size distributions and elemental composition by particle size of the stations particulate emissions. Southern Research Institute (SoRI) was given the responsibility for providing most of the latter determinations. Particle size distributions were measured using cascade impactors and electrical mobility techniques. Elemental composition was determined in six size fractions from samples obtained by means of the series cyclone system developed by SoRI. The investigation of the applicability of the diffusion technique was carried out as an adjunct to the latter measurement programs.

Experimental Method

A system using parallel plate diffusion batteries and the SoRI SEDS III sample extraction dilution system was developed to permit size segregated filter samples suitable for trace element analysis to be obtained. The samples nominally have the following size properties:

Filter Sample Type:	A μm	B μm	C μm	D μm
Lower Size Limit to the Sample:	0.02	0.04	0.08	0.16
Upper Size Limit to the Sample:	0.32	0.32	0.32	0.32

A schematic of the system is shown in Figure 1. The sample extraction and dilution system is illustrated in Figure 2. A single stage impactor pre-cutter is used on a sample drawn from the diluter to provide a uniform upper size limit of 0.32 μm diameter for each of the four diffusion battery filter samples. Thus the particles collected by each diffusion battery filter are effectively smaller than the D_{50} of the impactor stage and larger than the D_{50} of the diffusion battery. A fifth filter is used to obtain a sample directly from the impactor pre-cutter to establish inlet concentrations to the diffusion batteries. The filters have a 99.9%+ collection efficiency for all sizes of interest here.

Diffusion batteries may consist of a number of long, narrow, parallel channels, a cluster of small bore tubes, or a series of screens. Figure 3 shows a typical parallel channel (parallel plate) diffusion battery as used in this work. Figure 4 shows the aerosol penetration characteristics of the system used in this study.

Fuchs et al[1] presented a technique for calculating the particle size distribution from raw data, assuming that the size distribution was log normal. A modification of the latter technique to account for the truncation at each end of

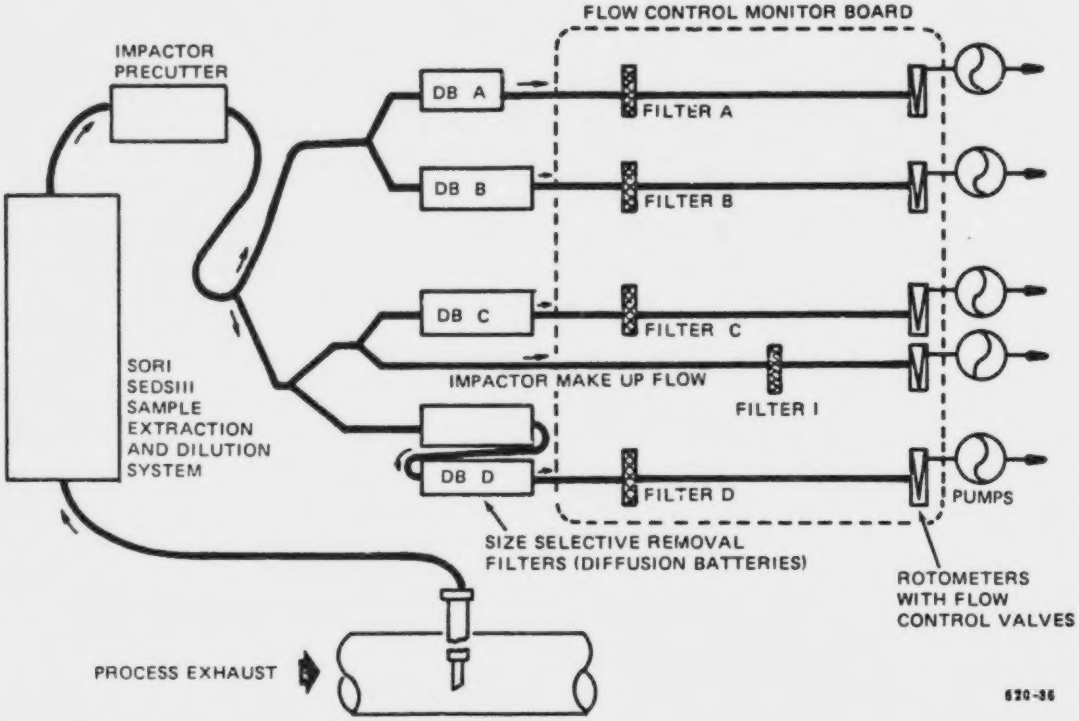
FLOW CONTROL MONITOR BOARD
IMPACTOR PRECUTTER
DB A
FILTER A
DB B
FILTER B
DB C
FILTER C
IMPACTOR MAKE UP FLOW
FILTER I
DB D
FILTER D
PUMPS
SORI SEDSIII SAMPLE EXTRACTION AND DILUTION SYSTEM
SIZE SELECTIVE REMOVAL FILTERS (DIFFUSION BATTERIES)
ROTOMETERS WITH FLOW CONTROL VALVES
PROCESS EXHAUST
620-36

Figure 1. Schematic of a novel diffusion sizing system for use in obtaining samples of ultrafine particle samples for elemental analysis.

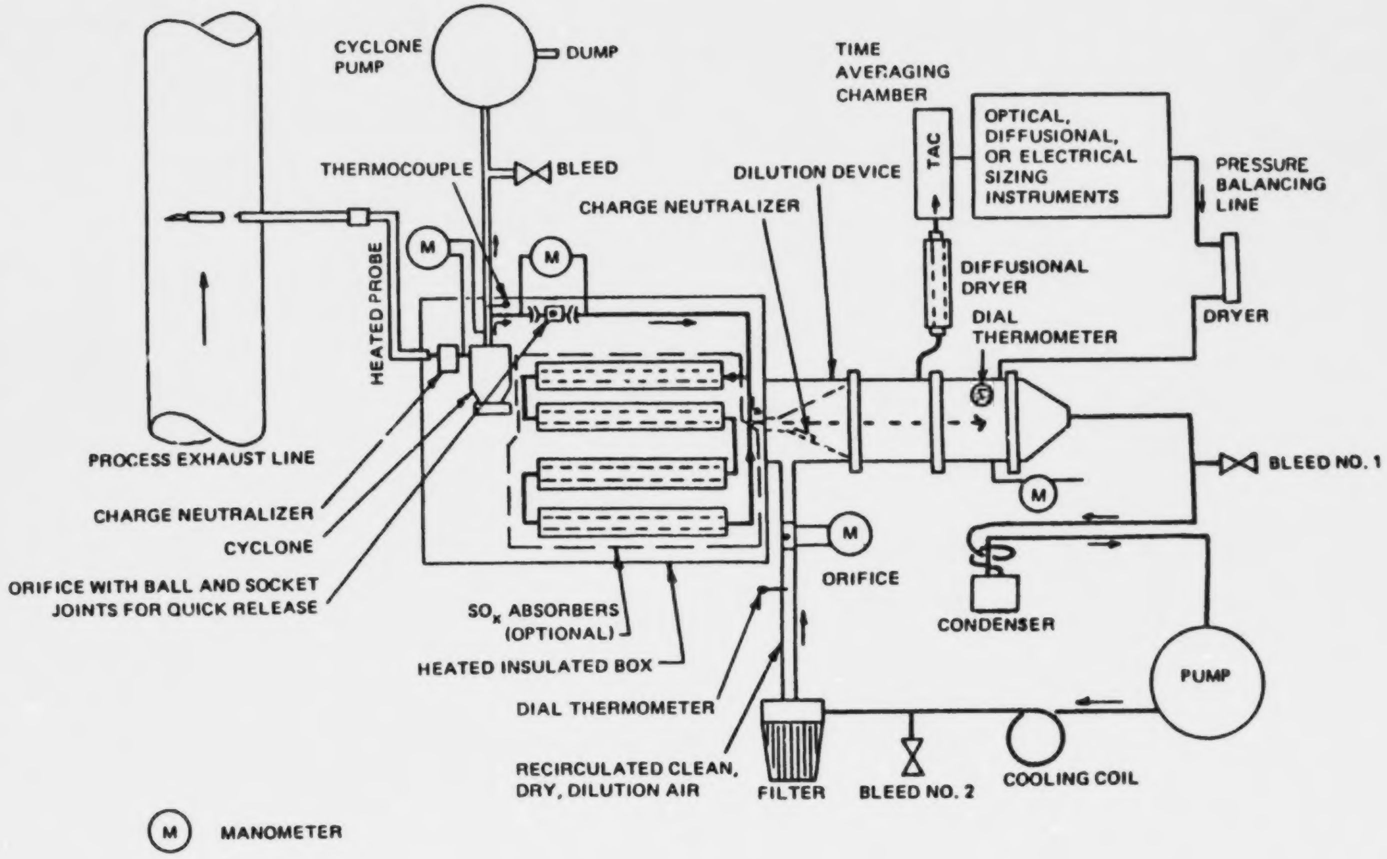
CYCLONE PUMP
DUMP
TIME AVERAGING CHAMBER
TAC
OPTICAL, DIFFUSIONAL, OR ELECTRICAL SIZING INSTRUMENTS
PRESSURE BALANCING LINE
DRYER
THERMOCOUPLE
BLEED
DILUTION DEVICE
CHARGE NEUTRALIZER
DIFFUSIONAL DRYER
DIAL THERMOMETER
HEATED PROBE
M
PROCESS EXHAUST LINE
CHARGE NEUTRALIZER
CYCLONE
ORIFICE WITH BALL AND SOCKET JOINTS FOR QUICK RELEASE
SO$_x$ ABSORBERS (OPTIONAL)
HEATED INSULATED BOX
DIAL THERMOMETER
RECIRCULATED CLEAN, DRY, DILUTION AIR
FILTER
BLEED NO. 2
COOLING COIL
PUMP
CONDENSER
ORIFICE
BLEED NO. 1
MANOMETER

Figure 2. Modified Southern Research Institute SEDS.

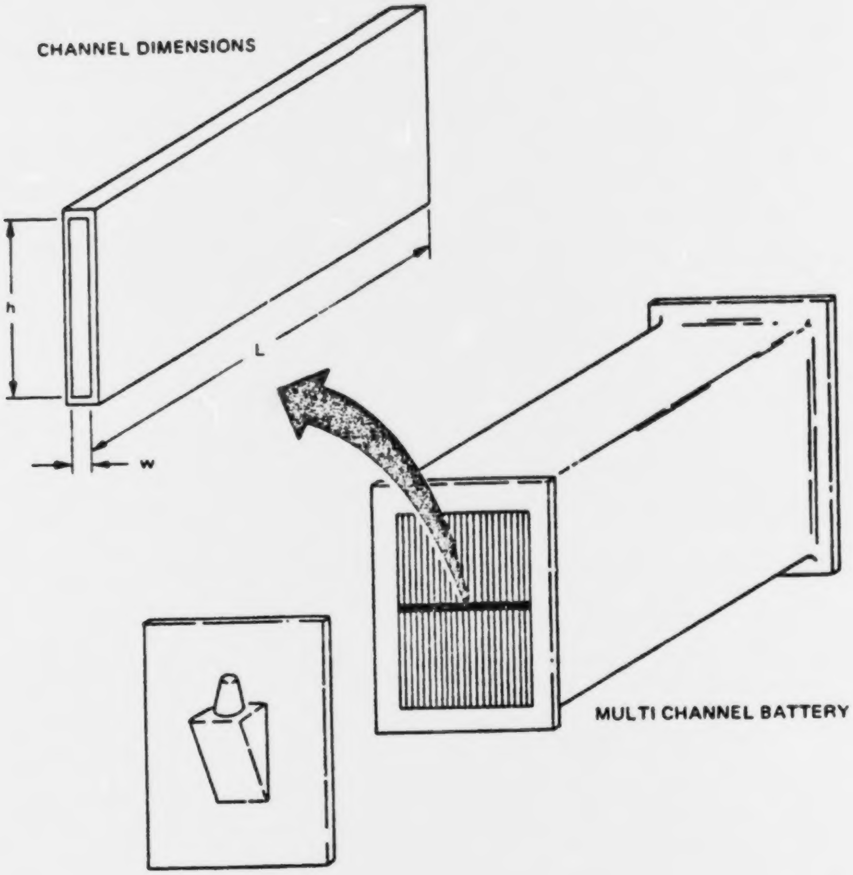
CHANNEL DIMENSIONS
h
L
w
MULTI CHANNEL BATTERY

Figure 3. A typical rectangular channel diffusion battery.

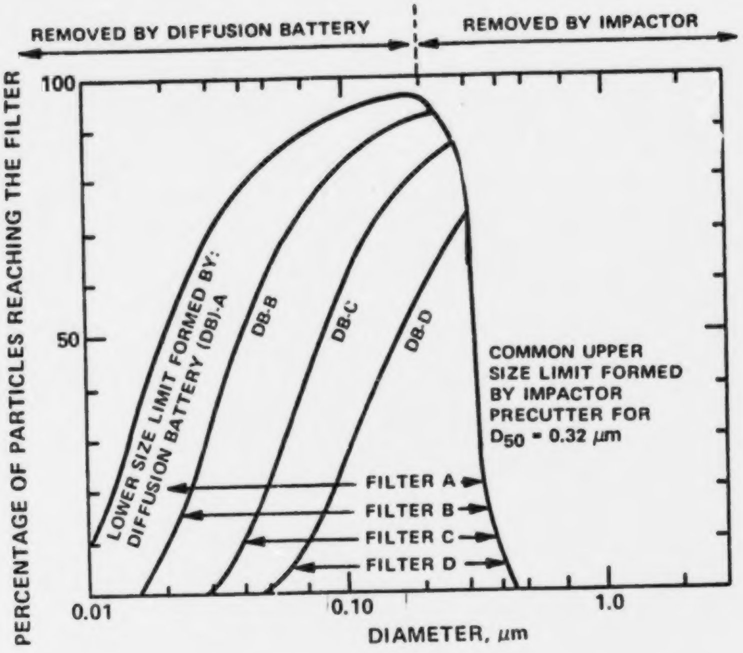

Figure 4. Percentage of initial particles, as a function of size, which reach and are captured by Filter A, Filter B, Filter C, and Filter D.

the size spectrum was used in this work. The truncation at large sizes results from the precutter, while diffusion losses in the probe and connecting tubing limits the minimum size particle which will be passed to the diffusion batteries to approximately 0.01 μm.

The monodisperse penetration of a rectangular plate diffusion battery is given by

$$P = \frac{n}{n_0} = 0.9104e^{-1.88522DY} + 0.0531e^{-21.431DY} + 0.015e^{-62.317DY} + 0.0068e^{-124.537DY} + \ldots \quad (1)$$

where D = Particle diffusivity, cm^2/sec,
Y = Diffusion battery flow rate-geometry constant, sec/cm^2,
n_0 = Diffusion battery inlet concentration, and
n = Diffusion battery outlet concentration.

The particle diffusivity, D, is given by

$$D = kTB , \qquad \text{where} \tag{2}$$

k = Boltzmann's Constant, gm cm^2/sec^2 °K,
T = Absolute Temperature, °K, and
B = Particle Mechanical Mobility, sec/gm.

The particle mechanical mobility, B, is given by

$$B = \left[1 + 2.49\ (\lambda/d) + .84\ (\lambda/d) e^{-(.44)(d/\lambda)} \right] /3\pi\mu d \tag{3}$$

where λ = gas mean free path, cm,
d = particle diameter, cm, and
μ = gas viscosity, gm/sec cm.

The diffusion battery flow rate-geometry constant, Y, is given by

$$Y = \frac{4LhN}{QW} \quad \text{where} \tag{4}$$

L = Channel length, cm,
h = Channel height, cm,
N = Number of channels,
Q = Flow rate, cm^3/sec, and
W = Channel width, cm.

Two diffusion battery geometries were used in this work having the following dimensions.

	Type 1	Type 2
L	45.72 cm	45.72 cm
h	10.15 cm	11.46 cm
W	0.10 cm	0.10 cm
N	13	98

Diffusion battery "A" was a "Type 1" geometry, "B" and "C" were single "Type 2" batteries, and "D" was two "Type 2" batteries in parallel.

The net penetration of a diffusion battery by a truncated polydisperse aerosol is given by the expression

$$P = \int_{d_1}^{d_2} f(d)\ p(d) dd \Bigg/ \int_{d_1}^{d_2} f(d) dd. \tag{5}$$

where

p(d) = monodisperse penetration,
f(d) = distribution function,
d_1 = minimum particle size in the truncated distribution,
and d_2 = maximum particle size in the truncated distribution.

Noting in Equation 1, that the flowrate and diffusion battery geometry variables are contained in the term "Y", one can conveniently use "Y" as a variable for plotting the predicted net penetrations of polydisperse aerosols which would result from the use of a series of diffusion battery measurements. In practice, log (1.8852Y) is a more useful parameter. Figure 5 shows plots of such predicted penetration vs. avg (1.9852y) curves for truncated log normal distributions having mass median diameters of 0.04, 0.08 and 0.16 μm and geometric standard deviations σg's, of 1.05 and 2.0. Vertical lines are drawn at values of log (1.8852y) corresponding approximately to the four diffusion battery conditions used in this study. Size distributions are then experimentally determined by plotting the measured penetrations at the corresponding values of log (1.8852y) and matching the experimental data points to the best fitting theoretical curves.

3. Analytical Methods

The diffusion battery filter samples, together with control filters for background correction, were analyzed for elemental composition by x-ray fluorescence and neutron activation analysis. The x-ray fluorescence analyses for the July and December 1979 samples were provided by the U.S. EPA, using wavelength dispersive methods. The August 1980 x-ray fluorescence analyses were done by Columbia Scientific Laboratories, using energy dispersive methods. All neutron activation analyses were performed by North Carolina State University.

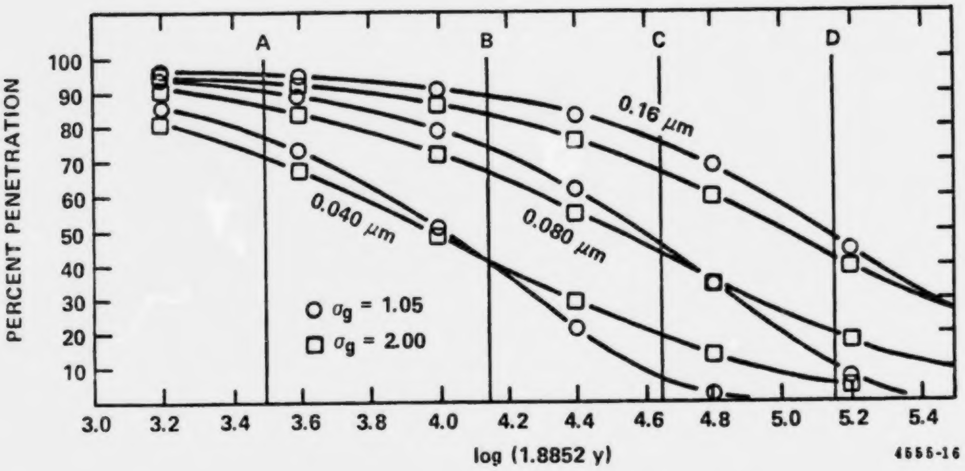

Figure 5. Theoretical penetrations of aerosols having truncated log-normal distributions through parallel plate diffusion batteries. The range of particle sizes in the truncated distributions is 0.01 μm to 0.5 μm. The calculations were based on standard air as a carrier gas at a temperature of 44°C and a pressure of 508 mm Hg.

As a rule, approximately 10 elements were detected by the x-ray techniques and approximately 20 elements by the neutron activation technique. Approximately 7 of these elements were detected by both techniques. In general, the comparability between the two techniques was fair, although certain elements notably aluminum and iron, showed rather large discrepancies. The latter were probably related to fundamental limitations of the neutron activation analysis technique for these elements.

4. Results and Discussion

The sampling was done at the 365 foot level of 700 foot stacks at the Salt River Project Navajo Generating Station. This station is comprised of three 850 MWe generating units with particulate emissions controlled by high efficiency "hotside" electrostatic precipitators. Diffusion battery sampling was done on two of the three units (units 2 and 3). Samples were obtained in July 1979, December 1979, and August 1980. Table 1 summarizes the measured particulate concentrations and size distribution parameters for the three test series. The data given in Table 1 for the December 1979 test was provided by M.J. Pilat, Inc. of Seattle, Washington. A typical overall size distribution for the three units during these tests is shown in Figure 6.

All samples obtained with the diffusion battery system were taken after dilution and drying. This was accomplished with the SoRI sample extraction dilution system which is normally used in conjunction with electrical aerosol size analyzers and optical particle counters to condition flue gases for use with such instruments. Table 2 presents a summary of the general results of the sampling in terms of sample time, the dilution correction factor, and gravimetrically determined weights of the various filter catches. This table also contains information on the sampling rates for each diffusion battery filter and the concentration of particles reaching the filter, as determined gravimetrically. In the cases of all the filters obtained during the July 1979 test series and the C and D diffusion battery filters for the December 1979 and August 1980 test series, the gravimetrically determined weights are not consistent with the expected diffusion losses through the batteries. The discrepancies are probably the result of a combination of errors in weighing the small catches and hygroscopic particles, which results in measured catch weights being higher than the actual weights of the particles on the filters.

The precollector used to eliminate particles larger than 0.32 micrometers was selected on an aerodynamic diameter rather than a Stokes diameter basis for the July 1979 and December 1979 test series, resulting in a pre-collector cut near the mass median diameter of the aerosol mode being sampled. This undesirably small precollector cut was corrected in the August 1980 test series for which the cut diameter was approximately 0.31 microns on a Stokes basis.

The results of the x-ray and neutron activation analyses are given in Tables 3 and 4 respectively in terms of concentrations of the elements in the flue gas at dry normal conditions. The concentrations of the metals are given as oxides. The results of the no-diffusion battery sample from the August 1980 test are invalid in terms of absolute concentration because of an internal leak which allowed some of the sample to bypass the filter. They are presented here because they are useful in terms of relative abundances of the elements. Concentrations, by size, of selected elements for the total aerosol are given in Table 5 for comparison purposes.

Table 1. Summary of Particle Concentrations from Cascade Impactors and EASA Data

DATE	UNIT	PARTICULATE CONCENTRATION (mg/DNM^3) TOTAL	PARTICULATE CONCENTRATION (mg/DNM^3) SUBMICRON MODE	MODAL DISTRIBUTION PARAMETERS FOR LOG NORMAL FITS (μm) LARGE PARTICLE MODE Mass Median Diameter Stokes	LARGE PARTICLE MODE Mass Median Diameter Aerodynamic	LARGE PARTICLE MODE σ_g	SUBMICRON MODE Mass Median Diameter Stokes	SUBMICRON MODE Mass Median Diameter Aerodynamic	SUBMICRON MODE σ_g
6/28/79	3	34.1		3.2	5.0				
6/30/79	3	20.6	0.078	2.9	4.5	2.4	0.128	0.26	1.44
7/02/79	3	27.5	0.070	4.2	6.5	2.4	0.120	0.25	1.48
7/03/79	3	23.6	0.047	3.7	5.7	2.4	0.148	0.29	1.63
12/7/79	1	40.7	0.058*	3.0	4.7	2.5	(0.06)*	(0.15)*	--
	1	57.4		3.8	6.0	3.4			
12/12/79	1	26.2	0.081*	4.3	6.7	2.8	(0.06)*	(0.15)*	--
12/13/79	1	23.3		3.4	5.4	3.3			
	1	29.4		4.0	6.3	4.0			
12/10/79	2	37.2		3.7	5.8	3.2			
12/11/79	2	46.6	0.307*	3.5	5.6	2.8	(0.12)*	(0.25)*	--
	2	54.0		4.6	7.3	4.1			
12/12/79	2	30.4	0.218*	3.2	5.1	2.8	(0.12)*	(0.25)*	--
12/9/79	3	51.2	0.343*	4.0	6.3	3.1	(0.17)*	(0.33)*	--
	3	46.6		3.7	5.9	3.4			
	3	53.7		4.0	6.2	3.2			
12/13/79	3	17.0	0.417*	2.2	3.5	2.7	(0.17)*	(0.33)*	--
8/24/80	1	27.1	0.073	4.5	7.0	3.0	0.332	0.58	2.19
8/25/80	1	38.3	0.213	5.5	8.6	3.1	0.403	0.70	2.12
8/19,20/80**	2	56.9	0.710	4.2	6.6	3.0	0.294	0.53	2.03
8/28/80	2	42.5		4.4	6.8	3.0			
8/29/80	2	84.4	0.347	2.8	4.6	2.5	0.080	0.18	1.26
8/23/80**	3	72.8	1.09	3.7	5.8	2.6	0.157	0.30	1.51
8/26/80	3	17.6	0.161	3.5	5.4	3.0	0.126	0.26	1.51
8/27/80	3	28.8	0.140	4.3	6.8	3.0	0.199	0.38	1.56

*Low pressure impactor data.
**Boiler upset.

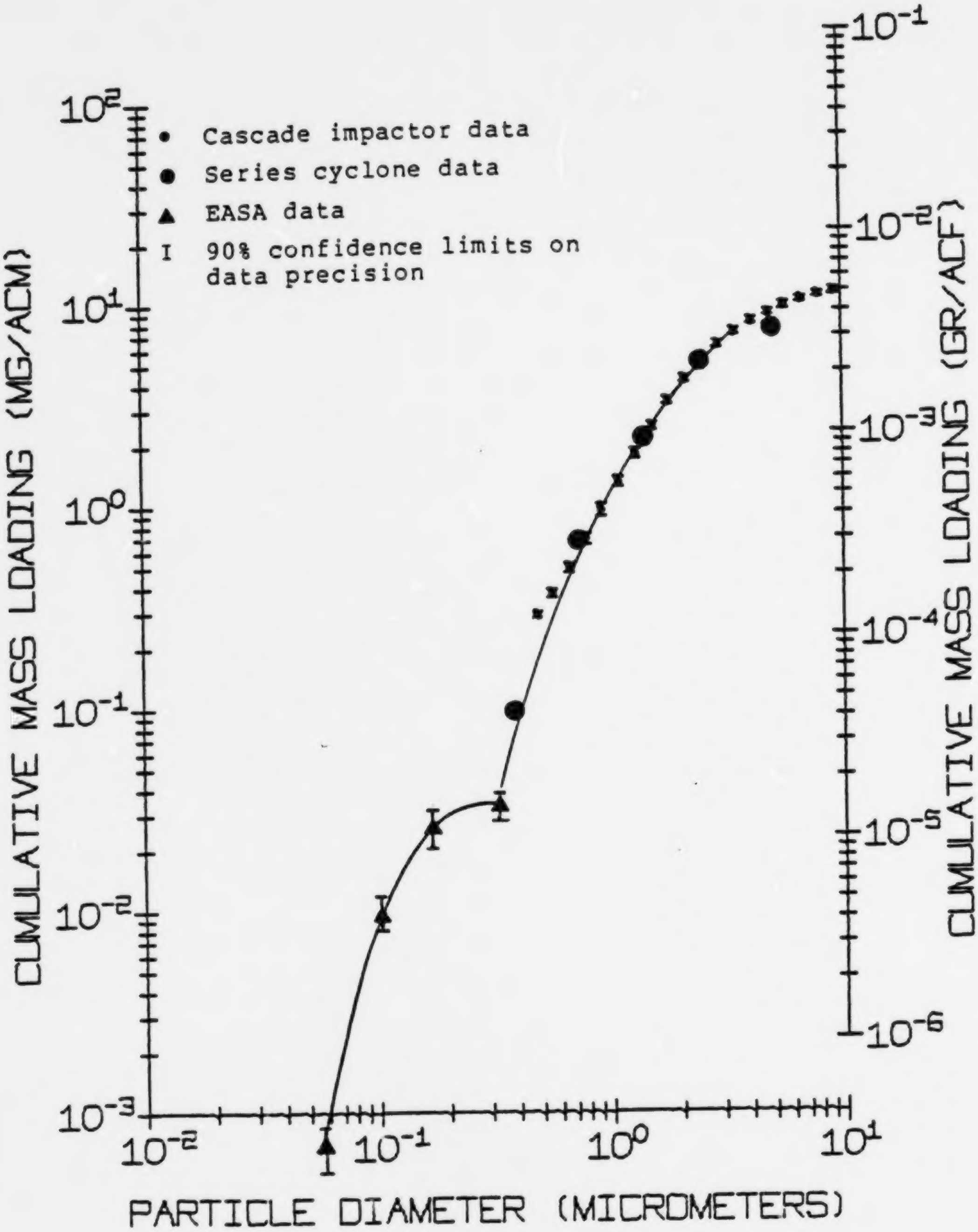

Figure 6. Grand average unit 3 size distribution on cumulative mass concentration versus particle Stokes diameter basis (ρ_p = 2.41 g/cc) 6/28/79-7/03/79.

Table 2. Summary of Diffusion Battery Sampling

Filter	July 23, 1979			December 11-15, 1979			August 19-20 and 25-29, 1980		
	UNIT 3			UNIT 3			UNIT 2		
	t=1220	DCF=10.5		t=5400	DCF=25.5		t=6532	DCF=13.6	
	Catch, mg	Flowrate, ℓpm	Concentration mg/DNM^3	Catch, mg	Flowrate, ℓpm	Concentration mg/DNM^3	Catch, mg	Flowrate, ℓpm	Concentration mg/DNM^3
I	.17	6.54	0.224	.62	6.78	0.432	(0.25)*	6.89	(0.076)*
A	.14	7.25	0.167	.48	7.38	0.308	0.75	6.98	0.224
B	.18	14.72	0.1053	.89	14.53	0.289	1.06	14.03	0.157
C	.11	4.52	0.2085	.34	4.61	0.349	0.36	4.31	0.174
D	.06	3.09	0.166	.51	3.12	0.772	0.37	2.99	0.254
MAXIMUM PARTICLE SIZE (STOKES DIA.):		0.204 µm			0.184 µm			0.314 µm	

*Filter Leaked

Table 3. Concentrations of Elements Determined by X-Ray Fluorescence, ng /DNM^3. (Concentrations of metals given as oxides)

	July 1979, Unit 3					December 1979, Unit 3					August 1980, Unit 2					
	I	A	B	C	D	I	A	B	C	D	I+	A	B	C	D	
Mg	706	661	484	213	-	1375	1130	1287	687	334	-	-	-	-	-	Mg
Al	1575	1416	1337	-	-	3920	4552	5082	2862	1924	8526	28148	23819	18450	-	Al
Si	5689	5451	5724	-	-	6640	14340	14817	7986	5198	17400	48233	43194	32103	12120	Si
P	-	-	-	-	-	1898	1771	1683	950	461	2529	8026	7342	5240	2808	P
S	4654	4499	4326	2167	-	8804	10532	9735	7242	4044	7830	28161	23184	21525	8436	S
Ca	3676	9359	8811	5355	2615	13601	11186	10890	7528	4255	5591	17413	14628	11700	6168	Ca
Ti	472	719	552	341	-	1378	1006	1014	-	342	1438	3553	2995	2731	1884	Ti
Fe	4815	4326	3945	2554	-	9115	6872	6171	-	-	2575	7484	6486	4576	2544	Fe
Ba	1790	2142	1760	1429	832	6464	5385	4884	3550	2485	1148	3742	3312	<2337	-	Ba
V											145	578	514	233	<168	V
K												242	215	<156		K

+Filter Leaked

Table 4. Concentrations of Elements Determined by Neutron Activation Analysis, ng/DNM^3. (Concentrations of metals given as oxides)

	July 1979					December 1979					August 1980				
	I	A	B	C	D	I	A	B	C	D	I	A	B	C	D
Ba	-	-	-	-	-	7254	8270	7091	3847	3931	2337	5316	3282	3914	929
Ti	-	-	-	-	-	< 3950	2478	1320	<2600	-	1638	3985	2659	4658	<1160
Mn	-	318	-	-	-	93.6	107	77.7	-	-	<1.1	30.2	22.9	<3	27.0
Mg	-	-	-	-	-	<12300	-	<3015	-	-	7118	3217	<1228	10860	<3950
V	244	266	239	213	85	325	271	240	153	109	1140	3008	2723	2100	1490
Cl	-	-	-	-	-	138	167	< 91	-	-	1080	893	0	908	1934
Al	13719	15253	8034	10348	4692	21879	15137	12625	9564	11158	187900	498230	421700	497200	499900
Ca	-	-	-	-	-	-	-	-	-	-	7570	12628	15935	6855	6185
Hg	< 67	192	68.8	15.1	16.6	52.1	40.2	15.0	23.5	63.0	-	53.6	-	-	-
Sm	.76	1.37	1.35	.66	.16	0.88	2.20	< .19	3.5	1.6	3.0	6.6	6.6	4.8	.72
Ce	95	<7	17.8	<12	<17	15.1	-	15.9	<11.3	-	-	58.7	43.6	17.8	17.3
U	43	14.6	27.7	<21	<31	19.1	7.9	11.4	<1.1	-	17.4	47.0	45.1	32.8	16.0
Se	100	56.5	47.6	<27	137	337	269	206	116	85.9	200	236	228	<15	38.9
Cn	234	158	42	563	167	18.7	-	-	-	-	121	190	272	188	222
La	< 7.7	2.83	< 3.4	15	13	10.8	-	< 1.9	-	-	10.6	17.6	10.4	22.6	8.3
Na	1115	2087	414	862	-	-	-	-	-	-	260	736	239	1139	235
As	89	49.6	43.6	<24	263	73.7	-	11.4	29	26.3	47.6	86.3	80	63.7	36.7
Sb	<1.6	21.8	14.8	20.9	<3.4	22.1	6.1	2.7	11.9	10.6	21.7	60.5	53.8	40.6	25.2
Br	0	42.4	15.8	26.7	8.4	-	27.4	<158	17.2	30.3	81.4	76.9	47.6	71.3	155
Sc	2.1	1.8	1.78	2.9	<.4	1.4	.77	.44	.94	-	1.5	4.4	4.6	7.3	3.5
Fe	<2820	12644	<1246	15892	11246	13338	2594	852	10945	3484	5851	14862	14338	9606	5339
Zn	<1000	< 898	936	<1438	1090	135	7.9	0	355	297	748	292	236	304	<257
Co	-	-	-	-	-	19.3	.81	.42	5.2	1.9	7.5	7.4	7.6	18.5	9.0

[+] Filter Leaked.

Table 5. Average Elemental Concentrations ($\mu g/m^3$), July and December 1979 by Particle Size (μm)

	Cyclone Samples (In Situ)						Diffusion Battery (Extraction)
Size Range	>8	3.8-8.0	2.4-3.8	1.2-2.4	0.63-1.2	<0.63	<0.32
Na	290	100	180	70	22	0.90	0.68
Mg	140	46	85	32	18	1.8	0.53
Al	2000	530	900	180	120	7.4	1.6
Si	4400	960	1500	490	200	13.0	4.6
S	150	82	120	31	23	3.6	3.0
Ca	1300	320	470	140	66	16	7.4
Fe	1000	240	400	130	56	13	3.9
As	110	32	50	21	12	4.6	3.4
Se	0.46	.14	0.42	0.12	.080	0.068	0.062
Cd	0.31	.12	0.45	0.27	.32	0.24	0.14
Sb	0.67	.33	0.38	0.085	.070	<.13	0.10
Ba	0.09	.13	0.21	0.075	.035	0.019	0.018
Hg	-	-	-	-	-	0.14	0.12

Table 6 gives total concentrations in the size range covered by the diffusion batteries from gravimetric determinations from the diffusion battery filters, determinations by integration of the elements (as oxides) from the x-ray and neutron activation analyses, Electrical Aerosol Size Analyzer data, and in the case of the December 1979 results, concentrations determined by use of low pressure cascade impactors. The low pressure impactor data was provided by M.J. Pilat, Inc. The gravimetric determinations in Table 4 are probably the least reliable of the various values as a result of weighing uncertainties in the catch weights of the diffusion battery filters. Referring to Table 2 it should be noted that the first three filters, I, A, and B, in each case show declining concentrations as would be expected from diffusion losses in the batteries. In the case of diffusion batteries filters C and D, the declining concentrations no longer occur, indicating that the catch weights are biased high. The elemental concentrations as determined from the filters for the most part do exhibit the expected decreases in concentration through the complete series (I,A,B,C,D).

Plots of the elemental penetrations versus diffusion battery parameter are given in Figures 7 and 8 for the August 1980 test. Also shown in Figures 7 and 8 are theoretical penetration curves for the size distributions measured using the Electrical Aerosol Size Analyzer during the time the diffusion battery samples were being taken. Results similar to those shown were obtained from the other two tests.

Although in principle one can determine size distributions for individual elements from the data, the uncertainties in the penetrations made that appear not to be worthwhile in the present case. However, certain trends could be determined. First, the individual elemental penetrations, with few exceptions, appear to be consistent with the range of theoretical penetrations for the size distributions determined by the electrical aerosol analyzer. Because of the scatter

Table 6. Total Concentration in the Size Range Covered by the Diffusion Batteries as Determined by Various Methods

	Concentration, mg/DNM^3					
Method	July, 1979		December, 1979		August, 1980	
	I	A	I	A	I*	A
(1) Gravimetric	224^+	167^+	432	308	76	224
(2) Integration of elements (metals as oxides)	43.4	46.5	73.2	73.2	55	165
(3) Electrical Aerosol Size Analyzer	46.4		-		216	
(4) Low Pressure Cascade Impactor	-		155^+		-	

***Filter leaked**

$^+$Very small catches resulted in large probable errors in weighing

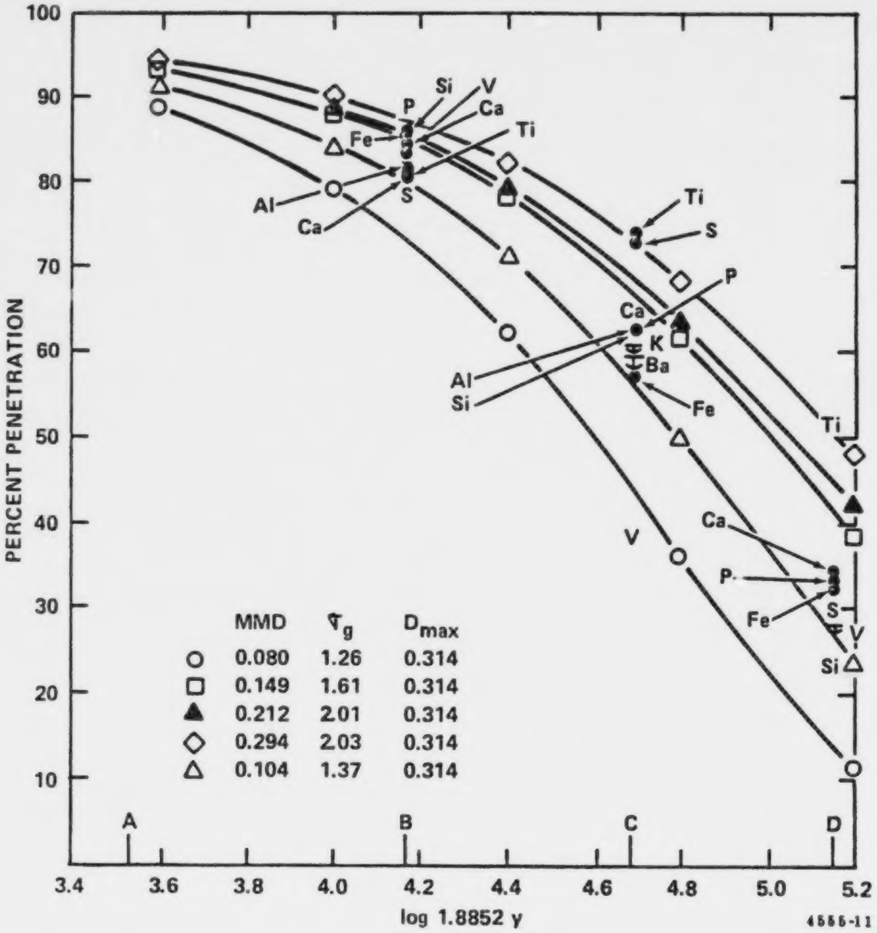

Figure 7. Elemental penetrations of diffusion batteries for Unit 2, August 1980 test from x-ray fluorescence analysis.

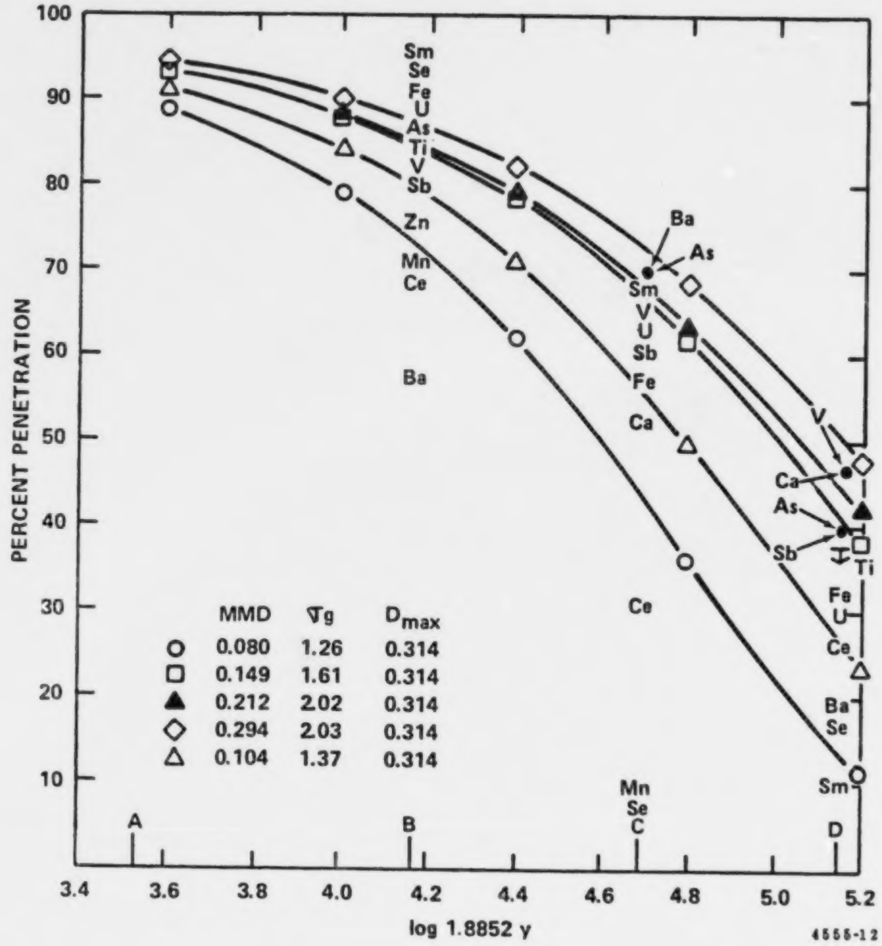

Figure 8. Elemental penetrations of diffusion batteries for Unit 2, August 1980 test from neutron activation analysis.

in the data it was difficult to be certain of any differences in the distributions by element for any one of the three tests. However, when the three tests were taken as a whole, certain trends did become apparent. Elements which consistently show lower penetrations than others almost certainly have somewhat smaller mean sizes than the bulk of the elements in the mode. Conversely, those which show consistently higher penetrations probably have larger than average sizes. Those elements which appeared to be in smaller particles than the average are cesium, magnesium, selenium, and mercury. Those which may exhibit size trends larger than the average are aluminum, calcium, arsenic, vanadium, and antimony.

Figures 9, 10, and 11 show plots of averages of the elemental penetrations for the three respective tests. The scatter resulting from experimental uncertainties is greatly reduced by such averaging, and it can be seen that the average penetrations of the elements are quite consistent with the theoretical penetrations of the distributions obtained with the electrical aerosol size analyzer. Thus we conclude that the concentrations and size distributions determined by the diffusional technique are consistent with those determined by the electrical aerosol size analyzer.

Elemental abundances relative to aluminum for the diffusion battery filters and the material collected in the first cyclone of the series cyclone runs that were obtained in parallel with the diffusion battery samples are given in Table 7. The catch in cyclone 1 of the series cyclone system can be taken to represent the abundances found in the gross flue gas aerosol less the submicron mode. Crustal abundances are also given in Table 7 for comparison. Table 8 tabulates those elements found to have strong, moderate, or slight enrichment, first relative to the crustal abundances, and second, relative to cyclone 1 abundances for the three tests. It can be seen that the elements exhibiting the greatest enrichments are typically those which might be expected to be volatized in the combustion process and subsequently recondense to form a submicron aerosol.

Table 9 presents concentrations determined from diffusion battery "A" filters. These represent, for practical purposes, the elemental concentrations as oxides in the submicron aerosol mode. For comparison, concentrations determined from the series cyclone and the backup filters are also tabulated in Table 9. Average concentrations as determined by the diffusion battery filters were approximately 20 to 70% of those from the series cyclone filters. The lower values in the diffusion battery filters are to be expected as a result of the smaller particle cutoff for these filters as compared to the upper limits of the particle size on the cyclone filters. The elements sulfur, mercury, antimony, chlorine, bromine, and perhaps manganese showed significant enrichment in the diffusion battery filters as compared to the cyclone filters. At least for the cases of sulfur, mercury, antimony, chlorine and bromine such results might be expected from probable condensation of vapor phase components of these elements upon cooling of the sample in the dilution system. This same type of enrichment probably occurs within the plume upon discharge to the atmosphere. The relative enrichment of these elements in the cooled, diluted gas relative to the gas at stack conditions was found to range from a factor of two to ten (2x to 10x).

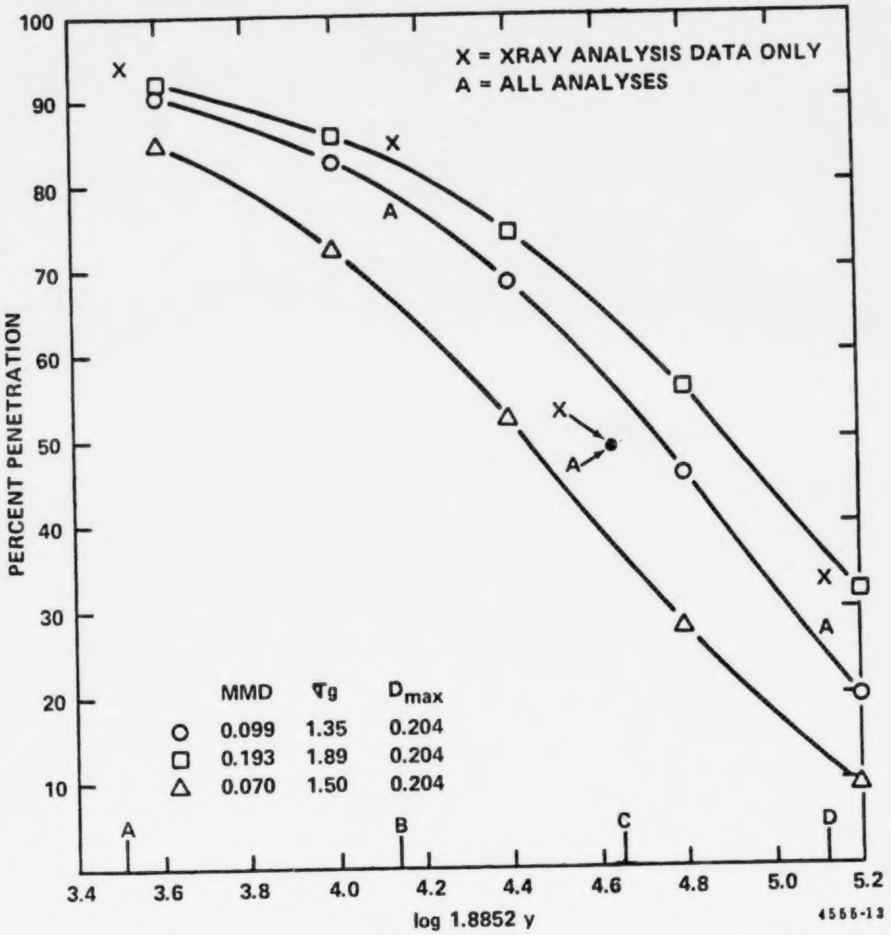

Figure 9. Average of elemental penetrations from July 1979, Unit 3 data.

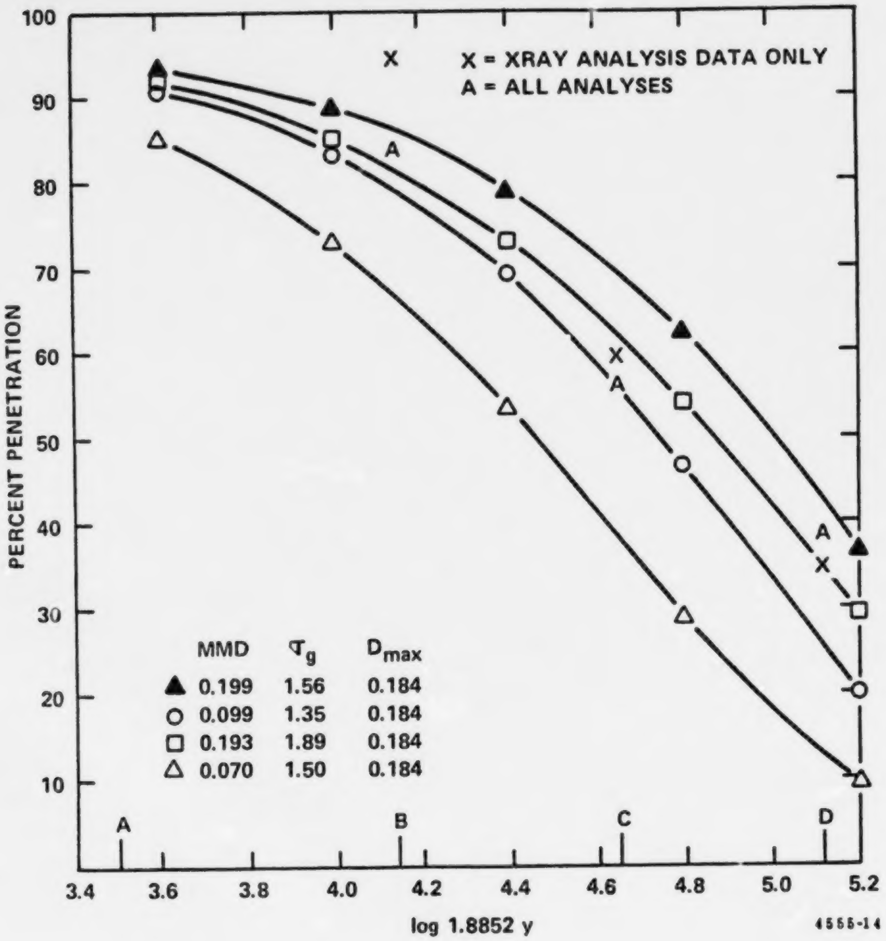

Figure 10. Average of elemental penetrations from December 1979, Unit 3 data.

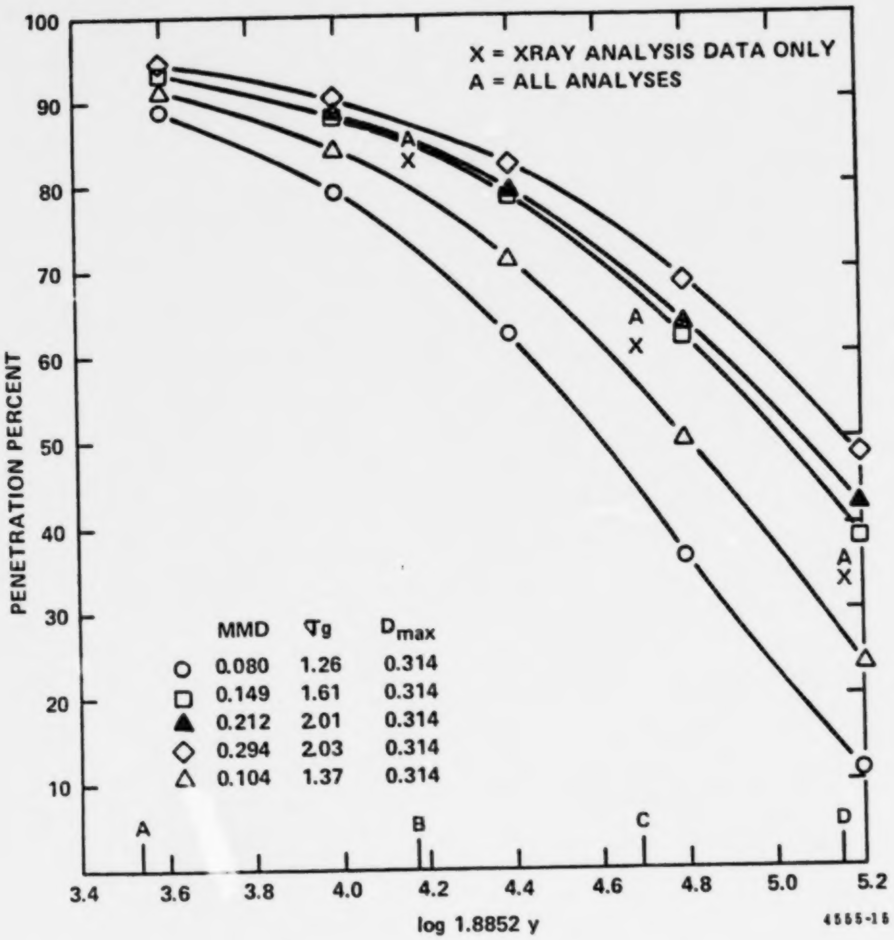

Figure 11. Average of elemental penetrations from August 1980, Unit 2 data.

Table 7. Elemental Abundances Relative to Aluminum and Enrichment Ratios

		July 1979						December 1979						August 1980					
	Crust**	D.B. "B" Filter		Cyclone 1		Enrichment* Ratio		D.B. "B" Filter		Cyclone 1		Enrichment* Ratio		D.B. "B" Filter		Cyclone 1		Enrichment* Ratio	
Element		XRF	NAA	XRF	NAA	Crust	Cyclone 1	XRF	NAA	XRF	NAA	Crust	Cyclone 1	XRF	NAA+	XRF	NAA	Crust	Cyclone 1
Na	0.348		0.083		0.00067	0.24	124	0.081		0.135		0.230	0.60		0.0142		0.076	0.041	0.19
Mg	0.257	0.41		0.091	0.064	1.59	5.5	0.29		0.061	0.082	1.13	4.75		<0.053		0.046	<0.21	<1.15
Al	1.000																		
Si	2.80	3.78		2.00		1.35	1.89	2.58		2.28		0.92	1.13	1.60		1.69		0.57	0.95
P	0.0145							0.27				18.6		0.25		0.040		17.2	6.25
S	0.0064	2.44		0.114		381	21	1.45				227		0.74		0.046		116	16.0
Ca	0.446	8.89		0.769		19.9	11.6	2.90		0.568		6.5	5.1	0.83	0.905	0.198		1.86	4.2
Ti	0.054	0.467		0.106		8.65	4.4	0.23	0.118	0.11	0.031	4.6	2.1	0.14	0.124	0.042	0.051	2.6	3.3
Fe	0.615	3.89	< 0.20	0.55	0.45	6.33	7.8	1.61	0.09	0.50	0.175	2.62	3.22	0.36	0.798	0.222	0.171	0.59	1.6
Ba	0.00308	2.22		0.058		721	38	1.63	1.35	0.051	0.0186	529	32	0.23	0.231	0.19		74.6	12
Mn	0.0123				0.00094						0.00096				0.0014	0.0040	0.0012	0.114	1.2
V	0.00185		0.031	0.0046	0.0013	16.8	24				0.0009			0.022	0.121	0.00037	0.0014	11.9	22.7
Cl	0.0039																		
Hg	6E-06		0.016		< .0002	2700	> 80		0.0022			366			< .00017			< 28	
Sm	8E-05		0.00027		7.6E-05	3.4	3.6		< 2E-05						0.00053		4.2E-05	6.6	12.6
Ce	0.00057		0.0034		< 4E-05	6.0	> 85		0.0024		0.00064	4.2	3.75		0.0028		0.00071	4.9	3.9
U	4.9E-05		0.0057		0.00012	116	48		0.0020		0.00034	41	59		0.0032		0.000073	65	44
Se	1E-06		0.0079		< 1E-06	7900	>8000		0.022		8.2E-05	22000	268		0.0128	0.0030	0.00031	12800	41
Cr	0.0025		0.00080		0.00044	0.32	1.8	0.032	0.002		0.00052	0.80	3.8		0.0172	0.0043	0.00037	6.9	46
La	0.00022		< .0007			< 3					0.00041	1.86			0.0071			9.9	
As	6.2E-05		0.0077		0.00020	124	39		0.00013		7.5E-05	2.1	1.7		0.0048		4.7E-05	77	101
Sb	1.2E-05		0.0029	0.00077		241	3.8		0.00034		2.3E-05	28	15		0.0035		3.1E-05	292	113
Br	2.0E-05		0.0037		2.3E-05	185	160		< .00024		5.4E-05	< 12	<4.4		0.0039		1.9E-05	195	205
Sc	6.2E-05		0.00027		0.00025	4.4	1.08		5.0E-05		0.00013	0.81	0.38		0.00017		0.00012	2.7	1.4
Zn	0.00162		0.17		0.0015	105	113		<0.01		0.0085	<6.2	<1.17		0.015			9.3	
Co	0.00028				0.009	0.002			0.00019		8.2E-05	0.68	2.3		0.00053		0.00013	1.9	4.1

**From Handbook of Chemistry and Physics, 41st Edition.

*Where both NAA and XRF values are available, the XRF result is quoted.

+XRF aluminum concentration value used for normalization.

Table 8. Elements Showing Slight to Strong Enrichments in Diffusion Battery Samples

	Enrichment Relative to Earth Crust			Enrichment Relative to Cyclone 1		
	Strong ($>10^2$)	Moderate (10^1-10^2)	Slight (3-10)	Strong ($>10^2$)	Moderate (10^1-10^2)	Slight (3-10)
July, 1979	S	Ca	Ti	Se	S	Mg
	Ba	V	Fe	Na	Ca	Ti
	Hg		Sm	Br	Ba	Fe
	U		Ce	Zn	V	Sm
	Se		Sc		Hg	Sb
	As				Ce	
	Sb				U	
	Br				As	
	Zn					
December, 1979	S	P	Ca	P	Ba	Mg
	Ba	U	Ti	S	U	Ca
	Hg	Sb	Ce	Hg	Sb	Fe
	Se		Se			Ce
						Cr
August, 1980	S	P	Sm	As	S	P
	Se	Ba	Ce	Sb	Ba	Ca
	Sb	V	Cr	Br	V	Ti
	Br	U	La		Sm	Ce
		As	Zn		U	Co
					Se	
					Cr	

Table 9. Elemental Concentrations (as Oxides), ng/DNM^3, from Diffusion Battery and Series Cyclone Filters

Element	July 1979 Unit 3							December 1979 Unit 3					August 1980 Unit 2						
	XRF			NAA				XRF		NAA			XRF			NAA			
	A* ng/DNM^3 <0.204 µm	F+ ng/DNM^3 <0.34 µm	F+ ng/DNM^3 <0.34 µm	A ng/DNM^3 <0.204 µm	F ng/DNM^3 <0.34 µm	F ng/DNM^3 <0.34 µm	A/F	A ng/DNM^3 <0.184 µm	F ng/DNM^3 <0.34 µm	A ng/DNM^3 <0.184 µm	F ng/DNM^3 <0.34 µm	A/F	A ng/DNM^3 <0.314 µm	F ng/DNM^3 <0.46 µm	F ng/DNM^3 <0.46 µm	A ng/DNM^3 <0.314 µm	F ng/DNM^3 <0.46 µm	F ng/DNM^3 <0.46 µm	A/F
Mg	661	2158	5810				0.165	1130	1677		6358	0.674				3217	15504	760	0.395
Al	1476	9072	28161	15253			0.076	4552	8789	15137	54810	0.518	28148	45630	28350	498250	1393000	151200	0.76
Si	5451	18660	56924				0.144	14340	21614			0.663	48233	79180					0.61
P		1099	2997					1771	2153			0.823	8026	5931	27480				0.48
S	4499	6550	13250				0.647	10532	9250			1.14	28161	14475	87500				0.55
Ca	9359	21140	37240				0.321	11186	15120			0.74	17413	16800	70000	12628	15400	22400	0.40
Ti	719	2271	4843				0.202	1006	1653	2478	3958	0.609	3553	4041	12959	2895	3490	2370	0.42
Fe	4326	13585	27313	12644	40612	51051	0.212	6872	9338	2594	13270	0.736	7484	15730	32890	14862	13914	31460	0.31
Ba	2142	2912	5376				0.517	5385	6339	8270		0.850	3742	3002	14560	5316			0.43
V				266	37.6	37.6	7.07			271	376	0.721	578	304	2130	3008	1342	1504	0.47
K		576	1560			6120			324				242	12248	1932				0.034
Mn				318			(∞)			107	90.3	1.18			774	30.2	2.6	38.7	1.46
Hg				192	130	270	0.96			40.2	80.0	0.50				53.6	30	<1	3.46
Sm				1.17	5.10	10.3	0.181			2.2	5.8	0.38				6.6	11.6	11.6	0.57
Ce				< 7	34.4	148	< .077				24.6	0.23				58.7	36.9	123	0.73
U				14.6	31.6	54.2	0.340			7.9	33.9	0.73				47.0	39.3	90.4	0.72
Se				56.5	310		0.182			269	367					236	296	860	0.41
Cr				158	1250	1125	0.133		250		462					190	1250	150	0.27
La				2.83	43.3	257	0.019				35.1					17.6	70	82	0.23
Na				2087			(∞)		729							736	2052	<13.5	0.71
As				49.6	80.5	116	0.505				79.2					86.3	66	277	0.50
Sb				21.8	19.2	25.2	0.982			6.1	24	0.25				60.5	24	112	0.89
Br				42.4			(∞)			27.4	4.0	6.85				76.9	50	60	1.40
Sc				1.8	8.46	18.3	0.135			0.77	6.1	0.126				4.4	15.3	15.3	0.29
Zn				< 898						7.9	384	0.02				292	< 161	24.8	>3.1
Co										0.81						7.4	12.7	12.7	0.58
Cl										167	100	1.67				833	< 210	90	>6.0

*A=Diffusion Battery Filter "A"
+F=Series Cyclone Backup Filter

CONCLUSIONS

The diffusional method was found to be capable of providing samples suitable for determining correlations between elemental composition and size distributions of ultrafine aerosols. However, long sampling times may be required to collect enough material for analysis. The use of compact screen type diffusion batteries operated in situ would reduce the sampling times used here by about a factor of ten.

The submicron mode in the aerosol produced by a pulverized coal boiler was found to differ significantly in chemical make up from the aerosol as a whole. In addition, significant enrichment in S, As, Se and Hg was found to occur in the submicron mode when the flue gases were cooled by mixing with filtered ambient air. However, all elements detected, with the exception of Hg were found to be in much higher concentrations in the large particle mode than in the submicron mode. No variation of elemental composition with particle size could be reliably established within the submicron mode.

ACKNOWLEDGEMENTS

The diffusion battery experiments were funded as a basic research effort by the Salt River Project. The impactor, cyclone and EASA sampling was jointly funded by the Salt River Project and the U.S. EPA during the 1979 tests and solely by the Salt River Project during the 1980 test. Dr. K. Knapp of the U.S. EPA provided the XRF analyses of the samples obtained in the July 1979 test.

REFERENCE

1. Fuchs, N.A. The Mechanics of Aerosols. Pergamon Press, New York, 1964.

Paper 2

AIRBORNE PARTICULATE SIZE DISTRIBUTION MEASUREMENTS IN SMELTER PLUMES

Walter H. Chan
Robert J. Vet*
Maris A. Lusis
Gregory B. Skelton+

Air Resources Branch
Ontario Ministry of the Environment

ABSTRACT

As part of the Sudbury Environmental Study to determine the fate of stack emitted pollutants in the form of dry deposition, airborne studies in the Falconbridge 93 m stack and the INCO 381 m chimney plumes were carried out in 1979 and 1980. Particle sizing measurements were made of the plume constituents with Andersen impactors mounted on a Hughes 500 C helicopter. This paper discusses (i) use of sticky and non-sticky substrates, (ii) particulate size distributions for constituents emitted by two nickel smelters at Sudbury and (iii) comparison of airborne and in-stack measurements.

INTRODUCTION

Sudbury, Ontario is an area of major environmental interest because of the magnitude of sulfur dioxide and particulate emissions due to smelting and mining activities. In 1973, the Ontario Ministry of the Environment (MOE) initiated a multi-disciplinary study, the Sudbury Environmental Study (SES), to assess the impact of the smelter sources on the local environment.

One of the study objectives is to define the fate of the pollutants due to chemical transformation, deposition and transportation (1). As part of our dry deposition monitoring program, measurements were made of the particle size distribution for sulfates and various trace metals, since the dry deposition rate is largely determined by the size of the particles concerned.

Conventionally, in-stack measurements are made for determining emission rates and the associated particle size information. However, the latter measurements may not truly represent reality because once the

---

Current affiliations: *Concord Scientific Corporation, 2 Tippett Rd., Downsview, Ontario, Canada M3H 2V2: +Skeltech, 517-1276 Islington Ave., Islington, Ontario, Canada M9A 3J9

particulates are emitted from the stack, changes of particle size may occur. Therefore an alternative approach was taken. Airborne studies were carried out in the Falconbridge 93 m smelter stack (March and September, 1979) and the INCO 381 m chimney (September, 1979 and February, 1980) plumes to obtain information on the size distribution of various particulate constituents in the plume. These measurements not only lead to better dry deposition estimates, but can also be used to provide useful information for the identification of the origin of ambient pollutants (by comparing sizing results obtained at the plume and ground levels) and the assessment of health effects which are a function of particle size.

In September of 1979, a joint in-stack sampling program by MOE and Falconbridge was carried out. A similar joint study was carried out in February, 1980 by MOE and INCO. Emissions of sulfur dioxide, sulfuric acid, particulates and trace elements as determined in these programs are reported elsewhere (2,3). In this account, only the airborne studies' results are described in detail, but references will be made to the in-stack measurements where applicable.

EXPERIMENTAL

Airborne Sampling Instrumentation

A Hughes 500C helicopter was used as the airborne platform in all field studies. The particle sizing instrumentation was attached to a boom which extended approximately 1 meter beyond the nose of the aircraft. It consisted of two Andersen 2000 Mark III Cascade Impactors. Each contained 8 impaction plates as well as a Whatman 40 back-up filter and was adapted for airborne use by attaching a rigid aluminum casing and a teflon-coated isokinetic nozzle. Effective 50% cut-off diameters of these stages ranged from 0.4 to greater than 9 µm.

The impaction plates in both samplers were covered with polyethylene disks to allow easy removal and analysis of the samples. One Andersen used plates covered with untreated polyethylene while the other used polyethylene coated with a thin layer of petroleum jelly. The latter was used to reduce bounce-off of large particles as suggested by other investigators (4).

All substrates and filters were cut from sheets using a stainless steel cutting die, and stored in a desiccator to prevent contamination. The polyethylene substrate coating solution was prepared by dissolving 10 gm of petroleum jelly in 100 ml of toluene (4). The substrates were dipped in this solution and placed in a fume hood to allow the toluene to evaporate before loading.

The two types of substrates from the March study were subjected to analysis for some selected parameters of interest. Upon examination of the data, it was found (5) that the results obtained with the sticky and non-sticky substrates were not identical and the discrepancies were more serious for large particles, indicating evidence of particle bounce on the non-sticky substrates. Therefore, from the September study onward sticky substrates were used to collect samples for trace metal analysis only and the non-sticky substrates for analysis of only $SO_4^{=}$ and NH_4^{+} (which were known to be in the small size fraction).

Calibrations of the in line flowmeters and rotameters used with the samples were carried out prior to the study, and an in-flight calibration of each rotameter was done during one flight. Typical flows for the particle sizing samplers were 29 l min^{-1}.

Experimental Design

Measurement flights were designed to maximize sampling time in the plume and to achieve proper isokinetic sampling. The flights therefore consisted of a number of passes starting 3 to 5 km downwind of the chimney and moving upwind through the plume along its centreline. An air speed was maintained at approximately 13 m sec^{-1} to obtain isokinetic sampling.

The Andersen samplers were changed only at the end of two to three 1-hour runs to collect cumulative samples. While airborne sampling was being carried out, MOE personnel were in the Falconbridge or INCO smelter documenting smelting process operations.

On September 10, 1979, and February 6, 1980 flights sampling background air were carried out. It was found that background contributions of the various parameters of interest were negligible. Therefore no background correction to the present results was necessary.

Chemical Analysis

After sampling, filters were stored in polyethylene bags and transferred to the Toronto laboratory for chemical analysis. Both aqueous and acid leachings were carried out at different stages as part of the extraction procedures for the analysis of $SO_4^{=}$, NH_4^{+} and trace metals.

For the March Falconbridge study, sample recovery method was similar for the Andersen sticky and non-sticky substrates, and Whatman 40 backup filters. Substrates were placed in acid-washed 20-ml screw cap scintillation vials. Doubly distilled water (~ 15 ml) was added and the sample was heated at 90°C on a hot plate for 4 hours. Samples were cooled, brought to 20 ml with doubly distilled water before trace metal analyses. Graphite furnace flameless atomic absorption spectroscopy was used for all metals except zinc and samples having iron and lead in high concentrations , where flame absorption spectroscopy was used.

For samples collected in the September Falconbridge study and the INCO studies, modified recovery procedures were adopted. The Andersen non-sticky polyethylene substrates and Whatman 40 backup filters were placed as received in calibrated 50 - ml polyethylene centrifuge tubes. Distilled water (25 ml) was added, the tubes tightly capped and placed in an oven at $85^{\circ}C$ overnight. There was no apparent loss of volume. The samples were well mixed and 5 ml taken by a syringe for $SO_4^=$ (Dionex ion chromatography) and NH_4^+ (phenate hypochlorite) analysis. Modifications of routine procedures were needed to allow analysis of 3 parameters on a 5 ml sample aliquot. The remaining 20 ml were acidified with HNO_3 (Suprapure, conc., 1.5 ml) and the tube resealed and again heated at $85^{\circ}C$ overnight. The volume was adjusted to 25 ml and the solution analyzed for metals by flameless atomic absorption, and for arsenic and selenium by hydride generation atomic absorption.

The Andersen sticky polyethylene substrates were placed in teflon tubes and low-temperature ashed for several days. In some samples not all the polyethylene filter had disappeared after this time; HNO_3 (conc. 1.5 ml) was added and the volume brought to 25 ml with distilled water. The tubes (screw top, Oak Ridge type) were capped and the samples placed in a hot block at $150^{\circ}C$ for 16 hours. Water vapor escaped despite the threaded top and after 16 hours 1 ml remained. The tubes were cooled, brought to 25 ml with distilled water, mixed and analyzed for metals by flameless a.a.s.

Most of the results used in the calculations are of samples with loadings equal to or greater than two times the blank values.

RESULTS AND DISCUSSIONS

Sticky vs Non-Sticky Substrates

The non-sticky substrate samples from Flight 2 of the March study were stored in petri dishes rather than in polyethylene bags upon unloading. This allowed the individual samples to be examined with scanning electon microscopy (SEM).

A visible impaction dot from each polyethylene substrate stage was cut out and the substrate was handled with platinum tweezers. The cut sample was then adhered to a carbon stub and coated with a silver paint before an evaporation process was carried out. The backup Whatman 40 cellulose filter was unsuitable for SEM analysis.

Details of the SEM results are reported elsewhere (5). The results, however, are summarized briefly below. On the upstream stages (i.e. stages 0,4 and 5), the major consitutents were S, Fe and Si with the presence of smaller quantities of K, Ca, Ti, Ni, Cu, Zn and Pb. There was also evidence of trace amounts of Al and Mg. On the last two stages, little trace metal loading was present and the content was dominated primarily by sulfur compounds which were most likely non-metal sulfates such as sulfuric acid and ammonium sulfate.

Comparisons of the expected and observed particle sizes (Table 1) suggested that particle bounce-off of larger size trace metal

Table l: Summary of the Observed Particle Size and Expected Effective Cut-Off Diameter (in um)

Stage Number	50% Effective Cut-Off Diameter	Approximate Observed Diameter
0	9.0	36
1	5.8	-
2	4.7	-
3	3.3	11
4	2.1	4
5	1.1	7
6	0.7	500-700
7	0.4	4-28

particulates and condensation and/or crystallization of the sulfur species had taken place after collection (note especially the particles on stages 6 and 7, which were found to be large sulfate crystals).

These SEM analysis results were further substantiated by the detailed chemical analyses of both the stick and non-sticky substrate samples (See Table 2). They both pointed to the fact that bounce-off problems did occur with non-sticky substrates under airborne sampling conditions. This was especially serious with particles in the coarse size range. Therefore in subsequent experiments sticky substrates only were used for coarse particle sampling.

Particle Sizing Results from Airborne Sampling of Smelter Plume

Introduction --

An excellent description of aerosol sizing data presentation has been given by Whitby (6) where it is shown that cumulative plots are quite useful in determining the aerodynamic mass median diameter of a sample. This approach however has some limitations in that the median obtained represents a rough average of the fine and coarse modes and it hides the modal characteristics of the distribution. However, for deposition calculation purposes, data generated by this technique are sufficient.

TABLE 2: SUMMARY OF MASS MEDIAN DIAMETERS (μm) from ANDERSEN SAMPLING IN THE FALCONBRIDGE 93 m STACK PLUME

	March 7, 1979		March 8, 1979		March 9, 1979	
Substrate Parameter	Sticky	Non-Sticky	Sticky	Non-Sticky	Sticky	Non-Sticky
Fe	> 9	4.5	> 9	3.8	8.65	3.60
Cu	> 9	4.28	7.35	4.36	8.20	3.45
Ni	> 9	6.5	>9	6.85	> 9	4.3
Pb	0.92	1.01	1.01	0.94	0.87	0.95
Zn	< 4.7	1.1 - 2.1	1.90	1.19	1.00	1.03
As	0.89	0.84	0.67	0.82	0.69	0.66
Cd	< 0.7	2.60	1.09	0.92	0.93	0.79
SO_4	0.44	0.60	0.40	0.59	0.48	0.62

An alternative plotting method is the differential plot which shows the different "modes" of particle size; it indicates the amount of sample which is found in each size range along a continuous spectrum. This latter plot has the advantage over the cumulative plot approach when data for some stages are missing. If a linear plotting co-ordinate is used, the ratio of modal areas underneath the modes could potentially be used as an indicator for particle source identification.

Falconbridge Results --

Results from size distribution probability plots of aerodynamic mass median diameters, and differential plots($\Delta m / \Delta \log Dp$ vs. Dp) are summarized in Tables 3 and 4.

Some general observations can be made of the two Falconbridge smelter studies:

1. The species measured can be classified into two categories according to the mass median diameters (MMD):

(a)Coarse particles (MMD > 2.5 μm): Fe, Cu, Ni, Al, and Mn
(b)Fine particles (MMD < 2.5 μm): Pb, Zn, Cd, As, SO_4 and NH_4^+.
The aluminum results should be accepted with reservation because the Andersen sampler is made of aluminum, and thus contamination is possible.

Table 3: Mass Median Diameter* (μm) by Andersen Sampling in the Falconbridge Smelter Plume

	March 1979			September 1979	
Flight	1	2	3	1	2
Parameter					
Fe	> 9	> 9	8.65	7.1	7.0
Cu	>9	7.35	8.20	5.9	4.4
Ni	>9	> 9	> 9	9	6.6
Pb	0.92	1.01	0.87	0.95	-
Zn	< 4.7	1.90	1.00	0.84	-
Al[+]	-	5.40	-	7.2	2.9
Mn	-	-	-	5.5	-
Cd	< 0.7	1.09	0.93	5.3	2.3
As	0.89	0.67	0.69	-	-
SO_4	0.60	0.59	0.62	0.82	0.64
NH_4	-	-	-	0.7	0.84

* All parameters were determined from sticky polyethylene substrates except SO_4 and NH_4 which were determined from non-sticky polyethylene substrates.

+ Probably contamination due to Al sampler.

TABLE 4: SUMMARY OF MODAL DIAMETER (μm) FROM AIRBORNE SAMPLING IN THE FALCONBRIDGE SMELTER STACK PLUME*(1979)

	Mar. 7	Mar. 8	Mar. 9	Sept. 9	Sept. 11
Fe	2.5, 4.7	0.9, 2.6	0.7, 3	1.2, 3.5	--
Cu	0.4, 2, 4.7	0.7, 2.2	0.7	0.9, 2.7	1.9
Ni	0.4, 2, 4.7	0.7, 3.3	1.1	1.1, 3.5	0.3
Pb	0.7, 4.7	0.7	0.7, 3.3	0.7, 4.7	--
Zn	0.4, 1.1, 4.7	0.7, 3.3	0.7, 3.3	0.7, 2.1, 4.7	--
Al	0.4, 2.1	0.8, 2.1, 4.7	1.7, 5	--	0.7, 2.1
Cd	0.4, 2.5	0.7	0.7, 2.1	0.7	0.7, 2.1, 4.7
As	0.6	0.7, 2.1	0.7, 3.3	--	--
NH_4	--	--	--	0.7, 2.5, 4.7	0.7, 3.3
SO_4	0.6	0.7	0.6	0.7, 3.3	0.6

* There is evidence of a mode larger than 9 μm for some heavy metals; however, this information is concealed due to the upper sampling limit of the sampler.

Large departures from log-normal size distribution are frequently observed in our results. Some of these may be only apparent due to difficulties in chemical analysis of very lightly loaded impactor substrates. Others may be a reflection of bimodal or trimodal chracteristics which are exemplified in the differential plots. The unusually high MMD's for Fe, Cu and Ni are somewhat unexpected and may be linked to the efficiency of the electrostatic precipitator.

2. The maxima determined from the differential plots for the two studies showed reasonably good consistency. Most particles display modes at about 0.4 to 0.7 μm and 2 to 3 μm, and some seem to have a third one around 5 μm. There is also evidence of a mode larger than 9 um for some of the metals; however, this information is concealed due to the upper sampling limit of the sampler.

INCO Results --

The mass median diameters (MMD) of the various species are given in Table 5 . Data collected in September, 1979 and February, 1980 are, in

Table 5: Mass Median Diameter (μm) of Particulate in the INCO 381 m Chimney Plume by Andersen Sampling

PARAMETER	MASS MEDIAN DIAMETER (μm)				
	Sept. 8 1979	Jan. 31 1980	Feb. 4 1980	Feb. 5* 1980	Feb. 7 1980
Fe	5.2	>9	>9	>9	>9
Cu	>9	>9	>9	>9	2.8
Ni	>9	>9	>9	>9	>9
Pb	1.0	1.05	0.92	1.7	1.15
Zn	1.1	1.1	0.96	6.6	2.1
Al	3.2	2.1	8.2	>9	5.6
Cr	-	3.8	1.0	-	-
Cd	3.1	1.5	1.9	1.1	3.4
Mn	4.2	-	-	-	-
Se	-	-	-	1.25	1.4
As	-	0.98	0.92	0.96	1.0
Mg	-	8.0	>9	>9	7.0
SO_4	0.48	0.98	0.93	1.1	0.94
NH_4	0.53	1.6	2.0	2.2	2.6

* Emissions on this date were atypical.
Particulate fallout near the stack was observed.

general, quite consistent except in the cases of Fe, Al, $SO_4^=$ and NH_4^+. In these cases, the MMD appeared to be larger in the February study but due to the limited sample size, it is difficult to attach any significance to this change. There seems to be considerable variability from one sample to another in the MMD of Cu, Al, Cr and Cd. The data can be broadly categorized into two classes: Fe, Cu, Ni, Al, Mg and Mn belong to the coarse particle range with MMD larger than 2.5 um; and Pb, Zn, Cr, Cd, Se, As, $SO_4^=$ and, NH_4, belong to the fine particle size range, with MMD less than 2.5 µm.

Differential plot results are summarized in Table 6. Generally, the distributions do not follow a log-normal pattern, but tend to be bimodal. Aside from the modes below 5 µm, there is some indication that a mode larger than 9 µm exists for some of the heavy metals. It should be noted that on February 5, 1980, particle fallout was observed near the stack. In general, MMD's determined on this day seem to be larger than those found on other days, and the results are probably atypical.

Comparison of Airborne and In-Stack Results

In September, 1979, three single-point in-stack particle sizing experiments were carried out at the 93 m Falconbridge stack. Although none of these runs coincided with the airborne flights, a comparison of the data from the two sets of measurements is still interesting and is given in Table 7. Also during the INCO February, 1980 airborne study, in-stack particle sizing experiments were also carried out in the 381 m stack but it was again not possible to synchronize the airborne and in-stack measurements (3). These data are summarized in Table 8.

In general, it seems that the size of the particulates emitted from Falconbridge containing Fe, Ni and Cu increases upon release into the atmosphere. Particle sizing results from the INCO studies on Fe, Ni and Cu are not very meaningful because of the upper limits of the sampling equipment. In order to make the comparison feasible, percentages of these species with 9 µm size are calculated from the raw data. For the three in-stack tests: Fe (30%, 31%, and 31% with an average of 31%), Ni (22%, 31% and 27% with an average of 27%) and Cu (36%, 50% and 31% with an average of 33%). For the airborne tests excluding the atypical run on February 5, 1980: Fe (31%, 16% and 22% with an average of 23%), Ni (10%, 20% and 30% with an average of 20%) and Cu (45%, 37% and 74% with an average of 52%). It seems that the sizes of Fe and Ni decrease whereas that of Cu increases upon release form the INCO stack into the atmosphere. Particulates containing volatile metals from the two sources such as Pb and Zn grow slightly or remain fairly constant in size upon release from the stack. In the case of $SO_4^=$, an unexpected phenomenon was observed for both sources , i.e. the size of the $SO_4^=$ particulate is apparently reduced upon release into the atmosphere. It is suspected that this may be due to sampling and analytical problems associated with the in-stack measurements. In the in-stack Andersen sampling, glass fiber filters were used and spurious sulfate formation due to SO_2 passage through the filter could potentially change the real

Table 6: Summary of Modal Diameter (μm) from Airborne Sampling in the INCO 381 m Chimney Plume[+]

	Sept. 8, 1979	Jan. 31, 1980	Feb. 4, 1980	Feb. 5, 1980**	Feb. 8, 1980
Fe	*, 3.3	1.2, 3.3	1.1, 3.4	3.3	-
Cu	*, 3.3	0.7, 3.3	0.7, 3.4	1.2	1.8
Ni	*, 3.3	3.3	3.3	2.1	3.1
Pb	*, 3.3	0.7, 3.3	1.1, 3.3	0.7	2.1
Zn	*, 2.1, -	0.7, 3.3	-	1.1	2.1
Al	*, 2.3, 4.2	1.1	-	-	-
Cr	-	0.7, 4.7	-	-	-
Cd	*, 2.0, 4.9	1.05, 3.3	-	0.75	0.76, 3.3
Mn	*, 3.5	-	-	-	-
Se	-	-	-	0.4, 1.1	2.1
As	-	0.7	1.1, 3.3	0.7	0.7
Mg	-	0.4, 3.3	-	-	4.7
SO_4	0.4, 4.5	0.4	1.1, 4.7	0.7,2.1	1.1,3.3
NH_4	(0.7), 4.5	0.7, 3.3	0.7, 4.7	0.4,2.6,4.7	0.68,4.7

[+] There is evidence of a mode larger than 9 μm for some heavy metals, but diameter cannot be defined due to sampler cut-off limits.

[*] Incomplete results due to loss of partial Andersen sample in the course of chemical analysis.

[**] Emissions on this date were atypical. Particulate fallout near the stack was observed.

Table 7: Comparison of Mass Median Diameter (μm) of Particulates Determined by In-Stack and Airborne Measurements at the 93 m Falconbridge Stack in 1979

Parameter Test	Fe	Ni	Cu	Pb	Zn	SO_4
In-stack						
#1(Aug. 28)	4.5	5.5	4.6	.58	.70	4.3
#2(Aug. 29)	3.5	3.9	3.1	.60	.68	2.2
#3(Aug. 30)	7.3	6.8	4.75	.70	.94	3.5
Airborne						
#1(Sept. 9)	7.1	9	5.9	.95	.84	.82
#2(Sept. 11)	7.0	6.6	4.0	-	-	.64

Table 8: Comparison of Mass Median Diameter (μm) of Particulates Determined by In-Stack and Airborne Measurements at the INCO 381 m Chimney in 1980

	Parameter					
	Fe	Ni	Cu	Pb	Zn	SO_4
In-Stack:						
Jan. 30, 1980	>13	>13	>13	.84	3.6	4.0
Feb. 1, 1980	>13	>13	8.7	2.7	.92	1.9
Feb. 2, 1980	>13	>13	>13	6.2*	8.0*	3.7
Airborne:						
Jan. 31, 1980	>9	>9	>9	1.05	1.1	0.98
Feb. 4, 1980	>9	>9	>9	0.92	0.96	0.93
Feb. 5, 1980+	>9	>9	>9	1.7	6.6	1.1
Feb. 7, 1980	>9	>9	2.8	1.15	2.1	0.94

* Results look suspiciously high.

+ Particle sizes probably atypical due to particle stratification and fall out.

size distribution (7). It has also been recognized that sizing measurements of sulfuric acid inside the stack using the existing method may not yield accurate results. If the in-stack sampling train collects preferentially non-volatile metal sulfates but not sulfuric acid which exists mainly as SO_3 vapor due to the high sampling temperature, potentially larger MMD of the sample and a lower emission rate of SO_4 could result as trace metal sulfates are in the larger particle size range than sulfuric acid. However, under airborne sampling conditions at ambient temperature, sulfuric acid is in the form of an aerosol in the fine particle size range, and will be collected without loss on the substrate. This speculation on the different particle size of $SO_4^=$ as measured in stack and airborne is further supported by the fact that higher $SO_4^=$ emission rates were observed in the airborne measurements relative to the in-stack measurements (8,9).

Since the number of samples in these experiments was small, and in no case were airborne and in-stack measurements made simultaneously, the above observations about differences in the two sets of measurements should be regarded with caution.

SUMMARY

A technique was described for determining plume particle size distributions of a number of constituents emitted by two nickel smelters at Sudbury, Ontario. It is felt that for particle deposition rate determinations, this technique is more useful than in-stack measurements, since the particle size distribution may change as the emissions emerge from the hot stack into the much cooler ambient air.

It was found necessary to use sticky substrates for the sample collection, as there was evidence of bounce-off problems for the larger particulates, on untreated substrates. In both smelters, the constituents could be separated into coarse particles having mass median diameter larger than 2.5 μm (these included Fe, Cu, Ni, Al and Mn), and fine particles (which included $SO_4^=$ and relatively volatile metals such as Pb, Zn, Cd and As). In many cases, a bimodal distribution (and in some cases a trimodal distribution) was observed. A comparison of in-stack and airborne size distributions suggested that changes can occur as emissions mix with the ambient air, but the sample size from these experiments was too small to draw any definite conclusions.

REFERENCES

1. Chan, W.H., M.A. Lusis and R.J. Vet. Sudbury Environmental Study: An Overview, paper 80-52.4A, presented at the 73rd Annual Meeting of the APCA. Montreal, June 22-27, 1980

2. Ozvacic, V. and J. McDonald. "Sulfur Dioxide, Sulfuric Acid, Particulate and Particle Size Determination at Falconbridge Smelter Stack, August, 1979" Ontario Ministry of the Environment report ARB-TDA-40-80, to be published.

3. Ozvacic, V. and J. McDonald. "Determination of the Extent of Particulate Stratification at the INCO 381 Meter Chimney at Copper Cliff Ontario", Ontario Ministry of the Environment report ARB-TDA-58-80

4. Rao, A.K. and K.T. Whitby. Non-ideal Collection Characteristics of Inertial Impactors - II Cascade Impactors J. Aerosol Sci. 9, 87 (1978)

5. Chan, W.H. and M.A. Lusis "An Airborne Study in the Falconbridge Smelter Plume - March, 1979" Ontario Ministry of the Environment internal report (1979)

6. Whitby, K.Y., The Physical Characteristics of Sulfur Aerosols, Atmos. Environ. 12, 135 (1978)

7. Harris, D.B., G. Clinard, L.G. Felix, G. Lacey and J.D. McCain. Substrate Collectors for Cascade Impactors, An Evaluation. Paper 13, Proceedings: Advances in Particle Sampling and Measurement, Asheville, North Carolina, May 1978.

8. Chan, W.H., R.J. Vet, G.B. Skelton and M.A. Lusis, "Size Distribution and Emission Rate Measurements of Particulates in the 93 m Falconbridge Smelter Stack Plume, 1979" Ontario Ministry of Environment report ARB - TDA 57-80, to be published.

9. Chan, W.H., R.J. Vet, M.A. Lusis and G.B. Skelton, "Size Distribution and Emission Rate Measuremtns of Particulates in the INCO 381 m Chimney and Iron Ore Recovery Plant Stack Plumes, 1979-80" Ontario Minsitry of Environment report ARB - TDA - 62-80, to be published.

ACKNOWLEDGMENTS

Thanks are due to the following persons whose contributions have made the studies possible:

DR. D. Lake of Cambrian College, Sudbury, for making laboratory space available for our use during these studies; Messrs L.Fitz, T. Van Rossam, J. Bassett, D. Bazinet and F. LaLonde of MOE and R. Laine of Falconbridge for documenting processes during these studies; Messrs S. Onlock and R. Regier for technical assistance; Messrs. R. Chiu, R. Regier, M. Talbot, R. Harvey and J.C. Cassagne for assisting in calculations; Mr. F. Tomasinni and Dr. B. Loescher for coordinating laboratory efforts; and Dr. D. Balsillie and Messrs. L. Fitz, J. McDonald, R. Potvin and J. Weglo for helpful discussions.

The work described in this paper was not funded by the U.S. Environmental Protection Agency. The contents do not necessarily reflect the views of the Agency and no official endorsement should be inferred.

The work described in this paper was not funded by the U.S. Environmental Protection Agency. The contents do not necessarily reflect the views of the Agency and no official endorsement should be inferred.

Paper 3

CHARACTERIZATION OF URANIUM OXIDE AEROSOLS PRODUCED BY HIGH ENERGY ENVIRONMENTS

R. P. Sandoval
Transportation Technology Center
Sandia National Laboratories

G. J. Newton
B. A. Wong
Inhalation Toxicology Research Institute

ABSTRACT

Radioactive aerosols generated by subjecting depleted uranium oxide and spent fuel pellets to high energy environments (explosively generated) have been experimentally quantified and characterized. These measurements are the results of a program at Sandia National Laboratories to determine the radiological source terms resulting from nuclear spent fuel shipping systems subjected to severe accident or sabotage. An aerosol containment and sampling system was assembled to collect and sample the aerosols generated. A variety of sampling devices was used to collect and size particles from 0.01 μm to 2 mm diameter. Special emphasis was placed on respirable aerosols (< 10 μm aerodynamic diameter) for consideration of potential health hazards and clean-up costs. Cellulose nitrate filters and cascade impactors provided samples for time-dependent measurements of particle size, concentration and elemental composition. Point-to-plane electrostatic precipitators were used to obtain samples for analyses by transmission and scanning electron microscopy as well as energy dispersive x-ray spectroscopy. Electrical aerosol analyzers were used to determine the size of particles less than 1.0 μm diameter and condensation nuclei counters measured total number concentration as a function of time. Mechanical sieving, followed by weighing and uranium fluorometric analyses, was used to size classify UO_2 particles from 37 μm to 2 mm diameter. Although large masses of the UO_2 fuel were disrupted, relatively small mass concentrations of respirable UO_2 were produced.

INTRODUCTION

Public concern has been focused on the risks that the transportation of nuclear materials poses to human health and the environment. Various scenarios involving accidents and sabotage of spent fuel transports have been studied in an effort to determine the resulting health consequences. A working draft environmental assessment study[1] was sponsored by the U.S. Nuclear Regulatory Commission (NRC) to evaluate the radiological consequences resulting from the transportation of radioactive materials (RAM) in urban areas for various types of transportation scenarios, including sabotage. This study predicted that tens of early fatalities and hundreds of latent fatalities could occur from the sabotage of spent fuel shipping systems, assuming certain attack modes.

Since no experimental data were available for these studies, the quantity and characteristics of the released radioactive material were estimated assuming anticipated damage to the package and contents and a particular attack mode. The NRC reacted to the "Urban Study"[1] by requiring restricted routing and physical protection measures for U.S. spent fuel shipments pending the availability of credible experimental data supporting or disproving these predictions.

In response to these experimental data needs, the Department of Energy (DOE) has initiated the Transportation System Safety Evaluation (TSSE) program at Sandia National Laboratories (SNL) to provide an experimental data base which characterizes the released radionuclides. This data base will be used to make realistic and improved human health risk assessments for the transportation of spent fuel in sabotage and accident produced environments. These risk assessments may, in turn, be used for public information, for policy formation and to assist the NRC in regulating spent fuel shipments.

The objectives of the TSSE program are to evaluate the effectiveness of the various attack devices to breach an LWR spent fuel cask and to determine the physical and chemical characteristics of the released radionuclides. Emphasis is placed on the respirable size range (less than 10 micrometers mass medium aerodynamic diameter) for health effects; however measurements of particles larger than 10 micrometers are also conducted for estimating clean-up and decontamination costs. The health consequences are estimated using this data base as input to the "Calculations of Reactor Accident Consequences" code (CRAC)[2] developed for reactor safety studies. This code is identical to that used to estimate health consequences in the "Urban Study."[1]

EXPERIMENTAL METHODS

Since no single aerosol instrument can size particles from 0.01 μm to about 2 mm diameter, the battery of instruments listed in Table 1 was selected to measure the size and mass of particles. For preliminary atmospheric tests, surrogate fuel pins consisting of depleted UO_2 fuel pellets and zircalloy cladding were placed between two simulated full scale generic cask walls and an Energy Intensive Device (EID) was fired at the test assembly. Samplers were placed at selected locations around the test site to measure the size and concentration of the aerosol. Modified Andersen Impactors were used to measure the particle size distribution of the aerosol cloud. High volume filters were used to measure the mass concentration of the aerosol. Samplers were analyzed gravimetrically for total mass, and fluorometric analyses were used to quantitate aerosolized uranium from which total UO_2 was calculated.

Aerosol size parameters as a function of time were determined from cascade impactor[3,4] samples obtained at various time intervals after EID detonation. Similarly, filter samples provide a time history of the change in mass concentration. Changes in morphology were shown by sequential electrostatic precipitator[5] (ESP) samples and changes in number concentration were shown by continuously recording condensation nuclei counters. The targets were: (1) steel blocks

Table 1

Sampling Instruments Used in Quarter Scale Chamber Tests

Instrument and Applicable Size Range	Purpose of Samples	Analytical Method
LMJ Cascade impactors 0.5 - 12 μm	Aerodynamic size, geometric standard deviation of total aerosol mass and UO_2 mass.	Gravimetric (Cahn microbalance) and fluorometry for determination of uranium.
Point-to-plane electrostatic precipitator TEM & SEM 0.01 - 12 μm	Particle morphology, count distribution and elemental distribution.	Transmission and scanning electron microscopy and energy dispersive x-ray analysis.
Filter 37 mm, sequential, 0.01 - 12 μm	Provide a time history of total aerosol and uranium mass after EID detonation. Samples for surface area measurements.	Gravimetric for total mass and uranium by fluorometry, BET nitrogen absorption for surface area measurements.
Filter 37 mm, front surface reentrant filter (FSRP) 0.01 - 12 μm	Sequential filter samples from filters inside chamber to compare with filters obtained by extractive techniques to address aerosol line losses.	Gravimetric for total mass of aerosol and uranium by fluorometric techniques.
[a]Condensation nuclei counter (CNC) 0.001 - 12 μm	Total count of aerosol particles vs. time after detonation.	Optical light scattering instrument.
[a]Electrical aerosol analyzer (EAA) Dia < 1.0 μm	Size distribution parameters for particles between 0.01 and 1.0 μm.	Electrical mobility.
Sieves (38 - 2000 μm)	Provide size distribution data on larger particles of surrogate spent fuel.	Mechanical sieving followed by weighing for total mass and fluorometry for uranium determination.

---

[a] Data from these instruments are not included in this report.

for test numbers 3 and 4 (see Table 2), (2) surrogate fuel pins placed on steel blocks in test 5, (3) a quarter-scale cask containing short sections of full scale surrogate fuel pins in test 6, and (4) a quarter-scale cask containing short sections of full scale surrogate fuel pins and water as a coolant in test 7. Results from these tests could then be used to predict results expected from full-scale casks containing spent fuel pins.

The confinement chamber (Figure 1) was a steel, cylindrical tank (14.3 mm thick walls) sealed at one end and having an airtight door at the other end. The length of the cylinder, exclusive of end caps, was 1.55 m and the internal diameter was 1.37 m. Total internal volume, including the end caps, was 2886 ℓ. The EID was mounted external to the chamber and fired into the chamber through a 6.4 mm diameter hole in a flanged assembly mounted external to the chamber. Between the EID and the chamber was an isolation slide valve. This valve was designed to close after the detonation of the EID to reduce the mass of combustion products entering the chamber. Five sampling ports penetrated the chamber in various locations. The ports were closed by remotely operated pneumatic valves. The valves were kept closed until after the detonation to prevent damage to the sampling equipment by the shock wave. All debris were collected from surfaces inside the test chamber and separated into obvious non-uranium-containing material and suspected uranium-containing material. All suspected uranium debris was sieved, the mass determined, and uranium fluorometric analyses performed. Energy dispersive x-ray analysis (EDXA) was used to determine the quantity of various elements in particles collected by the electrostatic precipitators.

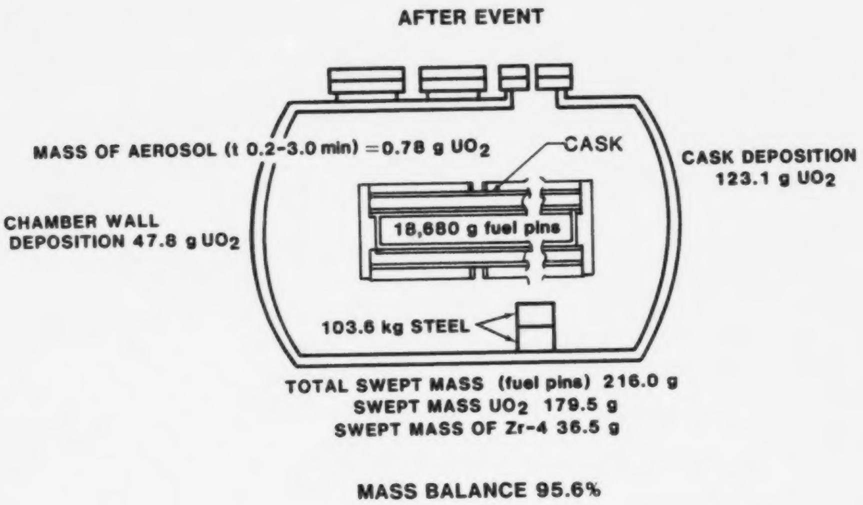
AFTER EVENT
MASS OF AEROSOL (t 0.2-3.0 min) =0.78 g UO_2
CASK
CASK DEPOSITION 123.1 g UO_2
CHAMBER WALL DEPOSITION 47.8 g UO_2
18,680 g fuel pins
103.6 kg STEEL
TOTAL SWEPT MASS (fuel pins) 216.0 g
SWEPT MASS UO_2 179.5 g
SWEPT MASS OF Zr-4 36.5 g
MASS BALANCE 95.6%

Figure 1. Schematic diagram of chamber test No. 6 showing a reconstruction of the results immediately after the Energy Intensive Device (EID) detonation.

Chamber tests consisted of placing the target assembly inside a large cylindrical chamber in order to retain all materials released by the EID's environment. The sampling procedure was designed to provide a time history of the aerosol in the chamber. From the aerosol time history, calculations could be performed to determine the initial release parameters. By developing such techniques on casks containing surrogate fuel, the results can be extrapolated and used in tests on casks containing spent-fuel where sampling might not be permitted until considerable time after detonation.

RESULTS AND DISCUSSION

Two preliminary atmospheric tests (1 and 2), conducted in July and August of 1979, demonstrated the feasibility of performing aerosol measurements following full scale explosive attacks on simulated cask walls and surrogate fuel (depleted UO_2). An estimate of the release was made based on an average UO_2 concentration, the total mass of disrupted fuel and by extrapolating to the estimated cloud size. Approximately 0.0018 of the removed fuel mass was released from the cask as respirable UO_2. A mass balance calculation was not possible because of the loss of surrogate fuel material to the surrounding area. For these reasons, and also in order to obtain time histories of aerosol parameters for future spent fuel experiments, subsequent tests were conducted within containment. Table 2 lists the two atmospheric tests and chamber tests conducted along with the purpose and results of each test.

Two chamber tests (No. 3 and 4) were conducted to evaluate aerosol measurement methods and techniques in explosive environments and to evaluate explosive actuated isolation valves. Test 5 verified the previous developmental tests with surrogate (depleted UO_2) fuel pins.

Test 6 involved a quarter-scale dry cask containing a short section of a 5 x 5 array of full scale surrogate fuel pins, and test 7 involved a quarter-scale cask containing a water coolant in the fuel cavity and a short section of a 5 x 5 array of full scale surrogate fuel pins. Figure 1 is a schematic of the set—up for test 6 and a reconstruction of events immediately after detonation. Total UO_2 aerosol mass (0.78 g) is the basis of the estimated aerosolized released fraction for test 6. Based on the removed surrogate fuel pin mass of 216 g (determined by weighing fuel pins before and after detonation), the aerosolized UO_2 release fraction for test 6 was 0.36%. Figure 2 shows a time history of the aerosol mass within the chamber based on sequential filter samples obtained from a sampling port located at the bottom of the chamber. The exponential decay of aerosol mass in Figure 2 indicates that the first filter sample (0.2 min to 3.0 min after detonation) is consistent with all subsequent filter samples obtained. Sequential cascade impactor samples were also taken to give a time history of aerosol size distribution parameters. Assuming a single log-normal aerosol size distribution, aerosol size reached a peak (3.5 μm) after approximately 12 minutes and then the size stabilized near a mass median aerodynamic diameter (MMAD) of 2.0 μm after 30 min. Similar trends were observed for the geometric standard deviation σ_g which stabilized at 2.0 after 30 minutes. Uranium dioxide concentration (fluorometric determination) as a function of total aerosol mass ranged from 7% at early times to about 2% at 10 minutes post detonation. Similar UO_2 aerosol percentages were also observed in EDXA studies of TEM samples obtained from ESP collected aerosols with peaks attributable to Pb, Cu, Al,

Table 2

Summary of Aerosol-Explosive Device Tests

No.	Date	Target	Test Type	Purpose and Results
1	7/79	Surrogate fuel pins between two open simulated cask walls	atmospheric (full scale EID)	Feasibility study using filters and cascade impactors to determine sensitivity of uranium analysis.
2	8/79	Surrogate fuel pins between two open simulated cask walls	atmospheric (full scale EID)	Repeat feasibility study using release fraction estimate (0.18% obtained) based on extrapolation to observed cloud size. Mass balance was not possible.
3	1/80	Thick steel target	chamber (1/4 scale EID)	Feasibility of chamber test, isolation valve and evaluation of aerosol sampling instruments, multi-component aerosol observed requiring several aerosol instruments for measurement of mass and size.
4	2/80	Thick steel target	chamber	(Same as Test #3)
5	3/80	Thick steel target	chamber (1/4 scale EID)	(Same as Test #3) Verification of method of uranium fluorometric analyses were obtained.
6	6/80	Quarter-scale cask containing short sections of a 5 x 5 array of surrogate fuel pins. No water coolant was used in this test.	chamber (1/4 scale EID)	Determined respirable UO_2 release fraction based upon removed fuel mass (0.0036) from dry quarter scale cask using quarter scale EID.
7	3/81	Quarter-scale cask containing short sections of a 5 x 5 array of surrogate fuel pins. Water was used as a coolant in fuel cavity.	chamber (1/4 scale EID and 1/4 cask)	Determined respirable UO_2 release fraction based upon removed fuel mass (0.00014) from a wet quarter scale cask using a quarter scale EID.

Fe, and U. In all analyses, including total field scan, small particle analysis and analysis of larger particles, the percentage of uranium by weight ranged from 1.6% to 2.0%.

Figure 3 is a schematic of the setup for test 7 and a reconstruction of events immediately after detonation. Total UO_2 aerosol mass (19.6 mg) is the basis of the estimated aerosolized released fraction for test 7. Based

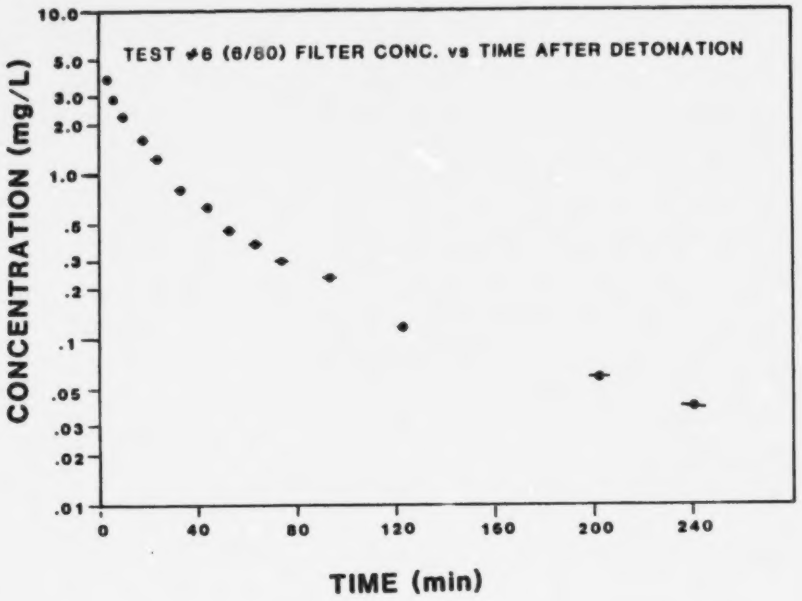

Figure 2. Time history of total aerosol mass within chamber for test No. 6 based on sequential filter samples.

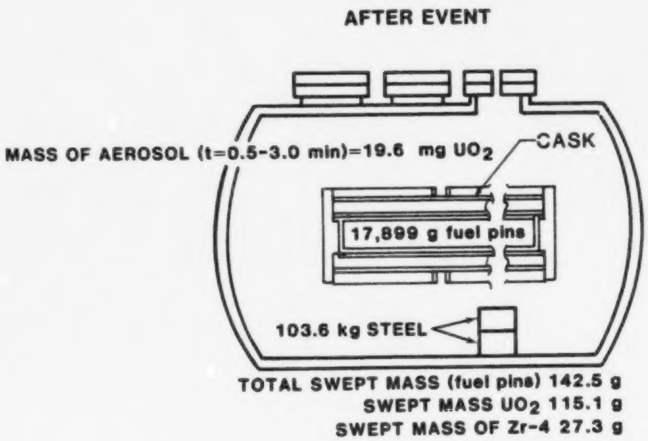
AFTER EVENT
MASS OF AEROSOL (t=0.5-3.0 min)=19.6 mg UO2
CASK
17,899 g fuel pins
103.6 kg STEEL
TOTAL SWEPT MASS (fuel pins) 142.5 g
SWEPT MASS UO2 115.1 g
SWEPT MASS OF Zr-4 27.3 g

Figure 3. Schematic diagram of chamber test No. 7 showing a reconstruction of results immediately after detonation.

on a removed mass of 142.5 g of fuel pins (zircalloy cladding and UO_2 fuel pellets), the aerosolized UO_2 release fraction for test 7 was 0.014%. Figure 4 shows a time history of the aerosol mass within the chamber based on sequential filter smaples, cascade impactor samples, and front surface reentrant filter samples. Good agreement is obtained among the varous sampling techniques. The early time aerosol mass concentration for the wet test No. 7 is an order of magnitude smaller than that for the dry test No. 6. Assuming a single log-normal aerosol size distribution for test 7, aerosol size reached a peak of 1 μm MMAD at approximately 5 minutes after detonation and then stabilized near a MMAD of 0.7 μm after 30 minutes. Uranium dioxide aerosol mass concentration (fluorometric determination) as a function of elapsed time after detonation is shown in Figure 5 for tests 6 and 7. Early time UO_2 aerosol mass concentration is forty times less for the wet test (No. 7) than for the dry test (No. 6). Approximately 1.4% of the total aerosol mass of test 7 was observed to be UO_2 using EDXA of ESP samples taken at 0.5 minutes post detonation.

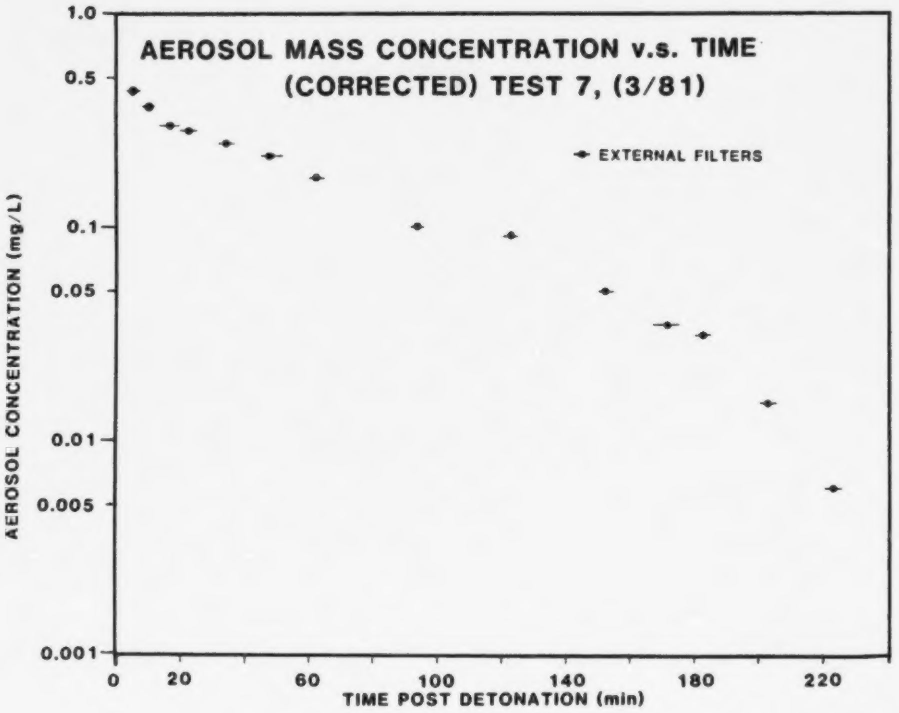

Figure 4. Time history of total aerosol mass in chamber for test No. 7 based on sequential filter samples, cascade impactor samples and front surface reentrant.

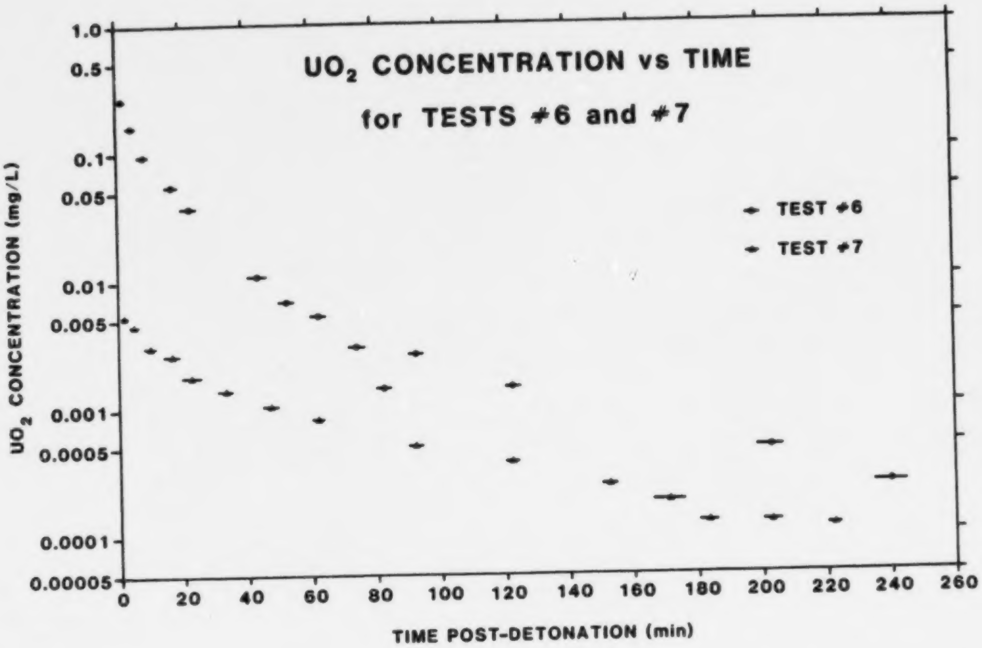

Figure 5. Comparison of UO_2 aerosol mass concentration as a function of time for test No. 6 and test No. 7.

SUMMARY AND CONCLUSIONS

Full scale atmospheric tests with large explosive devices and quarter-scale tests on nuclear spent fuel casks within containment have been conducted, and methods for aerosol measurements in explosive environments have been developed. A quarter-scale cask containing surrogate fuel (depleted UO_2 pellets) and a quarter scale cask containing water as a coolant and surrogate fuel (depleted UO_2) have been explosively breached using an energy intensive device. The released airborne and non-airborne composition using cascade impactors, cellulose nitrate filters, point-to-plane electrostatic precipitators, transmission and scanning electron microscopy, electrical aerosol analyzers, sieving techniques, and uranium fluorometric analyses. The airborne particulate size stabilized at $\approx 0.7\ \mu m$ MMAD, 30 minutes after EID detonation for test No. 7 (wet). Approximately 1.4% of the total airborne aerosol mass was UO_2 at 0.5 minutes post detonation. The airborne particulate size stabilized at a MMAD of $\approx 2.0\ \mu m$, 30 minutes after EID detonation for test No. 6 (dry). Approximately 2% of the total aerosol mass for test No. 6 was UO_2 at 10 minutes post detonation. The UO_2 mass concentration for test No. 6 at 0.2 minutes after detonation was 0.72 mg/l. The UO_2 mass concentration for test No. 7 at 0.5 minutes after detonation was 6.8 µg/l. The removed fuel mass for test No. 6 was 216 g and the removed fuel mass for test No. 7 for a similar EID was 142.5 g. A respirable UO_2 release fraction of 0.0036 based upon the removed UO_2 fuel mass was calculated for test No. 6. A respirable UO_2 release fraction of 0.00014 based upon the removed UO_2 fuel mass was calculated for test No. 7.

The large σ_g's calculated for cascade impactor samples and sieved debris suggest: (1) cascade impactors sample only a small portion (MMAD < 12 μm) of a size distribution that is probably multimodal, and (2) this unknown size distribution is probably formed as a result of several processes including vaporization and mechanical dispersion. Additional evidence on the multimodal aerosol size distribution is seen in the EAA data and on TEM photomicrographs. Further analyses are required to address the problem of a multimodal distribution including more detailed interpretation of the data from the electrical aerosol analyzers, condensation nuclei counters and electrostatic precipitator samples.

REFERENCES

1. Findley, N. C., D. C. Aldrich, S. L. Daniel, D. M. Erickson, C. Henning-Sacks, P. C. Kaestner, N. R. Ortiz, D. D. Sheldon, J. M. Taylor and S. F. Herreid, Transportation of Radionuclides in Urban Environs: Draft Environmental Assessment, NRC Research and Development Report, NUREG/CR-0743, SAND79-0369, Sandia National Laboratories, Albuquerque, NM, July 1980.

2. I. B. Wall, et al, Overview of the Reactor Safety Consequence Mode, NUREG 0340, U. S. Nuclear Regulatory Commission, Washington, DC, October 1977.

3. Mercer, T. T., M. I. Tillery and G. J. Newton, "A Multi-State Low Flow Rate Cascade Impactor," J. Aerosol Sci. 1: 9-15, 1970.

4. Newton, G. J., O. G. Raabe and B. V. Mokler, "Cascade Impactor Design and Performance," J. Aerosol Sci. 8: 339-347, 1977.

5. Morrow, P. E. and T. T. Mercer, "A Point-to-Plane Electrostatic Precipitator for Particle Size Sampling," Am. Ind. Hyg. Assoc. J. 25: 8-12, 1964.

The work described in this paper was not funded by the U.S. Environmental Protection Agency. The contents do not necessarily reflect the views of the Agency and no official endorsement should be inferred.

Paper 4

CHARACTERIZATION OF SUSPENDED PARTICLES IN THE SPACE SHUTTLE EXHAUST CLOUD

David C. Woods
NASA Langley Research Center

Raymond L. Chuan
Brunswick Corporation

ABSTRACT

Particles in the exhaust cloud, formed from the launching of the Space Shuttle on April 16, 1981, were sampled and characterized. Measurements were made in situ from aboard a small twin engine aircraft, instrumented with particle and gas sensors, as it made multiple passes through the cloud. Mass concentrations and particle size distributions were measured with a multistage impactor which contained a piezoelectric crystal microbalance in each stage for sensing mass as a function of particle diameter. An integrating nephelometer was used to measure scattering coefficient and to indicate when the aircraft entered and exited the cloud. Particles, collected in the various stages of the impactor, were analyzed by scanning electron microscopy and energy dispersive x-ray analysis to determine particle shape and elemental composition.

Two of several cloud segments which separated and moved in different directions at different altitudes were sampled. The size distributions measured in both cloud segments were monomodal. The first segment had a peak mass concentration at 0.11 μm geometric mean diameter and the second segment had a peak mass concentration at about 5.4 μm geometric mean diameter. Scanning electron microscope photographs showing agglomerates, consisting of a number of individual particles stuck together, suggest that coagulation may contribute to the 5.4 μm mode. Particles, approximately spherical in shape and containing aluminum, were found in all stages of the impactor covering a size range from ~0.11 to greater than 40 μm geometric mean diameter. These particles are presumed to be Al_2O_3 produced from the burning of the solid propellent which contains aluminum. Among the submicron size particles, in addition to aluminum, there were abundant amounts of sodium, sulfur, chlorine, potassium, and zinc with traces of calcium and iron.

INTRODUCTION

Since 1972, studies on the effluents from launch vehicles with solid propellent motors (Titan III) have been conducted by the National Aeronautics and Space Administration (NASA). Measurements from aboard a light aircraft equipped with sampling instruments (1) have been made during selected launches of Titan III vehicles in their low altitude exhaust clouds (ground clouds). These studies were aimed at determining possible tropospheric and ground-level environmental effects and providing data for use in developing dispersion models for predicting exhaust cloud behavior. Since the booster for the Space Shuttle includes two strap-on solid propellent motors, and because of the expected high frequency of Shuttle launches, it is considered essential to study and characterize Shuttle effluents and assess their possible environmental effects. NASA is now applying some of the measuring techniques developed for the Titan studies to measure and characterize effluents from Shuttle. Measurements were conducted when Space Shuttle I was launched on April 12, 1981.

The solid propellent rocket motor consists of an ammonium perchlorate oxidizer, an aluminized synthetic-rubber binder fuel, and various other additives to stabilize mass and to control the burning rate. The major constituents after combustion are hydrogen chloride (HCl), water vapor (H_2O), and aluminum oxide (Al_2O_3) particles. During the Shuttle I launch, HCl and Al_2O_3 particles were sampled in the exhaust cloud. The results of the HCl measurements are reported in reference 2. In this report, results of size distribution measurements (mass versus particle diameter) of the suspended particles in the cloud are presented.

It is believed that the Al_2O_3 particles and foreign debris particles entrained in the cloud play important roles in the evolution and dispersion of the cloud. For example, very large particles (>100 μm diameter) are expected to rain out of the cloud rapidly and sediment to the ground within a few kilometers of the launch site. Submicron particles, on the other hand, may serve as nuclei for condensation of the HCl vapor, thereby forming acid droplets which could grow and precipitate out along the cloud path. Coagulation among the particles will contribute to particle growth, causing a time varying size distribution and possibly forming particles large enough to be eventually removed from the cloud by settling. A possible deleterious effect on local agriculture may result. In addition, submicrometer- and micrometer-size particles may possibly reach stratospheric altitudes and remain suspended for long periods of time. It is, therefore, of interest to investigate the possible effects on climate, through scattering and absorption of solar and terrestrial radiation, by an accumulation and global distribution of particles in the stratosphere resulting from many Shuttle launches. Other concerns are the possible pulmonary effects on man and animals and possible participation of particles in chemical and physical processes with other constituents of the exhaust cloud.

Our efforts were focused on measuring the size distribution of these particles by use of an airborne cascade impactor with a real time measuring capability. Some limited post-flight analyses (Scanning Electron Microscopy (SEM)) have been performed on the size-segregated particles captured by the impactor. The scattering coefficient in the ambient air and in the exhaust cloud was measured with an integrating nephelometer. Selected results and discussion from these measurements are presented herein.

Measurements

The Space Shuttle I, "Columbia," was launched from the Eastern Test Range on April 12, 1981. After lift-off, the exhaust plume, because of weak inversion conditions, split into several cloud segments that moved in different directions and at different altitudes. The sampling aircraft (Cessna 402) penetrated one cloud segment (cloud A) at approximately 8.5 minutes after lift-off and followed it with repeated penetrations at roughly 2- to 5-minute intervals for about 37 minutes. This cloud moved in a northerly direction while rising from an altitude of 650 meters to 950 meters. The relative humidity in this cloud was about 60 percent. A second cloud segment (cloud B) moving eastward at a higher altitude, between 1350 and 1880 meters, was similarly sampled from 49 minutes after lift-off to 2 hours and 8 minutes after lift-off. This was a much drier cloud with a relative humidity of about 15 percent.

An integrating nephelometer aboard the aircraft measured scattering coefficient (b_{scatt}) in the ambient air and in the exhaust cloud. The scattering coefficient is related to aerosol concentration and, therefore, serves as an excellent means of mapping the cloud profile in addition to providing a rough indication of particle concentration. In figures 1(a) and 1(b), plots of b_{scatt} versus time after launch, as the aircraft flew through the two different cloud segments, are shown. The peaks and valleys in the curve are indicative of the patchiness of the cloud, indicating that the aerosol distribution is not symmetrical. In general, the mean value of b_{scatt} per pass through the cloud decreased as time progressed, suggesting that the cloud was expanding or dispersing with time. However, it was not possible to obtain an expression for decay because the exact path through the cloud center was not flown during each pass. For example, on one pass the aircraft may have flown through the center of the cloud and on another pass it may have flown near the edge, where the concentration would have been lower.

The particle size distributions were measured during each pass through the cloud by sampling the particles with a quartz crystal microbalance (QCM) cascade impactor (3). The QCM separates the particles into ten size intervals by inertial impaction. The mass of the particles that impact each stage of the cascade is measured in real time by a piezoelectric microbalance. The QCM covers a size range of 0.11 to greater than 40 μm geometric mean aerodynamic diameter.

Tables I(A) and I(B) list the mass concentration per log size interval ($\Delta C/\Delta \log D$), as measured by the QCM in cloud A and cloud B at various times after lift-off. Because of readout problems associated with liquid droplets impacting in stages 1 and 2 of the impactor, no useful data were obtained on concentrations for particles larger than 10.7 μm diameter. Size distribution plots ($(\Delta C/C)/\Delta \log D$ versus D) are shown in figure 2(a) for three passes through cloud B. ΔC is the mass concentration in a given stage of the

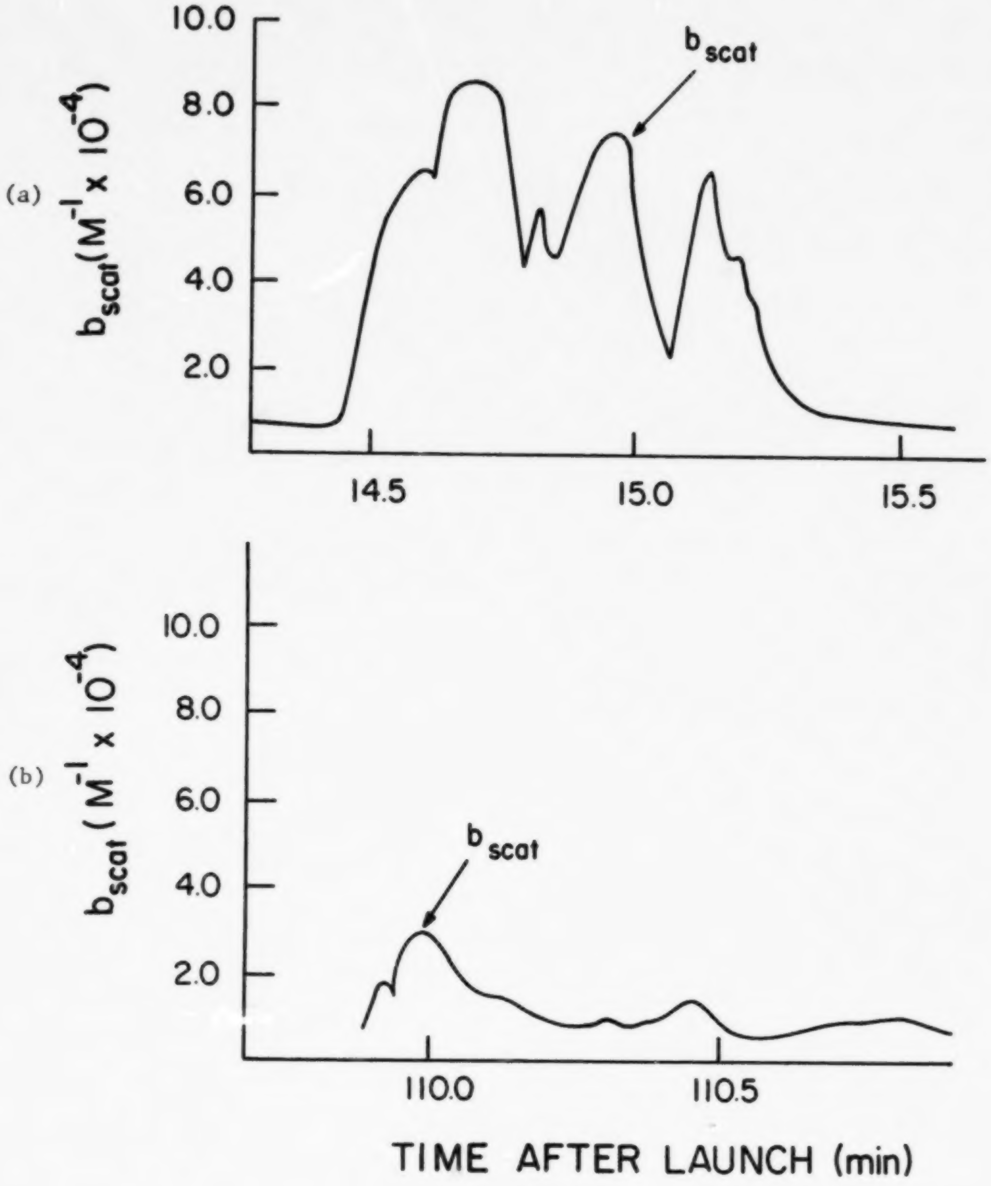

Figure 1. Scattering coefficient plots as a function of time after liftoff of Space Shuttle I measured with an integrating nephelometer in (a) cloud A and (b) cloud B.

TABLE I. MASS CONCENTRATION PER LOG SIZE INTERVAL MEASURED IN EACH STAGE OF THE QCM IMPACTOR. (A) FOR CLOUD A AND (B) FOR CLOUD B. ESTIMATED UNCERTAINTY IN MASS CONCENTRATION IS <1 $\mu g m^{-3}$.

($\Delta C/\Delta \log D$ μg m^{-3} μm^{-1})

		(A)			(B)		
		Pass 1	Pass 3	Pass 6	Pass 11	Pass 15	Pass 20
QCM stage	GMD (μm)	8.5 min AL*	19.1 min AL	31.1 min AL	57.8 min AL	95.6 min AL	109.8 min AL
3	10.7	34	2	0	40	30	18
4	5.4	12	2	0	163	152	110
5	2.6	21	3	4	66	70	50
6	1.32	18	6	5	68	68	22
7	.69	0	4	10	27	34	18
8	.33	19	10	9	11	8	6
9	.17	172	145	133	31	18	8
10	.11	321	229	203	22	22	19

*After lift-off

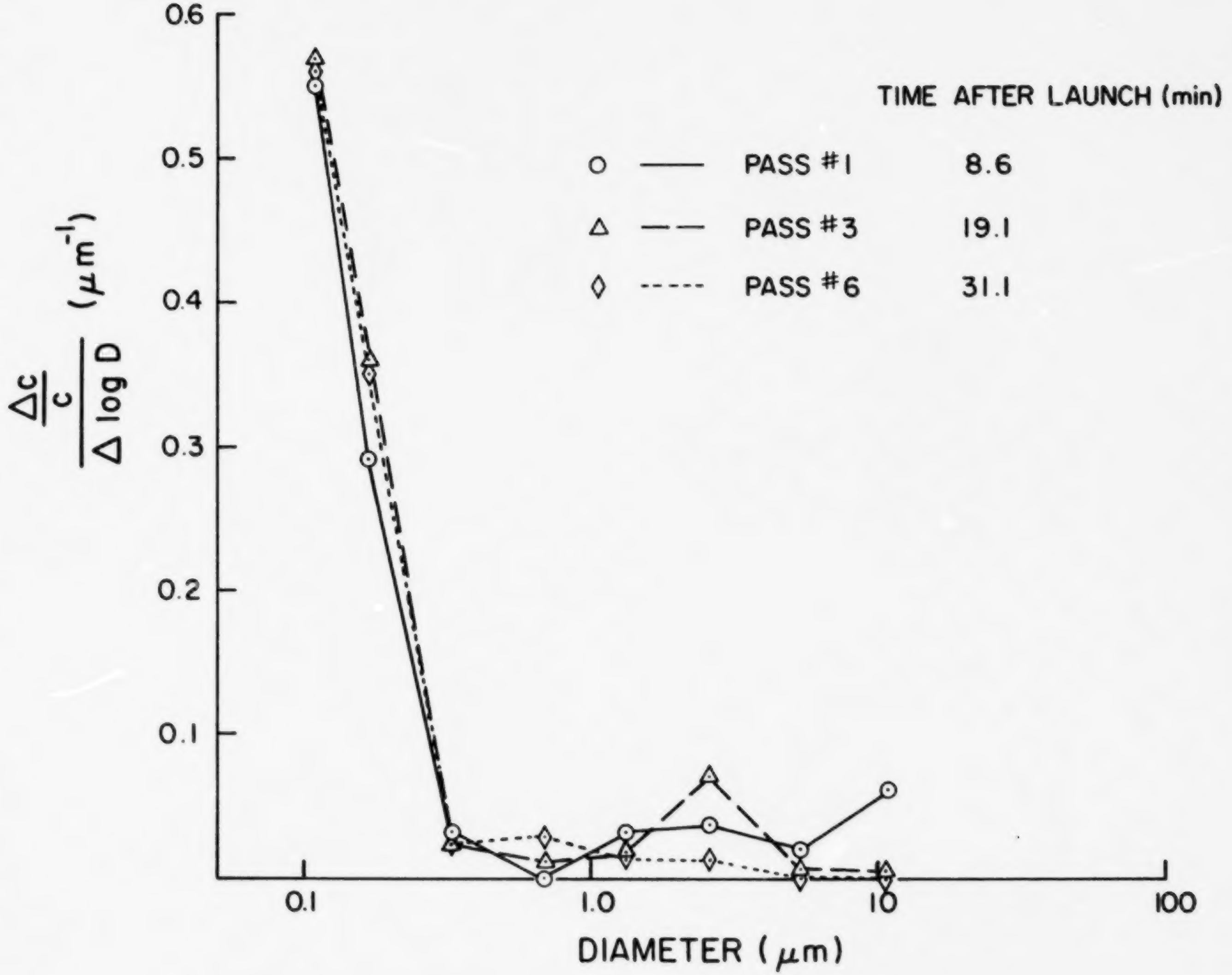

Figure 2(a). Size distribution plot for cloud A of normalized mass concentration per log size interval $\frac{\Delta C}{C}$ log D as a function of particle diameter D.

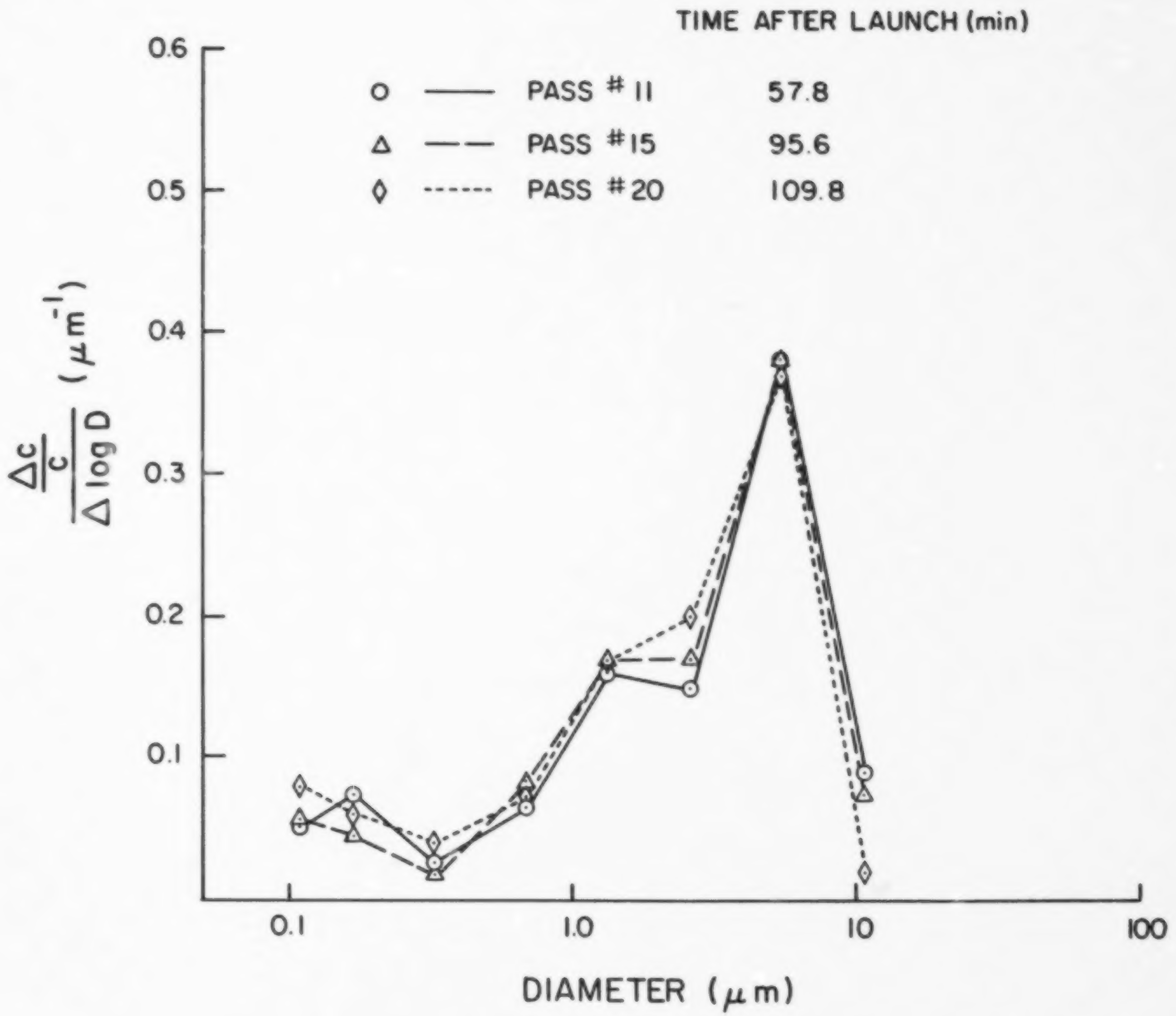

Figure 2(b). Size distribution plot for cloud B or normalized mass concentration per log size interval $\frac{\Delta C}{C}$ log D as a function of particle diameter D.

impactor; C is the total concentration summed over all sizes; and D is the geometric mean aerodynamic diameter. Figure 2(a) and the data in Table I(a) show that the size distributions measured in cloud A are all very similar. There is a relative abundance of very small particles. The peak concentration at 0.11 μm diameter or less represents at least 55 percent of the total mass summed over all sizes. More than 85 percent of the mass falls in the size range less than 0.17 μm diameter.

In sharp contrast to the size distributions in cloud A, the size distribution in cloud B (fig. 2(b)) has peak concentrations near 5.4 μm diameter with more than 35 percent of the mass at that size. In measurements of Titan exhaust clouds, bimodal size distributions were found (4) in contrast to the two single mode distributions found in the two separate cloud segments here. However, some of the Titan bimodal size distributions have peaks occurring at about the same sizes (0.11 and 5.4 μm geometric mean diameter) as were observed in the single mode distributions here (5). It is probable that the two cloud segments developed differently because they mixed with different types of air masses. There was, for example, a noted difference in altitude and relative humidities in the two clouds with cloud A having about 60 percent relative humidity and cloud B having about 15 percent relative humidity. It appears that coagulation may have contributed to the peak at 5.4 μm in cloud B. Evidence of coagulation is seen by the agglomerate in the SEM photograph in figure 3. These particles show only Al in the energy x-ray spectra and are presumed to be Al_2O_3 because of their shape. Note that the b_{scatt} values for cloud A are much higher than cloud B, which is consistent with the preponderance of small particles in cloud A versus cloud B since the nephelometer, and visibility, are much more sensitive to smaller particles.

The relatively low concentrations of particles larger than 10 μm, as indicated by the size distribution plots in figures 2(a) and 2(b), suggest that larger particles may not be present in the cloud. However, particles larger than 40 μm were found in stage 1 of the cascade impactor, as shown in figures 4(a) and 4(b). These large particles consist of smaller Al_2O_3 spheres which apparently combined in the cloud by coagulation. It was not possible to quantify these particles by mass because of the readout problems in stages 1 and 2 mentioned earlier. Compared to the smaller particles, the number of these large ones is relatively small, but because of their large size, the relative mass could be significant.

The small single spherical particles surrounded by the dark spots in figure 4(a) are Al_2O_3 spheres. The dark spots are thought to be caused by liquid coatings of HCl on the particles which later evaporated leaving the dark stains. There is also etching of the nickle electrode in these regions apparently caused by the HCl. Thus, we see evidence of the HCl condensing on the particles forming HCl droplets.

Spherical-shaped particles, showing energy dispersive x-rays for aluminum only, were found in stages 4, 5, 6, and 7, corresponding to geometric mean diameters of 5.4, 2.6, 1.3, and 0.69 μm, respectively. Figure 5(a) is an SEM photograph showing an example of these particles in stage 6. Figure 5(b) shows an aluminum mapping. The light spots indicate the presence of aluminum.

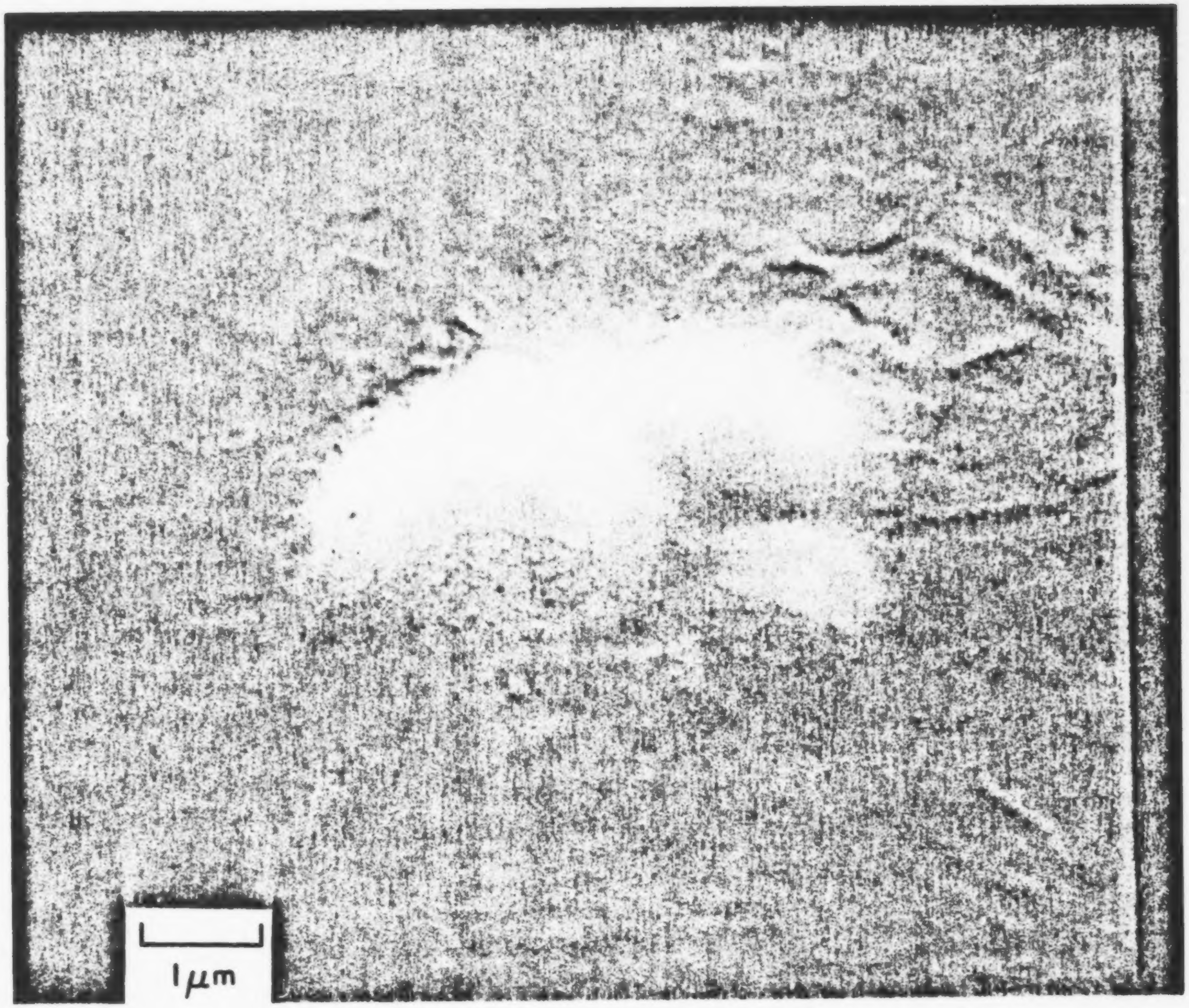

Figure 3. Scanning electron microscope photograph of seven aluminum oxide particles that coagulated and formed one large particle. These particles impacted in stage 4 of the QCM impactor which corresponds to a geometric mean aerodynamic diameter of 5.4 μm.

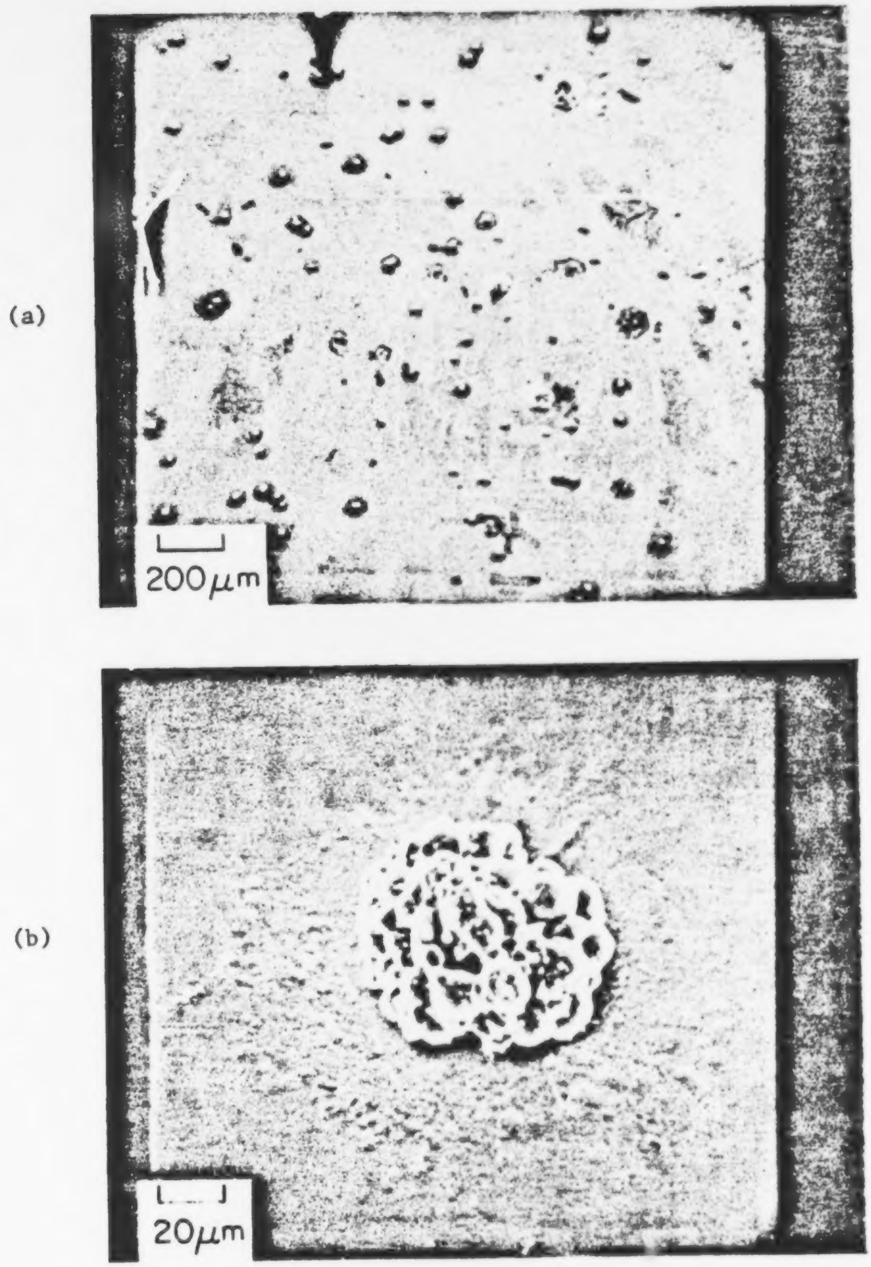

Figure 4(a). Scanning electron microscope photograph of aluminum oxide particles collected in QCM stage 1. Several of the large agglomerates are larger than 40 µm diameter. (b) Higher magnification of the large particle near the center of (a).

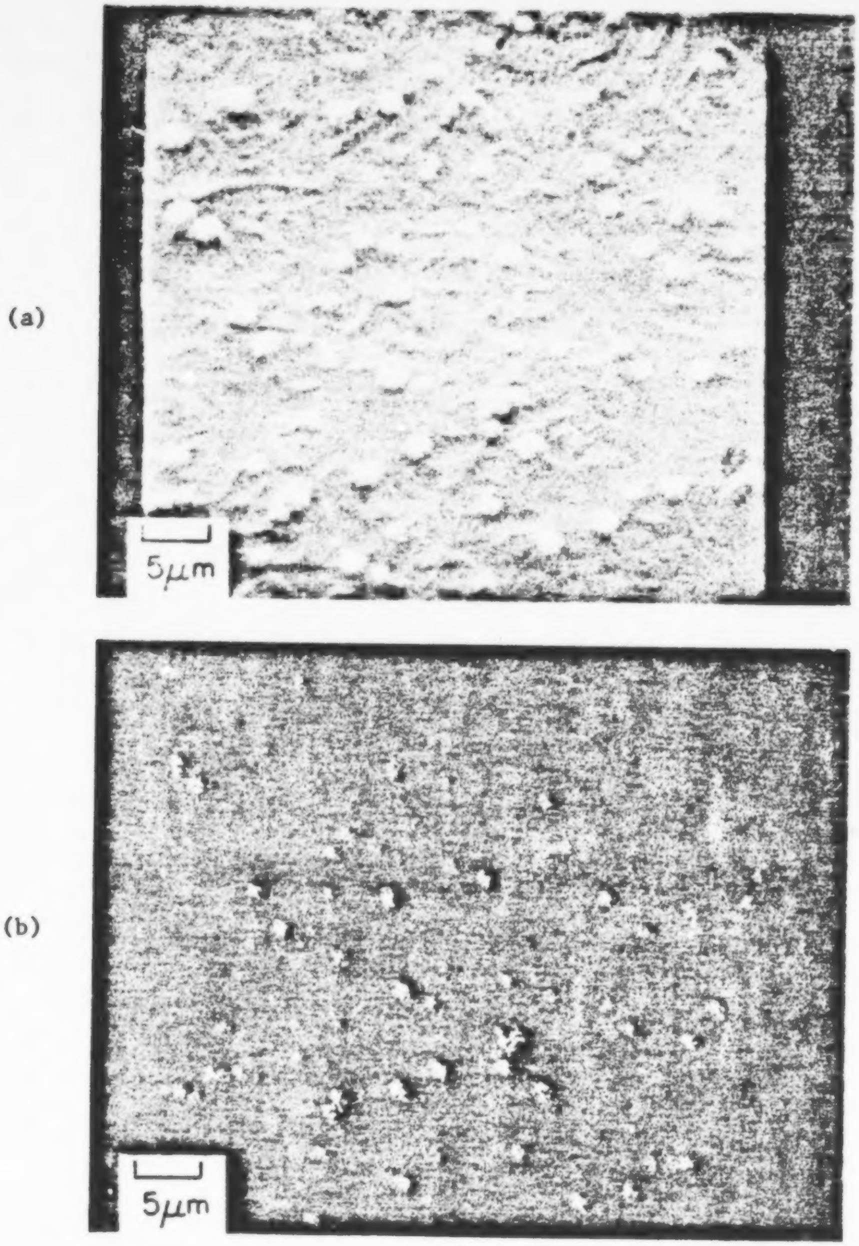

Figure 5(a). Scanning electron microscope photograph of aluminum oxide particles collected in stage 6 of the QCM impactor corresponding to a geometric mean aerodynamic diameter of 1.32 μm. (b) An x-ray energy mapping for aluminum of particles in (a).

These are presumed to be Al_2O_3 particles from combustion. Mixed with these Al_2O_3 particles in stages 5 and 6 is a background of amorphous material which shows a complex x-ray spectrum indicating the presence of: Na, Mg, Al, S, Cl, Ca, and Fe. These same materials have been found in the same size ranges in Titan exhaust clouds (6). In impactor stages 8, 9, and 10, corresponding to geometric mean diameters of 0.33, 0.17, and 0.11 μm, the morphology of the material becomes very complex and irregular with both solids and liquids present. X-ray energy scans show Na, S, Cl, Fe, Zn, and K, in addition to the Al. These elements are likely present in the background air.

CONCLUSIONS

Measurements in two separate segments of the Space Shuttle exhaust cloud revealed a difference in particle size distributions in the two clouds. The lower altitude cloud segment (between altitudes of 650 and 950 meters) was sampled up to 37 minutes after lift-off and had a peak mass concentration at 0.11 μm geometric mean diameter. A second cloud segment (between altitudes of 1350 and 1880 meters) was sampled from 49 minutes until more than 2 hours after lift-off and had a peak mass concentration at 5.4 μm. Post flight analysis of the size-segregated particles revealed the presence of some particles larger than 40 μm diameter. Evidence of coagulation among particles in the cloud is seen from scanning electron microscope photographs. The particles larger than 2.6 μm diameter are almost all Al_2O_3 spheres while the Al_2O_3 spheres 2.6 μm and smaller are mixed with amorphous materials consisting of Na, Mg, Al, S, Cl, Ca, and Fe. In addition, there is evidence of HCl condensing on the Al_2O_3 particles forming large droplets.

There has recently been some concern shown over the possible effects of the large particles containing HCl dropping out of the cloud. Future efforts will be directed toward quantifying these large particles in the cloud, and flights underneath the cloud will be made to detect the dropout of these particles.

REFERENCES

1. Wornom, D.E., D.C. Woods, M.E. Thomas, and R.W. Tyson. Instrumentation of Sampling Aircraft for Measurement of Launch Vehicle Effluents. NASA TMX-3500, 1977.

2. Sebacher, D.I., G.L. Gregory, R.J. Bendura, D.C. Woods, and W.R. Cofer. Hydrogen Chloride and Particulate Measurements in the Space Shuttle Exhaust Cloud. Proceedings of the 1981 Annual Meeting of the JANNAF Safety and Environmental Protection Subcommittee, Nov. 17-19, 1981.

3. Chuan, R.L. Rapid Measurement of Particulate Size Distribution in the Atmosphere. Fine Particles, Aerosol Generation, Measurement, Sampling, and Analysis. Edited by Benjamin Y.H. Liu, Academic Press, Inc., 1976.

4. Woods, D.C. Rocket Effluent Size Distributions Made With a Cascade Quartz Microbalance. Fourth Joint Conference on Sensing of Environmental Pollutants, Nov. 6-11, 1977.

5. Woods, D.C., and R.L. Chuan. Aerosol Characterization With a Quartz Crystal Microbalance Cascade Impactor. Proceedings, Advances in Particle Sampling and Measurement, Daytona Beach, FL, Oct. 1979.

6. Chuan, R.L., and D.C. Woods. Morphology and Elemental Composition Analysis by Size of Rocket Particulate Effluent. Proceedings of the Fourth Joint Conference on Sensing of Environmental Pollutants, Nov. 6-11, 1977.

The work described in this paper was not funded by the U.S. Environmental Protection Agency. The contents do not necessarily reflect the views of the Agency and no official endorsement should be inferred.

Paper 5

RECENT RESEARCH IN THE FIELD OF AEROSOL SAMPLING, MEASUREMENT, AND CHARACTERIZATION IN EUROPEAN COUNTRIES

K. R. Spurny
Frauenhofer Institute for Toxicology and Aerosol Research

H. Fissan
Aerosolmesstechnik, University of Duisburg

ABSTRACT

This review includes a general survey of the most important institutions working in the aerosol field in the West European countries as well as in the East European countries. Eight new aerosol measurement and analysis techniques developed in Western Europe recently are described and discussed. Five of these procedures are optical methods for the measurement of aerosol concentration and particle size distribution and three methods deal with chemical aerosol analysis.

INTRODUCTION

Aerosol physics and chemistry as well as colloid chemistry have their origin in Western Europe. Both these disciplines, of which the first can be considered as a branch of the second, started their development in the second part of the 19th century. T. Graham, who in 1861 studied membrane diffusion, is considered to be a founder of classical colloid chemistry and J. Aitken, who discovered in 1880 the function of atmospheric condensation nuclei, can be considered as the first aerosol chemist. England was therefore the womb of both these disciplines[1].

AEROSOL RESEARCH IN EUROPE

Theoretical as well as applied aerosol research has been developed in Europe in the first part of this century, but an extensive development started mainly since 1950. Austria, Germany, Great Britain, France, and Italy can be considered as the highest developed European countries in this field. Nevertheless, many smaller European countries, such as Belgium, the Netherlands, Denmark, and Sweden, possess non-negligible activities in applied aerosol research.

In East European countries, the highest development level in the field of theoretical and applied aerosol physics and chemistry is reached in Russia.

This research started also in the first part of this century and since 1950 has been disseminated in many university and governmental institutes. In other Eastern satellite countries mostly only applied aerosol research has been developed in some state institutions. This has been the case, e.g., in East Germany, Czechoslovakia, Poland, Hungary, and Bulgaria.

Three important European schools of aerosol physics have already reached international reputations - the Vienna School of Aerosol Physics (led by O. Preining), the French School (founded by J. Bricard) and the English School (led by C. N. Davies). No crystallized leading center or school exists up to now in Germany. But the entire research activities are very broad. Applied aerosol research is dominant. The most important aerosol groups are at the University in Mainz (founded by C. Junge), at the University of Duisburg (led by H. Fissan), at the University of Karlsruhe (led by F. Löffler), at the Technical University in Berlin (led by G. W. Israel) and at the University of Göttingen (led by J. Porstendörfer). Many non-university institutions are working in the field of applied aerosol research; e.g., a working group at the Atomic Research Center in Karlsruhe (led by W. Schikarski), a working group in the Institute of the Society for Radiation and Environmental Research in Frankfurt (led by W. Stahlhofen), a department of aerosol physics in the Fraunhofer Institute of Toxicology and Aerosol Research in Grafschaft (led by W. Stöber).

The majority of German and European aerosol scientists are integrated in the Association for Aerosol Research, which has its residence in Germany, and cooperates with the Journal of Aerosol Science, edited by C. N. Davies in London. This journal is also the associated journal with the Association for Aerosol Research. Important aerosol research activity in Italy has been developed in the Laboratorio di Fisica Sanitaria of the Italian Atomic Energy Commission in Bologna (led by V. Prodi).

Basic aerosol research in Russia has an old tradition and a high scientific level. Three most important aerosol schools can be distinguished in Russia - all situated in Moscow. The School of Aerosol Physics at the Karpov Institute of Physical Chemistry (founded by N. A. Fuchs), the Aerosol Filtration School at the same institute (founded by I. Petryanov), and the School of Physical Chemistry of Aerosols at the Academy of Sciences (founded by B. Deryaguin). Applied aerosol research has been developed at many state research institutes and institutions. Military aerosol research has the biggest research centers in the Karpov Institute and in some institutes of the Academy of Science in Novosibirsk.

A serious "brake" on aerosol research in Russia and in other East European countries seems to be a great technical underdevelopment in the field of modern equipment and in close contacts with West European and American aerosol researchers.

SOME NEW EUROPEAN EQUIPMENT AND METHODS

It is almost impossible to present in one short review a representative picture of the newest methods and equipment for aerosol sampling, measurement, and characterization in Europe. It is possible to say that applied European aerosol research has almost the same goals and practical motivations as similar research in the U.S. Also in Europe, the most important atmospheric environmental research is dealing with the problem of development of new energy sources: problems of ambient air contamination with fly ash, asbestos and mineral fibers, with organic carcinogenic and mutagenic pollutants, with radioactive aerosols, with the problem of surface dust sources, etc. Also the problems of new types of traffic aerosols (e.g., the exhaust aerosols of diesel engines) play an important role in the research activities.

Eight new aerosol measurement and analysis techniques developed in Western Europe recently were chosen in this review. Five of them are optical methods for the measurement of aerosol concentration and particle-size distribution and three methods deal with the chemical analysis of aerosols. Two of the optical methods were developed in Austria, and three in West Germany. The new methods for chemical analysis of aerosols were developed in West Germany and the Netherlands.

OPTICAL METHODS

The five optical methods describe the application of a new Aerosol-Telephotometer (ATP), of a Size Analyzing Nuclei Counter (SANC), of an Aerosol Filter-Photometer (AFP), a Multiple Color Photosedimentometer (MCPS) and an Optical Particle Counter-Laser Doppler Anemometer Combination (OPC-LDA).

AEROSOL TELEPHOTOMETER (ATP)

This equipment was developed and described at the Institute for Experimental Physics of the Technical University of Vienna by H. Horvath[2,3].

The extinction of light in the atmosphere is due to aerosol particles and gas molecules. Both absorption and scattering cause extinction of light. The extinction of radiation in the atmosphere is usually characterized by the extinction coefficient, normally measured in m^{-1} or km^{-1}. The atmospheric extinction coefficient can be measured directly by means of the mentioned telephotometer ATP. Basically the brightness of distant objects is measured with this instrument and compared with the brightness of the horizon; from this the extinction coefficient can be calculated. It permits a quick measurement of the atmospheric extinction coefficient under almost all conditions.

The ATP was built using a commercially available astronomical reflecting telescope with mirrors of approximately 110 mm diameter and 900 to 1200 mm focal length (Figure 1). When used as a telescope, the light enters the instrument, it is reflected on the first mirror, deflected by the second mirror, and forms a real image just outside the tube. This real image is viewed through a magnifying lens. For the purpose of photometry the magnifying lens is removed and replaced by the measuring unit. At the place where the image is formed a small adjustable stop is brought into position. The light passing through the stop is focussed on a photocell, the photocurrent is amplified by the amplifier integrated in the photocell and displayed. The whole system is battery-operated. The angle of view with the smallest stop is 3.8 minutes of arc or 0.0011 radians, thus allowing the measurement of an object 1.1 m in diameter at a distance of 1 km, or 11 m at 10 km.

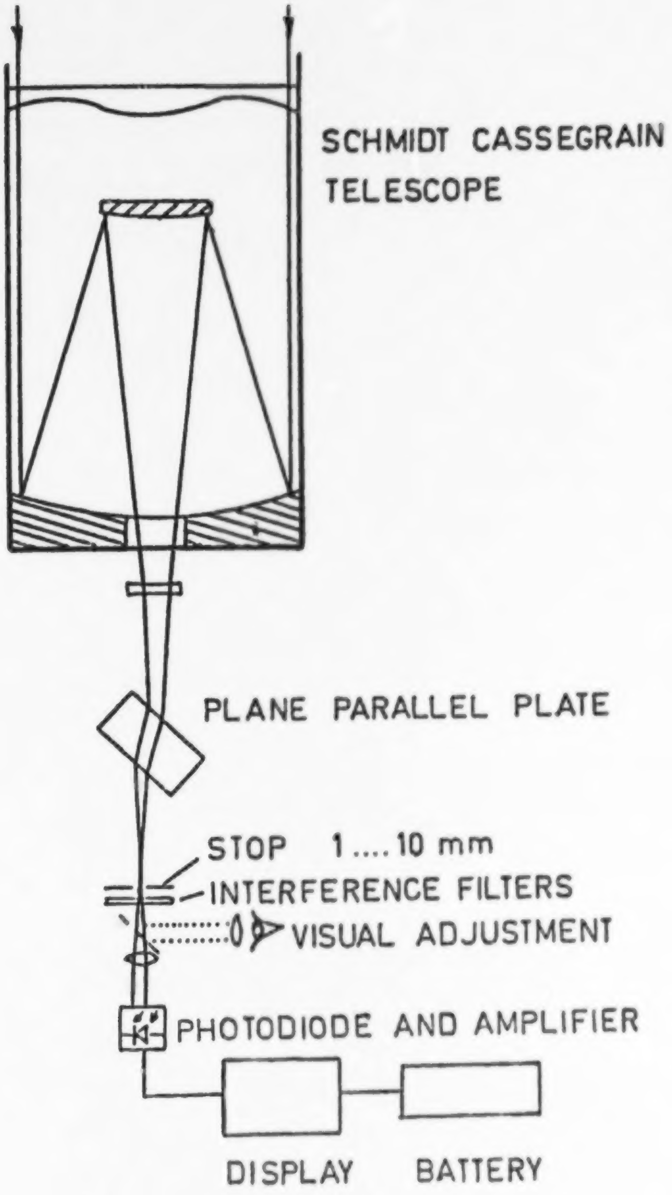
SCHMIDT CASSEGRAIN
TELESCOPE
PLANE PARALLEL PLATE
STOP 1.... 10 mm
INTERFERENCE FILTERS
VISUAL ADJUSTMENT
PHOTODIODE AND AMPLIFIER
DISPLAY
BATTERY

Figure 1. Astronomic reflective telescope used as a telephotometer.

Measurement - By means of the ATP the values of the contrast of the target at zero distance C(o) and of the contrast at the distance x, C(x) are measured. The atmospheric extinction coefficient b can then be determined:

$$C(x) = C(o) \cdot \exp(-b \cdot x)$$

Routine measurements of spectral extinction coefficients over extended periods performed in different locations in Europe have shown that in most cases the extinction coefficient of the particles b_p has a power law dependence with wavelength which can be represented by

$$b_p(\lambda) = k \cdot \lambda^{-\alpha}.$$

The wavelength dependence is most likely caused by the size distribution of the aerosol particles. The particle size parameter α is given by

$$\alpha = 2r\pi/\lambda$$

in which r is the particle radius.

An experimental example of such measurements in the atmosphere of Vienna is demonstrated in Figure 2. The agreement between both methods (filter sampling and extinction measurement) seems to be very good with a correlation coefficient of 0.75.

The measurements performed so far with the ATP have shown that it is a very versatile instrument, allowing measurements both in very clean and heavily polluted areas by selecting objects at a proper distance[4,5].

SIZE ANALYZING NUCLEI COUNTER (SANC)

This equipment was also developed at the Institute for Experimental Physics of the University of Vienna.

The operation of a classical condensation nuclei counter (CNC) is based on heterogenous nucleation of supersaturated vapor on aerosol particles and subsequent droplet growth. Thereby particles which are too small to be detected by most other methods grow to visible size and can be counted by optical techniques. Provided that each growing droplet corresponds to just one aerosol particle, the measured droplet concentration is equal to the aerosol number concentration. In most types of CNC's the required supersaturation is obtained by a fast expansion of a nearly saturated vapor-gas mixture. The number concentration of the formed droplets is then determined either by direct visual counting or by light extinction or light scattering techniques. While visual counting provides absolute number concentrations, most light extinction and light scattering techniques depend on empirical calibration by external reference standards.

The SANC was developed for the measurement of concentration and size in highly dispersed aerosols, as well as for investigation of heterogeneous nucleation and droplet growth in supersaturated vapor. In the SANC a process of controlled fast expansion in a chamber is used. The equipment consists of a humidifier, an expansion chamber, subpressure vessels, and pumps. Humidifier and expansion chamber are separately thermostatted; the connecting

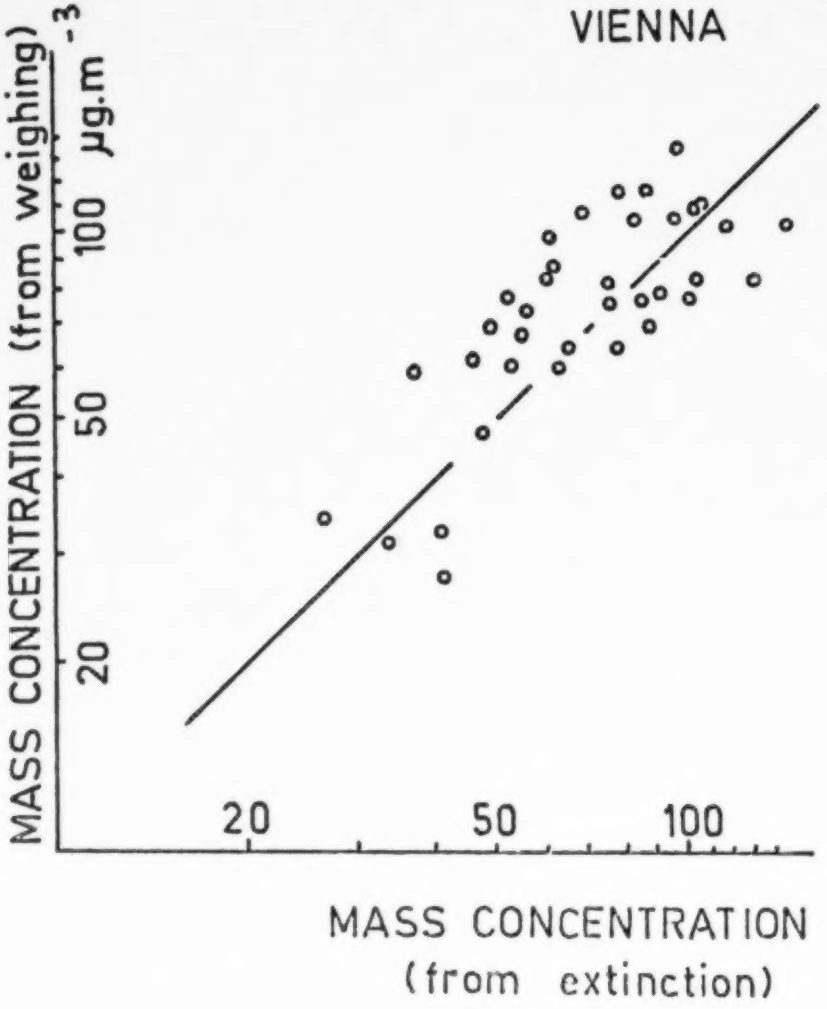

Figure 2. Measured concentration (filter sampling) and mass concentration obtained by optical measurements (extinction).

tubes are heated in order to avoid losses due to vapor condensation. The measuring process is controlled by an electronic control unit in connection with five solenoid valves. The finely dispersed aerosol (nuclei) first passes through the humidifier in order to obtain a nearly saturated vapor-gas mixture and then the humidified aerosol enters the expansion chamber. Subsequently an expansion with a duration of approximately 5-7 ms is facilitated by opening of a solenoid valve and thus connecting the expansion chamber to a subpressure vessel. Thereby vapor supersaturation is obtained in the expansion chamber and heterogeneous nucleation is caused by aerosol particles, acting as condensation nuclei. For observation, the droplets growing in the expansion chamber are illuminated by a He-Ne laser beam. The light flux scattered by the growing droplets is monitored under selectable scattering angles. Furthermore the laser light flux transmitted through the expansion chamber and the total gas pressure are monitored during expansion and droplet growth. These three signals are recorded by a digital transient recorder. Depending on the selected scattering angle, the experimental scattered light flux agrees with theoretical scattered light flux versus size curves calculated by means of Mie theory.

Figure 3 shows schematically the applications of SANC. The condensation process in the expansion chamber EXP is observed optically. The growing droplets are illuminated by a continuous-wave He-Ne laser. The light flux, transmitted through the expansion chamber, is measured by an optoelement OPT. The light flux scattered by the growing droplets under a fixed scattering angle is monitored by a photomultiplier PM with a high-voltage power supply HV. The scattering angle can be varied over a range from 15° to 165° by means of a process controlled step-motor STM. The anode current of the PM is converted into a voltage signal and amplified by a process controlled amplifier PAMP. The scattered light flux varies over several orders of magnitude depending on the scattering angle and the droplet concentration. The total pressure in the expansion chamber is measured by a fast piezoelectric pressure transducer PT with charge amplifier CHA.

The output signals of the optoelement OPT, of the process controlled amplifier PAMP, and of the charge amplifier CHA are recorded simultaneously by a process controlled digital transient recorder TR.

Figure 4 shows a typical set of measured curves. The upper curve shows the total pressure in the expansion chamber and the lower curves show the transmitted and scattered light fluxes as functions of time. After establishing the unique correspondence between experimental and theoretical light scattering extrema, droplet size and droplet concentration can be determined independently. From the position of the experimental light scattering extrema the droplet sizes at specific times can be obtained. On the other hand, from the height of the experimental maxima the droplet concentration can be evaluated.

The SANC can be therefore used for determination of Kelvin-equivalent size distributions of highly dispersed aerosols. To this end, measuring series have to be performed with stepwise increasing supersaturation and otherwise unchanged experimental conditions. Thereby gradually smaller particles are activated as condensation nuclei and cumulative Kelvin equivalent size distributions of the nuclei aerosols are obtained[6].

AEROSOL FILTER-PHOTOMETER (AFP)

This apparatus was developed at the Fraunhofer Institute for Toxicology and Aerosol Research at Grafschaft (Germany)[7].

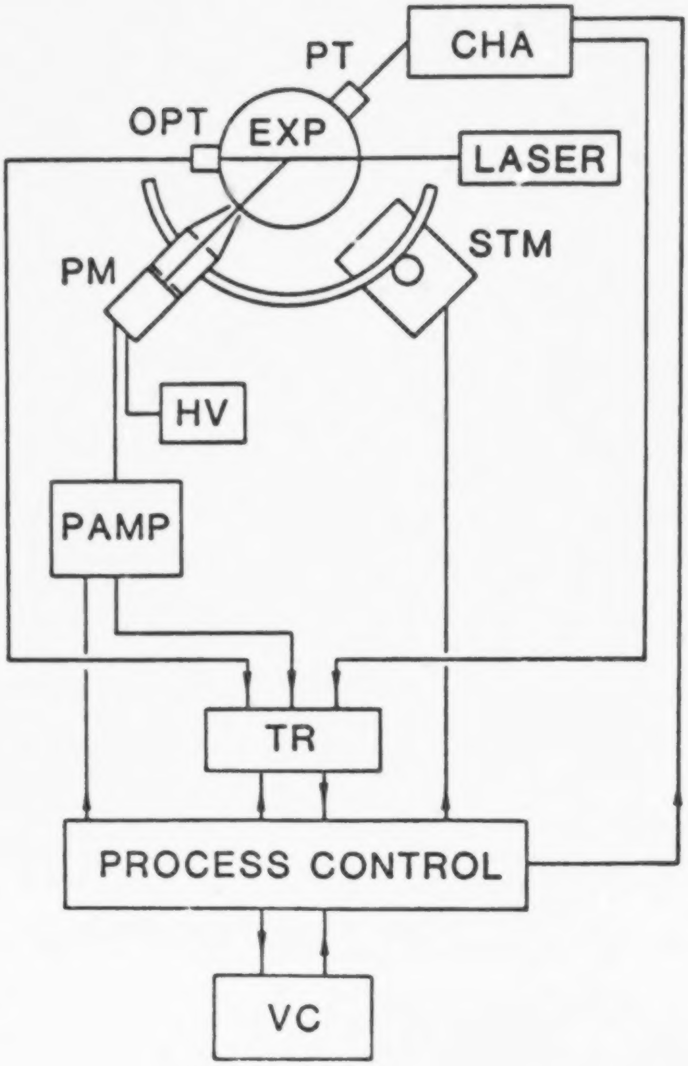
CHA
PT
OPT
EXP
LASER
STM
PM
HV
PAMP
TR
PROCESS CONTROL
VC

Figure 3. Schematic diagram of the SANC (description in the text).

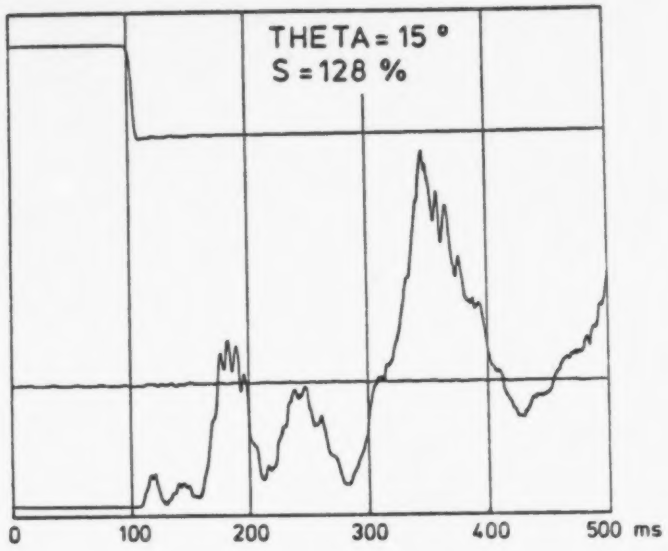

Figure 4. Typical set of measured curves (description in the text).

This method is based on changes in light transmission through metal-coated Nuclepore filters by deposited aerosol particles. Metal coating of smooth Nuclepore filters with their straight pores results in the transmission of light through the pores only. The pore size has to be comparable to the wavelength of the light. In this case wave optics control the light flux through the pores. Particles deposited near the pores are detected by a transmission change while the background transmission of the filter is greatly reduced. The sensitivity of the method is therefore very high. After calibration, the method yields integrated mass, and, by differentiating the output signal with respect to time, instantaneous concentration as well.

The schematic of the portable apparatus is shown in Figure 5. In order to achieve optimum sensitivity, a reference beam method was used. The light of an ordinary incandescent lamp is transmitted as a sample beam through the filter assembly, which continuously collects the particulate phase from the aerosol drawn through the filter by a suction pump. The reference beam is used as a comparative standard in detecting changes in the filter transmission. A chopper disk interrupts periodically both beams; the resulting signal is electronically amplified, rectified, and recorded. Before the measurement, the reference beam has to be adjusted by means of a beam attenuator in such a way that reference - and sample - beam intensities are equal; i.e., the output signal becomes minimal. The equipment has to be calibrated for each type of aerosol. Aerosol deposition on the filter between 2 and 20 $\mu g/cm^2$ can be well measured. Figure 6 demonstrates the view of a portable instrument. Presently a new microprocessor controlled version in being built.

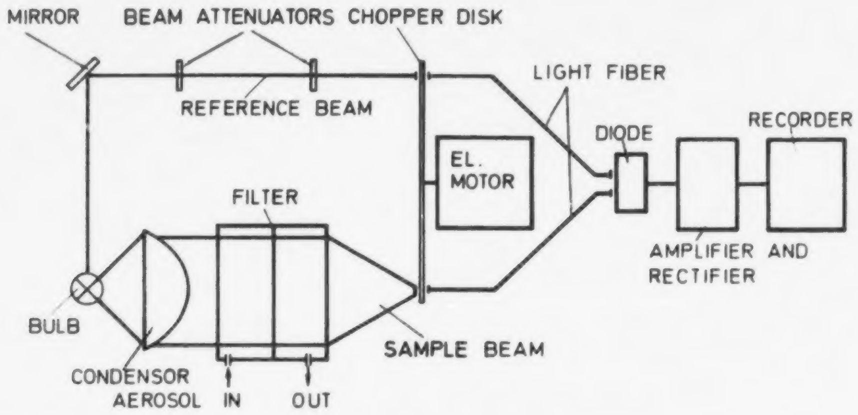
MIRROR
BEAM ATTENUATORS
CHOPPER DISK
LIGHT FIBER
REFERENCE BEAM
DIODE
RECORDER
EL. MOTOR
FILTER
AMPLIFIER AND RECTIFIER
BULB
SAMPLE BEAM
CONDENSOR
AEROSOL
IN
OUT

Figure 5. Scheme of the portable AFP.

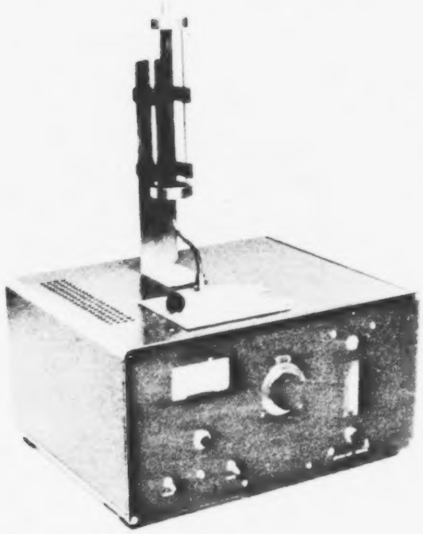

Figure 6. Front view of the portable instrument (AFP).

This new version will allow a real time printout of momentary concentration in $\mu g/m^3$ when a calibration constant has been keyed in.

The applications for the AFP include integrated and time resolved monitoring of various particulate air pollutants as well as occupational exposure monitoring.

MULTIPLE COLOR PHOTOSEDIMENTOMETER (MCPS)

This equipment has been developed and described at the Institute for Mechanical Engineering of the University in Karlsrugh by R. Weichert[8].

The photosedimentation carried out with light of different wavelengths is an alternative method for the particle size analysis of fine powders or of colloidal suspensions of any particulates. The theory of the multiple color photosedimentation is based on the assumption of wavelength-independent optical properties of the analyzed powders or particulates. Particles as small as 1 μm or even smaller can be measured.

The basis of photosedimentation is the attenuation of light by the settling particles. This attenuation, being caused by scattering and absorption, is described by a extinction efficiency which depends on the ratio of particle size to wavelength of the light, on the geometry of the optical measuring device, and on the optical constants, i.e., index of refraction and absorptivity of the analyzed material. A theoretical determination of the extinction efficiency according to the Mie theory was possible under simplifying assumptions. Nevertheless, the extinction efficiency can also be determined experimentally by calibration of a photosedimentometer with a material of known particle-size distribution.

The principle of the photosedimentometer MCPS is schematically shown in Figure 7. The light transmission through the settling suspension is measured at three wavelengths (0.5, 0.6 and 0.75 μm), filtered by three interference filters out of a white light beam. The filters are all mounted on a rotating wheel. The transmission of light through the well-thermostatted suspension is measured at different settling heights (H 1 to H 4, ranging from 6.5 mm to 250 mm). Hence wide-ranging particle sizes can be measured in a reasonable

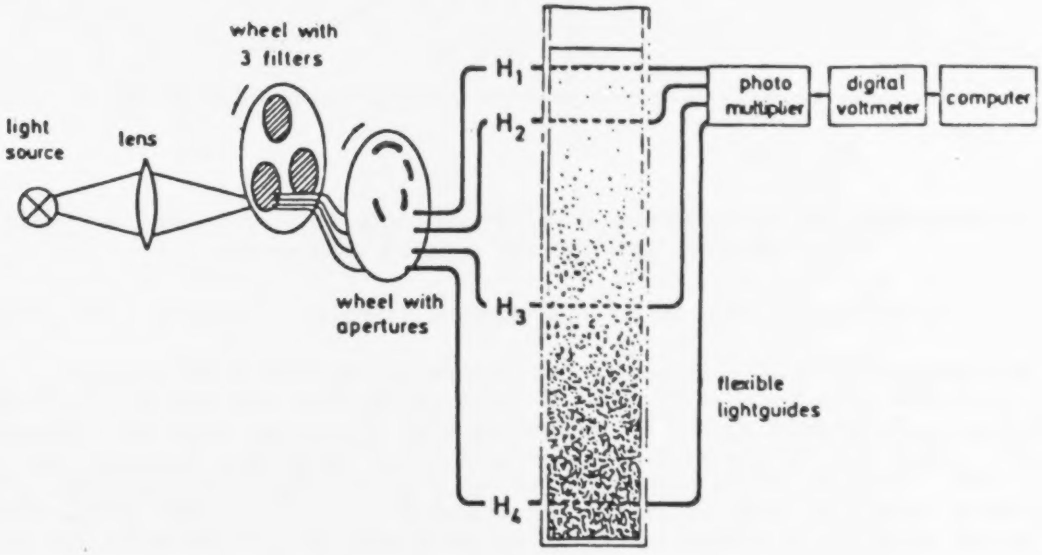

Figure 7. Scheme of the MCPS.

settling time. The light passing through the suspension is detected by a photomultiplier which is followed by a computer controlled digital voltmeter. The light intensities of the three wavelengths, measured at four heights, are stored at programmed time intervals. After the measurement, the stored data are evaluated by the theory.

In Figure 8 the particle-size distribution of a quartz powder, as determined by MCPS, is compared with conventional analysis by a sedimentation balance. The agreement is quite good.

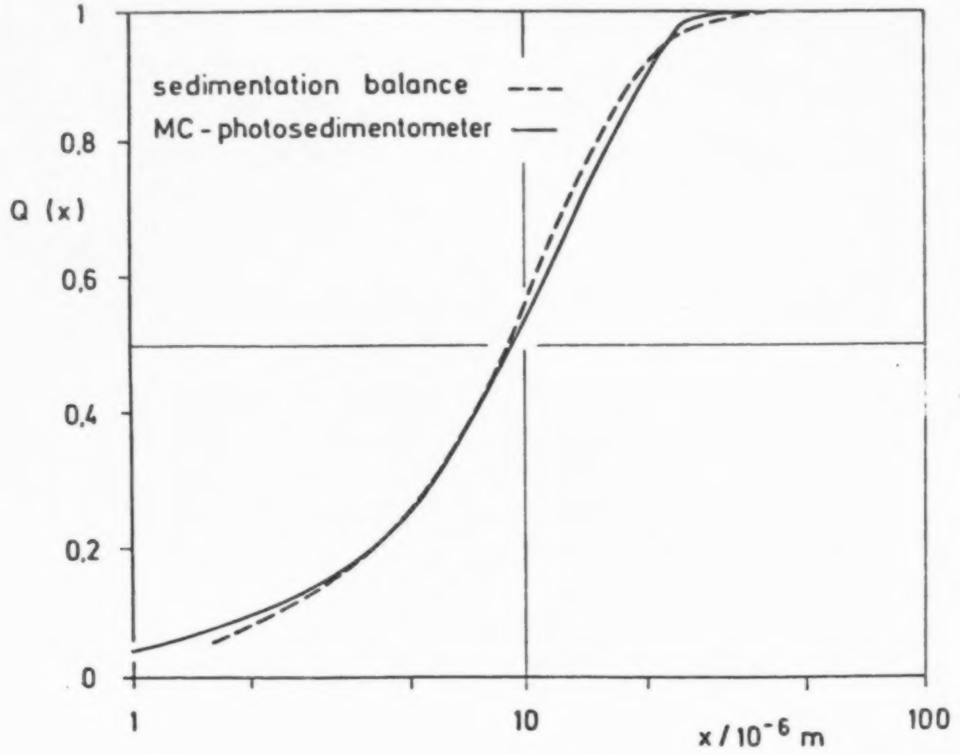

Figure 8. Particle size distribution of a quartz powder as determined by a sedimentation balance and the MCPS method.

COMBINATION OF OPTICAL PARTICLE COUNTER WITH LASER DOPPLER ANEMOMETER (OPC-LDA)

Also at the Institute for Mechanical Engineering of the University in Karlsruhe, an optical particle counter (OPC) has been developed, mainly by Umhauer. The main feature of this instrument, which is commercially available, is its optically determined scattering volume. Thus using a 90°-angle a very small scattering volume (110 µm x 110 µm x 110 µm) can be achieved. The advantage of using such a small scattering volume is that the number concentration can be as high as 10^5 particles/cm^3 with negligible coincidence losses[9].

Errors caused by particles moving through the edge of the scattering volume have been quantified and correction procedures have been developed.

The calibration curve strongly depends on refractive index. Therefore the instrument has been simulated using Mie theory, so that calibration curves can be calculated for spherical particles of known refractive index. For particles of unknown shape and refractive index a calibration procedure using a preimpactor has been developed in Duisburg[10].

B. Ruck from the Sonderforschungsbereich 80 of the University of Karlsruhe has combined the optical particle counter with a laser doppler anemometer (Figure 9). Thus it is possible to measure simultaneously the size and the velocity of a single particle (Figure 10). By measuring many particles, one gets the size distribution and the velocity distribution for particles of the same size (Figure 11).

There is especially interest in information of this kind, for instance in the field of droplet combustion.

CHEMICAL AEROSOL ANALYSIS

Three methods dealing with a new analytical procedure for detection of small amounts of sulfuric acid aerosols, with a thermoanalytical determination of HNO_3, H_2SO_4, and NH_3 in ambient air, and with a new procedure for mass spectroscopic analysis of single particles were selected in this review. A new type of analytical membrane filters made of mica is also mentioned.

SULFURIC ACID AEROSOL ANALYSIS

A new x-ray fluorescence method for the determination of sulfuric acid in sulfuric acid-containing aerosols was developed at the University of Dortmund (West Germany)[11]. The technique makes use of the reaction between sulfuric acid and potassium chloride yielding volatile hydrogen chloride and

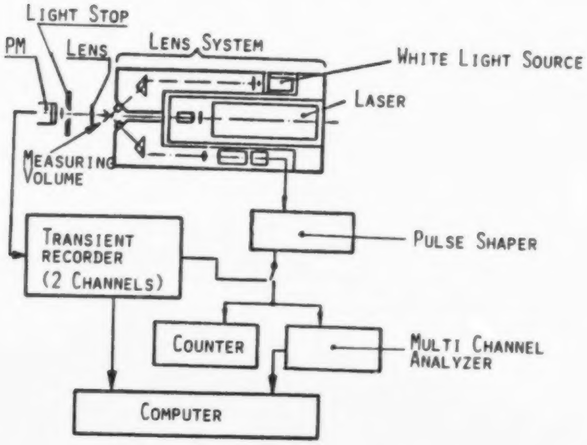

Figure 9. Scheme of combination of OPC (HC 15) with LDA.

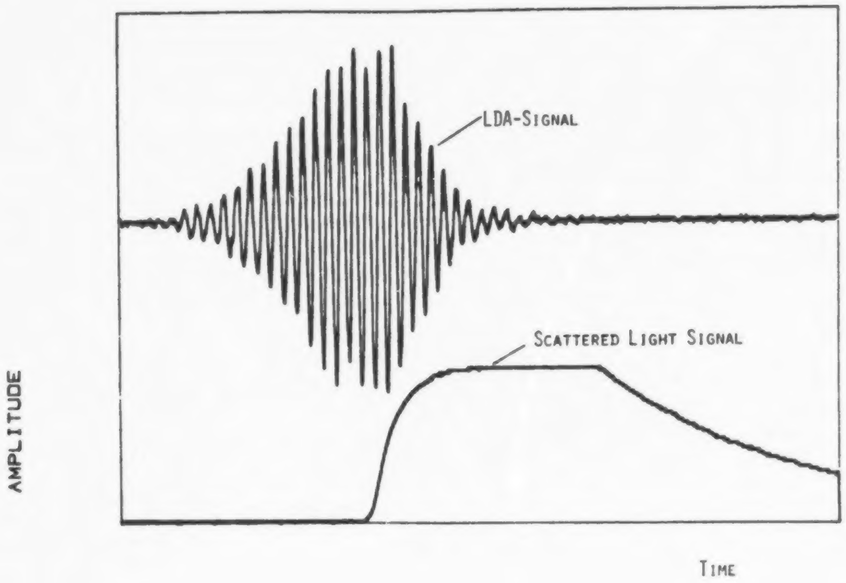

Figure 10. Signals of the combination of OPC (HC 15) and LDA.

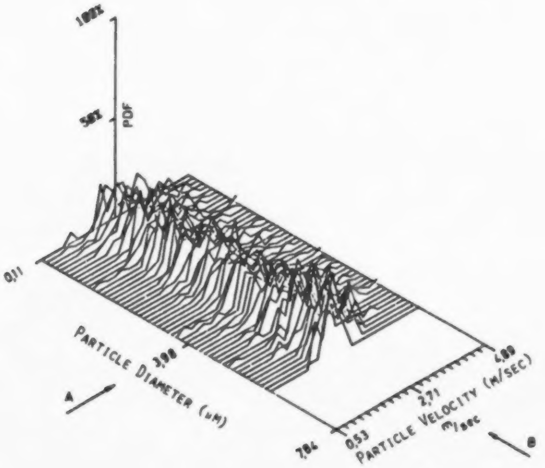

Figure 11. PDF of the particle velocities for different particle size classes.

thus changing the Cl/K-ratio. Nuclepore filters are first loaded with potassium chloride and then used for the collection of the aerosol. The chlorine and potassium x-ray signals are then measured before and after the sampling of the acid aerosol. The decrease of the Cl/K intensity ratio (Figure 12) is taken as a measure for the amount of sulfuric acid collected. SO_2 does not interfere with this procedure.

THERMO-DENUDER ANALYZER (TDA)

A new thermoanalytical method for specification of atmospheric strong acids has been developed and used for the measurement of the $HNO_3/H_2SO_4/NH_3$-system in ambient air[12].

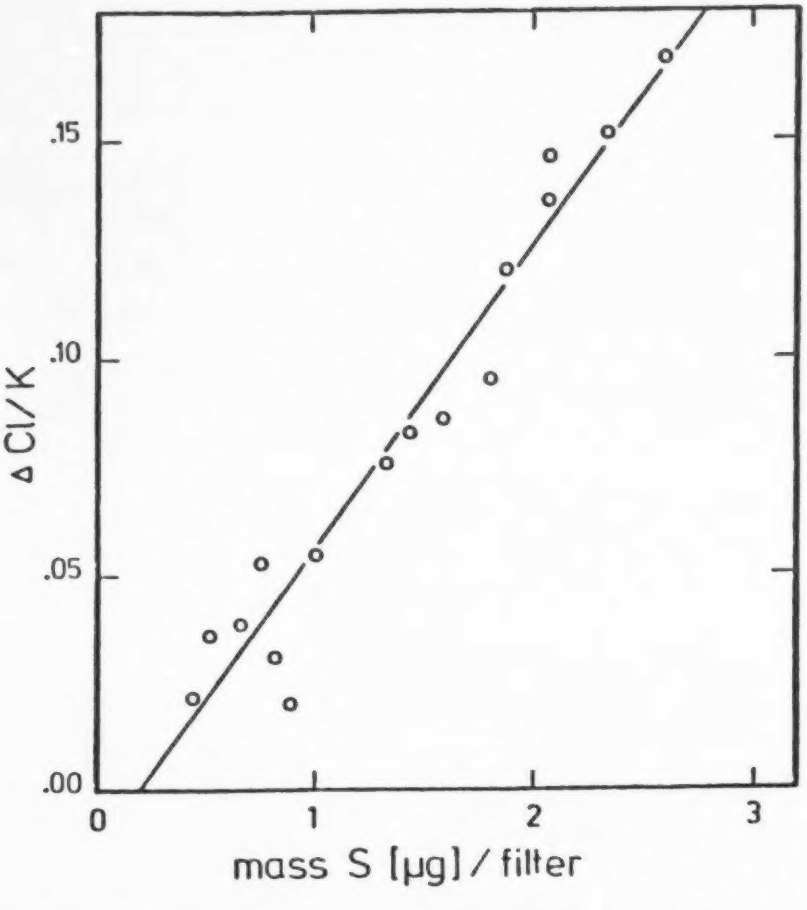

Figure 12. Calibration curve for the determination of H_2SO_4 by measuring the loss of Cl from KCl-loaded nuclepore filter.

A series of coated tubes operating at different temperatures were used to collect selectively nitrate and sulfate containing atmospheric trace compounds as well as free ammonia (Figure 13).

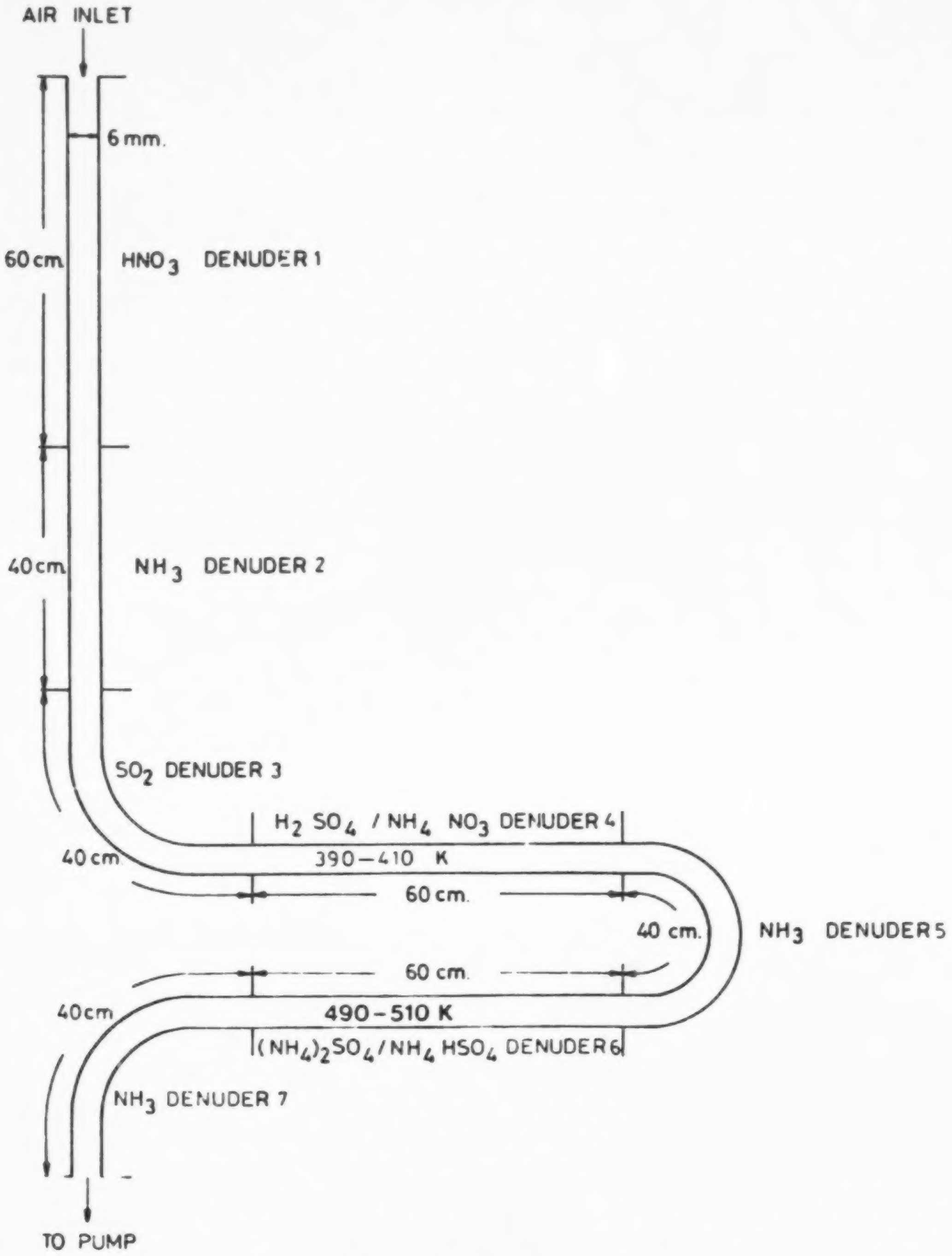
AIR INLET
6 mm.
60 cm
HNO_3 DENUDER 1
40 cm
NH_3 DENUDER 2
SO_2 DENUDER 3
H_2SO_4 / NH_4NO_3 DENUDER 4
390–410 K
40 cm
60 cm.
40 cm.
NH_3 DENUDER 5
60 cm.
40 cm
490-510 K
$(NH_4)_2SO_4$/NH_4HSO_4 DENUDER 6
NH_3 DENUDER 7
TO PUMP

Figure 13. Schematic of the denuder.

HNO_3 and NH_3 are collected at room temperature by NaF and H_3PO_4 coated tubes, respectively. H_2SO_4 and HNO_3 resulting from the dissociation of NH_4NO_3 are then collected by the NaF coating of a denuder tube heated to 390 to 410°K. The liberated NH_3 (from NH_4NO_3) is deposited in a subsequent H_3PO_4 coated tube. At 490-510°K ammonium sulfates decompose forming H_2SO_4 and NH_3. The fragments are trapped in the same way using tubes with an NaF and an H_3PO_4 layer, respectively. All tubes are washed with water. In the extracts NO_3^- and SO_4^{--} are determined by ion chromatography, NH_4^+ by means of ion selective electrode.

LAMMA PROCEDURE

The Laser Microprobe Mass Analyzer LAMMA 500^R originally had been designed for the analysis of biomedical samples, especially thin sections. The equipment and the procedure were developed at the University in Düsseldorf and in the Leybold-Heraeus GmbH Corp. in Cologne[13].

The principle of LAMMA is based on the excitation of a microvolume of the sample to an ionized state by a focused laser beam. The analytical information is derived from mass spectroscopy of these ions. It is obvious that all elements of the periodic table and their isotopes can be detected. Various applications have demonstrated that besides element detection, the instrument can also be used for the detection of organic and inorganic compounds.

The application of LAMMA has meanwhile been extended from biological work to quite different fields such as general chemistry, mineralogy, criminology, geology, and environmental research.

The LAMMA instrument as a new laser microprobe may also answer many questions of aerosol researchers. The LAMMA spectra (Figure 14) of positive and negative ions contain much information about atomic and molecular constituents of a single particle. In addition the sensitivity is high enough to detect trace contaminants in the ppm range and the measuring and data processing is fast enough to allow for the collection of statistically significant information on the particle population as whole[14].

Some other promising applications of the LAMMA procedure are the field of fibrous dusts and aerosols[15]. Mass spectra of asbestos and man-made mineral fibers obtained by LAMMA (Figure 15) are very reproducible and characteristic for each asbestos and glass type.

A very good differentiation could be found between serpentines and amphiboles. Also a differentiation between amosite and crocidolite was possible. LAMMA spectra could be considered as good fingerprinting for different asbestos minerals, glass fibers, and other natural and man-made mineral fibers. Further investigations in this field have also shown a significant chemical instability of chrysotile fibers in environmental samples, in acids and in living organisms (human lung tissue, spleen, etc.). Magnesium ions can be leached from the fiber relatively quickly; leaching of iron and silicon ions was also observed. In strong acids, entire (MgOH)-sheets of chrysotile were stripped, leaving a silica skeleton.

Results of analysis of chrysotile fibers (in human lung tissue and after extraction in acids) examined by LAMMA indicated that chemical changes

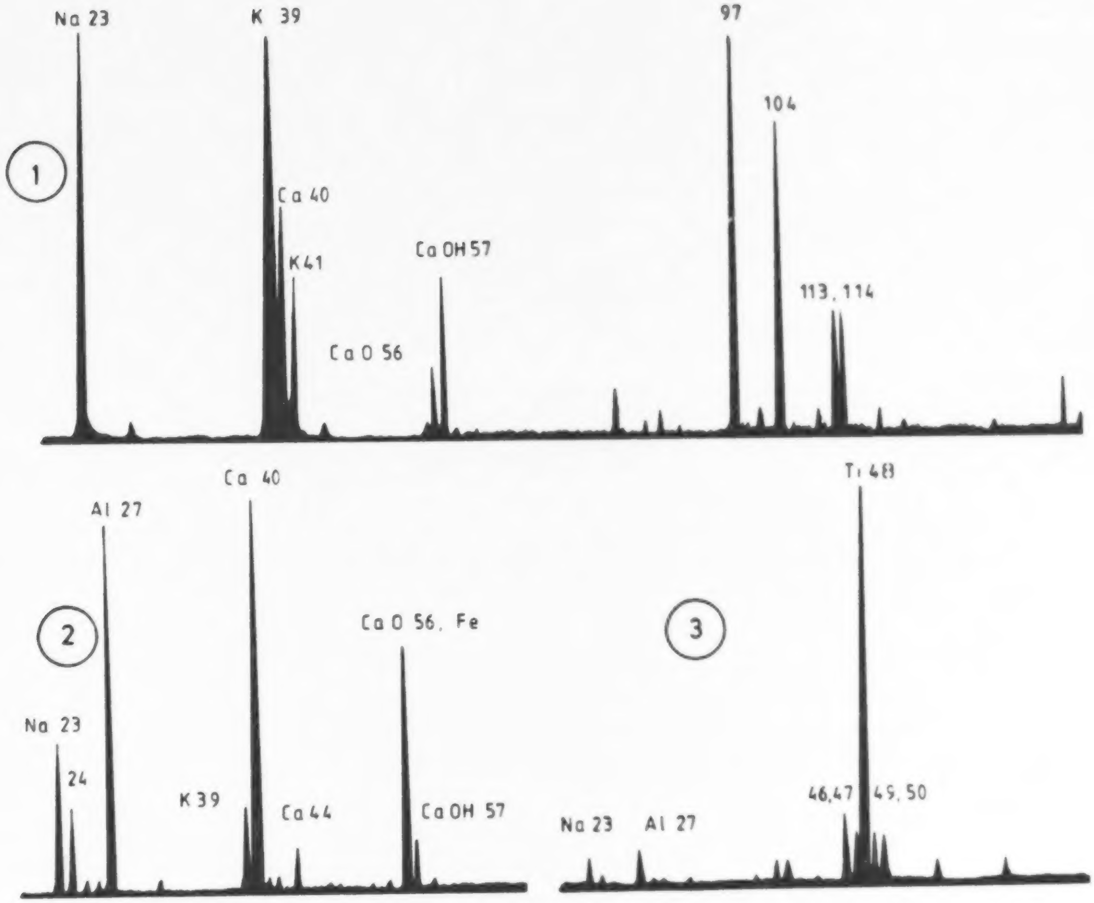

Figure 14. LAMMA spectra (positive ions) of three different dust particles sampled from the lung tissue of an asbestos worker after autopsy.

(leaching of Mg, Fe, and Si) in single fibers are of a statistical nature. Some chrysotile fibers showed insignificant changes after extraction with acids and after long residence time in human lung tissue. Mg, Fe, and/or Si were left in the majority of the chrysotile fibers. The leaching of Mg was not constant along the fiber axis. Also analysis of glass fibers has shown that they undergo chemical changes similar to those of chrysotile fibers.

The first applications of the LAMMA instrument to aerosol research show that this new microprobe can give very useful information concerning the chemical nature of the single particle material. The chemical histograms obtained by LAMMA analysis of an individual particle as well as those of particle populations are very helpful for both the identification of source specific particle properties as well as for the investigation of the chemical particle alteration in the gasborne and deposited states. This can also lead to a better estimate of particle-induced effects which, for example, are important in biology, medicine, meteorology, and other related fields.

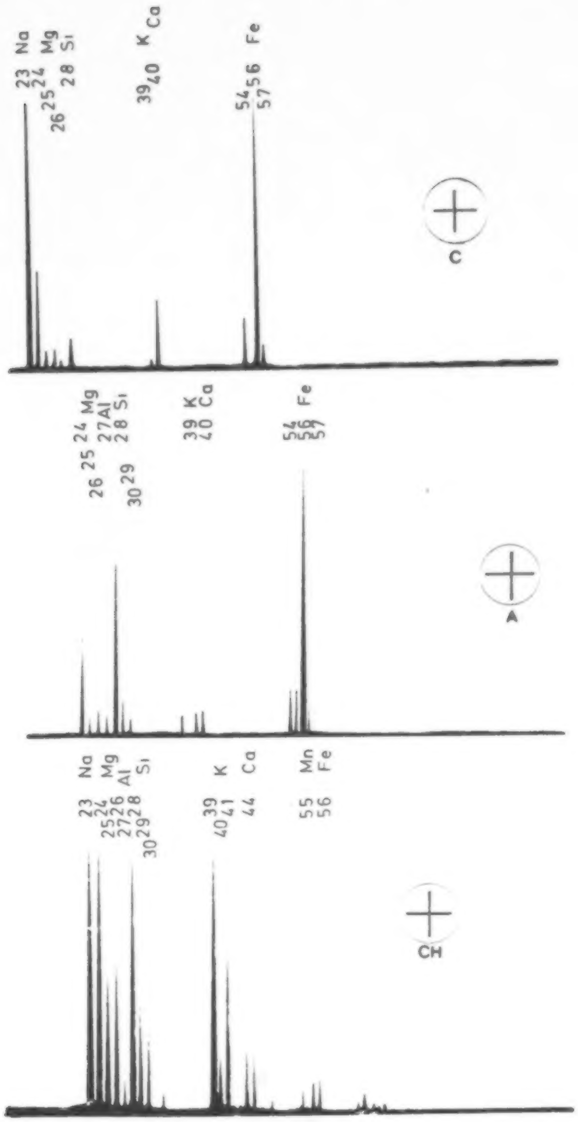

Figure 15. LAMMA spectra for positive ions of single fibers of crocidolite (C), amosite (A), and chrysotile (CH).

MICA NUCLEPORE FILTERS (MNPF)

In 1963 a new technology was developed in the United States for preparing thin, porous polycarbonate sheets. Filters produced by an irradiation procedure have a very uniform structure and excellent properties for sampling and analysis of colloids, suspensions, and aerosols. They have been commercially available more than 10 years as Nuclepore filters (Nuclepore Corp., Pleasanton, CA). Their filtration properties and applications in the aerosol field were also described in the literature in Europe.[16]

Using the same irradiation procedure, a new type of analytical filters was recently developed and described by P. Vater et al. at the University in Marburg (West Germany)[17]. These filters produced of mica and designated as nuclear track microfilters or "mica nuclepore filters" mean a new class of microsieves with high resistance to corrosion, chemical attack, and temperature.

Mica foils with diameters of 50 mm and thicknesses of about 50 µm are used for the preparation of MNPF. The foils are irradiated by the GSI accelerator with xenon, lead, or uranium ions of specific energies up to 8.5 MeV/amu at present doses of 10^3 to 10^6 cm^{-2}. The irradiated foils are then etched in hydrofluoric acid to the desired pore diameter. The side length of the rhomboidally shaped pore (Figure 16) depends linearly on the etching time and has a Gaussian distribution. The pore size remains constant throughout the thickness of the filter.

Application of these MNPF is envisioned in chemical engineering for filtration of hot aggressive liquids, in environmental science, in diagnostic medicine, in colloid chemistry, etc.

The application in the field of measurement and analysis of aerosols and dusts could be very successful and broad. The MNPF's seem to be a complementary filtration material in the group of membrane and Nuclepore filters.

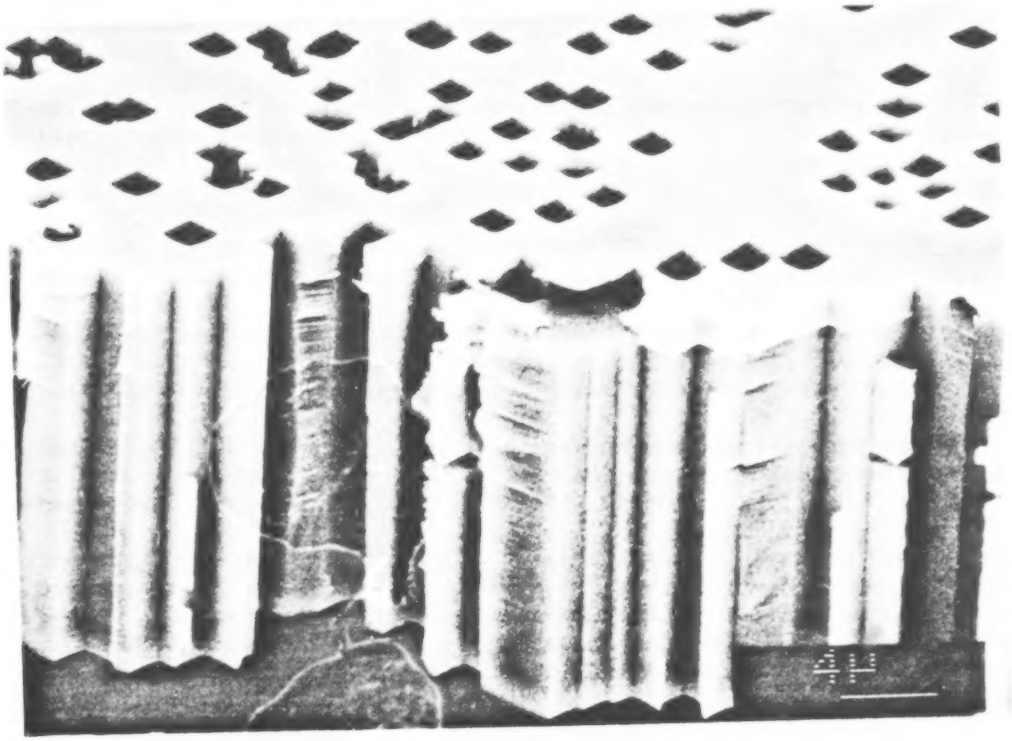

Figure 16. Scanning electron micrograph showing the rhomboidal shape of mica track microfilters (20 min. etching in 48% H_2F_2).

REFERENCES

1. Fuchs, N. A. Collection of Aerosol Abstracts. All-Union Institute of Technical and Scientific Information (Moscow), 1971.

2. Horvath, H., and G. Presle. Determination of the Atmospheric Extinction Coefficient by Measurement of Distant Contrasts. Appl. Optics 17: 1304-1314, 1978.

3. Presle, G., and H. Horvath. Visibility in Turbid Media with Colored Illumination. Atmos. Environ. 12: 2455-2459, 1978.

4. Horvath, H. The Influence of the Wavelength Dependent Extinction Coefficient of the Atmospheric Aerosol Visibility and its Measurement. Am. Ind. Hyg. Assoc. J. 41: 748-757, 1980.

5. Horvath, H. The University of Vienna Telephotometer. Atmos. Environ. In press, 1981.

6. Preining, O., P. E. Wagner, F. G. Pohl, and W. Szymanski. Heterogeneous Nucleation and Droplet Growth. Report from the Institute for Experimental Physics of the University of Vienna, 3: 1-269, 1981.

7. Holländer, W., J. Schörmann, W. Stöber, F. J. Mönig, and N. Schwarzer. Sensitive Integrated and Time-Resolved Aerosol Measurement of Light Transmission Changes of Metal-Coated Nuclepore Filters. Environ. Sci. Technol. 15: 471-473, 1981.

8. Weichert, R. Determination of Extinction Efficiency and Particle-Size Distribution by Photosedimentation Using Light of Different Wavelengths. Report of the Institute of Mechanical Engineering of the University in Karlsruhe. 1-8, 1981.

9. Umhauer, H. Partikelgrössenbestimmung in Suspensionen mit Hilfe eines Streulichtzählverfahrens. Chem. Ing. Tech. 52: 55-58, 1980.

10. Fissan,H. J., and C. Helsper. Simulation Studies and Data Reduction for Size Classifying Measurement Techniques. Proceedings: Advances in Particle Sampling and Measurement. EPA-600/9-80-004, Jan. 1980

11. Klockow, D., R. Niessner, and B. B. Jablonski. Application of the Sulfuric Acid-Halide Reaction to the Analysis of Sulfuric Acid Containing Aerosols. Analyt. Lett. 13: 1397-1408, 1980.

12. a. Niessner, R., and D. Klockow. A Thermoanalytical Approach to Speciation of Atmospheric Strong Acids. Intern. J. Environ. Anal. Chem. 8: 163-175, 1980. b. Slanina, J., L. v. Lamoen-Doornenbal, W. A. Lingerak, W. Meilof, D. Klockow, and R. Niessner. Application of a Thermo-denuder Analyzer to the Determination of H_2SO_4, HNO_3, and NH_3 in Air. Intern. J. Environ. Anal. Chem. 9: 59-70, 1981.

13. Hillenkamp, F., and R. Kaufmann (Ed.). LAMMA-Symposium, Düsseldorf, October 8-10 (1980). Fresenius Z. Anal. Chem. 308: 195-320, 1981.

14. Wieser, P., R. Wurster, and U. Haas. Application of LAMMA in Aerosol Research. Fresenius Z. Anal. Chem. 308: 260-269, 1981.

15. Spurny, K. R., J. Schörmann, and R. Kaufmann. Identification and Microanalysis of Mineral Fibers by LAMMA. Fresenius Z. Anal. Chem. 308: 274-279, 1981.

16. Spurny, K. R., and J. W. Gentry. Aerosol Fractionation by Graded Nuclepore Filters. Powder Technol. 24: 129-142, 1979.

17. Vater, P., G. Tress, R. Brandt, B. Genswürder, and R. Spor. Nuclear Track Microfilters Made of Mica. Nuclear Instrum. Methods. 173: 205-210, 1980.

Although the research described in this paper has been funded (wholly or in part) by the United States Environmental Protection Agency, it has not been subjected to Agency review and, therefore, does not necessarily reflect the views of the Agency and no official endorsement should be inferred.

Paper 6

AN INSTACK CASCADE IMPACTOR TO COLLECT SAMPLES FOR WDXRF ANALYSIS

L.G. Felix, J.D. McCain, D.H. Hussey, and R. Smith
Southern Research Institute

K. Knapp
U.S. Environmental Protection Agency

ABSTRACT

A five-stage cascade impactor has been designed and constructed which collects source emitted aerosols on a 47mm diameter substrate for subsequent wave dispersive x-ray fluorescence (WDXRF) analysis. Uniform particle deposition was achieved by using an oscillating drum beneath a slit nozzle. The sample is deposited on a rectangular area 31mm x 34mm. The impactor is constructed of 316 stainless steel and will fit through a 4-inch sampling port. A specially designed right-angle pre-impactor is used to reduce inlet losses and provide a 15 μm aerodynamic diameter cut.

Calibration studies were conducted with a prototype unit designed to allow various slit widths and jet to plate spacings. These studies provided the design criteria used for dimensioning the final impactor.

Special substrates and substrate coatings were found which offer good particle retention at sampling temperatures and provide low x-ray background.

With this sampling system, samples can be readily collected and directly analyzed by wavelength dispersive x-ray fluorescence analysis for elemental composition. No sample preparation is required other than mounting the substrate in a carrier for the analysis.

INTRODUCTION

A novel cascade impactor for in situ flue gas sampling has been developed. This device differs from all other in-stack impactor designs because it is intended to collect size segregated particulate matter samples so that no sample preparation is necessary in order to perform wavelength dispersive x-ray fluorescence (WDXRF) analysis on each stage catch.[1] The 47mm diameter collection substrates are coated with a high melting point-low WDXRF background polymer. This polymeric coating softens at stack temperatures and acts as a near-ideal impaction surface. This project was sponsored by the U.S. EPA under Contract 68-02-2992. The Project Officer was Dr. K.T. Knapp.

The impactor is designed to fit through a standard 4 inch sampling port. Requiring a fit through a 4 inch port precludes the use of a cyclone precutter to obtain an inhalable particulate (IP) cut. Since laboratory and field data have demonstrated that large sampling errors can be induced with bent or buttonhook nozzles,[2,3] an impactor precutter of Southern Research Institute design is used at the inlet to the impactor. This precutter eliminates sampling errors due to bent nozzles and provides the IP 15 micrometer aerodynamic cut at the design flowrate (22.65 lpm) and temperature (150°C). Four sampling nozzles are provided: 9.53mm, 6.35mm, 4.76mm and 3.18mm.

Figure 1 shows the disassembled impactor with the precutter attached. From this figure one can see that in concept, this impactor is very similar to the ambient air sampling impactor developed by Lundgren.[4] This design has five stages and an integral 47mm back-up filter. Each stage of the impactor is a drum. Substrates 47mm in diameter are mounted on each drum and held in place with spring clips spot welded to the drums. During sampling these drums rotate synchronously back and forth beneath the slits so that size segregated particulate samples are uniformly deposited onto each substrate on an area 31mm x 34mm. During WDXRF analysis an area 30mm in diameter in the center of each substrate is analyzed. Therefore, the edges of the sample are avoided, where some non-uniformity of deposition might occur. Nominal aerodynamic stage D_{50} values are 8, 4, 2, 1, and 0.5 micrometers at the design flowrate and temperature. The impactor is made out of 316 stainless steel.

Figure 2 shows the assembled impactor attached to a specially designed 10 foot sampling probe and I-beam support. Figure 3 shows the rear of the probe with the drive stepping motor and motor position indicator. Figure 4 shows a modified Andersen EPA control unit which provides flow and flow measurement, and Figure 5 shows the central control unit. The items shown in Figures 1 through 5, plus a punch designed to cut substrates constitute the equipment resulting from this development.

DESCRIPTION OF THE IMPACTOR

As Figure 1 shows the impactor is a five-stage device with an integral back-up filter. One of the oscillating drums which holds the collection substrates is shown in Figure 6. The locating pins and tabs which secure the edges of the 47mm diameter substrate are indicated. The punch which was designed to cut the collection substrates from sheet mylar also punches out small holes for the locating pins. Figure 7 shows the back-up filter assembly which slides in and out of the rear of the top shell of the impactor. It breaks apart into halves allowing the back-up filter to be easily installed or removed. As shown in Figure 2, the impactor requires attachment to a sampling probe which provides connection to the drive for the stages, a heated gas sampling line, and thermocouple sensors in the gas stream, impactor, and probe. Figure 8 shows the end of the impactor which attaches to the probe and illustrates how the impactor fits onto the probe. Male dovetails on the end of the probe engage female dovetail slots machined in the rear of the impactor. The arrangement of the dovetails allows only one orientation for the impactor-probe

Reproduced from
best available copy.

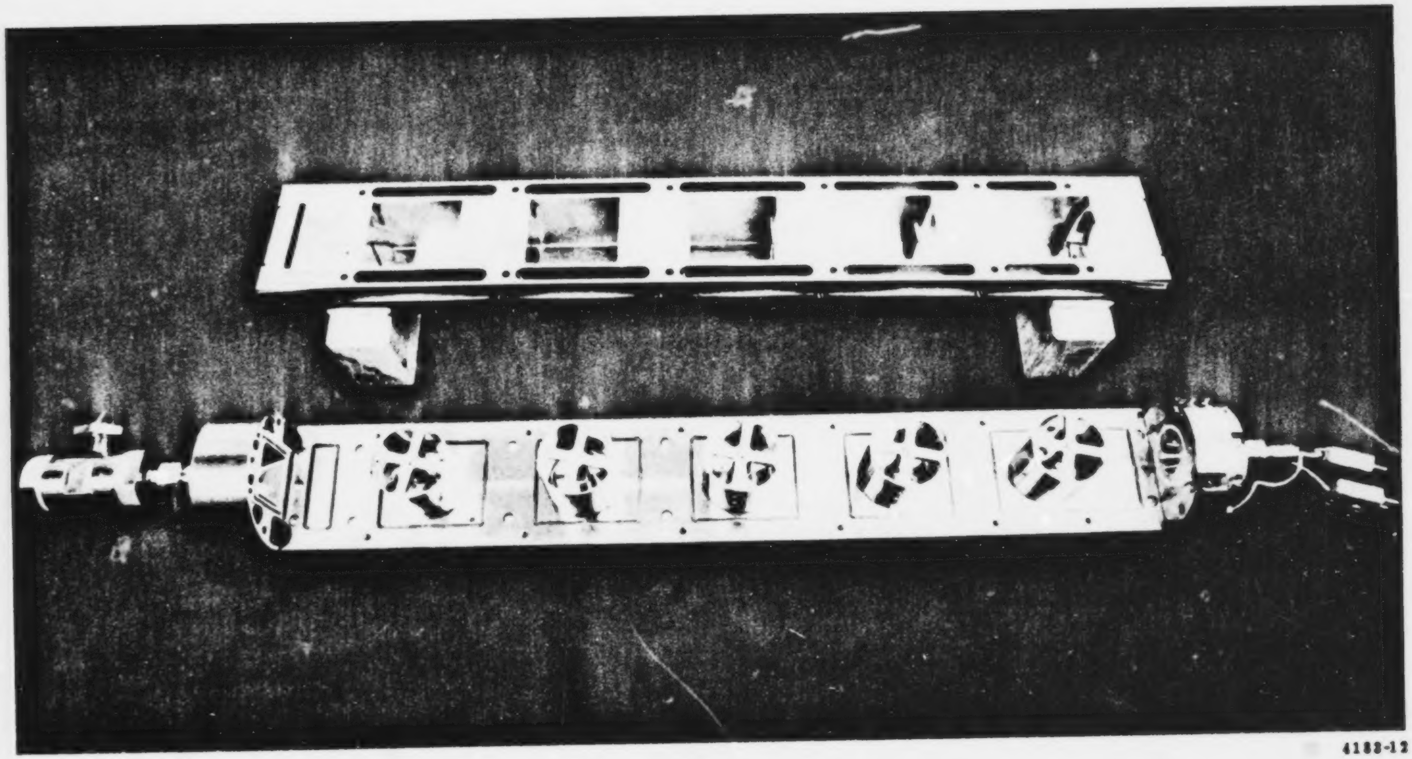

4188-12

Figure 1. The disassembled impactor with right angle impactor precutter attached.

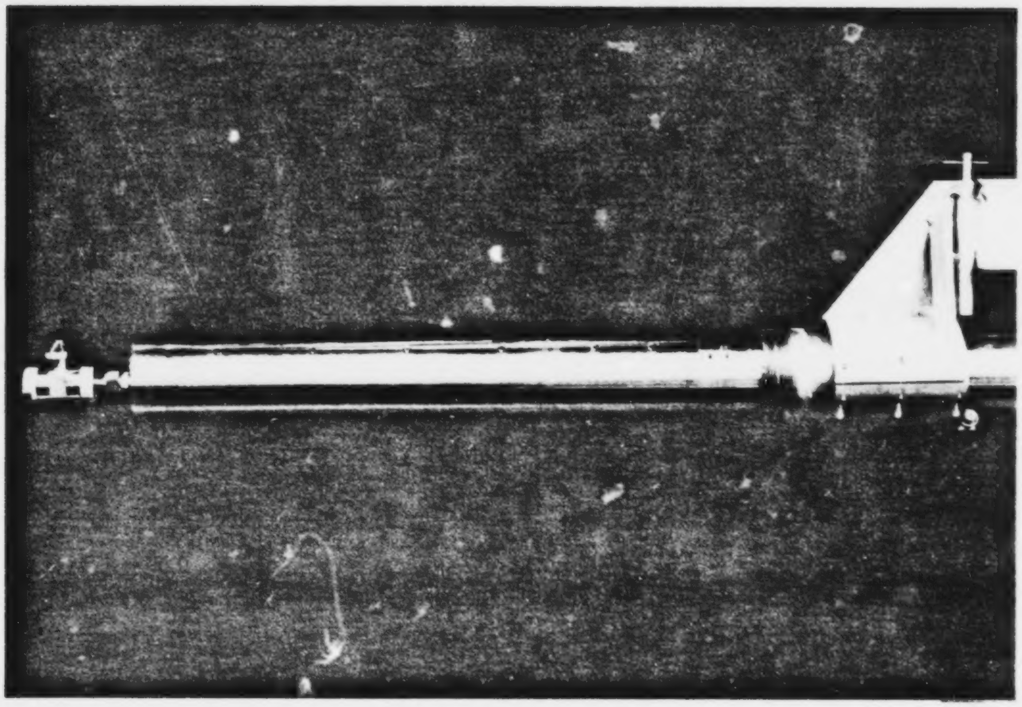

4183-16

Figure 2. The impactor attached to the 10-foot sampling probe and I-beam support.

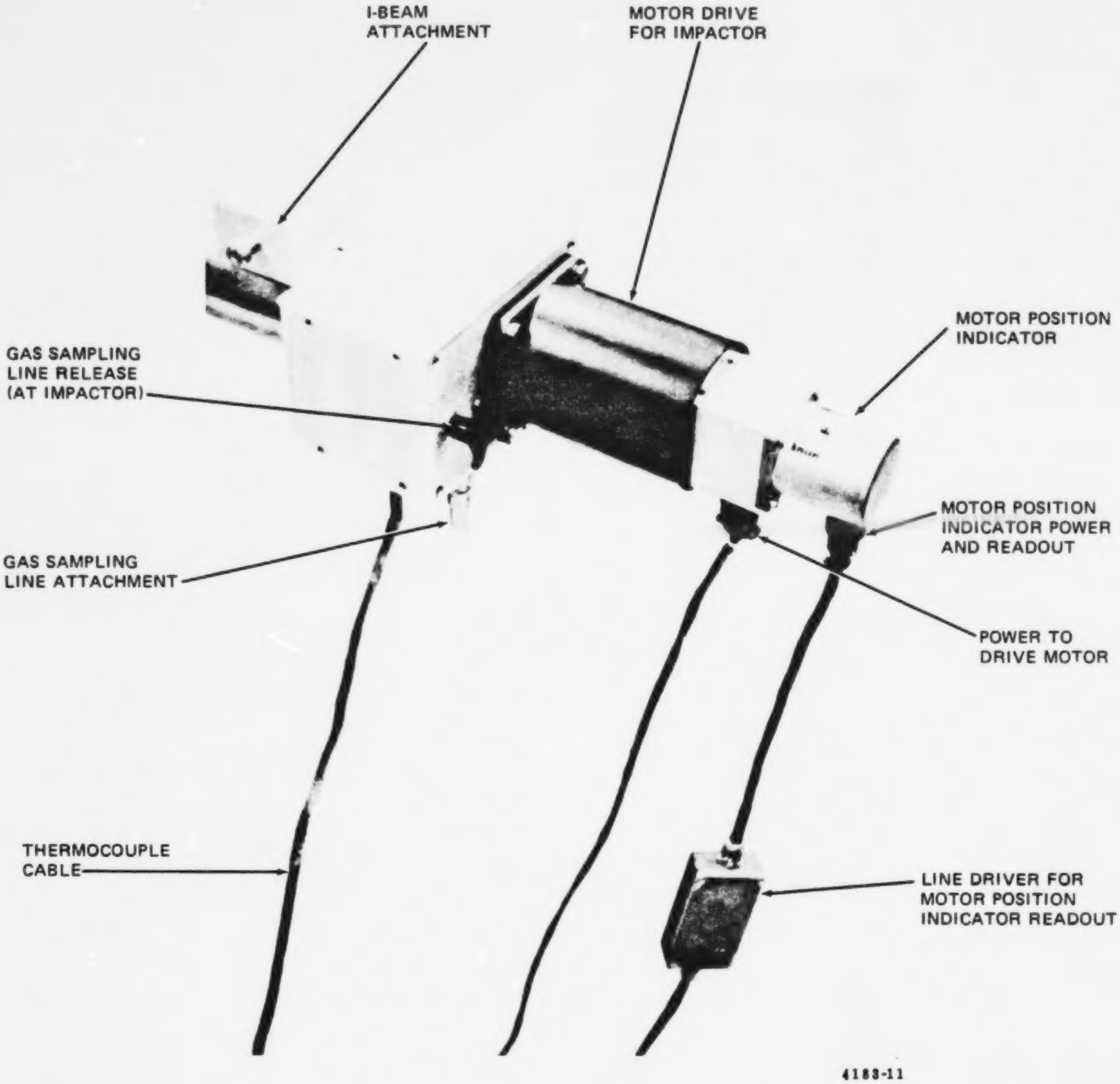
I-BEAM ATTACHMENT
MOTOR DRIVE FOR IMPACTOR
MOTOR POSITION INDICATOR
GAS SAMPLING LINE RELEASE (AT IMPACTOR)
MOTOR POSITION INDICATOR POWER AND READOUT
GAS SAMPLING LINE ATTACHMENT
POWER TO DRIVE MOTOR
THERMOCOUPLE CABLE
LINE DRIVER FOR MOTOR POSITION INDICATOR READOUT
4183-11

Figure 3. Rear end of probe showing various component parts.

Reproduced from best available copy.

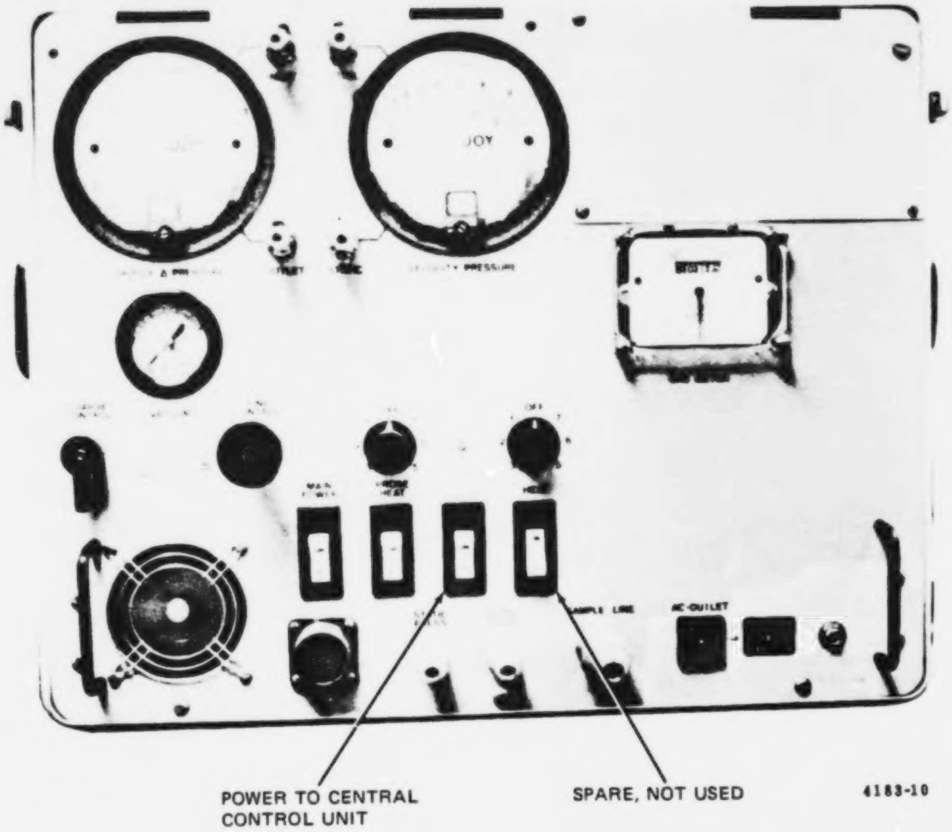
JOY
JOY
VELOCITY PRESSURE
OFF
MAIN POWER
PROBE HEAT
SAMPLE LINE
AC OUTLET
POWER TO CENTRAL CONTROL UNIT
SPARE, NOT USED
4183-10

Figure 4. The modified Andersen EPA control unit.

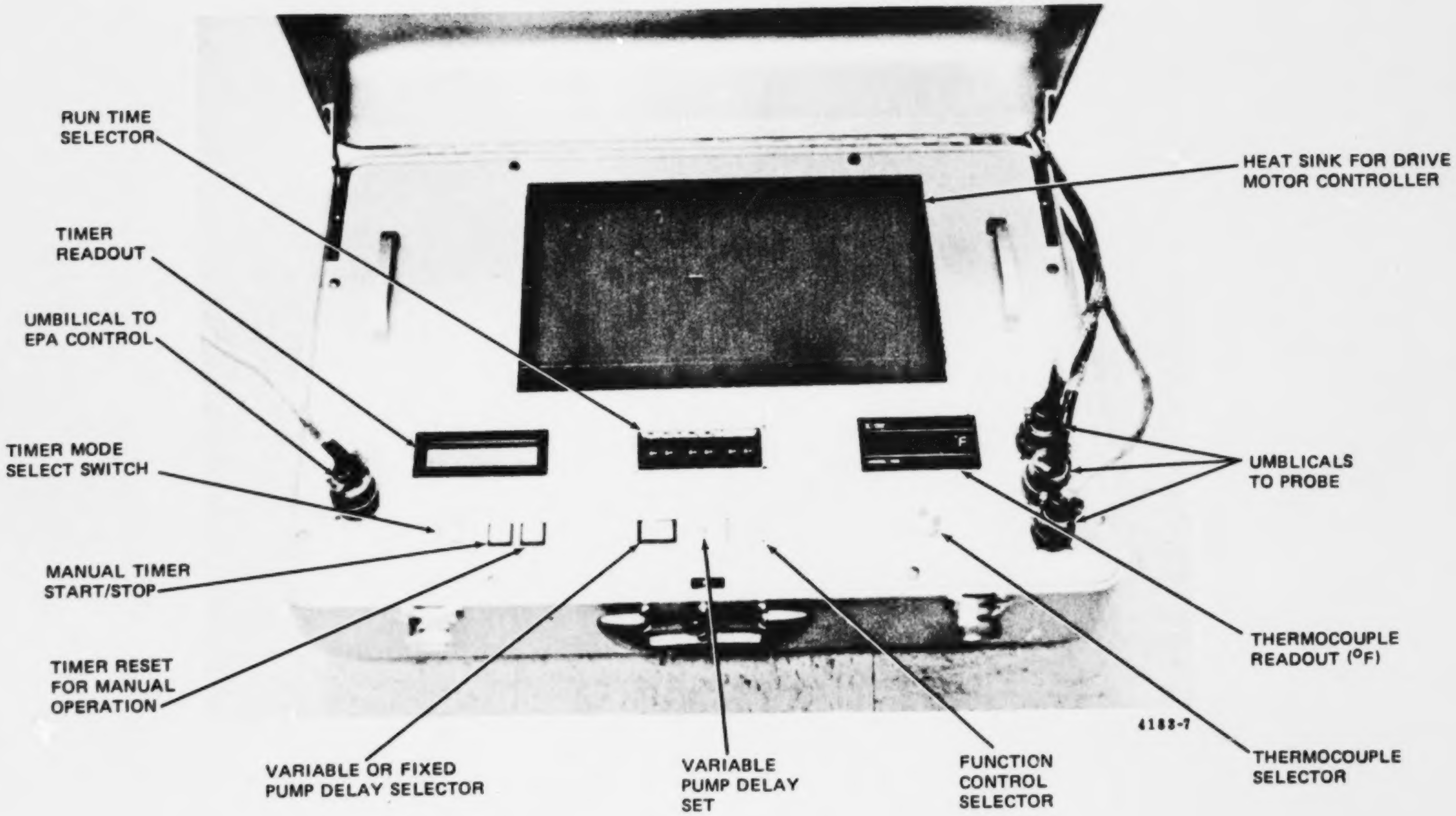
RUN TIME SELECTOR
TIMER READOUT
UMBILICAL TO EPA CONTROL
TIMER MODE SELECT SWITCH
MANUAL TIMER START/STOP
TIMER RESET FOR MANUAL OPERATION
VARIABLE OR FIXED PUMP DELAY SELECTOR
VARIABLE PUMP DELAY SET
FUNCTION CONTROL SELECTOR
THERMOCOUPLE SELECTOR
THERMOCOUPLE READOUT (°F)
UMBLICALS TO PROBE
HEAT SINK FOR DRIVE MOTOR CONTROLLER
4183-7

Figure 5. The central control unit.

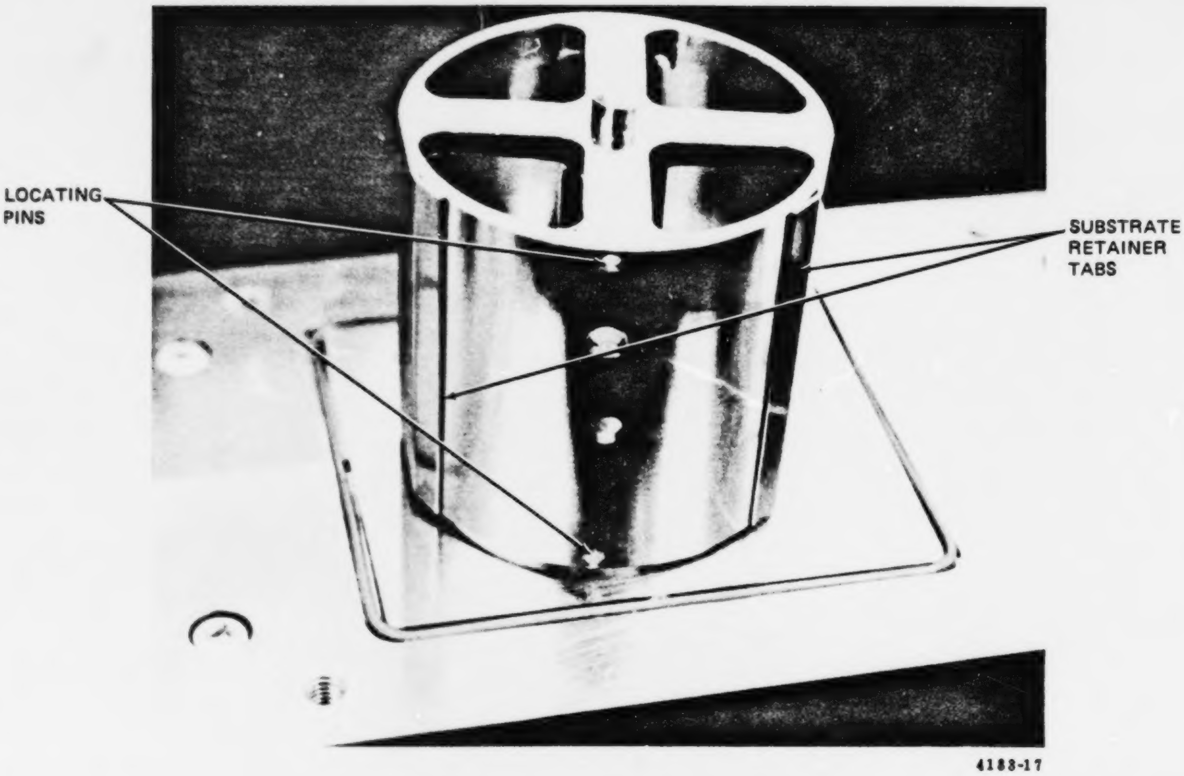
LOCATING PINS
SUBSTRATE RETAINER TABS
4183-17

Figure 6. Typical collection drum showing the substrate locating pins and retaining tabs.

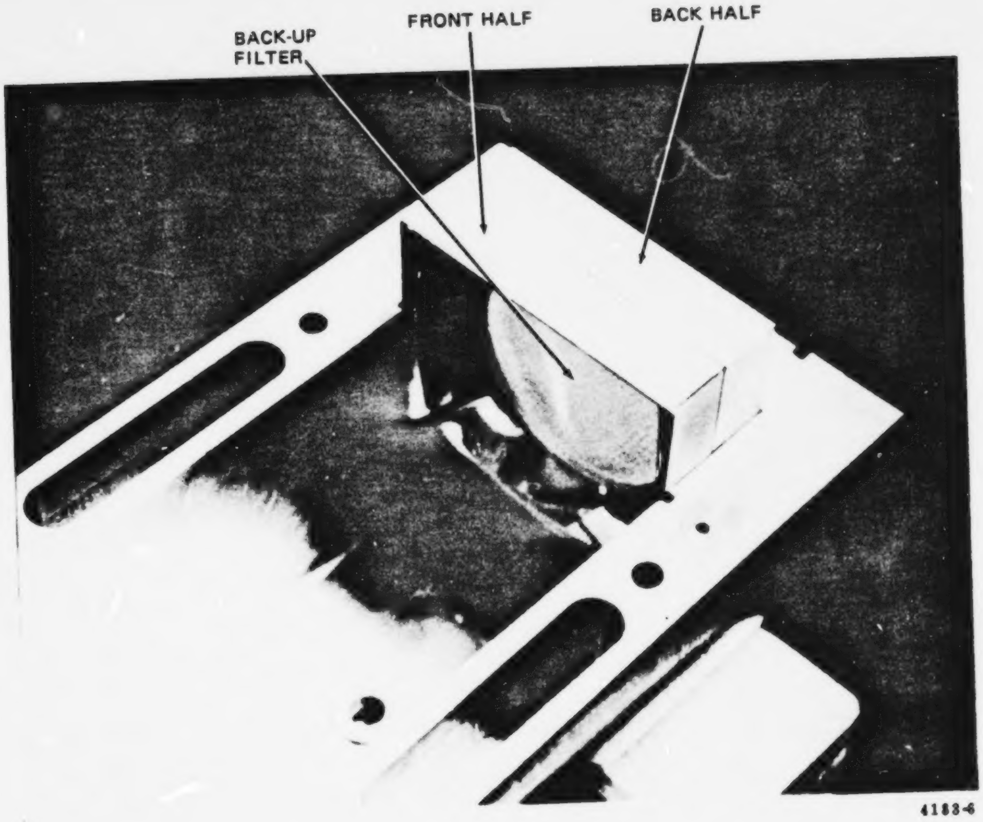
BACK-UP FILTER
FRONT HALF
BACK HALF
4183-6

Figure 7. Back-up filter assembly.

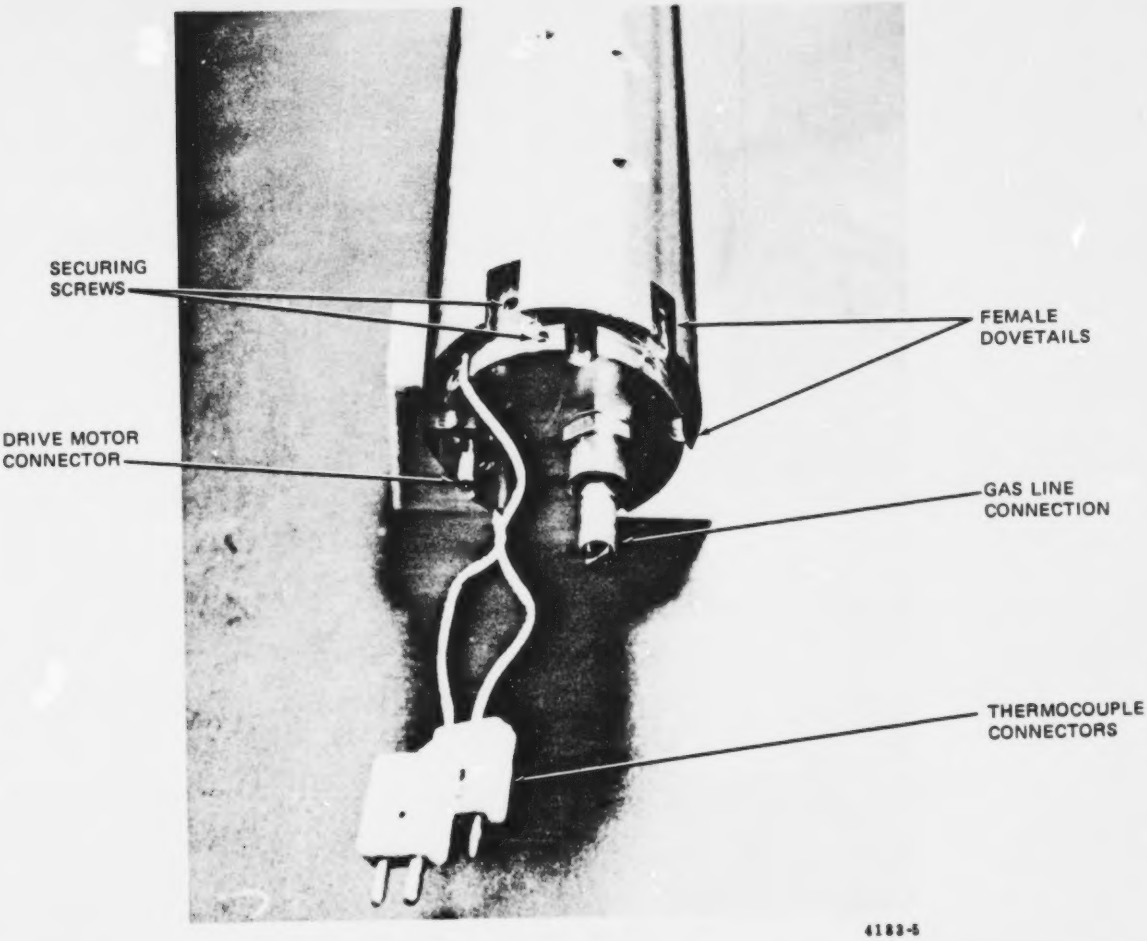
SECURING SCREWS
FEMALE DOVETAILS
DRIVE MOTOR CONNECTOR
GAS LINE CONNECTION
THERMOCOUPLE CONNECTORS
4183-5

Figure 8. End of impactor showing attachment points for the probe, gas line connection, thermocouple connectors and drive connection.

assembly. Figure 8 also shows thermocouple, gas sampling and drive connections on the probe and impactor. The thermocouple connections must be made before the impactor is mounted on the probe; other connections to the probe are made automatically when the impactor is properly seated. Allen screws located in dovetail slots on the impactor are backed out through mating threaded holes in the male probe dovetails to secure the impactor, and are left flush with the surface of the probe.

When the impactor is properly seated on the probe a quick connect gas sampling fitting is automatically secured. For disassembly this connection is broken by pulling on the "T" handle at the rear of the probe (see Figure 3), turning the handle a quarter turn and then pushing the handle. Pulling on the "T" handle while the impactor is secured to the probe will not result in any leakage or break in the connection since there is no free room for disconnection while the impactor is bolted to the probe.

Disassembly and Assembly of the Impactor

Disassembly and assembly of the impactor is carried out with the impactor removed from the probe. The first step in disassembly is to remove the 12 bolts holding the top shell of the impactor to the bottom half. Second, remove the three bolts on either end of the impactor which hold the inlet and exit transforms to the top shell. Third, loosen the two bolts which secure the inlet transform to the lower half of the impactor. Finally roll the impactor over and lift the lower half up and off of the upper half leaving the upper half on the workbench. Potential damage to substrates can be eliminated by replacing some of the 12 top to bottom half securing bolts with threaded rods about 6 inches long. These rods will keep the two halves from hitting during disassembly or assembly.

When this stage of disassembly is reached, substrates can be removed or replaced along with the back-up filter. The impactor is then reassembled and rebolted. During assembly each bolt should be checked to be sure it is coated with anti-seize compound. If anti-seize compound is not used on all threaded connections, then galling will almost certainly result.

The impactor is then re-attached to the probe and it is ready to use for resampling. Since the probe is quite heavy it is anticipated that it will remain on the sampling platform attached to the I-beam support and the impactor will be mounted and dismounted for each run.

CALIBRATION STUDIES

A prototype impactor was constructed early in the project. The prototype is a single stage slit impactor with a drum upstream and downstream of the jet. The upstream drum is fixed and the downstream drum is connected to an oscillating electric motor through a pressure seal. The slit jet is designed so that various slit widths and jet to plate spacings can be used. The impaction substrate used in the calibration studies was a thin coating of petroleum jelly applied directly to the collection drum.

The first study conducted with the prototype was a study of the uniformity of the particle deposition pattern. Figure 9 shows a diagram of the experimental apparatus.

The particle deposition pattern on the collection drum of the breadboard impactor was checked by sampling an ammonium fluorescein aerosol. A solution of ammonium fluorescein was made by dissolving one gram of fluorescein in 20 ml of ammonium hydroxide. The solution was then diluted 20:1. A small amount of solution was placed in a DeVilbiss medical nebulizer and dispersed into a plenum. The impactor sampled the particles at the rate of 28.3 lpm from the bottom of the plenum. A jet width of 0.2mm and a jet to plate spacing of 0.5mm was used. The deposition pattern observed was uniform with no irregularities.

A second set of experiments were conducted with the prototype to measure collection efficiency as a function of slit width and jet to plate spacing.

Figure 10 shows a diagram of the calibration apparatus used for making collection efficiency measurements with the prototype. As this figure shows, a Climet Instruments Model 208 optical particle counter in conjunction with a Canberra Series 30 multichannel analyzer was used to measure aerosol concentration upstream and downstream of the prototype. Collection efficiency was determined by comparison of the two concentration measurements.

Two slit widths and two sizes of monodisperse aerosols were used in the calibration study. The slit widths were 0.315mm (12.4 mils) and 0.787mm (31 mils) and the particle sizes used were 1.099 micrometers and 2.02 micrometers. Dow Polystyrene Latex and Polyvinyltoluene Latex monodisperse suspensions were dispersed to generate the aerosols.

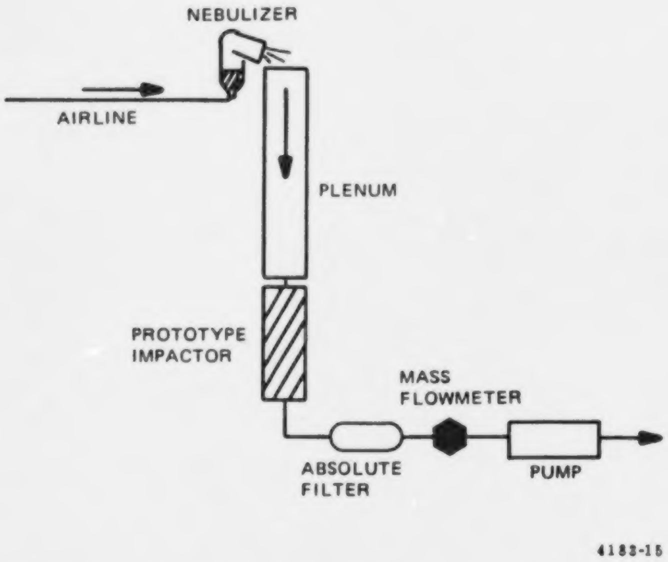

Figure 9. System to determine particle deposition in the prototype impactor.

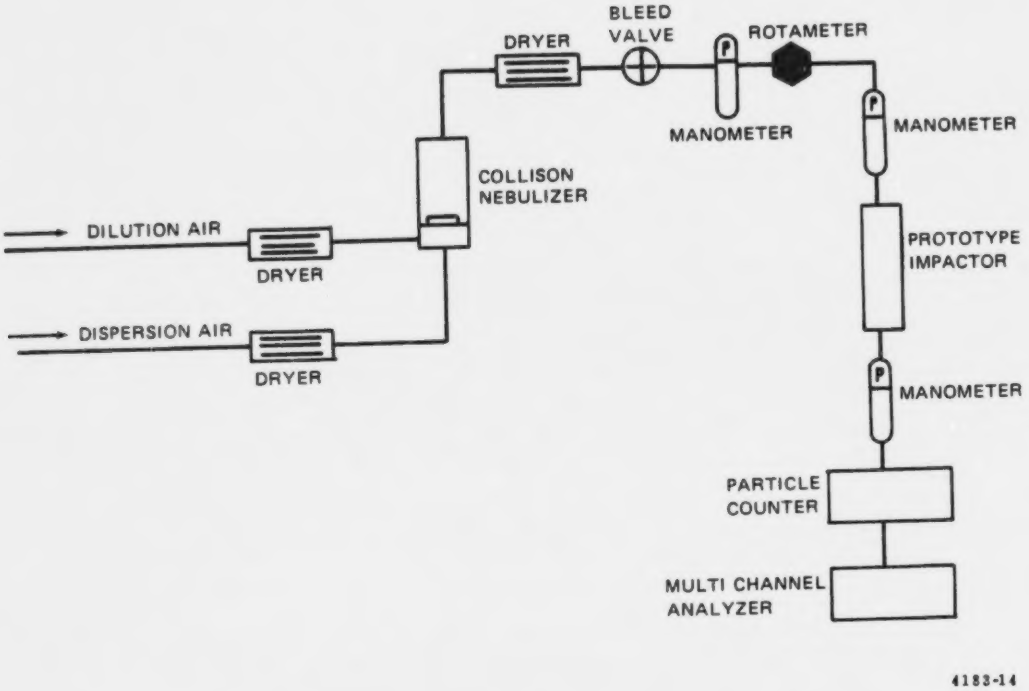
BLEED VALVE
DRYER
ROTAMETER
P
MANOMETER
P
MANOMETER
COLLISON NEBULIZER
DILUTION AIR
DRYER
PROTOTYPE IMPACTOR
DISPERSION AIR
DRYER
P
MANOMETER
PARTICLE COUNTER
MULTI CHANNEL ANALYZER
4183-14

Figure 10. System to study the collection efficiency and D_{50} of the prototype impactor for different slit widths and jet-to-plate spacings.

During tests with 2.02 micrometer diameter aerosols, particle impaction losses made necessary the removal of the rotameter. It was replaced with a length of stainless steel tubing with pressure taps on either end. Pressure drop across the tube was correlated to flow by making a series of flow-pressure drop measurements with the tube and pressure taps connected to a NBS traceable laminar flow element calibration device. With the tube in the system, flowrate was measured by noting the pressure drop across the tube.

Figures 11 and 12 summarize the calibration data, showing collection efficiency as a function of the Stokes number[5], $\sqrt{STK}$. In Figure 12, data set I and data set II are for the same configuration, taken approximately two weeks apart. The data shown in Figure 11 were taken during the two week span.

Marple's theory[5] predicts a value of 0.73 for $\sqrt{STK}$ for a slit nozzle configuration at 50% collection efficiency. This number compares well with the results we obtained with the prototype for the 1.099 μm particle size and for the experimental data from data set I. The data from data set II do not agree as well and the reason for this may be that the drum was not oscillating when some of the measurements were made.

From this study we conclude that the behavior of real slit impactors can be described by theory using a $\sqrt{STK_{50}}$ value of 0.73 as predicted by Marple.[5]

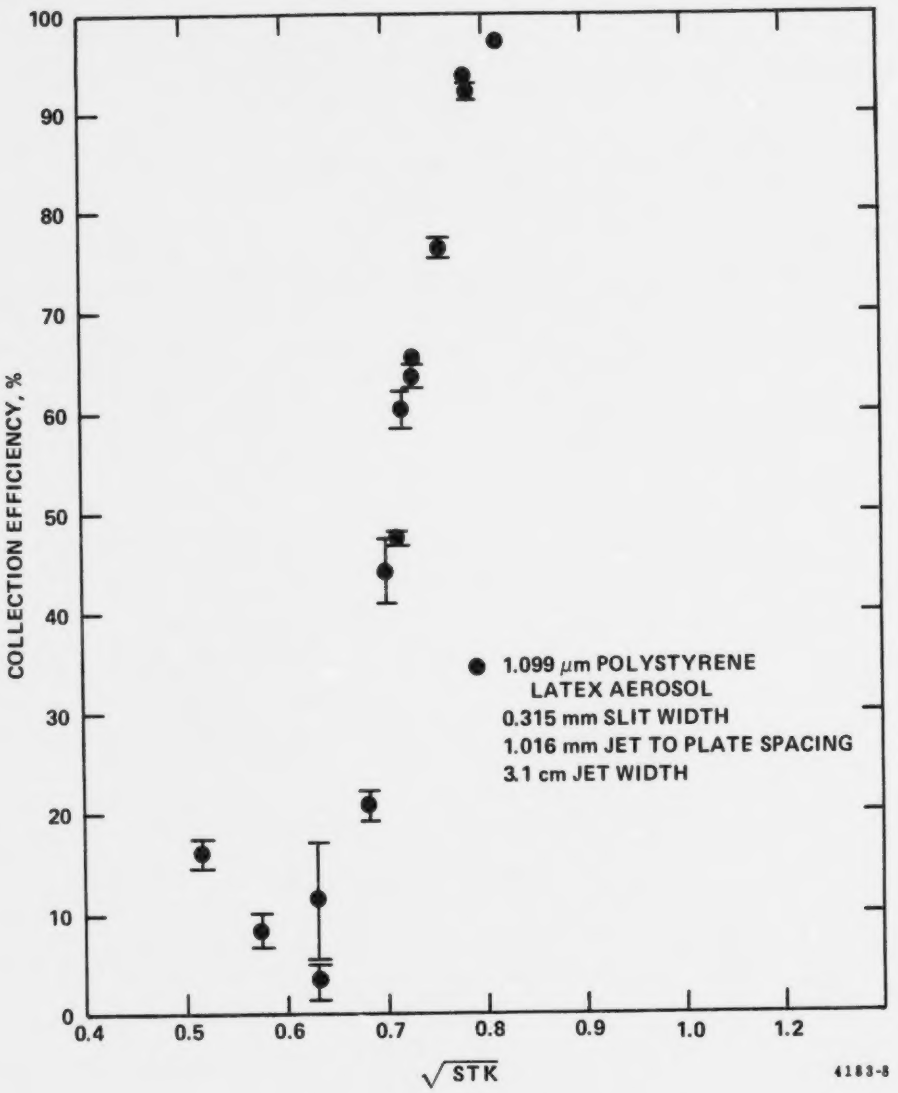

Figure 11. Collection efficiency versus $\sqrt{STK}$ for 1.099 micrometer polystyrene latex aerosol.

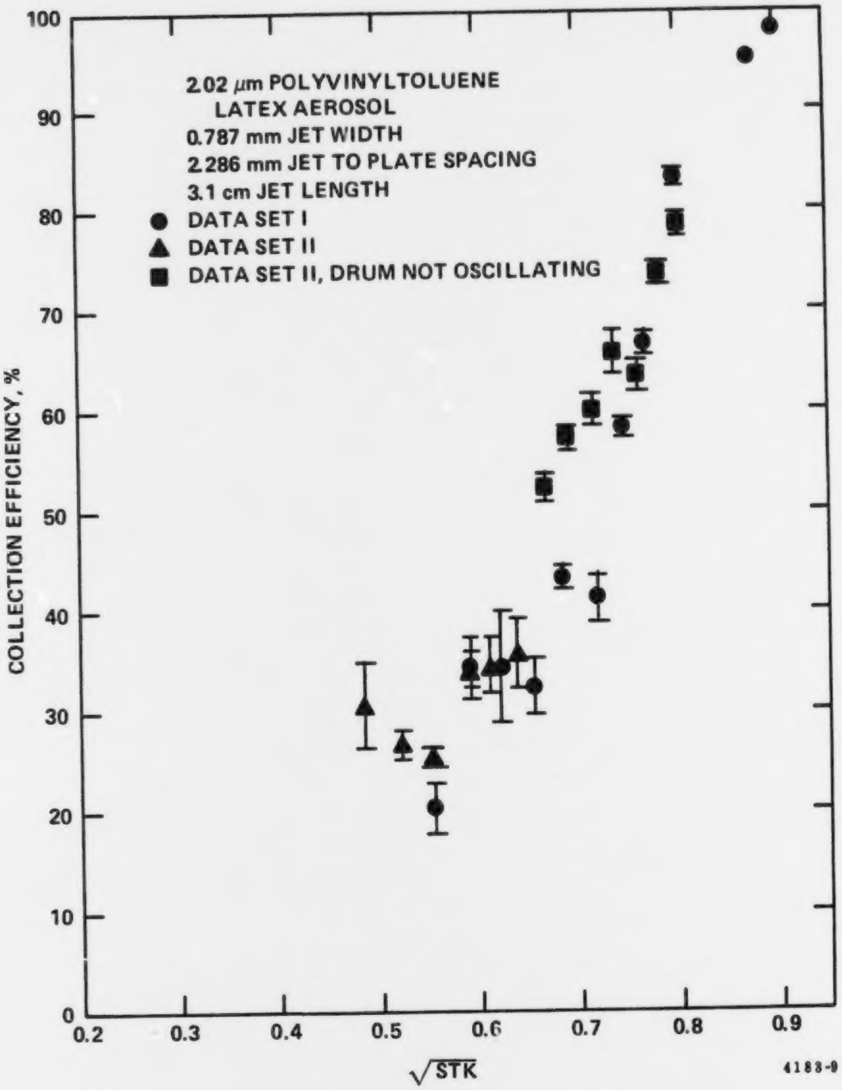

Figure 12. Collection efficiency versus $\sqrt{\mathrm{STK}}$ for 2.02 micrometer polyvinyltoluene latex aerosol.

Therefore, we proceeded with the design of the in-stack unit selecting jet widths according to slit impactor theory. The pertinent interior dimensions of the in-stack unit are given in Table 1.

SUBSTRATE DEVELOPMENT

Shortly after project initiation we were advised by the Project Officer that the most common greases used for impaction substrate coatings[6] were not suitable for this work. This is because these greases contain unacceptably high amounts of metals which are expected to occur in trace quantities in typical samples to be obtained with the impactor.[7] Therefore, other substrate coatings were investigated.

After consulting with the Project Officer and polymer chemists at Southern Research Institute, work began on the selection of a chemically stable high melting point polymer as a substrate coating and substrate materials which would be compatible with the coatings.

Table 2 lists the potential substrate materials which were found. These materials were chosen because they would be compatible with potential substrate coatings, are unaffected by high temperatures and are essentially inert. Mylar and Kaptan were chosen for substrate materials. Mylar is the first choice because it has a much lower X-ray background than Kaptan.

After evaluating the adhesion properties of a number of polymers on Mylar and Kaptan substrates, six were chosen for testing as impaction media at various temperatures. The six compounds are listed in Table 3.

TABLE 1. INTERIOR DIMENSIONS OF THE IN-STACK IMPACTOR*

Stage	Aerodynamic D_{50} (micrometers)	Slit Width (mm)	Jet-to-Plate Spacing (mm)
Precutter	14.9	--	
1	8.0	2.64	5.46
2	4.0	1.35	2.79
3	2.0	0.686	1.52
4	1.0	0.356	1.14
5	0.5	0.188	0.89

*Design flowrate = 22.65 lpm (0.8 cfm) at 150°C (302°F).
Slit length is 31mm for all stages.

TABLE 2. POSSIBLE SUBSTRATE MATERIALS FOR THE IMPACTOR

Identity and Composition	Chemical Characterization
Mylar (Du Pont) Polyethylene terphthalate (linear polymer)	Fusible, m.p. 250°C, softening point 230°C. Solvent swelling by ketones, aromatics, alcohols, dioxane. Attacked by alkali, some acids (as HCl).
Kaptan H (Du Pont) - Polyimide Polycondensation between an aromatic tetrabasic acid and an aromatic amine. (May be combined with Teflon FEP resin to make a heat sealable structure).	Infusible. No known organic solvents. High temperature stability: 200°C+. Subject to slow oxidative degradation.
Tedlar (Du Pont) - polyvinyl fluoride. Contains 0.05 to 1.0 wt % of dimethylacetamide residual	Heat sealable at ∿200°C. Resists solar degradation. Partially soluble in a few polar solvents above 150°C. Compatible with adhesives: acrylics, polyesters, epoxies, rubber.
Kynar (3M) - polyvinylidene fluoride	Heat sealable at 190°C, m.p. 158°C, High temperature stability 140°C. Similar to Tedlar in properties.
Lexan (GE) polycarbonate	Heat sealable at 135°C. Softening temperature 125°C. Soluble in chlorinated hydrocarbons. Partially soluble in aromatics, ketones and esters (they act as stress-crazing agents).
Polysulfone (U.C.)	Melting temperature 300°C, softening temperature 235°C. However, presence of 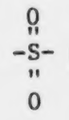 $-\overset{\overset{O}{\|}}{\underset{\underset{O}{\|}}{S}}-$ group is expected to interfere in X-ray measurements.

TABLE 3. SUBSTRATE COATINGS

Coating	Composition: % Vinyl Acetate	% Ethylene	Ring and Ball Softening Point	Flow-Melt Point
EY903*	45%	55%	144°C (292°F)	-
EY904*	47%	53%	132°C (270°F)	-
EY906*	55%	45%	129°C (265°F)	-
EY907*	60%	40%	158°C (316°F)	-
49032**	-	-	-	110°C (230°F)
49000**	-	-	-	130°C (266°F)

*Vynathene, U.S. Industrial Chemicals

**Polyester, DuPont

Mylar and Kaptan substrates were coated with the six polymers by a spin casting technique as well as dipping, both of which leave a uniform thin coating on the substrate. The Vynathenes and Dupont polyester materials are soluble in methyl ethyl ketone. The spin casting technique uses a rapidly spinning cup with the substrate held on the side of the cup. A solution of the substrate coating is poured into the cup while the cup is rotating. The cup is rotated until the solvent has evaporated.

In order to determine suitability of the polymer coatings as impaction substrates, the system shown in Figure 13 was used. A Collison nebulizer redispersed 2.02 micrometer polyvinyltoluene latex spheres (PVTL). An optical particle counter in conjunction with a multichannel analyzer (MCA) was used to measure the concentration of the PVTL particles upstream and downstream of the impaction stage. The collection efficiency was determined by comparing the two concentration measurements.

Samples of the candidate substrates were cut to fit a Brink BMS-11 impactor collection plate. A flowrate and jet diameter combination was chosen such that 2.02 micrometer PVTL particles would have an impaction efficiency near 100%, but the jet velocity would be high enough to result in significant losses due to particle bounce when no adhesive coating was used on the substrate. Velocities on the order of 35 m/s and 70 m/s were used.

Many of the candidate materials did not appear to be effective in reducing particle bounce when tested at ambient temperatures (∿20°C). Subsequently, collection efficiency measurements were made at 93°C by placing the impactor stage in a 93°C oven. Preliminary tests on several substrates showed that the

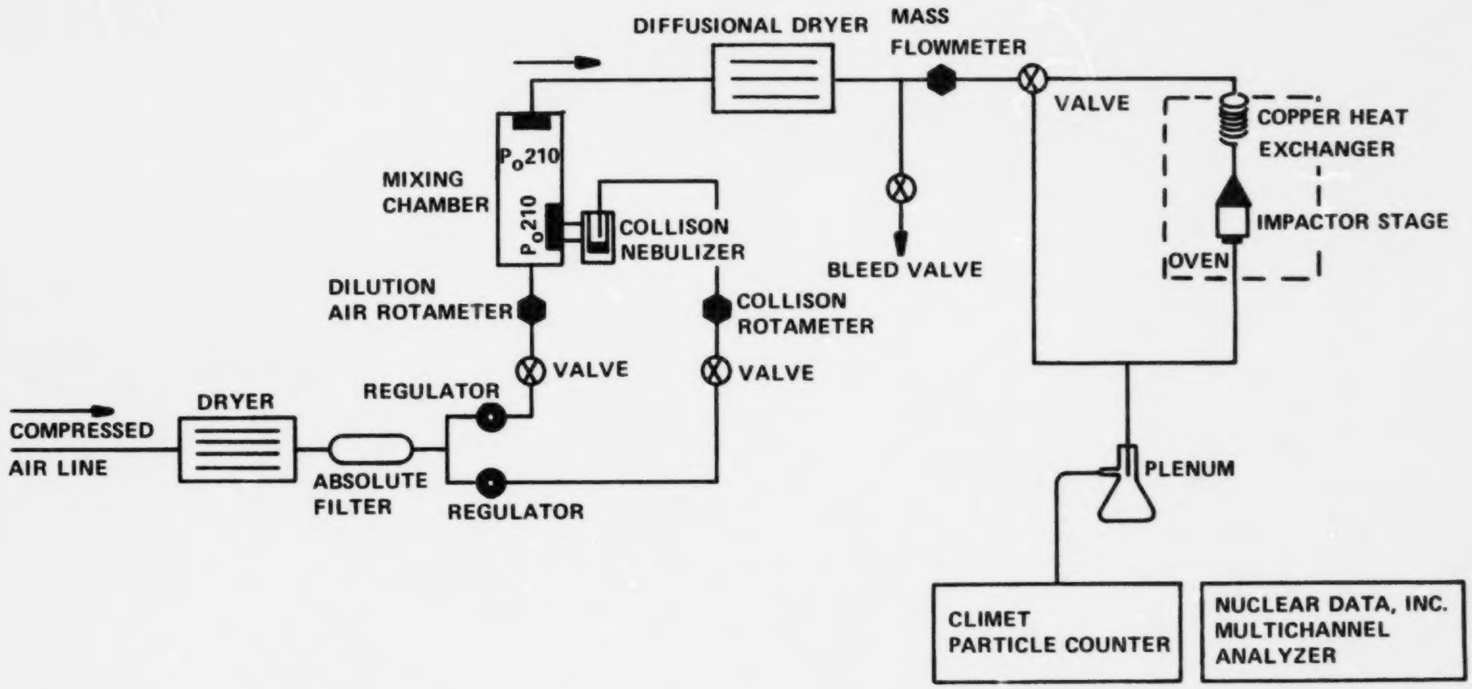
DIFFUSIONAL DRYER
MASS FLOWMETER
VALVE
COPPER HEAT EXCHANGER
IMPACTOR STAGE
OVEN
MIXING CHAMBER
P_o210
P_o210
COLLISON NEBULIZER
BLEED VALVE
DILUTION AIR ROTAMETER
COLLISON ROTAMETER
VALVE
VALVE
REGULATOR
COMPRESSED AIR LINE
DRYER
ABSOLUTE FILTER
REGULATOR
PLENUM
CLIMET PARTICLE COUNTER
NUCLEAR DATA, INC. MULTICHANNEL ANALYZER

Figure 13. System to determine the collection efficiency of candidate substrate materials.

efficiencies increased slightly. A copper heat exchanger was then added to the system so that the aerosol would equilibrate to 93°C before passing through the impactor. Collection efficiency improved substantially with all spun cast substrates, but not for the dipped substrates.

Glass fiber, bare metal, petroleum jelly, and Apiezon L were used as control substrates and the efficiency for each was periodically checked. All collection efficiencies are listed in Table 4.

Weight stability was determined for each substrate at progressively higher temperatures. The results of these tests are shown in Table 5.

After reviewing the behavior of the polymer coatings as impaction substrates and their stability at elevated temperatures we concluded that the best material was the EY907 Vynathene on Mylar. This is the recommended substrate for use with the impactor.

SAMPLING WITH THE IMPACTOR

All sampling functions are carried out with the central control unit and the modified Andersen EPA Control Unit. The EPA control unit (Figure 4) has been modified by the removal of the temperature monitor to the central control unit. Main power to all units is provided at the MAIN POWER switch. Power for the central control unit is switched at the third switch from the left, originally used as a vacuum pump on/off switch. The central control unit (Figure 5) controls all sampling and switches the vacuum pump in the EPA unit on and off. Once sampling has commenced, all flowrate adjustment and control was handled with the EPA unit operating as detailed in the operating instructions for the EPA Control Unit.[7]

Once the flowrate has been determined and initial settings have been made, all functions are initiated by the central control unit. The various functions of this unit are shown in Figure 5.

Looking from the left, the first control is the TIMER MODE SELECT switch. There are two positions, AUTOMATIC and MANUAL. The timer is a Intersil ICM-7045 complementary MOS Precision Timer chip. The readout for this timer is located above the mode selector and is labelled TIMER READOUT. In the AUTOMATIC mode the timer is used to measure the sampling time and is automatically started and stopped by the FUNCTION CONTROL switch. In the MANUAL mode, the timer is activated by the MANUAL TIMER START/STOP switch and reset by the MANUAL TIMER RESET switch. Four possible functions are possible in the manual operating mode: the standard, sequential, split, and the rally mode.

The rocker switch to the right of the timer controls is labelled VARIABLE/FIXED PUMP DELAY SELECTOR. This control allows the turn on of the vacuum pump in the EPA Controller Unit to be delayed for up to 30 seconds after the impactor drive has been turned on. The start of the timer is also delayed if the TIMER MODE SELECT switch is in the AUTOMATIC position. The delay time is adjusted with the SET PUMP DELAY potentiometer located between the VARIABLE/FIXED PUMP DELAY SELECTOR switch and the FUNCTION CONTROL switch. If the FIXED PUMP DELAY is selected, then the pump and timer turn on almost instantaneously after the START function is selected.

TABLE 4. COLLECTION EFFICIENCIES OF COPOLYMER/THIN FILM SUBSTRATES

SAMPLES SPUN CAST AT 3500 RPM. FILMS ~ 0.005 cm THICK. DRY COATING ~ 0.0013 cm THICK.												Dipped Samples, Each Layer ~18-20Å 1-5 Layers, 2-25 Layers, 3-10 Layers.			CONTROL SUBSTRATES			
EY903/ Mylar	EY903/ Kapton	EY904/ Mylar	EY904/ Kapton	EY906/ Mylar	EY906/ Kapton	EY907/ Mylar	EY907/ Kapton	49032/ Mylar	49032/ Kapton	49000/ Mylar	49000/ Kapton	EY903/ Kapton^1	EY903/ Kapton^2	49032/ Kapton^3	Glass Fiber	Vase- line	Bare Metal	Apiezon L
CONDITIONS: Samples tested with the second stage of a Brink BMS-11 Impactor at ambient																		
68%	55%	59%	62%	52%	48%	52%	49%	57%	57%	-	-	61%	60%	68%	-	98%	54%	-
CONDITIONS: Samples tested with the first stage of a Brink BMS-11 Impactor at ambient																		
67%	56%	67%	65%	74%	71%	80%	62%	46%	39%	63%	46%	52%	50%	52%		96%	74%	77%
																95%	46%	87%
																95%	89%	
																	57%	
																	66%	
																	64%	
															Averages	95%	66%	82%
CONDITIONS: These samples were tested with Stage 1 at 93°C (200°F)																		
76%	77%	72%															37%	
64%	73%	73%	66%	76%													42%	
85%	73%	65%	66%	80%													29%	
	65%																29%	
																	36%	
Averages																	12%	
75%	72%	70%	66%	78%													31%	
CONDITIONS: These samples were tested with Stage 1 at 93°C. A copper heat exchanger was added to system so as to allow aerosol time to heat to 93°C.																		
87%	93%	94%		81%	84%	89%	91%	87%	87%	75%	.58%	Sample	40%	60%	63%		59%	83%
89%	87%	92%	82%	83%	91%	96%	94%	57%	86%	79%	46%	Supply	45%	65%	72%		71%	78%
83%	88%	84%	81%	74%		97%	87%	85%	84%		63%	Depleted	69%	40%	57%		54%	71%
								85%		73%			26%	40%	61%		30%	87%
								56%					87%	58%	64%		46%	
								62%							65%		55%	
															42%			
															65%			
Averages															45%			
86%	89%	90%	81.5%	79%	87.5%	94%	91%	72%	86%	76%	59%		53%	53%	59%		52.5%	80%

TABLE 5. WEIGHT STABILITY OF SUBSTRATES

Substrate	INITIAL WEIGHT (mg)	WEIGHT AFTER BAKING[a] (mg)	WEIGHT CHANGE (mg)	WEIGHT AFTER BAKING[b] (mg)	WEIGHT CHANGE (mg)	WEIGHT AFTER BAKING[c] (mg)	WEIGHT CHANGE (mg)	WEIGHT AFTER BAKING[d] (mg)	WEIGHT CHANGE (mg)	WEIGHT AFTER BAKING[e] (mg)	WEIGHT CHANGE (mg)	WEIGHT AFTER BAKING[f] (mg)	WEIGHT CHANGE (mg)	INITIAL WEIGHT (mg)	WEIGHT AFTER BAKING[g] (mg)	WEIGHT CHANGE (mg)
EY903/ Mylar	52.77	52.72	0.05	52.72	0.00	52.71	0.01	52.73	-0.01	52.73	0.00	51.52	1.21	51.53	51.02	0.51
EY903/ Kapton	52.18	52.05	0.13	52.05	0.00	51.96	0.09	51.93	0.03	51.80	0.07	51.33	0.47	51.33	50.97	0.36
EY904/ Mylar	50.91	50.89	0.02	50.89	0.00	50.89	0.00	50.88	0.01	50.68	0.20	50.27	0.31	50.37	50.18	0.19
EY904/ Kapton	53.26	53.15	0.11	53.13	0.02	53.04	0.09	53.00	0.04	52.90	0.10	52.70	0.20	52.70	52.23	0.47
EY906/ Mylar	54.05	54.02	0.03	54.03	-0.01[h]	54.03	0.00	54.02	0.01	53.71	0.31	53.26	0.45	53.27	53.09	0.18
EY906/ Kapton	56.86	56.73	0.13	56.71	0.02	56.62	0.09	56.56	0.06	56.50	0.06	56.16	0.34	56.15	55.43	0.72
EY907/ Mylar	51.77	51.71	0.06	51.72	-0.01	51.70	0.02	51.72	-0.02	51.68	0.04	51.38	0.30	51.38	51.12	0.26
EY907/ Kapton	51.25	51.14	0.11	51.10	0.04	51.00	0.10	50.98	0.02	50.91	0.07	50.73	0.18	50.72	49.92	0.80
EY903/ Kapton(1)[i]	12.86	12.85	0.01	12.85	0.00	12.85	0.00	12.85	0.00	12.85	0.00	12.84	0.01	12.85	12.83	0.02
EY903 Kapton(2)[i]	20.38	20.36	0.02	20.36	0.00	20.35	0.01	20.36	-0.01	20.35	0.01	20.35	0.00	20.35	20.33	0.02
49032/ Kapton(3)[i]	39.16	39.12	0.04	39.09	0.03	39.08	0.01	39.10	-0.02	39.10	0.00	39.08	0.02	39.08	39.06	0.02
49032/ Mylar	56.09	55.91	0.18	55.89	0.02	55.86	0.03	55.87	-0.01	55.85	0.02	55.82	0.03	55.82	55.55	0.27
49032/ Kapton	61.05	60.89	0.16	60.77	0.12	60.64	0.13	60.62	0.02	60.42	0.20	60.19	0.23	60.19	59.60	0.59
49000/ Mylar	46.66	46.65	0.01	46.64	0.01	46.62	0.02	46.62	0.00	46.61	0.01	46.58	0.03	46.59	46.56	0.03
49000/ Kapton	50.38	50.35	0.03	50.36	-0.01	50.33	0.03	50.35	-0.02	50.32	0.03	50.23	0.09	50.24	50.19	0.05

[a] 2 hours at 121°C

[b] 4 additional hours at 121°C

[c] 2 hours at 149°C

[d] 2 additional hours at 149°C

[e] 2 hours at 177°C

[f] 4 hours at 177°C

[g] 2 hours at 204°C

[h] Negative sign indicates weight gain.

[i] Dipped substrates. Each layer is 18-20 A° thick.
(1) 5 layers, (2) 25 layers, (3) 10 layers.

The main control switch which governs all the motor drive and flow functions is the FUNCTION CONTROL switch. When the main power switch on the EPA Control Unit is turned on, the upper left quadrant of the FUNCTION CONTROL switch is illuminated and the word RESET appears. Depressing the switch once causes the upper right quadrant of the switch to be illuminated and the word START to appear. At this point, pump delays can be selected, the timer mode is set, and the RUN TIME SELECTOR is set for hours, minutes, and seconds of run time. The RUN TIME SELECTOR is programmed by lever switches. The first two digits are hours (maximum of 99); the second two digits are minutes (maximum of 59); and the third two digits are seconds (maximum of 59). Depressing the FUNCTION CONTROL switch starts the vacuum pump and timer, after any programmed delay, and illuminates the lower left and right quadrants of the FUNCTION CONTROL switch. The lower left quadrant is red and reads ABORT: the lower right quadrant is clear and labelled RUN. If for any reason the run should be stopped before the set run time has elapsed, pressing the FUNCTION CONTROL switch will stop the vacuum pump and leave the TIMER READOUT displaying the elapsed time. If the run proceeds normally, the run time set on the RUN TIME SELECTOR elapses, and the ABORT and RUN lights on the FUNCTION CONTROL switch are extinguished. Pushing the FUNCTION CONTROL switch again has no effect. This was intended so that a completed run would not be ruined. In order to make another run and start the RESET, START, ABORT/RUN sequence again, power to the control unit must be turned off and then back on.

On the right side of the central control unit a Type K digital thermocouple readout is located along with a THERMOCOUPLE SELECTOR switch. Six temperatures can be monitored: STACK, IMPACTOR, PROBE INLET, PROBE OUTLET, GAS METER INLET, and GAS METER OUTLET. The STACK temperature is monitored by a shielded thermocouple which extends through the front of the impactor, shown in Figure 5. The IMPACTOR temperature is monitored in the middle of the impactor out of the gas path. The PROBE INLET and OUTLET and GAS METER INLET and OUTLET temperatures are monitored at the obvious locations. In the case of the probe, temperatures are monitored beneath the heating tape at the surface of the gas line.

RESULTS AND CONCLUSIONS

Results

The impactor has been used for stack sampling at a kraft recovery boiler, a smelt tank, and a power boiler associated with a pulp and paper mill. These measurements were conducted as part of multiple source/multiple receptor study performed in an industrial region containing an oil-fired power plant, a contact sulfuric acid plant and a pulp and paper mill. The above study was funded by the U.S. Environmental Protection Agency under Contract 68-02-3460.

The samples obtained in this study are under analysis and no results are yet available. However, preliminary comments can be made about how well the impactor functioned and the performance of the substrate materials.

The impactor met all of its design objectives and performed well. Samples were obtained for WDXRF analysis.

The substrate coating material was found to react with sulfur components in the flue gas at sampling temperatures above about 100°C. Since the sampling times were short, this did not present a problem except at the power boiler where even with short sampling times, the stack temperature was high enough to liquify the EY907 substrate coating. For this reason, an alternate substrate coating was used, A-Fax 500 (Hercules Chemical Co.)

A-Fax 500 is an amorphous polypropylene . At sampling temperatures characteristic of the power boiler it performs well and does not react with sulfur oxides in flue gases, although its X-ray background may be higher than EY907. We have used this material as an impaction substrate for other stack sampling and used it for sampling at the power boiler. Samples were obtained for WDXRF analysis.

CONCLUSIONS

The impactor designed and built on this project has proven itself in the field. It is a unique tool for obtaining samples for X-ray analysis with no sample preparation. For many aerosol sampling situations this presents a new opportunity to obtain a size segregated sample from which a size distribution and elemental composition as a function of particle size may be obtained without destroying the sample.

Although quite expensive to build, the impactor is easy to operate and is rugged enough to survive many field testing expeditions without major repair.

ACKNOWLEDGEMENTS

The design and construction of this impactor was carried out under USEPA contract 68-02-2992. Sampling with the impactor was funded on USEPA contract 68-02-3460. The Project Officer for both contracts is Dr. K.T. Knapp.

We are indebted to Mr. Donald L. Duke of Dr. Knapp's staff for the initial suggestion to use a polymeric material for a substrate coating.

REFERENCES

1. Wagman, J., R.L. Bennett, and K.T. Knapp, "Simultaneous Multiwavelength Spectrometer for Rapid Elemental Analysis of Particulate Pollutants," X-Ray Fluorescence Analysis of Environmental Samples, Ann Arbor Science Publishers, Inc., Ann Arbor, Michigan, (1977).

2. Knapp, K.T., "The Effects of Nozzle Losses on Impactor Sampling." In: Proceedings, Advances in Particle Sampling and Measurement, W.B. Smith, Editor. U.S. Environmental Protection Agency Report EPA 600/9-80-004, January, 1980.

3. Felix, L.G., and McCain, J.D., "Errors in Recovered Size Distributions Caused by Impactor Sampling with Bent Nozzles," Presented at the 74th Annual Meeting of the Air Pollution Control Association, Philadelphia, Pa. Paper 81-7.4 (1981).

4. Lundgren, D.A., "An Aerosol Sampler for Determination of Particle Concentration as a Function of Size and Time," J. APCA, 17, 4 (1977), pp. 225-228.

5. Marple, V.A., and Liu, B.Y.H., "Characteristics of Laminar Jet Impactors," Environ. Sci. Technol. 8, 7 (1974), pp. 648-654.

6. Felix, L.G., Clinard, G.I., Lacey, G.E., and McCain, J.D., "Inertial Cascade Impactor Substrate Media for Flue Gas Sampling," U.S. Environmental Protection Agency Report EPA-600/7-77-060, June 1977.

7. Operating Instructions for Andersen Samplers, Inc., Emission Parameter Analyzer, Bulletin WP-53-1. Available from Andersen Samplers, Inc., 4215-C Wendell Dr., Atlanta, GA 30336.

This paper has been reviewed in accordance with the U.S. Environmental Protection Agency's peer and administrative review policies and approved for presentation and publication.

Paper 7

SOURCE ASSESSMENT SAMPLING SYSTEM (SASS) VERSUS DILUTION TUNNEL SAMPLING

Raymond G. Merrill, Jr., Joellen Lewtas, and Robert E. Hall
U.S. Environmental Protection Agency
Research Triangle Park, North Carolina

INTRODUCTION

Two sampling methods have received increased attention recently because of their ability to collect particulate and organic emissions from combustion sources (1,2). One method of sampling, represented by the Source Assessment Sampling System (SASS), is designed to collect and size-classify particulate and to collect nonparticulate organic and inorganic materials at source conditions. The second method, represented by various types of dilution tunnels, is designed to collect total particulate and particulate bound organic material at conditions which approximate ambient environment.

Both methods of sampling were evaluated by EPA at its combustion research facility in Research Triangle Park, NC, using a typical residential oil furnace. The data acquired in these tests demonstrate the strengths and weaknesses of each method and the possible applications of the two methods to stationary source sampling.

DESCRIPTION OF THE SAMPLING SYSTEMS

SASS

The SASS was designed to collect sufficient quantities of stationary source particulate and gaseous emissions to allow particulate size characterization and inorganic, organic, and bioassay analyses (3,4).

The SASS train consists of a stainless steel probe that connects to three cyclones and a filter in an oven module, a gas treatment section, and an impinger series (see Figure 1). Size fractionation is accomplished in the cyclone portion of the SASS train, which incorporates the three cyclones in series to provide large collection capacities for particulate matter nominally size-classified into three ranges: (a) >10 μm, (b) 3 μm to 10 μm, and (c) 1 μm to 3 μm. By means of a standard 142-mm or 230-mm filter, a fourth cut, <1 μm, is also obtained. The gas treatment system follows the oven unit and is composed of four primary components: the gas cooler, the sorbent trap, the aqueous condensate collector, and a temperature controller. Volatile organic material is collected in a cartridge or "trap" containing XAD-2 sorbent, a

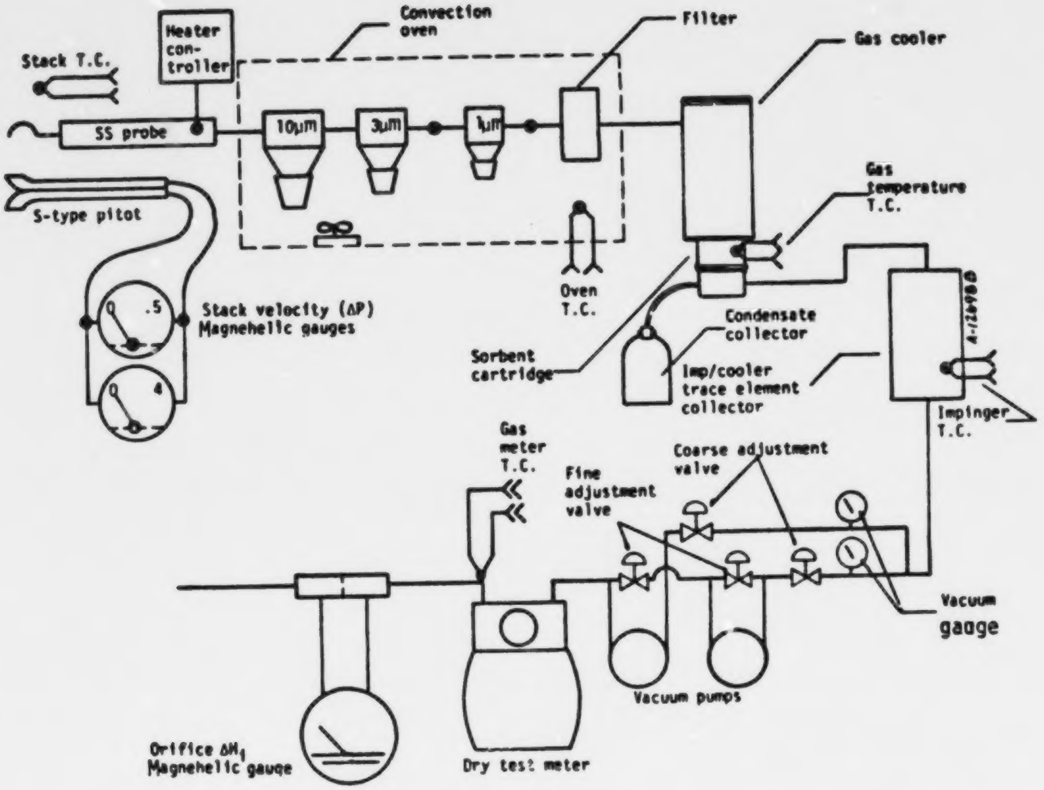
Convection oven
Filter
Gas cooler
Heater controller
Stack T.C.
SS probe
10μm
3μm
1μm
S-type pitot
Gas temperature T.C.
Stack velocity (ΔP) Magnehelic gauges
.5
4
Oven T.C.
A-12490
Condensate collector
Sorbent cartridge
Imp/cooler trace element collector
Impinger T.C.
Gas meter T.C.
Coarse adjustment valve
Fine adjustment valve
Vacuum gauge
Vacuum pumps
Orifice ΔH, Magnehelic gauge
Dry test meter

Figure 1. SASS flow diagram.

micro-reticular resin with the capability of absorbing a broad range of organic species. Volatile inorganic elements are collected in a series of impingers that follow the condenser and sorbent system. The last impinger in the series contains silica gel for moisture removal. Trapping of some inorganic species also may occur in the sorbent module.

Particulate material sampled by the SASS train in the furnace tests is collected at 205°C and gas-phase organic material is cooled and collected at 20°C in the gas conditioning module. In order to obtain the 30 dscm SASS sample under conditions typical of home furnace use, the furnace is operated for 25 cycles of approximately 10 minutes on followed by 20 minutes off. The SASS train is started 20 seconds before burner start-up and left on for 40 seconds following burner shutdown. SASS sampling flow rate is held at 0.11 dscm per minute.

Dilution Tunnel

Dilution sampling systems are designed to collect cooled particulate and particulate bound flue gas materials at approximately ambient environment conditions. Dilution of flue gas is accomplished with filtered ambient air which cools the source sample to approximately 32°C and allows condensable material to absorb on the particulate material. The particulate material is collected on an inert (Teflon) coated fiberglass filter. No particulate size fractionation is accomplished in the primary collection apparatus.

For the oil heater tests, a dilution tunnel consisting of a 12.7 meter long steel tube 0.45 meters in diameter was used as shown in Figure 2. The source stream and filtered dilution air are admitted in one end of the tunnel and drawn through the tunnel to the filter module. Dilution air enters through a laminar flow element where the flow rate is measured. Cooled source sample and dilution air are drawn through a 50 by 50 cm Teflon-coated filter and pumped to an exhaust stack through another laminar flow element where the final flow rate of source plus dilution air is measured.

The dilution tunnel is operated on the same cycle as the SASS train (i.e., 10 minutes on, 20 minutes off, starting 20 seconds before start-up, and sampling 40 seconds after burner shutdown).

DESCRIPTION OF THE DOMESTIC FURNACE TEST

The tests were conducted using a conventional (10 year old) commercial Williamson home furnace with a non-flame retention burner fired with No. 2 fuel oil. Figure 3 is a schematic of the residential warm air furnace. Source sampling and monitoring was accomplished before and after the furnace barometric damper. Only the results of sampling after the damper are presented here since the source and dilution data are directly comparable for this portion of the source stream.

Flue gas analyzers and a SASS probe were inserted into the stack above the atmospheric damper. All material in the flue gas stream which passes these sampling probes was directed through the dilution tunnel and filter. All samples were taken in duplicate, and the results reported are the average of two sampling runs.

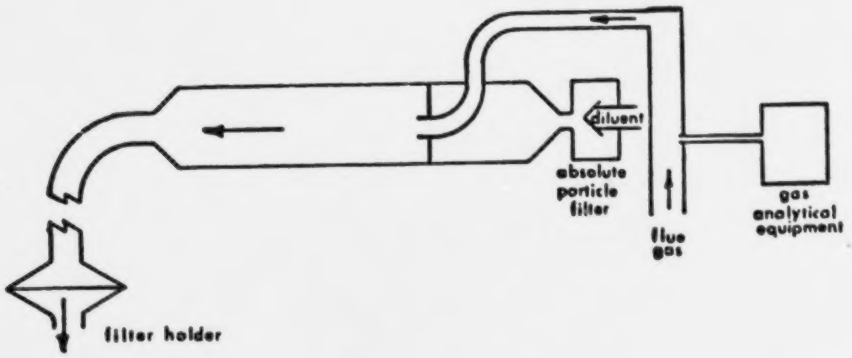

Figure 2. Dilution tunnel system for collection of particulate.

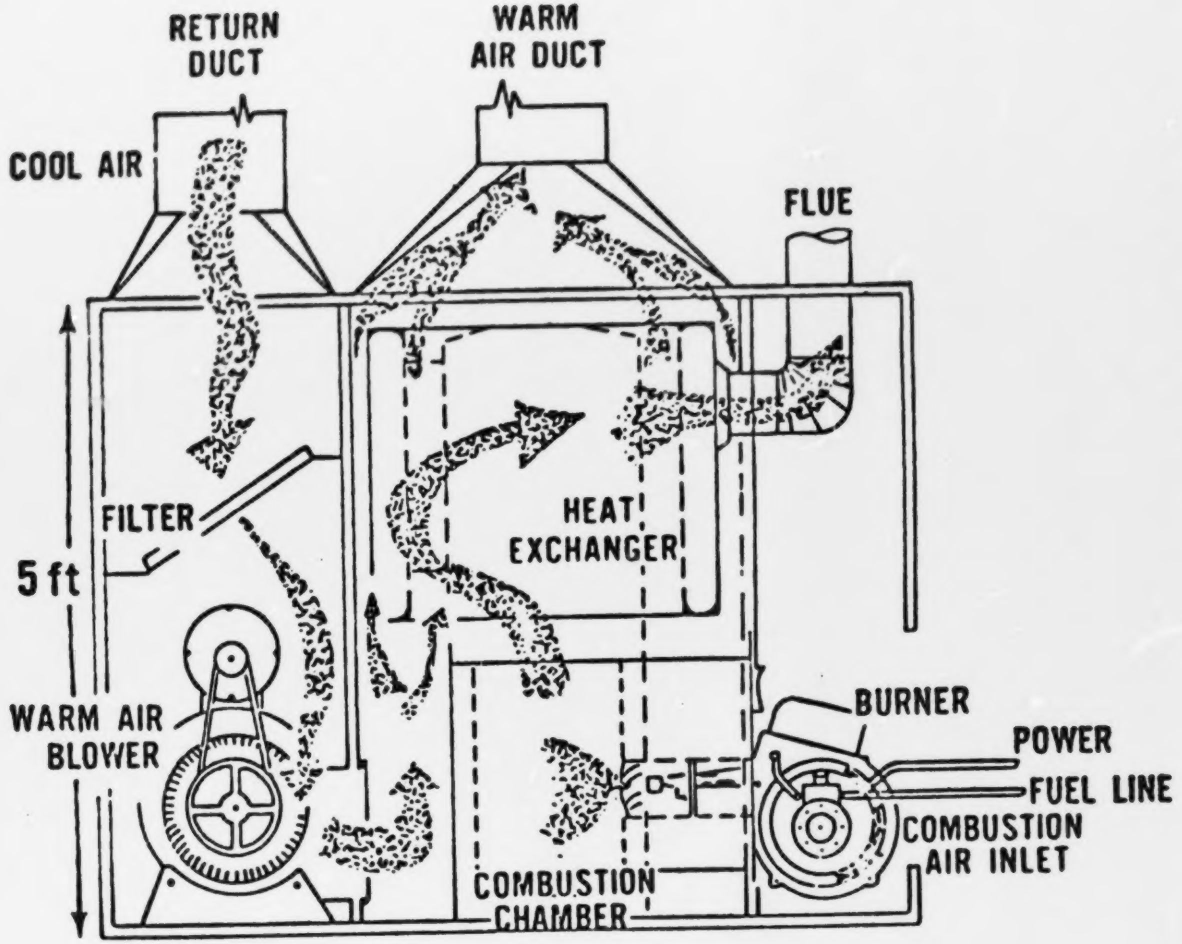
RETURN DUCT
WARM AIR DUCT
COOL AIR
FLUE
FILTER
5 ft
HEAT EXCHANGER
WARM AIR BLOWER
BURNER
POWER
FUEL LINE
COMBUSTION AIR INLET
COMBUSTION CHAMBER

Figure 3. Residential warm air furnace.

SAMPLE ANALYSIS

Bulk Solids

Bulk solids from the SASS train were recovered from the probe, cyclones, and fiberglass filter. Solvent from probe and cyclone particulate washes were allowed to evaporate, and the residual was weighed. Filters were weighed after reaching constant weight in a desiccator.

Bulk solids on the dilution tunnel filters were determined by weighing after the filters had reached constant weight in a desiccator. No attempt was made to recover particles from the tunnel itself.

Extractable Organic Materials

In addition to total particulate mass, the total extractable organic material was recovered from both sampling systems. Limited bioassay and chemical analyses were performed on the organic extracts.

Organic samples from the SASS train were prepared by Soxhlet extraction with dichloromethane as described in the IERL-RTP Level 1 Procedures Manual (5). Since the amount of organic extract from the SASS particulate was extremely small, it was combined with the extract of the XAD-2 module.

Dilution tunnel filters (50 by 50 cm) were cut into 6 by 13 cm sections and extracted with dichloromethane in a Soxhlet extractor. These samples were filtered through a medium porosity frit glass funnel to remove fine particles.

Total semiquantitative organic analysis of the samples was performed using selected Level 1 procedures shown in Figure 4. Samples were concentrated using Kuderna-Danish apparatus. Total chromatographic organic (TCO) analysis for components boiling between 100 and 300°C was performed by gas chromatography. Gravimetric analysis for components boiling above 300°C was performed by taking an aliquot of each sample to dryness in a preweighed pan and weighing the residue.

Ames reverse mutation assays were performed with and without S9 microsomal activation on organic extract samples. Only results from TA-98 are reported. Results are reported as the best-fit computer-modeled slope of the experimentally observed response per microgram of organic material added to the plates.

RESULTS

The first indication of a difference in the sampling characteristics of these two systems appears in the mass of particulate caught. For the residental home heater studies, the dilution tunnel retained 1.5 times the weight of material per cubic meter collected by the SASS (Table 1). The extra mass of the particles collected in the dilution tunnel is due to the presence of condensed organic material on the filtered particulate present because the tunnel operates at ambient temperature. Organic material in the SASS train remains in the vapor phase as it passes the 200°C oven cyclones and filter and condenses or absorbs on the XAD-2 after cooling to 20°C in the gas cooler.

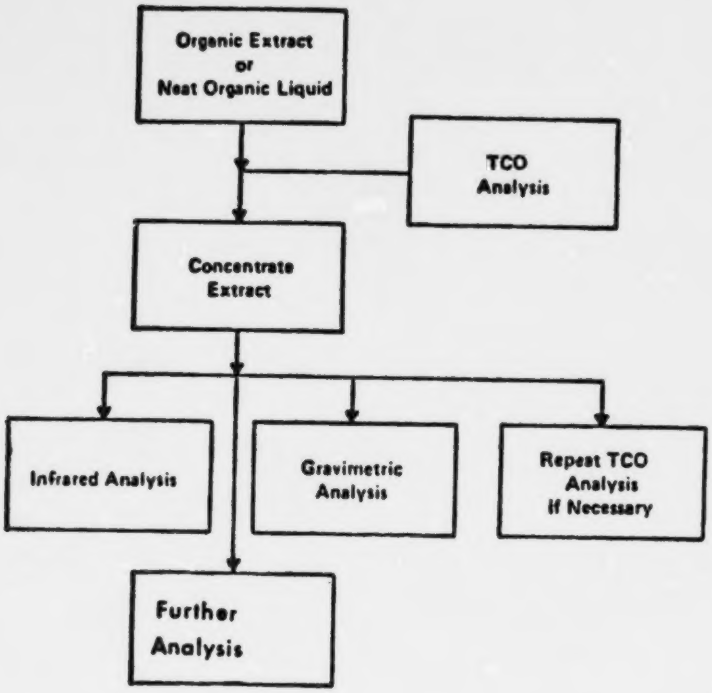
Organic Extract
or
Neat Organic Liquid
TCO
Analysis
Concentrate
Extract
Infrared Analysis
Gravimetric
Analysis
Repeat TCO
Analysis
If Necessary
Further
Analysis

Figure 4. Total extractable organic analysis of SASS and dilution tunnel samples.

TABLE 1. TOTAL PARTICULATE MASS - SASS VS DILUTION TUNNEL

	SASS[a]	DILUTION TUNNEL[b]
Condition 1, mg/dscm[c]	1.62	2.41
Condition 2, mg/dscm[d]	2.65	3.25

[a] Collected at 205°C.

[b] Collected at approximately 32°C.

[c] Equivalent to Bacharach Smokespot 1.

[d] Equivalent to Bacharach Smokespot 3.

A better example of the differences in the sampling systems can be seen by comparing total organic mass collection (Table 2). The SASS method collected 17 to 20 times more total organic mass than the dilution tunnel. SASS samples showed greater concentration of organic material in the flue gas due to the ability of the SASS train to collect and retain organic material of lower boiling point (100°-300°C) than the dilution tunnel.

The dilution sampling method did not collect any of the 100°C to 300°C organic material in these tests. In addition, the chemical analysis revealed that only 20% of the organic material boiling above 300°C was retained on the particulate in the dilution tunnel.

Most of the organic material which is collected by SASS and not by the dilution tunnel was chemically characterized as unburned fuel. The Ames reverse mutation assays results indicate that the organic material collected by both systems which boils above 300°C has similar biological activity (Table 3). The total SASS sample, including all organic material boiling above 100°C, is difficult to assay because it is toxic to bacteria; however, these samples seem to contain materials of higher biological activity than the dilution tunnel (2).

CONCLUSIONS

The results from these tests confirm the design constraints of each of the sampling systems. The dilution tunnel collects particulate and material bound to particulate at temperatures near ambient. Samples taken this way retain less of the total organic emission by percent; but, because of the dilution tunnels' high sampling rate (4.3 dscm per minute), the total material collected provides enough sample for chemical and bioassay analyses.

The SASS method collects the entire particulate and condensable organic mass in separate parts of the sampling apparatus. The SASS method is much more efficient than the dilution tunnel at collecting organic material boiling between 100 °C and 300 °C. The SASS method is much better than the dilution method in accounting for the total condensable emissions from a source, since the dilution tunnel collects only 5% of the organic mass collected by the SASS.

TABLE 2. TOTAL ORGANIC MASS CATCH - SASS VS DILUTION TUNNEL

	SASS	DILUTION TUNNEL
	FILTER AND XAD-2	FILTER
Condition 1, mg/dscm[a]	6.9	0.36
Condition 2, mg/dscm[b]	4.2	0.25

[a] Equivalent to Bacharach Smokespot 1.

[b] Equivalent to Bacharach Smokespot 3.

TABLE 3. MUTAGENICITY[a] OF ORGANICS

	SASS (GRAV) -S9	SASS (GRAV) + S9	DILUTION -S9	FILTER +S9
Condition 1[b]	2.96	2.51	2.15	5.11
Condition 2[c]	1.32	2.58	1.97	5.47

[a] Revertants per µg of organics in strain TA98.

[b] Equivalent to Bacharach Smokespot 1.

[c] Equivalent to Bacharach Smokespot 3.

REFERENCES

1. Huisingh, J., et al. Application of Bioassay to the Characterization of Diesel Particle Emissions. In: Application of Short-term Bioassays in the Fractionation and Analysis of Complex Environmental Mixtures. EPA-600/9-78-027, NTIS PB 299429, Sept. 1978.

2. Lewtas, J. Comparison of the Mutagenic and Potentially Carcinogenic Activity of Particle Bound Organics from Wood Stoves, Residential Oil Furnaces, and Other Combustion Sources. In: Proceedings of the International Conference on Residential Solid Fuels, Portland, Oregon (in press) 1981.

3. Blake, D. Source Assessment Sampling System: Design and Development. EPA-600/7-78-018, NTIS PB 279757, Feb. 1978.

4. Dorsey, J.A., L.D. Johnson, and R.G. Merrill. A Phased Approach for Characterization of Multimedia Discharges from Processes. In: ACS Symposium Series No. 94, pp. 29-48, Nov. 1978.

5. Lentzen, D.E., et al. IERL RTP Procedures Manual: Level 1 Environmental Assessment (Second Edition). EPA-600/7-78-201, NTIS PB 293795, Oct. 1978.

This paper has been reviewed in accordance with the U.S. Environmental Protection Agency's peer and administrative review policies and approved for presentation and publication.

Paper 8

A STACK DILUTION SAMPLING SYSTEM FOR THE MEASUREMENT OF CONDENSIBLE VAPORS IN PROCESS EMISSIONS

A.D. Williamson, J.D. McCain, and W.B. Smith
Southern Research Institute

D.B. Harris
Technical Support Staff
Industrial Environmental Research Laboratory--RTP
U.S. Environmental Protection Agency

ABSTRACT

In order to measure the condensible portion of process emissions a stack dilution sampling system (SDSS) has been designed, characterized in various laboratory studies, and demonstrated in the field at several plants. The principal component of the sampling train is a cylindrical dilution chamber into which the flue gas is directed after passing through the EPA dual cyclone IP sampling train. In the dilution chamber the flue gas is mixed with a standard dilution air and the resulting aerosol-laden mixture is analyzed. Laboratory characterization experiments have verified that thorough mixing of the sample and dilution streams does indeed occur, and that a condensation aerosol can be formed in the diluter. Field demonstrations of the SDSS have been conducted at a domestic oil-fired heater, a coal-fired power plant, two kraft recovery boilers, and a continuous drum mix asphalt plant. Future tests are also planned.

INTRODUCTION

The Environmental Protection Agency has been given the responsibility to set air pollution emission factors for a size specific particulate standard based on the Inhalable Particulate (IP) fraction of particulate emissions. As part of the IP program, a secondary goal of high priority is the measurement of the condensible fraction of process streams. For the present purposes, a condensible compound may be defined as a substance which exists in solid or liquid phase in typical concentrations at ambient conditions, but which has a vapor pressure sufficiently large that significant vapor concentrations can exist at stack temperature.

The contribution to mass emissions of condensed vapors can be quite high under some circumstances. For example, in a coal-fired boiler burning 10 percent ash coal with a particulate control device having 99 percent efficiency, the emitted fly ash will amount to 0.1 percent of the original coal mass. If the coal contains 1 percent sulfur, and if 1.7 percent of this amount is oxidized to sulfuric acid, the amount of acid vapor formed would equal 0.05 percent of the original coal mass. If all of the acid condensed, it would account for one third of the total solid emissions from the utility stack. In other processes, notably smelters, the fraction of mass emitted as vapors and condensing at the stack/ambient interface may far exceed the mass existing in solid form within the stack.

The accurate measurement of the concentrations of condensible vapors and determination of their physical and chemical state after emission into the atmosphere is an important and challenging task. Obviously, instack particulate sizing or mass measurement devices will underestimate the amount of condensible vapors present by neglecting the vapor-phase concentration. In principle, condensible vapors could be collected on cold filters or traps, in impingers, or in sorbent modules. All these techniques, however, are subject to losses on the surfaces of the sampling device, low efficiency of capture of the submicron condensation aerosol, possible aerosol formation due to chemical reactions, or other such artifacts. Furthermore, no information can be obtained on the size distribution of the captured aerosol. It is obvious that, at least in principle, the best way to measure the properties of the aerosol found after emission into the ambient environment is to simulate the process of cooling, dilution, and mixing that occurs in the actual plume. In order to meet the IP program goal of obtaining measurements of condensible matter, a dilution system was designed to simulate the plume/ambient mixing process as closely as possible within the size constraints of a field sampling train. This paper describes the design and laboratory characterization of this Stack Dilution Sampling System (SDSS) and the preliminary results of initial field sampling studies with the device.

DESIGN OF STACK DILUTION SAMPLING SYSTEM

The relative importance of the design parameters for the dilution sampler may be estimated by considering the details of the condensation process. The stack gas initially contains both condensible vapors and particles which can serve as condensation nuclei. As the gas mixes with ambient air the vapors are diluted and cooled, a process which may create a transient supersaturation of the condensible. The condensible vapor concentration is then depleted by condensation/adsorption on the particles (and perhaps self-nucleation). Hygroscopic particles will in addition take up water from the atmosphere. The growth of particle mass is then terminated as the temperature of the plume drops to near-ambient levels and the vapor phase condensibles are depleted to their equilibrium concentration. As the cooled plume continues to spread, further alteration of the particle size distribution may occur by coagulation or evaporation, but these processes may be assumed to be slower than the condensation phase considered here. In this critical phase, the evolution of particles depends on the interacting processes of molecular transport, mixing and cooling dynamics, condensation, and adsorption.

From this qualitative account we may infer that the parameters most critical to plume simulation of condensation are the rate of cooling, the rate and dynamics of mixing, and the composition of the stack mixture. While it may not be necessary to mix and cool at the same rate as a typical source, it appears desirable that the relative rates of cooling, diffusion, and vapor to particle deposition be comparable to those occurring in the plume environment. For this reason a design was chosen to give a relatively gentle mixing process over a mixing time of seconds. The final size distribution is expected to be relatively insensitive to the details of the mixing process after the initial cooling phase has depleted the condensible vapor concentration. Thus, extraction and further dilution should not be a problem.

A second factor expected to be critical to the final size distribution is the relative humidity of the dilution air. The amount of water condensed on hygroscopic aerosols will directly depend on humidity. Since there is considerable variation of ambient humidity, this variable should be controlled in all dilution sampling experiments if the size distribution of the condensed aerosol is of interest.

In short, the parameters expected to be critical to the performance of the dilution sampler are the mixing time (that is, the turbulent mixing length divided by the average velocity), the residence time, and dilution air humidity. Other design parameters are constrained either by the sampling requirements (such as the sample temperature and flow rate) or by practical necessity (such as total size and weight of the instrument).

The mixing mechanism chosen for the present device is injection of a jet of extracted stack gas into the center of a confined stream of dilution air moving at a lower velocity. This choice seems to be the closest approximation to a jet exhausting from a stack exit into nearly stagnant ambient atmosphere. The diameters of the sample inlet tube and the overall dilution chamber were chosen to give cross-sectional areas for sample gas and dilution air inlets to the dilution chamber that are proportional to the mass flows of these two gas streams. Thus, if the sample gas temperature were the same as the 21°C dilution air, the two streams would merge isokinetically. Heated sample gas streams will have extra velocity, as indeed occurs in a buoyant plume. Other geometric specifications were chosen to meet the target flowrate and mixing time specifications. A summary of the specifications used in the design is given in Table 1.

The system as designed for field use is shown in Figure 1. The principal component of the diluter is the cylinder in which flue gas is mixed with filtered air and the resulting aerosol-laden mixture analyzed. Stack gases are extracted into the EPA IP Dual Cyclone Sampler, in which particles with aerodynamic diameters greater than 15 μm are captured in one cyclone (Cyclone X) and inhalable particles in the 2.5-15.0 μm size range are captured in a second (Cyclone III). Particles with aerodynamic diameters less than 2.5 μm pass through the sampler and remain in the gas stream as it passes through a heat-traced flexible hose into the cylindrical dilution chamber. The sample gas is introduced through a tube oriented along the axis of the cylinder and the dilution air is introduced as an annular sheath around the sample. As the sample is cooled by dilution, condensible vapors form particles under conditions close to those

TABLE 1. SPECIFICATIONS FOR STACK DILUTION SAMPLING SYSTEM

GEOMETRIC	
• Active length of dilution chamber:	122 cm
• Diameter of dilution chamber:	21.3 cm
• Diameter of sample inlet tube:	4.27 cm
• Active dilution volume:	43600 cm^3
FLOW	
• Sample flow (determined by IP cyclone train):	∿17 ℓ/min
• Sample velocity:	∿27 cm/sec at 150°C
• Dilution air flow:	425 ℓ/min
• Dilution air velocity:	20 cm/sec
• Dilution ratio:	∿25:1 (up to 40:1 possible)
• Residence time:	6.2 sec
GAS CONDITIONS	
• Sample gas: T < 250°C; particles > 2.5 μm removed by cyclones	
• Dilution air: T = 21.1°C; relative humidity 24%; filtered ambient air	
SAMPLE COLLECTION	
• Particulate collected on hi-vol filter	
• Optional impactor gives cuts at 0.5, 1.0, 2.0, 4.0 μm	
• Optional extraction of diluted stream for sizing by optical counter, electrical mobility analyzer, CN counter, etc.	

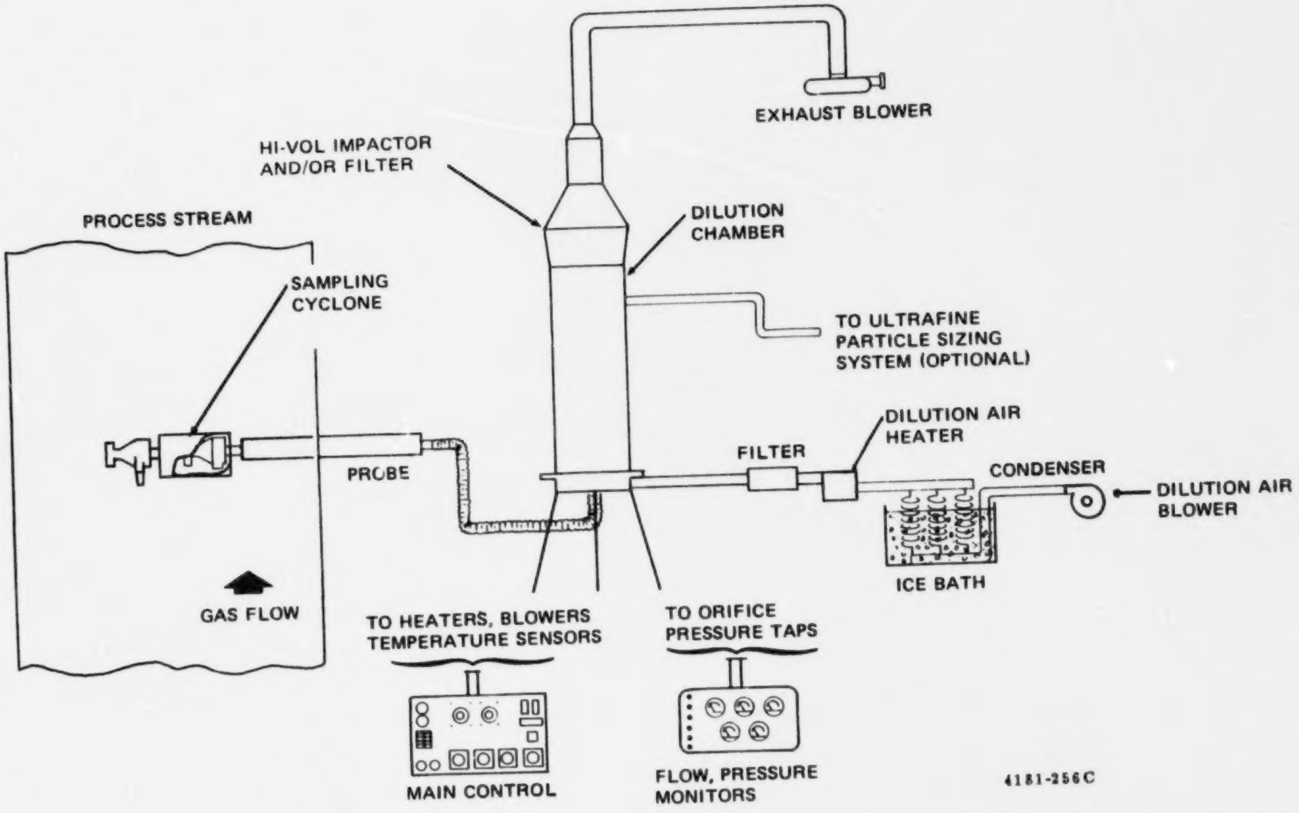
EXHAUST BLOWER
HI-VOL IMPACTOR AND/OR FILTER
PROCESS STREAM
DILUTION CHAMBER
SAMPLING CYCLONE
TO ULTRAFINE PARTICLE SIZING SYSTEM (OPTIONAL)
DILUTION AIR HEATER
FILTER
PROBE
CONDENSER
DILUTION AIR BLOWER
ICE BATH
GAS FLOW
TO HEATERS, BLOWERS TEMPERATURE SENSORS
TO ORIFICE PRESSURE TAPS
MAIN CONTROL
FLOW, PRESSURE MONITORS
4181-256C

Figure 1. Diagram of stack dilution sampling system.

which occur in actual plumes. The system is designed for a "standard" dilution air at 21°C, 24 percent relative humidity, mixing time of 6.2 seconds, and a dilution ratio of 25:1. All of these parameters can be adjusted to some extent. The diluter can be adapted to a variety of sampling devices to measure the condensed and diluted aerosol. The total flow is normally directed into a cascade impactor or filter; alternately, portions of the diluted stream can be extracted, further diluted if necessary, and sampled using an electrical aerosol analyzer, optical particle counter, or diffusion batteries with a condensation nuclei counter. The standard SDSS is limited to stack temperatures below 250°C by the Teflon components in the current design. More extreme temperatures can easily be accommodated by replacing the affected parts with ceramic or metal substitutes.

LABORATORY CHARACTERIZATION OF SAMPLER

In order to assess the suitability of the sampler design to simulate the conditions of real plume formation, several tests were run to investigate the flow and mixing behavior in the diluter. These tests were performed on a clear plastic prototype rather than the stainless steel SDSS actually used for field sampling. The major result of the laboratory studies was to confirm that adequate mixing was occurring in the body of the diluter and that condensation aerosol formation could be studied.

The initial studies of mixing behavior consisted of experiments using smoke to visualize air flow in the sample and dilution lines. These tests showed nearly uniform flow in both streams at the point of introduction without obvious density gradients or turbulent eddies at that point. When smoke was introduced in the sample line, the system gave a good visual presentation of plume-like behavior, with eddy formation in the lower half of the dilution chamber leading to breakup of the original smoke stream and large-scale mixing that appeared uniform over a time average at the top of the chamber. Qualitative differences in the mixing were noted when a cold smoke aerosol is used as opposed to a hot (93°C) smoke stream.

In order to study mixing of the diluted stream in a more quantitative fashion, studies were made of the radial distribution of both condensed and nonvolatile test aerosols. Nebulized table salt solutions were used to form a nonvolatile salt test aerosol. A condensible aerosol was generated by forming a glycerol smoke, then passing a portion of this stream through a heated tube to vaporize portions of the glycerol. The test aerosol was injected in the sample gas stream. At the top of the diluter, a probe was positioned to withdraw a sample from an arbitrary point along the diameter of the diluter tube. The aerosol concentration at this point was monitored using an electrical aerosol analyzer or condensation nuclei counter. In this manner a profile of the particle distribution across the diluter could be obtained.

Figure 2 shows the concentration of the salt aerosol across a diameter of the diluter for various sample temperatures. The degree of mixing is enhanced dramatically as the temperature of the sample is raised. This effect is expected, since the velocity mismatch is designed to be zero for ambient sample temperatures and increases with temperature above ambient. As the

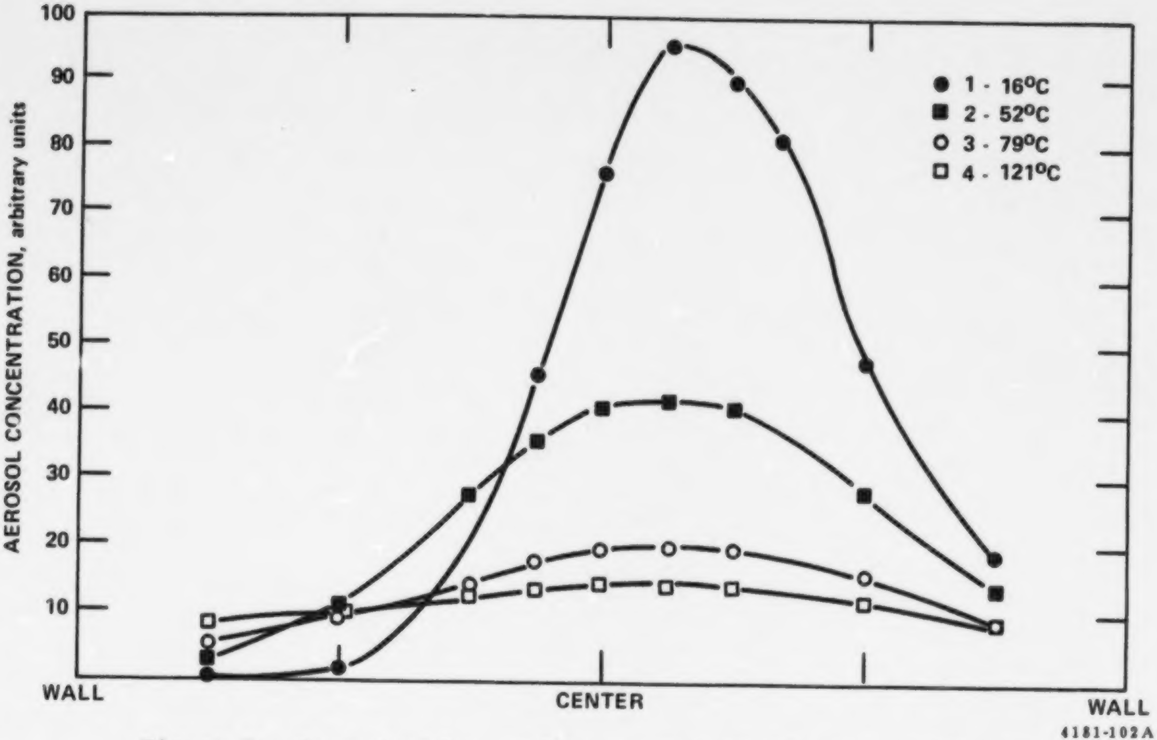

Figure 2. Concentration profile of salt aerosol across diluter.

sample temperature is increased, the transfer of momentum to the dilution air becomes greater and mixing more thorough. As can be seen in Figure 2, for sample temperatures typical of stack conditions substantial mixing has occurred over the entire diameter of the diluter tube. These results indicate that dilution factors, local temperatures, and vapor saturations calculated on the basis of total mixing will be meaningful.

Profiling tests were also performed using the glycerol smoke aerosol. At sample temperatures over about 65°C, a substantial fraction of the original aerosol evaporates in the sample line and recondenses as it is cooled by dilution. Between 93 and 150°C, evaporation is complete and a detached plume of glycerol condensation smoke is observed in the diluter. In this system, as in field samples containing condensible vapors, molecular diffusion could conceivably aid in the mixing process. Results of these tests are illustrated in Figure 3. The dependent variable in this figure is the half-width of the concentration profile relative to the diameter of the diluter tube. As was evident in Figure 2, the half-width of the profile increases with temperature above ambient. Data from the salt aerosol and the glycerol smoke fall along the same curve, indicating that the main mixing mechanism is probably turbulent mixing in macroscopic eddies. This behavior corresponds to what is expected for real plumes.

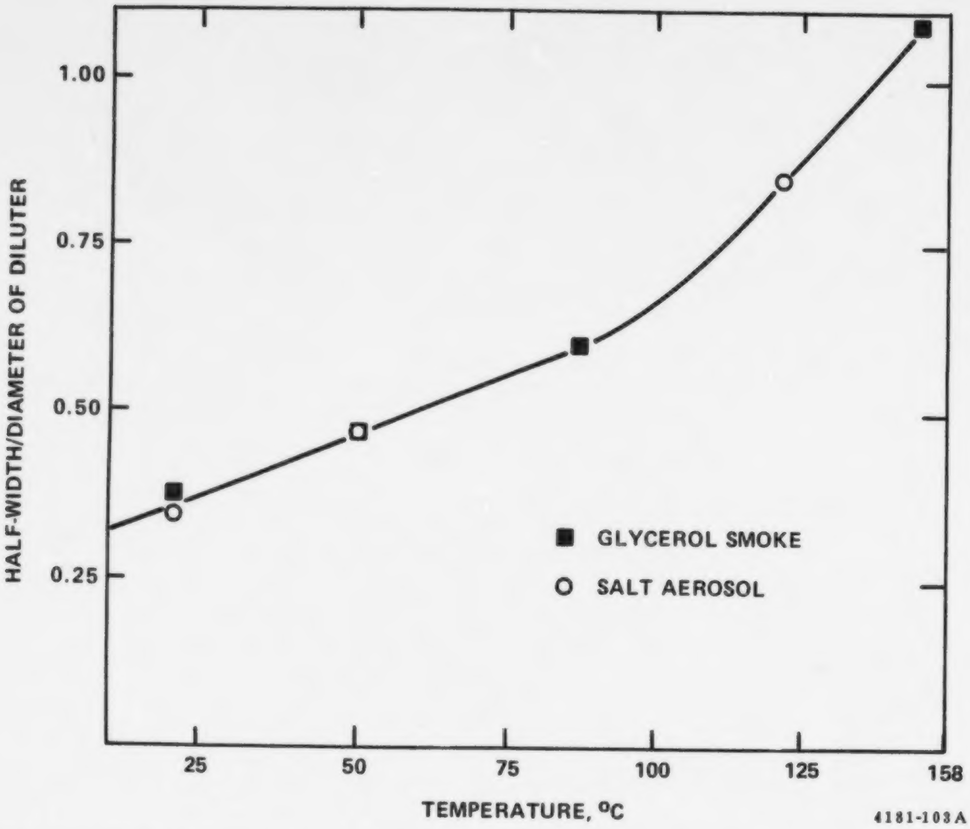

Figure 3. Temperature dependence of cross-section of diluted aerosol plume.

After in-house laboratory characterization, the SDSS was tested at the EPA facilities in Research Triangle Park, North Carolina. The SDSS was one of a battery of devices used to sample the effluent of a domestic oil-fired heater. Other sampling devices included SASS trains, gas analyzers, and an automotive dilution tunnel. Analysis of extracts from the SASS sorbent module demonstrated that most of the emissions were light (TCO fraction) organic compounds, whose vapor pressures were too high to be captured in any of the particulate sampling devices, including the dilution systems. However, both the SDSS and the automotive dilution tunnel captured about 25 percent more mass than the SASS trains, indicating that condensation did significantly increase the particulate loading under the conditions similar to those at the flue exit.

FIELD DEMONSTRATION OF SDSS

A more dramatic confirmation of the operating behavior of the system was obtained in a test at a power plant fueled by high-sulfur coal. The dilution sampling system was used to sample the emissions of a 50 MW boiler downstream of the ESP. Since independent measurements recorded sulfur trioxide (SO_3)

levels of 7 to 8 ppm in the same duct during the sampling periods, it was anticipated that a measurable amount of sulfuric acid would be detected in the SDSS. Since the duct did not have the 6-in. (15.24 cm) ports required for the IP dual cyclone train, only the smaller cyclone was used on the probe of the SDSS. In addition, a Teflon-membrane hi-volume filter was used to ensure low sulfate background and minimize artifact sulfuric acid formation due to the high concentrations of SO$_2$ in the stack gas. Aside from these changes, the dilution sampler was operated in a standard manner. Results of this test are summarized in Table 2. The mass train and impactor measurements are consistent with a stack particulate loading of 36 mg/m^3 actual gas volume during the approximate time period of the SDSS test, with approximately 2 mg/m^3 in the fine fraction as defined by the cut of stage 4 of the modified U.W. Mark V impactors used. In contrast, the fine particulate plus condensible mass as measured by the SDSS was about 26 mg/m^3. Although some differences are to be expected because the impactors and mass trains were run at different times in different positions in the duct, the order of magnitude increase in mass is clearly beyond experimental uncertainty. To obtain further evidence that sulfuric acid condensation was occurring in the SDSS, a portion of the diluted stream was extracted into the Southern Research Institute Ultrafine Particle Sizing System for size analysis of the particulate matter smaller than 1.0 μm. As shown in Figure 4, the size distribution of particulate after dilution was dominated by a mode centered at about 0.08 μm. In contrast, the size distribution in the stack peaks at larger diameters with an integrated mass roughly 5 percent of that observed in the diluted sample. The data in Figure 4 indicate that a sulfuric acid mist is formed by condensation in the SDSS and, presumably, in the plume of the power plant under test.

Although the test at the utility boiler confirmed the operation of the SDSS, certain aspects of the IP protocol could not be followed. A particular omission was the required comparison of the concentrations measured by the SDSS with those measured in simultaneous samples with the standard dual cyclone train.

Two field sampling tests using the SDSS have been completed as part of the IP emission factor measurements program of the EPA. In the first of these tests, the SDSS was used as part of the IP sampling at two kraft recovery boilers, one of which used a Direct-Contact Evaporation (DCE) drying process

TABLE 2. COMPARATIVE MASS LOADINGS (IN mg/acm) IN TEST OF UTILITY BOILER BURNING HIGH-SULFUR COAL--PRELIMINARY DATA

Sample		Fine (<2 μm)	Coarse (>2 μm)	Total
Method 17	(2/4/81)			35.7
Impactor	(2/3/81)	2.0	21	23
Impactor	(2/4/81)	2.2	24	27
SDSS	(2/3/81)	25		
SDSS	(2/4/81)	27		

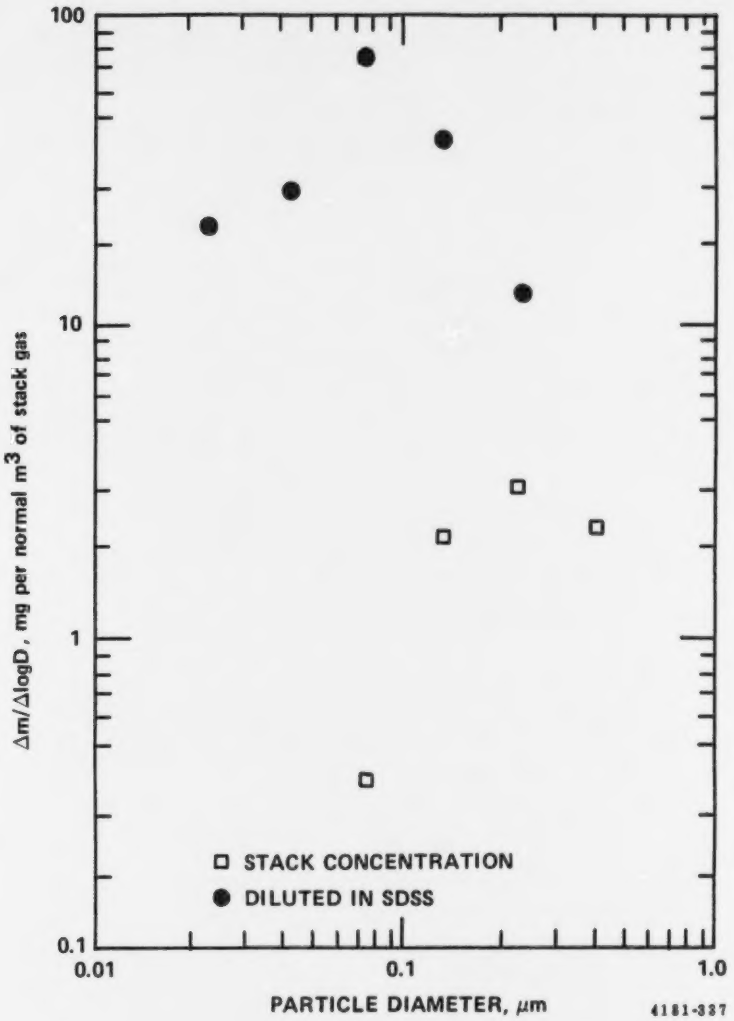

Figure 4. Submicron size distribution in stack gas from coal-fired boiler before and after dilution in Stack Dilution Sampling System. Note evidence of sulfuric acid condensation mode.

and the other a non-DCE process. The second IP test series was conducted at a stationary continuous drum mix asphalt plant. All three sites were sampled downstream of highly efficient particulate control devices. Both recovery furnaces were equipped with electrostatic precipitators, and the asphalt plant with a baghouse. At all three sites the SDSS samples were taken concurrently with a standard dual cyclone IP train with instack filter which was inserted in a second port 90 degrees around the stack from the SDSS port. The loading measured on the instack filter of the standard IP cyclone train was compared with the loading on the SDSS filter and the probe washes. In this way the condensible fraction of the emissions could be separated from the fine particulate fraction which was also collected in the SDSS.

The results of the three field tests are summarized in Tables 3 and 4. Table 3 contains the results of the two kraft recovery boiler tests. The first test, at a recovery boiler which did not use a direct contact evaporation (DCE) process, gave fine particulate concentrations over a factor of five higher in the out-of-stack (SDSS) compared to the instack backup filter on the standard dual cyclone (IP) train. In contrast, tests at the second boiler, which used a DCE process, showed only a factor of two higher loadings in this size fraction in the SDSS runs. These differences may be rationalized by a recent study showing that DCE recovery boilers tend to have approximately one fourth the concentrations of gaseous (SO_2) and condensible (SO_3/H_2SO_4) sulfur oxides found in the non-DCE boilers.[1]

TABLE 3. RESULTS OF STACK DILUTION SAMPLING SYSTEM AND INHALABLE PARTICULATE TESTS ON TWO KRAFT RECOVERY BOILER ESP EXHAUST STREAMS

Run	Sample Volume, dnm^3	Catch Weights, mg				Mass Concentrations, mg/dnm^3				
		Cyclone X	Cyclone III	Probe Wash	Filter	Cyclone X	Cyclone III	Filter+ Probe	Total	Method 5
BOILER A - non-DCE PROCESS										
1-SDSS	2.029	53.11	2.85	128.96	5.00	26.17	1.40	66.01	93.58	--
2-SDSS	2.000	3.11	0.22	157.56	35.20	1.55	0.11	96.28	97.94	172
2-IP	2.194	12.23	5.38		33.19	5.77	2.45	15.13	23.15	
3-SDSS	1.793	0.69	0.05	99.79	10.2	0.38	0.03	61.35	61.75	45.3
3-IP	2.28	4.10	4.57		26.14	1.80	2.00	11.46	15.26	
BOILER B - DCE PROCESS										
4-SDSS	1.854	0.86	5.96	12.83	28.0	0.46	3.21	22.02	25.69	
4-IP	2.180	8.68	13.48	--	25.06	3.98	6.18	11.50	21.66	
5-SDSS	1.888	3.06	12.85	24.06	20.4	1.62	6.80	23.54	31.97	
5-IP	2.121	13.98	20.55	--	27.08	6.59	9.69	12.77	29.05	
6-SDSS	1.888	1.97	6.82	13.51	3.80	1.04	3.61	9.17	14.36	
6-IP	2.090	4.52	5.43	--	14.30	2.16	2.60	6.84	11.60	
7-SDSS	1.882	2.35	4.93	10.08	19.9	1.25	2.62	15.93	19.80	
7-IP	1.930	0.55	3.94		14.8	0.28	2.04	7.66	9.99	

TABLE 4. RESULTS OF STACK DILUTION SAMPLING SYSTEM TESTS AT A CONTINUOUS DRUM MIX ASPHALT PLANT

Run	Sample Volume, dnm^3	Mass Concentrations, mg/dnm^3			Percent Condensibles
		Cyclone X	Cyclone III	Filter + Probe	
1-IP	1.765	5.78	1.57	1.59	
1-SDSS	1.559	19.03	2.80	--	--
2-IP	1.681	18.76	0.94	1.49	
2-SDSS	1.375	14.92	2.01	15.78	43.7
3-IP	2.104	36.74	4.36	1.66	
3-SDSS	1.704	25.61	5.52	19.79	35.6
4-IP	1.155	9.70	2.14	2.42	
4-SDSS	1.112	14.47	2.13	27.81	57.2
AVERAGE-IP		17.75	2.25	1.79	
AVERAGE-SDSS		18.51	3.11	21.13	45.3

The results of condensibles testing at a continuous drum-mix asphalt plant are shown in Table 4. At this plant the fine particle and condensible fraction measured in the SDSS was an order of magnitude higher than that measured by the instack filter. When total emissions are considered, the condensible fraction averaged 40 percent. At this source the condensible fraction is expected to be mainly volatile hydrocarbons evaporated from the asphalt recycle mix.

The results of both field tests confirm that particulate collected from these sources after dilution is altered by the addition of condensible vapors. Further tests at other sources are anticipated in the course of the EPA IP emission factor measurement program.

ACKNOWLEDGEMENTS

This research was supported by the U.S. Environmental Protection Agency under Contract No. 68-02-3118, D.B. Harris, Project Officer. Field tests at the kraft recovery boilers were performed via subcontract from Acurex Corporation under EPA primary Contract No. 68-02-3159. Field tests at the asphalt plant were performed via subcontract from Midwest Research Institute under their EPA primary Contract No. 68-02-3158. Ultimate EPA program manager for both field tests is D.L. Harmon.

REFERENCES

1. Jain, A.K., Blosser, R.O., Newport, D.B., and Oglesby, H.S. Evaluation and Application of SO_x Measurement Procedures for Kraft Recovery Furnaces. EPA-600/S2-80-186, U.S. Environmental Protection Agency, Cincinnati, Ohio, 1980.

Paper 9

PASSIVE REMOTE SMOKE PLUME OPACITY MONITOR

Pedro Lilienfeld
Paul Elterman
Roger Stern
Gary Woker
GCA/Technology Division

ABSTRACT

The development and testing of a novel, remote, passive optical sensor for the measurement of the visual opacity of plumes emitted from smoke stacks is reported. The operation of this instrument is based on the extinction of polarized Rayleigh scattered sky light as it traverses a smoke plume. A two-color measurement of the polarized component of sky light attenuated by the plume is compared with the same components of direct sky light adjacent to the plume. The Remote Opacity Monitor (ROM) operates as a tripod-mounted telephotometer which is focused and aligned on the top of the stack, after which the instrument automatically indicates the visual obscuration of the plume in the units of percent opacity. The prototype ROM (ROM-X) exhibits a typical 2-sigma noise level of about ± 1% opacity with a measurement time constant of 30 seconds. Preliminary comparison tests on oil-fired power plants and "smoke school" generated plumes with in-stack transmissometers were performed. Correlation coefficients for the latter tests were found to be about 0.99 for black smokes and 0.98 for the combined data for black and white smokes.

INTRODUCTION

Remote monitoring of the opacity of plumes emerging from smoke stacks is presently based on visual observations performed by trained observers (EPA Method 9) (1). This offers a rapid and "portable" method of plume particulate emission assessment wherein the human eye-brain combination serves as a transmissometer-contrast photometer. The obvious disadvantages of the visual method reside in: (1) its subjectivity, and (2) its compatibility with continuous recording and/or data transmission. Thus, a considerable effort has been dedicated during the last decade to the development of alternate monitoring techniques which could either complement or even supplement the visual opacity technique.

Optical transmissometry through the stack, the reference method against which visual opacity determinations are compared, although in fairly widespread use at present, represents an intrinsically permanent and non-transportable monitoring system requiring both acquiescence and investment by the source operator; in contrast, a remote opacity sensor would be compatible with nonintrusive and objective inspection procedures, at the same time as it would eliminate the errors associated with the subjective judgement of "smoke inspectors".

Heretofore the only method for remote plume opacity measurements, that has shown promise is based on lidar techniques (2). Its routine use, however, has not materialized so far because of the inherently high complexity and cost of such systems, as well as the attendant dangers resulting from the requirement for high-energy lasers (3). Contrast photometry, and direct sun-light attenuation have been investigated within this context, but practical constraints associated with such approaches (i.e. uniqueness and variability of solar position, and absence of adequate contrast targets) have militated against their routine implementation.

We report here the development and testing of a passive remote plume opacity monitor whose operation is based on sensing the attenuation of the plane-polarized component of sky light as it traverses a smoke plume.

OPTICAL DESIGN

The remote opacity monitor (ROM) consists of a tripod mounted polarization photometer. As shown in figure 1, a zoom and a Barlow lens combination are used to form an image of the smoke stack and plume. The basic 85mm to 200mm telephoto lens permits the operation over a range of instrument-to-stack distances of 20 to 100 times the stack diameter. Typically, for a 3m diameter stack the ROM-X can be placed at any distance ranging from 60 to 300m.

The light forming this image first passes through a rotating half-wave plate which rotates the plane of polarization of the sky light at twice the rotational frequency of the plate. Unpolarized light from both the plume and sky are unaffected.

After passing through the half-wave plate, the light is separated by the first 45° beamsplitter so that approximately 30% of the light is imaged on to the eyepiece reticle for viewing as shown in figure 2. This configuration allows the operator to aim and focus the ROM prior to measurement, and to monitor the viewing region during measurement. The light passed by the first beamsplitter is separated into two channels by the second (50-50) beamsplitter. In the first channel the light passes through a blue (pass) optical interference filter centered at 490 nm and polarizer while in the second channel the light passes through a red (pass) optical interference filter centered at 630 nm and polarizer. The light in each channel is imaged onto two detectors, one which views the center of the plume slightly above the stack, and one which views a small region of sky adjacent to the plume. Thus there are a total of four detectors illuminated, a "blue plume", a "red plume", a "blue sky", and a "red sky" detector. The regions of the sky and plume viewed by these detectors are indicated by the two circles on the eyepiece reticle as shown in figure 2.

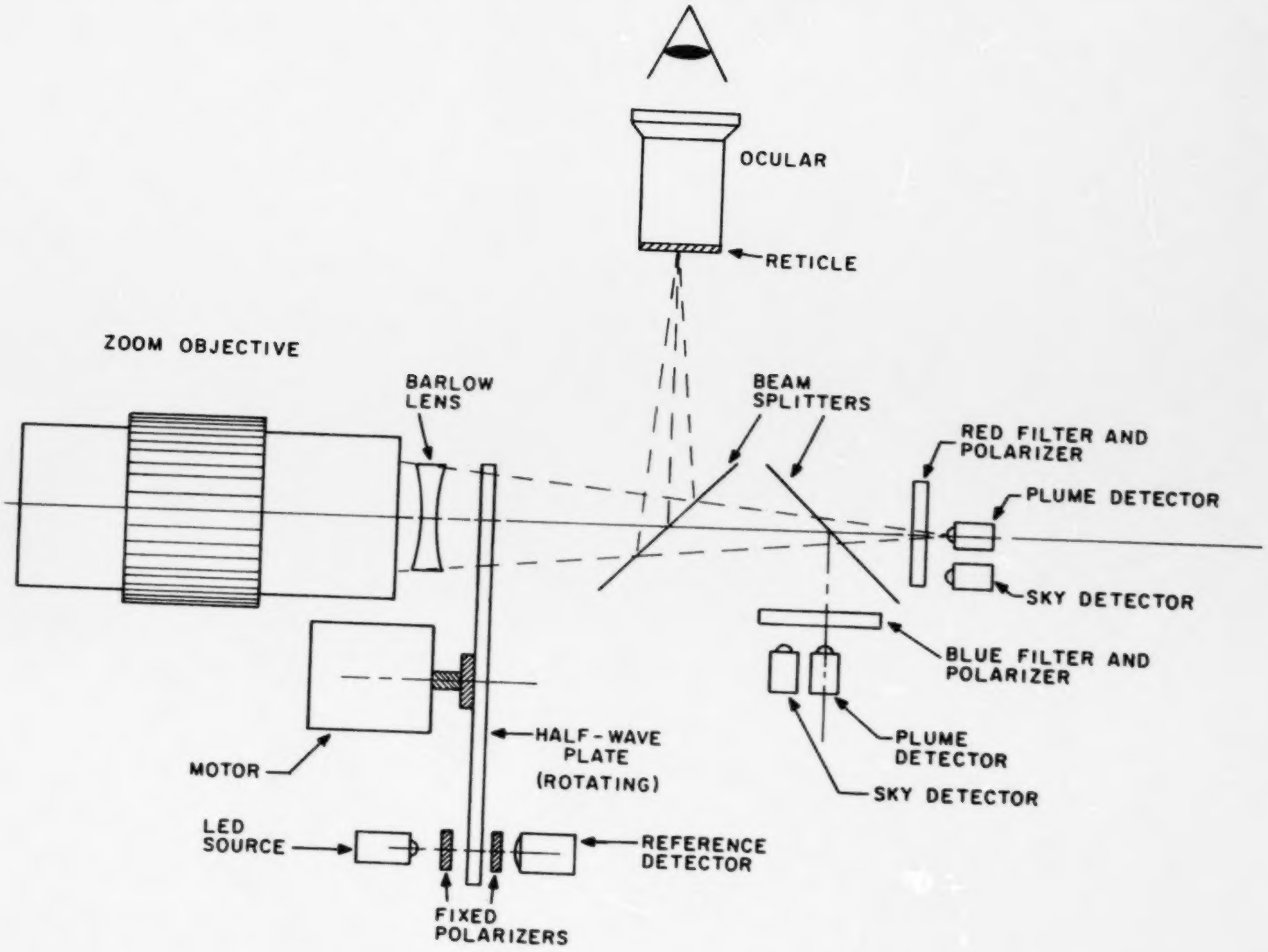
OCULAR
RETICLE
ZOOM OBJECTIVE
BARLOW LENS
BEAM SPLITTERS
RED FILTER AND POLARIZER
PLUME DETECTOR
SKY DETECTOR
BLUE FILTER AND POLARIZER
PLUME DETECTOR
SKY DETECTOR
MOTOR
HALF-WAVE PLATE (ROTATING)
LED SOURCE
REFERENCE DETECTOR
FIXED POLARIZERS

Figure 1. Optical configuration of ROM.

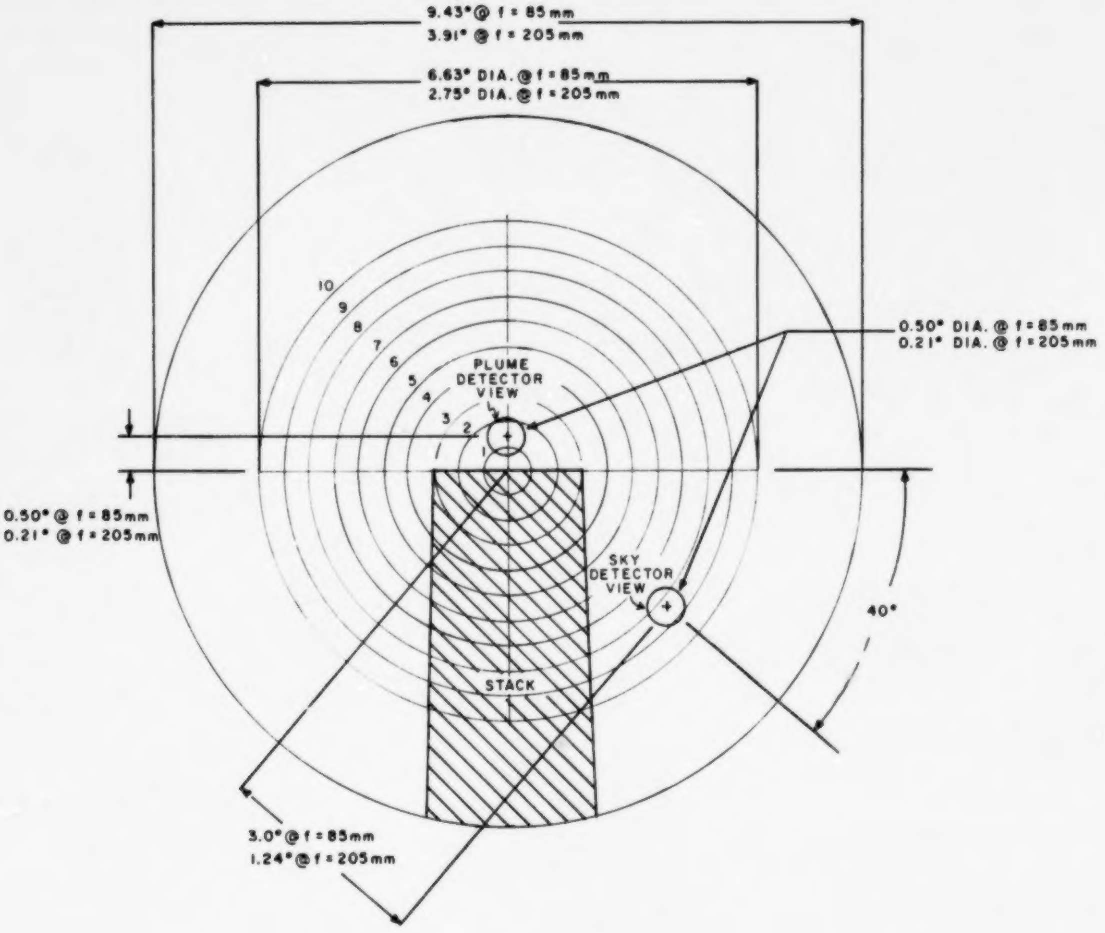
9.43°@ f = 85 mm
3.91° @ f = 205 mm
6.63° DIA. @ f = 85 mm
2.75° DIA. @ f = 205 mm
10
9
8
7
6
5
4
3
2
1
PLUME DETECTOR VIEW
0.50° DIA. @ f = 85 mm
0.21° DIA. @ f = 205 mm
0.50° @ f = 85 mm
0.21° @ f = 205 mm
SKY DETECTOR VIEW
40°
STACK
3.0°@ f = 85 mm
1.24°@ f = 205 mm

Figure 2. Angular view of ROM as viewed through eyepiece.

As previously mentioned, all of the imaged light passes first through a rotating half-wave plate (rotating with an angular frequency ω) and then through a polarizer. The combination of these two optical elements intensity modulates the polarized light entering the ROM at 4ω while leaving all unpolarized sky and plume light unmodulated. In the same manner, the LED reference source and detector generate a 4ω reference signal which is used by the lock-in electronics to discriminate against all signals other than those modulated at 4ω - i.e. only polarized light is detected.

SIGNAL PROCESSING

Figure 3 depicts a simplified block diagram of the electronic signal processing circuitry of the ROM. The four signals, red sky, blue sky, red plume, and blue plume, are detected by four hybrid silicon photodiode-amplifier detectors. These signals are further amplified by four adjustable preamplifiers whose gains are set such that the responses of all detector channels to white light (i.e. the solar spectrum) are equal. After this equalization step, the "red plume" signal is subtracted from the "blue plume" signal by means of a differential amplifier while the "red sky" signal is similarly subtracted from the "blue sky" signal. This procedure has the effect of cancelling the unwanted contribution of small amounts of polarized white plume light while leaving the predominantly blue sky signal light only partially reduced. The differential signals (Δsky, Δplume) are next detected by two lock-in amplifiers. As discussed in the optical design section, the reference signal is derived from an LED and reference detector pair in combination with the rotating half-wave plate. Proper reference phase is manually adjusted by means of an electronic phase shifting network and control pot (not shown in the simplified block diagram). The filtered D.C. signal from the lock-in amplifiers is fed to a divider, the output of which is proportional to the ratio (Δplume/Δsky) or equivalently the transmission T, of the plume.

Prior to the measurement of a plume opacity, the divider output signal is adjusted for unity (zero opacity), viewing a clear sky, by adjusting the gain of the divider with the system zero adjustment control located on the panel. The divider output is subtracted from one and integrated with a selectable 2 or 30 second time constant and then displayed on an LCD digital readout directly in the units of percent opacity. Two warning dots flash on the display if (a) the amplifier gain is set so high that saturation occurs, or if (b) the divider denominator signal is too low for proper operation. If both indicators flash, sky-light polarization is insufficient, precluding an accurate opacity measurement. This latter warning signal removes any subjective judgements from the plume opacity determinations. In addition to the digital display, the plume is available as an analog output for recording.

FIELD EVALUATION

Power Plant Tests

During late October 1979, several sets of opacity measurements were made at a nearby power plant using the prototype ROM (ROM-X). Two of the three smaller stacks were measured. Each plume had a grayish-white appearance.

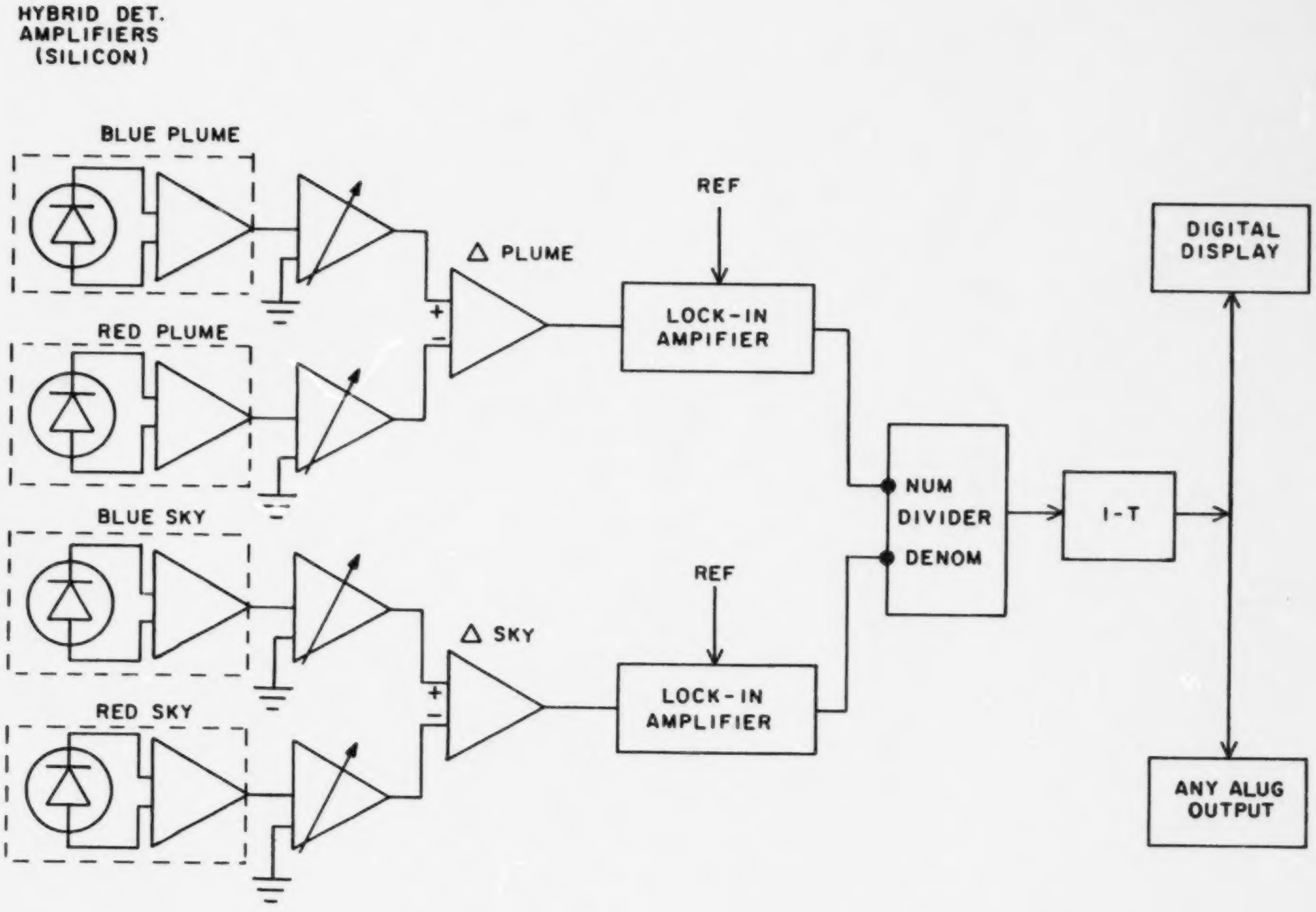
HYBRID DET.
AMPLIFIERS
(SILICON)
BLUE PLUME
RED PLUME
BLUE SKY
RED SKY
+
−
Δ PLUME
Δ SKY
REF
LOCK-IN
AMPIFIER
LOCK-IN
AMPLIFIER
NUM
DIVIDER
DENOM
I-T
DIGITAL
DISPLAY
ANY ALUG
OUTPUT

Figure 3. Simplified ROM signal processing block diagram.

Weather conditions were unfavorable, and considerable problems were had with intermittent low clouds and strong wind. The wind tended to blow smoke from an adjacent stack into the instrument's field of view. Only intermittent short term measurements could be taken.

The power plant monitoring system consists of two transmissometers measuring across the two effluent ducts feeding into the common base of the stack under scrutiny. The reference opacity values were determined by averaging the outputs of the two transmissometers. This assumed equal flow rates in the two effluent ducts, a condition which may not always have existed during these tests.

The ROM-X data were taken by observing the digital display and periodically recording its readings. A readout time constant of 30 seconds was used whenever possible.

Figure 4 shows the relationship between the ROM-X readings and the average of the two transmissometer outputs. The plotted points are of the observed ROM-X averages and the averages of the two transmissometers as mentioned above. Plotted data points are those for which the reading from both instruments remained reasonably stable for periods of at least 5 minutes. The bars in the vertical direction are the range of ROM-X readings during each sampling period, while the bars in the horizontal direction are the range of transmissometer averages for the same period.

Smoke Generation Tests

During late January 1980, a transportable "smoke school" generator was borrowed from the EPA to conduct a series of more controlled experiments with the ROM-X prototype. The smoke generator has a 10-inch diameter by 16 foot smokestack with a built in transmissometer. The transmissometer output is fed into a control unit with 0 percent and 100 percent adjustments and a digital display with direct indication of percent opacity. The device can generate white or black smoke at any selectable opacity. Black smoke is produced by partial combustion of toluene, while white smoke is generated by vaporizing diesel fuel. Smoke generated in this fashion tends to have a fairly narrow particle size distribution. Plumes with narrow size distributions scatter light which is more polarized and varies more with scattering angle than plumes with broad particle size distributions. Therefore, the amount of polarized light scattered per unit opacity was expected to be higher for these smokes than for those of industrial plumes, and consequently the error caused by plume-scattered light was expected to be higher.

Comparisons of the opacity readings of the ROM-X and the transmissometer were made by recording simultaneously both outputs on a dual-pen chart recorder. A low-pass filter was added to the transmissometer output to achieve a time constant comparable to that of the ROM-X (30 seconds). Figure 5 depicts a typical recording of this type, obtained over a period of 30 minutes. The two traces are offset along the time axis to permit a clear distinction between them. The amplitude of the ROM-X readings slightly exceed those of the transmissometer because the extended path length of observation resulting from the vertical angle of observation and the then prevailing wind direction.

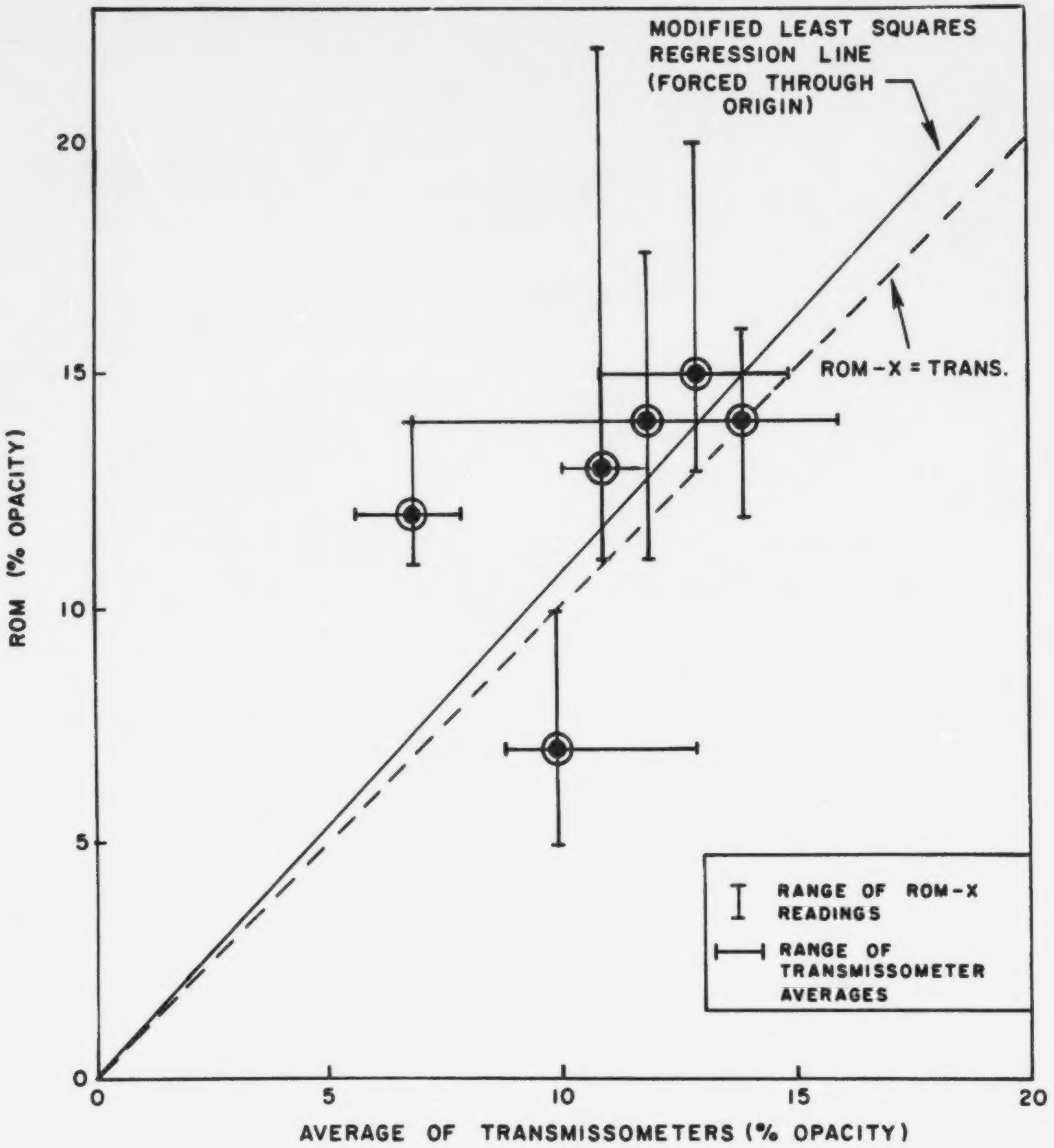

Figure 4. Boston Edison measurements.

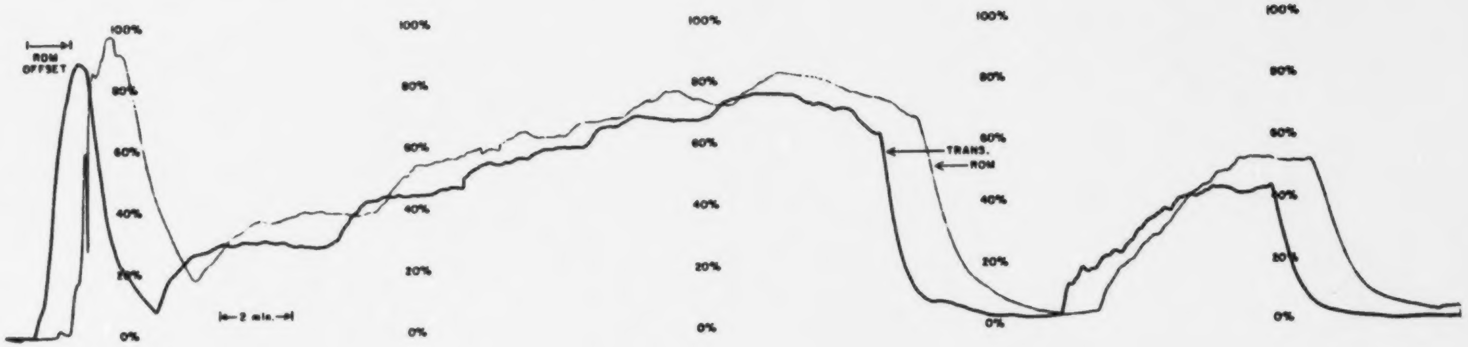

1/27/80 1500 to 1530 Scattering Angle = 100°
Solar Zenith Angle = 70° to 75°
Plume illuminated by sun

Figure 5. Black smoke strip chart recording for both the ROM-X and transmissometer

Figure 6 is a plot of data points (corrected for vertical angle), i.e. ROM-X measurements versus transmissometer readings, for both black and white smoke obtained over a period of several hours, without any adjustments of the operating parameters of the ROM-X.

As can be discerned from this plot and the recording of figure 5, the agreement between the two methods of measurement, i.e. the remote sensing instrument under scrutiny and the standard transmissometer, was excellent. For all conditions of operation, i.e. for black and white smokes and during different days and solar angles (i.e. time of day) the correlation coefficient between the data obtained by the two methods fluctuated between 0.96 and 0.99, which is a rather remarkable degree of agreement considering that the transmissometer is an active system whereas the ROM-X is based on a passive sensing principle.

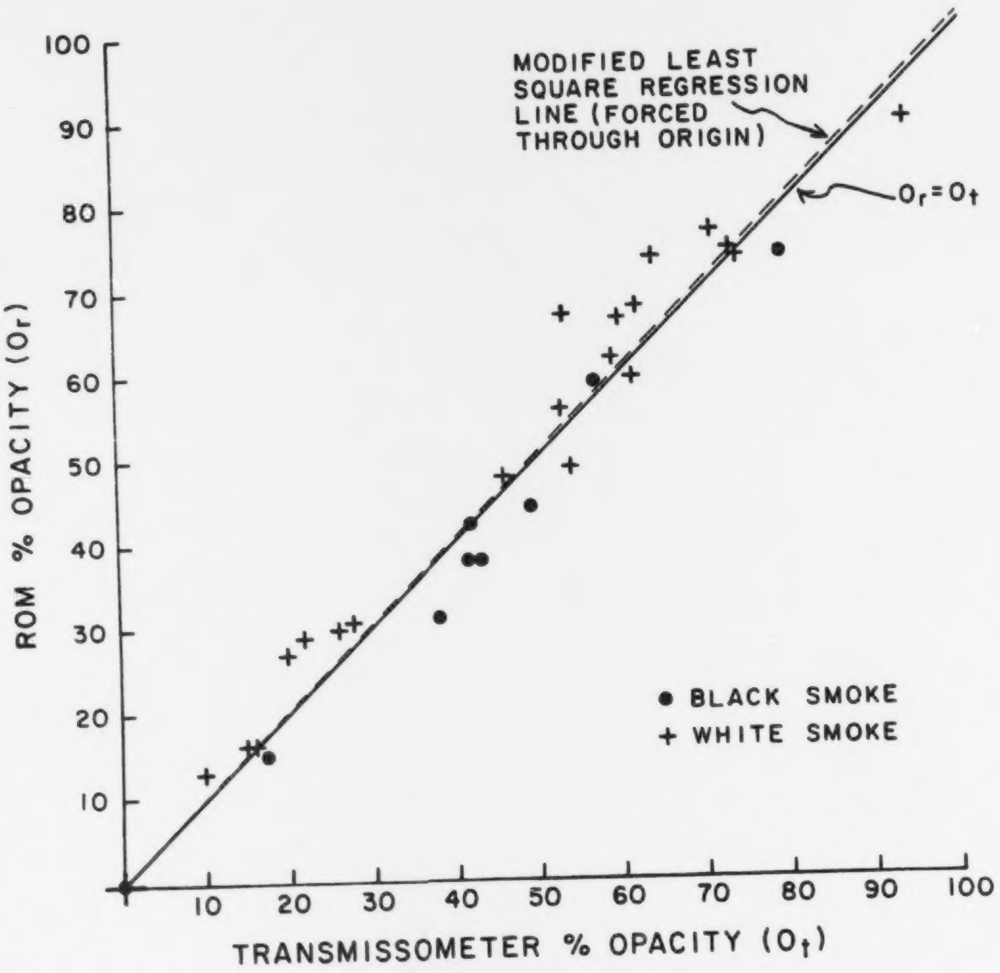

Figure 6. ROM-X versus transmissometer.

SUMMARY AND CONCLUSIONS

A Remote Plume Opacity Monitor (ROM) has been developed and field tested. This instrument, which makes use of the polarization and color properties of the background sky light, remotely measures the opacity of smoke plumes by the attenuation of this background light. Field tests performed on a power plant stack emission and the plume emitted by a "smoke school" generator indicate excellent agreement with concurrent in-stack transmissometer measurements. The more controlled "smoke school" tests were performed over a range of about 10% to 100% opacity, both with black as well as white smoke plumes. The resulting data indicate correlation coefficients between 0.96 and 0.998 for all test runs performed with the adjustable smoke generator, combining the results of black and white smoke.

The development of a commercial version of this instrument is presently underway. This device will integrate all optical and electronic components in a single rechargeable battery-powered unit, compatible with typical field applications.

REFERENCES

1. Federal Register, 40 CFR 60, Method 9. Visual Determinations of the Opacity of Emissions from Stationary Sources.

2. Saraf, D.G. Continuous Reading Lidar Technique for Measuring Plume Opacity. EPA-600/2-79-023. February 1979.

3. Uthe, E.E., et al. Study of Laser Backscatter by Particulates in Stack Emissions. Final Report EPA-R2-72-089, Stanford Research Institute, Menlo Park, California, 1972.

4. Sekera, Z. Light Scattering in the Atmosphere and the Polarization of Sky Light. J. Opt. Soc. Am., Volume 47, p. 484. 1957. Numerous other publications.

5. Newberger, H. Arago's Neutral Point: A Neglected Tool in Meterological Research. Bull. Am. Met. Soc., Volume 31, No. 4, p. 119. 1950.

6. Lilienfeld, P., Woker, G., Stern, R., and McVay, L., Passive Remote Smoke Plume Opacity Sensing: a Technique. Applied Optics, Volume 20, p. 800 1981.

The work described in this paper was not funded by the U.S. Environmental Protection Agency. The contents do not necessarily reflect the views of the Agency and no official endorsement should be inferred.

The work described in this paper was not funded by the U.S. Environmental Protection Agency. The contents do not necessarily reflect the views of the Agency and no official endorsement should be inferred.

Paper 10

ULTRA-FINE CASCADE IMPACTOR PARTICLE SIZE DATA RELATIONSHIPS TO OPACITY: CASE HISTORIES

Phillip A. Nelson
Washington State Department of Ecology

David S. Mummey and Wesley D. Snowden
Alsid, Snowden & Associates

ABSTRACT

Four cases of ultra-fine cascade impactor samples are reported and related to high-opacity plumes. Sulfate, heavy metals, sodium chloride, and magnesium oxide condensation particles are included in the paper. Importance of condensation particle formation mode is related to the opacity in the cases studied. Data presentation techniques are illustrated to assist in interpretation of the particle size results. Observations on the control devices utilized on the high opacity plumes are also included in the paper.

BACKGROUND

The relationship between plume opacity and physical properties of an aerosol has become increasingly important in recent years. Under most circumstances the attainment of acceptable emission levels must include consideration of plume opacity as well as particulate mass or concentration standards. Until recently no techniques were available for relating aerosol properties to plume opacity other than reliance on previous experience. Techniques utilized in this paper have shown fairly good agreement between in situ opacity measurements and aerosol mass concentration for various sources. These sources include cement kilns, Kraft recovery furnaces, lignite-fired boilers, and other source types. These correlations, however, have proven to be source specific and must be obtained on a process-by-process basis.

The in-stack light extinction properties of an aerosol can be expressed in terms of the fractional light transmittance, T, which can be estimated by the Bouguer law,

$$T = \frac{I}{I_o} = \exp(-bL) \qquad (1)$$

where $b(n^{-1})$ is the extinction coefficient of the aerosol over the light path length, L(m). I and Io are the transmitted and incident light, respectively. The extinction coefficient can be calculated from light scattering theory using the Mie equation.

Pilat and Ensor[1] have shown that the aerosol mass concentration is related to optical transmittance through a modified form of the Beer-Lambert law such that

$$\ln\frac{I}{I_o} = \frac{WL}{k\rho} \qquad (2)$$

where W is the particulate mass concentration, ρ is the average particle density, and K is the ratio of the specific particle volume-to-light extinction coefficient. The parameter K can be calculated provided the particle size distribution, particle refractive index, and wavelength of the incident light are known. Ensor and Pilat[2] have provided figures for determining a value for K as a function of the log-normal particle size distribution parameters and the refractive index of the aerosol.

When the particle size distribution cannot accurately be approximated by the log-normal model, it is necessary to calculate a value of K using the actual size distribution in the following manner. Thielke and Pilat[3] reasoned that each component of the aerosol size distribution scatters and/or absorbs light independently such that

$$\ln\frac{I}{I_o} = L(b_1 + b_2 + \ldots\ b_n) \qquad (3)$$

where b_n is the extinction coefficient of the nth size increment in the overall particle size distribution. Based on the definition of K, Equation 2 was put in a form similar to Equation 3 by Thielke and Pilat giving

$$\ln\frac{I}{I_o} = -LW\left\{\frac{f_1}{K_1\rho_1} + \frac{f_2}{K_2\rho_2} + \ldots\ldots\ \frac{f_n}{K_n\rho_n}\right\} \qquad (4)$$

where f_n is the fraction of total mass, ρ_n is the particle density, and K_n is the monodisperse specific volume extinction coefficient ratio characteristic of the nth particle size increment.

TEST METHODS

A majority of the data presented in this paper was collected in a cascade impactor; other test techniques specifically utilized to determine high temperature condensation products were also utilized. The cascade impactor used for all of the tests was developed to obtain a higher density of data within the condensation mode range of the particulate size distribution. This high resolution impactor (U.S. Patent No. 4,189,937) has a total of 14 jet stages with particulate cuts ranging from 18 micron aerodynamic particle diameter to 0.15 micron particle diameter. The high resolution impactor was designed to operate as a high pressure drop device; thus the static pressures on the intermediate and especially the lower stages are very much less than atmospheric pressure. At this greatly reduced operating pressure of the lower stages of the impactor, the particles of a given diameter may be required at atmospheric pressure. Through the use of this principle the high resolution impactor is able to size particles of a much smaller size than is possible in a conventional cascade impactor. A schematic of the sampling system is given in Figure 1.

Test data for one of the case histories required the characterization of various condensing constituents within the flue gas. To collect this data, EPA Method 8 was utilized to obtain the SO_3 concentrations present within the flue gas and the back half (condenser section) of the EPA Method 5 train was utilized to collect any hydrocarbons present.

CASE HISTORIES

Petroleum Coke Calciner

A series of six cascade impactor runs were made on the effluent of a petroleum coke calciner, at various operating conditions. The effluent was known to have sulfuric acid in the exhaust.

The method of calculating opacity was that described by Thielke and Pilat.[3] In this method the scattering and absorption contribution to light attenuation is calculated for each size fraction f. For this calculation, a number of constants need to be known. The sulfuric acid aerosol was assumed to be 60% strength, due to considerations of equilibrium with concentrations of acid and water vapor. The specific gravity was taken to be 1.45, the density of 60% acid at 100°C. The scattering component of light attenuation is a function of index of refraction, which was determined to be 1.398 at the conditions of temperature and concentration of acid. The absorption coefficient was assumed to be 0.02. Most atmospheric aerosols have a value of this coefficient between 0.02 and 0.05. The D_{50} diameters are calculated to be actual (not aerodynamic) values based on the known or assumed densities of the particles.

From the size distributions shown in Figure 2, it is clear that the particles collected have a bimodal distribution, that is, there are aerosols from two separate sources. The two modes separate at about 1 micron diameter. Particles smaller than 1 micron are assumed to be sulfuric acid and were given the properties above described. Particles larger than 1 micron were arbitrarily given the values of 1.3, 1.0, and 1.0 for index of refraction, absorption coefficient, and specific gravity. Any error that may be introduced from these assumptions will be small because the contribution to light attenuation from particles in this size range is quite small.

The value L, the optical path length, is equated to stack diameter. The total mass concentration W is expressed in grams per cubic meter of gas at stack conditions, including water vapor.

A sample calculation is shown in Table 1. A tabular summary of all case histories is presented in Table 2. Table 2 includes particle mass loading, calculated opacities, and any observed or measured opacities for each case.

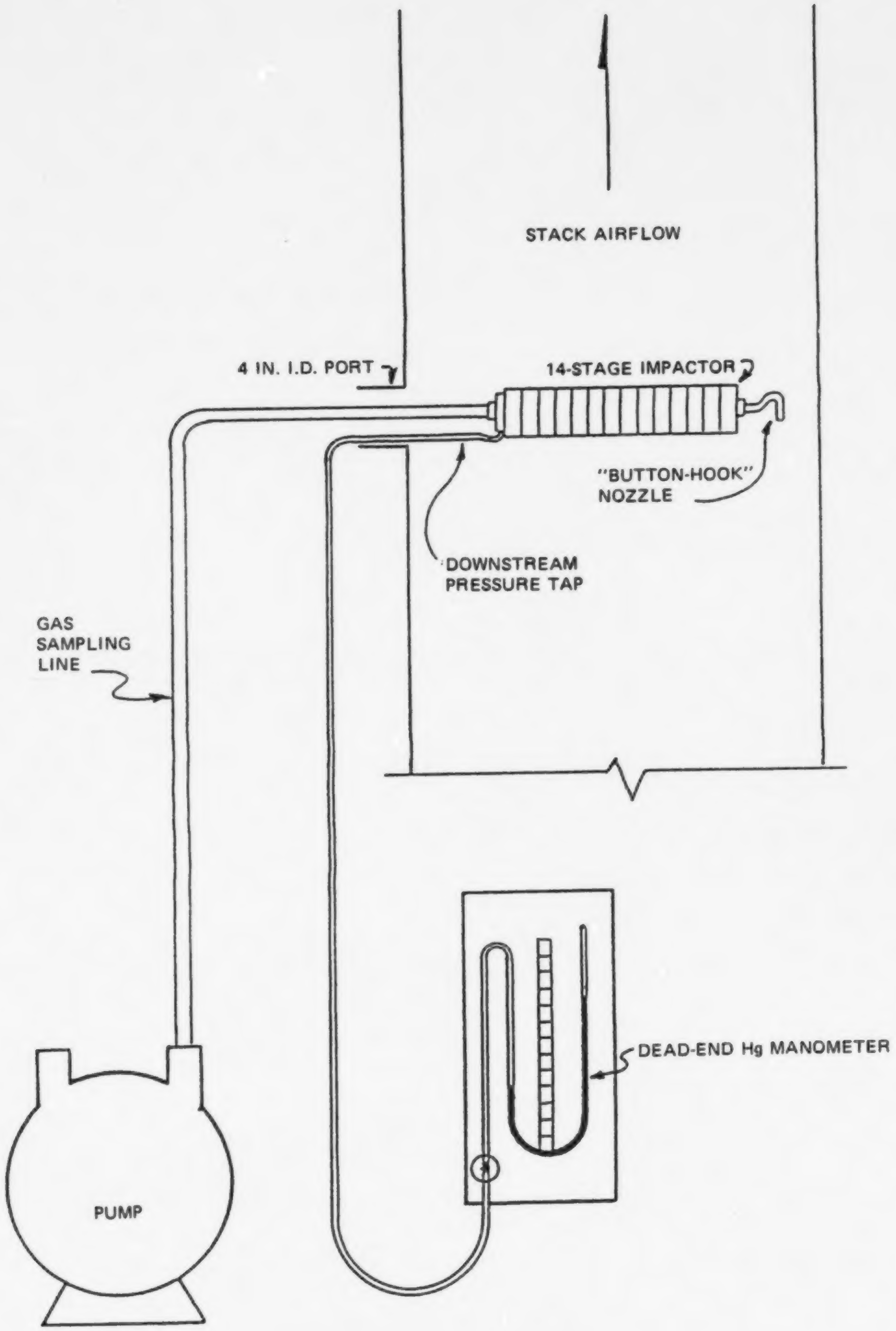
STACK AIRFLOW
4 IN. I.D. PORT
14-STAGE IMPACTOR
"BUTTON-HOOK" NOZZLE
DOWNSTREAM PRESSURE TAP
GAS SAMPLING LINE
DEAD-END Hg MANOMETER
PUMP

Figure 1. Nelson high resolution cascade impactor.

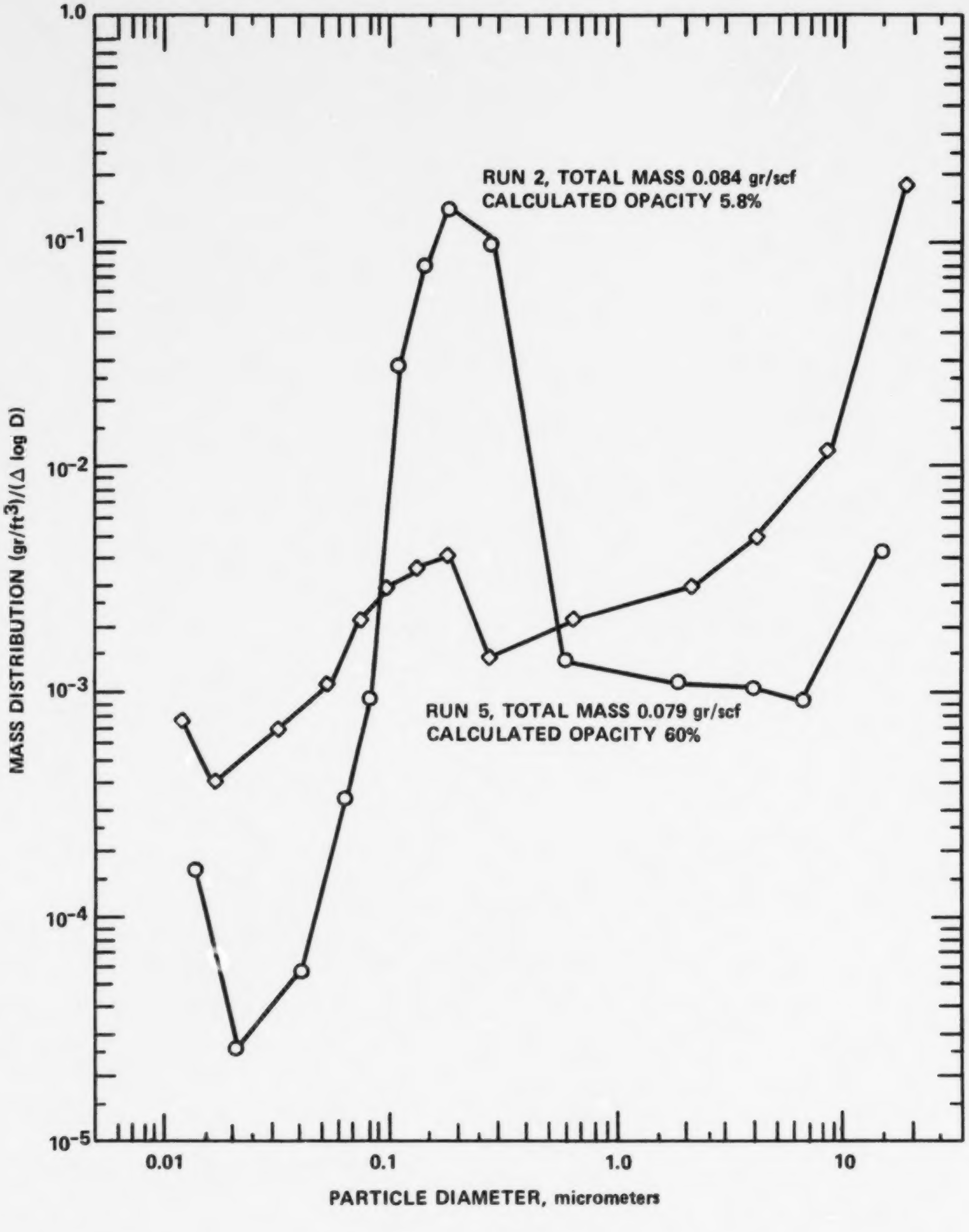

Figure 2. Two size distributions of exhaust gas from coke calciner with approximately equal total mass concentrations.

Table 1. Opacity calculation for run 2 of coke calciner

d50 microns	f weight fraction	n1 index of refraction	n2 index of absorbance	K cu.cm/cu.m.	ρ g/cu.cm.	$f/K\rho$
16.7	.8549	1.3	1.0	9.0	1.0	.0950
7.78	.0562	1.3	1.0	3.8	1.0	.0148
4.12	.0226	1.3	1.0	2.0	1.0	.0133
1.97	.0145	1.3	1.0	1.0	1.0	.0145
.651	.0117	1.398	.02	.32	1.43	.0255
.264	.0064	1.398	.02	.15	1.43	.0298
.158	.0104	1.398	.02	.25	1.43	.0241
.119	.0056	1.398	.02	.37	1.43	.0110
.093	.0045	1.398	.02	.55	1.43	.0057
.074	.0039	1.398	.02	.85	1.43	.0035
.053	.0027	1.398	.02	1.65	1.43	.0011
.032	.0027	1.398	.02	3.7	1.43	.0005
.015	.0014	1.398	.02	5.5	1.43	.0002
.011	.0024	1.398	.02	5.5	1.43	.0003
						.2443

W = .1188 g/cubic meter stack conditions

L= 2.438 meters

$\ln (I/I_o) = -LW \; f/K\rho$

$I/I_o = .932$ therefore opacity = 1 - .932 = .068

Table 2. Comparison of Opacity Results

	TOTAL MASS CONC g/cubic meter	PERCENT OPACITY		
		CALCULATED	TRANSMISSOMETER	TRAINED OBSERVER
COKE CALCINER				
Run 1	.0285	3.4	N/A	35*
Run 2	.1188	5.8	N/A	55*
Run 3	.1093	9.2	N/A	25*
Run 4	.0594	7.2	N/A	40* & 60*
Run 5	.1364	60.0	N/A	45*
Run 6	.1592	13.6	N/A	40*
HOG FUEL BOILER (Salt-Laden fuel).	.1527	16.0	N/A	20
SOAP DRYER	.0503	7.7	8	
FERROUS MELTING FURNACE				
- Particulate	.01167			
- Hydrocarbon	.0324	7.8		
- Sulfuric Acid**	.0419	18.4		
		=====		
TOTAL		34.4		40

* Readings by trained observer after plume had condensed in ambient air. Whenever plume was detached from the top of the stack, the opacity was less than 10%.

** Diluted to 60% H2SO4

Returning to Figure 2, note that the size distributions of runs 2 and 5 have approximately the same total mass concentration. However, run 5 has a large concentration of particles in the size region of 0.1 to 0.4 micron diameter, whereas most of the mass in run 2 is concentrated above the 1 micron size. The calculated opacities are 60.0 percent and 5.8 percent, respectively for run 5 and run 2. This is because the particles in the 0.1 to 0.4 micron size range are much more efficient at scattering visible light than are the particles with a size greater than 1 micron.

Hogged Fuel Boiler

Testing was performed on the effluent from a hogged fuel boiler which used fuel that had been derived from salt-water borne logs. The size distribution curve of this source also indicates a bimodal distribution as in the previous case. The small particle fraction had been shown by analysis to be sodium chloride. The handbook value of 1.54 for index of refraction was used. Lin and Baker[4] reported that the value of the absorption coefficient is zero. Likewise the density of sodium chloride was taken from the handbook to be 2.165 g/cm^3. A calculated value of 16 percent opacity agreed reasonably well with a value of 20 percent from a trained observer. This is considered good because the variance of an observer is plus or minus 5% opacity. The results are presented in Table 2.

Soap Dryer

A calculation of the results from a soap dryer is also included in Table 2. In this case an index of refraction was taken to be 1.47, that of palmitic acid. The absorption coefficient was taken to be 0.02. As shown in Table 2, the calculated value of 7.7% agrees closely with the opacity meter value of 8%.

Ferrous Metal Melting

A series of tests were taken at the exhaust to a baghouse following a foundry cupola to determine the cause of its opacity. Both cascade impactor tests as well as total particulate tests were obtained to determine what influences the particulate loading had upon the plume opacity. Two SO_2/SO_3 sample analyses were obtained to determine the effect of possible condensing sulfuric acid aerosols upon the opacity.

The particulate data was analyzed to obtain the particle size distribution present as well as the total particulate. The total particulate test results (EPA Method 5) were broken down into total particulate present as well as condensing species. The condensation products were analyzed for both hydrocarbons and sulfates. A series of selected particulate samples were analyzed using an elemental x-ray analysis package used in conjunction with a scanning electron microscope.

The results of the previous tests were utilized to calculate the opacities of each of the following plume components: total particulate loading, hydrocarbon condensation, and diluted sulfuric acid droplets. The particulate size distribution at unit density with the following refractive index components: 1.5 - 0.05 i gave a K value of 0.101. Inputing the mass loading rate results in a particulate contribution to the total opacity of 8.2%. A typical hydrocarbon K value, presented by Ensor and Pilat[1] for veneer dryers, is 0.36. Due to the composition of veneer dryer emission, primarily hydrocarbons, this K factor was applied to the total measured hydrocarbon mass concentration values and gave a hydrocarbon contribution to the total opacity of 7.8%. The SO_3 tests revealed a concentration of 6.7 ppm SO_3 within the stack gas. Again as with the calciner operation the SO_3 will combine with the water in the flue gas and form sulfuric acid aerosols, and these will be diluted within the flue gases to a 60% H_2SO_4 + 40% H_2O solution. Using the same refractive index as in the calciner example, 1.398 - 0.0 i, a mass loading of 0.0419 g/m^3, and a K value calculated from an aerosol size distribution characteristic of condensing aerosols, 0.26, the calculated opacity due to sulfuric acid aerosols is 18.4%.

The total opacity of the three components would be the summation of the three components, 34.4%. This result agrees relatively well with the observed opacity of 40%. It should be noted that it is assumed that each of the components remains homogeneous with relation to each of the other opacity-causing species. The results are summarized in Table 2.

SUMMARY

There are many sources of error in the method. Some are associated with the assumption that must be made about constants that are not available. It is believed that the greatest potential source of error is in the graphical determination of the "K" parameter for the particles in the size range of 0.1 to 0.4 microns in diameter (see Thielke and Pilat, reference 3). A computer program to actually calculate the K value would reduce the error in the determination of the K value.

This method of calculation of opacity is seen as having a great potential benefit because the method reveals the quantitative contribution to opacity of the various components of the atmospheric emission. The calculation method is rendered especially useful by the availability of the high resolution cascade impactor. The high resolution cascade impactor provides detailed data in the size range between 0.1 and 1.0 microns in diameter, the size range which has the most influence on the overall plume opacity.

REFERENCES

1. Pilat, M. J., and D. S. Ensor. Plume Opacity and Particulate Mass Concentration. Atmos. Environ. 4:163-173, 1970.

2. Ensor, D. S., and M. J. Pilat. Calculation of Smoke Plume Opacity from Particulate Air Pollutant Properties. J. Air Pollut. Control Assoc. 21(3): 490-501, 1971.

3. Thielke, J. F., and M. J. Pilat. Plume Opacity Related to Particle Mass Concentration and Size Distribution. Atmos. Environ. 12:2439-2447, 1978.

4. Lin, C., and N. Baker. Absorption Coefficient of Atmospheric Aerosols: A Method for Measurement. Appl. Opt. 12:1356-1363, 1973.

Paper 11

PARAMETERS FOR AMBIENT SAMPLING OF INHALABLE PARTICULATE MATTER

Charles W. Lewis and Robert K. Stevens
Inorganic Pollutant Analysis Branch
Environmental Sciences Research Laboratory -- RTP
U. S. Environmental Protection Agency

ABSTRACT

EPA has been considering the potential usefulness of a new category of aerosol, referred to as Inhalable Particulate Matter. Some discussion of the inhalable particles concept is given, along with some of the current proposals for the parameters that would define an ambient inhalable particles sampler. The proposals include the consideration that the resulting sampler have the flexibility for multiple uses, such as source apportionment analysis and visibility monitoring, in addition to the fundamental use as a routine mass monitor.

INTRODUCTION

The present National Ambient Air Quality Standard (NAAQS) for particulate matter is expressed in terms of Total Suspended Particulate (TSP), which is defined operationally by the sampling characteristics of the Hi-vol sampler. During the approximately ten years in which the TSP/Hi-vol standard has been in use, a number of undesirable features have become apparent. These include the following:

(1) poor inlet characteristics -- Hi-vol effectiveness (sampling efficiency vs. particle size) depends strongly on ambient wind speed and direction; TSP includes large particles that are seldom associated with adverse health effects.

(2) filter artifact -- Hi-vol glass fiber filters are subject to gas-to-particle conversion, in which more sulfate and nitrate appear on the filter than is present in the atmosphere.

(3) no size separation -- TSP ignores the bimodal nature of atmospheric aerosol by grouping together fine and coarse particles whose chemistry and origins are quite different.

The work of Stevens and Dzubay[1] was one of the earliest published attempts to provide an aerosol inlet that would correct the deficiencies of the Hi-vol inlet. The resulting inlet had an upper cutpoint near 20 μm (but with considerable wind speed dependence) and was used with a prototype dichotomous sampler designed to separate particles into two size fractions. While a 20 μm choice could be regarded as an improvement on the considerably larger cutpoint of the Hi-vol, it had no precise theoretical basis in terms of demonstrated health effects.

EPA is currently reviewing the NAAQS for particulate matter and considering a new size specific standard, defined in terms of Inhalable Particles (IP), as an alternative to the TSP standard. This leads naturally to a consideration of characteristics that would be desirable in an IP sampler. The set of parameters defining an IP sampler (besides being consistent with the meaning of IP) should avoid recognized deficiencies of the Hi-vol and, if possible, provide sufficient flexibility for uses other than routine mass monitoring. This paper discusses the current meaning of IP, along with possible characteristics of an IP sampler.

IP SAMPLER PARAMETERS

In this section we present some recent considerations on inlet characteristics, filter medium, flow rate, and the question of fine/coarse particle separation, within the framework of the design of an ambient IP sampler.

Inlet Effectiveness Curve

The effectiveness curve of a sampler inlet specifies the fraction of particles able to penetrate the inlet as a function of particle size, for a particular choice of particle approach velocity. It is the effectiveness curve which provides the operational definition of what is to be meant by IP. A critical parameter of an effectiveness curve is its D_{50} value, i.e., the particle size for which the sampling effectiveness is 50%. Most discussion concerning IP has centered around two D_{50} alternatives, 15 and 10 μm (aerodynamic equivalent diameter). Both possibilities stem from the desire to protect the lower respiratory system, or thoracic region (i.e. beyond the larynx) under conditions of mouth breathing. This is in accord with the general view that adverse health effects of ambient aerosols are most likely to be associated with particles that penetrate to the lower respiratory system.

In addition to the D_{50} choice a complete definition of IP requires that the full effectiveness curve be specified. The debate over both these matters has been lengthy, and has been shaped by several key papers.[2,3,4] Without attempting to re-trace the developments it can be noted that the most recent recommendations (within EPA[5] and by vote of the national members of the TC 146 Committee of the ISO[3]) have favored D_{50} = 10 μm, and an effectiveness curve shape which mirrors observed penetration to the lower respiratory system (thoracic region) as a function of particle size. Parenthetically, the term "thoracic particles" (TP) has been informally used[5] recently to designate particles penetrating to the thoracic region, but without implying any specific D_{50} value. Figure 1 shows experimental data for the fraction of aerosol that is deposited in the upper respiratory system relative to what has entered. Since

$$\text{Penetration} = 1 - \text{Deposition} \qquad (1)$$

where penetration is to the lower respiratory system, and deposition is in the upper respiratory system, the desired inlet effectiveness curve for IP may be obtained from a simple transformation of Figure 1 (invert and re-number the

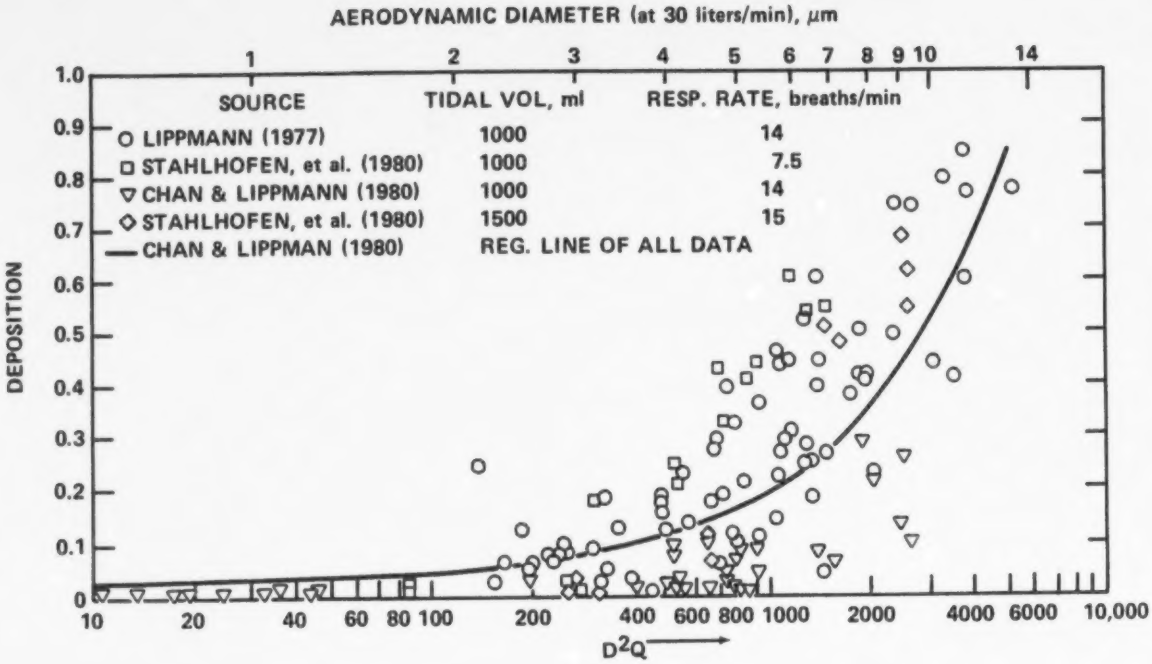

Figure 1. Deposition of monodisperse aerosols in extrathoracic region for mouth breathing in humans as a function of D^2Q, where Q is the average inspiratory flow rate in liters/min. The data are the individual observations cited by the various investigators. The solid line is the overall regression derived by Chan and Lippmann (1980).

vertical axis). The solid line through the data is referred to as the Chan-Lippmann curve[6], and serves as a convenient analytical representation of the data.

The effectiveness curve of a real sampler inlet cannot be expected to exactly match the ideal one (whether the Chan-Lippmann curve or another) so that tolerance limits need to be specified for judging the acceptability of a candidate IP_4 inlet. The most recent proposal for tolerance criteria is that of Rodes et al[4]. This proposal can be expressed in terms of two requirements: (1) D_{50} must be in the range 9 to 11 µm for windspeeds in the range 2 to 24 km/h. (2) The total mass collected should be within ± 15% of that collected by an "ideal" inlet (e.g., Chan-Lippmann) under ambient conditions.

Requirement (2) may be expressed in the form

$$\left| \int \frac{dM}{dLogD} \left[E_1(D) - E_2(D)\right] dLogD \right| \le 0.15 \int \frac{dM}{dLogD} \cdot E_1(D)\, dLogD, \qquad (2)$$

where

$$\frac{dM}{dLogD} = \text{aerosol mass distribution,}$$

$E_1(D)$ = Chan-Lippmann (or equivalent) curve,

$E_2(D)$ = inlet effectiveness.

To make use of inequality (2) a selection has to be made for the ambient aerosol mass distribution. In general, it is expected to be bimodal. Beyond this, however, it is difficult to avoid a rather arbitrary choice, such as one of the distributions reported by Lundgren and Paulus[7] that have been frequently used before. In this circumstance it is well to recall that before the bimodal model came into fashion, a commonly used approximation to ambient aerosol size distributions was the Junge distribution,

$$\frac{dM}{dLogD} = \text{constant} \qquad (3).$$

For this choice, inequality (2) takes on a very simple form involving only $E_1(D)$ and $E_2(D)$. A suitable lower limit for the integrals would be 1 µm, since practically any inlet will have an effectiveness of 100% for smaller particle sizes. In this case the magnitude of the constant in inequality (2) could be increased somewhat and still keep the total mass difference within 15%. Use of the Junge distribution also reveals the insight that to obtain good agreement in total mass collection it is more important to match E_1 and E_2 at small values of D than at large values, due to the inverse weighting that occurs in the integrand (dLogD = dD/D).

The two acceptance requirements, which may be regarded as an "integral mass criterion", are in contrast with the "performance envelope criterion"[8] which had been previously considered. A performance envelope proposed earlier for 15 µm is shown in Figure 2. EPA supported the development of several 15 µm inlets intended to satisfy the criteria of Figure 2. Using four different designs of 16.7 LPM inlets developed for the dichotomous sampler, EPA conducted a series of ambient intercomparison measurements over the course of a year in Durham, NC. In spite of significant differences in the extent to which individual inlets satisfied the criteria of Figure 2, the differences in the total mass collected were on average well under 10 percent[9]. This suggested that the performance envelope approach (and the difficult wind tunnel measurements on which it was based) might be unnecessarily stringent in obtaining good ambient mass collection agreement. Adoption of the "integral mass" approach would be consistent with this finding.

Filter Medium

A primary concern in the choice of a filter medium for an IP sampler is freedom from gas-to-particle artifact formation. There is ample evidence that 1 to 6 µg/m^3 of the sulfate measured on glass fiber filters taken from Hi-vol samplers can be due to the conversion of SO_2 on the filter.[9,10] In the case of

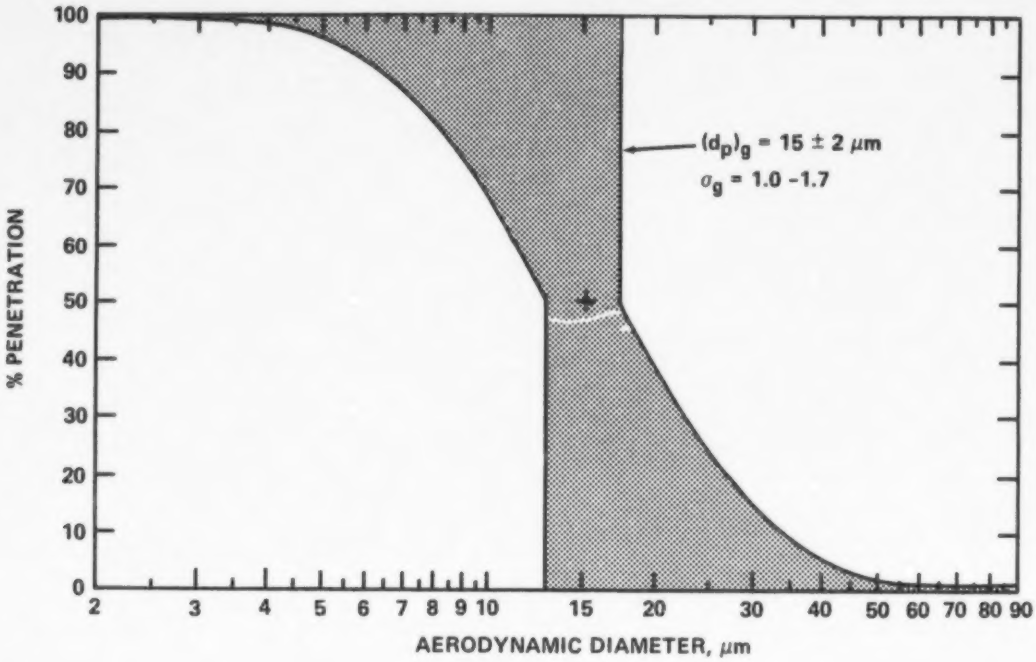

Figure 2. Performance envelope for IP inlet (15μm).

nitrate, artifact formation from the conversion of (gaseous) nitric acid on glass fiber filters has been observed to average 10 μg/m^3 for 24-h sampling periods in California,[11] and up to several times this amount for shorter sampling periods.[12] Nitrate artifact is of lesser importance in other parts of the U.S. Teflon and microquartz filters seem to offer the best possibilities for minimizing sulfate and nitrate artifact formation. Other advantages and disadvantages of Teflon and microquartz are indicated in Table 1. The cost penalty for use of Teflon filters would be substantially reduced by the introduction[13] of a new Teflon filter (2 μm pore size, 3 mg/cm^2) expected by mid-1982.

Flow Rate

Presently there are three flow rates that are most frequently discussed with respect to an IP sampler: 40 CFM, the nominal flow rate of the Hi-vol; 4 CFM; and 16.7 LPM (0.59 CFM), the flow rate of the dichotomous sampler. For all three, 10-and/or 15-μm inlet development work has occurred. The choice of flow rate and filter medium need to be considered together. For example, choosing the new Teflon filter material, the projected filter costs[13] at the three flow rates ($4, $2, and $1) differ substantially. In this case the intermediate flow rate is quite attractive because sufficient material is collected to avoid the expense of micro-balance equipment for the mass determination, and the filter cost is probably not prohibitive.

TABLE 1. TEFLON VS. MICROQUARTZ CHARACTERISTICS

Teflon	Microquartz
Hydrophobic	Slightly hygroscopic
Strong	Moderately fragile
Excellent for aerosol mass, X-ray fluorescence, and X-ray diffraction measurements	Excellent for aerosol carbon measurement
Limited loading characteristics	Excellent loading characteristics
Expensive	Inexpensive

Size Separation

Size separation means that the mass collected by an IP sampler is deposited on two filters, one for fine and one for coarse particles. Since the concept of IP as outlined does not involve any such size separation, it may seem odd to consider the desirability of this in an IP sampler. There are two different reasons why this is an appropriate concern. The first relates to the preservation of the chemical character and total mass of the collected aerosol. Since fine particles are predominantly acidic, while coarse particles are largely basic, the commingling of fine and coarse particles on the same filter substrate can lead to reactions (e.g., $H_2SO_4 + CaO \rightarrow CaSO_4 + H_2O$) that not only change the chemistry of the collected aerosol, but may also lead to a mass loss if the reaction products are volatile. Evidence for this effect has been reported in a number of cases.[14,15,16]

The second reason for size separation is to make an IP sampler flexible enough that it can be useful for purposes other than solely as a compliance monitor. A prime example is the increasing interest in Source Apportionment Analysis[17], in which ambient aerosol samples are subjected to a variety of physical/chemical and mathematical analyses with the objective of determining the percentage contribution made to the total ambient loading by potential sources. The attractiveness of Source Apportionment Analysis is that the same sampler that demonstrates non-compliance with an ambient air quality standard simultaneously provides the data from which the most cost-effective control strategy to achieve compliance can be devised. It is generally recognized that effective source apportionment procedures require the use of size separated fine and coarse samples. The previous identification of Teflon and quartz as filter media of first choice for an IP sampler is also consistent with source apportionment needs. These filter types support the large variety of physical and chemical aerosol characterizations that are required as inputs to source apportionment analysis (see Table 1).

The close relationship between visibility and fine particle concentration[18] provides another use for an IP sampler that includes size separation.

Finally, the acquisition of separate fine and coarse particle data bases could provide the raw material for possible future refinement of ambient air quality standards.

SUMMARY

Possibilities for the parameters associated with an ambient IP sampler have been discussed. The discussion has emphasized recent changes that have occurred as a result of the evolution of the IP concept. Additionally, the discussion has stressed the desirability of an IP sampler that has the flexibility for uses beyond the fundamental one of a routine mass monitor.

REFERENCES

1. Stevens, R. K. and T. G. Dzubay. Recent Developments in Air Particulate Monitoring. IEEE Trans. Nucl. Sci. NS-22:849-855, 1975.

2. Miller, F. J., D. E. Gardner, J. A. Graham, R. E. Lee, W. E. Wilson, and J. D. Bachmann. Size Considerations for Establishing a Standard for Inhalable Particles. J. Air Pollut. Control Assoc. 29:610-615, 1979.

3. ISO [International Standards Organization] Size Definitions for Particle Sampling. Am. Ind. Hyg. Assoc. J. 42:64-68, 1981.

4. Rodes, C. E., K. A. Rehme and L. J. Purdue. Particle Collection Criteria for 10 Micron Samplers. U. S. Environmental Protection Agency internal report, Environmental Monitoring Systems Laboratory, Research Triangle Park, NC (September 1981).

5. OAQPS [Office of Air Quality Planning and Standards] Review of the National Ambient Air Quality Standards for Particulate Matter: Revised Draft Staff Paper. U.S. Environmental Protection Agency, Research Triangle Park, NC (October 31, 1981).

6. Chan, T. C. and M. Lippmann. Experimental Measurements and Empirical Modelling of the Regional Deposition of Inhaled Particles in Humans. Am. Ind. Hyg. Assoc. J. 41:399-409, 1980.

7. Lundgren, D. A. and H. J. Paulus. The Mass Distribution of Large Particles. J. Air Pollut. Control Assoc. 25: 1227-1231, 1975.

8. Ranade, M. B., and E. R. Kashdan. Critical Parameters for the Federal Reference Method for the Inhalable Particulate Standard. Final Report Technical Directive 222, EPA Contract 68-02-2720, Research Triangle Institute, Research Triangle Park, NC (September 1979).

9. Shaw, R. W., R. K. Stevens, C. W. Lewis, and J. H. Chance. Comparison of Aerosol Sampler Inlets. Paper 81-5.3, Air Pollution Control Association, 74th Annual Meeting, June 21-26, 1981, Philadelphia.

10. Stevens, R. K., T. G. Dzubay, G. Russwurm and D. Rickel. Sampling and Analysis of Atmospheric Sulfates and Related Species. Atmos. Environ. 12:55-68, 1978.

11. Appel, B. R., S. M. Wall, Y. Tokiwa and M. Haik. Interference Effects in Sampling Particulate Nitrate in Ambient Air. Atmos. Environ. 13:319-325, 1979.

12. Spicer, C. W. and P. M. Schumacher. Interferences in Sampling Atmospheric Particulate Nitrate. Atmos. Environ. 11:873-876, 1977.

13. Whatman Paper Division, Clifton, NJ.

14. Harker, A. B., L. W. Richards and W. E. Clark. The Effect of Atmospheric SO_2 Photochemistry upon Observed Nitrate Concentrations in Aerosols. Atmos. Environ. 11:87-91, 1977.

15. Pierson, W. R., W. W. Brachaczek, T. J. Korniski, T. J. Truex and J. W. Butler. Artifact Formation of Sulfate, Nitrate, and Hydrogen Ion on Backup Filters: Allegheny Mountain Experiment. J. Air Pollut. Control Assoc. 30:30-34, 1980.

16. Davis, B. L., L. R. Johnson, R. K. Stevens, D. F. Gatz and G. J. Stensland. Observation of Sulfate Compounds on Filter Substrates by Means of X-Ray Diffraction. Proceedings, Heterogenous Catalysis Workshop, State University of New York, Albany, June 28-July 3, 1981.

17. Gordon, G. E. Receptor Models. Environ. Sci. Technol. 14:792-800, 1980.

18. Lewis, C. W. On the Proportionality of Fine Mass Concentration and Extinction Coefficient for Bimodal Size Distributions. Atmos. Envrion. (in press).

Although the research described in this paper has been funded (wholly or in part) by the United States Environmental Protection Agency, it has not been subjected to Agency review and, therefore, does not necessarily reflect the views of the Agency and no official endorsement should be inferred.

Although the research described in this paper has been funded (wholly or in part) by the United States Environmental Protection Agency, it has not been subjected to Agency review and, therefore, does not necessarily reflect the views of the Agency and no official endorsement should be inferred.

Paper 12

AN AMBIENT AIR INLET FOR COLLECTION OF TTP AND RSP AEROSOL FRACTIONS

Andrew R. McFarland
Carlos A. Ortiz
Clayton M. Rue

Air Quality Laboratory
Department of Civil Engineering
Texas A&M University

ABSTRACT

An aerosol sampling inlet has been developed which enables either the collection of the TTP aerosol fraction or the simultaneous collection of both the TTP and RSP fractions. The TTP and RSP aerosols are defined in terms of the particulate matter which passes through separators with aerodynamic cutpoint sizes of 10 and 2.5 µm, respectively. The system is designed to operate at a flow rate of 113 L/min (4 cfm) with the entire flow passing through a single filter when the sampler is in the TTP-only mode and with the flow split into two equal parts when it is operated in the simultaneous TTP/RSP mode.

Both wind tunnel and laboratory tests have been used to evaluate the performance of the system for the collection of the TTP fraction. The results of wind tunnel testing with liquid aerosols showed the inlet to provide a cutpoint of 10 ± 0.5 µm for wind speeds of 2, 8 and 24 km/hr. Slope of the fractionation curve, calculated as a geometric standard deviation, is 1.58. Static tests in the laboratory with solid particles showed no significant particle bounce problems.

The cyclone separator for stripping the non-RSP aerosol from the distribution has a cutpoint of 2.5 ± 0.3 µm with the penetration curve having a slope of 1.26.

Tests were conducted to determine the uniformity of particle deposition on the filters. With the system in the TTP-only mode, 10.4 µm particles were collected on 102 mm filters. The coefficient of variation for 10 subsamples cut from the filters was less than two percent. Nine subsamples were removed from the RSP fraction filters. For 2.5 µm aerosols, the coefficient of variation of sample uniformity across the filters was less than one percent. Correspondingly, the variation in TTP filter deposits for 10 µm particles was less than three percent with the system operated in the TTP/RSP mode.

INTRODUCTION

The current EPA standard method for sampling particulate matter from the ambient atmosphere, the Hi-Vol approach, has been shown to have biases. Lee and Wagman[1], and Spicer et al.[2] identified artifact problems associated with the sampling of acid gases wherein particulate matter may be formed (or lost) in the glass fiber filter. Stevens et al.[3] have shown the use of teflon filters greatly reduces these sampling anomalies; however, the present cost of teflon filters (approximately $25 for the 8-inch by 10-inch Hi-Vol size) precludes universal useage of this media.

The Hi-Vol sampler has a second limitation, one which cannot be eliminated without mechanical design changes. The size distribution of particulate matter collected on the Hi-Vol filter depends upon both environmental and operational conditions. Of particular importance is the observation that large particles are collected to varying degrees, depending upon wind speed and direction. For example, in wind tunnel tests in which the Hi-Vol was rotated at 1 RPM, McFarland and Ortiz[4] noted the Hi-Vol to have cutpoints of ~45, 44 and 30 μm for wind speeds of 2, 8 and 24 km/hr, respectively. Here, cutpoint is defined as the aerodynamic particle size for which 50 percent of the aerosol can penetrate through the inlet system and be deposited on the filter.

Under the Clean Air Act Amendments of 1977[5] Congress directed EPA to review the existing ambient air standards and, where appropriate, to make necessary modifications. Since the primary ambient air standards are directed towards air quality levels which are compatible with human health, EPA gave consideration to specification of sampling criteria wherein the collected particulate matter would have size ranges which could penetrate the human respiratory system. Miller et al.[6] identified two size ranges of interest, 0-2.5 μm aerodynamic diameter, the respirable particle fraction (RSP), and 0-15 μm, which was termed the inhalable particle fraction (IP). RSP was deemed to be the aerosol which would penetrate the lung system to the gas exchange region and IP was considered to represent the aerosol which could penetrate to the main bronchial tubes of "mouth breathers." An ad hoc committee of the International Standards Organization (ISO)[7] reviewed existing lung penetration data and suggested that a size range of 0-10 μm would provide a sample which would be more representative of the aerosol which can penetrate into the thoracic region. This 0-10 μm size range has been termed the total thoracic particle fraction (TTP). ISO also suggested that the fractionation curve should be a log-normal function with a slope (geometric standard deviation) of 1.5. With respect to the RSP fraction, the ISO ad hoc committee noted that a cutpoint of 2.5 μm would be appropriate for providing a size range which would be similar to that which can be inspired into the lower lung regions of sensitive individuals in the population (the young, the sick and infirm). The shape of the RSP curve suggested by ISO is one which does not permit more than 90 percent of the smallest particle ($\leq$ 1.4 μm) to pass through the separator. In practice, it would be difficult to design a separator which would accomplish this goal.

In the present study, a 113 L/min sampler has been developed which over-comes the Hi-Vol limitations and which meets the ISO suggested cutpoints. This sytem, Figure 1, is designed to provide either the TTP fraction or both the TTP and RSP fractions. When operated in the TTP-only mode, sample collection takes place on 102 mm filters and when operated in the combined TTP/RSP mode, collection takes place on two 64 mm filters. Because of the reduced filter size in comparison with the Hi-Vol, operation with teflon filters may be economically feasible. Currently, a single 102 mm teflon filter costs approximately $5.00.

With reference to Figure 1, a flow rate of 113 L/min of ambient aerosol is drawn into the 10 μm sampling inlet where particles larger than the TTP range are stripped from the distribution. For operation in the combined TTP/RSP mode, the aerosol is drawn through a flow splitter. Half of the aerosol flow, 56.6 L/min, containing the TTP particles passes through the center of the splitter and then to a filter for particle collection. The remaining aerosol is directed through a cyclone, Figure 2, which separates the non-RSP from the RSP aerosol. The latter fraction is then drawn through a second collection filter. When operated in the TTP-mode, the flow splitter and cyclone are removed from the system and all of the aerosol from the inlet is drawn through a single filter, McFarland and Ortiz[8].

During the development work, several different designs for each of the components were evaluated. The results which will be presented will be only those for the final selections of apparatus.

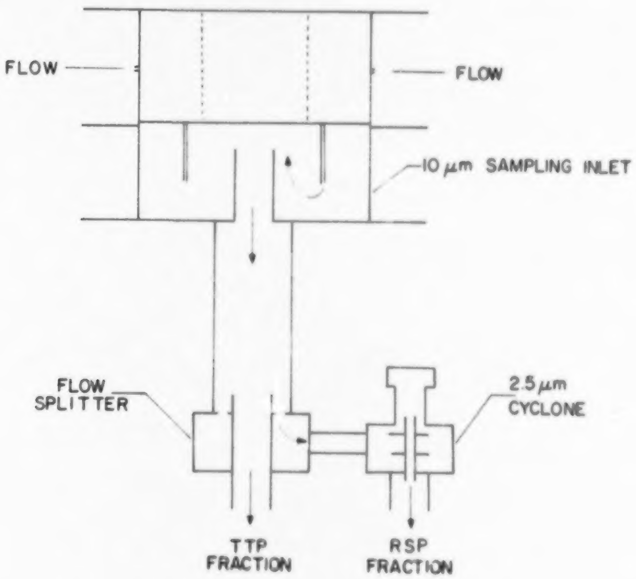

Figure 1. Aerosol sampler for TTP and RSP fractions.

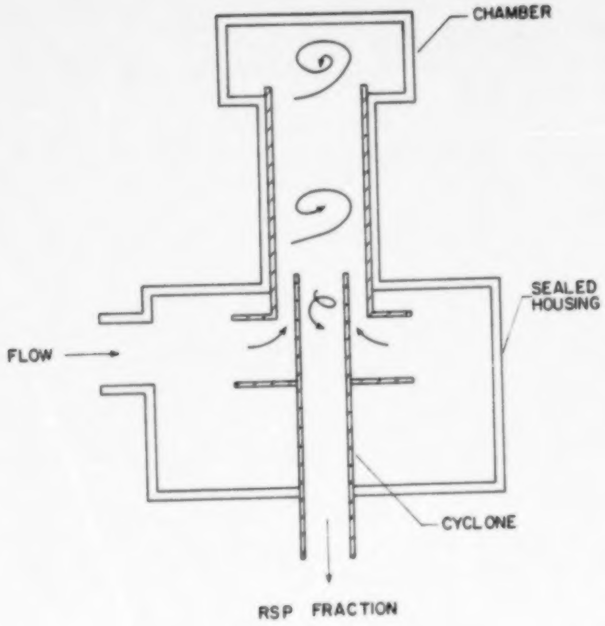

Figure 2. Configuration of cyclone used for separation of non-RSP from RSP aerosol.

METHODOLOGY

A combination of wind tunnel and laboratory tests was used to characterize the performance of the sampling system. The 10 μm sampling inlet was tested in the TTP-only mode in an aerosol wind tunnel which has a basic cross section of 1.5 m x 1.5 m with a test section which is expanded to 2.4 m x 2.4 m. Aerosol generated with a vibrating jet atomizer [9,10] was drawn into the wind tunnel entrance, mixed with ambient air, and passed into the test section. The test aerosol was formed from oleic acid disolved in ethanol. An analytical tracer, sodium fluorescein, was added to the mixture in the ratio of 1 gm fluorescein per 10 mL of oleic acid.

The wind tunnel test procedures consisted of sequentially operating the test inlet and an isokinetic sampler. The process was repeated to provide at least three isokinetic samples and two inlet samples. Sampler effectiveness, E, for a given test was computed from:

$$E = \frac{C_s}{C_{iso}} \tag{1}$$

where: C_s = wind tunnel aerosol concentration determined from test inlet

C_{iso} = aerosol concentration determined from isokinetic sampler

Particle size for a given test was determined by first collecting an aerosol sample on an oil-phobically treated glass slide and then microscopically measuring the droplets. The observed size was converted to equivalent aerodynamic size using the approaches of Olan-Figueroa et al.[11] and McFarland and Ortiz[8].

By varying particle size at a fixed wind speed, the so-called inlet effectiveness curves could be developed. These tests were conducted for wind speeds of 2, 8 and 24 km/hr. Quantification of the amount of aerosol collected by each sampling filter was performed by first eluting the fluorescein tag with ethanol and then mixing the ethanol with a measured volume of water. A 4-mL sample of the mixture was placed in a cuvette, one drop of 1N NaOH was added to stabilize fluoresence, and a reading taken with a Turner Model 111 Fluorometer.

To determine if the inlet has dry particle carry-over problems, a set of static tests was conducted in the laboratory. The roof of the inlet was replaced with a vertical cylinder which was fitted with internal cones to direct the aerosol towards the jet inlets. Nearly monodisperse plant pollens were aerosolized into the cylinder with the aid of a gooseneck atomizer, Whitby et al.[12]. A charge neutralizer, consisting of a 10 mCi line source of Kr-85, was placed in the cylinder. Aerosol penetration through the inlet (effectiveness) was determined by comparing the mass of pollen collected on the filter with that which was dispersed into the cylinder.

Aerosol samples are frequently subjected to chemical analyses in which either a small segment of the filter is removed for testing or only a small portion of the sample is instrumentally viewed, e.g. X-ray fluorescence analysis. As a consequence, uniformity of sample deposits is desirable. Experiments were performed in which the inlet was operated in the wind tunnel, with a 1.65 km/hr wind speed and with an aerosol of 10.4 μm aerodynamic diameter. Ten subsamples of 13.5 mm diameter were removed from each filter and were fluorometrically analyzed.

To characterize the performance of the system in the TTP/RSP mode, two types of laboratory experiments were performed. First, to examine the capabilities of the flow splitter, the inlet was replaced with a 1-m vertical drift tube and the cyclone was removed. Monodisperse 2.5 and 10 μm aerosols from a vibrating jet atomizer were introduced into the drift tube and sampled with the TTP and RSP filters. Additional experiments were conducted to determine the uniformity of deposits of 10 μm aerosols on the TTP filter. Second, to determine the fractionation characteristics of the cyclone, a set of experiments was performed in which aerosol was introduced from a flow tube into the cyclone housing. With the cyclone in place in the housing, the system was operated at a flow rate of 56.6 L/min. The aerosol passing through the cyclone was either collected on the RSP filter and measured fluorometrically or it was sampled with an optical counter (Climet Model CI-208) for a direct concentration reading. Next the cyclone was removed and the measurement process repeated. Aerosol penetration was calculated from the ratio of the concentration of aerosol passing through the cyclone to the concentration which was determined with the cyclone removed.

Measurements were made of the uniformity of deposits of 2.5 μm particles on the RSP filter. Here 9 subsamples of 11.0 mm diameter were removed from each 64 mm filter and the relative amount of fluorescein on each subsample was determined.

RESULTS

The results are shown in Figure 3 for wind tunnel tests with monodisperse oil droplets for the system operated in the TTP-only mode. Since the data for all three wind speeds are nearly the same, only a single curve is shown. The cutpoint size for the inlet is 10 ± 0.5 µm. Slope of the fractionation curve s_g, defined as a geometric standard deviation, can be calculated from:

$$\ell n^2 s_g = \Sigma\, \Delta E_i\, (\ell n\, D_i - \ell n D_{.5})^2 \qquad (2)$$

where: ΔE_i = ith increment of the effectiveness curve

D_i = midpoint particle diameter of the i^{th} interval, µm

$D_{.5}$ = cutpoint particle diameter, µm

For the curve drawn in Figure 3, the slope is 1.58.

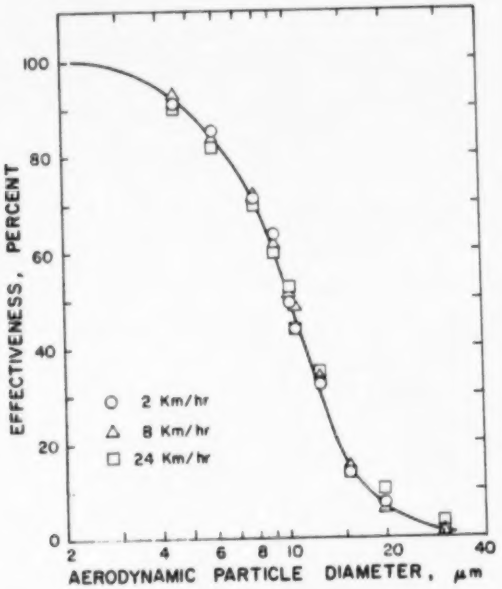

Figure 3. Sampling performance of inlet in TTP mode. Flow rate = 113 L/min. From McFarland and Ortiz[8].

The data in Figure 3 are replotted in Figure 4 to show a comparison with the ISO suggested curve which has a cutpoint of 10 μm and a slope of 1.5. In addition, error bars are shown for the experimental data. Effectiveness values for all three wind speeds at a given particle size were pooled and the standard deviation computed. The error bars represent ± 1 standard deviation from the mean.

To interpret the effect of the slope of the fractionation curve upon the amount of aerosol which will be sampled, three cases of atmospheric particle size distributions were generated, Figure 5. These were formed by using multiple log-normal fits to approximate three cases of actual distributions observed by Lundgren[13]. To these three size distributions were applied the fractionation curves of ISO, the test inlet, and step cut inlet with a cutpoint of 10 μm and slope of 1.0. The results, Table 1, show the fraction of total aerosol which would be collected by a filter following the fractionation stage. It may be observed from Table 1 that there is little difference in the TTP mass associated with the use of inlets with any of the three fractionation curves.

With respect to the uniformity of deposits on the filters for the inlet operated in the TTP-only mode, the results given in Table 2 show that the coefficient of variations for three tests ranged from 0.90 to 1.98%. Here the coefficient of variation is the ratio of the standard deviation to the mean of the mass collected on the 10 subsamples cut from each filter.

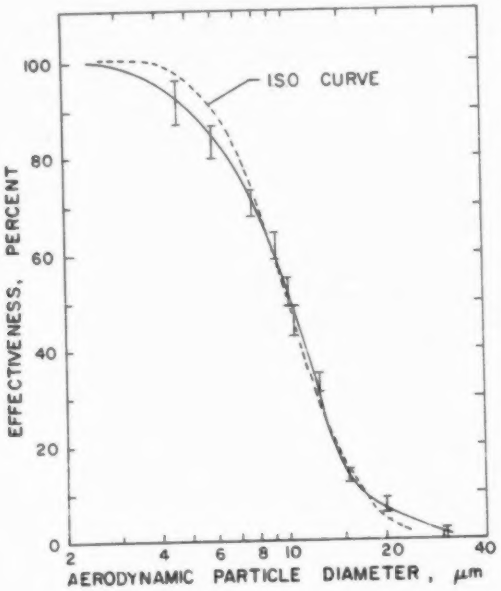

Figure 4. Comparison of sampling effectiveness of inlet with ISO curve. Wind speeds of 2, 8 and 24 km/hr. Error bars are ± 1 standard deviation. From McFarland and Ortiz[8].

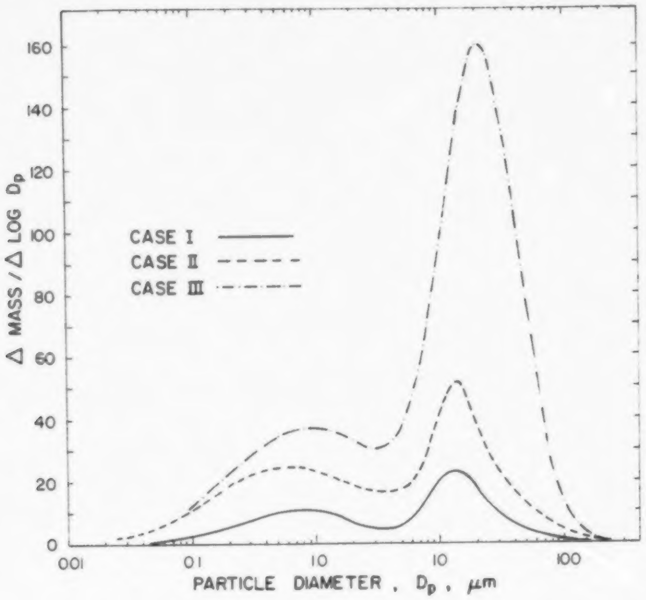

Figure 5. Case examples of atmospheric size distributions generated from composite of log-normal functions.

TABLE 1. PERCENT OF AEROSOL MASS TRANSMITTED THROUGH GIVEN INLETS FOR THREE AEROSOL SIZE DISTRIBUTIONS

	Inlet		
Size Distribution	ISO[a]	Step[b]	Test Inlet[c]
Case I	61.7%	62.1%	61.9%
Case II	65.5	65.9	65.5
Case III	42.8	42.8	41.9

[a] ISO effectiveness curve: Cutpoint 10 μm, Slope = 1.5

[b] Step effectiveness curve: Cutpoint 10 μm, Slope = 1.0

[c] Test inlet effectiveness curve: See Figure 3.

TABLE 2. UNIFORMITY OF DEPOSITS ON SAMPLING FILTERS

Mode of Operation	Filter Element	Particle Size	Number of Subsamples	Coefficient of Variation of Deposits
TTP-only	TTP	10.4 μm	10	1.67% 0.90 1.98
TTP/RSP	TTP	10.0	9	3.06 2.80
TTP/RSP	RSP	2.5	9	0.60 0.13

With the sampler operated in the combined TTP/RSP mode, the uniformity of filter deposits for the RSP fraction were examined with the use of 2.5 μm aerosols. The results of duplicate tests, Table 2, show the coefficients of variation for the 9 subsamples from each test to be 0.60 and 0.13 percent. Experiments to determine the uniformity of particle deposits on the TTP filter were conducted with 10 μm aerosols, Table 2. The results of two tests showed coefficients of variation for the subsamples from each filter to be 3.06 and 2.80 percent.

The results of static tests to determine dry particle sampling characteristics are shown in Figure 6. For these tests, the inner region of the inlet was operated with a heavy grease coating (silicone stopcock grease) on the internal surfaces in the fractionator and with the surfaces dry. It may be noted that use of grease does not substantially change the aerosol penetration. The curve resulting from dynamic testing, Figure 3, is shown in Figure 6 for comparative purposes. Considering the difference in methodology, the agreement is good between the static tests with dry particles and the wind tunnel tests with liquid droplets.

Evaluation of the splitter which is used for dividing the TTP and RSP flows was conducted with 2.5 and 10 μm aerosols. For 10 μm particles, the average of three tests showed that 49.8% of the aerosol was deposited on the TTP filter and 50.2% was drawn into the RSP flow line. Tests with 2.5 μm particles showed similar results.

Figure 7 shows the performance of the cyclone used to separate the non-RSP aerosol from the RSP. The fractionation curve has a cutpoint of 2.5 ± 0.3 μm aerodynamic diameter with a slope of 1.26. At least three data points were taken at each particle size. The mean standard deviation of effectiveness values for the eleven particle sizes is 1.6 percent. Polystyrene spheres were used as the test particles for the 1.35 μm aerodynamic diameter and polyvinyl toluene was used for the 2.38 μm size. Experiments with these two aerosols were evaluated with the optical counter. All other tests were conducted with the fluorescein-tagged oleic acid aerosols. The smallest oleic acid aerosols size, 2.37 μm was chosen to coincide with that of the polyvinyl toluene aerosol. Mean effectiveness calculated from tests with the polyvinyl toluene was 43.8 percent and that for the oleic acid aerosol was 43.1 percent.

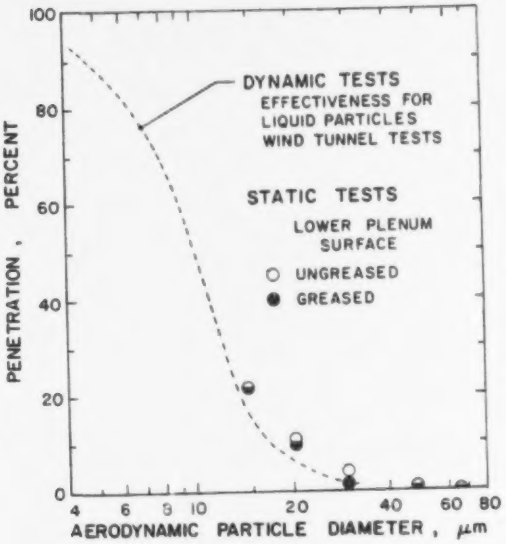

Figure 6. Static tests of inlet with dry particles. Flow rate = 113 L/min. From McFarland and Ortiz[8].

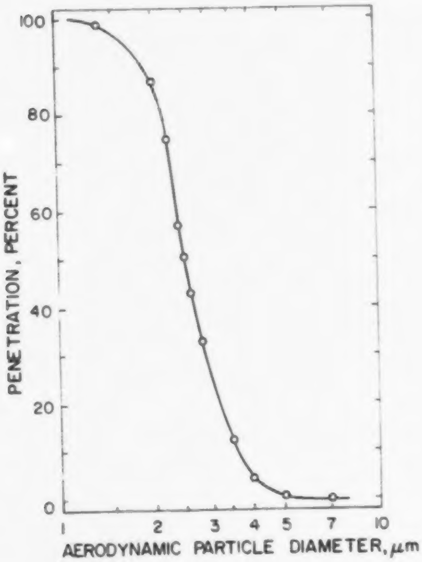

Figure 7. Sampling performance of RSP fractionator. Flow rate = 56.6 L/min.

SUMMARY AND CONCLUSIONS

A 113 L/min aerosol sampler has been developed to provide TTP and RSP aerosol fractions. Particles larger than 10 μm are removed by a fractionation stage within the inlet. The aerosol can then either be drawn through a single filter to provide a TTP-only fraction or through a flow splitter and cyclone to provide both TTP and RSP. When operated in the TTP/RSP mode, half of the flow, 56.6 L/min, is drawn through the TTP filter and the other half through the cyclone and thence through the RSP filter.

Wind tunnel test data for the inlet in the TTP mode shows the cutpoint to be 10.0 ± 0.5 μm with a fractionation curve slope of 1.58. Uniformity of deposits of 10 μm particles on the filter are represented by a coefficient of variation of less than two percent. Static tests with dry particles showed there to be little evidence of bounce or re-entrainment problems.

Calculations were made of the TTP aerosol which would be transmitted through the test inlet, an inlet with an ISO curve (10 μm cutpoint and 1.5 slope), and a step inlet (10 μm cutpoint and 1.0 slope) for three cases of atmospheric size distributions. Little differences were observed in the results for the TTP fractions between any of the inlets, indicating that slope of the fractionation curve over the range of 1.0 to 1.58 is not of great importance.

The flow splitter was shown to divide a 10 μm aerosol into two equal mass fractions, indicating that it performs as required. With the flow splitter in place, the uniformity of deposits of 10 μm aerosol on the TTP filter was characterized by a coefficient of variation of less than three percent.

Tests with the RSP cyclone showed a cutpoint of 2.5 ± 0.3 μm and a fractionation curve slope of 1.26. For 2.5 μm aerosol, the uniformity of deposits on the RSP filter was represented by a coefficient of variation of less than one percent.

ACKNOWLEDGEMENTS

The assistance of Mr. Robert E. DeOtte, who performed the numerical calculations, and Messrs. Dwight C. Russell, and Randall O. Guantt, who helped with the experimentation, is gratefully acknowledged. Support for this study was provided by EPA under Cooperative Agreement CR807732010.

REFERENCES

1. Lee, R.E., Jr. and J. Wagman. A sampling anomaly in the determination of atmospheric sulfate concentration. Am. Ind. Hyg. Assoc. J. 27:266-71, 1966.

2. Spicer, C.W., P.M. Schumacher and J.A. Kouyoumjian. Sampling and analytical methodology for atmospheric particulate nitrate. Report EPA - 600/2-78-067. U.S. EPA, Research Triangle Park, NC, 1978.

3. Stevens, R.K., T.G. Dzubay, G. Russwurm and D. Rickel. Sampling and analyses of atmospheric sulfates and related species. Atmos. Environ. 12:55-68, 1978.

4. McFarland, A.R. and C.A. Ortiz. Aerosol characterizations of ambient particulate samplers used in environmental monitoring. Progress Report. EPA Contract 68-02-2720. Air Quality Laboratory, Texas A&M University, College Station, TX, Nov. 1980.

5. 42 U.S.C. § 7409 (d) (1).

6. Miller, F.J., D.E. Gardner, J.A. Graham, R.E. Lee, Jr., W.E. Wilson and J.D. Bachmann. Size considerations for establishing a standard for inhalable particles. J. Air Pollut. Contr. Assoc. 29:610-15, 1979.

7. International Standards Organization. Report of ad hoc working group to Technical Committee 146 - Air Quality. Recommendations on size definitions for particle sampling. Am. Ind. Hyg. Assoc. J. 42:A64-A68, 1981.

8. McFarland, A.R. and C.A. Ortiz. A 10 μm cutpoint ambient aerosol sampling inlet. Accepted for publication in Atmos. Environ., 1981.

9. Raabe, O.G. and G.J. Newton. Development of techniques for generating monodisperse aerosols with the Fulwyler droplet generator. In Fission Products Annual Report LF-43. Lovelace Biomedical and Environmental Research Institute, Albuquerque, NM, 1970.

10. Berglund, R.N. and B.Y.H. Liu. Generation of monodisperse aerosol standards. Env. Sci. & Technol. 7:147-53, 1973.

11. Olan-Figueroa, E., A.R. McFarland and C.A. Ortiz. Flattening coefficients of aerosols collected on treated slides. Paper accepted for publication in Atmos. Environ., 1981.

12. Whitby, K.T., D.A. Lundgren, A.R. McFarland and R.C. Jordan. Evaluation of air cleaners for occupied spaces. J. Air Pollut. Contr. Assoc. 11: 503-11, 1961.

13. Lundgren, D.A. and H.J. Paulus. The mass distribution of large atmospheric particles. J. Air Pollut. Contr. Assoc. 25:1227-31, 1975.

Paper 13

A 10 MICRON CUTPOINT INLET FOR THE DICHOTOMOUS SAMPLER

James B. Wedding
Aerosol Science Laboratory
Civil Engineering Department
Colorado State University

Michael A. Weigand and Theodore C. Carney
Research Institute of Colorado

Ralph E. Baumgardner
U.S. Environmental Protection Agency

ABSTRACT

The United States Environmental Protection Agency is considering an alternative standard requiring the collection of a specific size fraction of atmospheric aerosol termed the thoracic fraction. This new standard assists in providing the impetus for the inlet development described herein.

An acceptable ambient air inlet for the dichotomous sampler has been designed, fabricated and performance tested. The device operates at 16.7 l/min and has an aerodynamic particle size of 10 μm associated with a 50% effectiveness value, which is commensurate with the anticipated changes in the Air Quality Standards. The system is independent of all environmental conditions, most importantly windspeed. The inlet employs a unique, omni-directional cyclone fractionator. Under static conditions the inlet was tested with solid particles by Dr. Walter John and exhibited no evidence of particle bounce.

INTRODUCTION

The U.S. Environmental Protection Agency (EPA) under the auspices of the Clean Air Act Amendment of 1977 is mandated to review the total suspended particulates (TSP) standard for its applicability to the protection of health and welfare. The present standards for particulate matter are 75 $\mu g/m^3$ average annual limit (geometric mean) and 260 $\mu g/m^3$ 24 hour limit (geometric mean) for particles <45 μm. EPA is considering an alternative standard requiring the collection of a specific size fraction of atmospheric aerosol. The principal impetus for this new approach are data that indicate that protection of public health may be better served by considering only inhalable particles (IP). An initial definition for IP was given by Miller **et al.**[1] (1979) as the size fraction represented by particles with aerodynamic diameters from 0 - 15 μm. Up until 1972 characterization of atmospheric particulate matter had been accomplished through the use of the standard hi-vol sampler which measured TSP and operated at a nominal flow rate of 1.41 m^3/min (50 cfm). The principal design criteria for the hi-vol required unquantitative specifications for inlet size and employed glass fiber filters. Inlets to permit collection of the early IP fraction were developed by several investigators including Wedding et al. (1981)[2] and Liu et al. (1981)[3]. The hi-vol approach has been shown during performance characterization tests to have a number of deficiencies. First, Lee and Wagman (1966)[4] and later Spicer et al. (1978)[5] have documented that the use of glass fiber filters lead to the formation of artifact. Secondly, the wind tunnel testing by Wedding et al. (1977)[6] and Ortiz et al. (1980)[7] have shown that the inlet characteristics of the hi-vol sampler are strongly a function of particle size, wind speed and direction. Irrespective of the proven drawbacks of the hi-vol sampling approach, it may nevertheless continue to serve as the basis for the atmospheric monitoring of aerosols as explained presently.

The International Standards Organization (ISO, 1981)[8] proposed consideration of a standard based upon those particles deposited in the tracheobronchial and alveolar regions of the human respiratory tract. This has subsequently been referred to as thoracic deposition or TTP (Total Thoracic Particles). Relying on this information, recent experimental data and scientific opinions, the Clean Air Scientific Advisory Committee (CASAC) has recommended to EPA that the 10 μm size range be selected. A recent EPA staff paper published by the Office of Air Quality Planning and Standards has thus proposed that the new primary standard be based on either 10 or 15 μm and additionally that the new average annual limits be set somewhere in the range of 55 - 120 $\mu g/m^3$ (arithmetic mean) with the 24 hour limit set somewhere within the range of 150 to 350 $\mu g/m^3$. This amounts to essentially a relaxation by about a factor of 2 - 3 in the existing standard. As IP is a relatable but varying fraction of TSP, depending on the ambient size distribution, it is felt that a need exists to monitor with instruments that sample only IP or TTP. Existing data suggest that few locations would be expected to violate the new standards. Thus, one may feel that monitoring with the hi-vol approach alone would be sufficient. This would result in an inaccurate calculation as the relationship of TTP to TSP would vary with location and meteorology. Additionally, this approach would be shortsighted because there is an inadequate monitoring data base to accurately set new standards. By not monitoring the specific size fraction that appears to be most deleterious to public health, the next five year review of the Clean Air Act may again see an attempt to establish meaningful air quality standards based upon inadequate data. In the opinion of these authors , it would be more conservative to keep average air quality standards at least as good or better than they were in the past, instead of risking the many unknowns that reside in the approach of allowing air quality to deteriorate. This would require that the new standard be kept at the lower limit of the proposed range, as one must consider the conversion from geometric to arithmetic mean (75 $\mu g/m^3$ geometric ~ 85 $\mu g/m^3$ arithmetic mean), as well as the fact that particles <10 μm comprise roughly 55% of the mass of particles < 45 μm.

Anticipating sampling apparatus that would monitor the 10 μm standard, the Environmental Monitoring Systems Laboratory of the Environmental Protection Agency during fiscal year 1981 proceeded to develop samplers to collect particles penetrating to the thoracic region of the respiratory tract.

The deposition of particles in the thoracic fraction is shown graphically Figure 1, taken from a regression fit by Chan and Lippman (1980)[9] on available experimental data on the respiratory tract. Also shown in Figure 1 is an ideal inlet for assessing the true ambient particle concentration and defined by a log-normal effectiveness curve having a D_{50} = 10 µm and a unity slope ($\sigma_g = 1.0$). Note also that an ideal inlet could be defined as one whose performance characteristics allows collection of the mass representative of the TTP fraction. The performance characteristics of these then will have a D_{50} = 10 µm and a slope that allows collection of mass representing TTP. D_{50} is defined as the particle size associated with a sampling effectiveness of 50%, and where effectiveness is defined as the ratio of mass deposited on the collection substrate of the sampler to the total airborne mass approaching the inlet with the proper corrections made for sampling volumes.

The research reported herein consists of the development of an ambient aerosol sampling inlet for the dichotomous sampler with a 50% cutpoint of 10 µm and a flow rate of 16.67 lpm. Wind tunnel testing was performed to determine the operational characteristics of the device at three different wind speeds of 2, 8 and 24 km/hr for a series of nominal aerodynamic particle sizes of 1 - 20 µm.

DESIGN RATIONALE AND INLET DESCRIPTION

The Wedding Inlet to the Dichotomous Sampler is illustrated in Figure 2. Design rationale is based upon the need for an Ambient Aerosol Sampling Inlet capable of collecting all particles of interest with the same D_{50}, slope (σ_{16}, σ_{84}) and shape of the collection effectiveness versus aerodynamic diameter curve - independent of the sampling conditions. At this time a need exists for an Inlet that is capable of immediate retrofit use on the Dichotomous Sampler with a D_{50} equal to 10 microns. This is because it is believed that the new Air Quality Standards will be based on a D_{50} = 10 µm and arises principally from the thoracic fraction curve as shown in Figure 1. The resulting effectiveness curve for an Inlet is the product of the fractionating device efficiency used to establish the desired D_{50} and the efficiency of the Inlet geometry which both transports the aerosol to the fractionator and protects the system from environmental factors. The choice of the fractionator device is practically limited to a conventional impactor, a virtual impactor or a cyclone. The conventional impactor suffers from particle bounce problems which may be reduced for a time with an appropriate coating or angled collection surface to alter the particle trajectory. These fractionators will always require unpredictable periodic maintenance. The virtual impactor may be a candidate but to date no workable prototypes have emerged. The cyclone, if designed to be omni-directional, is the best candidate as the slope of the fractionation curve is comparable to that of an impactor and has been shown to be unsusceptible to particle bounce problems. It is for these reasons that the cyclone approach was adopted as the fractionating element for this proposed IP Inlet. The inlet depicted in Figure 2 utilizes the omni-directional cyclone allowing aerosol entry from any angle of approach. An angular impetus is imparted to the particle motion by

Reproduced from best available copy.

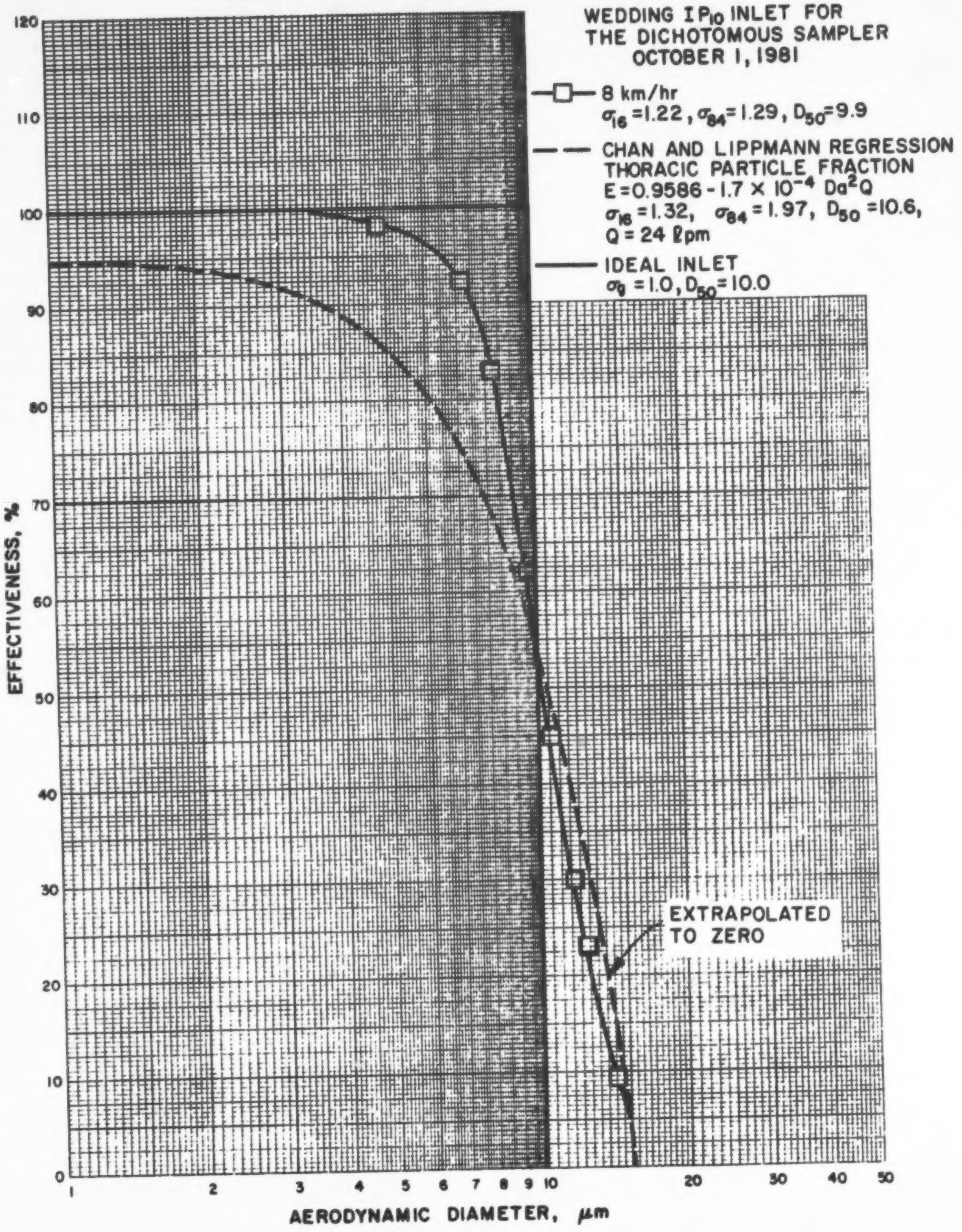

Figure 1. Wedding IP_{10} inlet performance curve at 8 km/hr and the thoracic fraction penetration curve vs. the ideal inlet curve.

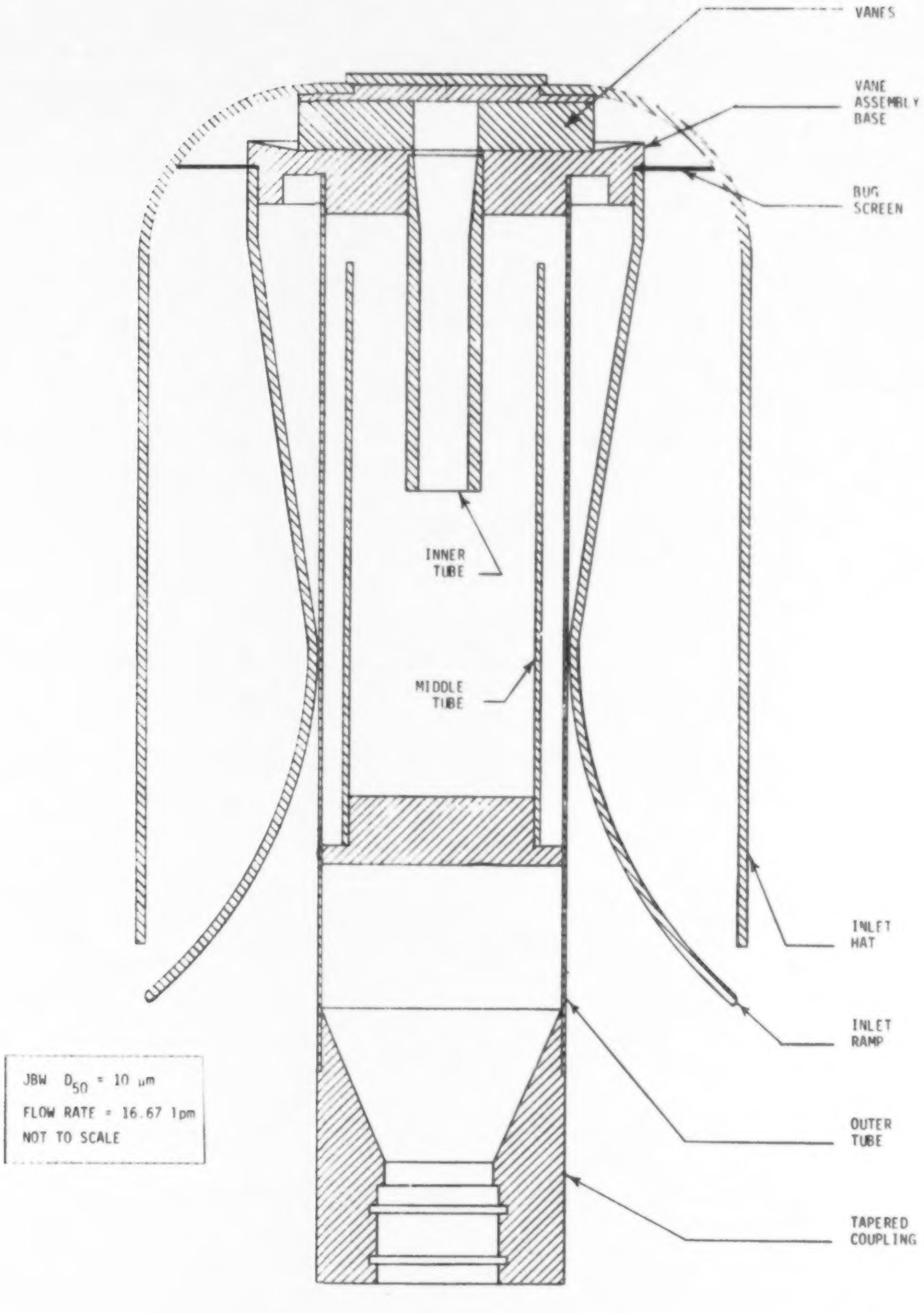
VANES
VANE ASSEMBLY BASE
BUG SCREEN
INNER TUBE
MIDDLE TUBE
INLET HAT
INLET RAMP
OUTER TUBE
TAPERED COUPLING
JBW D_{50} = 10 µm
FLOW RATE = 16.67 lpm
NOT TO SCALE

Figure 2. Wedding IP$_{10}$ inlet for the dichotomous sampler.

evenly spaced entrance vanes of a two-dimensional nature. The body of the cyclone is cylindrical in cross-section. As the particles enter the Inlet they follow the fluid streamlines along the lower radius and enter the cyclone fractionator through the vane system. Particle removal is realized on the inner collection tube. The flow with unremoved particles then enters the middle tube where the trajectory is altered and flow continues in an upward ascension. An additional turn is made to alter the flow into a downward trajectory to allow the particles to ultimately deposit on the collection substrate for subsequent mass analysis. Note that essentially 100% of the mass that deposits in the cyclone fractionator is removed by the inner tube and that there are no losses in the vane structure, middle or outer tubes. This is important, as then the inner and middle tube may act as a collection reservoir.

EXPERIMENTAL MEASUREMENTS

Inlet testing at a sampling rate of 16.67 lpm was performed in the closed loop Aerosol Science Laboratory Wind Tunnel at Colorado State University (Figure 3). The tunnel has a cross-sectional dimension of 1.22m square at the test section. The longitudinal component of turbulence intensity at the test location was found by hot-wire anemometer measurements to be 4%. The longitudinal macroscale was ~ 20cm. The tests utilized monodisperse aerosols with aerodynamic diameters of 1 to 20 μm generated by a vibrating orifice atomizer operating in an inverted position. Particles employed in the study were made from an oleic acid - ethanol mixture tagged with uranine. The aerosol was sized both by calculation and microscopically. The spread factor, or ratio of measured to actual diameter for this size range on oil phobic (coated with 3M fluorocarbon) glass slides has been found to be 1.39. The equivalent spherical diameter was converted to aerodynamic diameter using the specific gravity of pure oleic acid, 0.895. Measurements with a Casella impactor have found doublets do not exceed 4% at the test section. Aerosol from the atomizer was injected through a 15.24cm diameter tube containing a Kr-85 charge neutralizer. The pipe diverged into an annular region between two cones. Six pipes spaced around the annular region led the aerosol into the tunnel. This injection system produced a particle concentration profile across the test section which was found to be independent of wind speed over the range of 0.5 to 40 km/hr. Variation of the concentration across the width of the inlet never exceeded 10.2%.

The inlet was tested at wind speeds of 2, 8 and 24 km/hr. The velocities were measured upstream of the test section with a calibrated hot wire anemometer (TSI temperature compensated probe and TSI constant temperature anemometer). The anemometer was calibrated using a precision pitot tube and micromanometer. To determine the inlet effectiveness, the aerosol concentration was sampled isokinetically before and after each test using two sampling manifolds 0.90m wide with six sampling nozzles spaced at equal intervals (~12.5cm) in the same horizontal plane and at the same location in the test section as the inlet opening. Each nozzle led to a 47mm Gelman AE glass fiber filter. The inlet was mounted on a vertical tube approximately 1 m long, connected to a Millipore filter holder on the bottom. The sampling effectiveness of the inlet was determined by comparing the quantity of aerosol passed

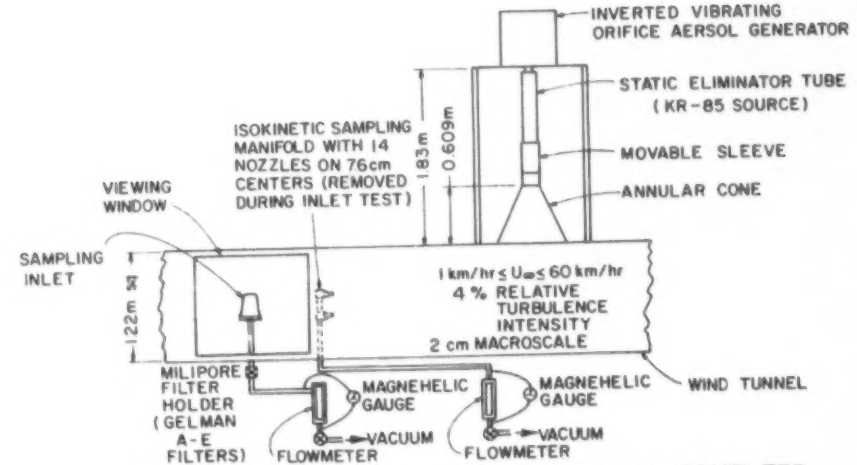
INVERTED VIBRATING ORIFICE AERSOL GENERATOR
STATIC ELIMINATOR TUBE (KR-85 SOURCE)
MOVABLE SLEEVE
ANNULAR CONE
ISOKINETIC SAMPLING MANIFOLD WITH 14 NOZZLES ON 76cm CENTERS (REMOVED DURING INLET TEST)
1.83m
0.609m
VIEWING WINDOW
SAMPLING INLET
1.22 m
1 km/hr ≤ U∞ ≤ 60 km/hr
4 % RELATIVE TURBULENCE INTENSITY
2 cm MACROSCALE
MILIPORE FILTER HOLDER (GELMAN A-E FILTERS)
MAGNEHELIC GAUGE
MAGNEHELIC GAUGE
WIND TUNNEL
VACUUM
VACUUM
FLOWMETER
FLOWMETER

TESTING FACILITY FOR AMBIENT AEROSOL SAMPLERS

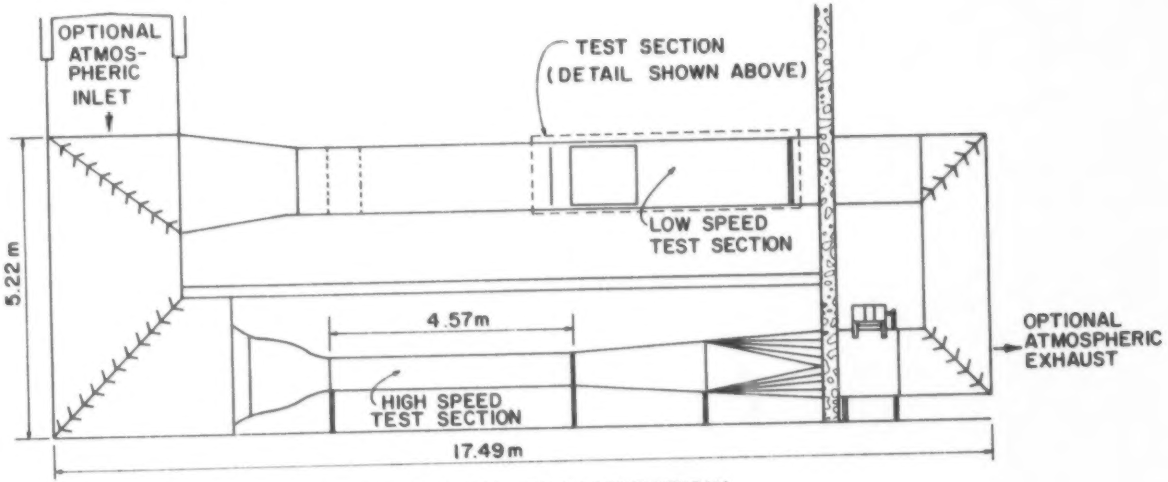
OPTIONAL ATMOS-PHERIC INLET
TEST SECTION (DETAIL SHOWN ABOVE)
LOW SPEED TEST SECTION
5.22 m
4.57m
HIGH SPEED TEST SECTION
OPTIONAL ATMOSPHERIC EXHAUST
17.49m

EXPERIMENTAL CONFIGURATION:
AEROSOL SCIENCE LABORATORY TEST FACILITY

Figure 3. Aerosol Science Laboratory Test Facility, Colorado State University.

by the inlet and deposited on the filter to that collected by the isokinetic sampling probe with appropriate corrections for differences in sampling volume and pressure drops as monitored in the lines. Collection substrates were washed in 50 ml of pure ethanol, then diluted 1:1 with distilled deionized water which served as a buffer to stabilize fluorescence. A 4 ml aliquot of each sample solution was measured for uranine content with an Aminco fluorometer.

RESULTS AND DISCUSSION

The results of the performance testing of the Wedding IP Inlet are shown in Figure 4. Each plotted point represents the average value of at least 8 data points taken on different days. Additionally, the D_{16}, D_{84}, and D_{50} values are tabulated along with σ_{16} and σ_{84} values. σ_{16} is defined as the ratio D_{16}/D_{50} and σ_{84} defined as the ratio D_{50}/D_{84}. The D_{50} values for the windspeeds of 2, 8 and 24 km/hr are 10.6, 10.4, and 9.75, respectively. Thus, it is seen that the D_{50} shift is less than 1 micron. The three curves at all 3 windspeeds are essentially parallel to each other with nearly identical σ_{16} and σ_{84} values as noted in Figure 4. Note that the performance curves are thus nearly logarithmic which means that $\sigma_{16} = \sigma_{84} = \sigma g$. The fact that the inlet performance is independent of windspeed results from the unique inlet housing design and sharp cut characteristics of the cyclone fractionator.

Independent tests utilizing solid particles were performed by Dr. Walter John at the Air and Industrial Hygiene Laboratory in Berkeley, California to determine if the fractionator suffered from particle bounce. These tests indicated the following: "Tests on the Wedding Inlet revealed negligible solid particle bounce."(1981)[10]Note that the Inlet for the Dichotomous Sampler must have small σ_{16} values (steep fractionation curve), and be windspeed independent to avoid errors in a coarse fraction collected mass.

Quantitative assessment of the influence of inlet performance characteristics on collected mass and how this collected mass relates to the actual ambient mass distribution, as well as particles penetrating to the thoracic region of the respiratory tract, was recently investigated in a paper by Rodes et al (1981)[11]. A regression analysis of available deposition data taken from Chan and Lippman (1980) was used to represent particle penetration to the thoracic region of the respiratory tract. This regression curve along with the 8 km/hr effectiveness curve for the Wedding Inlet is shown in Figure 1. In the Rodes et al paper, a mathematical analysis of the mass collected by the Wedding Inlet as well as the TTP fraction, was undertaken. The results of that analysis show that the mass collected by the Wedding IP Inlet and that collected by the lung in the TTP fraction are essentially identical. In the fine fraction collected mass, no sampling bias would be found between the mass collected by the Wedding Inlet or the TTP fraction. In the coarse fraction, or total IP, the Wedding IP_{10} Inlet collects almost exactly the same amount of mass as would be collected in the thoracic region of the respiratory tract.

Additional tests are underway to further quantify the sampler performance when the approaching mean wind vector does not lie parallel to the horizontal plane. This is important as many samplers are placed upon the roof tops of buildings where the angle to the approach flow of the Inlet may be as much as

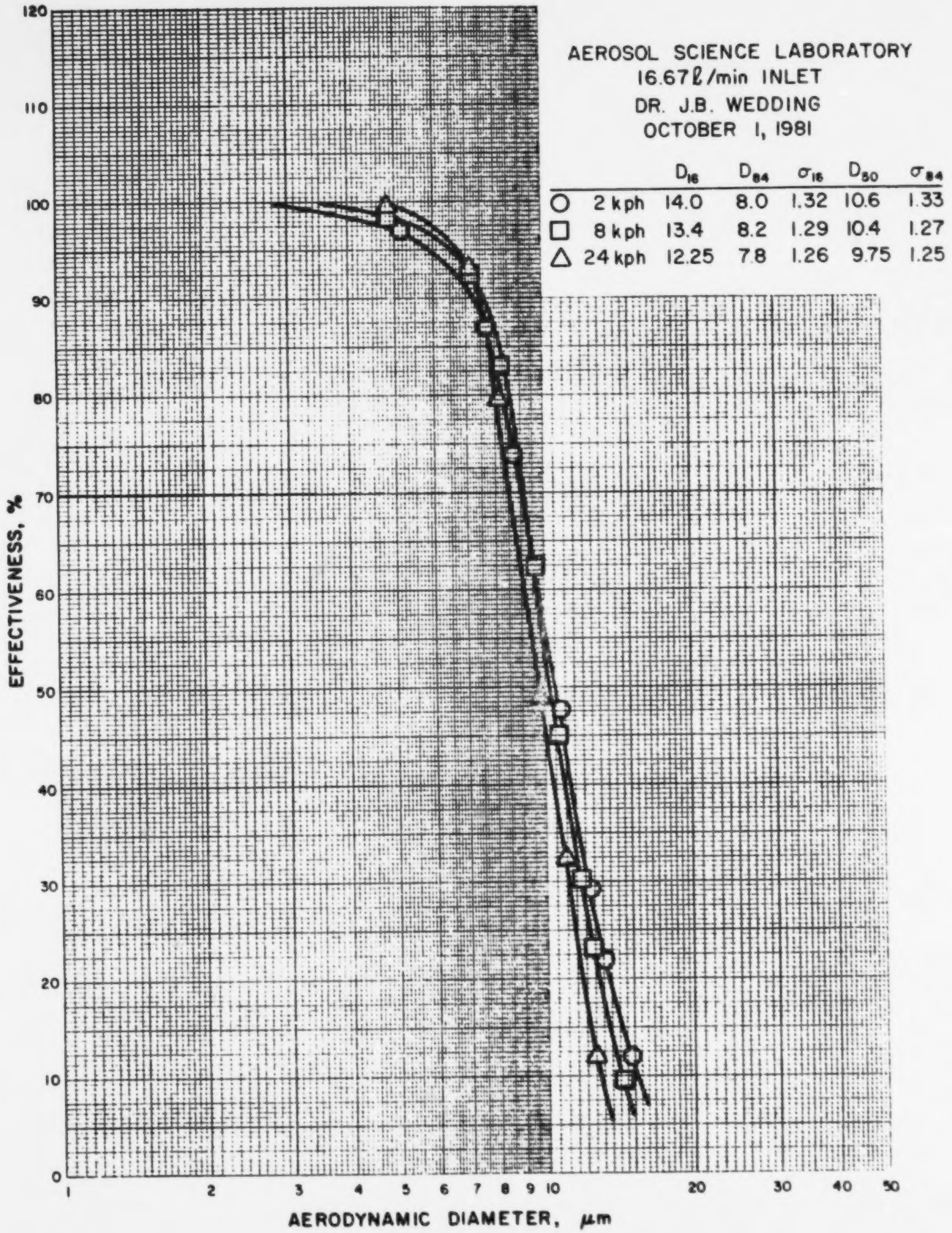

Figure 4. Performance curves for the Wedding IP_{10} inlet for the dichotomous sampler.

Reproduced from best available copy.

30 - 45 degrees. Note that tests of this type must be performed at angles greater than 10 to 15 degrees which is the minimum angle for separated flow to occur on prismatic bodies. Tests conducted at angles less than 10 to 15 degrees will probably show no significant difference in sampling effectiveness.

Finally, a series of tests were performed at flow rates other than 16.67 lpm to see what effect this would have on the inlet performance curve. Tests were conducted at 15 and 17 lpm and there was no discernible effect in sampler performance.

SUMMARY AND CONCLUSIONS

1. An acceptable IP Inlet for $D_{50} = 10\mu m$ has been designed, fabricated, and performance tested. It is believed to represent a completely viable candidate for use on the EPA IP network as an immediate retrofit for the Dichotomous Sampler. The unit has been found to have small σ_{16} values to insure windspeed independency and has been shown by computer analysis to collect essentially the same mass as that collected in the thoracic region of the respiratory tract.

2. In static tests with solid particles, the inlet displayed no particle bounce problem.

3. The inlet can be operated in the field for an indefinite period of time without any maintenance whatsoever.

4. The unit was operated at two different sampling rates in addition to the 16.67 lpm standard flow rate. At both 15 and 17 lpm flow rates, there was no detectable change in the effectiveness values.

ACKNOWLEDGMENTS

Financial support for this investigation was provided by the U.S. Environmental Protection Agency under Cooperative Agreement Nos. CR808011-02 and CR807753. The EPA project officers for the cooperative agreements were Mr. Ralph Baumgardner and Mr. Charles Rodes.

The invaluable assistance of Mike Ligotke in the lab is duly noted and greatly appreciated.

REFERENCES

1. Miller, F.J., Gardner, D.E., Graham, J.A., Lee, R.E., Jr., Wilson, W.E. and Bachman, J.D., "Particle Size Considerations for Establishing a Standard for Inhaled Particles", Draft. U.S. Environmental Protection Agency, Research Triangle Park, NC, 1979.

2. Wedding, J.B., "Ambient Aerosol Sampling: History, Present Thinking and a Proposed Inlet for Inhalable Particulate Matter", Accepted by Env. Sci. Technol., 1981.

3. Liu, B.Y.H. and Pui, D.Y.H., Atmos. Environ., 15: 4, 589 - 600, 1981.

4. Lee, R.E., Jr. and Wagman, J., Am. Ind. Hyg. Assoc. J. 27, 266 - 271, 1966.

5. Spicer, C.W., Schumacher, P.M. and Kouyomjian, J.A., "Sampling and Analytical Methodology for Atmospheric Particulate Nitrate", Report No. EPA-600/2-78-067, 1978.

6. Wedding, J.B., McFarland, A.R. and Cermak, J.E., Env. Sci. Technol. 11: 387 - 390, 1977.

7. Ortiz, C.A., McFarland, A.R. and Rodes, C.E., "Wind Tunnel Studies of the Hi-Vol and Membrane Aerosol Samplers", Accepted for publication in J. Air Pollut. Contr. Assoc., 1980.

8. ISO TC146, Am. Ind. Hyg. Assoc. J. 42, A64 - A68, 1981.

9. Chan, T.L. and Lippman, M., Am. Ind. Hyg. Assoc. J. 41, 399 - 409, 1980.

10. John, W., Air and Industrial Hygiene Laboratory, California Department of Health, Berkeley, CA 80266, Private Communication, March 1980.

11. Rodes, C.E., Carney, T.C. and Wedding, J.B., "A Quantitative Technique for Determining the Impact of Non-Ideal Ambient Sampler Inlets on the Collected Mass", Submitted to Atmos. Env., 1981.

Although the research described in this paper has been funded (wholly or in part) by the United States Environmental Protection Agency, it has not been subjected to Agency review and, therefore, does not necessarily reflect the views of the Agency and no official endorsement should be inferred.

The work described in this paper was not funded by the U.S. Environmental Protection Agency. The contents do not necessarily reflect the views of the Agency and no official endorsement should be inferred.

Paper 14

APPLICATIONS OF THE "APPARENT DIAMETER" METHOD FOR UNIMODAL AND BIMODAL DISTRIBUTIONS

James W. Gentry
Institute for Physical Science and Technology
University of Maryland

J. San, F. Farzaneh, and P. K. Yu
Department of Chemical Engineering
University of Maryland

ABSTRACT

A method for unambiguously determining the parameters for log normal distributions based on the "apparent diameter" or "apparent diffusion coefficient" method is discussed.

In the paper, the limitations of using the Nyström method for analyzing penetration measurements are demonstrated using the L-1 and L-∞ condition numbers. This easy-to-apply mathematical property can be readily adapted for the evaluation of any data reduction procedure.

The Park-Gentry procedure is extended to bimodal distributions and to fibers. Limitations as well as advantages of the procedure are demonstrated.

Thirdly, it is shown that for an important sub-class of problems, the Park Gentry conjecture:

$$\int_0^\infty F(D)\ \mathrm{Ln}D\ dD = \int_0^1 \mathrm{Ln}\ \bar{D}\ d\ Pt = \int_0^1 \mathrm{Ln}\ \bar{D}\ d\ \overline{Ef}$$

is true; and furthermore, that there are no other analogues to the equation.

INTRODUCTION

The base problem is to determine an unknown size distribution function $\underline{f}(D)$ from a series of experimental measurements of the fractional penetration $\overline{Pt}(Z_k)$ at different operating conditions (i.e. flow rate, residence time, etc.) Z_k. Usually, $Pt(D_j Z_k)$ the theoretical penetration will be known as a function of size D_j and operating conditions Z_k. In developing an inversion algorithm it is desirable:

1. That the algorithm provide non-ambiguous estimates of the distribution;
2. That the inversion algorithm be relatively insensitive to experimental error;
3. That the algorithm be easy to apply;
4. That the algorithm require as few a priori constraints regarding functional form of size distribution as possible; and
5. That the algorithm be suitable for as wide a range of classifiers (i.e. diffusion batteries, elutriators, inertial impactors, filters, etc.) as possible.

Mathematically, the problem can be stated as finding a method to solve the integral equation:

$$\int_0^\infty Pt(D,Z_k) \cdot f(D)\, dD = \overline{Pt}(Z_k) \tag{1}$$

with as few a priori constraints on f(D) and $Pt(D,Z_k)$ as possible and with the experimental penetration $\overline{Pt}(Z_k)$ subject to random fluctuations $\Delta\overline{Pt}(Z_k)$.

In this paper, we discuss the application of the "apparent diameter method". In procedures based on this and related methods, the behavior of the apparent diameter (or apparent diffusion coefficient) as a function of experimental penetration $\overline{Pt}$ and/or operating variables Z_k is examined. The apparent size ($\bar{D}$) is defined by the relation:

$$Pt(\bar{D},Z_k) = \overline{Pt}(Z_k) \tag{2}$$

From this relation, it is clear that the apparent diameter corresponds to the hypothetical diameter of a monodisperse aerosol having a theoretical penetration at conditions Z_k equal to the experimentally measured penetration. Of course, since the efficiency (ef) is defined as 1-Pt, equations (1) and (2) could be expressed in terms of the efficiency.

In the investigation described here, we were unable to develop an algorithm which meets all the desirable criteria for inversion algorithms listed above. Our procedure does require an a priori assumption regarding the distribution function. Non-ambiguous estimates of the size distribution were obtained only if an a priori constraint on the distribution function being limited to functions characterized by two adjustable parameters were imposed. However, the algorithm does impose two mathematical constraints on the parameters of more complex distributions in lieu of specifying the parameters.

Below, we briefly describe the limitations of earlier algorithms which led to the development of our algorithm. Secondly, the algorithm is described in its most restrictive form--i.e. with a constraint of an a priori assumption that the size distribution function be log normal. Thirdly, tests of the algorithm with simulated and real penetration or efficiency measurements are described. Finally, a discussion of the application to more complex distributions is presented. In evaluating the algorithm, the primary criterion is how well does the algorithm meet the desirable characteristics of an inversion algorithm described above.

In one important respect it does not. Specifically, the method cannot be used for cases where the penetration is not monotonic, for the method is dependent on a unique single size satisfying equation (2). In practice, this constraint does not restrict the use of the method in the inversion of measurements with diffusion batteries, elutriators, cyclones, settling chambers, or inertial impactors (provided there is no size dependent re-entrainment or bounce). It is not applicable to filters and is probably not applicable to light scattering. [In the case of light scattering, the penetration in equation (1) is replaced with the amount of light scattered.]

CONDITION NUMBERS AND THE NYSTRÖM METHOD

Inversion algorithms based on Nyström[1] type methods have an inherent attraction in that no a priori assumption is necessary regarding the shape of the size distribution function. Typically, in this method the integral equation is replaced by a series of algebraic equations having the form:

$$[Pt]_{jk}\, f_k = \overline{Pt}_j \qquad (3)$$

where $\overline{Pt}_j$ is the experimental penetration at operating conditions Z_j, f_k is the frequency of particles in the kth size class, and $[Pt]_{jk}$ is the theoretical penetration associated with particles of size class k and operating conditions Z_j. The repeated subscript implies a summation over all size classes.

Unfortunately, it soon became evident that for many experimental measurements especially those with diffusion batteries, solution of equation (3) results in non-feasible (negative) values of f_k. This problem could be moderated by adjustment of the matrix elements $[P]_{jk}$ either by defining them as products of penetrations from several stages as for example in inertial impactors or by overspecifying the equation (i.e. measuring the penetration at more conditions than the number of unknown size classes). Although these techniques do reduce the probability of obtaining non-feasible values, there is no assurance that either the method will converge to the correct value or that the solution is restricted to positive frequencies. Furthermore, these methods are especially vulnerable to small fluctuations in the measured penetration.

An indication of the sensitivity of the solution to small fluctuations is given by the relation:

$$\frac{||\Delta f||_p}{||f||_p} \leq C(N:P)\frac{||\Delta ft||_p}{||Pt\;||_p} \qquad (4)$$

The expression relates the relative error in the penetration to a corresponding relative error in the frequency. The incremental and total values of penetration and frequency are expressed in terms of the pth norm which is defined by:

$$||f||_p = (|f_1|^p + |f_2|^p + \ldots |f_k|^N)^{1/p} \qquad (5)$$

where N is the total number of collocation points. The condition number C(N:P) depends only on the elements Pt_{ij} of the matrix and on the particular norm used. Two of the more convenient norms are those where p=1 and $p \to \infty$. (In this case, the norm is the value of the element with the largest maximum value.) For these cases, the condition numbers are defined by:

$$C(N;P) = ||Pt_{jk}||_p \cdot ||Pt^{-1}_{jk}|| \tag{6}$$

where

$$||Pt_{jk}||_1 = \text{Maximum of} \sum_{j=1}^{N} |Pt_{kj}| \tag{7}$$

and

$$||Pt_{jk}||_\infty = \text{Maximum of} \sum_{j=1}^{N} |Pt_{jk}| \tag{8}$$

Three points should be made regarding the condition numbers. Clearly the condition number will depend on the particular norm chosen; although all are related. Secondly, the condition number will always be positive and greater than one [except for the special case of N=1 where the condition number is identically one and the inequality in equation (4) becomes an equality.] Thirdly, the condition number can be changed by scaling. We have found that scaling the matrix $[Pt_{jk}]$ by normalizing either the largest term in each row (p=1) or the sum of the absolute values of each element in a row ($p=\infty$) to the value one gives a satisfactory scaling.

The important point is that the condition number provides an indication of the sensitivity of the solution vector to fluctuations in the penetration measurements. Originally developed as a criterion for evaluating the uncertainties owing to round off error in digital computer calculations, the condition numbers can provide an indication of the sensitivity of a distribution to measurements and a guide to their optimal location. Were the condition number to be greater than 10^2 for a normalized penetration matrix, there is considerable doubt if the resulting solution vector would consist of feasible values for a relative error of over 1% in the penetration measurements. Since for diffusional deposition such condition numbers are the rule rather than the exception, it is not surprising that Nyström methods have largely been abandoned. We have found that the condition number increases as the number of collocation points increase. More important, the condition number is a strong function of the classifier index n defined by the relation:

$$\overline{Ef} = 1 - \overline{Pt} \to D^n \tag{9}$$

as

$$\overline{Ef} \to 0 \text{ or } \overline{Pt} \to 1$$

For diffusion batteries n=2/3, elutriators n=2, and for inertial impactors n>4. From our calculations simulating power law classifiers, we found that very large condition numbers were obtained when n was less than 1. Specifically for N=7, the condition number was ~100 for n=1.1, $\sim 10^3$ for n~0.9, $\sim 10^4$ for n~0.8, and $\sim 10^6$ for $n \sim 10^6$. For n>2.0, the condition number was ~10. For condition numbers greater than 10^2, Nyström type methods are not recommended. Based on these results, we conclude that Nyström methods are unsuitable for diffusion battery measurements and questionable for elutriator or gravitational classifiers.

THE "APPARENT DIAMETER" ALGORITHM[2]

The apparent diameter (or diffusion coefficient) is defined by the relation given in equation (2). If the theoretical penetration were a monotonic function of D then for each value of the experimental penetration there is only one value of the apparent diameter. Furthermore, the apparent diameter is a monotonic function of penetration. (For diffusion batteries, the apparent diffusion coefficient increases with penetration whereas for elutriators, the apparent diameter increases. For simulated measurements, the apparent diameter when plotted as a function of the penetration yields a flat curve at penetration values near one, and is almost vertical at penetrations near zero. Although the curve is very steep at penetrations ranging between 35-40%, it appears that for diffusion battery measurements, the apparent diffusion coefficient is equal to the log mean diffusion coefficient for a log normal equation. That is:

$$\bar{D}^* \; (@\; 0.35 < \overline{Pt} < 0.4) = \text{Exp} \int_0^\infty \text{Ln}D^* \, F(D^*) \, dD^* \qquad (10)$$

The algorithm described by equation (10) was developed independently[3,4] by Megaw and Nolan. It had two limitations: first, no information was provided regarding the standard deviation (polydispersity) of the distribution; secondly, the value of the characteristic penetration (the penetration where the apparent diameter is equal to the log mean diameter) was not precisely defined but ranged between 0.35 and 0.4. Subsequently, we were able to show that the characteristic penetration depends upon the degree of polydispersity accounting for this lack of precision.[5]

The second idea incorporated into our algorithm was the use of asymptotic conditions as the penetration approaches one. In an earlier application of this idea, Pollack[6] developed a method applicable as the penetration approaches zero. Unfortunately, this method fails when applied to measurements with any experimental uncertainty. Our application to the other asymptotic condition (as the penetration approaches one) proved to be more fruitful in that the curve of the apparent diameter or diffusion coefficient is almost level.

These two ideas were incorporated along with the assumption that the distribution function is log normal to produce the algorithm. The steps in the algorithm were as follows:

1. From the experimental penetration measurements, the apparent diameter (or diffusion coefficient) was calculated and plotted as a function of experimental penetration.

2. Secondly, the value of $\text{Ln}D_1$ was obtained by numerical integration of LnD over penetrations from 0 to 1.

3. Finally, the value of the standard deviation was obtained by first extrapolating LnD to a fractional penetration, then calculating σ (the standard deviation) from:

$$\lim_{Pt \to 1} \bar{D}^n = D_1^n \, \text{Exp} \, \frac{n^2 \sigma_1^2}{4} \qquad (11)$$

where n is the classifier index defined in equation (9) and D_1 is the log mean diameter determined in step 2 of the algorithm.

It is important to note that equation (11) follows directly from the assumption that the distribution can be represented by a log normal distribution and the asymptotic expression for the efficiencies. No other assumptions or restrictions are required. On the other hand, that

$$\int_0^1 \mathrm{Ln}\bar{D}\ d\,\overline{Pt} = \mathrm{Ln}D_1 = \int_0^\infty F(D)\ \mathrm{Ln}D\ \delta D \qquad (12)$$

is a conjecture. Based on extensive numerical simulations, equation (12) appeared to be valid for distributions consisting of one or two log normal distributions.

In order to examine equation (12) analytically, it is necessary to find an inverse expression giving the diameter (or diffusion coefficient) as a function of penetration. A special case of such functions which also has the asymptotic form of equation (9) is the power law expression defined by:

$$Pt(D,Z) = 1 - \left[\frac{D}{D(Z)}\right]^n \qquad D<D(Z) \qquad (13a)$$

$$Pt(D,Z) = 0 \qquad D \geq D(Z) \qquad (13b)$$

where D(Z) is a characteristic diameter depending only on the operating conditions (flow rate, instrument length, etc.) and independent of the particle size distribution. With this assumption, one can derive an expression relating the efficiency and apparent diameter to two parameters:

$$\bar{q}_1 = \frac{n\sigma_1}{2} \qquad (14a)$$

and

$$\tau_1 = \frac{1}{\sigma_1}\ \frac{\mathrm{Ln}D(Z)}{D_1} \qquad (14b)$$

The two equations can be combined yielding an equation relating the apparent diameter to the efficiency (or penetration) with $\bar{q}_1$ as a parameter. With the power law expression for the efficiency, one can derive analogous closed form expressions for a size distribution consisting of an arbitrary sum of log normal distributions. When the penetration approaches one, this expression becomes:

$$\underset{Pt\to 1}{\mathrm{Lim}}\ \bar{D}^{n} = \sum_{j=1}^{J} C_j D_j^n \exp \bar{q}_j^{2} \qquad (15)$$

where C_j, D_j, and $\bar{q}_j$ are the parameters of the constituent log normal distributions. Generally, the classifier index n will be known; consequently, there will be 3J-1 unknown parameters in equation (15). [One unknown was eliminated by the condition that ΣC_j must be units.]

The second relation which can be obtained is that:

$$\int_{o}^{1} \mathrm{Ln}\bar{D}\ d\ \overline{Pt} = \sum_{j=1}^{J} C_j\ \mathrm{Ln}\ D_j \qquad (16)$$

a direct consequence of equation (12).

Recently, we were able to show that for power law efficiencies and with a distribution function consisting of a sum of log normals that:

$$\int_{o}^{1} H(\bar{D})\ d\ \overline{Pt} = \int_{o}^{\infty} H(D)\ F(D)\ \delta D \qquad (17)$$

if H(D) = LnD (equation 16) or H(D) = 1 (normalization) but for no other H(D). Since almost any function can be approximated by an arbitrary sum of log normal distributions, this result indicates that for power law classifiers, equation (12) is valid for an arbitrary size distribution function. Furthermore based on previous simulations, it appears likely that the equation holds for cases where the theoretical penetration is monotonic. A second very important result is that the method does not hold for other H(D).

The method of proof was to evaluate the objective function ψ:

$$\psi(H) = \int_{o}^{1} H(\bar{D})\ d\ \overline{Pt} - \int_{o}^{\infty} H(D)\ F(D)\ \psi D \qquad (18)$$

The second integral can be evaluated if the functional form F(D) is known (i.e. series of log normal distributions). The first integral requires the assumptions of both the power law classifier and the distribution. The resulting expression ψ can be shown to be constant (i.e. independent of polydispersity) only if H(D) is LnD or 1. The final step of the proof is to show that the constant is equal to zero for LnD.

APPLICATION TO BIMODAL DISTRIBUTIONS

In applying the method, non-ambiguous solutions are obtained only if the function can be represented by a single log normal. However, for more complicated distributions, equations (15) and (16) are constraints. This suggests a generalized procedure.

First, the data are analyzed as if the distribution were a single log normal. From the asymptotic limit as the penetration approaches one and from the integral of $\mathrm{Ln}\bar{D}$ with respect to penetration yields D_1 and $_1$. These parameters can then be used to simulate the $\mathrm{Ln}\bar{D}$ as a function of penetration curve. If the simulated data and experimental measurements agree, then one concludes that:

1. The distribution function is log normal (or can be represented by a log normal within experimental error); and
2. The parameters are given unambiguously by equations (11) and (12).

If the simulated data do not agree with the experimental measurements, then the hypothesis of a single log normal is rejected, and the examination of multimodal distributions is begun. The major problem is that even for a bimodal distribution there are five parameters with two constraints:

$$\int_0^1 \mathrm{Ln}\bar{D}\, d\,\overline{Pt} = C_1 \,\mathrm{Ln}\, D_1 + (1-C_1)\,\mathrm{Ln}\, D_2 \tag{19}$$

and

$$\lim_{Pt\to 1} \bar{D}^n = C_1 D_1^n \exp \bar{q}_1^2 + (1-C_1)\, D_2 \exp \bar{q}_2^2 \tag{20}$$

where

$$\bar{q}_j = \frac{n\sigma_j}{2}$$

We have examined a number of special cases, but have found no clearcut rule. Comaprison of the frequency distributions with the corresponding $\mathrm{Ln}\bar{D}$ vs. penetration (or efficienty) plots show that when there is a significant difference in the frequency curves, the difference is manifest in the LnD penetration plot. These comparisons are significant in that the asymptotic limit of $\mathrm{Ln}\bar{D}$ and its integral are chosen to be the same for the bimodal as the unimodal distribution.

To illustrate the algorithm, we first consider the simulation of penetration measurements for an elutriator. The experimental penetrations, the flow rate, the apparent diffusion coefficient and its logarithm are given in TABLE I.

TABLE 1. SIMULATED PENETRATION MEASUREMENTS FOR TEST PROBLEM

Flow Rate	Penetration	Apparent Diameter	$\mathrm{Ln}\bar{D}$
0.1	0.00	1.0	0
0.5	0.00	2.2	0.77
1.0	0.00	3.2	1.15
4.6	0.06	6.6	1.89
10.0	0.14	9.3	2.23
46.4	0.45	16.0	2.77
100.0	0.63	19.2	2.95
464.0	0.88	23.3	3.15
1000.0	0.94	24.2	3.19

The apparent diameter is then plotted as a function of penetration as in Figure 1. These "experimental" data are represented by solid circles ●. The points are extrapolated to a penetration of 1 yielding a value of 3.2. Next, the integral of:

$$\int_0^1 \mathrm{Ln}\bar{D}\, d\,\overline{Pt}$$

is calculated. Five point Gauss-Hermite quadrature was used giving the value of 2.71. (It was assumed that the penetration through the elutriator was:

$$Pt(D,Q) = 1 - \frac{0.1\, D^2}{Q}$$

where Q is the flow rate.)

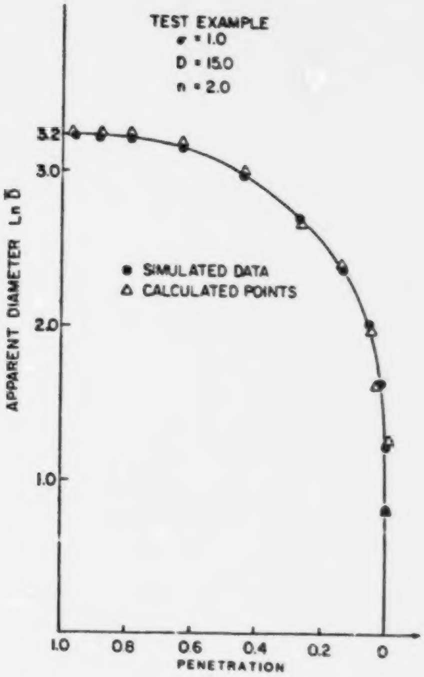

Figure 1. Test example.

The values of the parameters of a log normal distribution with an asymptotic limit of $\mathrm{Ln}\bar{D} = 3.2$ and an integral of 2.7 is $\sigma_1 = 1.0$ and $D_1 = 15$. With these parameters, simulated values for the experimental flow rates are determined. These points are shown by the triangles Δ. Since the triangles and circles fall on a common curve, one can conclude that the experimental measurements are consistent with an assumed log normal distribution ($\sigma_1 = 1.0$; $D_1 = 15$) and the use of more complicated distributions is not justified.

In Figure 2, an example is presented of the method on bimodal distributions chosen so that $C_1 = 0.9$ and $C_2 = 0.1$. The distributions are chosen to yield the same intercept and integral. In this case, one obtains observable differences in that the LnD vs. penetration curves only if the curves are separated. The significance lies in that one would not be able to distinguish by this method alone between bimodal distributions with peaks lying close together. Probably the only feasible approach is by independent measurements of moments (i.e. volume or mass distributions as well as number distributions.) In short, the use of the apparent diameter does yield all the available information in the distribution, but it does not increase the precision of the analysis. Its advantages lie in that the parameters generated by the method are non-ambiguous and that it incorporates trends in the data in an efficient manner.

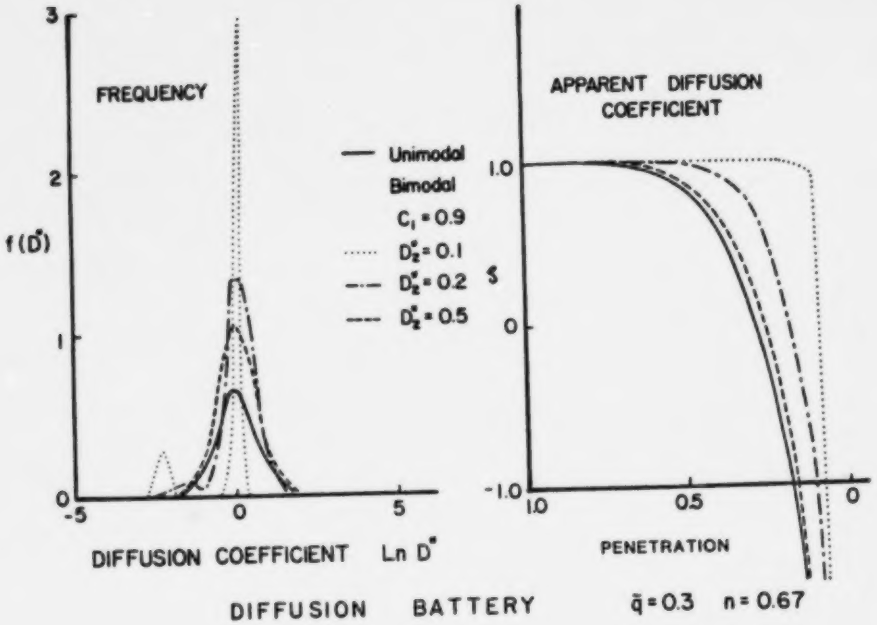

Figure 2. Application of bimodal distribution.

ACKNOWLEDGEMENT

All the authors wish to acknowledge the financial support of the State of Maryland Department of Natural Resources under Grant # P 678004.

REFERENCES

1. Nyström, E.J. Über die Praktische Auflösung von Integralgleichungen mit Anwendungen auf Randwertaufgaben. Acta Math. 54:185-204, 1930.

2. Park, Y.O., W.E. King, J.W. Gentry. On the Inversion of Penetration Measurements to Determine Aerosol Product Size Distributions. Ind. Eng. Chem. Prod. Res. Dev. 19, 2:151-157, 1980.

3. Megaw, W.J., and R.D. Wiffin. Measurement of the Diffusion Coefficient of Homogeneous and Other Nuclei. J. Rech. Atmos. 1:113, 1963.

4. Nolan, P.J., and J.A. Scott. Observations on the Heterogeneity of Condensation Nuclei. Proc. Royal Irish Acad. 63A:35, 1963.

5. Yu, P.Y., J. San, J.W. Gentry. Application of the "Apparent Diameter" Method for Inversion of Penetration Methods: Fibers and Isometric Particles. International Symposium on Aerosols in the Mining and Industrial Work Environment. Minneapolis, Minnesota, November, 1981.

6. Pollak, L.W., and A.L. Metniecks. On the Determination of the Diffusion Coefficient of Heterogeneous Aerosols by the Dynamic Method. Geofis. Pura Appl. 37:183-190, 1957.

The work described in this paper was not funded by the U.S. Environmental Protection Agency. The contents do not necessarily reflect the views of the Agency and no official endorsement should be inferred.

Paper 15

RECENT ACTIVITIES OF THE NATIONAL BUREAU OF STANDARDS AND THE AMERICAN SOCIETY FOR TESTING AND MATERIALS IN DEVELOPING PARTICULATE STANDARD REFERENCE MATERIALS

R. Keith Kirby
U.S. Department of Commerce
National Bureau of Standards

ABSTRACT

Four years ago an ASTM Coordinating Committee (S-21) was formed for the purpose of obtaining the cooperation of industry to assist NBS in the certification of Standard Reference Materials (SRM's) for particle size metrology. These SRM's will probably include monosize particles and distributed size particles. In general, these SRM's will be used to calibrate particle sizing equipment, but they will also provide for traceability in the marketplace and can be used to develop accurate secondary reference materials. The progress that has occurred to date in this activity and the NBS SRM program will be discussed.

INTRODUCTION

The Standard Reference Material (SRM) Program at the National Bureau of Standards (NBS) celebrated its 75th year this year. During most of these years the emphasis has been on metallic compositional reference materials. During the last 10 years, however, there has been a large increase in requests for SRM's in clinical chemistry, environmental analysis and nuclear materials as well as in physical science and in engineering. An SRM is a material or device for which a chemical or physical property has been certified by NBS. SRM's are primary reference materials that can be used to calibrate measurement systems, to evaluate measurement methods, and to provide traceability to the basic units of measurement. By making SRM's available to commerce, NBS provides a "third party role" in the specification and verification of products. In general, measurements leading to certification are made at NBS in such a way that an accurate value (the present best estimate of the true value and its uncertainty) for the property is obtained. When measurement techniques are not available at NBS, certification is still possible by using networks of cooperating qualified laboratories.

PRESENT SRM'S

At this time NBS has only a few SRM's for particle metrology. These include glass spheres with size distributions in the range 35 to 120 μm (SRM 1004), 100 to 310 μm (SRM 1017a), and 225 to 780 μm (SRM 1018a). These three SRM's are for calibrating sieves. A cement standard (SRM 114m) can be used to check the sieve size and Blaine and Wagner measures of surface area. An SEM magnification standard (SRM 484b) and a linewidth standard for optical microscopes (SRM 474) are also available. The SEM standard is made by electroplating alternate layers of nickel and gold. The ∿0.06 μm layers of gold are spaced at varying distances apart (1,2,3,5, and 50 μm) by the nickel and when viewed edge on with an SEM appear as bright lines. If properly etched, this standard can also be used with an optical microscope as a stage micrometer. The linewidth standard is made with photomask techniques and linewidths, spacings between lines, and midline separations are certified from 1 to 12 μm. This SRM is only certified for use in calibrating optical microscopes to measure linewidths on anti-reflectance chromium photoplates and is not readily available as the certification is very painstaking. Some work in progress at NBS will result in new SRM's for counting asbestos fibers, for inhalable alpha quartz, and for a submicrometer powder for measurement of size using x-ray diffraction.

RESEARCH ASSOCIATE PROGRAM

In responding to requests for new types of SRM's, NBS must try to finance their production while maintaining the continuity of supply of existing SRM's with an essentially constant amount of funding. (Each year the Office of Standard Reference Materials uses the income generated by sales in the previous year to support these production activities.) To help produce those SRM's that are needed by an industry, NBS has sought their help in producing them. The NBS Research Associate Program can be used for this purpose. This program enables an expert from industry to work at NBS on projects of mutual interest to the sponsor and NBS. Except for the use of laboratories and clerical help at NBS, the sponsor financially supports the Research Associate (RA).

Such a program was started in 1976 through the American Society for Testing and Materials (ASTM) Coordinating Committee S-17 for the production of metal, alloy and metal bearing ore SRM's. Funds obtained from industry provide ASTM the capital to support the RA who works with this committee, industry, and NBS to produce these SRM's. During these five years the program has been an outstanding success in that over 75 SRM's have been certified and are now on sale. In this effort there has been a tremendous amount of industrial cooperation which has ranged from the initial monetary donations, to the donation of materials, and to extensive laboratory analyses. As a consequence, NBS has been able to certify many more reference materials than its limited resources alone would have produced and industry has obtained the SRM's that were needed.

ASTM COORDINATING COMMITTEE

Four years ago a workshop was held at NBS to evaluate the feasibility of establishing a program in fine particles similar to that in metals. The result is that a new ASTM Coordinating Committee (S-21) was organized and has started work. The progress in S-21 has been slow, however, because of the diverse nature of the industries involved. Basic membership of S-21 includes representatives from sixteen technical committees as shown in Table 1. The interest of these members run from metal and inorganic powders, to pigments and toners, to air and water-borne particulates and wear particles, and to foods and drugs. Strong support in the Committee also comes from the manufacturers of measuring instruments.

Table 1

VOTING AND EX-OFFICIO MEMBERS OF S-21

B-09	Metal Powders and Metal Powder Products
C-01	Cement
C-05	Manufactured Carbon and Graphite Products
C-09	Concrete and Concrete Aggregates
C-21	Ceramic Whitewares and Related Products
D-01	Paint and Related Coatings and Materials
D-18	Soil and Rock for Engineering Purposes
D-22	Sampling and Analysis of Atmospheres
D-32	Catalysts
E-29	Particle Size Measurement
E-34	Occupational Health and Safety
F-01	Electronics
F-05	Business Copy Products
F-07	Aerospace Industry Methods
F-21	Filtration
G-02	Erosion and Wear
Duke Scientific	
Eastman Kodak	
Pennwalt Corp	
Portland Cement Association	
Pratt and Whitney Aircraft Corp	
Rush/Presbyterian Medical School	
Travenol Laboratories	

The current chairman of S-21 is David W. Johnson from Bell Laboratories who has supplied a very strong and dedicated leadership. The scope of S-21, like that of S-17, is direct and limited. It allows the Committee to solicit funds to support the RA, to determine the needs of industry, to select candidate SRM materials in the area of particle metrology, and to set priorities for their preparation and certification. The program has received enough funds to run three years starting this Fall. In accomplishing its goals the Committee will support and direct the activities of the RA who in turn will work with the Committee, industry, and the NBS Technical Divisions. Russell Obbink, who has recently retired from the Aluminum Company of America, has been hired by ASTM as the Research Associate.

Before S-21 can recommend that an SRM be produced by NBS through the RA Program, it must satisfactorily answer the following questions:

1) Can the uses for which this SRM are intended be satisfied by an existing primary reference material? In other words, does NBS or some other national authority have a certified reference material that will serve the purpose?

2) Is the material likely to be homogeneous and stable and can it be duplicated at some future time at reasonable cost?

3) Will the SRM have an impact on industrial and national needs and not just meet the needs of a limited interest group?

Suggestions for SRM's can be submitted directly to S-21 (or to NBS) but are best directed through any of its members. The meetings of S-21 are, of course, open to anyone who wishes to attend. ASTM Headquarters in Philadelphia can be contacted for the committee's schedule of meetings.

NBS ACTIVITIES

S-21 has set its priorities (indicated in Table 2) for the production of SRM's. The most important ones are the monosize spheres in the range 0.1 to 100 µm. Work leading to the certification of 1-µm spheres has already started at NBS under the direction of George Mullholland. This work, which is described in detail by Swyt and Lettieri[1], will use a unique electron microscope, a light scattering technique, and electrical sensing particle counters.

Table 2

PROPOSED FINE PARTICLE SRM's

Monosized Polymer Spheres
    0.1, 0.3, 1, 10, 30, 100 µm
Distributed Nonspherical Garnet or Quartz Powders
    0.7 to 7, 8 to 30, 20 to 75 µm
Surface Area
    10 and 150 m^2/g

The material that has been obtained has an average diameter of about 0.91 µmm and will be available as a 0.5 percent suspension in water. Preliminary measurements indicate that the deviation of the particles from sphericity is less than one percent and that the distribution of sizes has a standard deviation of less than 0.01 µm.

The polystyrene spheres will first be examined for sphericity and the presence of debris by using a conventional SEM A unique electron microscope that has a stationary electron beam and a special scanning stage, will then be used to measure the diameters of about a hundred spheres along a single axis. The scanning stage is a variation of a "spring hinge" that is moved by a piezo-electric transducer and has micropositioning capability. The movement of the stage is measured with an interferometer so that the diameter of a single sphere can be determined with an accuracy of about 0.01 µm. This method is, of course, very tedious and exposes the polystyrene particles to high vacuum and to electron irradiation.

The light scattering technique using a 5-mW HeNe will be used to determine the average diameter of the population as suspended in water. The variation of intensity of the scattered light will be detected by a photomultiplier as it is rotated through nearly 300 degrees. The intensity pattern that is obtained will be analyzed to provide the mean particle size based on independent measurements of size distribution and index of refraction.

The size distribution, especially concerning the presence of outliers and agglomerates, will be obtained through the combined efforts of NBS and cooperating laboratories using different types of flow through counters and microscopic techniques. It is hoped that these measurements will be completed by Spring of 1982 and that the SRM will be available for sale later that year. Work will also be started on 10-µm spheres using essentially the same measurement techniques.

SUMMARY

In summary, work has started on the development of particulate SRM's by the cooperative effort of NBS and industry acting through ASTM. The first SRM to be certified in this effort will be a narrow distribution of polystyrene spheres that has an average diameter of about 0.91 µm.

REFERENCES

1. D. A. Swyt and T. R. Lettieri, Techniques for the Dimensional Calibration of Standard Microscopic Particles, Proceedings of the 1980 Fine Particle Society Fall Meeting (in press).

Paper 16

RECENT DEVELOPMENTS IN THE APPLICATION OF FINITE DIFFERENCE SOLUTIONS TO THE STUDY OF FLOW FIELDS AND PARTICLE TRAJECTORIES

V. A Marple and D. J. Rader
Particle Technology Laboratory
University of Minnesota

ABSTRACT

The finite difference numerical solution of the fluid mechanics Navier-Stokes equation in two dimensions has been useful in understanding the flow fields of aerosol systems such as inertial impactors and inlets. Upon solving for the flow field, particle trajectories can be numerically calculated to provide information on collection or sampling efficiencies. This procedure is now being expanded to three dimensions so that such devices as cyclones or inlets in a cross-wind can be studied.

For two dimensional analysis, the value of the stream function and the vorticity are calculated at a set of grid node points. However, for three dimensional analysis, the value of the pressure is determined at the grid node points but the velocity vector components are calculated at control volume interfaces between the grid node points. Thus, the three dimensional procedure is somewhat more complicated than that for the two dimensions.

In this paper the equations to be solved will be presented and the general solution procedure described. In addition, preliminary results of calculations using the technique will be presented.

INTRODUCTION

The numerical finite difference solution of the Navier-Stokes equations and the subsequent numerical solution of the particle trajectories has been useful in studying several aerosol systems such as inertial impactors [1,2], filter fibers[3] and virtual impactors[4]. However, the stream function technique employed in these studies is generally limited to two dimensional analysis. Thus, the three dimensional flow occuring in a cyclone or near an inlet in cross flow cannot be analyzed by this particular technique.

Since many important aerosol systems are three dimensional in nature, a general numerical solution technique is being developed by which the three dimensional Navier-Stokes equations can be solved. The present formulation is based on methods described by Patankar[5] for the solution of a general class of differential equations to which the Navier-Stokes equations belong. The Patankar method is used to calculate the variation of a conserved quantity in time and space under the combined effects of convection, diffusion and local sources or sinks. Although the technique is applicable to rectangular, cylindrical and spherical coordinate systems, the work reported here is being presented in cylindrical coordinates so it can be directly applied to the study of cyclones, a device commonly used in aerosol studies.

GENERAL CONSERVATION EQUATIONS

Since the Navier-Stokes equations are a special case of the general conservation equation, it is informative to first discuss the general equation. For the conservation of any specific quantity, $\phi(\underset{\sim}{r},t)$ expressed on a unit mass basis, Equation 1 can be written:

$$\frac{\partial}{\partial t}(\rho\phi) + \nabla\cdot(\rho\underset{\sim}{u}\phi) = \nabla\cdot(\Gamma_\phi\nabla\phi) + S_\phi \tag{1}$$

where: t = time

ρ = fluid density

$\underset{\sim}{u}$ = fluid velocity vector

$\Gamma\phi$ = diffusion coefficient for ϕ

S_ϕ = source term for ϕ.

Physically, Equation 1 represents the conservation per unit volume of a specific quantity, ϕ, within an infinitesimally small control volume about $\underset{\sim}{r}$. Thus, the net rate of accumulation of ϕ within the control volume $(\partial/\partial t(\rho\phi))$ is determined by the convection $(\nabla\cdot(\rho\underset{\sim}{u}\phi)$ and diffusion $(\nabla\cdot\Gamma\phi\nabla\phi)$ of ϕ across control volume boundaries and by the generation (S_ϕ) of ϕ within the volume itself. Equation 1 can be simplied by introducing the local flux vector, $\underset{\sim}{J}$ of the quantity ϕ:

$$\underset{\sim}{J}_\phi = \rho\underset{\sim}{u}\phi - \Gamma_\phi\nabla\phi \tag{2}$$

into Equation 1 which then becomes

$$\frac{\partial}{\partial t}(\rho\phi) + \nabla\cdot\underset{\sim}{J}_\phi = S_\phi \tag{3}$$

Note that the fluid continuity equation, a special case of Equation 3, may be obtained by taking $\phi = 1$ and $S_\phi = 0$. Thus, Equation 1 simplifies to:

$$\frac{\partial\rho}{\partial t} + \nabla\cdot(\rho\underset{\sim}{u}) = 0 \tag{4}$$

In general, a numerical solution for a given ϕ will require the transformation of Equation 3 from a continuous differential equation to a discrete set of algebraic equations. The present method requires that the region of interest first be partitioned into a set of three-dimensional control volumes appropriate to the particular choice of ϕ and coordinate system. Equation 3 is then integrated over each control volume subject to certain assumptions discussed in detail by Patankar[5]. The integrations ultimately yield a system of n equations (one for each control volume) in n unknowns (the values of ϕ within each control volume), which is then solved by a convenient computational method.

In cylindrical coordinates, Equation 3 can be expressed as

$$\frac{\partial}{\partial t}(\rho\phi) + \frac{1}{r}\frac{\partial}{\partial r}(rJ_r) + \frac{1}{r}\frac{\partial J_\theta}{\partial \theta} + \frac{\partial J_z}{\partial z} = S_\phi \tag{5}$$

$$\begin{aligned} J_r &= \rho v_r \phi - \Gamma \frac{\partial \phi}{\partial r} \\ J_\theta &= \rho v_\theta \phi - \Gamma \frac{1}{r}\frac{\partial \phi}{\partial \theta} \\ J_z &= \rho v_z \phi - \Gamma \frac{\partial \phi}{\partial z} \end{aligned} \tag{6}$$

INTEGRATION OF CONSERVATION EQUATIONS

A typical control volume appropriate for cylindrical coordinates is shown as the shaded section in Figure 1. This is a control volume about some arbitrary grid point P. The adjacent grid points in the r, θ, and z directions are N and S, E and W, and T and B, respectively. The boundary areas of the control volume are denoted by the dashed lines and labeled as n, s, e, w, t, and b. Although the grid lines do not have to be equally spaced, the grid lines and control volume surfaces are spaced so that the grid lines are midway between the control volume surfaces (i.e. P is midway between the w and e, s and n, and t and b surfaces).

By integrating Equation 5 over the control volume in Figure 1 and time, τ, the following integral equation is obtained:

$$\begin{aligned} &\int_w^e \int_s^n \int_b^t \int_\tau^{\tau+\Delta\tau} r \frac{\partial}{\partial t}(\rho\phi)\, dt\,dz\,dr\,d\theta + \int_\tau^{\tau+\Delta\tau} \int_s^n \int_b^t \int_w^e \frac{\partial J_\theta}{\partial \theta}\, d\theta\,dz\,dr\,dt \\ &+ \int_\tau^{\tau+\Delta\tau} \int_b^t \int_w^e \int_s^n \frac{\partial}{\partial r}(rJ_r)\, dr\,d\theta\,dz\,dt \quad \int_\tau^{\tau+\Delta\tau} \int_w^e \int_s^n \int_b^t r \frac{\partial J_z}{\partial z}\, dz\,dr\,d\theta\,dt \\ &= \int_\tau^{\tau+\Delta\tau} \int_w^e \int_s^n \int_b^t rS_\phi\, dz\,dr\,d\theta\,dt \end{aligned} \tag{7}$$

For the unsteady term, ϕ is assumed constant and equal to its center point value throughout the control volume at each instant of time. The variation with time of the remaining terms is handled by assuming that the values at the end of the

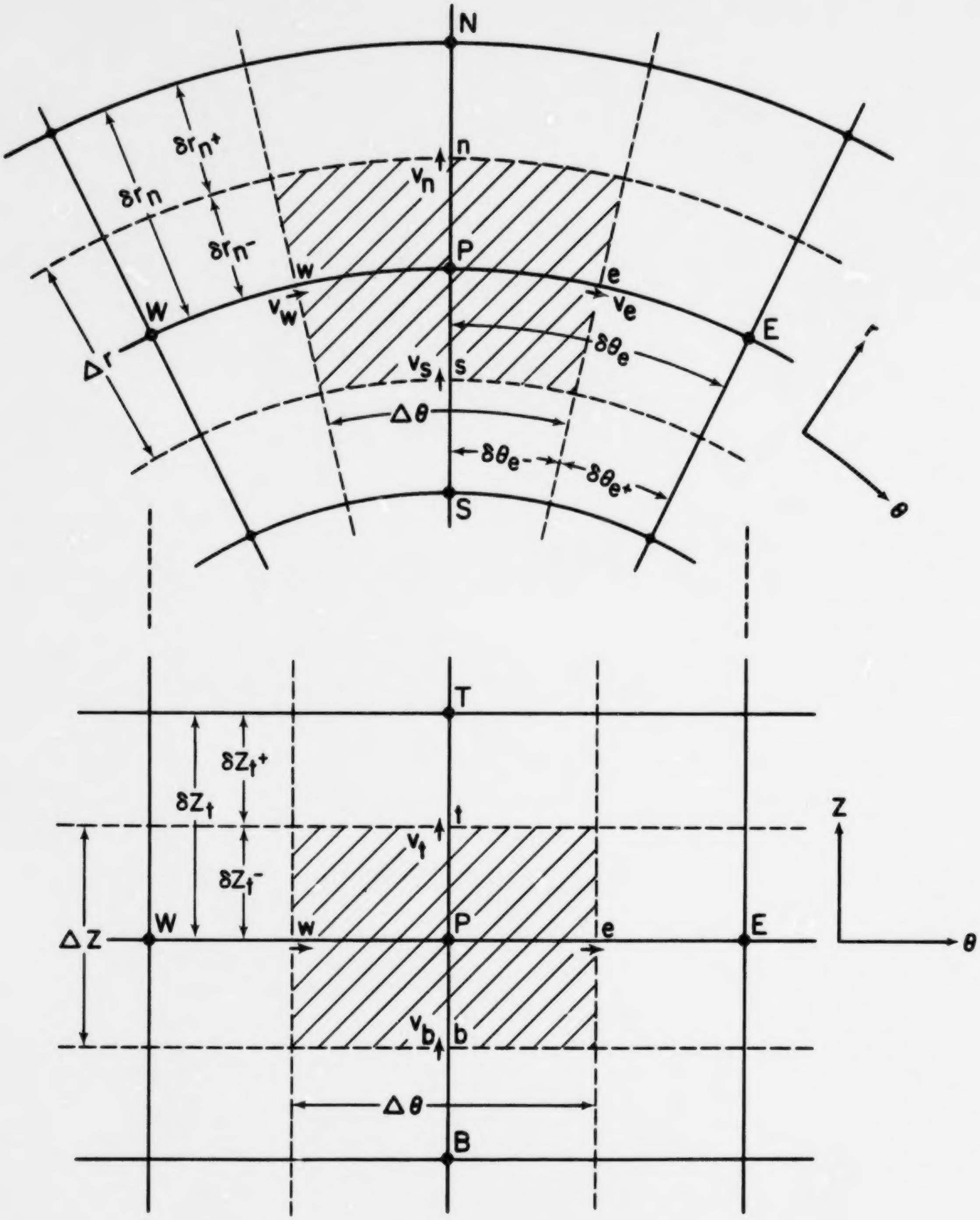
N
n
v_n
δr_{n^+}
δr_n
δr_{n^-}
P
w
e
W
E
v_w
v_e
Δr
$\delta \theta_e$
v_s
s
$\Delta \theta$
$\delta \theta_{e^-}$
$\delta \theta_{e^+}$
S
r
θ
T
δZ_{t^+}
δZ_t
t
v_t
δZ_{t^-}
Z
ΔZ
W
w
P
e
E
θ
v_b
b
$\Delta \theta$
B

Figure 1. Control volume for typical point P.

time step had prevailed from the start. This is the fully implicit method described by Patankar[5]. With these assumptions the integrals in Equation 7 may be evaluated to yield the following discretized equation:

$$[(\rho\phi)_p - (\rho\phi)^\circ_p]\,\frac{r_n + r_s}{2}\,\frac{\Delta r\Delta\theta\Delta z}{\Delta t} + (J_e - J_w)\,\Delta z\Delta r + (r_nJ_n - r_sJ_s)\Delta\theta\Delta z$$

$$+ (J_t - J_s)\,\frac{r_n + r_s}{2}\,\Delta r\Delta\theta = (S_c + S_p\phi_p)\,\frac{r_n + r_s}{2}\,\Delta r\Delta\theta\Delta z \tag{8}$$

where $\Delta r = r_n - r_s$

$\Delta\theta = \theta_e - \theta_w$

$\Delta z = z_t - z_b$

$(\rho\phi)_p - (\rho\phi)^\circ_p$ = change in $\rho\phi$ over time period $\Delta\tau$.

The continuity equation is again a special case of Equation 8 with $\phi = 1$ and $S_\phi = 0$. Thus, the continuity equation is:

$$(\rho^\circ_p - \rho^\circ_p)\,\frac{r_n + r_s}{2}\,\frac{\Delta r\Delta\theta\Delta z}{\Delta t} + (F_e - F_w)\Delta z\Delta r + (r_nF_n - r_sF_s)\,\Delta\theta\Delta z$$

$$+ (F_t - F_b)\,\frac{r_n + r_s}{2}\,\Delta r\Delta\theta = 0 \tag{9}$$

where $F_e = (\rho v_\theta)_e$ $F_w = (\rho v_\theta)_w$ $F_n = (\rho v_r)_n$ $F_s = (\rho v_r)_s$ $F_t = (\rho v_z)_t$

$F_b = (\rho v_z)_b$

By multiplying Equation 9 by ϕ_p and subtracting the product from Equation 8, the general discretization equation is:

$$(\phi_p - \phi^\circ_p)\,\frac{\rho^\circ_p}{\Delta t}\,\frac{r_n + r_s}{2}\,\Delta r\Delta\theta\Delta z + [(J_e - \phi_pF_e) - (J_w - \phi_pF_w)]\,\Delta z\Delta r$$

$$+ [r_n(J_n - \phi_pF_n) - r_s(J_s - \phi_pF_s)]\,\Delta\theta\Delta z + [(J_t - \phi_pF_t) - (J_b - \phi_pF_b)]\,\frac{r_n + r_s}{2}\,\Delta r\Delta\theta$$

$$= (S_c + S_p\phi_p)\,\frac{r_s + r_n}{2}\,\Delta r\Delta\theta\Delta z \tag{10}$$

Before Equation 10 can be simplified further, the terms such as ($J_i - F_i \phi_P$) where i = e, w, etc. must be discussed. For example, $J_e - \phi_P F_e$ is to be evaluated at position e in Figure 1 in terms of values at the grid points P and E. A power law technique described in detail by Patankar[5] will be used here. By using this technique a typical term $J_e - F_e \phi_P$ can be expressed as:

$$J_e - F_e \phi_P = D_e A_e (\phi_P - \phi_E) \qquad (11)$$

where $De = \Gamma e/\delta x_e$

δx_e = distance between grid points P and E

$A_e = A(|P_e|) + [-P_e, 0]$

$A(|P_e|) = [0, (1 - 0.1|P_e|)^5]$

$Pe = \left(\frac{\rho u \delta x}{\Gamma_\phi}\right)_e$ = Peclet number at e

[a, b] = Maximum of a or b.

In addition, the harmonic mean is used for Γ such that D_e is expresed as follows,

$$D_e = \frac{\Gamma_P \Gamma_E}{r_P \delta\theta_{e^-} \Gamma_E + r_P \delta\theta_{e^+} \Gamma_P}$$

A typical term $J_w - F_w \phi_P$ is expressed as

$$J_w - F_w \phi_P = D_w B_w (\phi_W - \phi_P) \qquad (12)$$

where $B_w = A(|P_w|) + [P_w, 0]$ and A, P, and D are expressed as in Equation 11.

Equation 10 can now be rewritten as:

$$a_P \phi_P = a_E \phi_E + a_W \phi_W + a_N \phi_N + a_S \phi_S + a_T \phi_T + a_B \phi_B + b$$

$$a_E = (D_e A(|P_e|) + [-F_e, 0])\, \Delta z \Delta r \quad D_e = \frac{\Gamma_e}{r_p \delta\theta_e};\ F_e = (\rho v_\theta)_e;\ P_e = \frac{F_e}{D_e}$$

$$a_W = (D_w A(|P_w|) + [F_w, 0])\, \Delta z \Delta r \quad D_w = \frac{\Gamma_w}{r_p \delta\theta_w};\ F_w = (\rho v_\theta)_w;\ P_w = \frac{F_w}{D_w}$$

$$a_N = (D_n A(|P_n|) + [-F_n, 0])\, r_n \Delta\theta \Delta z \quad D_n = \frac{\Gamma_n}{\delta r_n};\ F_n = (\rho v_r)_n;\ P_n = \frac{F_n}{D_n}$$

$$a_S = (D_s A(|P_s|) + [F_s,\ 0])\, r_s \Delta\theta\Delta z \quad D_s = \frac{\Gamma_s}{\delta r_s};\ F_s = (\rho v_r)_s;\ P_s = \frac{F_s}{D_s}$$

$$a_T = (D_t A(|P_t|) + [-F_t,\ 0])\, \frac{r_n + r_s}{2}\, \Delta r\Delta\theta \quad D_t = \frac{\Gamma_t}{\delta z_t};\ F_t = (\rho v_z)_t;\ P_t = \frac{F_t}{D_t}$$

$$a_B = (D_b A(|P_b|) + [F_b, 0])\, \frac{r_n + r_s}{2}\, \Delta r\Delta\theta \quad D_b = \frac{\Gamma_b}{\delta z_b};\ F_b = (\rho v_z)_b;\ P_b = \frac{F_b}{D_b}$$

$$a_P = a_E + a_W + a_N + a_S + a_T + a_B + \left(\frac{\rho_P^\circ}{\Delta_T} - S_P\right) \frac{r_n + r_s}{2}\, \Delta r\Delta\theta\Delta z$$

$$b = (S_C + \phi_P^\circ \frac{\rho_P^\circ}{\Delta T})\, \frac{r_n + r_s}{2}\, \Delta r\Delta\theta\Delta z \qquad (13)$$

As desired, Equation 13 represents a set of algebraic equations relating the value of ϕ_P to each of its neighbors (ϕ_E, ϕ_W, etc.). There will be one equation such as 13 for each of the control volumes in the calculation field. If there are n control volumes, the problem has been reduced to the solution of n simultaneous equations in n unknowns.

MOMENTUM EQUATIONS

The Navier-Stokes equations of motion for an incompressible fluid with constant viscosity are a statement of momentum conservation in three orthogonal directions: r, θ and z in the cylindrical coordinate system. As a special case of the general conservation equation, the momentum equations may be solved using the method outlined above, in which ϕ is repaced by the appropriate momentum per unit mass: v_r, v_θ and v_z. Note that Γ becomes the fluid viscosity in this case and that the source terms (S_ϕ) are defined so as to include the pressure gradient and additional terms resulting from the choice of a curvilinear coordinate system (e.g. centripetal accelerations).

However, some special considerations are required when ϕ is replaced by a velocity in Equation 10. First, the solution of Equation 10 requires that the flow field be known, since quantities such as $Fe = (\rho v_\theta)e$ need to be calculated. This difficulty is handled by iteration - at each step the previous flow field is used as a guess, and then updated once the new velocities are calculated. Since the solution of each momentum equation requires a complete flow field, the three equations are solved together by a systematic iteration technique.

A second difficulty involves determining the pressure field, since no obvious "pressure equation" is available. The present method employs a modified form of the continuity equation and the flow field of the most recent iteration to arrive at a correction for the pressure at each grid point. Velocities are also corrected at this point so that, after each iteration, the resulting velocity field satisfies the continuity equation. The conservation of flow obtained at the end of each iterative step in the calculation is physically appealing, and helps insure convergence.

Finally, to exclude certain physically unrealistic solutions, it is desirable to shift the location at which the velocities are calculated. Thus, the values of density and pressure are stored at the main grid points as shown in Figure 1, while v_r, v_θ and v_z are stored at staggered locations as shown in Figures 2, 3 and 4. Staggering the grid implies that the control volumes associated with each variable are also shifted, as indicated by the shaded regions in Figures 1-4. This method entails the storage of additional geometric quantities - lengths, areas and volumes for each particular control volume set - and requires that certain interpolations be performed. Otherwise, the derivations above are quite valid provided that the integration of Equation 7 is made over the correct control volume.

The above discussion briefly outlines the technique employed to calculate the fluid flow field. The system of four equations -three momentum and continuity - in four unknowns - v_r, v_θ, and v_z - is solved as a set by an iterative method. For complete details of this numerical method of flow analysis, the reader is referred to Patankar[5].

APPLICATION TO THREE DIMENSIONAL ANALYSIS

The methods described in the above section have been incorporated into a computer program. Most of the work to date has been in the solution of special two dimensional test problems to check the accuracy of various parts of the program. However, the program was applied to determining the flow field of a cyclone of simple design shown in Figure 5. The program can eventually be used to analyze cyclones with conical rather than flat bottoms, but the flat bottom case was chosen for the initial work because of its simplicity.

The grid used for analyzing this cyclone is shown in Figure 6. There are 11, 14, and 12, grid lines in the r, z, and θ directions, respectively.

Because of its spiral nature, the flow field is rather difficult to show in three dimensions. Thus, the resulting flow field is presented in several two dimensional plots of one pathline. In Figure 7, the plot of the pathline in the r-z coordinates shows the r-z position of the pathline as it swirls in an angular direction inside the cyclone. The pathline starts at some angular position θo indicated by "0" on Figure 7. For every 360° of angular rotation, a data point is indicated on the streakline with an adjacent number demoting the number of 360° rotations from the inlet. For example, the first rotation is from point "0" to "1", the second from "1" to "2", etc. For each 360° rotation there also is an r-θ plot of the pathline, shown in Figure 8.

It is interesting to note that in this cyclone the air flows downward to the bottom, then upward to the outside of the exit tube, then downward to the inlet of the exit tube, and finally upward and out the exit tube. It is expected that if the inlet area were wider and/or the exit tube larger, the air would only flow downward to the bottom and then upward out the exit tube.

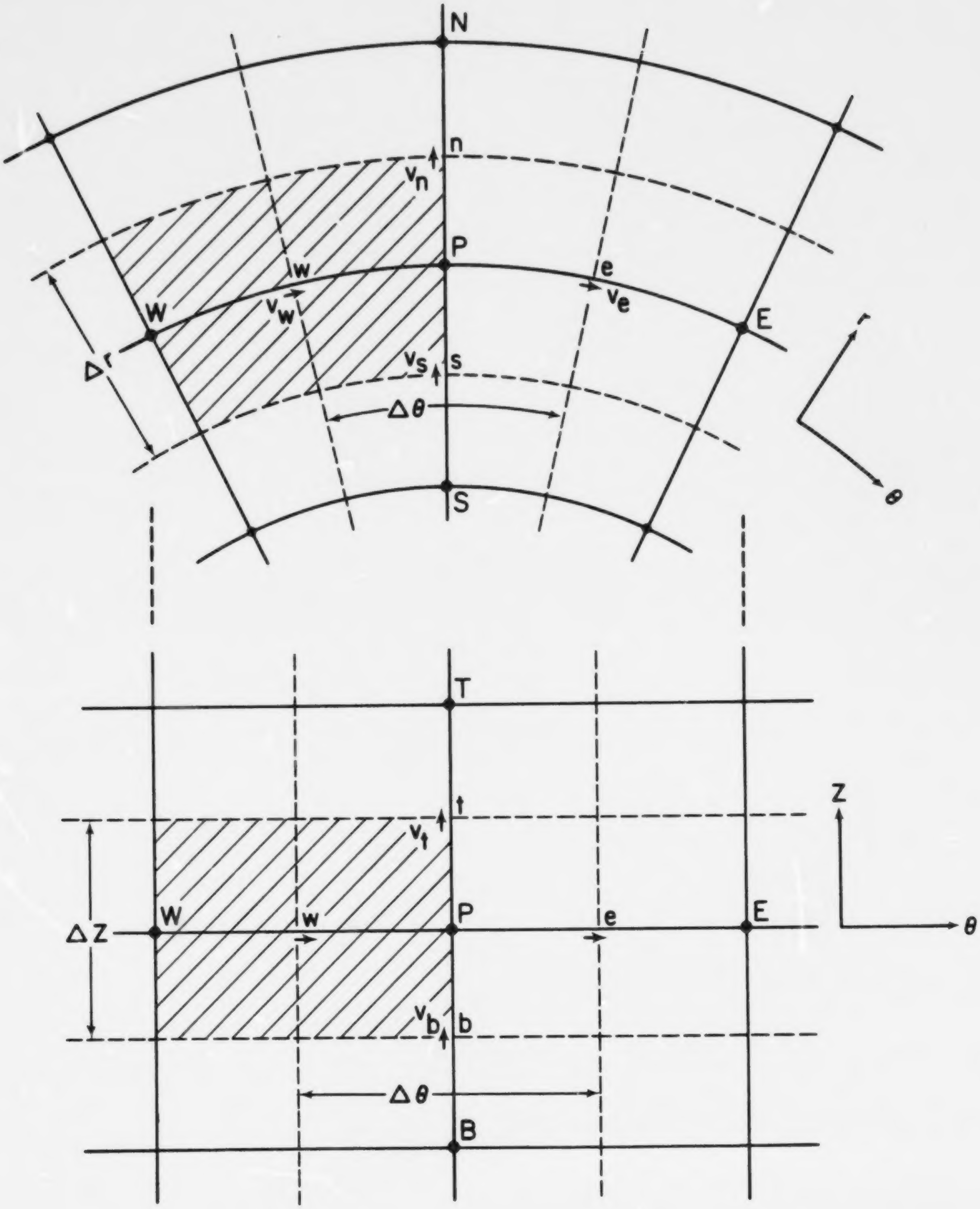
N
n
v_n
P
w
v_w
W
e
v_e
E
v_s
s
Δr
$\Delta\theta$
S
r
θ
T
t
v_t
Z
ΔZ
W
w
P
e
E
θ
v_b
b
$\Delta\theta$
B

Figure 2. Control volume for typical v_θ.

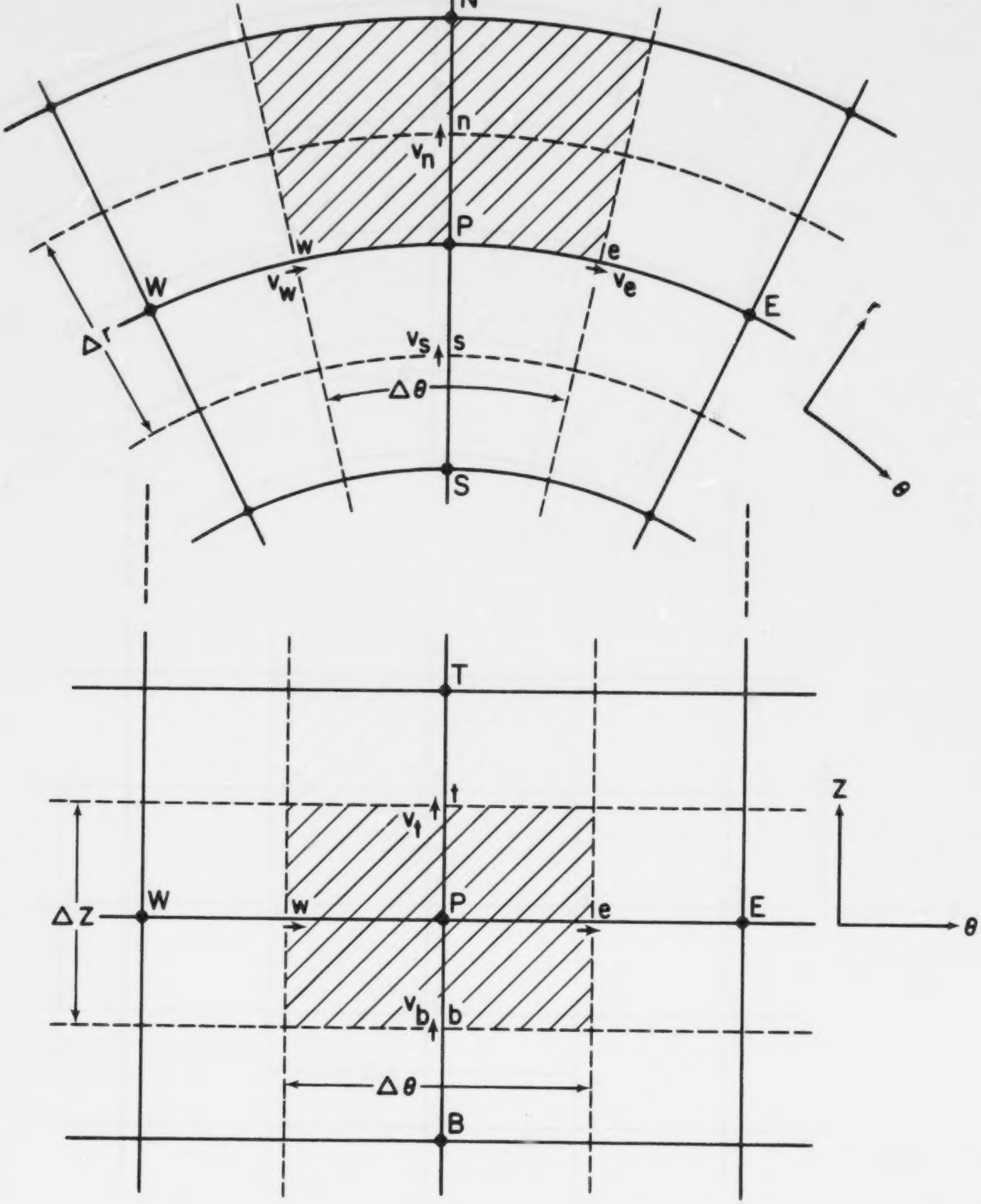
N
n
v_n
P
w
e
v_w
v_e
W
E
Δr
v_s
s
$\Delta\theta$
S
r
θ
T
t
v_t
Z
ΔZ
W
w
P
e
E
θ
v_b
b
$\Delta\theta$
B

Figure 3. Control volume for typical v_r.

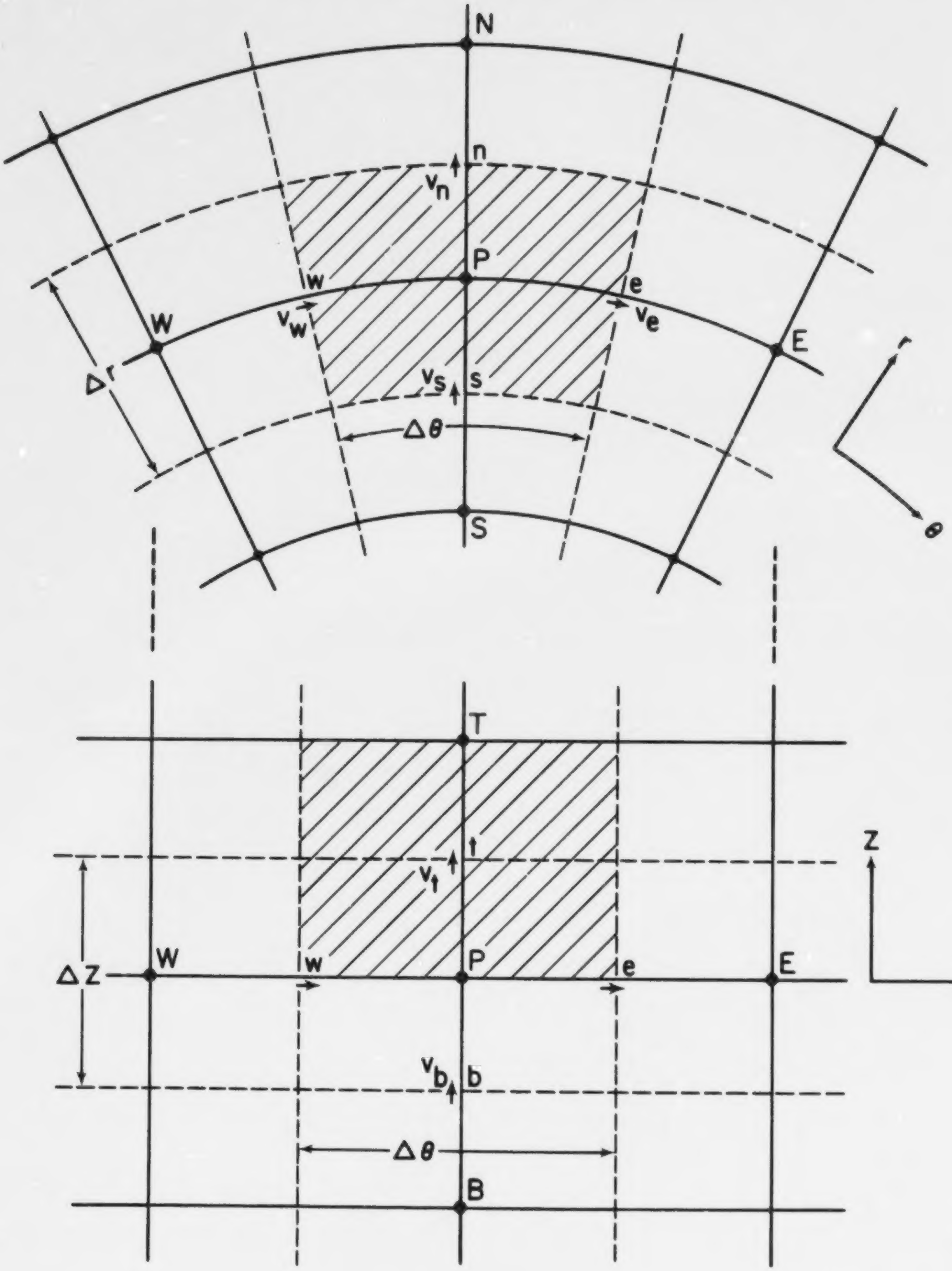
N
n
v_n
P
w
e
v_w
v_e
W
E
Δr
v_s
s
$\Delta\theta$
S
r
θ
T
v_t
t
Z
W
w
P
e
E
ΔZ
θ
v_b
b
$\Delta\theta$
B

Figure 4. Control volume for typical v_z.

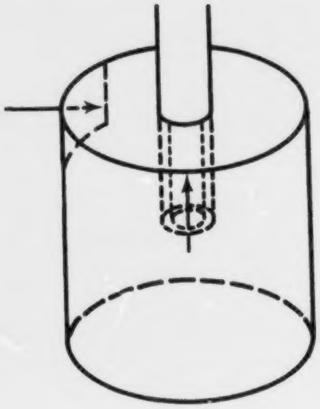

Figure 5. Schematic of cyclone used in initial calculations.

CONCLUSIONS

Using the above methods, a computer program has been written which solves the Navier-Stokes equations in three dimensional cylindrical coordinates. While still in the testing stages, the program has been applied to the solution of the flow field in a cyclone. Once the flow fields of such systems are known, particle trajectories may be calculated using an extension of methods developed by Marple[1]. At present, work on a three dimensional particle trajectory program is continuing.

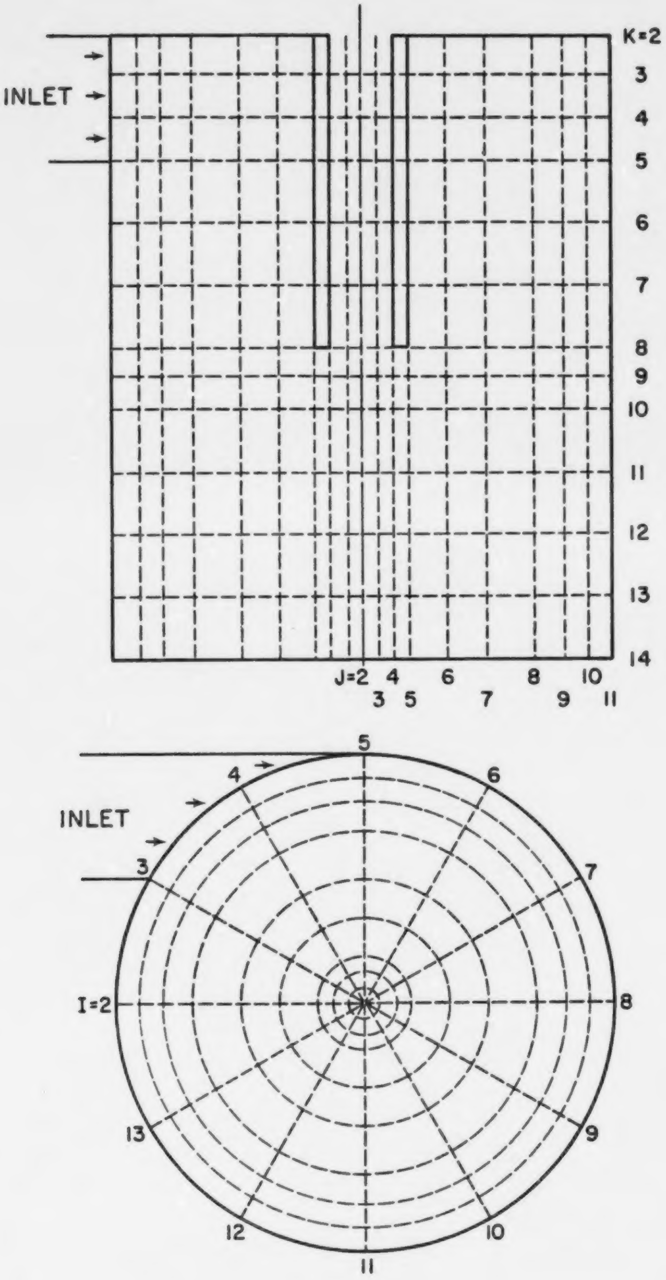
INLET
K=2
3
4
5
6
7
8
9
10
11
12
13
14
J=2
3
4
5
6
7
8
9
10
11
5
4
6
INLET
3
7
I=2
8
13
9
12
10
11

Figure 6. Arrangement of cyclone grid lines.

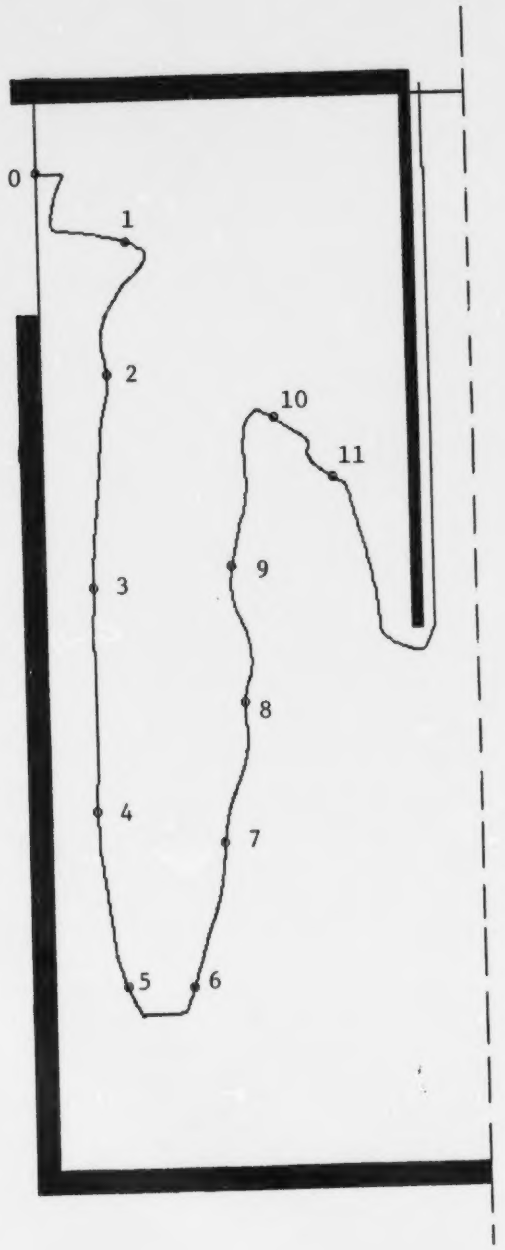
0
1
2
3
4
5
6
7
8
9
10
11

Figure 7. r-z pathline in cyclone.

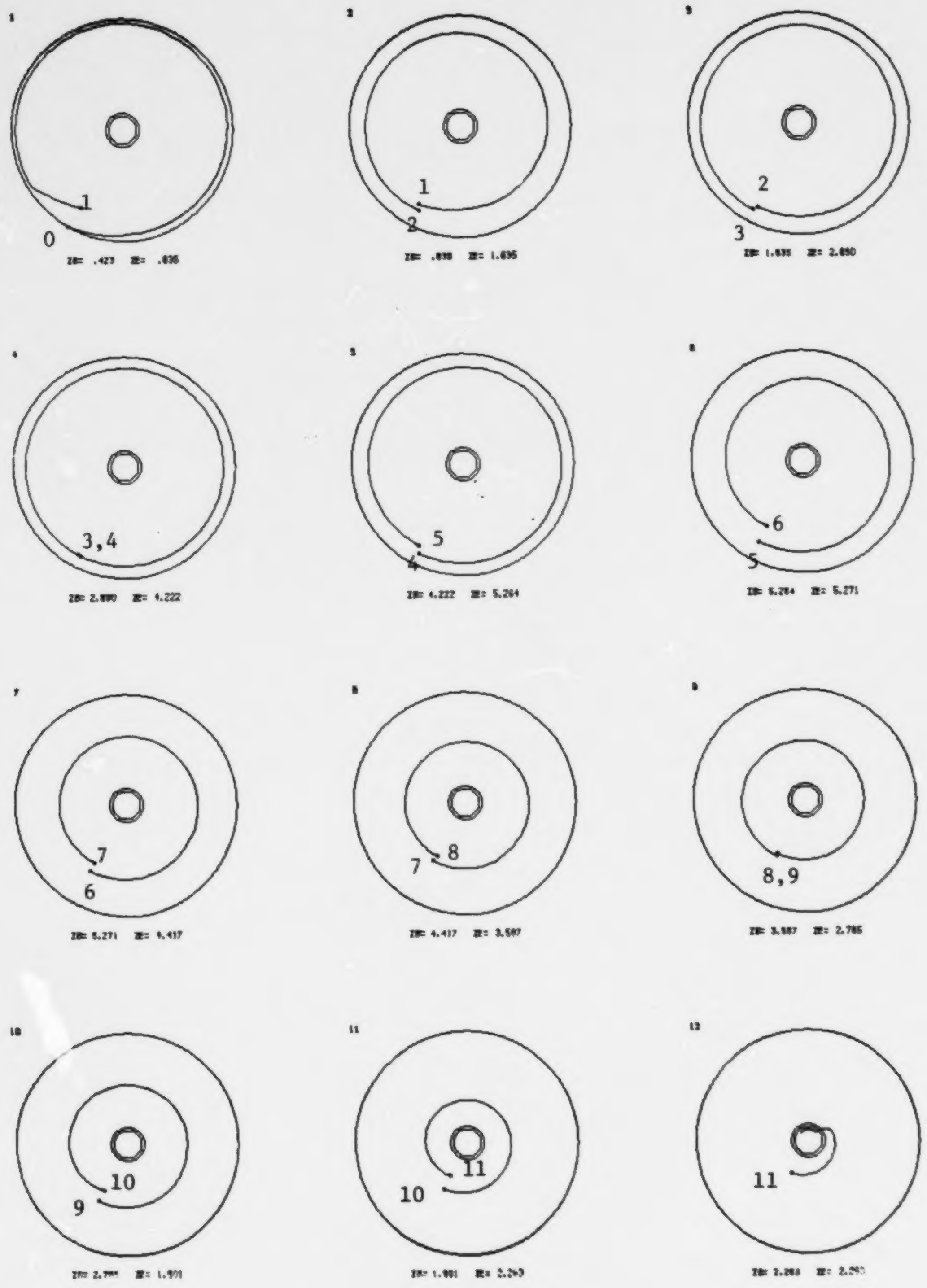

Figure 8. r-θ pathline in cyclone.

REFERENCES

1. Marple, V. A. "A Fundamental Study of Inertial Impactors", Ph.D. thesis, University of Minnesota, Minneapolis, Minnesota, 1970.

2. Schott, J. H. "Jet-cone Impactors as Aerosol Particle Separators", M.S. thesis, Chemical Engineering Department, University of Minnesota, Minneapolis, Minnesota, 1973.

3. Yeh, H. C. and B. Y. H. Liu "Aerosol Filtration by Fibrous Filters--Part I. Theoretical", J. Aerosol Sci. 5:191-204, 1973.

4. Marple, V. A. and C. M. Chien, "Virtual Impactors: A Theoretical Study", Environ. Sci. Technol. 14:976-985, 1980.

5. Patankar, Suhas V. Numerical Heat Transfer and Fluid Flow, McGraw-Hill Book Company, 1980.

The work described in this paper was not funded by the U.S. Environmental Protection Agency. The contents do not necessarily reflect the views of the Agency and no official endorsement should be inferred.

Paper 17

AN INDUSTRY RESPONSE TO MEETING ITS PARTICLE SIZING INFORMATION NEEDS

Timothy J. Abrott
Jerry E. Whyte
Weyerhaeuser Company

ABSTRACT

Industrial efforts to control process particulate emissions rely upon the ability to characterize both the existing emissions stream and the performance of potentially-applicable control technologies. In an effort to implement a sound technical approach and develop a generalized data base, an emphasis on particle size distribution and fractional collection efficiency evaluations is essential. Practical experience utilizing the cascade impactor particle sizing technique suggests numerous short-comings as commonly implemented.

The relevant particle sizing issues for industrial process emission and control technology characterizations have been identified. Proposed responses to each issue have been formulated. The program stresses identification of and solutions to weaknesses in industrial particle sizing technology. Evolution of a reasonable and defensible industrial particle sizing methodology is the goal of this program.

The program is being actively pursued. Problems being addressed include inherent cascade impactor hardware inefficiencies, sampling technique and sample analysis errors, and process-related sampling condition impacts. Extension and coalescence of each study into a particle sizing method relevant to industrial information needs will be discussed.

INTRODUCTION

Weyerhaeuser Company's interest in particle sizing is basic to all industry - good particle size data contributes to the achievement of particulate emission standards for the lowest cost. With emission control costs approaching 10% of the facility capital cost, and rising rapidly as regulations become more stringent, the importance of obtaining accurate/precise particle size data escalates. Poor particle size data may result in over-control, under-control or selection of the incorrect generic control device altogether, all of which carry serious economic penalties.

Our specific particle sizing information needs and how we are meeting them are the subject of the following discussion. Common particle sizing problems and research recommendations are detailed. The program represents a rational approach to the issue of quality assurance in industrial particle sizing.

PARTICLE SIZING DATA USES

Weyerhaeuser Company has an agressive R&D program to identify, develop and implement the most cost-effective solutions to its emissions problems. Benefits to the company result from avoiding control strategy failures, maintaining existing operations within compliance limits, increasing in-compliance process operation rates, and minimizing emission control costs. Accurate and precise particle size emissions data are essential to realize these overall benefits. The specific uses of particle size data in obtaining Weyerhaeuser Company's objective are reviewed below.

Particle size data are essential to this program for the generalization of a particulate emissions/control data base. All collection devices are characterized by a set of a performance curves of collection efficiency versus particle size. These are specific for particulate type and set of operating conditions. The definition of this set of curves will build a performance data base which may be reliably extrapolated from source to source. This technique applies to both the extrapolation of a pilot-scale device to full-scale and of an existing full-scale installation to a proposed future installation. An accurate performance comparison of competing technologies may also be made from an efficiency versus particle size data base.

While in many cases empirical performance data are adequate for routine control device specification, modeling to understand the active mechanisms behind collector efficiencies may provide additional valuable information. Definition of the most appropriate operating or design guidelines based on a mechanism model can lead to significant efficiency improvements. Major collection mechanisms perform as a function of particle size, thus attempts at control device model development must rely on particle size data.

As a prerequisite to the use of a generalized control technology performance data base, the ability to accurately measure end-of-pipe particle size distributions is required. The size distribution to be controlled may then be entered into the performance data base, and the most reasonable collection device selected. Additionally, collector outlet particle size data may be utilized to assess the performance of the existing control system. An unusual outlet size distribution will identify collection mechanism problems. Significant cost savings will result from identifying and fixing an existing unit in lieu of additional collector installation.

Recent Environmental Protection Agency (EPA) activities indicate development of a size-specific ambient particulate standard by the EPA. This would presumably regulate the source discharge of total thoracic particulate matter (TTP), especially in areas not achieving the TTP standard . However, based on the current state-of-the-art of particle sizing technology, it is questionable just how accurately this particle fraction may be measured. Should the regulations be approved, incorporation of a standard, defensible particle sizing technique would be required.

While emissions control is often considered a problem best addressed by end-of-pipe collector addition, significant opportunities have been identified for control through process operation modifications. Particle size distribution data may be used as an indicator of process efficiency, especially for combustion systems. The data provided can help tune the process mechanisms, often with attendant process efficiency benefits. The reduction in need for additional end-of-pipe emissions control can be significant. The required sampling upstream of the primary collector can, however, present some of the most significant problems associated with particle sizing.

PARTICLE SIZING PROBLEMS

The most common instrument used in fulfilling industrial particle sizing needs is the cascade impactor. This instrument offers the advantages of durability and relative ease of operation required for routine industrial sampling. The problems of particle sizing with the cascade impactor have been discussed by numerous authors[1-5], making cascade impactors the most studied and understood of any stack particle sizing device. However, the problems still have not been adequately resolved by the impactor manufacturers, regulatory agencies, or academic community. Based on practical experience, the short-comings of the cascade impactor sizing technique will be discussed below.

Cascade impactor sizing problems may be classified into three general groups: 1) inherent impactor inefficiencies, 2) sampling technique and sample analysis errors, and 3) process-related sampling impacts. Both equipment inefficiencies and technique and analysis errors may be encountered and addressed in the laboratory as well as the field. However, the process-related impacts, while manifesting themselves principally on the full-scale industrial process level, can be as significant and much harder to remedy.

The major inherent source of error in a cascade impactor is the result of "nonideal" configuration (nonperpendicular jet orientation, noncylindrical jets (round jet impactors), etc.) causing variability in distribution of effective jet velocities and orientations to the impaction surface. Nonideal flow patterns increase wall losses through wall impaction and settling. Impactor entry configuration to the first stage has been a very significant problem in some designs. While perhaps not easily overcome, the inherent inefficiencies are quantifiable for incorporation into data analysis methods.

Additional impactor sizing problems result from the sampling technique itself. Particle bounce and re-entrainment are significant problems as higher impaction jet velocities are used to separate the finer particles. Impaction substrate materials are often specific to a limited range of operating conditions. These ranges of conditions have not been well defined in some cases. Operation outside the temperature range for a grease substrate will lead to volatilization mass loss of the substrate (Figure 1). In low-loading situations the grease loss may overshadow the sample mass collected. (Figure 2).

Sample analysis and data interpretation are further areas of concern. Preparation and handling errors may be minimized in the laboratory, however field sampling seldom offers equivalent sample analysis conditions. A quantification of analysis errors is essential for each situation to

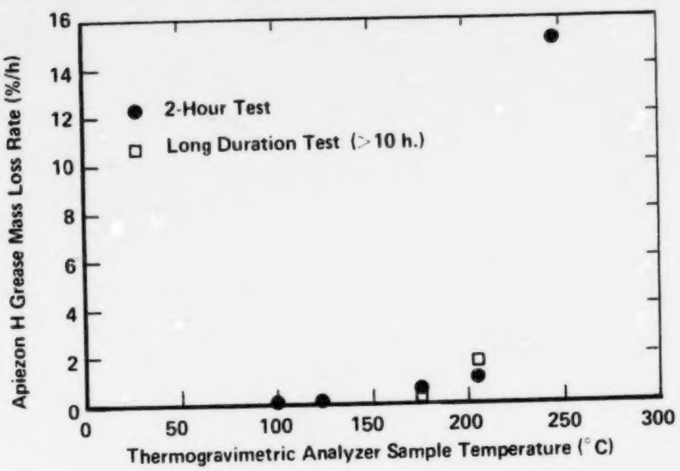

Figure 1

Curve of Apiezon H Grease Mass Loss Rate vs. Temperature for a Thermogravimetric Analyzer Sample. Initial Solvent Mass Loss from Application of 5% (Mass) Apiezon H Grease in Toluene Solution Eliminated from Mass Loss Rate Calculations.

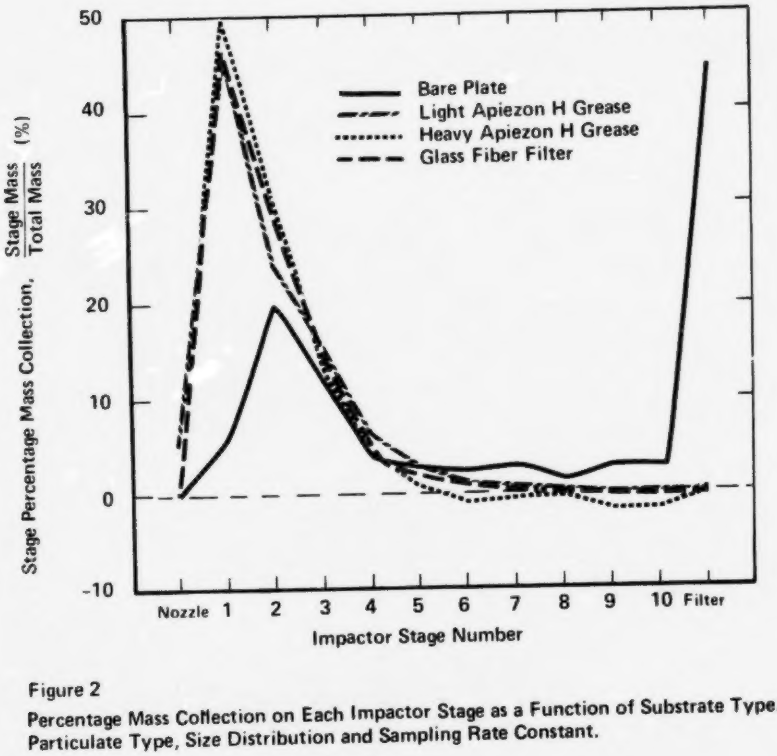

Figure 2

Percentage Mass Collection on Each Impactor Stage as a Function of Substrate Type. Particulate Type, Size Distribution and Sampling Rate Constant.

determine the significance of the data obtained. A standard data interpretation technique should be defined to incorporate sampling error analysis. Incorrect data interpretation can prove costly in an industrial emissions control device specification.

Process-related impacts on particle size measurements are perhaps the most difficult to overcome. Representative samples are difficult to obtain in an industrial process due to variations in particulate mass and size emissions, resulting from process variations, and particulate maldistributions at the sampling point. The maldistribution problem can perhaps be resolved by multiple samples; however, unless they can all be performed simultaneously, the effect of process variation will become significant. Use of multiple simultaneous samples is possible, but practically limited to a relatively small number of samples. The selection of sampling locations and assumed representative "equal areas" becomes significant, with no accepted rational means of selection.

The process variation and particulate maldistribution uncertainties discussed above are magnified at process outlet/primary collector inlet locations. High particulate loadings significantly reduce allowable sampling duration. Stage overloading, particle bounce and re-entrainment are the result of excessive sample collection. Because a significant large particle fraction may be found at this type of location, preseparation may be necessary to minimize overloading and bounce problems. In some cases an important portion of the particulate mass may be too large to enter the sampling nozzle and will thus remain unmeasured. While data from the stages themselves may still be analyzed, the absence of the large particle fraction must be considered.

Too little attention has been paid to sampling system configuration and its effect on the measured size distribution. While buttonhook nozzles are commonly used in industrial source sampling, seldom are the influences on the size distribution reaching the impactor taken into account. The particles caught in the nozzle are often those which the first few impactor stages were designed to collect. When the nozzle catch is assumed to represent particles which would have been caught on the top stage (the accepted procedure), a skewed particle size distribution results.

The problems outlined are significant. The benefits in resolution of these problems to provide the required data to optimize existing processes/control systems and to specify new control devices are also significant. Our particle sizing program discussed below is specific to our priority needs and is a step toward optimizing control technology implementation. While our program represents a start, a great deal more should be done. Because these problems are common to a great many organizations utilizing particle sizing data, the rationale for further EPA investigation and pursuit of the needs appears strong.

PARTICLE SIZING PROGRAM

Responses to each of the above identified issues relating to industrial particle sizing technology have been developed. Both near-term and long-term approaches are defined. While the program is presently focusing on development of the cascade impactor sizing technique, other techniques will be investigated as required in the future. The goal will be evolution of a useful and defensible particle sizing methodology.

The major components of the near-term program are:

1. Cascade impactor calibration.
2. Impactor plate preparation, handling and analysis error evaluation.
3. Sampling rate effects study.
4. Small duct sampling configuration study.
5. Visual sample examination technique development.
6. Data interpretation technique development.
7. Cascade impactor cross-correlation development with other sizing devices.

The issues to be addressed by each program component are given in Table 1. The long-term portion of the program is highly dependent on near-term results. Thus, it is not clearly defined in needs or scope at present.

A cascade impactor calibration program is currently nearing completion at Southern Research Institute. It attempts to address impactor sizing performance as a function of flowrate and substrate quality (i.e., the ability to control particle bounce and reentrainment). A "good" substrate is being simulated by a Vaseline coating on each plate. A substrate exhibiting high particle bounce results from an Apiezon H grease coating at ambient temperature. The objective is to identify the impaction jet velocities for which bounce becomes a problem, as well as the influence upon the data collected. Additionally, the effects of wall and buttonhook nozzle losses upon the resulting size distributions will be assessed.

As a parallel effort to the calibration work, a four-phase program has been formulated to address errors introduced by impactor plate preparation, handling and analysis techniques. The program is presented in Figures 3-6. A weighing error analysis represents Phase 1 of the program (Figure 3). Parallel procedures are followed for a grease substrate, bare plate, and fiberglass filter substrate. Quantification of weighing uncertainties for each substrate type will result.

An analysis of grease mass loss at a given sampling temperature as a function of pretreatment temperature constitutes Phase 2 (Figure 4). Temperature range selections were based on an earlier Thermogravimetric Analyzer study of mass loss versus time and temperature for Apiezon H grease. The resulting mass loss rate curve versus temperature was given as Figure 1. A sharp degradation above 200°C was observed, thus limiting our Phase 2 study to this maximum temperature.

TABLE 1. PARTICLE SIZING PROGRAM

ISSUE	NEAR-TERM APPROACH	LONG-TERM APPROACH
Non-Ideal Impactor Behavior	. Calibrate cascade impactors . Perform sampling rate effects study with particulate matter of interest	. Additional work as necessary
Non-Ideal Substrate Behavior	. Calibrate cascade impactor . Perform sampling rate effects study with particulate matter of interest	. Additional work as necessary
Sample Analysis and Data Interpretation Techniques	. Perform impactor plate preparation, handling and analysis error evaluation . Develop visual sample examination technique . Incorporate all data into data interpretation technique	. Additional work as necessary
Process-Related Influences	. Control process variations best as possible . Continue single-point sampling with replication	. Investigate duct stratification effects . Develop long period sampling capability
Primary Collector Inlet Particle Sizing	. Identify impactor pre-separation device . Correlate bulk collected sample sizing techniques with impactor sizing	. Develop large particle sizing capability . Develop high particle mass loading sizing capability
Sampling Configuration Influences	. Calibrate cascade impactors with buttonhook nozzles . Determine small duct sampling configuration requirements	. Additional work as necessary

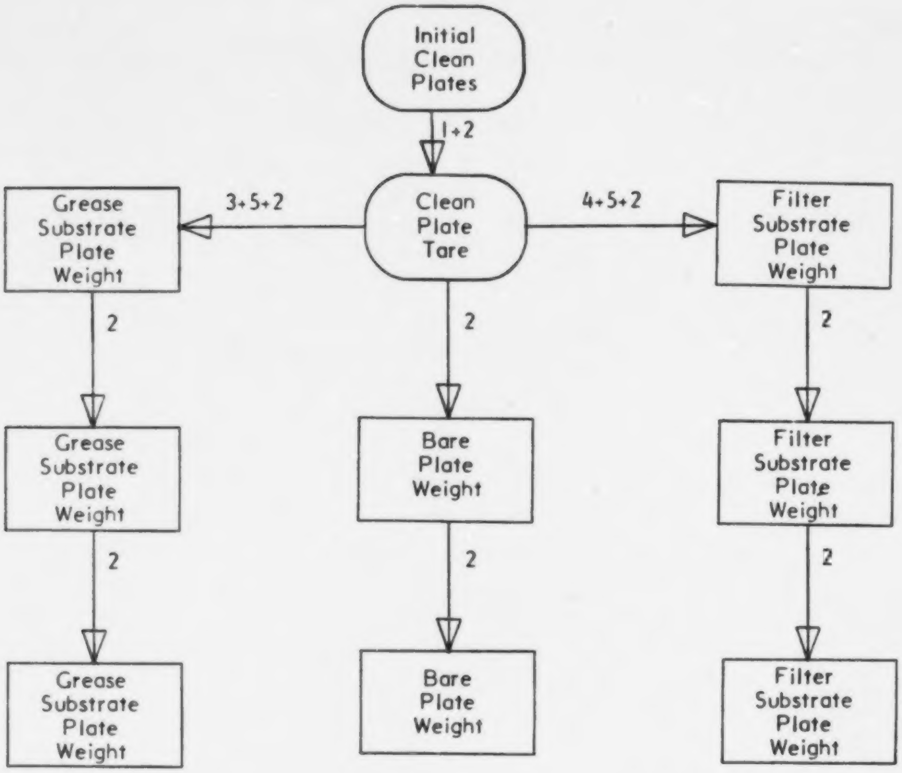
Initial Clean Plates
1+2
Clean Plate Tare
3+5+2
4+5+2
Grease Substrate Plate Weight
Filter Substrate Plate Weight
2
Bare Plate Weight
2
Grease Substrate Plate Weight
Bare Plate Weight
Filter Substrate Plate Weight

1. Residue removal: Use new impaction plates, wash with acetone, rinse with distilled water, evaporate to dryness by furnace treatment.
2. Dessication at room temperature, 2 hr minimum.
3. Add Apiezon H grease (5% Apiezon H in toluene solution) to each plate, approximately 5 mg (following toluene evaporation) per plate.
4. Add fiberglass filter mat substrate to each plate.
5. Toluene/water removal: furnace treatment at 125°C for 1 hr.
6. Conditioning A: furnace treatment at 125°C for 1-1/2 hr.
7. Conditioning B: furnace treatment at 150°C for 1-1/2 hr.
8. Conditioning C: furnace treatment at 175°C for 1-1/2 hr.
9. Conditioning D: furnace treatment at 200°C for 1-1/2 hr.
10. Temperature simulation: furnace treatment at 175°C for one hour.
11. Sampling simulation: load impactor plates into cascade impactor body.
12. Sampling simulation: unload impactor plates from cascade impactor body.
13. Sampling simulation: sample filtered gas flow on Multiclone Test Facility, 14 lpm at 175°C for one hour.
14. Conditioning: conditions to be determined from Series II results.

Figure 3. Phase 1 - weighing error investigation.

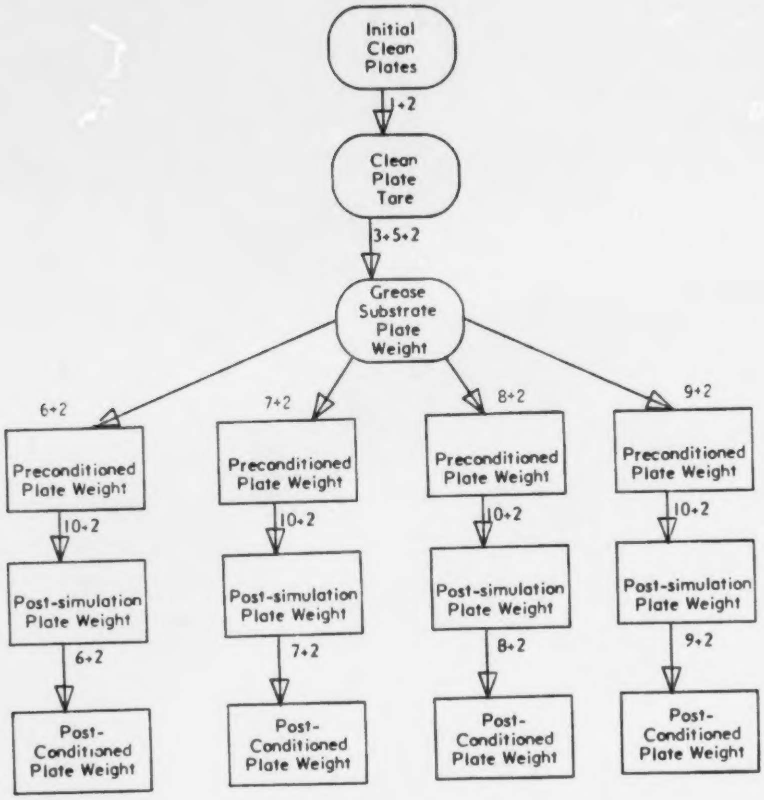
Initial Clean Plates
1+2
Clean Plate Tare
3+5+2
Grease Substrate Plate Weight
6+2
7+2
8+2
9+2
Preconditioned Plate Weight
Preconditioned Plate Weight
Preconditioned Plate Weight
Preconditioned Plate Weight
10+2
10+2
10+2
10+2
Post-simulation Plate Weight
Post-simulation Plate Weight
Post-simulation Plate Weight
Post-simulation Plate Weight
6+2
7+2
8+2
9+2
Post-Conditioned Plate Weight
Post-Conditioned Plate Weight
Post-Conditioned Plate Weight
Post-Conditioned Plate Weight

1. Residue removal: Use new impaction plates, wash with acetone, rinse with distilled water, evaporate to dryness by furnace treatment.
2. Dessication at room temperature, 2 hr minimum.
3. Add Apiezon H grease (5% Apiezon H in toluene solution) to each plate, approximately 5 mg (following toluene evaporation) per plate.
4. Add fiberglass filter mat substrate to each plate.
5. Toluene/water removal: furnace treatment at 125°C for 1 hr.
6. Conditioning A: furnace treatment at 125°C for 1-1/2 hr.
7. Conditioning B: furnace treatment at 150°C for 1-1/2 hr.
8. Conditioning C: furnace treatment at 175°C for 1-1/2 hr.
9. Conditioning D: furnace treatment at 200°C for 1-1/2 hr.
10. Temperature simulation: furnace treatment at 175°C for one hour.
11. Sampling simulation: load impactor plates into cascade impactor body.
12. Sampling simulation: unload impactor plates from cascade impactor body.
13. Sampling simulation: sample filtered gas flow on Multiclone Test Facility, 14 lpm at 175°C for one hour.
14. Conditioning: conditions to be determined from Series II results.

Figure 4. Phase 2 - conditioning temperature investigation.

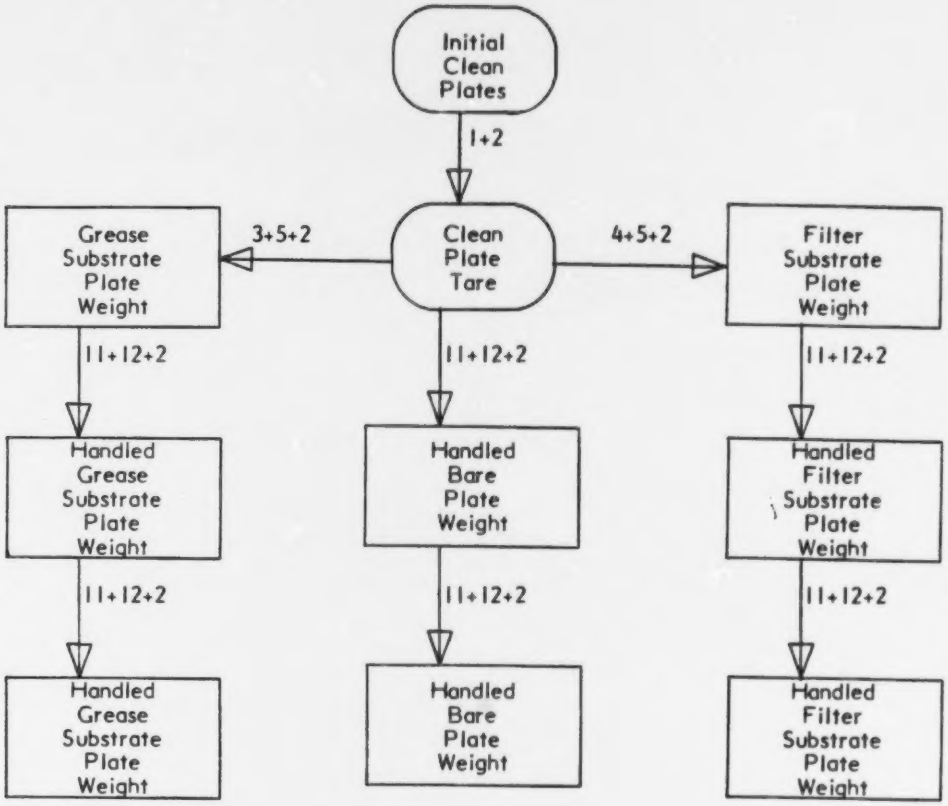
Initial Clean Plates
1+2
Clean Plate Tare
3+5+2
4+5+2
Grease Substrate Plate Weight
Filter Substrate Plate Weight
11+12+2
11+12+2
11+12+2
Handled Grease Substrate Plate Weight
Handled Bare Plate Weight
Handled Filter Substrate Plate Weight
11+12+2
11+12+2
11+12+2
Handled Grease Substrate Plate Weight
Handled Bare Plate Weight
Handled Filter Substrate Plate Weight

1. Residue removal: Use new impaction plates, wash with acetone, rinse with distilled water, evaporate to dryness by furnace treatment.
2. Dessication at room temperature, 2 hr minimum.
3. Add Apiezon H grease (5% Apiezon H in toluene solution) to each plate, approximately 5 mg (following toluene evaporation) per plate.
4. Add fiberglass filter mat substrate to each plate.
5. Toluene/water removal: furnace treatment at 125°C for 1 hr.
6. Conditioning A: furnace treatment at 125°C for 1-1/2 hr.
7. Conditioning B: furnace treatment at 150°C for 1-1/2 hr.
8. Conditioning C: furnace treatment at 175°C for 1-1/2 hr.
9. Conditioning D: furnace treatment at 200°C for 1-1/2 hr.
10. Temperature simulation: furnace treatment at 175°C for one hour.
11. Sampling simulation: load impactor plates into cascade impactor body.
12. Sampling simulation: unload impactor plates from cascade impactor body.
13. Sampling simulation: sample filtered gas flow on Multiclone Test Facility, 14 l pm at 175°C for one hour.
14. Conditioning: conditions to be determined from Series II results.

Figure 5. Phase 3 - handling error investigation.

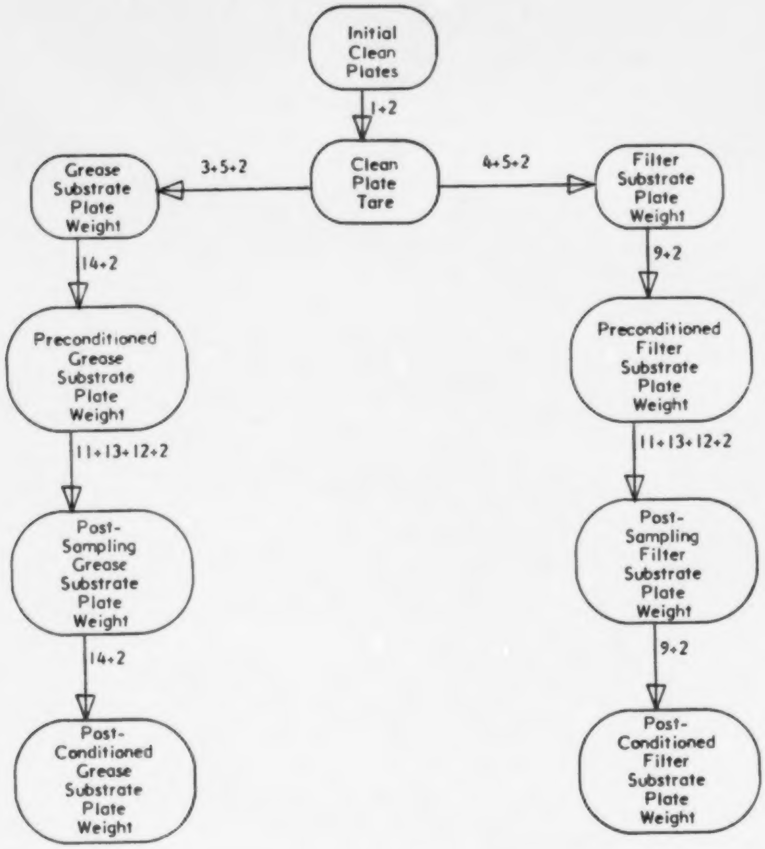
Initial Clean Plates
1+2
Clean Plate Tare
3+5+2
4+5+2
Grease Substrate Plate Weight
Filter Substrate Plate Weight
14+2
9+2
Preconditioned Grease Substrate Plate Weight
Preconditioned Filter Substrate Plate Weight
11+13+12+2
11+13+12+2
Post-Sampling Grease Substrate Plate Weight
Post-Sampling Filter Substrate Plate Weight
14+2
9+2
Post-Conditioned Grease Substrate Plate Weight
Post-Conditioned Filter Substrate Plate Weight

1. Residue removal: Use new impaction plates, wash with acetone, rinse with distilled water, evaporate to dryness by furnace treatment.
2. Dessication at room temperature, 2 hr minimum.
3. Add Apiezon H grease (5% Apiezon H in toluene solution) to each plate, approximately 5 mg (following toluene evaporation) per plate.
4. Add fiberglass filter mat substrate to each plate.
5. Toluene/water removal: furnace treatment at 125°C for 1 hr.
6. Conditioning A: furnace treatment at 125°C for 1-1/2 hr.
7. Conditioning B: furnace treatment at 150°C for 1-1/2 hr.
8. Conditioning C: furnace treatment at 175°C for 1-1/2 hr.
9. Conditioning D: furnace treatment at 200°C for 1-1/2 hr.
10. Temperature simulation: furnace treatment at 175°C for one hour.
11. Sampling simulation: load impactor plates into cascade impactor body.
12. Sampling simulation: unload impactor plates from cascade impactor body.
13. Sampling simulation: sample filtered gas flow on Multiclone Test Facility, 14 lpm at 175°C for one hour.
14. Conditioning: conditions to be determined from Series II results.

Figure 6. Phase 4 - sampling gas flow investigation.

Phase 3 (Figure 5) deals with handling-induced errors from impactor plate loading/unloading in a laboratory setting. Grease, fiberglass filter and bare plate substrates are evaluated. These results will be specific to the laboratory handling environment evaluated. More significant handling errors might be expected in a field situation. Incorporation of this study phase into every field study will help quantify errors resulting from handling in dirty environments.

The fourth phase (Figure 6) deals with additional substrate mass loss which may result from sampling a hot gas stream. A prefilter system will be used to eliminate particle loading into the impactor. Following a "typical" impactor warm-up time, a sample of a heated gas stream will be drawn. Any additional volatilization effect over that quantified in Phase 2 will be determined. Incorporation of data from all four phases should yield valid error estimates for future sample analysis.

The sampling rate effects study is designed to identify valid sampling rates and substrates for control of bounce and reentrainment of particulate matter from key forest products process operations. This study will be performed on a pilot-scale hot-flow facility to insure controllability and reproducability of conditions. The data will provide specific impactor performance information for the particulate matter of interest for direct comparison to the laboratory calibration results.

The importance of obtaining particle sizing data from pilot-scale evaluations has identified the need to minimize small duct sampling configuration effects on particle size measurement. Typical duct diameters range from 25-50 cm. Gas flow within the duct will be significantly affected by an in-duct impactor. While the problem could be avoided with a buttonhook nozzle and an out-of-duct arrangement, the added nozzle uncertainties are prohibitive. Our study will identify and design a straight nozzle (length, diameter, etc.) to sample the required range of flowrates experienced in small-duct sampling.

The visual sample examination and data interpretation techniques will lead to a standardization of particle sizing interpretation. Samples will be visually ranked for nonideal effects (scour, wall loss, nozzle loss) to provide a record of valid and questionable data. Data analysis will be performed with error estimate incorporation to enable review of the data in light of all caveats. The intent is to ensure that valid and questionable data are interpreted as such. A need for careful interpretation of results is emphasized by the large dollar decisions which are based on the particle size data.

Following development of the cascade impactor technique, the correlation of impactor data with that of other particle sizing techniques will be evaluated. Present plans involve cross-correlation with in-house laboratory techniques applicable to bulk collected samples. These will include the Bahco and Malvern Particle Size Classifiers. Because each technique may be appropriate only for selected sample needs, the correlation development will be essential for comparison of results. Additional in-stack devices will also be compared at a future date.

SUMMARY

Particle sizing data are important to industry's efforts to control particulate emissions. Additionally, the validity of particle sizing information is essential to any reasonable implementation of a size-specific particulate emission standard. The problems with the technology as currently practiced, however, are significant. Many of the short-comings are hardware and technique related. Because particle sizing problems are common to most industries and accurate sizing is necessary for a timely and cost-effective attainment of clean air goals, the rationale for continued EPA investigation appears strong.

As a result of the significance of Weyerhaeuser Company's own particle sizing needs, we have embarked on a program to address both general and company-specific concerns. The major issues have been defined. A multi-faceted program has been composed to address them on both near-term and long-term bases. Results are being assessed for incorporation into a practical and defensible particle sizing technique.

REFERENCES

1. Fegley, M. J., D. S. Ensor, and L. E. Sparks. The Propagation of Errors in Particle Size Distribution Measurements Performed Using Cascade Impactors. Presented at the 68th Annual Meeting, Air Pollution Control Association, Boston, Massachusetts, June 1975.

2. Smith, W. B., K. M. Cushing, and J. D. McCain. Particulate Sizing Techniques for Control Device Evaluation. EPA-650/2-74-102, U.S. Environmental Protection Agency, Research Triangle Park, North Carolina, 1974.

3. Cushing, K. M., J. D. McCain, and W. B. Smith. Experimental Determination of Sizing Parameters and Wall Losses of Five Source-Test Cascade Impactors. Environmental Science and Technology, 13(6):726-731, 1979.

4. McCain, J. D. and J. E. McCormack. Nonideal Behavior in Cascase Impactors. In: Proceedings: Advances in Particle Sampling and Measurement. EPA-600/9-80-004, U.S. Environmental Protection Agency, Research Triangle Park, North Carolina, 1980.

5. Knapp, K. T. The Effects of Nozzle Losses on Impactor Sampling. In: Proceedings: Advances in Particle Sampling and Measurements. EPA-600/9-80-005, U.S. Environmental Protection Agency, Research Triangle Park, North Carolina, 1980.

The work described in this paper was not funded by the U.S. Environmental Protection Agency. The contents do not necessarily reflect the views of the Agency and no official endorsement should be inferred.

Paper 18

A NEW PIEZOELECTRIC QUARTZ CRYSTAL FOR PARTICLE MASS DETERMINATION

H. Fissan
D. F. Schulze-Froehlich*
Aerosolmesstechnik, University of Duisburg

ABSTRACT

Quartz crystals are used for direct particle mass determination, since deposited particles cause a frequency shift. The sensitivity of quartz crystals is strongly dependent on the particle distribution over the surface of the crystal, which is dependent on the particle deposition mechanism. In cases where only a portion of the active surface of the quartz crystal is covered with particles, for instance in an impactor, the sensitivity distribution over the surface of the quartz crystal is of importance for estimating the actual sensitivity of the crystal. For the normally used plane-parallel (pp) quartz crystals the sensitivity distribution is known only for special cases.

On the other hand there exists a general theory for plano-convex (pc) quartz crystals, which allows the determination of the sensitivity distribution and knowing the particle distribution also the determination of the actual sensitivity of the pc quartz crystal.

In this paper, pc quartz crystals are introduced and are compared with pp quartz crystals. The measured sensitivities of pc quartz crystals used in an impactor are compared with calculated sensitivities using the theory.

INTRODUCTION

Quartz crystals are used for measuring particle masses. Some of their advantages in comparison with a normal balance are high sensitivity, quasi-continuous measurement, collection and mass analysis of particles at the same time, and electrical output signal. There are two processes involved. In a first step the particles are deposited on the surface of the quartz crystal. In a second step the quartz crystal changes its frequency, since its mass is increased by the deposited particles.

Thus far quartz crystals have been used in a centrifuge[1], in electrostatic precipitators[2,3], and in impactors[4].

In a centrifuge the active surface of the quartz crystal is covered with a homogeneous layer of particles; in the case of an electrostatic precipitator the layer is less homogeneous, whereas in the case of impactors the particles are normally distributed only over a certain area of the active surface.

---

*Present address, H. Steinelke, D4836 Herzebrock 1, Dieselstrasse 80-86, West Germany.

All quartz crystals do have a sensitivity distribution over the surface. For the theoretical determination of the characteristics of a quartz crystal in the case of an inhomogeneous layer this sensitivity distribution has to be known.

The sensitivity distribution of the thus far used plane-parallel (pp) quartz crystals is only roughly known, whereas a checked theory exists for plano-convex (pc) quartz crystals[5].

In this paper pc quartz crystals are described and compared with pp quartz crystals. For application in impactors, the characteristics of pp and pc quartz crystals are compared theoretically if possible and experimentally determined.

QUARTZ CRYSTALS INVESTIGATED

Figure 1 shows the geometries as well as the most important design parameters of the two types of quartz crystals investigated. The pp AT quartz crystal, with total diameter D, thickness d, and electrode diameter D_E has been used thus far. The pc AT quartz crystal, with total diameter D, total thickness T, thickness of the plane-parallel plate d, and radius of calotte R has been developed by Sauerbrey[6] for a special purpose in the field of communication techniques. He also developed and checked a theory for describing the sensitivity distribution, based on a comparison with spherical optical resonators used as laser resonators[5].

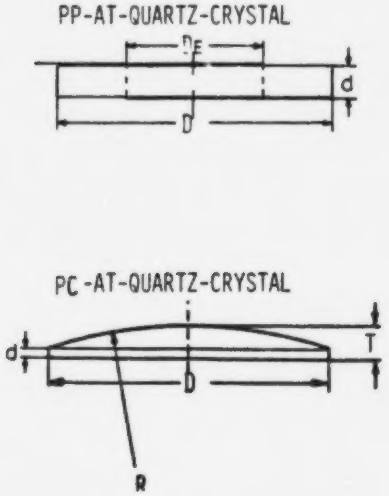

Figure 1. Geometries of pp and pc quartz crystals.

Sauerbrey himself proposed to use pc quartz crystals for particle mass determination, because of their advantage of having known sensitivity distribution. Thus it is possible to design a quartz crystal for a certain application with the necessary sensitivity and also to check the results of calibration experiments.

The characteristics of quartz crystals depend not only on the particle distribution on their surfaces, but also on temperature and humidity changes and adsorption of gases[8]. These effects are more or less the same for both types of quartz crystals, since they are both of the same AT cut. These problems are not considered further in this paper.

CHARACTERISTICS OF QUARTZ CRYSTALS: HOMOGENEOUS LAYER OVER TOTAL ACTIVE SURFACE

Very often it is assumed that the particles are distributed homogeneously over the active surface. The main steps for the derivation of the characteristics for both types of quartz crystals are then as given in Figure 2. The derivation is basically the same. The only differences are that instead of thickness d the maximum thickness t is chosen for the pc quartz crystal. The cut-dependent frequency constant N_{pc} is only slightly different from N_{pp} (a few percent), since t is small compared to R in all practical cases. Thus the overall sensitivity $\bar{S}_{opc}$ is only slightly different from $\bar{S}_{opp}$.

In deriving the characteristic Equation 4 in Figure 2 several assumptions have been made, which are less fulfilled with increasing particle mass. Therefore the actual curves characteristic of both types of quartz crystals become non-linear and approach asymptotically a constant frequency difference with increasing particle mass. Normally only the linear portion of the characteristic curve, where Equation 4 in Figure 2 holds, is used.

For the calculation of the overall sensitivities $\bar{S}_{opp}$ and $\bar{S}_{opc}$ the active surface A has to be known. Sauerbrey[9] has only shown that for a pp AT quartz crystal with f = 14 MHz the active surface is equal to the area covered by the electrodes. Later on Sauerbrey[10] has shown that the active surface also depends on the thickness of the electrodes. The assumed Gaussian sensitivity distribution is not valid in all cases. The eigenfunctions of plane-parallel plates are very complex, so that all components of the three-dimensional vibration can have comparable amplitudes[5].

In the case of pc quartz crystals, the vibrations with large amplitudes are concentrated in the center, so that effects caused by the holders are less likely to occur. In this case the active surface and the overall sensitivity can be calculated using the available theory for the sensitivity distribution as shown in the preceding section.

CHARACTERISTICS: INHOMOGENEOUS LAYER

All quartz crystals show a sensitivity distribution S (R, ξ) in which R and ξ are polar coordinates.

	pp - Quartz	pc - Quartz
(1)	$\frac{\lvert\Delta f\rvert}{f} = \frac{\Delta d}{d}$	$\frac{\lvert\Delta f\rvert}{f} = \frac{\Delta d}{t}$
(2)	$\lvert\Delta f\rvert = \frac{f}{\rho_Q A d}\Delta m$	$\lvert\Delta f\rvert = \frac{f}{\rho_Q A t}\Delta m$
(3)	$f = N_{pp}\frac{1}{d}$ $N_{pp} = 1662{,}5\,KHz \cdot mm$	$f = N_{pk}\frac{1}{t}$ $N_{pc} = N_{pp}\left(1 + 0{,}49\sqrt{\frac{t}{R}}\right)$
(4)	$\lvert\Delta f\rvert = \underbrace{\left(\frac{f^2}{\rho_Q\ A\ N_{pp}}\right)}_{\overline{S}_{opp}}\Delta m$	$\lvert\Delta f\rvert = \underbrace{\left(\frac{f^2}{\rho_Q\ A\ N_{pc}}\right)}_{\overline{S}_{opc}}\Delta m$

Figure 2. Characteristics for homogeneous layer.

If the particles are inhomogeneously distributed, the particle mass per unit area $\Delta\ \Psi = \Delta m/\Delta A$ also depends on the location on the quartz crystal. In this case the characteristics of quartz crystals starting with equation 2 in Figure 2 are given by:

$$\Delta f = \frac{f}{\rho_Q \cdot t} \cdot \frac{\int_0^{2\pi}\int_0^{R_D} \Delta\ \Psi\ (R,\xi)\ S(R,\xi)\ R\ dR\ d\xi}{\int_0^{2\pi}\int_0^{\infty} S\ (R,\xi)\ R\ dR\ d\xi} \qquad (1)$$

in which R_D is the radius up to which particles have been deposited. This relationship holds also for pp quartz crystals with d instead of t. This equation also shows that there is no unique relationship between frequency shift and total particle mass in the case of inhomogeneous and changing particle distribution on the quartz surface. Besides that, the sensitivity distribution $S(R,\xi)$ has to be known.

THE SENSITIVITY DISTRIBUTIONS OF QUARTZ CRYSTALS

As mentioned earlier, there does not exist a general theory to describe the behavior of pp quartz crystals, since the behavior depends on many parameters. Sauerbrey[5] applied the theory for laser resonators to pc quartz crystals and determined the amplitude distribution. This theoretical distribution has been compared with experimentally determined amplitude distributions, showing a good agreement.

For a round plate pc quartz crystal the sensitivity shows a Gaussian distribution

$$S(R) = \exp\left[-\frac{R^2}{w^2}\right]^2 = \exp\left[-\frac{R^2}{Ro^2}\right], \text{ with } R_o = \frac{w}{\sqrt{2}} \qquad (2)$$

The width of the amplitude distribution (1/e-value of amplitude) is given by

$$w = (1.07 \pm 0.05) \sqrt[4]{R\,t^3} \qquad (3)$$

Using a published design theory[11], 3 different pc quartz crystals have been designed and produced. The actual parameters of these quartz crystals are given in Table 1.

Table 1. Dimensions of pc Quartz Crystals Investigated[11]

No.	Frequency (MHz)	T (mm)	d (mm)	D (mm)	R_E (mm)	R (mm)
1	4.090	0.417	0.156	15	4	100
2	2.009	0.864	0.36	20	8	100
3	1.416	1.235	0.574	23	10	100

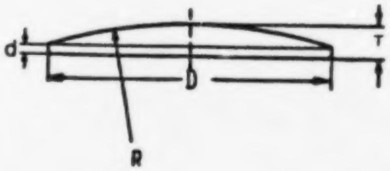

Using the data of Table 1, the widths of the amplitude distributions have been calculated in Table 2.

Table 2. 1/e-Radius w of Amplitude Distributions[11]

No.	Frequency F (MHz)	w (mm)
1	4.090	1.756
2	2.009	3.03
3	1.416	3.96

These values have been introduced in Equation 2 to calculate the relative sensitivity distributions (Figure 3). With decreasing frequency the distribution becomes broader.

EXPERIMENTALLY DETERMINED CHARACTERISTICS OF PP AND PC QUARTZ CRYSTALS IN AN IMPACTOR

To demonstrate the importance of particle distribution and also the advantage of having a theory to calculate the behavior of quartz crystals, a one-stage impactor with exchangable nozzles and quartz crystals as collection plates was developed[11]. Liquid monodisperse oleic acid particles doped with fluorescein were produced with a vibrating orifice generator. Liquid particles are used to exclude adhesion problems at the quartz surface. The diameter of these particles was just a little bit larger than the effective cut-off diameter of the nozzle used. The time constancy of the generator was monitored by an optical particle counter.

The frequency change was monitored as a function of time. After a certain sampling time, the quartz crystals were washed and, using a fluorometer, the deposited particle mass was determined. These experiments were performed for each quartz crystal using different nozzles (particle size) and collection periods.

The frequency shift as a function of particle mass is plotted in Figure 4 for a 5-MHz pp AT quartz crystal.

The characteristic curves do show different slopes in such a way that the larger the ECD the smaller the integral sensitivity. Investigation of the quartz crystals under a microscope after particle deposition yielded a method for determining the deposition area, since the deposited particles caused a change in color of the quartz crystal. The particles are distributed over a defined area (R_D) more or less homogeneously.

To demonstrate the errors involved using overall sensitivities with the electrode radius R_E for the determination of the active surface, the ratio of the integral sensitivity S_{R_D} to the overall sensitivity is shown in Figure 5 for quartz crystals with different frequencies and for different deposition areas (R_D).

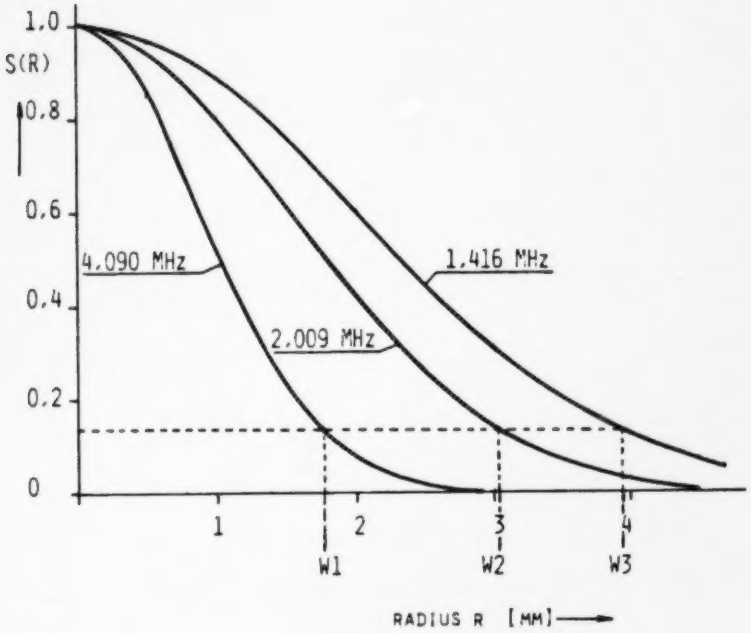

$$S(R) = \left(\frac{a}{a_0}\right)^2 = \left[\exp -\frac{R^2}{w^2}\right]^2 = \exp\left[-\frac{R^2}{R_0^2}\right]$$

$$R_0 = \frac{w}{\sqrt{2}}$$

Figure 3. Sensitivity distributions of pc AT quartz crystals.

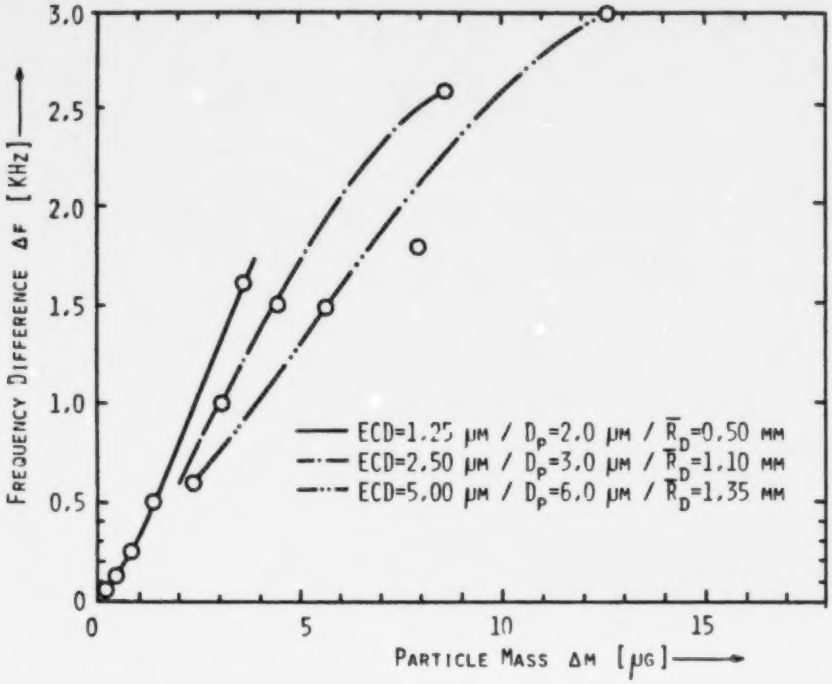

Figure 4. Characteristics of a quartz crystal (5.000 MHz pp AT quartz crystal).[11]

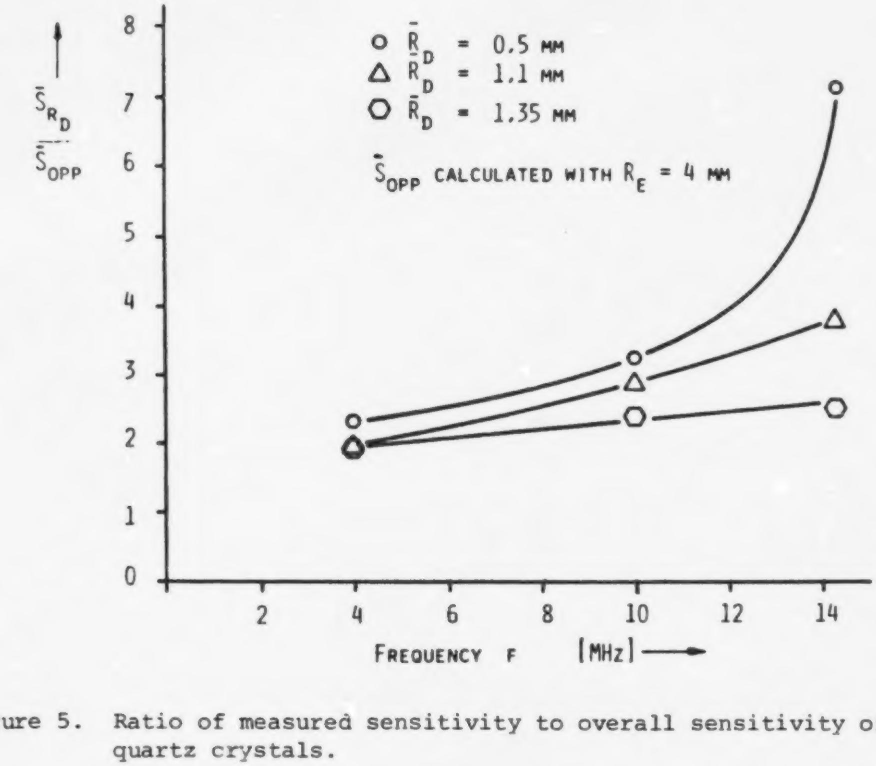

Figure 5. Ratio of measured sensitivity to overall sensitivity of pp AT quartz crystals.

In the case of the smallest deposition area the measured integral sensitivity is larger by a factor of seven compared with the calculated overall sensitivity for a 14-MHz quartz crystal. The smallest factor for the investigated cases is two.

In Figure 6 the characteristic curves of a 4.1-MHz pc AT quartz crystal are shown for the same particle deposition areas. Again the slope is decreasing with increasing deposition area. Despite the fact that the frequency is

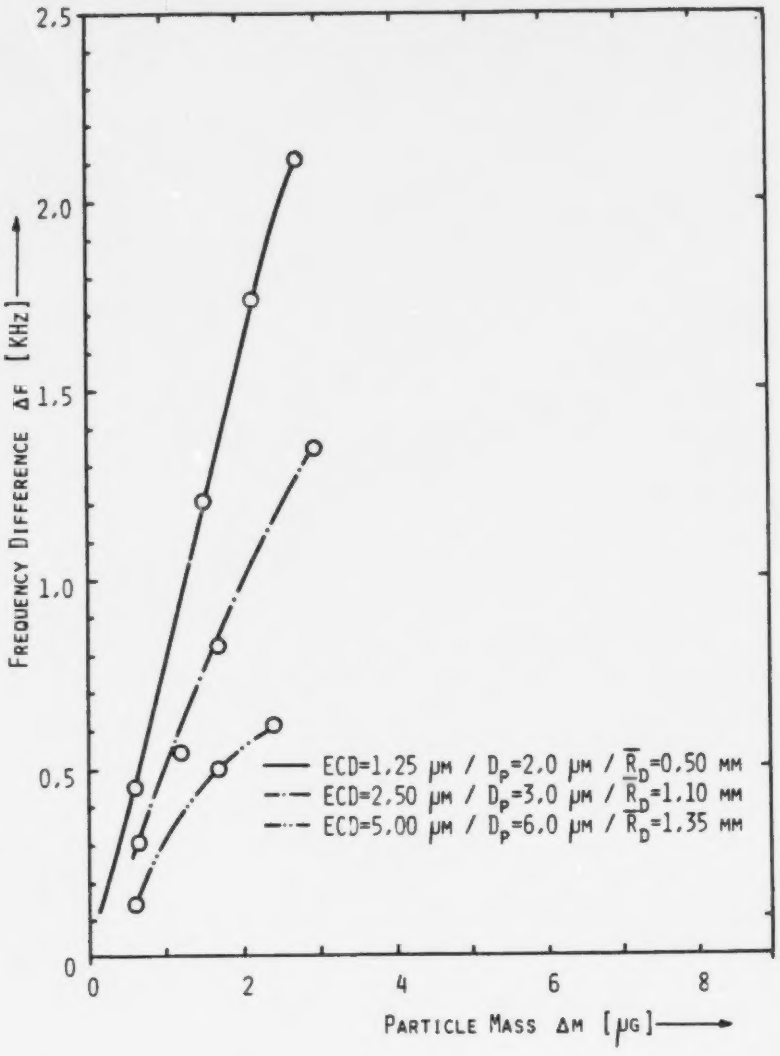

Figure 6. Characteristics of a quartz crystal (4.090 MHz pc AT quartz crystal).[11]

lower (pc quartz 4.1 MHz; pp quartz 5 MHz) the sensitivities of the pc quartz are larger by a factor of two when compared with the 5-MHz pp quartz crystal. It also has been observed[11] that the linearity of the characteristic curves, at least in this application, was better than those of pp quartz crystals.

In order to check whether the observed lack of repeatability of pp quartz crystals is especially true for pc quartz crystals, a set of four crystals with slightly different parameters and with different off-sets of the center of the calotte have been investigated. The characteristic curves are plotted in Figure 7. They show a high degree of repeatability.

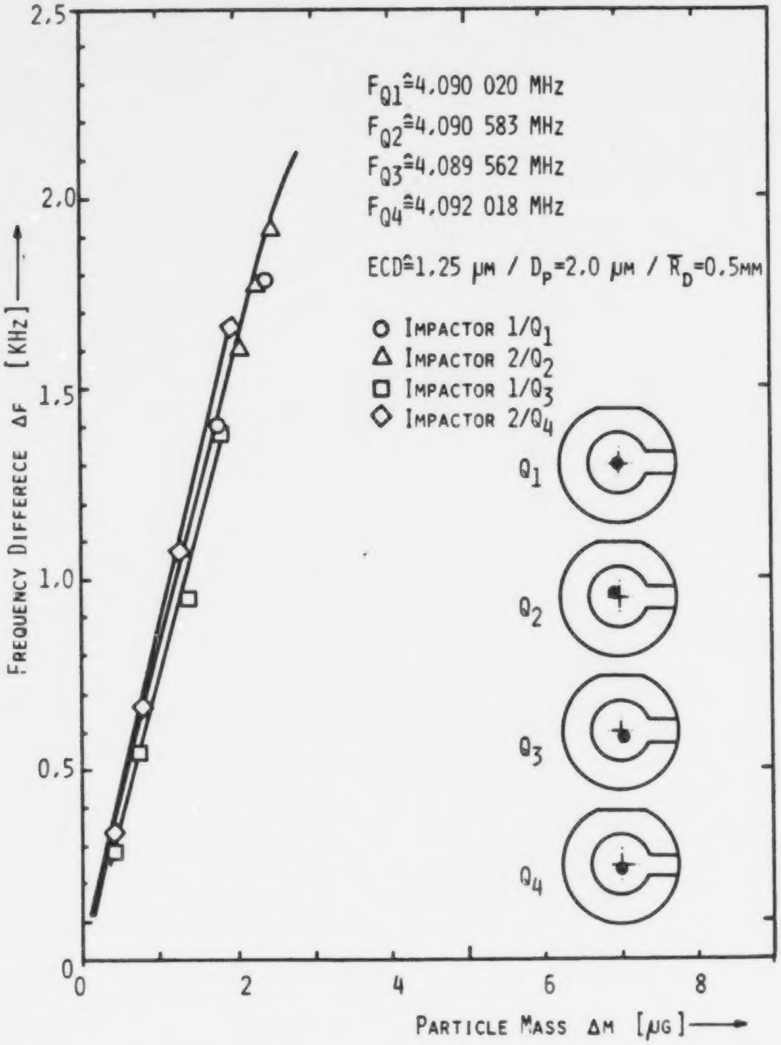

Figure 7. Repeatability of pc quartz crystals.[11]

In Table 3 the measured integral sensitivities $\overline{S}\ (R_D)$ for three different quartz crystals are shown as well as the calculated overall sensitivities $\overline{S}_{opp}$, which are almost equal to $\overline{S}_{opc}$. The difference is even greater than in the case of pp quartz crystals.

Table 3. Comparison of Sensitivities of pc Quartz Crystals

No.	F_O (MHz)	$\overline{S}\ (R_D)$ (Hz/µg)	$\overline{S}_{opp}$ (Hz/µg)	R_E (mm)
1	4.090	734	73.22	4
2	2.009	73	4.358	8
3	1.416	22	1.374	10

$\overline{S}\ (R_D)$ = Measured sensitivity for $R_D = 0.5$ mm

$\overline{S}_{opp}$ = Calculated overall sensitivity using the theory for pp quartz crystals

MODELING OF THE CHARACTERISTICS OF A PC QUARTZ CRYSTAL USED IN AN IMPACTOR[7]

Modeling the characteristics of a pc quartz crystal is possible with the assumptions of:

- rotational symmetry
- particle mass per unit area independent of radius R.

In the demonstrated impactor application using one nozzle the first assumption is fulfilled, whereas the second assumption is only fulfilled to a certain degree.

Introducing these assumptions into Equation 1 yields:

$$|\Delta f| = \frac{f}{\rho_Q t}\ \Delta\Psi\ \frac{2\pi\int_0^{R_D} S\ (R)\ R\ dR}{2\pi\int_0^{\infty} S\ (R)\ R\ dR} \qquad (4)$$

with

$$\Delta\Psi = \frac{\Delta m}{\Delta A}\ ;\ \Delta A = \pi\ R_D^{\ 2} \quad \text{and}$$

$$2\pi\int_0^{\infty} S\ (R)\ R\ dR \cong \pi\ R_O^{\ 2} \qquad (5)$$

$$|\Delta f| = \frac{f}{\rho_Q t} \cdot \frac{1}{\pi\ R_D^{\ 2}} \cdot \frac{2\pi\int_0^{R_D} S\ (R)\ R\ dR}{\pi\ R_O^{\ 2}}\ \Delta m \qquad (6)$$

The integral $\int_0^{R_D} S(R)\, R\, dR$ can be solved for small values of R_D ($R_D \leq w$) by expanding Equation 2 in a series; for larger values of R_D numerical or graphical methods have to be applied.

The result of such a calculation is shown in Figures 8, 9, and 10 as a full line.

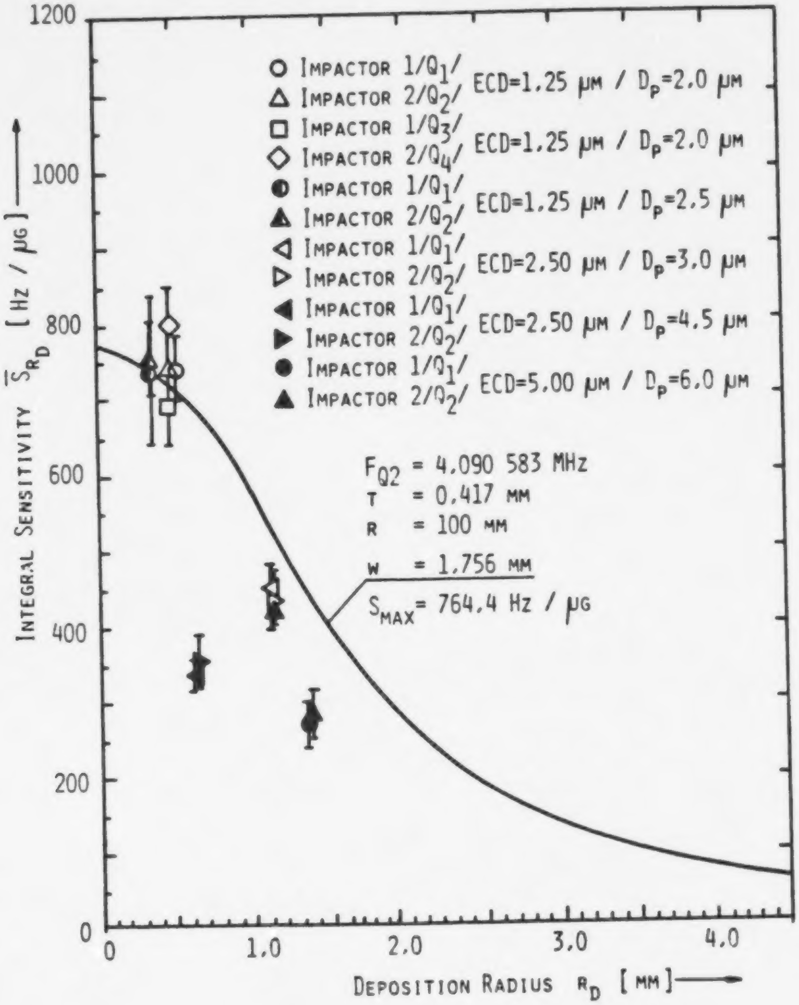

Figure 8. Calculated and measured integral sensitivities of a pc AT quartz crystal.

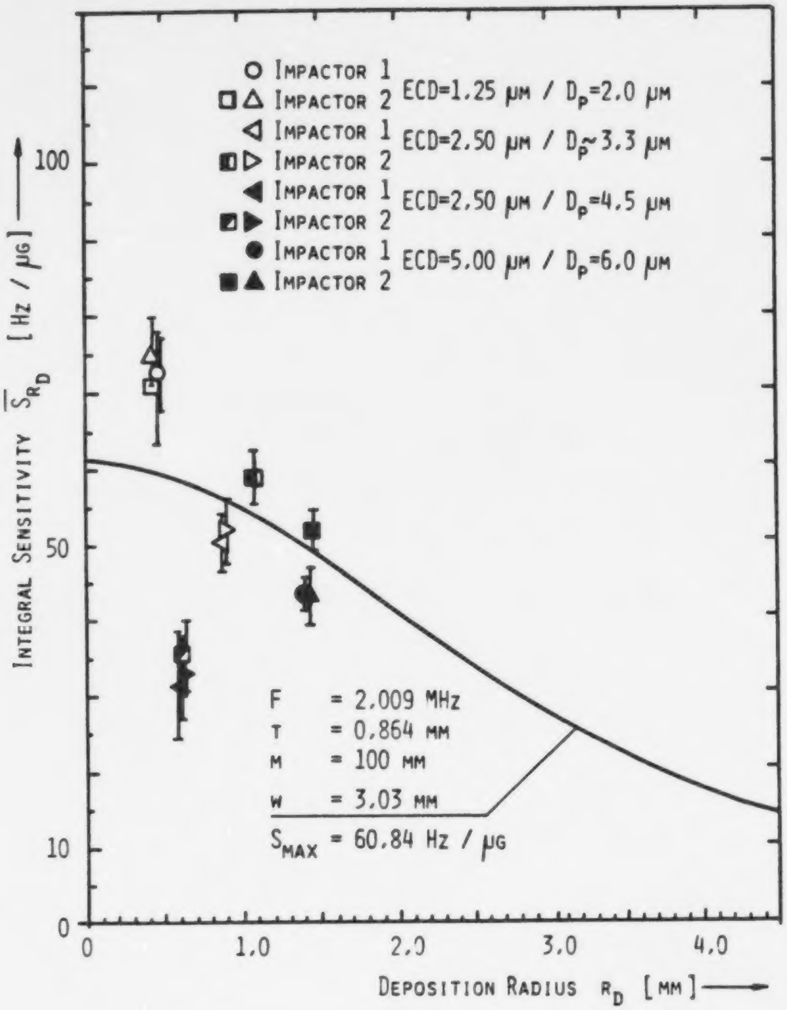

Figure 9. Calculated and measured integral sensitivities of a pc AT quartz crystal.[11]

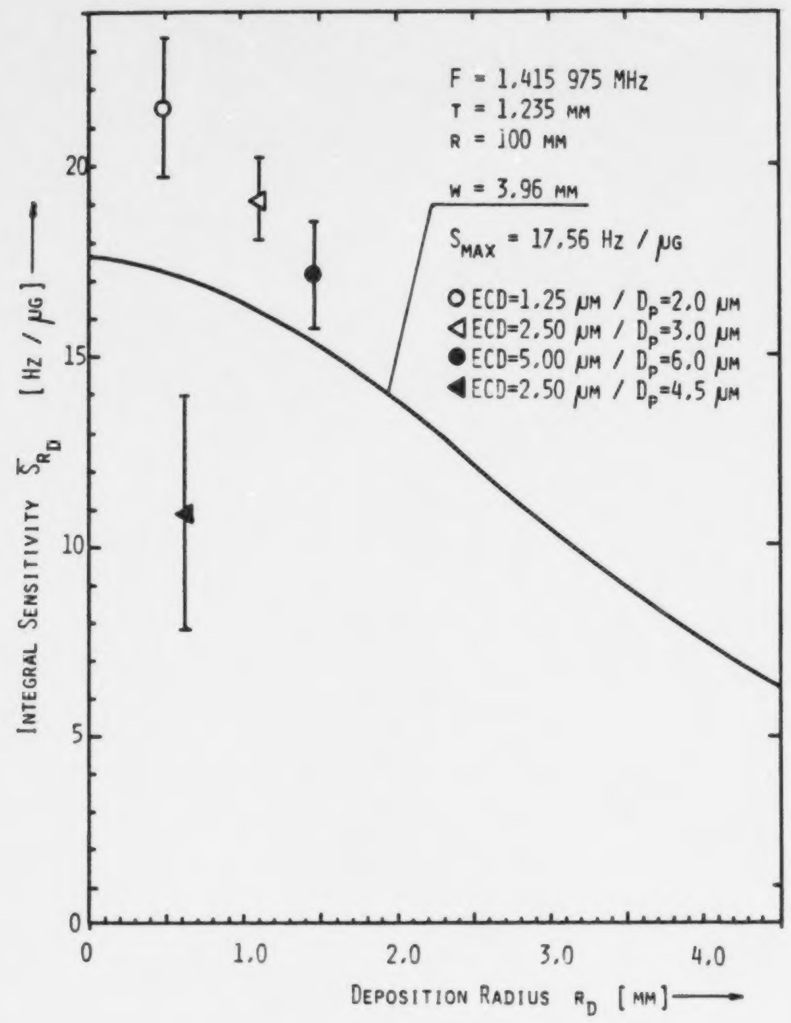

Figure 10. Calculated and measured integral sensitivities of a pc AT quartz crystal.[11]

The calculated and measured integral sensitivities are plotted as functions of deposition radius R_D on an absolute scale. For all three investigated pc quartz crystals the agreement between experiment and theory is rather good, except for the measurement points at $R_D = 0.6$ mm. These sensitivities are too small compared to theory in all cases. The corresponding characteristics are non-linear. The reason for this effect is not quite clear yet.

According to Equation 1, one gets a unique relationship between frequency shift and total deposited particle mass, if the sensitivity is constant over the crystal surface. This is never the case. But using the theory, it is possible to design a quartz crystal with a flat sensitivity distribution. To get a flat sensitivity distribution the width of the amplitude has to be large; this means that the maximum thickness t and the radius of the calotte have to be large. For t, Equation 3 in Figure 2 has to be fulfilled, so that for large t-values the frequency f and the radius R have to be small.

To show the flattening of the sensitivity distribution, the integral sensitivity $\bar{S}_{R_D}$ divided by the maximum sensitivity in the center $\bar{S}$ ($R_D = 0$) is plotted as a function of deposition radius in Figure 11, using the parameters of the investigated pc quartz crystals.

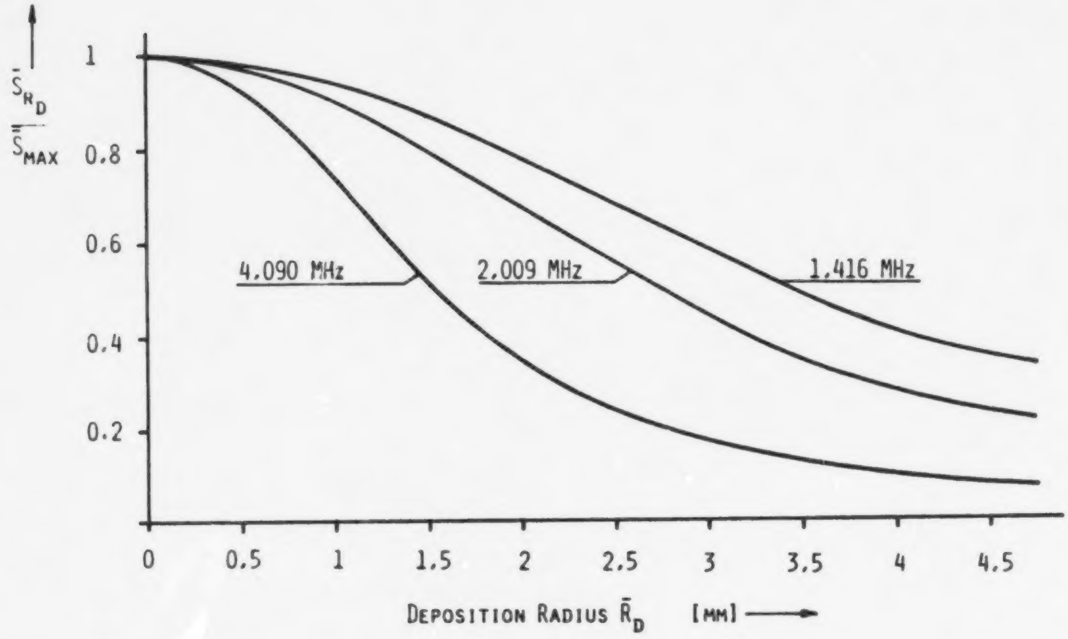

Figure 11. Integral sensitivity ratios for several pc AT quartz crystals.

The figure clearly demonstrates the increasing constancy of the sensitivity curve with decreasing frequency. The effect is less strong with increasing radius R, but it is also a possibility to influence the shape of the sensitivity distribution.

CONCLUSIONS

Quartz crystals are increasingly used for direct particle mass determination. There exists only a unique relationship between observed frequency shift and deposited particle mass, if the particles are deposited homogeneously. In certain applications, especially in impactors, only a portion of the active surface of the quartz crystal is covered with particles more or less homogeneously. In order to be able to predict the characteristics in such cases, which is of interest for the design of quartz crystals and their calibration, one has to know the sensitivity distribution.

For the thus far used pp quartz crystals there is no theory available, but for the newly introduced pc quartz crystals a theory has been developed by Sauerbrey.

Using this theoretical approach it has been shown that for pc quartz crystals one can predict the characteristics for cases where only a portion around the center of the quartz is covered with particles.

In summary the advantages of pc quartz crystals in comparison with pp quartz crystals are:

- higher degree of linearity of the characteristic curve, at least in the investigated case of an impactor with liquid particles
- higher degree of repeatability
- theory available, which allows a better design of quartz crystals for certain applications.

REFERENCES

1. Mönig, F. J., N. Schwarzer, and W. Stöber. Bestimmung der Aerosol-Masseverteilung in einer Aerosol-Zentrifuge mit Hilfe von Schwingquarzen. Gesellschaft für Aerosolforschung e.V. (Hrsg.) 1973: 58-61.

2. Olin, J. G., and G. J. Sem. Piezoelectric Microbalance for Monitoring the Mass Concentration of Suspended Particles. Atmospheric Environment 5: 653-668 (1971)

3. Sem, G. J., and K. Tsurubayaschi. A New Mass Sensor for Respirable Dust Measurement. American Industrial Hygiene Association Journal 1975 , 791-800.

4. Wallace, D., and R. L. Chuan. A Cascade Impaction Instrument Using Quartz Crystal Microbalance Sensing Elements for "Real-Time" Particle

Size Distribution Studies. Presented at: 8th Materials Research Symposium, Methods and Standards for Environmental Measurements (Sept. 20-24, 1976).

5. Sauerbrey, G., and G. Jung. Schwingungsmoden plankonvexer Quarzplatten. Zeitschrift für Angewandte Physik 24 (1968) 2, 100-108.

6. Sauerbrey, G. Design of Plano-Convex Crystal Plates. Frequency 6 (1968) 23, 23-24.

7. Sauerbrey, G. Private Communication.

8. Daley, P. S. and D. A. Lundgren. The Performance of Piezoelectric Crystal Sensors Used to Determine Mass Concentrations. American Industrial Hygiene Association Journal 1976 , 518-532.

9. Sauerbrey, G. Verwendung von Schwingquarzen zur Wägung dünner Schichten und zur Mikrowägung. Zeitschrift für Physik 155 (1959), 106-222.

10. Sauerbrey, G. Einfluss der Elektrodenmasse auf die Schwingungsfiguren dünner Quarzplatten. Archiv der Elektrischen Übertragung 18 (1964), 617-624.

11. Schulze-Fröhlich, D. F. Grundlagenuntersuchung an massesensitiven Schwingquarzen als Impaktions-flächen. Peter D. Lang, Frankfurt/Main. European University Studies, Technical Sciences Bd./Vol. 3.

ACKNOWLEDGEMENT

This research was supported by the Ministerium für Wissenschaft und Forschung des Landes, Nordheim-Westfalen, West Germany.

The work described in this paper was not funded by the U.S. Environmental Protection Agency. The contents do not necessarily reflect the views of the Agency and no official endorsement should be inferred.

Paper 19

RAPID TESTING OF FILTER EFFICIENCY WITH A COMPUTERIZED QCM CASCADE IMPACTOR

Raymond L. Chuan and Cam de Pierre
Defense Division
Brunswick Corporation

ABSTRACT

Using the basic technique of the quartz-crystal-microbalance (QCM) Cascade Impactor, described at the Second Symposium on Advances in Particulate Sampling and Measurement, a method for the rapid determination of filter efficiency has been developed, taking advantage of the real-time mass-measuring capability of the QCM and combining it with a microprocessor for control and data reduction. A further adaptation is the use of a small precision volume for on-line transfer of high concentration aerosol stream into the instrument whereby mass concentration as high as 10 g/m^3 can be measured without the need for sample dilution. The usual time-mode of QCM operation, whereby the aerosol sample flows through the instrument for a measured length of time, is used for measuring the concentration downstream of the filter under test. In this manner, a dynamic range of concentration measurement of 10^7 - from 10^{-6} to 10 g/m^3 has been achieved. A typical filter efficiency test can be completed in less than five minutes, with upstream and downstream mass concentration in up to ten size bands - from 0.05 to 25 μm - presented in histogram form by the built-in computer. The equipment, procedure, and test results involving several types of filters, using Arizona Road Dust as test aerosol, will be presented.

INTRODUCTION

The determination of filter efficiency inherently involves the measurement of aerosol concentration over a very wide dynamic range, typically of the order of 10^6 (for a filter efficiency of 99.999%, for example). Most conventional instruments can cope with the low end of the concentration range, but must resort to dilution or other indirect means to measure at the high end. If gravimetric measurement is required - as would be in most cases where aerosol concentration is expressed in terms of mass - the low end measurement, especially when size distribution is required, would normally take many hours. Thus the characterization of a particular filter - over a range of parameters involving concentration, face velocity, pre-accumulated material, etc. - may well consume several weeks. With the advent of the quartz crystal microbalance (QCM) cascade impactor (1) it is possible to make nearly instantaneous measurements of aerosol mass concentration over discrete size bands, thus greatly facilitating the determination of filter efficiency. The present paper describes a sampling arrangement with the QCM cascade impactor system which allows mass concentration measurements to be made over the range of 10 microgram/cubic meter (μg/m^3) to 10 grams/m^3, in times of the order of a few minutes. The high concentration aerosol upstream of the filter is measured in the so-called volume-transfer-mode; while the low concentration aerosol downstream of the filter is measured in the usual time-mode of the QCM instrument.

SAMPLING MODES OF THE QCM CASCADE IMPACTOR

In the conventional mode of operation of a cascade impactor, an aerosol sample is pumped through at a constant volume flow rate, $\dot{V}$ for a certain length of time, Δt. The mass collected on a stage i, ΔM_i, will yield the mass concentration, C_i, in the size range appropriate to stage i through the relationship

$$C_i = \frac{\Delta M_i}{\Delta t} = \frac{k_i \Delta f_i}{\Delta t}$$

Where Δf_i is the frequency shift in stage i and k_i the conversion factor (from frequency to mass).

Operating in this mode poses no particular problem in the case of a conventional cascade impactor, since ΔM_i is usually measured in milligrams, $\dot{V}$ in tens of liters per minute, and Δt in tens of minutes. For example, an aerosol sample with a mass concentration of 1 milligram per cubic meter (mg/m^3) in some size range would require 10 minutes sampling time at 100 ℓ/min to yield a sample of 1 mg for weighing. With a QCM instrument, on the other hand, only about 10 nanograms (ng) would give a very strong signal, so that at the same 1 mg/m^3 concentration, and at a flow rate of 1 ℓ/min, the sampling time required is only 10^{-2} min, or 0.6 sec which is, in practice, too short for accurate timing of the opening and closing of the sampling valve in the instrument. At higher concentration than 1 mg/m^3, it is clearly impractical to use the time mode operation of the QCM.

The usual solution is to resort to sample dilution, which in this example would be by a factor of 10 to 100,000 (the latter for a concentration of 10 g/m^3), which is cumbersome and lacks accuracy even at the low end, and would be quite impractical at the high end. The alternative is to inject into the instrument a fixed discrete volume of the aerosol sample, instead of timing a constant flow rate. This method, named the volume-transfer-mode, is analogous to the sample injection technique used in gas-chromatography, and is described below.

The volume-transfer-mode is accomplished through the sliding valve arrangement shown schematically in Fig. 1. The valve is made up of three flat rectangular sections, with the center piece as the volume transfer slider. The slider has three passages of which the middle is the transfer volume V_t. During standby, the slider is extended and the transfer volume is aligned with the volume mode sample inlet. High concentration sample is continuously drawn from the source, such as an aerosol chamber, through the transfer volume with an auxiliary pump at a reasonably high flow rate of a few liters per minute. The transfer volume becomes a part of the closed loop in which the aerosol to be measured is circulated in and out of the source. When a measurement is to be made, the slider is pushed in and the sample trapped in the transfer volume is moved over to the inlet of the instrument and drawn into the cascade impactor by the continuously flowing clean filtered air.

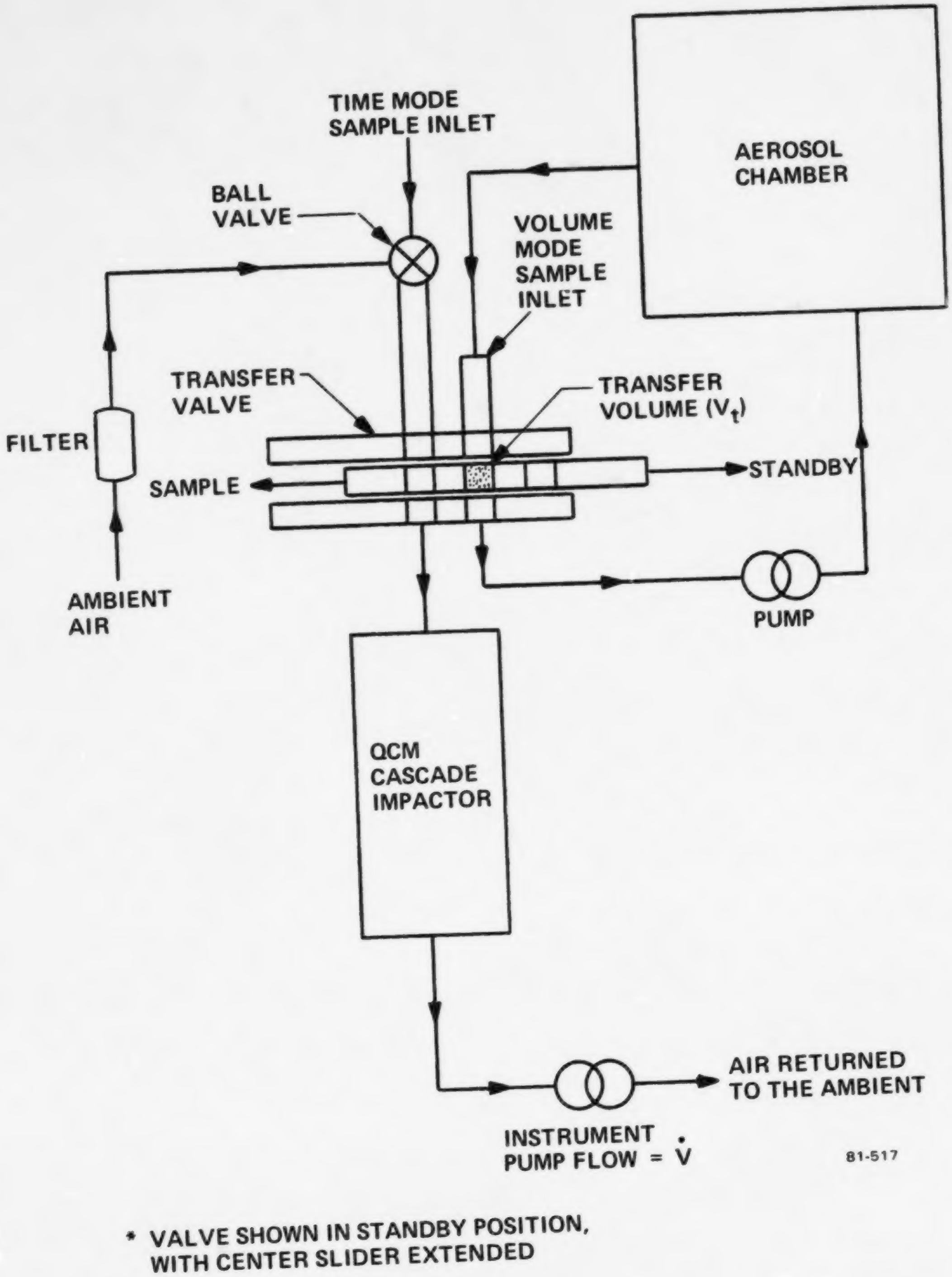
TIME MODE SAMPLE INLET
BALL VALVE
AEROSOL CHAMBER
VOLUME MODE SAMPLE INLET
TRANSFER VALVE
TRANSFER VOLUME (V_t)
FILTER
SAMPLE
STANDBY
AMBIENT AIR
PUMP
QCM CASCADE IMPACTOR
AIR RETURNED TO THE AMBIENT
INSTRUMENT PUMP FLOW = $\dot{V}$
81-517
* VALVE SHOWN IN STANDBY POSITION, WITH CENTER SLIDER EXTENDED

Figure 1. Schematic of volume transfer mode of QCM operation.

In the example given earlier, the desired sampling time of 10^{-2} min would mean a sampled volume of $10^{-2}\ell$ (at a flow rate of 1ℓ/min), or 10 mℓ, which means that in the volume-transfer-mode, the transfer volume V_t would be 10 mℓ. Actually, it is not necessary to accomplish the measurement in just one transfer of the pre-set volume. It is quite satisfactory to transfer the volume several times by sliding the transfer valve back and forth. In this case, the concentration is calculated as

$$C_i = \frac{\Delta M_i}{NV_t} = \frac{k_i \Delta f_i}{NV_t}$$ where N is the number of volumes transferred.

The instrument used for the measurements reported herein has a flow rate of 240 mℓ/min, so that the practical limit on concentration measurement in the time mode, assuming a crystal collection of 10 ng and a sampling time of 5 sec would be 0.5 mg/m^3. If, instead of the time mode, a transfer volume of 100 μℓ is used once (at the same concentration of 0.5 mg/m^3), a concentration of 100 mg/m^3 can be sampled with only a 10 ng deposition on the crystal. With the same 100 μℓ transfer volume, a concentration of 10 g/m^3 would produce a deposition of 1000 ng on the crystal, which is still within the capacity of the crystal. Thus, it is seen that by judicious choice of two or three transfer volumes (ranging from about 30 μℓ to 300 μℓ), a wide range of aerosol concentration from about 1 mg/m^3 to 10 g/m^3 can be conveniently measured. At somewhat lower concentration than 1 mg/m^3 more than one transfer can be made, with the largest transfer volume, to produce sufficient deposition on the crystal. Practically speaking, five to ten transfers are not considered cumbersome or time consuming - which would extend the range to 0.1 mg/m^3, giving a dynamic range of 10^5 in measurement with the volume-transfer-mode.

At lower than about 0.1 mg/m^3, one would shift to the time-mode of operation. For example, at 0.01 mg/m^3, it would require about 250 sec (at 240 mℓ/min) to produce a 10 ng deposition on the crystal, which is still an acceptable sampling time. By combining the time-mode with the volume-transfer-mode, one now achieves a dynamic range of 10^6 in the measurement capability.

QCM FILTER TESTING SYSTEM

The testing set-up for rapid filter efficiency determination is shown schematically in Fig. 2. The aerosol sample flows through a plenum chamber from which a sampling flow loop is maintained with a pump. The transfer volume in the QCM volume transfer valve forms a part of this loop. Thus high concentration aerosol can be introduced into the QCM cascade impactor without interrupting the flow into the filter under test.

After flowing through the filter, across which the pressure drop is measured, the aerosol stream goes through a second plenum chamber from which a sample can be drawn directly into the cascade impactor, operating in the time-mode. Thus, by operating alternately in the volume-transfer- and time-modes, the filter efficiency can be rapidly determined.

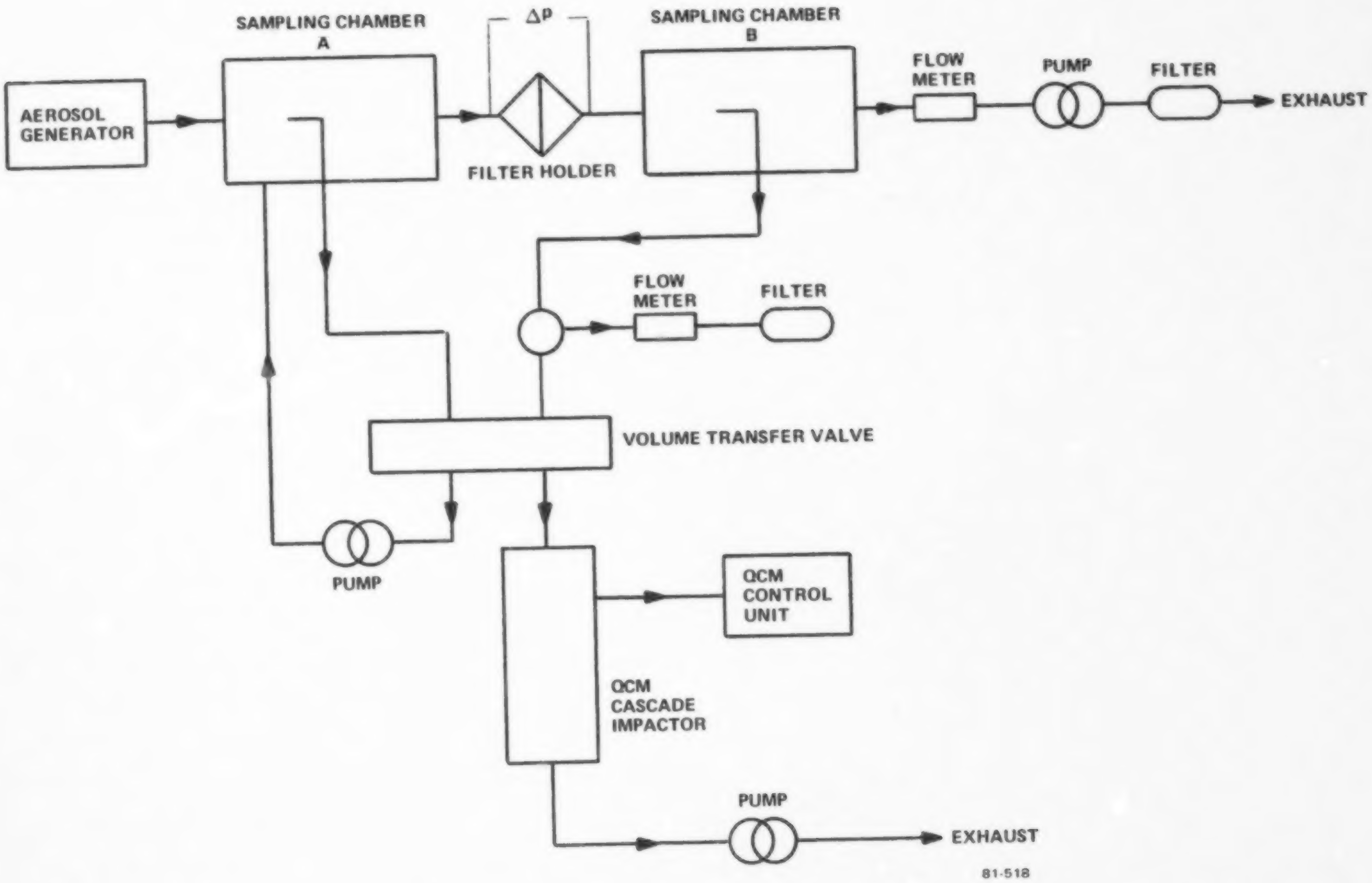
SAMPLING CHAMBER A
ΔP
SAMPLING CHAMBER B
AEROSOL GENERATOR
FILTER HOLDER
FLOW METER
PUMP
FILTER
EXHAUST
FLOW METER
FILTER
VOLUME TRANSFER VALVE
PUMP
QCM CONTROL UNIT
QCM CASCADE IMPACTOR
PUMP
EXHAUST
81-518

Figure 2. Schematic of filter efficiency test apparatus.

After a sample is introduced into the impactor, in either mode, about 90 seconds is needed for all the aerosol to traverse the ten stages, after which the built-in microprocessor is commanded to compute and print the results - in terms of the mass concentration in each stage, the total aerosol concentration and the normalized size distribution in the form of a histogram.

TEST RESULTS

Some tests have been conducted to assess the efficacy of the system described herein. A new type of low pressure drop electret filter medium is used for these tests, with samples held in a standard 47-mm filter holder. Representative results are shown in Figs. 3-6, which are reproductions of the instrument print-outs. The 50% cut-off diameters (for particles of mass density 2 g/cm^3) are listed below:

Channel (Stage)	50% Cut-off Diameter
1	25 μm
2	12
3	6
4	3
5	1.6
6	0.8
7	0.4
8	0.2
9	0.1
10	0.05

The print-out on the left in each figure gives the data for the aerosol upstream of the filter, and that on the right for the downstream side. The volume-transfer-mode is used for the high concentration upstream, and N shows the number of transfers made (the volume being 300 μℓ). The total aerosol mass concentration and that in each size band are shown, as well as the QCM frequency shift for each stage. The latter is shown for diagnostic purposes in case anomalies turn up in the data. Since the digital frequency counting has a ± 1Hz uncertainty, it is desirable to introduce sufficient material into the impactor so that the least count in the stage with the lowest concentration is 2 or greater. The least count in the case with N = 2 is approximately 1-2 mg/m^3, whereas the least count in the time mode, used downstream of the filter, with a sampling time of 90 seconds, is between about 2 to 4 μg/m^3 (depending on the stage). This resolution limit explains the apparent anomaly in Fig. 3 wherein stages 2, 3, 4 and 10 show zero mass upstream, but finite mass downstream. Improvement in resolution is achieved by increasing the amount of sample injection, as examplified by Fig. 4, where for upstream sampling ten transfers are made.

Figs. 3 and 4 are the results for a filter medium commercially designated Filtret G-1300. It is seen in Fig. 3 that at a face velocity of 500 cm/min the pressure drop is only 0.33 in. H_2O, while achieving 99.6 to 99.9% capture over the size range from 0.1 μm to 1.6 μm. A thinner filter, Filtret

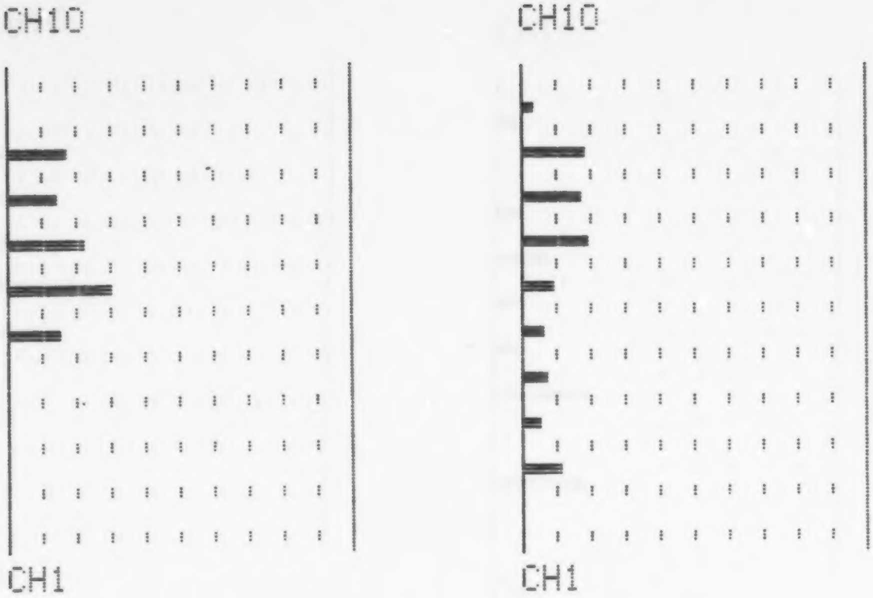

```
N=002 ⑬

TOTAL     16.47870

CH  ΔF      mg/m3
 1 0000    0.00000
 2 0000    0.00000
 3 0000    0.00000
 4 0000    0.00000
 5 0002    2.55360
 6 0004    4.94760
 7 0003    3.71070
 8 0002    2.31420
 9 0002    2.95260
10 0000    0.00000
```

```
ΔT=090 ⑭

                                CAPTURE
TOTAL     0.06518               99.6%

CH  ΔF      mg/m3
 1 0000    0.00000
 2 0002    0.00760
 3 0001    0.00380
 4 0002    0.00493
 5 0002    0.00426      99.8
 6 0003    0.00620      99.9
 7 0006    0.01240      99.7
 8 0006    0.01160      99.5
 9 0005    0.01233      99.6
10 0001    0.00206
```

Figure 3. Face velocity = 500 ml/min cm^2
Δp = 0.33 in. H_2O, Filtret G-1300.

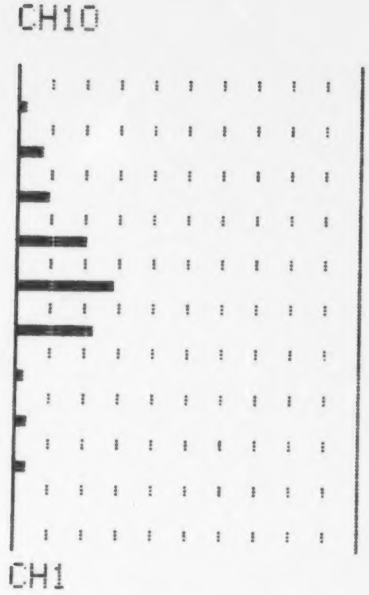

```
N=010 ㊸

TOTAL      12.24132

CH   ΔF      mg/m3
 1 0000    0.00000
 2 0001    0.45486
 3 0001    0.45486
 4 0001    0.29526
 5 0011    2.80896
 6 0014    3.46332
 7 0010    2.47380
 8 0005    1.15710
 9 0003    0.88578
10 0001    0.24738
```

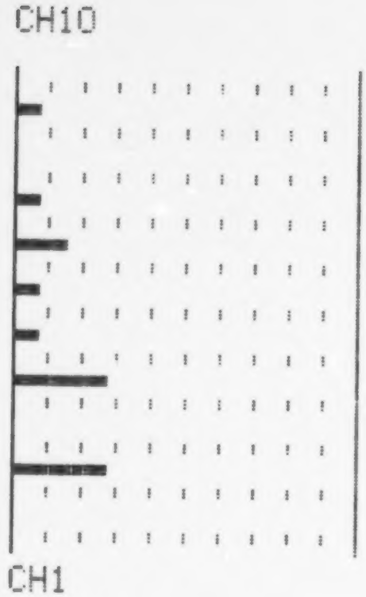

```
ΔT=060 ㊹
                              CAPTURE
TOTAL       0.04100           99.7%

CH   ΔF      mg/m3
 1 0000    0.00000
 2 0002    0.01140            97.5
 3 0000    0.00000            100.0
 4 0003    0.01110            96.2
 5 0001    0.00320
 6 0001    0.00310            99.9
 7 0002    0.00620            99.7
 8 0001    0.00290            99.7
 9 0000    0.00000            100.0
10 0001    0.00310            98.7
```

Figure 4. Face velocity = 500 ml/min cm^2
Δp = 0.33 in. H_2O.Filtret G-1300.

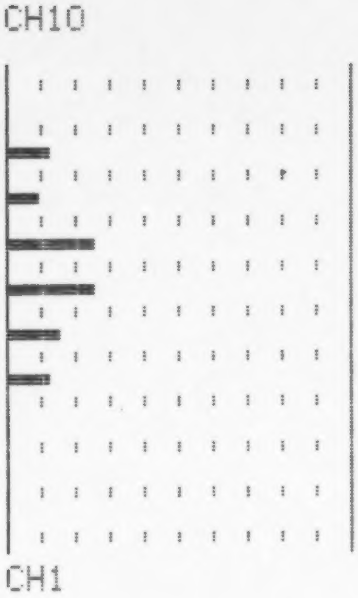

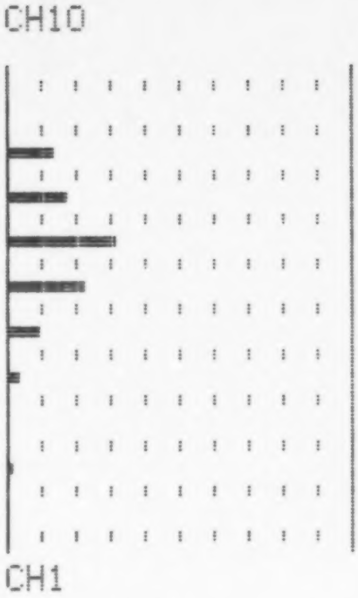

N=003 ㉕

ΔT=040 ㉖

TOTAL 16.27920

TOTAL 0.53880

CAPTURE
96.7%

CH	ΔF	mg/m^3	CH	ΔF	mg/m^3	
1	0000	0.00000	1	0000	0.00000	
2	0000	0.00000	2	0001	0.00855	
3	0000	0.00000	3	0000	0.00000	
4	0002	1.96840	4	0003	0.01665	**99.1**
5	0003	2.55360	5	0011	0.05280	**97.9**
6	0005	4.12300	6	0026	0.12090	**97.1**
7	0005	4.12300	7	0036	0.16740	**95.9**
8	0002	1.54280	8	0022	0.09570	**93.8**
9	0002	1.96840	9	0013	0.07215	**96.3**
10	0000	0.00000	10	0001	0.00465	

Figure 5. Face velocity = 500 ml/min cm^2
Δp = 0.25 in. H_2O, Filtret G-1150.

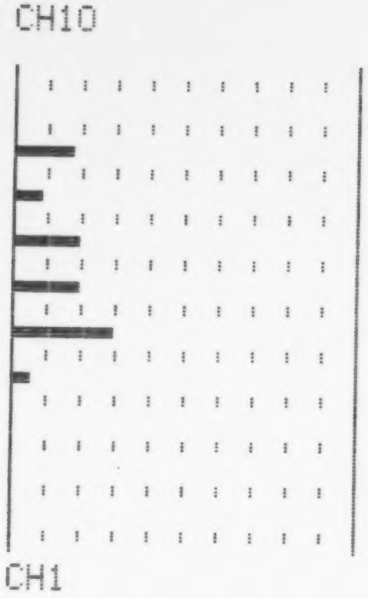

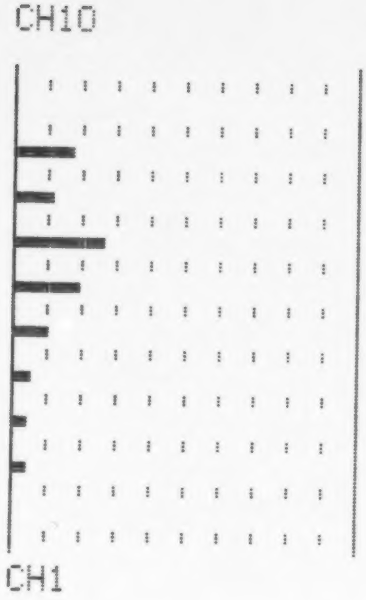

```
N=003 ㉝

TOTAL      17.18360

CH   ΔF       mg/m³
 1 0000     0.00000
 2 0000     0.00000
 3 0000     0.00000
 4 0001     0.98420
 5 0006     5.10720
 6 0004     3.29840
 7 0004     3.29840
 8 0002     1.54280
 9 0003     2.95260
10 0000     0.00000
```

```
ΔT=025 ㉞

TOTAL        0.30528     CAPTURE
                         98.2%

CH   ΔF       mg/m³
 1 0000     0.00000
 2 0001     0.01368
 3 0001     0.01368
 4 0002     0.01776      98.2
 5 0004     0.03072      99.4
 6 0008     0.05952      98.2
 7 0011     0.08184      97.5
 8 0005     0.03480      97.7
 9 0006     0.05328      98.2
10 0000     0.00000
```

Figure 6. Face velocity = 250 ml/min cm^2
Δp = 0.08 in. H_2O, Filtret G-1150.

G-1150, shows somewhat lower capture efficiency as seen in Fig. 5, with a lower pressure drop at 0.25" H_2O. The capture efficiency is also not constant over the size range, being highest at the large end. Fig. 6 shows the results for G-1150 operated at a lower face velocity, 250 cm/min. With a pressure drop of only 0.08" H_2O, this filter medium achieves an overall capture efficiency of 98.2%, with the highest efficiency of 99.4% in the size band 1.6 μm.

RANGE EXTENSION

The examples given here have been obtained with an instrument operating at a flow rate of 240 mℓ/min, and with a transfer volume of 300 μℓ, which is suitable for a range of aerosol mass concentration from about 10 $\mu g/m^3$ (measured with the time-mode) to about 500 mg/m^3 (measured with the volume-transfer-mode). The upper end can be extended by using a smaller transfer volume. A 30 μℓ volume would enable one to measure up to 10 g/m^3 without overloading the crystals. Fig. 7 shows an example with direct sampling of inhaled cigarette smoke.

On the other hand, if one desires to extend the low end, it would be necessary to increase the flow rate. It is possible, within the limitations imposed by the size of the sensing crystal, to increase the flow rate to about 3 ℓ/min. With this higher flow rate and a longer sampling time (up to about 10 minutes), the lower limit in concentration resolution can be extended to about 0.1 $\mu g/m^3$. Some QCM instruments with very stable electronics have been built and operated successfully at these extreme conditions (2).

REFERENCES

1. R. L. Chuan, "Fine Particles, Aerosol Generation, Measurement, Sampling, and Analysis", B.Y.H. Liu, Ed. (Academic Press, New York, 1975) p. 763

2. R. L. Chuan, D. C. Woods and M. P. McCormick, Science 211, 830 (1981)

The work described in this paper was not funded by the U.S. Environmental Protection Agency. The contents do not necessarily reflect the views of the Agency and no official endorsement should be inferred.

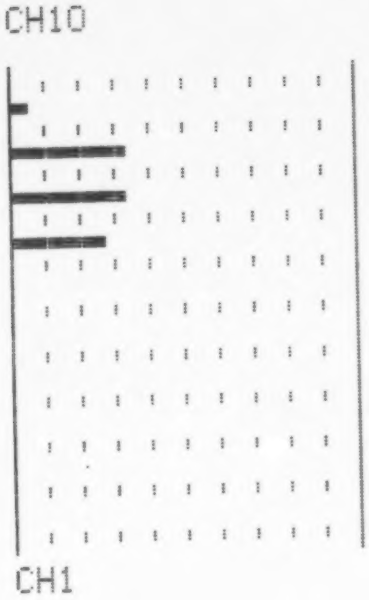

```
 N=001

TOTAL    10190.460

CH  ΔF        mg/m3
 1 0001     6.14460
 2 0001     4.54860
 3 0000     0.00000
 4 0001     2.95260
 5 0004    10.21440
 6 0011    27.21180
 7 1113  2753.3394
 8 1473  3408.8166
 9 1156  3413.2056
10 0228  564.02640
```

Figure 7. Inhaled cigarette smoke (Kent #3 Long Filter).

The work described in this paper was not funded by the U.S. Environmental Protection Agency. The contents do not necessarily reflect the views of the Agency and no official endorsement should be inferred.

Paper 20

NEW AUTOMATIC PIEZOELECTRIC AEROSOL MASS MONITOR

Frederick R. Quant
Gilmore J. Sem
TSI Incorporated

ABSTRACT

Automated measurements of aerosol mass concentrations are being made with a newly developed piezoelectric microbalance. The monitor performs real-time unattended measurements of concentrations from several micrograms (μg) per m^3 to 10 milligrams (mg) per m^3. Fine particles in the 0.01 μm to 10 μm diameter range are precut by a user-selected impactor and then electrostatically precipitated onto the vibrating piezoelectric crystal sensor which detects the true mass concentration. A built-in automatic sensor cleaning system prevents overloading and minimizes errors caused by humidity fluctuations which are an inherent problem of any particle accumulating detector. An internal microcomputer controls the instrument, optimizing operational flexibility. Printed results include: date, time, concentration and averaged concentration.

The paper presents a description of the instrument and data from an indoor monitoring program with concentrations in the 10-200 $\mu g/m^3$ range. In one case two instruments are operated side-by-side giving very repeatable results.

INTRODUCTION

A respirable aerosol mass monitoring instrument has been developed that continuously samples and records aerosol mass concentrations automatically. The mass of aerosol particles is sensed by a piezoelectric microbalance technique that has proven to be accurate and truly mass sensitive[1,2]. The instrument, which has a measuring range from 10 $\mu g/m^3$ to 10 mg/m^3, was used to monitor several offices in both smoking and non-smoking areas. Presented here are:

1) A description of the instrument and its operation,
2) Aerosol mass concentration data from two instruments in a side-by-side comparison, and
3) Mass concentration recorded in several offices.

DESCRIPTION AND OPERATION

The instrument is an automatic respirable aerosol mass monitor (Model 5000) manufactured by TSI Incorporated. Figure 1 shows a view of the monitor which consists of three separate cabinets containing the sensor, data processor, and cleaning reservoir.

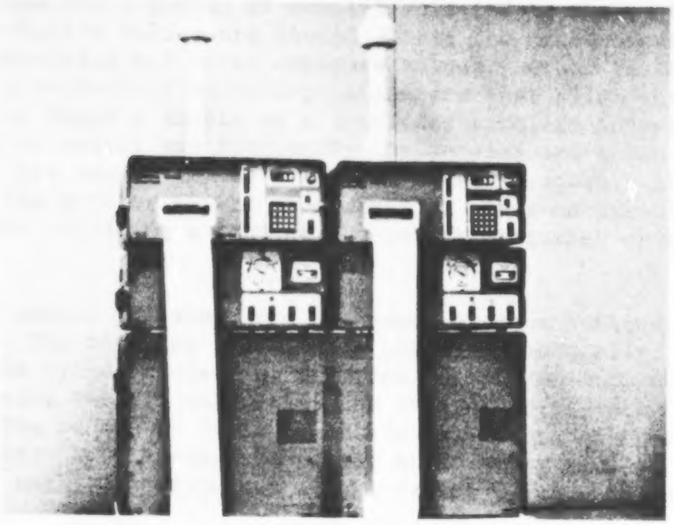

Figure 1. Two aerosol mass monitors in accounting office.

Aerosol is drawn into the monitor's inlet stack at about 150 lpm and is isokinetically sampled within the sensor at 1 lpm. By use of an inlet stack, the loss of larger respirable particles is reduced. Once inside the instrument, the nonrespirable particles are removed by a 3.5 μm impactor or cyclone. Impactors with cut sizes from 0.5 to 10 μm and a 3.5 μm cyclone are available but not used for this experiment. The aerosol then enters the sensing chamber where it is electrostatically precipitated onto the piezoelectric quartz crystal sensor. As particles adhere to the crystal, its oscillatory frequency decreases due to the added mass. The frequency is electrically mixed with a reference frequency of a slightly higher value. The resulting difference frequency is on the order of a few kilohertz and increases in direct proportion to the mass deposited on the sensor.

The microcomputer contained within the processor cabinet initiates a sample measurement by activating the precipitator 30 seconds prior to the measurement of the sensor frequency. At the end of the sample period, the processor measures the sensor frequency and calculates the aerosol mass concentration by:

$$C = \frac{\Delta f}{\Delta t} \frac{60{,}000}{K}$$

where: C = aerosol mass concentration, $\mu g/m^3$
Δf = (sensor final frequency) - (sensor start frequency), Hz
Δt = length of sample, seconds
K - sensor mass sensitivity, 180 Hz/μg

This concentration value is recorded by the printer along with time of day, start and final frequencies, and average concentration. The average concentration is calculated for a number of samples selected by the operator. Up to 100 previous concentration values are stored within the microcomputer. The average is useful for smoothing and total exposure values. Other features of the processor include a variety of operating parameters that allow the user to set up the instrument to begin a sample at a specified time, to adjust the length of the sample, and to select how frequently the samples are taken. Another feature terminates the sample in the event the sensor frequency shifts beyond a preset limit. The printer may be programmed to print-on-demand up to once every two seconds providing a copy of the sensor frequency change over the sample period.

After each sample is taken, the processor gives a command to clean the sensor crystal. The cleaning cycle takes place automatically, lasting 2 minutes. During the cycle, a cleaning solution is sprayed onto the crystal followed by rinsing water. Meanwhile, the crystal is wiped by 8 motor-driven wiper blades. The sensor is dryed by an air jet generated through use of the internal air pump. By cleaning the sensor after every sample, the particle deposit remains small and minimizes errors caused by changes in humidity.

SIDE-BY-SIDE COMPARISON

Two instruments were operated side-by-side in an accounting office, as shown in Figure 1. The office contained three smokers, none of whom were normally closer than 5 meters from the instruments. The office has a floor area of approximately 130 meters^2 and is subdivided into cubicles with half-wall partitions. The total occupancy of the office is normally 16 persons. The two instruments were operated side-by-side for three days (158 half-hour samples). The data is displayed graphically in Figure 2. Correlation between the two instruments was excellent. The three peaks over 80 $\mu g/m^3$ are caused by smokers in close proximity to the instrument. Because the sampling stacks of the 2 instruments were separated by about 70 cm, they measured aerosols of differing concentration during these peaks. The average difference in measurements between the instruments was 1.61 $\mu g/m^3$ and 2.51 $\mu g/m^3$ when including the differences measured on the three peaks. The average mass concentration during the three day period was 42 $\mu g/m^3$. Cyclic, diurnal mass concentrations were observed with peaks at noon between 50 and 70 $\mu g/m^3$ and minimums of about 30 $\mu g/m^3$ in the early morning before employees arrived.

OFFICE COMPARISONS

A single instrument was used to measure the week-long aerosol concentrations in an engineering office and a research office. The engineering office has approximately 130 m^2 of floor area and contained two smokers, one of whom was in a cubicle adjacent to the instrument. The measured concentrations are displayed in Figure 3. A cyclic diurnal variation of aerosol mass concentration is evident. The daytime concentrations are higher than those in the accounting office. Even more pronounced is the variation of concentrations in consecutive half-hour measurements. A dip in concentration occurs each day around noon corresponding to the employee lunch period. On Friday,

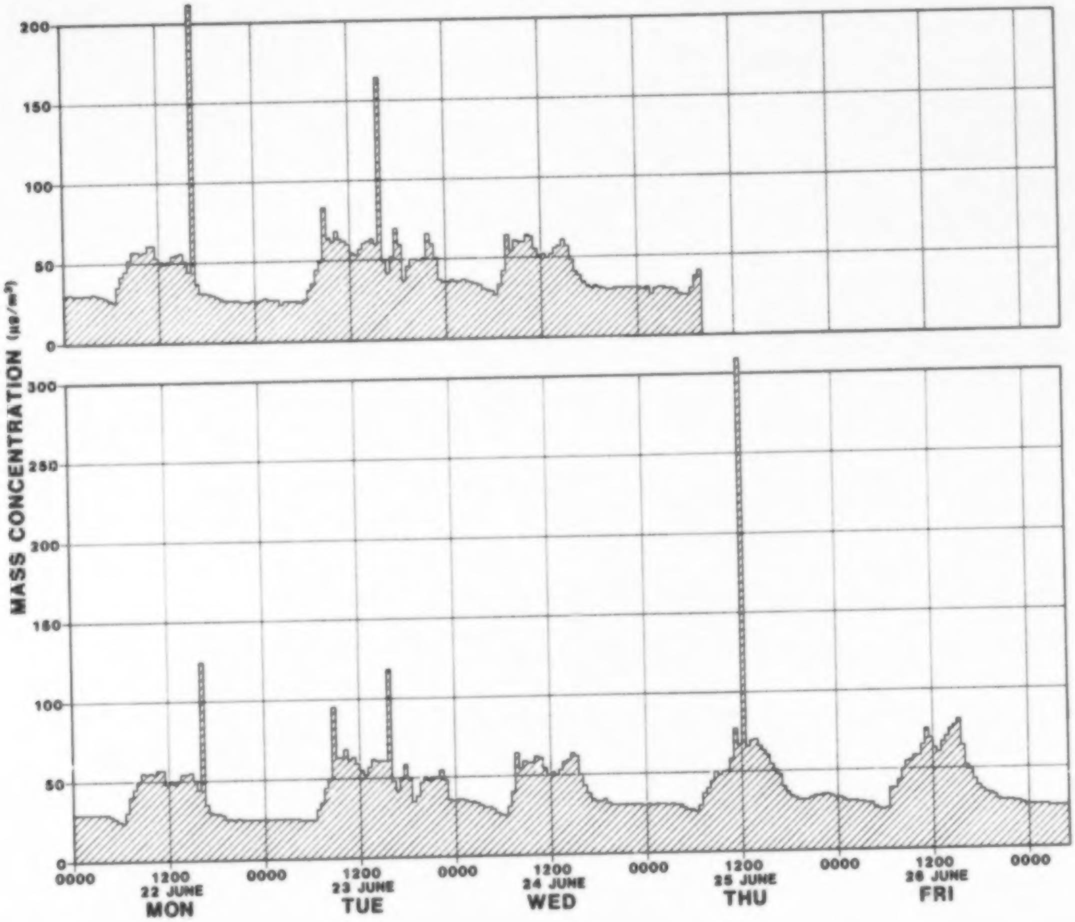

Figure 2. Aerosol mass concentrations in accounting office as measured by two side-by-side instruments.

a holiday, concentrations decayed to a nominal weekend level of about 35 $\mu g/m^3$. On Wednesday, the smoker adjacent to the instrument was absent, causing considerably lower concentrations for that day. The decay of aerosol concentration follows an exponential characteristic. A manual fit was applied to Tuesday's data and a time constant of 1.8 hours was determined. The data matched the exponential curve well, though a better fit could have been realized if shorter samples of 10 or 15 minutes were used. The primary source of aerosol, the smoker, left the office between 3:30 and 4:00 p.m. each day, providing a good step function.

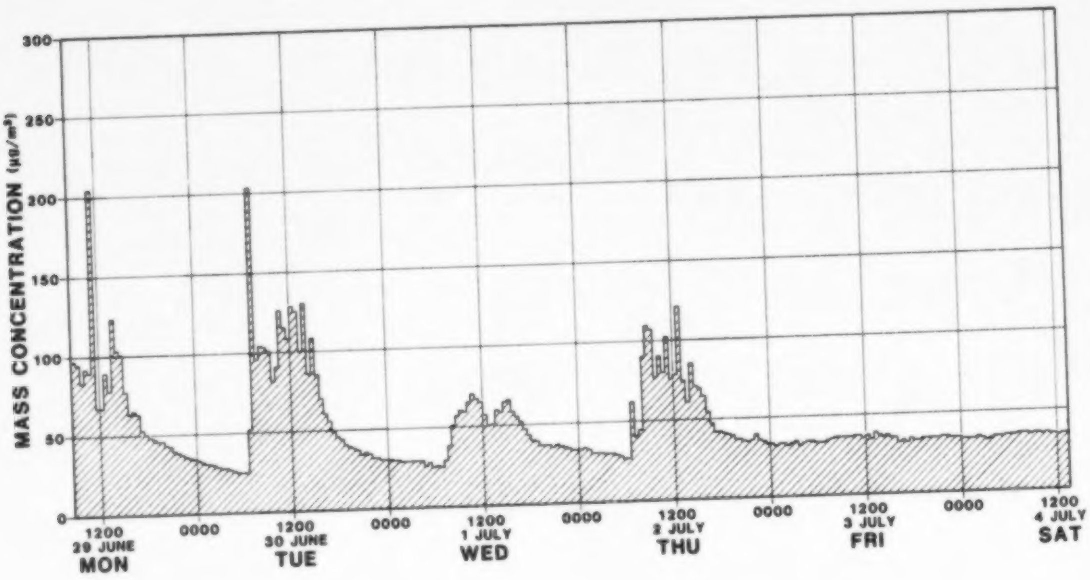

Figure 3. Aerosol mass concentrations in engineering office.

The research office is larger than either the accounting or engineering offices with approximately 280 m^2 of floor area. About 15 people normally occupy the office in cubicles along its perimeter. The monitor was located at one end of the office about 10 meters from the only smoker in the room. Figure 4 shows the data. The usual cyclic diurnal variation is again seen. Consecutive concentration measurements were considerably more stable then those observed in the engineering office. The single large peak was caused by a smoker from another area curiously watching the instrument. The decay characteristics of the office concentrations did not tend to be exponential. The observed decay appeared to have a longer time constant, probably caused by the poorer ventilation in the research area in the vicinity of the instrument.

CONCLUSIONS

The automatic respirable aerosol mass monitor, with its internal microcomputer, is capable of making unattended measurements for periods as long as several weeks. It allows experimental measurement of aerosol variations and trends over periods ranging from minutes to weeks. Two monitors are highly repeatable in side-by-side comparisons. Concentration measurements made in commercial offices displayed cyclic variations with noon peaks of 50 to 150 $\mu g/m^3$ and with evening and early morning minimums around 35 $\mu g/m^3$. Large variations in consecutive aerosol concentration measurements were found with the monitor in close proximity to a smoker. These large variations and peaks make the selection of sampling location of the measuring instrument very important when making total exposure measurements.

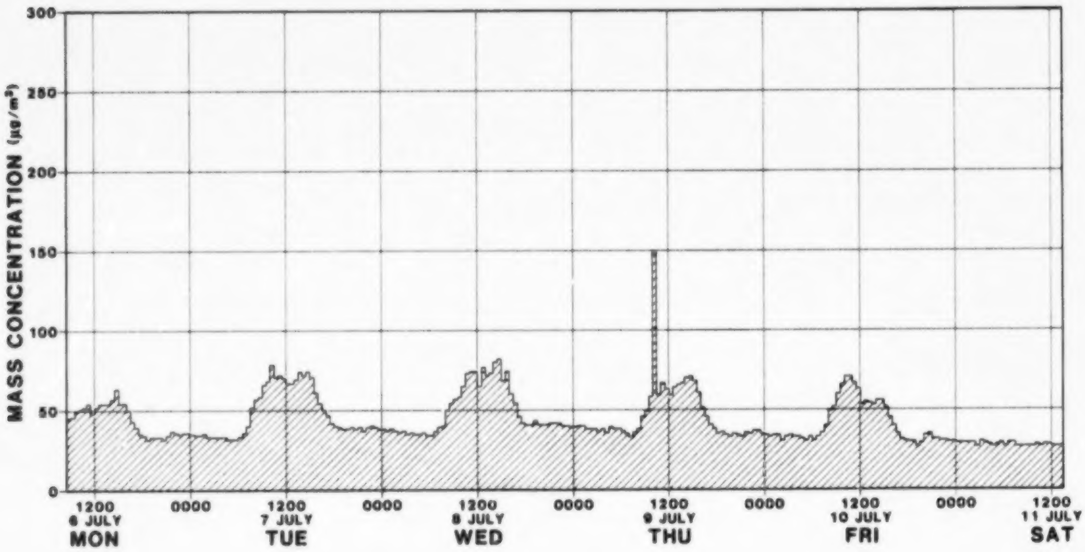

Figure 4. Aerosol mass concentration in research office.

REFERENCES

1. Sem, C.J., K. Tsurubayashi, and K. Homma. Performance of the Piezoelectric Microbalance Respirable Aerosol Sensor. Am. Ind. Hyg. Assoc. J. 38:580-588, 1977.

2. Tsurubayashi, K., and H. Kano. Field Testing of Automatic Piezoelectric Microbalances for Outdoor Aerosol Mass Concentration Measurements. EPA-600/9-80-004, Proceedings: Advances in Particle Sampling and Measurement (Daytona Beach, FL, October 1979), W.B. Smith, ed., pp. 217-241, 1980.

The work described in this paper was not funded by the U.S. Environmental Protection Agency. The contents do not necessarily reflect the views of the Agency and no official endorsement should be inferred.

Paper 21

A NEW PRACTICAL TECHNIQUE FOR REAL-TIME PARTICULATE MASS MONITORING

Hiroshi Noguchi, Nobuhisa Mori
and Tokuta Inoue
Higashifuji Technical Center
Toyota Motor Co., Ltd.

ABSTRACT

A new instrument has been developed for the continuous measurement of diesel particulate emissions in conjunction with the dilution tunnel method. The pressure drop caused by the loading of particulate on a sampling filter is monitored continuously and the instantaneous particulate mass emission is calculated. The accuracy, linearity, and time resolution of this instrument have been examined. In addition, the continuous particulate emission data provided with this technique are compared with FTP test results by a dilution tunnel-microbalance method. These results show the usefulness of this technique for diesel particulate mass monitoring during a transient cycle, such as LA#4.

INTRODUCTION

A dilution tunnel system was proposed by the Environmental Protection Agency in 1979 as a regulatory sampling and measurement method for diesel particulates determination. This system was designed to determine the total mass of diesel particulates emitted during a transient test cycle such as LA#4, in which exhaust gas containing particulates was mixed and diluted with air at the mixing point and vacuumed into a sampling line, and then the particulates were sampled on a particulate filter set into the sample line. In this method, six samples are needed for one FTP test and they are weighed by a microbalance after 1 - 56 hours stabilization. A typical dilution tunnel and the handling procedure of particulate filters are shown on Figure 1 and Figure 2.

On the other hand, there has been an obvious need for detailed information on the transient, instantaneous emission rate of diesel particulates. In the past few years, several methods for real-time particulate mass monitoring,

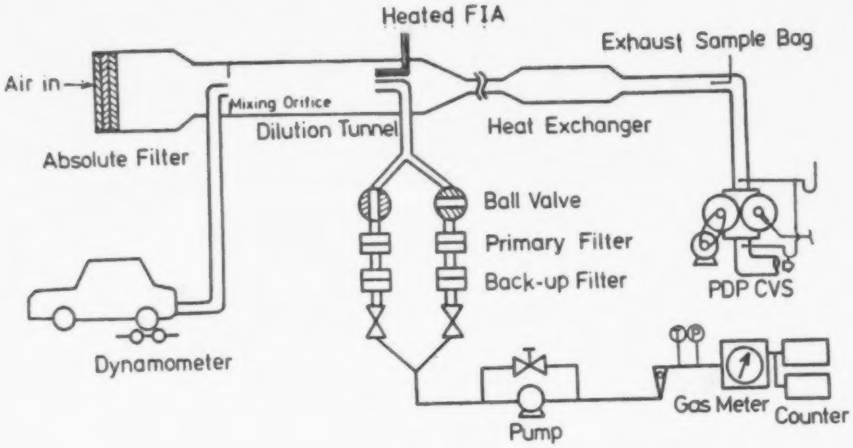
Heated FIA
Exhaust Sample Bag
Air in
Mixing Orifice
Dilution Tunnel
Heat Exchanger
Absolute Filter
Ball Valve
Primary Filter
Back-up Filter
PDP CVS
Dynamometer
Pump
Gas Meter
Counter

Figure 1. Dilution tunnel system.

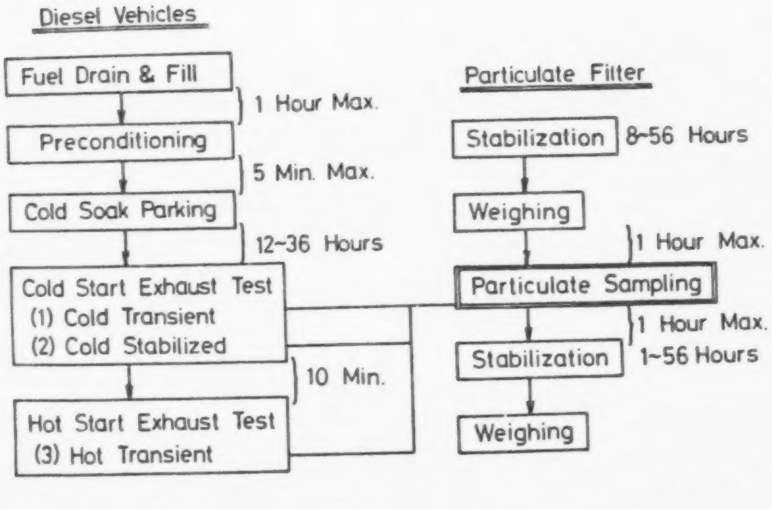
Diesel Vehicles
Fuel Drain & Fill
1 Hour Max.
Preconditioning
5 Min. Max.
Cold Soak Parking
12~36 Hours
Cold Start Exhaust Test
(1) Cold Transient
(2) Cold Stabilized
10 Min.
Hot Start Exhaust Test
(3) Hot Transient
Particulate Filter
Stabilization
8~56 Hours
Weighing
1 Hour Max.
Particulate Sampling
1 Hour Max.
1~56 Hours
Stabilization
Weighing

Figure 2. Handling procedure of particulate filter.

such as smoke opacity meter, light scattering, photoacoustic measurement and piezoelectric crystal microbalance have been introduced and applied for diesel particulate emission measurement and other research needs. Although these methods have significant advantages respectively, they also have a problem to be improved, and furthermore, correlation data between these methods are not well known. In this paper, a new practical technique (Pressure Drop Monitoring) is proposed for real-time particulate mass monitoring, which is under development in our laboratory. Principle and performance of this technique are described below.

PRINCIPLE AND SCHEME OF PRESSURE DROP MONITORING

Principle

The Pressure Drop Monitoring (PDM) technique is based on the Carman-Kozeny equation. The pressure drop across a particulate filter is proportional to the filter face velocity and viscosity coefficient of sample flow and also is approximately proportional to particulate mass collected on that filter within a fixed range. A relationship between particulate mass concentration (C) and the rate of pressure drop increase (dp/dt) can be written as follows.

$$C = K \left[\frac{\mu_0}{\mu} \cdot \frac{273 + T_0}{273 + T} \right] \frac{1}{Q^2} \cdot \frac{dp}{dt} \qquad (1)$$

where C : particulate mass concentration

P : pressure drop across filter

Q : sample flow rate

μ : coefficient of viscosity

T : temperature of sample gas across filter

t : time

K : constant

Schematic Diagram of Pressure Drop Monitoring

A schematic diagram of Pressure Drop Monitoring is shown in conjunction with a regulatory dilution tunnel system in Figure 3. The Pressure Drop Monitoring system is composed of several elements, such as thermometer, differential pressure transducer, flow control device, and calculator. The sample flow rate (Q) is kept at a constant level by an orifice, pressure sensor, valve, servomotor, and controller. The pressure drop signal (ΔP), together with sample flow rate (Q) and gas temperature (T), are fed into a calculator which calculates the particulate mass/unit volume (C) based on the calibration curve each second. A constant (K) has to be determined in advance for the real-time particulate mass calculation and the pressure drop across a particulate filter has to be correlated with the particulate mass collected on that filter for the estimation of particulate total mass.

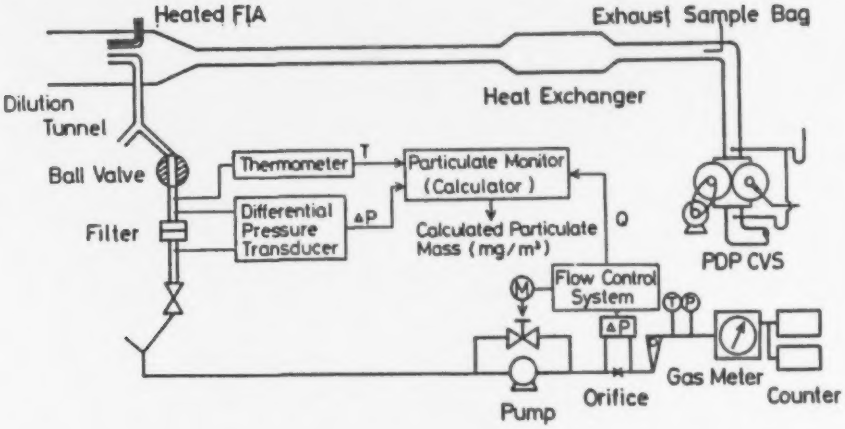
Heated FIA
Exhaust Sample Bag
Dilution Tunnel
Heat Exchanger
Ball Valve
Thermometer
T
Particulate Monitor (Calculator)
Filter
Differential Pressure Transducer
ΔP
Calculated Particulate Mass (mg/m³)
Q
PDP CVS
M
Flow Control System
T
P
ΔP
Gas Meter
Orifice
Counter
Pump

Figure 3. Schematic diagram of pressure drop monitoring.

RESULTS AND DISCUSSION

Deviation of Sample Flow Rate

Relationships between particulate loading and sample flow rate are shown in Figure 4. A dotted line shows the sample flow rate of a commonly used regulatory dilution tunnel system and a solid line shows the flow rate controlled by the above flow control device of the PDM method. The sample flow rate at the regulatory dilution tunnel was found to decrease gradually with increased pressure drop, and it became about 10% lower at the test end. On the other hand, the sample flow rate controlled by the flow control device was kept at a constant level, and its deviation was within 1% during the test. Particulate mass concentration C is significantly affected by the deviation of sample flow Q as described in Equation 1.

Comparison of Particulate Filters

A comparison of particulate filters is shown in Figure 5, concerning the pressure drop increase due to the particulate loading. These tests were carried out operating a diesel engine at a light load condition. The sample flow rate and gas temperature were kept at a constant level during these tests. The filters tested were two fluorocarbon-coated filters (Types A and B) and a fluorocarbon-based filter (Type C); they are commonly used for particulate sampling in the regulatory dilution tunnel system. As a result of these tests, a fluorocarbon-coated filter (Type A, Pallflex TX40HI20WW) was selected for the PDM method. Another fluorocarbon-coated filter was sometimes broken and the initial pressure drop of the fluorocarbon-based filter was found to be too high for the PDM method.

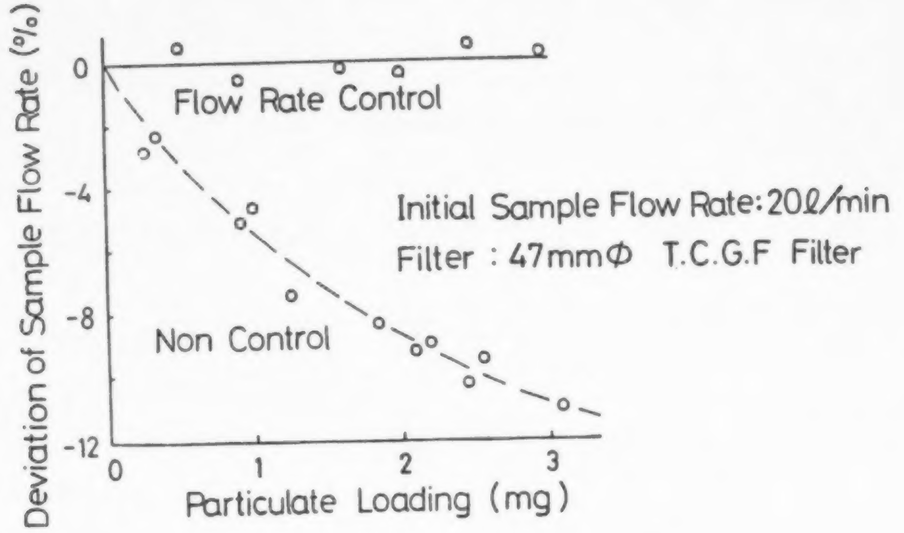

Figure 4. Relationship between particulate loading and sample flow rate.

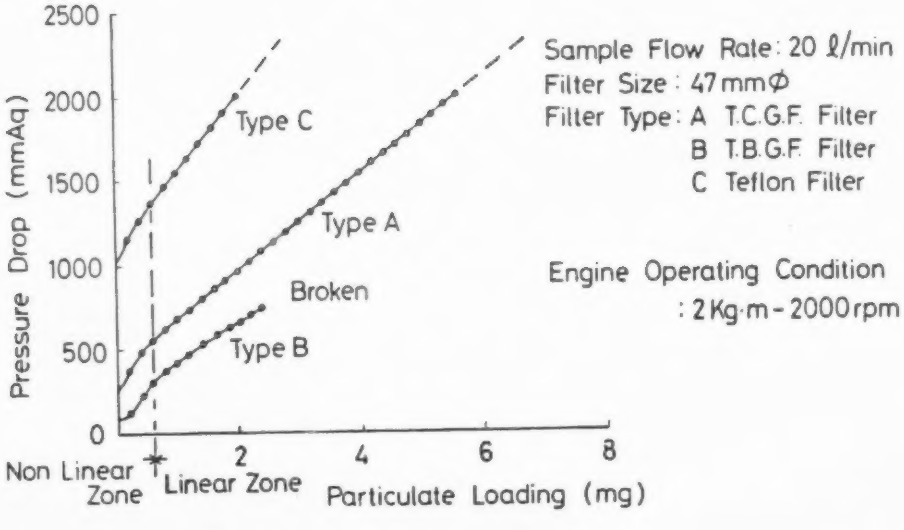

Figure 5. Comparison of particulate filters.

Relation between Particulate Loading and Pressure Drop

A typical relationship between particulate loading on a filter and the pressure drop across the filter is shown in Figure 6. The relationship has linearity except for the first stage within 0.5 - 0.6 mg of particulate loading and it shows that particulate filters should accumulate particulates of 0.5 - 0.6 mg before the tests to obtain more accurate results in PDM method.

Tests were repeated 24 times operating a diesel engine at a light load and a heavy load condition using 24 particulate filters, and then a calibration coefficient ($\bar{a}$) was determined for the estimation of particulate total mass. The calibration coefficient ($\bar{a}$) was 614.4 mmAq/mg at 35 ℓ/min sample flow rate and 30°C gas temperature, and the coefficient of variation was 0.045 for these data.

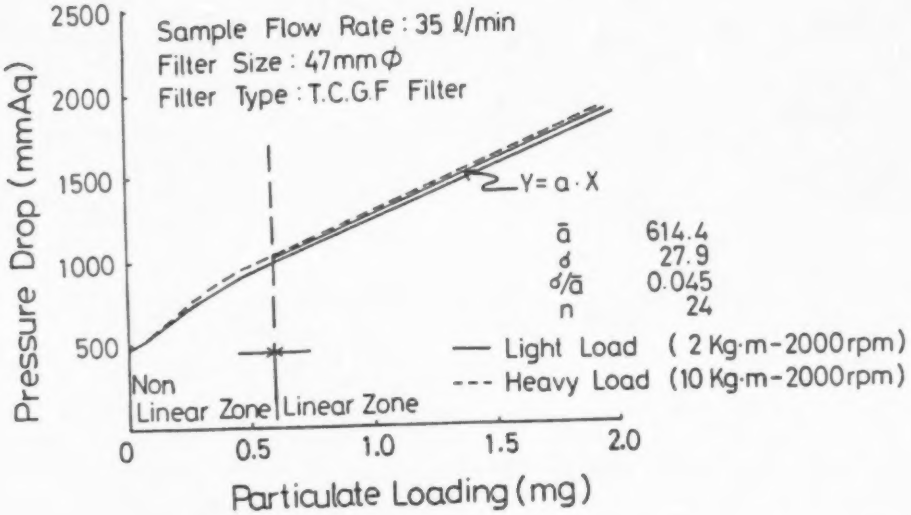

Figure 6. Relationship between particulate loading and pressure drop.

Real-Time Particulate Mass Monitoring

A real-time particulate emission trace of our production diesel vehicle is shown in Figure 7. Dotted lines show vehicle speed during a part of the LA#4 driving cycle. The pressure drop (ΔP) starts at about 1000 mmAq and ends at 2250 mmAq. The mean increase of pressure drop is about 2.5 mmAq/sec. Another solid line changed rapidly, showing the particulate mass concentration, and it varies in the range of 0 to 40 mg/m^3. Time resolution is one second.

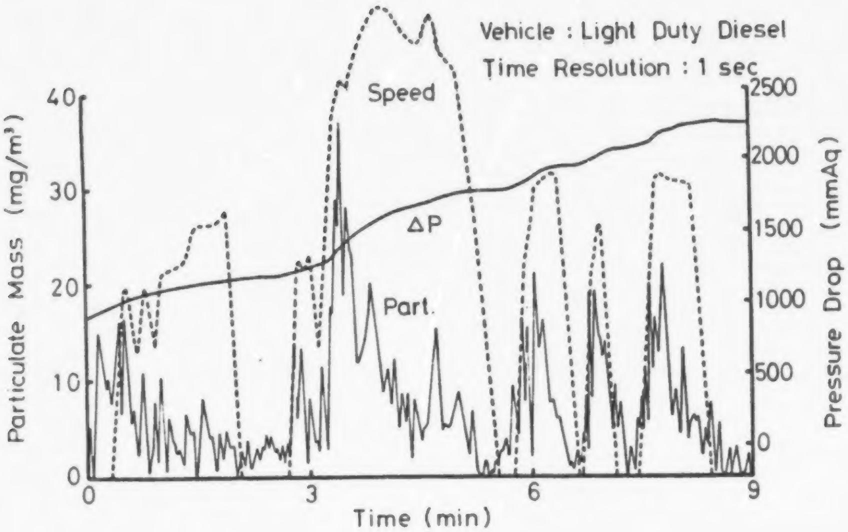

Figure 7. Real-time particulate mass emission trace.

The transient particulate mass emission rates at various vehicle operating conditions are found in this trace, and they are remarkably higher in the high load conditions.

Comparison of FTP Data and PDM Data

A comparison of the total mass particulates of FTP weighed data and those of PDM data is shown in Table 1. After the LA#4 tests were repeated 10 times, FTP weighed data and PDM data were compared for the same samples. The mean value of total mass particulate ($\overline{x}$) was 1.989 mg for FTP and 1.909 mg for PDM, and difference of these data was about 4%. The coefficient of variation was 0.041 for FTP and 0.070 for PDM.

Table 1. Comparison of FTP weighed data and PDM data

Vehicle : Light Duty Diesel
Test : LA#4 0-505 (Hot)

Test Number	FTP Weighed (mg) (A)	PDM (mg) (B)	(B)/(A)
1	1.952	1.820	0.932
2	1.969	1.740	0.884
3	1.909	1.704	0.893
4	2.014	2.001	0.994
5	2.015	1.958	0.972
6	1.984	1.922	0.969
7	1.966	1.885	0.959
8	2.201	2.168	0.985
9	1.953	1.929	0.988
10	1.930	1.958	1.015
Mean Value ($\bar{x}$)	1.989	1.909	0.959
Standard Deviation (σ)	0.081	0.133	
$\sigma/\bar{x}$	0.041	0.070	

CONCLUSIONS

A new practical technique (Pressure Drop Monitoring) has been developed for real-time particulate mass monitoring.

- Accuracy (variation of calibration coefficient) : 0.045 as coefficient of variation
- Time resolution : one second

Total mass particulate emission data for PDM and the data of FTP weighed method were compared for the same samples, and good agreement was obtained between these data.

- PDM data are about 4% lower than FTP weighed data.
- The coefficient of variation is 4% for FTP weighed data and 7% for PDM data.

The work described in this paper was not funded by the U.S. Environmental Protection Agency. The contents do not necessarily reflect the views of the Agency and no official endorsement should be inferred.

Paper 22

COHERENT DETECTION OF PHASE-SHIFTED LIGHT FROM SUBMICRON PARTICLES

Donald R. Pettit
Thomas W. Peterson
Department of Chemical Engineering
University of Arizona

ABSTRACT

A single particle counting instrument, called the coherent optical particle spectrometer (COPS), has been developed for sizing airborne particles. By utilizing the van Cittert-Zernike conditions, phase-shifted light from small particles at the focal point of a lens can be shown to be coherent. The magnitude of this phase shift can then be measured via optical heterodyne detection of the coherently superimposed carrier and local oscillator beams, using a shot-noise-limited square-law detector.

Phase modulation occurs as single particles flow through the focal point of the lens, yielding a pulse the height of which represents the power in the phase-modulated side-bands. This signal can be related to the particle diameter. Theoretical estimates for an ideal minimum detectable particle diameter are of the order of 5×10^{-3} micrometers (μm), and for a practical system are of the order of 5×10^{-2} μm. Detection of only those particles in the focal point region suggests that in-situ measurements are possible.

An apparent monotonic calibration curve of signal height vs. particle diameter has been established experimentally with polystyrene latex spheres in the range 0.085 to 3.0 μm diameter. TiO_2 smokes with typical diameters of 0.01 to 0.02 μm have also been detected, as have water droplet fogs with typical diameters of 5 μm and above. Tobacco smoke was found with this technique to range between 0.1 and 2.0 μm with an average size of 0.3 μm, based on the previously determined calibration curve.

INTRODUCTION

Considerable interest exists in the ability to determine the size distribution of airborne particulate matter. Atmospheric aerosols, industrial aerosols, combustion-generated aerosols, and the like can quite easily span a range of particle diameters from 0.001 to 10 μm. Because of the variable effect of particle size on visibility degradation, health, in-plant corrosion, etc., it is important to determine not only the total aerosol burden suspended in a gaseous medium (e.g., $\mu g/m^3$ of all suspended material), but the size distribution of that suspended material as well.

Currently, there is no single technique available for continuously determining the size distribution of aerosols over the entire range of interest. Typically two instruments are utilized to span this range. For particles between 10^{-3} and 1.0 μm, particle size is often determined on the basis of the electrical mobility of the particle. A complete description of the instrument used to measure electrical mobility is found in a paper of Liu and Pui[1]. For particles greater than about 0.1 μm diameter a variety of optical detection techniques have been utilized. Both monochromatic and polychromatic light sources have been used, as have a wide range of detection systems. General reviews of optical particle counting (OPC) techniques are given by Whitby and Willeke[2] and Willeke and Liu[3]. The minimum detectable particle size via optical techniques is nominally greater than 0.1 μm, due to signal-to-noise limits of background scattering from air molecules. Table 1 lists references to articles describing a variety of unique optical particle counters, either available commercially, available as a research tool, or proposed conceptually. Table 2 lists references of articles providing comparison of one or more OPC's. A complete list of applications of OPC's would be too lengthy to present here, but useful applications include atmospheric aerosol measurement, clean room measurements, source-related measurements (combustion, etc.) and characterization of particle physics and chemistry.

While laser-based instruments are included in the list of OPC's, no laser-based instrument to date utilizes the principle of coherent optical particle detection. Instead, the laser is used simply as a concentrated light source from which the intensity of scattered light is measured. Typically, the particle moves across a viewing zone that may contain a network of interference fringes so velocity as well as size can be ascertained. In coherent optical particle detection the particle size is determined from the phase shift due to the presence of the particle in the light beam. This measurement is made possible by utilizing the coherent properties of light available from the laser.

In summary, two separate instruments utilizing distinctly different physical principles are required to determine the size distribution of suspended airborne particulate matter. It would be quite useful, therefore, to develop a single particle counting instrument (as opposed to ensemble techniques, which measure average quantities only) which (1) measures particles over the entire size range of interest, (2) measures particle concentrations typical of atmospheric or industrial particle loadings, and (3) shows promise for application under in-situ measurement conditions.

Such a technique is available using the principles of optical heterodyne detection (OHD), as described by Jacobs[21], Gould, et al.[22], and Bassan and Ciliberto[23]. The major advantage of the OHD technique over other methods is the ability to span nearly the entire particle size range of interest for aerosol concentrations typical of both atmospheric and industrial process conditions. It is not a "high-powered" laser technique, in that relatively "weak" laser sources are acceptable. Therefore all the problems of open-cavity or strongly focused laser systems (such as particle evaporation) are avoided. Furthermore, by careful optical configuration, the control volume size is not defined by beam intensity gradients, flow constraints, or optical masks. The major difference between this OHD technique and other particle-size instruments

TABLE 1. OPTICAL PARTICLE COUNTERS

Reference	Instrument(s)	Light Source	Size Range, μm	
Colak and Yeh[4]	Theoretical	Laser	-	Considered scattering from moving particles in a strongly focused laser beam.
Hirleman[5]	MRSPC (Multiple ratio single particle counter)	Laser	0.4-3.0	Multiple-angle measurements of light scattered from single particles. View volume ~ 10^{-6} cm^3.
Hirleman[6]	Theoretical	Laser	-	Proposed technique for simultaneous size and velocity measurements.
Knollenberg and Luehr[7]; Knollenberg[8]	ASAS (Active scattering aerosol spectrometer)	Open cavity laser (~1W)	0.05-5.0	Open cavity laser measures forward (4°-22°) and backward (176°-158°) scattered light. Sample cross-section ~0.02mm^2.
	LAS (laser aerosol spectrometer)	Laser	0.3-1.0	Particle in sample volume determined by double pulse height analysis.
	FSSP (Forward scattering spectrometer probe)	Laser	0.4-6	Particle in sample volume determined by transit-time analysis.
Lepper[9]	Climet CI-208	Quartz-halogen lamp	0.3-10	15°-105° scattered light detected. Maximum allowable concentration < 10^3 cm^{-3}.

TABLE 1. (Cont'd)

Reference	Instrument(s)	Light Source	Size Range,μm	
Lieberman[10,11,12]	Royco 225	Incandescent	0.3-15	11°-30° scattered light detected.
	Royco 226	Laser	0.12-6.1	35°-120° scattered light detected.
	Royco 203,220	Incandescent	0.2-8	42°-138° scattered light detected.
Muly and Frock[13]	Leeds and Northrup Microtrac	Laser and incandescent	0.5-20	Multiple angle near-forward scattered laser light plus right angle scattered white light.
Rimberg[14]	Prototype Laser method	Laser	0.5-2.0	Utilizes both laser and ellipsoidal mirror to maximize intensity of scattered light from particle.
Wyatt and Phillips[15]	Science Spectrum Differential II	Laser	0.1-5.0	Angular dependence of light scattered from single stationary particles measured by rotating photomultiplier.

TABLE 2. OPTICAL PARTICLE COUNTER COMPARISONS

Reference	Instruments(s)	Remarks
Clark and Avol[16] (1979)	Climet 208 Royco 220	Examined performance relative to pulse height analysis, pulse shape and noise level.
Gebhart et al.[17] (1975)	LASS and LASI (Laser aerosol size spectrometer and low-angle scattering instrument)	Discusses laser vs. white light, responses to particle shape, refractive index, differences in response of particles above and below the wavelength of light.
Hirleman[18] (1980)	Laser-based single particle counters	Reviewed radiation-cross-section, scattering ratio, interferometric techniques. Discussed size range, dynamic range, sample space, particle shape and refractive index effects.
Houser[19] (1980)	Various laser-based techniques	Reviewed laser based particle counters based on scattering intensity ratioing, interferometry, and holography.
Rimberg[14] (1979)	Prototype laser method Bausch and Lomb 40-1 Royco 220	Examined advantages of new laser-based method over commercial instruments with respect to size resolution, count inefficiency, multi-valued response, and refractive index.
Tang et al.[20] (1979)	Science Spectrum Differential II Climet CI-208	Utilized both instruments in the measurement of growth rates of hygroscopic aerosols.

TABLE 2. OPTICAL PARTICLE COUNTER COMPARISONS

Reference	Instruments(s)	Remarks
Clark and Avol[16] (1979)	Climet 208 Royco 220	Examined performance relative to pulse height analysis, pulse shape and noise level.
Gebhart et al.[17] (1975)	LASS and LASI (Laser aerosol size spectrometer and low-angle scattering instrument)	Discusses laser vs. white light, responses to particle shape, refractive index, differences in response of particles above and below the wavelength of light.
Hirleman[18] (1980)	Laser-based single particle counters	Reviewed radiation-cross-section, scattering ratio, interferometric techniques. Discussed size range, dynamic range, sample space, particle shape and refractive index effects.
Houser[19] (1980)	Various laser-based techniques	Reviewed laser based particle counters based on scattering intensity ratioing, interferometry, and holography.
Rimberg[14] (1979)	Prototype laser method Bausch and Lomb 40-1 Royco 220	Examined advantages of new laser-based method over commercial instruments with respect to size resolution, count inefficiency, multi-valued response, and refractive index.
Tang et al.[20] (1979)	Science Spectrum Differential II Climet CI-208	Utilized both instruments in the measurement of growth rates of hygroscopic aerosols.

based on laser light sources is the use of the coherent properties of the light. The OHD technique herein described utilizes a near-forward gathering collector, but does not depend on the detection of light at any one particular angle. Since the technique to be described depends on the coherent detection of phase-shifted light, the instrument is appropriately referred to as a coherent optical particle spectrometer (COPS).

THEORY

If a single particle is allowed to interact with light at the focal point of a lens, the van Cittert-Zernike theorem (Born and Wolf[24]; Gould et al.[22]) will show that the gathered light is coherent if the interaction is contained in a region smaller than the resolution limit of the gathering lens. This gathered light will exhibit an average phase shift determined by the solid angle of view of the lens. If this beam is coherently superimposed with a local oscillator beam upon a shot-noise-limited square law detector, the power in the phase-shifted side bands can be measured and related (via scattering mechanisms) to the particle diameter.

Consider the following conditions for a COPS (Figure 1). A Jamin interferometer is used to separate the laser light into two beams, a subject beam and local oscillator beam, and recombine them in a coherent manner at a photodetector. In the path of the subject beam a pair of lenses is arranged so the beam emerging from the second lens remains collimated. The subject beam makes one path through the view volume and only near-forward light is detected. The local oscillator beam, with adjustable relative phase, passes undisturbed to the photodetector. Now consider single spherical particles passing at a constant rate through the beam waist perpendicular to the optical axis. If the particle is smaller than the resolution limit of the second lens, the gathered light will be coherent (as specified by the van Cittert-Zernike theorem) and will contain average phase shift information determined by the characteristics of the particle. The subject beam is then coherently superimposed with the local oscillator at the photodetector. The subject beam will be phase modulated by the particles at a frequency equal to the rate of particles passing through the beam waist and can be detected with optical heterodyne techniques.

Since this technique is based on measuring single particles as they pass through an optical viewing volume, it is important to define the radial and axial extent of this viewing zone. It would be desirable to have a viewing volume such that any particle contained inside will give the same signal regardless of its internal position or trajectory, with the boundaries of the region being sharply defined.

The physical geometry of the optical viewing volume for the COPS is shown in Figure 2. A Gaussian beam waist is provided by the primary lens, which has an aperture large enough to pass the power in the subject beam. The light is focused to a waist diameter d_w, defined by the $e^{-\pi}$ wave field amplitude point. The axial waist length Z_w is the collimated portion of the beam and extends one Rayleigh length in each direction from the beam waist. The Rayleigh length is the distance where the beam spreads to $\sqrt{2}$ times the beam waist diameter.

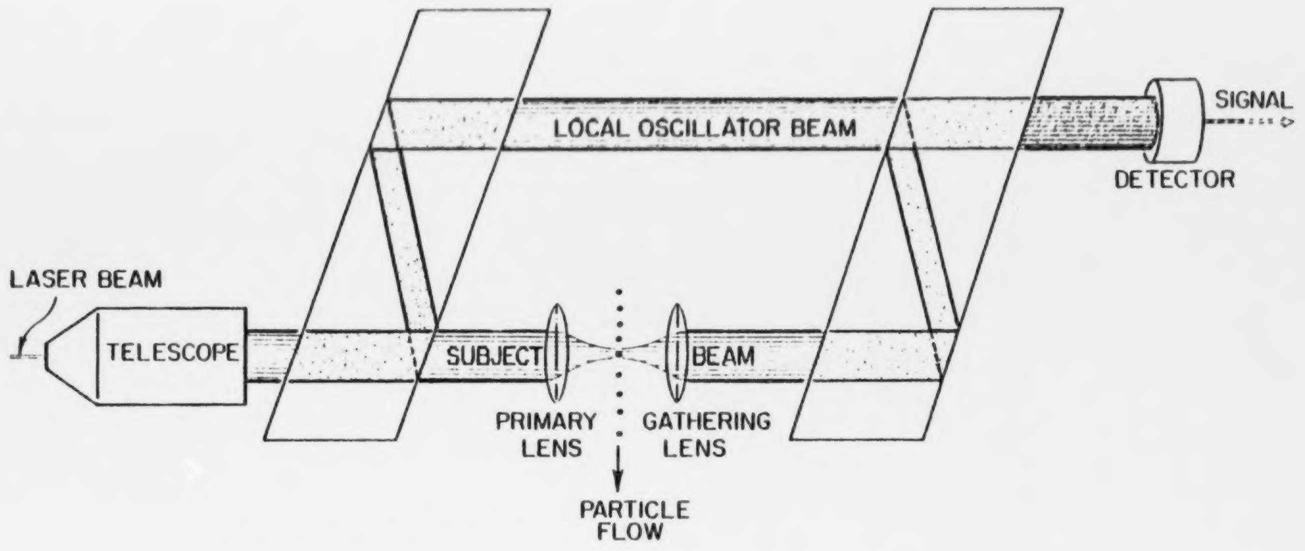
LOCAL OSCILLATOR BEAM
SIGNAL
DETECTOR
LASER BEAM
TELESCOPE
SUBJECT
BEAM
PRIMARY LENS
GATHERING LENS
PARTICLE FLOW

Figure 1. Jamin interferometer, showing local oscillator and subject beams.

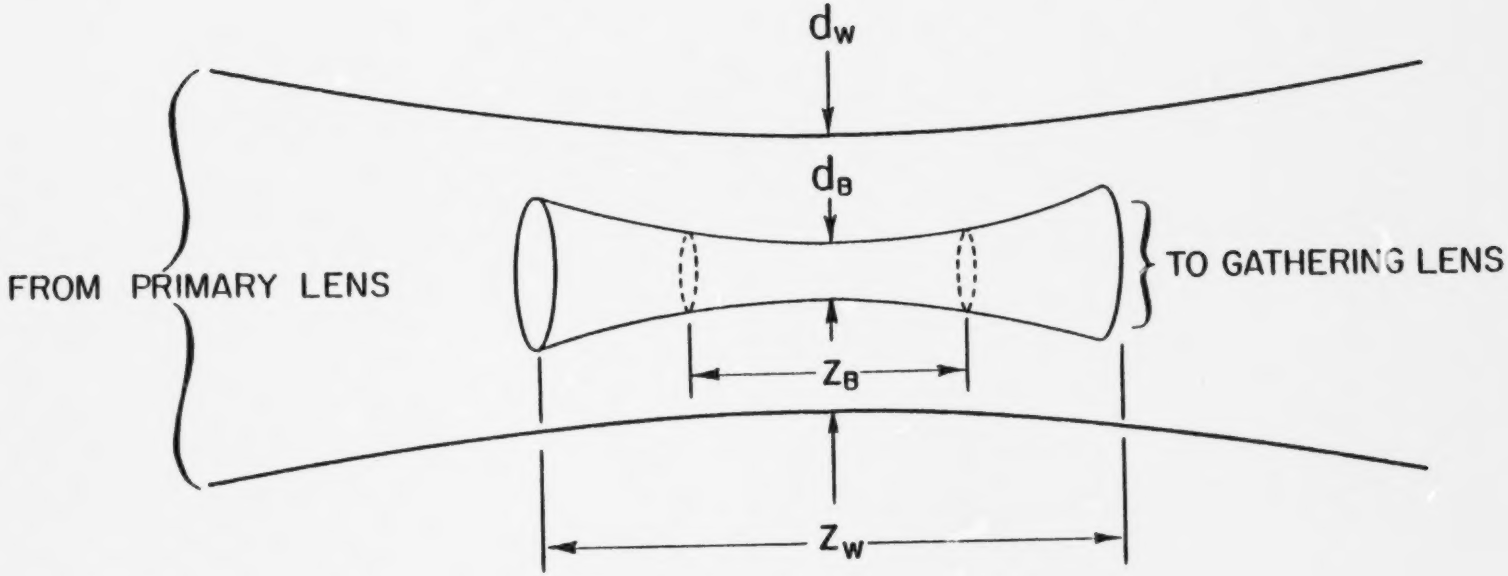
d_W
d_B
FROM PRIMARY LENS
TO GATHERING LENS
Z_B
Z_W

Figure 2. Geometry of the optical viewing volume of the coherent optical particle spectrometer.

The gathering lens is responsible for defining the limits of the viewing volume with its depth of focus and resolution-limited blur spot diameter, d_B. Phase-shifted light by particles within d_B will not be resolved into independent wave fronts and will appear as coherent plane waves downstream of the gathering lens, as shown by the van Cittert-Zernike theorem.

The radial extent of the viewing volume will be determined by d_B. Phase-shifted light from particles within this zone will be imaged as coherent plane waves propagating down the optical axis that are parallel and coincident with the local oscillator beam. Light scattered by particles radially outside this zone will be imaged as coherent plane waves propagating at an angle to the optical axis and will not be measured by the coherent detection methods.

The axial extent of the zone where the van Cittert-Zernike theorem applies will be determined by the depth of focus of the gathering lens. The axial extent of the optical viewing volume, Z_B, extends plus and minus one depth of focus from the focal point. Phase-shifted light from particles to the right of the axial region will not be imaged as coherent plane waves, and will not contribute to signals measured by the coherent detection techniques. Particles to the left of this axial region will likewise impart a phase shift, with a portion of this light propagating forward into the optical viewing volume and being imaged as coherent plane waves, extending the axial distance of the viewing volume somewhat further to the left of the focal point than one depth of focus.

In order to assure a signal that is independent of particle position within the viewing volume, a uniform intensity of incident light should exist throughout. This can be arranged by coordinating the geometry of d_W and Z_W from the primary lens with d_B and Z_B from the gathering lens. The intensity within the viewing volume will be given by $I(z,r)$ where z and r denote axial and radial coordinates from the origin at the beam waist.

The radial intensity across the beam at any position z is Gaussian and described by Gaskill[25] as:

$$\frac{I(z,r)}{I(z,o)} = \exp \{-2\pi \left(\frac{r}{b}\right)^2\} \tag{1}$$

where r = radial distance from centerline
b = Gaussian beam radius to $e^{-\pi}$ point in wave field amplitude
$I(z,o)$ = centerline intensity at position z

If d_B is centered in d_W and $(d_B/d_W) \leq 0.1$, then the radial intensity profile incident on d_B will not vary more than 6% and can be assumed sufficiently uniform to be constant in the radial direction.

The axial intensity at centerline is given by:

$$\frac{I(z,o)}{I(o,o)} = \left(\frac{d_W}{d_Z}\right)^2 \tag{2}$$

where d_W = diameter at beam waist to $e^{-\pi}$ point in wave field amplitude
d_z = beam diameter to $e^{-\pi}$ point at axial position z from beam waist
$I(o,o)$ = centerline intensity at beam waist

The beam diameter at axial position z from the waist is given by:

$$d_z = d_W \sqrt{1+(z/Z_R)^2} \tag{3}$$

where Z_R = Rayleigh length = $\frac{{d_W}^2}{4\lambda}$

Let axial position z be defined as a fraction of the Rayleigh length, so that:

$$z = Z_R/\gamma \tag{4}$$

where $\frac{1}{\gamma}$ = fraction of Rayleigh length from beam waist, then Equations 2 through 4 yield:

$$\frac{I(z,o)}{I(o,o)} = \frac{1}{1+(\frac{1}{\gamma})^2} \tag{5}$$

From Equation 5, if d_W and d_B axially coincide and $Z_B \leq (Z_R/5)$, then the axial centerline intensity profile within Z_B will not vary more than 1% and therefore will not compound the radial intensity profile error.

The integrated power from centerline to radial position r is given by Gaskill[25] as:

$$\frac{P(r)}{P_{tot}} = 1 - \exp\{-\frac{\pi}{2}(\frac{r}{b})^2\} \tag{6}$$

where r = radial position from centerline
b = beam radius to $e^{-\pi}$ in wave field amplitude
P_{tot} = total power in the beam

For the case of constant radial intensity ($\frac{d_B}{d_W}$ = 0.1), only 1.56% of the total beam power is contained within the blur spot diameter d_B and therefore contributes to particle measurement.

It is difficult to construct any sort of optical viewing volume where the edges are defined by sharp boundaries. There is always going to be a "fuzzy zone" surrounding the edges, so particles of a given diameter that happen to pass close to a boundary will result in a different signal than those that pass directly through. It would be desirable to minimize this fuzzy zone so particle counting errors are small.

The radial edges of the viewing volume are determined by the degree of non-parallelism between the scattered light and the local oscillator beam. Coherent detection methods are quite sensitive to misalignment, giving a rather sharp radial boundary. The axial distance of the photodetector from the interferometer will affect this sensitivity.

The trailing edge of the viewing volume will be sharply defined by the depth of focus where the van Cittert-Zernike theorem applies. The leading edge will be the fuzziest boundary because particles further to the left will phase shift light that could propagate forward into the viewing volume and be counted as smaller particles. Experimental results with monodisperse aerosols will be needed to practically define the magnitude of this problem.

It is interesting to note that if one overfills the primary lens aperture with the laser beam and clips 8% of the transmitted subject beam power, the centerline intensity at the beam waist (I(o,o)) is actually increased by nearly 40%. This and other peculiarities of working with Gaussian beams is treated by Gaskill[25].

Consider the following example for specifying the design of the viewing volume. The radial diameter (d_B) should be substantially greater than the maximum particle diameter $(d_p)_{max}$. This will minimize near-miss errors, wherein the particle straddles a boundary and is only partially contained within the viewing volume. For a $(d_p)_{max}$ of 5 µm, a d_B of 25 µm would be sufficient. Once a gathering lens with a given d_B is specified, the depth of focus is determined. For d_B of 25 µm, a corresponding Z_B of 100 µm is typical (Driscoll[26]). To insure a uniform radial intensity within d_B, d_w must be 250 µm. The corresponding Rayleigh length for a He-Ne laser with this beam waist is 26 mm, thus requiring Z_B to be less than or equal to 5.2 mm. This is obviously true for the above case.

The signals generated by uniformly spaced monodisperse aerosols passing through the viewing volume can be examined in either the time or frequency domain. In the time domain, pulses will occur with spacings given by the interval between particles passing through the beam. The pulse height will be given by the power measured in the phase-modulated side bands. The power in the phase-modulated side bands is related to the magnitude of the phase shift, which in turn can be related to the particle diameter.

The phase modulation process can be illustrated with a phasor diagram as shown in Figure 3. The subject beam with power P_s and electric field E_s is sub-divided into the carrier beam of power P_c with electric field of E_c, which is the light incident on the scattering cross sectional area of the particle, and the noncarrier with power P_n and electric field of E_n. The total power in the subject beam P_s is equal to the sum of P_n and P_c. The electric fields E_n and E_c are shown as phasors in Figure 3 where the phase shift $\Delta\phi$ is due to E_c incident on the particle and is approximated by two side-bands each with electric field E_{pm} that rotate in opposite directions at the modulation frequency ω. This rotation results in E_c swinging through an arc given by particle phase shift $\Delta\phi$, causing the carrier to be phase-modulated. For small angle modulation, the phase shift can be represented sufficiently by two side bands. Since E_c and E_n have identical phase, the resultant phase shift $\Delta\phi'$ (which is the phase shift measured by the OHD technique) will be the vector sum of E_c, E_n and E_{pm}.

In addition to the phase-modulated side bands, there will be amplitude-modulated side bands E_{am}, due to scattering and absorption, rotating at the same frequency but resulting in their sum changing the length of E_c.

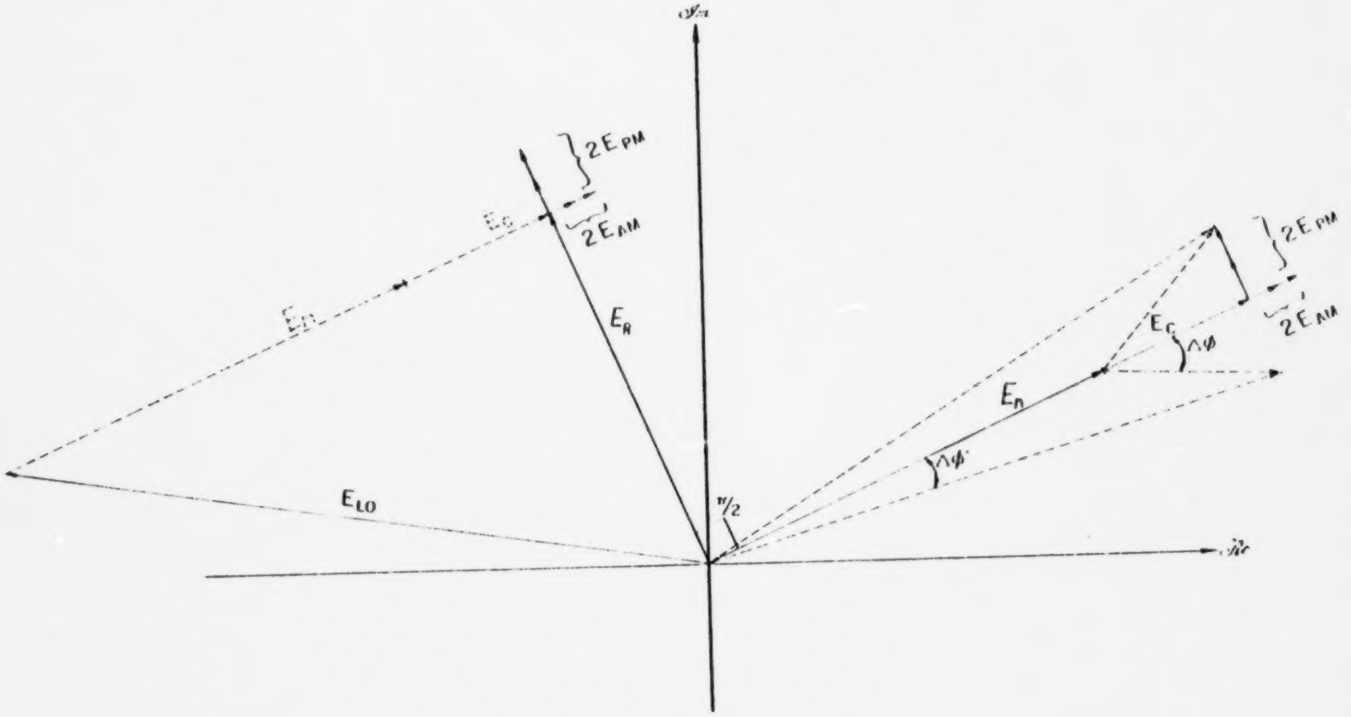
ℐm
2E PM
2E AM
E_C
E_n
E_R
E_LO
Δφ
Δφ
π/2
2E PM
2E AM
E_C
ℛe

Figure 3. Phasor diagram of the coherent optical particle spectrometer, showing phase-modulated side bands (E_{pm}), amplitude-modulated side bands (E_{am}), and the resultant in quadrature (E_R).

The local oscillator beam with power P_{LO} and electric field E_{LO} is adjusted so the phase of the resultant vector E_r (given by the sum of E_c, E_n, E_{pm}, E_{am}, and E_{LO}) is in quadrature to the carrier E_c. When E_r differs in phase from E_c by $\pi/2$, then the phase-modulated side bands on the carrier will appear as amplitude-modulated side bands on the resultant, and the amplitude-modulated side bands on E_c will appear as phase-modulated side bands on E_r (Figure 3). In this way, it is possible for a photodetector to measure the power in the phase-modulated side bands in terms of amplitude fluctuations, without detecting any effect from the amplitude modulation.

The power in the side bands P_{pm} can be found by considering small angle modulation, where:

$$E_{pm} \simeq \left(\frac{E_n+E_c}{2}\right)\Delta\phi' \tag{7}$$

Since we detect the power in both side bands together

$$P_{pm} \simeq \left(\frac{E_n+E_c}{2}\right)^2 (\Delta\phi')^2 \tag{8}$$

where P_{pm} is the power in both phase-modulated side bands.

For small angle modulation, the resultant phase shift in the subject beam $\Delta\phi'$ can be related to the phase shift due to the particle $\Delta\phi$ by:

$$\Delta\phi' \simeq \left(\frac{E_c}{E_c+E_n}\right)\Delta\phi \tag{9}$$

Substituting for $\Delta\phi'$ yields:

$$P_{pm} = \frac{\Delta\phi^2 P_c}{2} \tag{10}$$

Hence, the power in the phase-modulated side bands is due to the magnitude of the particle phase shift $\Delta\phi$ and the power in the carrier. The power in P_n does not interfere with the detection of the phase-modulated side bands because it is in phase with P_c and is balanced by the local oscillator when in quadrature.

To determine the theoretical signal as a function of particle size, the signal-to-noise ratio expression for a shot-noise-limited photodetector is used. For optical heterodyne detection, this is given as (Jacobs[21]):

$$(S/N)_p = \frac{\eta p}{h\nu\Delta f} \tag{11}$$

where η = photodetector quantum efficiency
h = Planck's constant
ν = frequency of carrier light
Δf = band width of electronics in signal processor
p = power in signal that is being measured
$(S/N)_p$ = power signal to noise ratio

For phase modulation, P is equal to the power in the phase-modulated side bands and is given by Equation 10.

The signal-to-noise ratio expression then becomes:

$$(S/N)_p = \frac{\eta \Delta\phi^2 P_c}{2h\nu\Delta f} \tag{12}$$

When the particle is inside the optical viewing volume, the incident intensity will be uniform, so the power in the carrier is given by:

$$P_c = P_B \frac{C_{scat}}{\pi/4 \; d_B^2} \tag{13}$$

where P_B = power contained within d_B
C_{scat} = particle scattering cross section

For the conditions of small angle modulation, the particles would be in the Rayleigh scattering regime so the scattering cross section is given by Kerker[27] as:

$$C_{scat} = \frac{24\pi^3 V^2}{\lambda^4} \left(\frac{n^2-1}{n^2+2}\right)^2 \tag{14}$$

where V = particle volume = $\pi/6 \; d_p^3$
n = particle refractive index
λ = wavelength of light
d_p = particle diameter

Using equation 6 to find P_B results in:

$$P_B = P_S \left[1 - \exp\left\{-\frac{\pi}{2} \left(\frac{d_B}{d_w}\right)^2\right\}\right] \tag{15}$$

where P_s = power in subject beam

P_S will be approximately one half the total power of the laser, depending on the reflection losses from the interferometer. Combining Equations 12 through 15 gives:

$$(S/N)_p = \frac{4\eta\Delta\phi^2 d_p^6 P_s \left[1-\exp\left\{-\frac{\pi}{2} \left(\frac{d_B}{d_w}\right)^2\right\}\right]}{3h\nu\Delta f \; d_B^2} \left(\frac{\pi}{\lambda}\right)^4 \left(\frac{n^2-1}{n^2+2}\right)^2 \tag{16}$$

The particle phase shift, $\Delta\phi$, is a function of particle diameter and refractive index and can be determined rigorously by numerical solution of the scattering equations (Dave[28], Wiscombe[29,30], Fymat and Mease[31]). Equation 16 assumes $d_B/d_W \leq 0.1$ for uniform intensity profiles and is limited to Rayleigh particles for scattering cross section and small angle modulation, where the phase shift can be represented by two side bands. These latter requirements make Equation 16 useful for estimating the minimum detectable particle size.

Using Equation 16 to estimate the minimum detectable particle size, consider nonabsorbing spherical particles passing singly through the beam waist perpendicular to the optical axis. If an estimate for the minimum detectable particle is all that is desired, then the particle phase shift can be taken as the order of:

$$\Delta\phi = \frac{2\pi(n-1)d_p}{\lambda} \tag{17}$$

Combining Equations 16 and 17, and introducing a factor α to account for the amount of phase-shifted light collected by the gathering lens yields:

$$(S/N)_p = \frac{16\eta\alpha d_p^8 \; P_s\left[1-\exp\left\{-\frac{\pi}{2}\left(\frac{d_B}{d_w}\right)^2\right\}\right]}{3h\nu\Delta f}\left(\frac{\pi}{\lambda}\right)^6\left[\frac{n-1}{d_B}\right]^2\left(\frac{n^2-1}{n^2+2}\right)^2 \tag{18}$$

where α = fraction of phase-shifted light collected by gathering lens.

Equation 18 can be used to estimate the minimum detectable particle size by selecting suitable values for the parameters indicative of experimental conditions. Typical values for the parameters that are fixed are:

silicon photodiode: $\eta = 0.50$
lens components: $\alpha = 0.10$ (ten percent of phase-shifted light collected)
$(d_B/d_w) = 0.1$ (to ensure uniform radial intensity)
particles: $n = 1.5$

Parameters that are somewhat flexible and can fall over a range of values are Δf, d_B and P_s. By rearranging Equation 18 and requiring the S/N ratio to be greater than one, a range of $(d_p)_{min}$ can be obtained for various values of these parameters, as given in Table 3. Table 3 contains both the "best case" combinations of Δf, d_B and P_s that could be proposed for a research environment and combinations that would be suitable for a commercial particle counting instrument.

If, for example, an electrodynamic balance (Davies and Ray[32]) were used to stabilize a particle oscillating at a precise frequency through the optical view volume, a 1 Hz bandwidth is feasible. High power levels (argon lasers, etc.) are also possible, since evaporation of Rayleigh particles by high incident intensities is difficult (Hunt[33]). With a 1 Hz bandwidth, 2 μm blur spot, and 1 watt subject beam, the mimimum detectable particle is approximately 5 x 10^3 μm. For a practical particle counting instrument, a bandwidth of at least 20 KHz is required to assure that randomly spaced particles are detected. Laser power should not be excessive (5 mW is quite reasonable), and a blur spot at least 5 times the maximum particle diameter will minimize near-miss problems. As can be seen in Table 3, minimum detectable particle sizes range from 0.04 to 0.07 μm, with maximum particle sizes (to minimize near-misses) of 0.4 to 5.0 μm. An instrument could be designed with an adjustable blur spot to allow both low and high-end limits to be reached.

TABLE 3. ESTIMATES OF MINIMUM DETECTABLE PARTICLE SIZE FOR VARIOUS d_B, P_s AND Δf

d_B[μm]	$(d_p)_{max}$[μm]	P_s	Δf[Hz]	$(d_p)_{min}$ [μm]
2	≈ .4	1 W	1	0.005
		1 W	20 K	.02
		5 mW	1	.01
		5 mW	20 K	.04
5	≈ 1.	1 W	1	.007
		1 W	20 K	.02
		5 mW	1	.01
		5 mW	20 K	.05
25	≈ 5	1 W	1	.01
		1 W	20 K	.04
		5 mW	1	.02
		5 mW	20 K	.07

With coherent detection, there is no background signal associated with scattered light because of the interferometric configuration that is responsible for measuring the phase shift. Statistical fluctuations of molecular cluster populations below the detection limit could impart a background noise on the refractive index, but the bandwidth and other experimental parameters will most likely dictate the lower detection limit.

With intensity measurements of scattered light, on the other hand, the background scattering of the gas molecules in the viewing volume is the same order as a single 0.1 μm particle, and thus the detection limit of a technique based on light scattering is established at that level. Experimental configurations can reduce the background scattering and possibly lower the limit by at most a factor of two (Hirleman[18]).

EXPERIMENTAL WORK

Apparatus

In Figure 4, the equipment is shown to include a Jamin interferometer, which provides a stable means of combining with the local oscillator beam the phase-shifted light from a single pass through the optical viewing volume. A 5X microscope objective is used as the primary lens and a 3.5X objective is used as the gathering lens in the subject beam. The primary lens provides a beam waist of 200 μm in diameter with a waist length of 1000 μm. The gathering lens has a blur spot diameter of 20 μm with a depth of focus of 80 μm and is

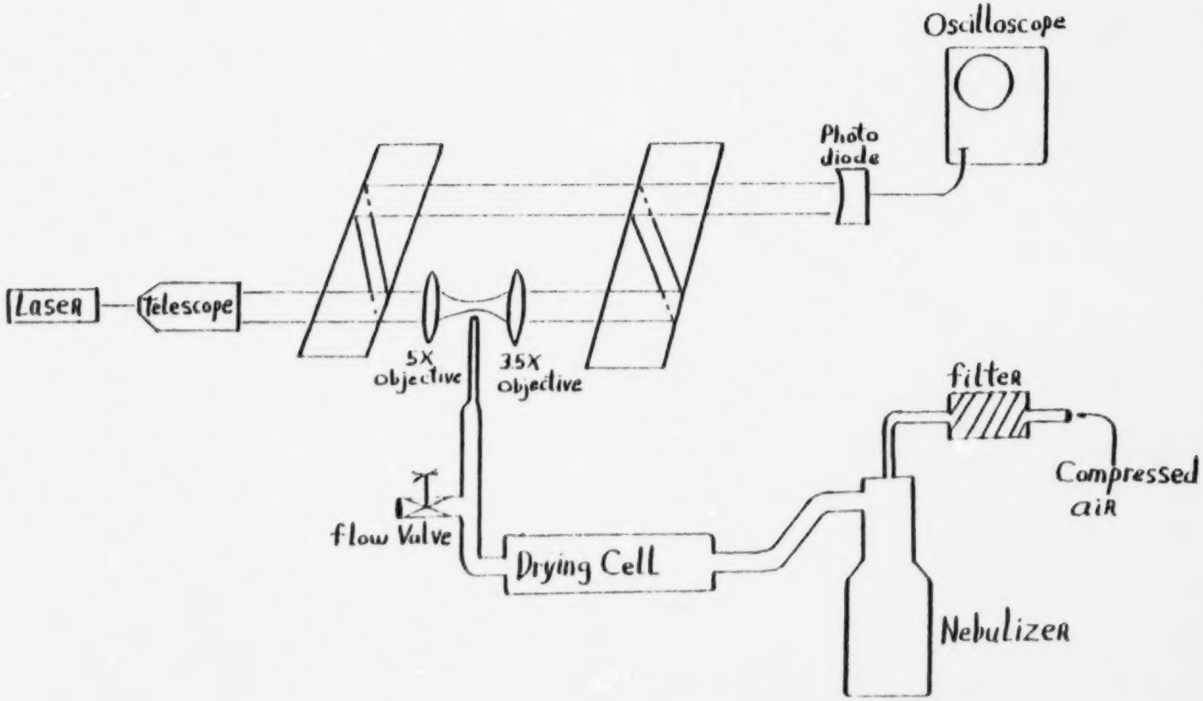
Oscilloscope
Photo diode
Laser
Telescope
5X objective
35X objective
filter
Compressed air
flow Valve
Drying Cell
Nebulizer

Figure 4. Calibration of coherent optical particle spectrometer using nebulized polystyrene latex spheres.

centered in the beam waist region of the primary lens. This assures a constant radial and axial intensity profile within the viewing volume. A photo diode is used with an oscilloscope to view the signal in the time domain. The light intensity incident on the photo diode is more than sufficient to shot-noise-limit the detector. A beam-expanding telescope enlarges the fringe pattern so that it can be readily seen, aiding the interferometer adjustment into quadrature. A 0.5 milliwatt helium-neon laser is used with a randomly polarized beam. A glass pasteur pipette with a tip diameter of 1.0 millimeter (mm) is used to direct the flow of aerosol sample through the focal point region, perpendicular to the subject beam. To minimize room vibrations, the entire system is assembled on an optical bench.

The calibration system for generating standard particles consists of a source of compressed air, a submicron filter, a nebulizer with distilled water suspensions of standard polystyrene latex (PSL) spheres, a drying cell, and a flow-regulating valve. Calibration particles were available from 0.085 μm to 3.0 μm in diameter. These particles were directed through the focal point region with the pipette, where faint light scattering could be seen with the eye. The signal was read from the oscilloscope for each particle size and a calibration curve established.

Results

Figure 5 shows the apparently monotonic calibration curve for COPS with signal voltage (pulse height) as a function of particle diameter using PSL spheres of 0.085, 0.22, 0.55, 0.95, 2.0 and 3.0 μm. For each calibration particle, the dot indicates the most frequent pulse height, and the "error bars" indicate the minimum and maximum pulse heights seen at least once. While an absolute monotonic relationship cannot be proclaimed (Cooke and Kerker[34]), the signal spread for COPS was primarily the result of the deviation from monodispersity of the calibration aerosols. Nebulized PSL spheres can deviate markedly from a monodisperse aerosol due to trace contaminants in the liquid vehicle (distilled water) and residual surfactants present from the stock PSL suspensions (Cooke and Kerker[35]; Fuchs[36]). The smaller the PSL spheres, the wider the deviation.

Figure 6 shows the direct signal voltage output as a function of particle diameter for PSL spheres of 0.55, 0.95, 2.0 and 3.0 μm as measured with a Climet (Model 208) OPC. Using the average value to define the calibration curve, the signal spread (shown by error bars about the average) can be used to estimate the size range of each calibration aerosol. The same procedure can be done with the COPS calibration curve (Figure 5) and Table 4 compares these size ranges. As can be seen from Table 4, the size range for each calibration aerosol is of the same order for both instruments.

Clearly, further work is needed to establish the resolution, extent of viewing volume, and character of the COPS calibration curve. Experiments with calibration aerosols that more closely approach a monodisperse system will be required to answer these questions. However, it is apparent from repetitive calibration runs similar to the experiment above that the COPS signal voltage-particle size relationship is at least as "unique" as that relationship for a "conventional" OPC. The advantage, of course, is the wider range in particle

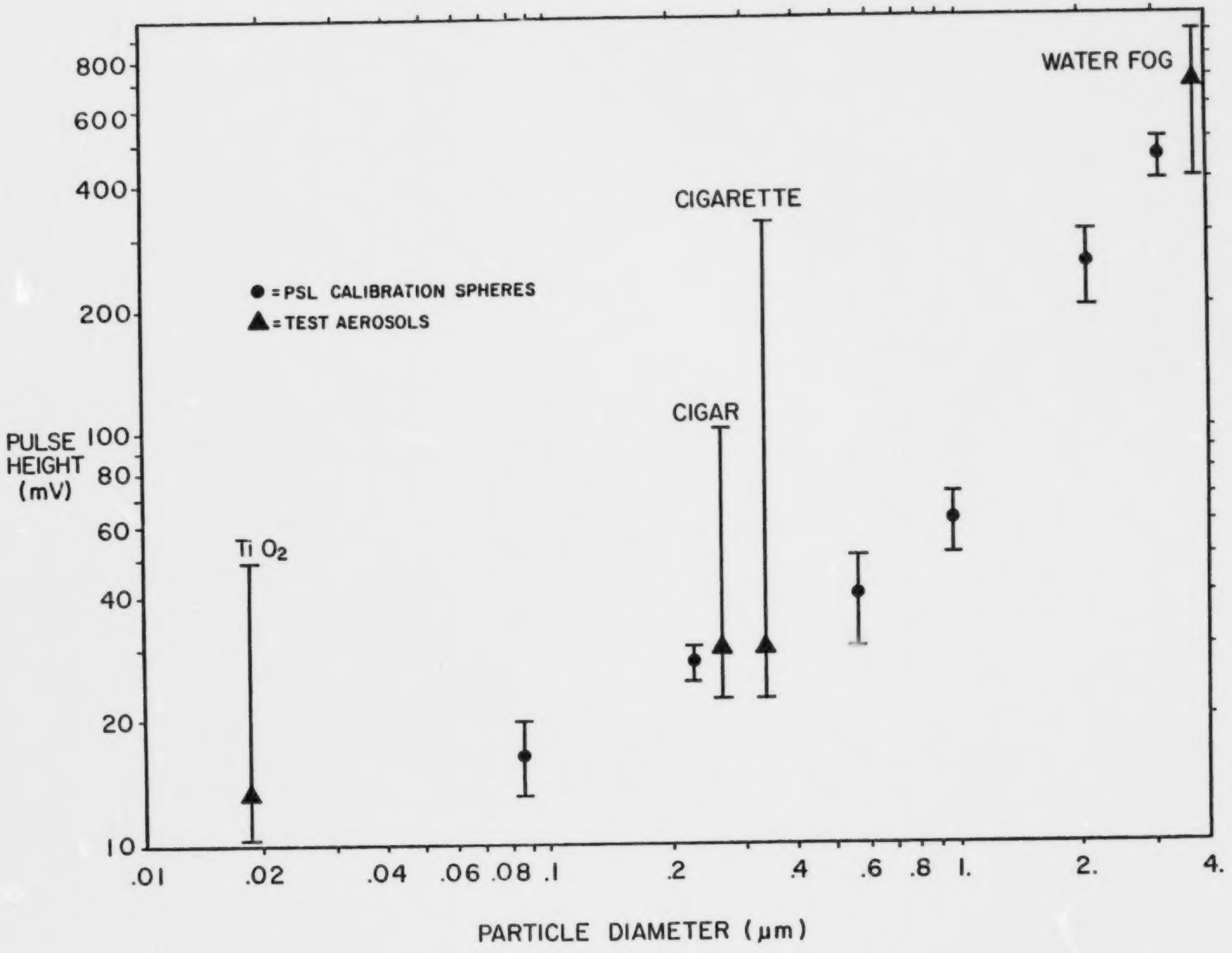

Figure 5. Calibration of pulse height (millivolts) vs. particle diameter (μm) for the coherent optical particle spectrometer: PSL spheres (●); test aerosols (▲).

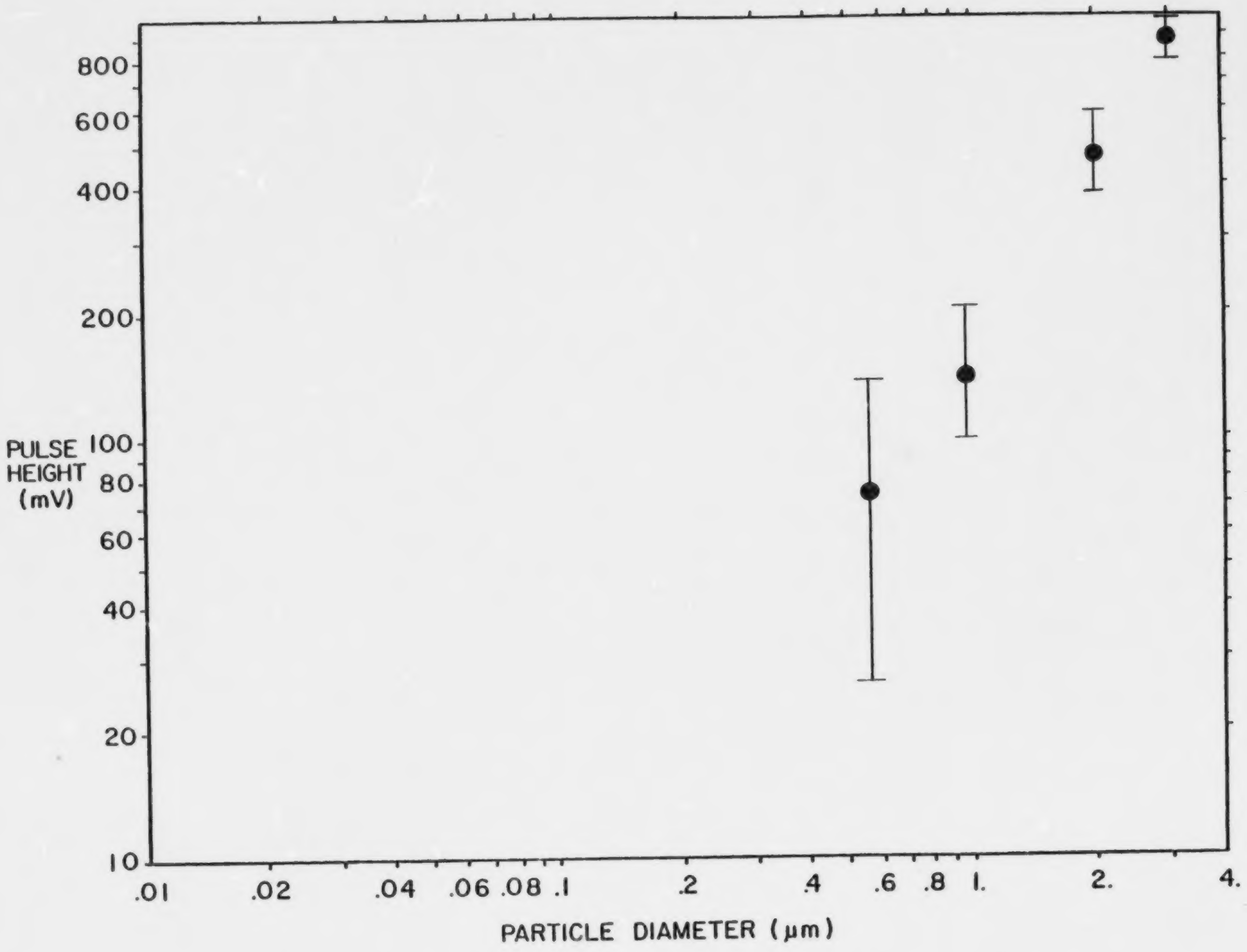

Figure 6. Calibration curve of pulse height (millivolts) vs. particle diameter (μm) for a Climet Model 208 optical particle counter; PSL spheres (●).

TABLE 4. PARTICLE SIZE RANGES FOR PSL CALIBRATION AEROSOLS

	Particle Size Range (μm) about PSL Diameter (μm)					
Instrument	0.085	0.22	0.55	0.95	2.0	3.0
COPS	(≈0.035)-0.13	0.18-0.30	0.26-0.78	0.78-1.1	1.8-2.2	2.8-(≈3.2)
Climet OPC (Model 208)	--	--	(≈0.3)-1.0	0.7-1.3	1.8-2.5	2.8-(≈3.2)

size covered by the COPS. The signal from COPS appeared as a string of pulses spaced at irregular intervals much like that from a conventional OPC. Decreasing and then increasing the aerosol flow rate through the pipette caused the oscilloscope signal to respectively range from an occasional blip to a thick "grassy" signal. Flow rates were balanced with total aerosol number concentrations to yield distinct separable peaks, usually resulting in signal frequencies in the range of 1-5 KHz.

Experiments were made to determine that phase modulation, and not amplitude modulation, was being measured. With particles directed at the focal point region, the local oscillator beam was blocked and the signal was lost for all but the larger particles. Particles of 0.55 μm and up showed a detectable amplitude-modulated signal that was at least a factor of five smaller than the same phase-modulated signal. When the local oscillator and subject beams were moved out of quadrature, the phase-modulated signal was attenuated or lost completely, demonstrating the sensitivity of the interferometric technique to measure phase modulation in terms of amplitude fluctuations at the photodetector.

There were two possible fringe locations for quadrature with the COPS system that give distinctly different signals. Quadrature could be maintained slightly shifted up from the dark fringe so when a particle passes through the viewing volume, the resultant phase shift caused the fringe to move from dark to bright. This was registered at the detector as an increase in intensity and gave a signal pulse that went up on the voltage scale of the oscilloscope. Quadrature could also be maintained slightly shifted down from the bright fringe, so when a particle was counted, the phase shift caused the fringe to move from bright to dark. This was registered at the detector as a decrease in incident intensity and caused the signal pulse to go down on the voltage scale. When the interferometer was adjusted, the signal pulses could be seen pointing up (dark quadrature) then disappearing (out of quadrature) and finally pointing down (bright quadrature). If the local oscillator beam was blocked at any position during the adjustment, the signal would reduce to residual amplitude-modulated pulses that would be pointing downwards, as extinction measurements should.

When the pipette tip was slightly translated along the optical axis away from the beam waist, the phase-modulated signal was lost even though particles were still passing through other sections of the beam. This verifies a small viewing volume where the van Cittert-Zernike theorem applies. If the pipette was tilted so that particles passed through at nonperpendicular angles, the pulse height remained the same. This demonstrates that Doppler shifts imposed on the phase-shifted light did not significantly affect the phase-modulated signal.

The COPS was also used to measure "unknown" test aerosols of tobacco smokes, titanium dioxide smokes and water droplet fogs. The approximate average pulse heights, as well as the spread in pulse heights measured, are also shown in Figure 5. Due to instrument limitations, all measurements were made visually from an oscilloscope. Quantitative analysis of the number distribution was not possible with this simple procedure, but reliable and reproducible estimates of signal mean and spread were obtained. As before, the signal spread is an indication of polydisperse conditions for each test aerosol.

Mouth drawn cigarette and cigar smoke were blown through a silica gel drying cell and into the focal point region of COPS. The average pulse heights for both tobacco smokes, according to the PSL calibration, correspond to a particle diameter of approximately 0.3 μm. The cigar smoke distribution ranged from 0.1 to 1.0 μm while the cigarette smoke was found to be between 0.1 to 2.0 μm. The generally accepted size range for tobacco smoke is between 0.01 and 1.0 μm (Perkins[37]). Also measured by the COPS was nebulized distilled water fog. The average pulse height fell above the largest PSL sphere, with a pulse-height spread corresponding to particles greater than 3.0 μm diameter. The water fog was measured by the Climet CI-208 OPC to be predominantly 5 μm and larger.

Refractory particles of titanium dioxide (TiO_2) were made by reaction of titanium tetrachloride with room-temperature air. A TSI, Inc. (Model 3030) electrical aerosol analyzer (EAA) was used to establish the TiO_2 distribution as shown in Figure 7. The TiO_2 aerosol consisted of small particles with diameters ranging from 0.005 to 0.5 μm. A single mode was found in the interval between 0.01 and 0.02 μm, and was at least an order of magnitude (in number concentration) greater than any other size interval. Shown in Figure 5 is the average pulse height generated by the TiO_2 aerosol on the COPS. The average pulse height fell below the smallest (0.085 μm) PSL calibration sphere and was placed in Figure 5 between 0.01 and 0.02 μm, based on the EAA distribution in Figure 7. The signal spread from the TiO_2 aerosol ranged from the background noise of COPS to a value that corresponds to a particle diameter of 0.7 to 0.8 μm.

In order to test the in-situ capabilities of COPS, a fuel-rich laminar diffusion flame of natural gas was stabilized in a 20 mm diameter pyrex glass chimney. When the flame was placed in the focal point region of the COPS, as shown in Figure 8, the interferometer could be readjusted into quadrature over the receptor area of the photodetector, even though the fringe pattern was distorted on the edges by the cylindrical geometry of the chimney.

Titanium tetrachloride was then introduced into the natural gas stream and the sizes of titanium dioxide particles produced in the flame zone were measured with COPS. The pulses fell in the same size range as was previously determined for titanium dioxide, but visual inspection of the signals indicated more frequent pulses in the larger range than seen for TiO_2 formation at room temperature.

OTHER CONSIDERATIONS

Stray Light

Only light that is coherently superimposed with the local oscillator beam will contribute to the power measured in the phase-modulated sidebands. Consequently, light scattered by particles outside of the viewing volume, room lights, window lights, and light from emission within the volume (such as a flame zone) will contribute only to additive noise superimposed on the particle

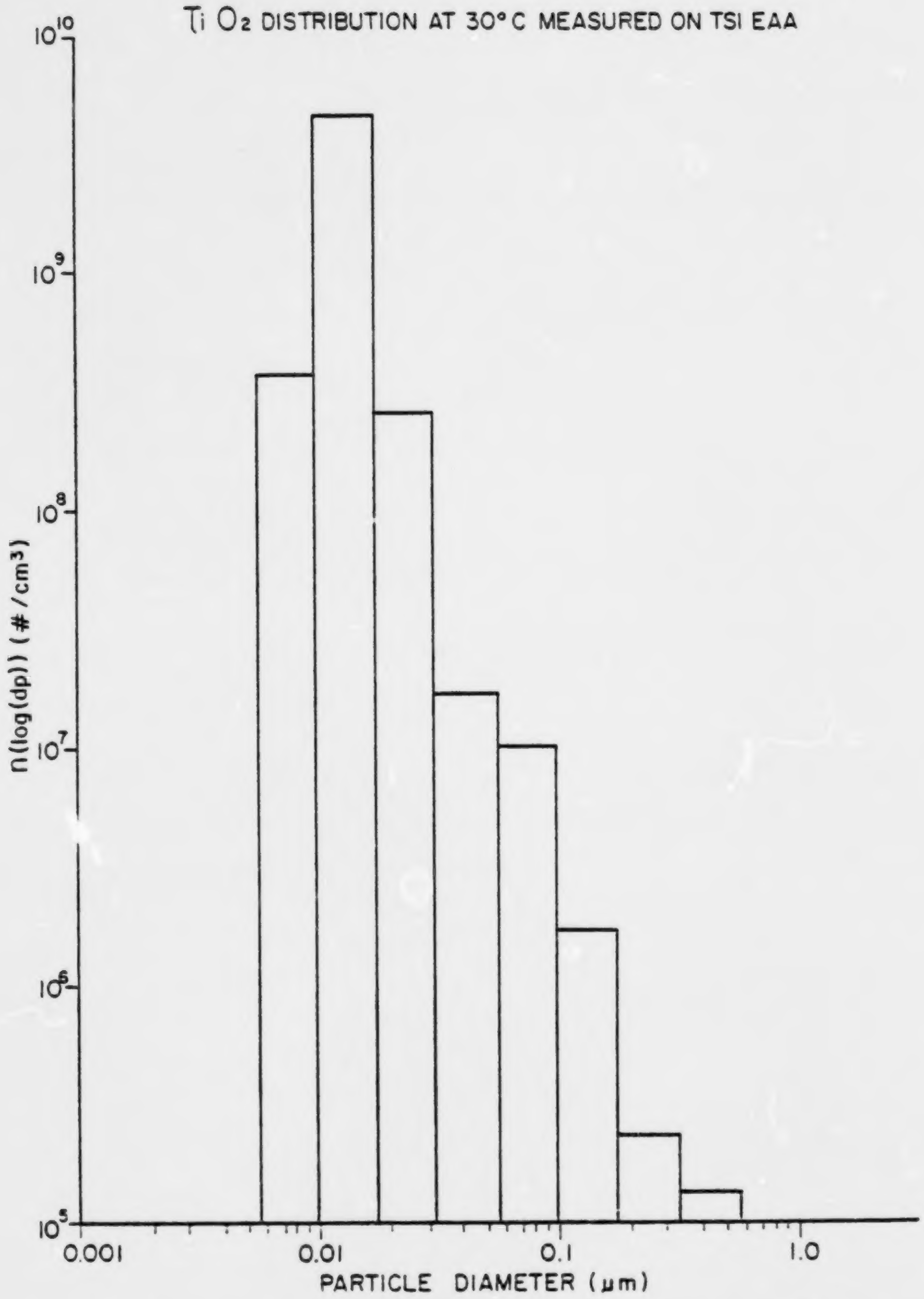

Figure 7. Titanium dioxide test aerosol as measured by electrical aerosol analyzer.

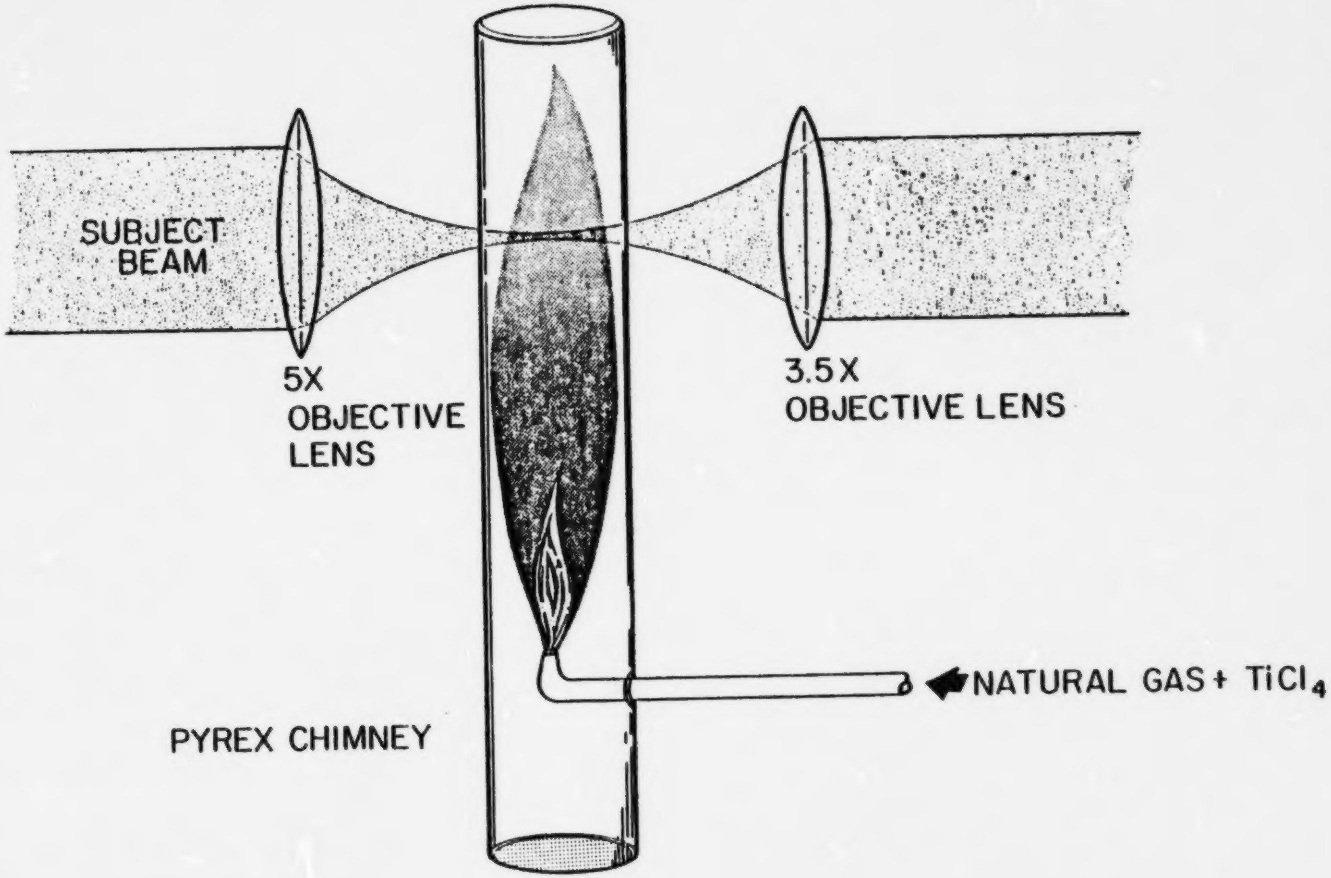
SUBJECT BEAM
5X OBJECTIVE LENS
3.5X OBJECTIVE LENS
PYREX CHIMNEY
NATURAL GAS + $TiCl_4$

Figure 8. Experimental apparatus for in-situ particle measurement.

signals. This noise will consist of DC terms and low frequency AC terms which can be filtered out electronically, since the particle signal frequencies are much greater than those of the stray light.

Experimentally, the effect of stray light was found to be minimal. Constant sources such as window light and flame emissions added a DC component to the signal, while overhead florescent lights imposed a 60 Hz noise component, all without affecting the signal height. With the room lights on, minor shielding of the photodetector from direct exposure to the light fixtures was all that was required to perform the experiments. This insensitivity to stray light is a characteristic of the COPS that is not available in standard light scattering instruments.

Particle Coincidence and Maximum Aerosol Densities

The COPS technique assumes that only one particle at a time passes through an optical viewing volume defined by the resolution limit and depth of focus of the gathering lens. Coincidence errors will result if this is not the case, and the total aerosol density must be sufficiently low to make this problem statistically insignificant.

A conservative estimate of the count loss due to coincidence is summarized by Whitby and Willeke[2] as:

$$\frac{N_i}{N_t} = \exp\,(-N_t v) \tag{19}$$

where N_i and N_t are the indicated and actual particle concentrations respectively, and the optical viewing volume is given by v. Table 5 shows the maximum allowable number concentration for varying blur-spot diameters, assuming no more than 5% coincidence loss. The COPS obviously has the capability of measuring particle concentrations in many cases without sample dilution.

TABLE 5. TOTAL ALLOWABLE NUMBER CONCENTRATIONS FOR COINCIDENCE ERROR OF LESS THAN 5%

d_B[μm]	Z_B[μm]	N_{tot} [#/cm^3]
2	≈ 5	10^9
5	≈ 15	10^8
25	≈ 100	10^6

Polydisperse Aerosol

Extending the time domain signal for a monodisperse aerosol to the polydisperse case, the COPS will output a series of pulses, one for each particle, at irregular intervals. Each pulse height is indicative of the diameter of the particle in the viewing volume at that instant. Each pulse can be electronically sorted by height, and counted to obtain a complete aerosol size distribution from this single-particle counting process.

Partial Eclipses of the Incident Beam

As with any laser-based optical technique, errors can result from particle "near-misses", where only a portion of the particle cross sectional area eclipses the incident light beam. Near-misses can be minimized by making the viewing volume dimensions much greater than the largest particle intended to be measured. The previous discussion of the viewing volume indicates that there will be a trade off between viewing volume size, maximum and minimum detectable particle size, and total aerosol density, to be determined by the specific application.

Random Particle Trajectories

If particles travel perpendicularly to the optical axis defining the viewing volume, Doppler shifts will be minimal. If particles travel at any other angle, there will be larger Doppler shifts in the phase-shifted light due to velocity components along the optical axis. These Doppler shifts will not affect the power in the phase-modulated side bands and hence will not affect the pulse height as registered by the electronics. The Doppler shift will result in adding higher and lower frequency components to the pulses, but the time domain signal will still show a one-to-one correspondence between pulse height and particle size. An elegant discussion of this problem is given by Colak and Yeh[4], who conclude that, compared to a plane incident wave, a strongly focused Gaussian beam can indeed alter the bandwidth and frequency shift of the light scattered from a moving particle.

Particles of Irregular Shape

Particles of irregular shape will behave differently than spherical particles but discrepancies will be minimized if gathered light is limited to forward angles (Pollack and Cuzzi[38]; Zerull et al.[39]).

Complex Refractive Index

Particles with complex refractive index will impart a phase shift due to transmitted as well as diffracted light. For strongly absorbing particles, the phase shift will be due to diffraction. It is important, as for any optical particle counting technique, to calibrate the COPS with particles similar to the ones to be measured.

Other COPS Configurations

Any type of interferometer that can coherently superimpose the subject and local oscillator beams can be used in the COPS. The Jamin was chosen because of its inherent stability to room vibration, ease of optical alignment, and single subject beam pass through the viewing volume. A Mach-Zehnder interferometer would be optically the same as the Jamin but would not have the vibration and alignment stability.

In addition to particle size, particle velocity could possibly be measured by looking at the pulse width in the time domain. Over any given sampling interval, some particles are going to travel close to the diameter chord of the viewing volume and give a maximum pulse width. By knowing the viewing volume diameter and maximum pulse width, the particle velocity can be found. This velocity would be limited to flow perpendicular to the subject beam and could be used to estimate gas velocity if the particles were small.

SUMMARY

Theory shows that phase-shifted light from small particles is coherent if gathered at the focal point of a lens. Coherent detection techniques can then be used to measure the extent of the phase shift due to the presence of the particles. The phase shift can be related to particle diameter, and theoretical estimates yield a minimum detectable particle diameter of the order of 0.005 μm in a research environment and 0.04 for a practical particle counting instrument. Maximum total aerosol densities range from 10^6 to 10^9 cm^{-3}, depending on the configuration of the viewing volume. Particles are counted singly as they travel through an optically defined viewing volume. Parameters such as beam power, configuration of viewing volume, and electronic bandwidth affect minimum and maximum detectable particle size and total aerosol density. An optimum arrangement must be reached for each application of interest.

An experimental Coherent Optical Particle Spectrometer (COPS) was made using a Jamin interferometer, two low power microscope objectives, and a helium-neon laser. An oscilloscope was used to process the signal from a photo diode. Standard polystyrene latex spheres of known size were used to determine a calibration curve in the range 0.085 to 5.0 μm diameter that was apparently monotonic. Aerosol flow rate showed a direct correlation with the pulse frequency. Signal rates of 1-5 kHz were typical with pulses being distinctly separated. Experiments showed that only particles passing through the focal point region were counted. When the local oscillator beam was blocked, the signal was reduced to residual amplitude-modulated pulses from the larger size particles. Particles traveling at non-perpendicular angles to the subject beam did not affect the signal height.

Titanium dioxide particles with typical diameters of 0.01 to 0.02 μm have been detected, as have water droplet fogs with typical diameters of 5 μm and larger. Tobacco smoke was measured with COPS to be between 0.1 and 2.0 μm. Particles of titanium dioxide were detected in-situ within a laminar fuel-rich diffusion flame of natural gas.

ACKNOWLEDGEMENT

The authors express their appreciation to Professor Steve Jacobs from Optical Sciences for his interest in this work, and his generosity in the use of laboratory equipment during the initial development of the COPS. Special thanks also go to Dr. A. Richard Kassander, Vice-President for Research, for supporting the present work on this project.

NOMENCLATURE

b = beam waist radius to $e^{-\pi}$ point in wave field amplitude
d_B = blur spot diameter given by gathering lens
d_p = particle diameter
d_w = beam waist diameter from primary lens to $e^{-\pi}$ in wave field amplitude
d_z = beam diameter at axial position z from beam waist to $e^{-\pi}$
E_s = electric field in subject beam
E_{LO} = electric field in local oscillator beam
E_c = carrier electric field, i.e., electric field incident on particle cross sectional area
E_n = non-carrier electric field in subject beam
E_{pm} = electric field in each phase-modulated side band
E_{am} = electric field in each amplitude-modulated side band
E_r = electric field resultant (sum of E_n, E_c, E_{LO}, E_{am}, E_{pm})
Δf = bandwidth of signal processing electronic
h = Planck's constant
$I(z,r)$ = Intensity where z and r denote axial and radial coordinates from origin at beam waist
$I(z,o)$ = centerline intensity at axial position z
$I(o,o)$ = centerline intensity at beam waist
n = particle refractive index
N_i = measured aerosol number concentration
N_T = actual aerosol number concentration
P_s = power in subject beam
P_{LO} = power in local oscillator beam
P_c = carrier power in subject beam, i.e., power incident on particle cross sectional area
P_B = power contained within d_B
P_n = non-carrier power in subject beam
P_{pm} = power in both phase-modulated side bands
P_{am} = power in both amplitude-modulated side bands
r = radial coordinate from center of beam
$(S/N)_p$ = power signal to noise ratio
v = volume of optical viewing zone
z = axial coordinate from beam waist
Z_B = axial extent of optical viewing volume
Z_R = Rayleigh length
Z_w = waist length of beam given by primary lens, i.e., $2Z_R$
η = quantum efficiency of photo detector
α = fraction of phase-shifted light collected by gathering lens
$1/\gamma$ = fraction of Rayleigh length from beam waist
λ = wave length of light in carrier beam

ν = frequency of light in carrier beam
ω = frequency of particle modulation
$\Delta\phi$ = phase shift due to presence of particle
$\Delta\phi'$ = resultant phase shift in subject beam

REFERENCES

1. Liu, B. Y. H., and D. Y. H. Pui. J. Aerosol Sci. 6:249, 1975.

2. Whitby, K. T., and K. Willeke. In: Aerosol Measurement, D. A. Lundgren, ed. Univ. Presses of Florida, Gainesville, 1979. p. 241.

3. Willeke, K., and B. Y. H. Liu. In: Fine Particles, B. Y. H. Liu, ed. Academic Press, NY, 1975. p. 697.

4. Colak, S., and C. Yeh. Appl. Opt. 19(2):256, 1980.

5. Hirleman, E. D., and S. L. K. Wittig. Combustion Inst. 16th Symp., 1977. p. 245.

6. Hirleman, E. D. Opt. Lett. 3(1): 19, 1978.

7. Knollenberg, R. G., and Luehr. In: Fine Particles, B. Y. H. Liu, ed. Academic Press, NY, 1975. p. 669.

8. Knollenberg, R. G. In: Aerosol Measurement, D. A. Lundgren, ed. Univ. Presses of Florida, Gainesville, 1979. p. 271.

9. Lepper, J. M. Jr. In: Aerosol Measurement, D. A. Lundgren, ed. Univ. Presses of Florida, Gainesville, 1979. p. 194.

10. Lieberman, A. In: Aerosol Measurement, D. A. Lundgren, ed. Univ. Presses of Florida, Gainesville, 1979. p. 183.

11. Lieberman, A. Opt. Eng. 19(6):870, 1980.

12. Lieberman, A. Amer. Lab. 61, July, 1980.

13. Muly, E. C., and H. N. Frock. Opt. Eng. 19(6):861, 1980.

14. Rimberg, D. In: Aerosol Measurement, D. A. Lundgren, ed. Univ. Presses of Florida, Gainesville, 1979. p. 321.

15. Wyatt, P. J., and D. T. Phillips. J. Colloid Interface Sci. 39:125, 1972.

16. Clark, W. E., and E. L. Avol. In: Aerosol Measurement, D. A. Lundgren, ed. Univ. Presses of Florida, Gainesville, 1979. p. 219.

17. Gebhart, J., J. Heyder, C. Roth, and W. Stahlhofen. In: Fine Particles, B. Y. H. Liu, ed. Academic Press, NY, 1975. p. 793.

18. Hirleman, E. D. Opt. Eng. 19(6):854, 1980.

19. Houser, M. J. Opt. Eng. 19(6):873, 1980.

20. Tang, I. N., H. R. Munkelwitz, and J. G. Davis. In: Aerosol Measurement, D. A. Lundgren, ed. Univ. Presses of Florida, Gainesville, 1979. p. 231.

21. Jacobs, S. Electronics 29, July, 1963.

22. Gould, G., S. F. Jacobs, J. T. LaTourrette, M. Newstein, and P. Rabinowitz. Appl. Opt. 3(5):648, 1964.

23. Bassan, M., and S. Ciliberto. Opt. Acta 27(8):1253, 1980.

24. Born, M., and E. Wolf. Principles of Optics, Pergamon, NY, 1959. p. 508.

25. Gaskill, J. D. Linear Systems, Fourier Transforms, and Optics, Wiley, NY, 1978. p. 420.

26. Driscoll, W. G., Ed. Handbook of Optics, McGraw-Hill, NY, 1978. pp. 2.29, 6.2.

27. Kerker, M. The Scattering of Light and Other Electromagnetic Radiation, Academic Press, NY, 1969. p. 37.

28. Dave, J. W. IBM Scientific Center, CA , Report 320-3237, 1968.

29. Wiscombe, W. J. NCAR Tech. Note NCAR/TN-140+STR., 1979.

30. Wiscombe, W. J. Appl. Opt. 19(9):1505, 1980.

31. Fymat, A. L., and K. D. Mease. Appl. Opt. 20(2):194, 1981.

32. Davis, E. J., and A. K. Ray. J. Colloid Interface Sci. 75(2):566, 1980.

33. Hunt, A. J., Lawrence Berkeley Laboratory Report LBL-9317, May, 1979.

34. Cooke, D. D., and M. Kerker. Appl. Opt. 14(3):734, 1975.

35. Cooke, D. D., and M. Kerker. J. Colloid Interface Sci. 42(1):150, 1973.

36. Fuchs, N. A. J. Aerosol Sci. 4:405, 410, 1973.

37. Perkins, H. C. Air Pollution, McGraw-Hill, NY, 1974. p. 225.

38. Pollack, J. B., and J. N. Cuzzi. In: Light Scattering by Irregularly Shaped Particles, Schuerman, D. W., ed., Plenum Press, NY, 1980. p. 113.

39. Zerull, R. H., R. H. Giese, and S. S. Weiss. In: Light Scattering by Irregularly Shaped Particles, Schuerman, D. W., ed., Plenum Press, NY, 1980. p. 273.

Paper 23

DEVELOPMENT OF AN AERODYNAMIC PARTICLE SIZER

Jugal K. Agarwal and Richard J. Remiarz
TSI Incorporated

ABSTRACT

A new real-time aerodynamic particle sizer was developed and now is commercially available. In this instrument, the velocity of accelerating particles exiting from a thin plate orifice is measured by using a laser velocimetry technique.

The accelerating orifice assembly consists of an 0.8 mm inner nozzle and a 1.0 mm outer orifice. About 20 percent of the sampled flow passes through the inner nozzle; the remaining 80 percent of the flow passes through a filter and a flowmeter and is reintroduced into the orifice assembly as sheath air. This approach confines the sampled aerosol particles to the center portion of the accelerating orifice.

The laser beam from a 2 mW He-Ne laser is split by a calcite plate. The two beams are focused into two rectangular spots near the accelerating orifice. The light scattered by the particles is collected and focused onto a photomultiplier tube. A particle passing through two spots will produce two pulses. The velocity of the particle is measured by measuring the transit time between the two pulses.

A microcomputer is used to analyze and display the particle size data. Initial experiments showed that this instrument could be used to test the performance of a 10 mm nylon cyclone. Such experiments took only a few minutes and gave penetration curves with virtually no data scatter.

INTRODUCTION

When studying particle behavior, the most desirable parameter for characterization of a particle is its aerodynamic diameter - "the diameter of a unit density sphere with the same settling velocity as the particle in question." Traditionally, this characterization has been done with inertial, centrifugal, or cyclonic separation followed by a manual counting or weighing procedure. This procedure is tedious and time consuming, and has instigated development of several techniques for real time aerodynamic characterization of particles. In most of these techniques, the particles were first made to acquire a velocity which is related to their aerodynamic diameter. The velocity of the individual particle was then measured and the aerodynamic particle diameter was inferred from the measured particle velocity.

William Yanta (1) measured the particle velocity after a normal shock in a Mach 3 nozzle with a laser Doppler velocimeter and showed that the measured particle velocity correlated to the particle size. Dahneke (2) accelerated particles in a free jet expanding into a vacuum and measured the terminal velocity of the particles. Chabay and Bright (3) measured the settling velocity of the particles in a chamber. Kirsch and Mazumder (4) subjected particles to acoustic excitation and measured the phase difference between the acoustic excitation and particle oscillation. Russo et al (5) measured the velocity of decelerating particles near the stagnation line of a cylinder in the flow. Wilson and Liu (6) reported experimental and theoretical studies involving particle velocities near the exit of a converging nozzle. They have reported the measured velocities of particles of a known diameter in the range of 0.5 to 11.3 μm under various flow conditions.

Agarwal and Fingerson (7) described an Aerodynamic Particle Sizer (APS) in which the aerosol was introduced into a chamber through an accelerating nozzle and the velocity of the particles just downstream of the nozzle was measured by a laser Doppler velocimeter. The velocity information of the individual particles was then recorded by a microcomputer. At the end of the sampling cycle, the microcomputer calculated the aerodynamic diameter of the particles and displayed the particle size distribution in the form of a histogram. They reported the size distribution measurement of several monodisperse as well as polydisperse aerosols.

This paper describes a new commercial real-time aerodynamic particle sizer. In this instrument, the particles first acquire a velocity which is related to their aerodynamic diameter. The velocity of each particle is then measured by using a laser velocimeter.

DESCRIPTION

The APS is shown in Figure 1. It consists of two modules: (i) the sensor and (ii) the microcomputer for data analysis and display. A brief description of the two modules is given below.

SENSOR

The main part of the sensor module is an accelerating orifice and a laser velocimeter which is schematically shown in Figure 2. It consists of a 1.0 mm diameter outer orifice and a 0.8 mm diameter inner nozzle. About 20 percent of the sampled aerosol goes through the inner nozzle. The remaining 80 percent

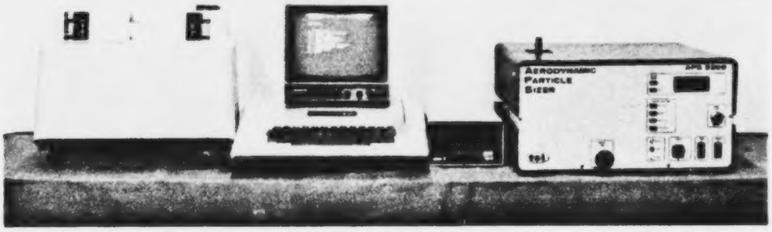

Figure 1. Photograph of aerodynamic particle sizer.

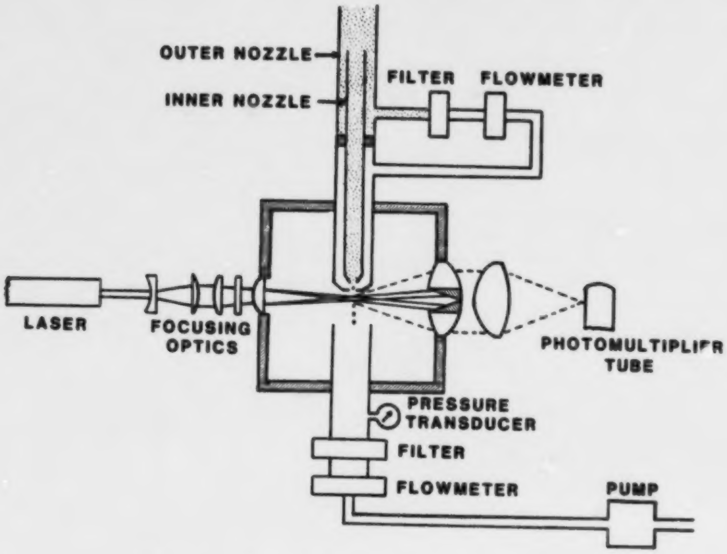

Figure 2. Schematic of sensor.

of the sampled aerosol passes through a filter and flowmeter and is reintroduced to the system as sheath air. The primary function of the sheath air is to confine the aerosol particles to the central region of the jet where the air velocity is uniform.

An air velocity of approximately 150 m/sec is maintained through the orifice by maintaining the sensing chamber at a pressure of 125 cm of water below the ambient inlet pressure. This is achieved by using a pressure transducer with an electrical output and feeding back the output of the pressure transducer to the vacuum pump.

The velocities of the individual particles exiting from the outer orifice are measured by a two-spot laser velocimeter. The velocimeter uses a polarized 2 mW He-Ne laser as its light source. As shown in Figure 2, the laser beam is first expanded by using a combination of a negative and a positive lens. It is then focused by another positive lens. A calcite plate placed after the focusing lens splits the beam by polarization. A final cylindrical lens makes two flat beams with rectangular cross-sections in front of the orifice. The main beams are then absorbed in a beam stop. The light scattered by the particles exiting from the accelerating orifice is collected (in the near forward direction) and focused onto a photomultiplier tube. A particle passing through the two beams produces two electrical pulses. The time interval (transit time, τ) between the two pulses is inversely proportional to the particle velocity and directly proportional to particle aerodynamic diameter.

A peak detecting circuit generates a digital level pulse for each particle pulse greater than a minimum threshold (see Figure 3). The time between these pulses is then measured by a high speed digital clock with 2 ns resolution. The measured transit time value is passed onto a Multi-Channel Accumulator (MCA) where the channel corresponding to the transit time value is incremented

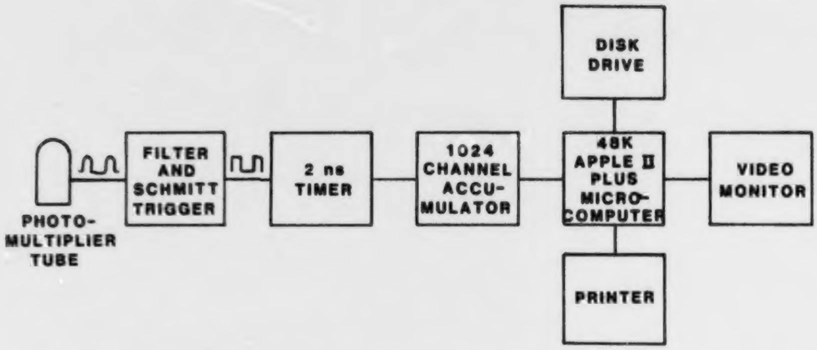
DISK DRIVE
PHOTO-MULTIPLIER TUBE
FILTER AND SCHMITT TRIGGER
2 ns TIMER
1024 CHANNEL ACCU-MULATOR
48K APPLE II PLUS MICRO-COMPUTER
VIDEO MONITOR
PRINTER

Figure 3. Block diagram of signal processing and data analysis.

by one. At the end of the sample period, the particle size distribution is determined from the MCA counts. The MCA has a total of 1024 accumulators, each capable of storing more than 10 million counts. The triggering circuit is located on a printed circuit board in common with the photomultiplier tube amplifier. The timing circuit and the MCA are located on separate printed circuit boards.

The total air flow and sheath air flow are measured by two thermal flowmeters. The true aerosol flow is calculated from the difference between the two flows.

In addition to the orifice assembly, laser velocimeter, timer, MCA, and flowmeters, the sensor module also houses a vacuum pump, and power supplies for the laser, photomultiplier tube, flowmeters, and vacuum pump.

MICROCOMPUTER FOR DATA ANALYSIS AND DISPLAY

The instrument uses an Apple II Plus (with 48K memory) microcomputer for data analysis and display. The microcomputer system includes an Apple Disk II drive and controller, a video monitor and an IDS 445 impact printer.

When the computer is instructed to take a sample, it clears all of the accumulators, starts and stops the sampling, reads the accumulators and translates the numbers stored in various accumulator bins to a particle size distribution using a pre-stored calibration curve.

The sample time is programmable from 1 second to 65536 seconds, 20 seconds being the default value. The computer can display the particle size distribution results in one of ten formats: accumulator bins vs. accumulator number in each bin; aerodynamic particle diameter vs. number, surface area, or mass concentration; aerodynamic particle diameter vs. cumulative number, surface areas, or mass; or in a normalized (percentage) format of the latter three quantities. For the size distribution displays, the particle size range is divided into 32 equal logarithmic channels per decade of size range. The instrument has the capability of providing a hard copy of all the graphic displays on 8 1/2 x 11 inch paper. In addition, the data for each channel can be printed in tabular form.

CALIBRATION

Calibration of the APS was carried out with two types of monodisperse aerosols. Monodisperse aerosols in the size range from 0.546 to 2.02 μm were generated by atomizing a dilute suspension of monodisperse polystyrene latex (PSL) particles. Dioctyl phthalate (DOP) particles in the size range of 3.15 to 15.76 μm were generated using a TSI Model 3050 Vibrating Orifice Monodisperse Aerosol Generator.

A PSL aerosol generation system was developed to facilitate the development of the APS. The system is schematically shown in Figure 4. It consists of four atomizers, each containing one size of PSL particles. The compressed air input to the atomizers is connected through solenoid valves and the outputs of the atomizers are connected to a common diffusion dryer (TSI Model 3062). The diffusion dryer consists of two coaxial cylinders; the outer one of plastic and the inner one of wire mesh. The space between the two cylinders is filled with silica gel. As the aerosol passes through the unobstructed inner cylinder, moisture diffuses to the silica gel. The aerosol then passes through a heated glass tube (TSI Model 3072) to ensure complete drying of the PSL particles.

Any one of the atomizers can be brought into operation by simply opening the appropriate solenoid valve. This system allows the generation of a particular size of PSL particles by turning on one switch and enables calibration of the instrument with four sizes of monodisperse aerosols in less than 10 minutes.

Figure 5(a) through 5(f) show the photodetector output for various calibration aerosols. It should be pointed out that these photographs are the superimpositions of several traces generated by the calibration aerosol particles, rather than single sweeps. The good repeatability of traces show that (1) the particles are monodisperse, (2) they have the same velocity, and (3) all the particles go through a region of uniform light intensity.

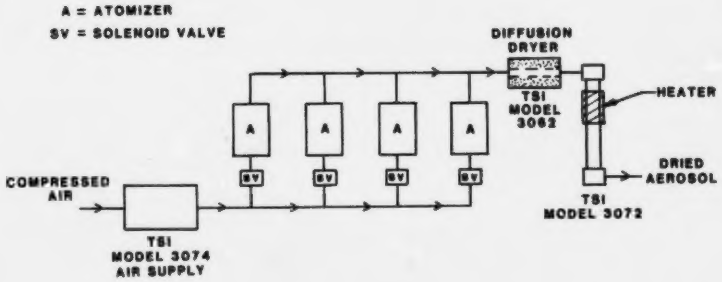

Figure 4. PSL aerosol generation system.

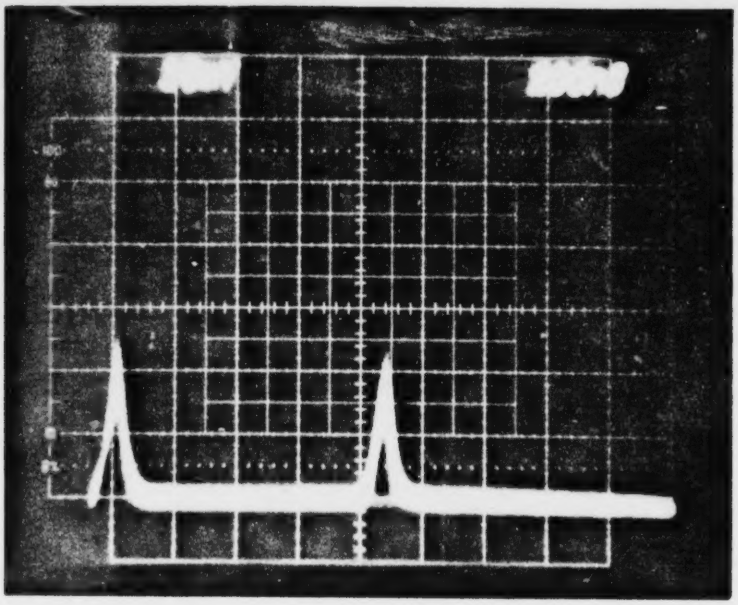

Figure 5(a). Photodetector output with 0.797 μm PSL particles.

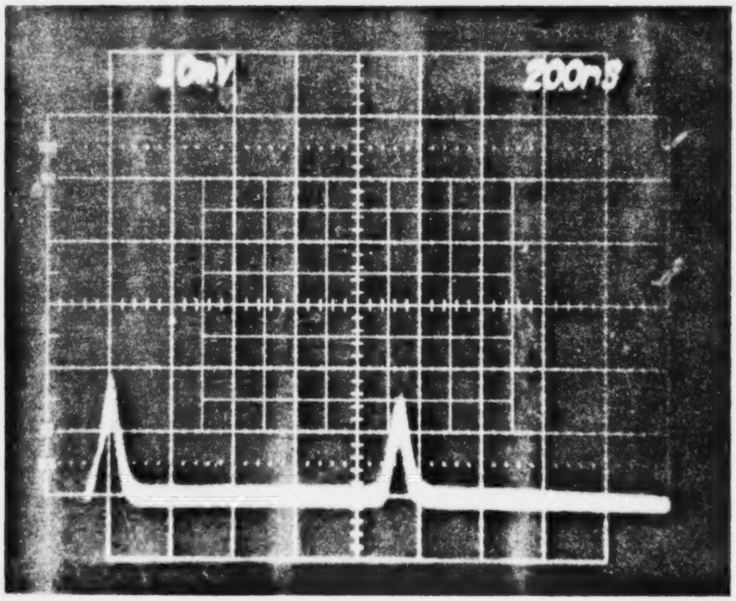

Figure 5(b). Photodetector output with 1.091 μm PSL particles.

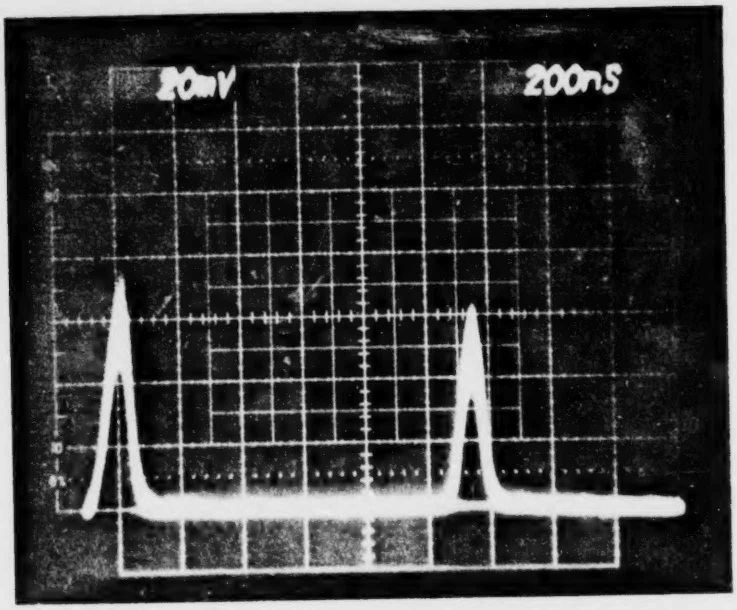

Figure 5(c). Photodetector output with 2.02 µm PSL particles.

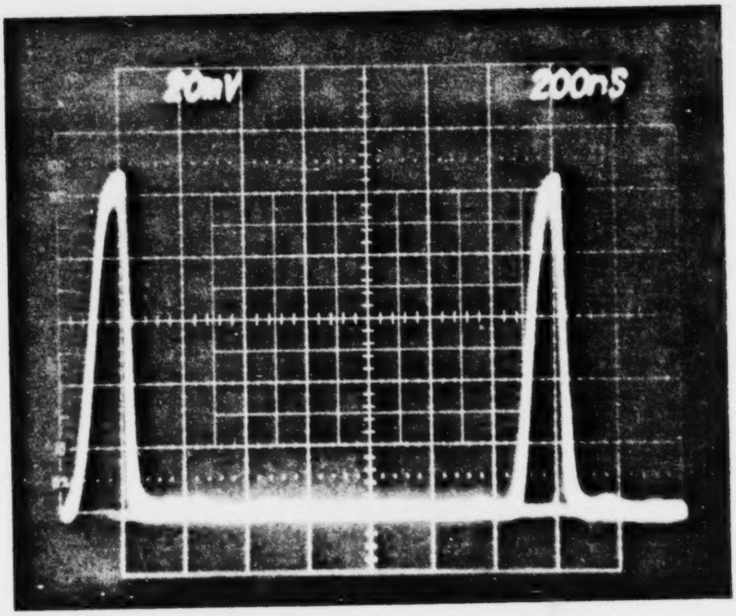

Figure 5(d). Photodetector output with 3.44 µm PSL particles.

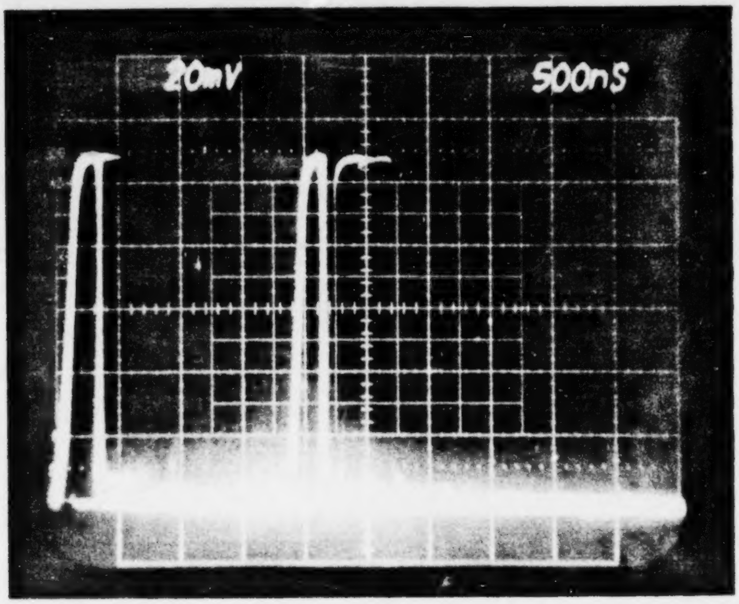

Figure 5(e). Photodetector output with 5.39 μm DOP particles.

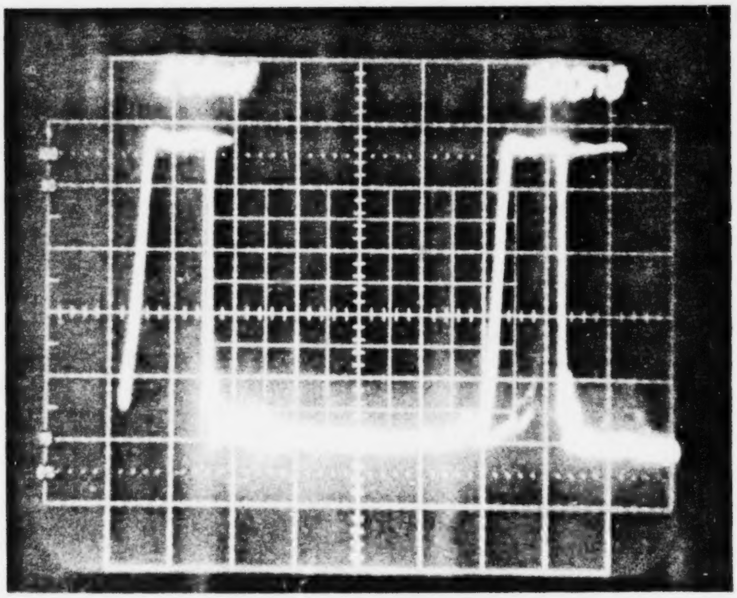

Figure 5(f). Photodetector output with 12.95 μm DOP particles.

Also note that the signal from 1.091 µm PSL particles is smaller than the signal from 0.797 µm PSL. Since the APS determines the particle size by measuring the time between the two pulses, this causes no problem. This is an important advantage of the APS over the typical OPC in which the height of such pulses is used to measure the particle size.

The calibration procedure of the instrument consisted of generating a monodisperse aerosol of specific size, sampling the aerosol by the instrument and noting the accumulator number containing the maximum counts. Since each accumulator is only 4 ns wide, the transit time is calculated by multiplying the accumulator number by 4. Then a monodisperse aerosol of another size is generated and the procedure is repeated.

The aerodynamic diameter, D_a, of the calibration aerosol is calculated from its geometric diameter, D_p, and density, ρ_p, using the following equation:

$$\sqrt{C(D_a)} \cdot D_a = \sqrt{C(D_p) \cdot \rho_p} \cdot D_p$$

where C(D) is Cunningham slip correction for a particle of diameter D. Table 1 shows the geometric and aerodynamic diameter of various calibration aerosols and the corresponding transit time as measured by the aerodynamic particle sizer. Figure 6 shows the calibration points in graphical format.

Figure 7 shows the accumulator bin output for an aerosol containing 0.797, 1.091, 2.02, and 3.44 µm PSL particles. Such an aerosol was generated by opening all four solenoid valves simultaneously in the particle generation system shown in Figure 4. Figure 8 shows the size distribution of the same aerosol.

TABLE 1. CALIBRATION DATA POINTS

Geometric Diameter (µm)	Particle Density (gm/cm^3)	Aerodynamic Diameter (µm)	Channel Number	Transit Time (ns)
.546	1.027	.554	202.5	810
.797	1.05	.819	217	868
1.091	1.05	1.12	233	932
2.02	1.027	2.05	286	1144
3.153	.9861	3.13	343.5	1374
3.972	.9861	3.94	380	1520
6.792	.9861	6.74	497	1988
8.816	.9861	8.75	555	2220
11.614	.9861	11.53	639	2556
15.76	.9861	15.65	753	3012

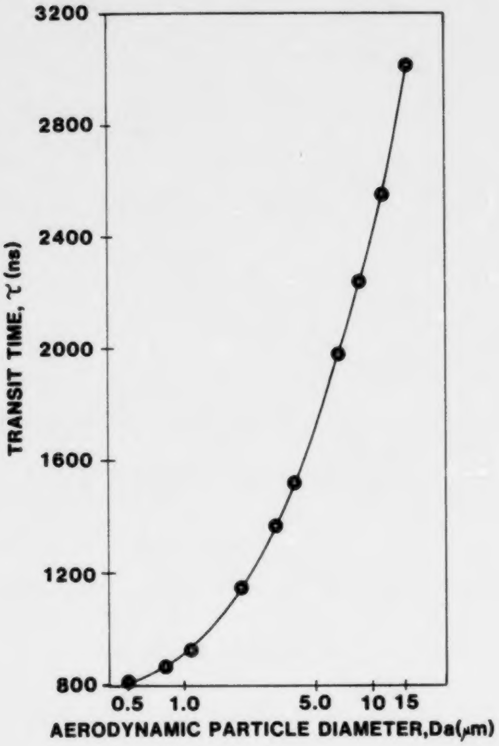

Figure 6. Calibration curve for APS.

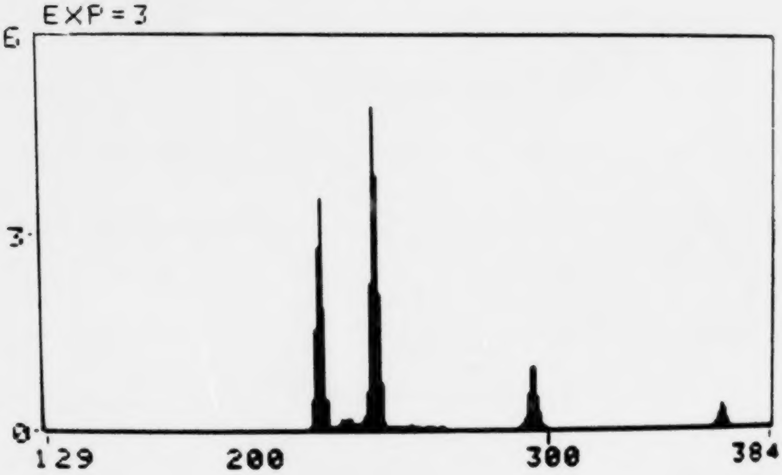

Figure 7. Accumulation bin output with an aerosol containing 0.797, 1.091, 2.02, and 3.44 μm PSL particles.

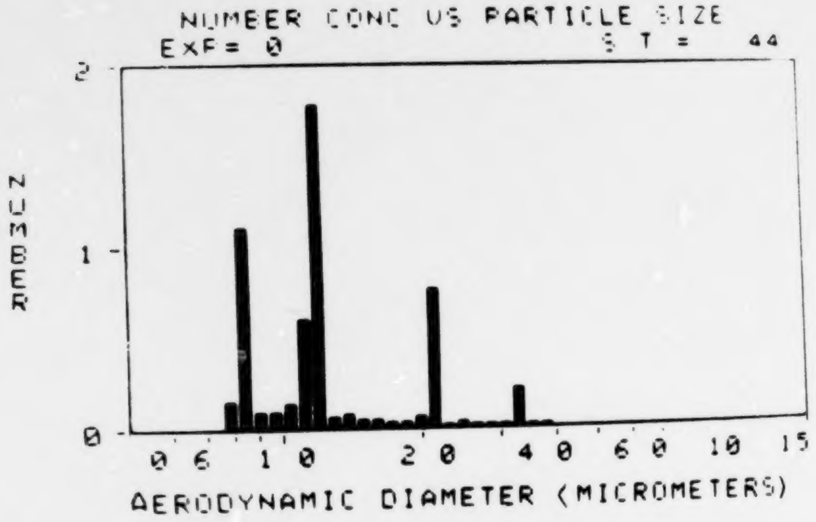

Figure 8. Size distribution of an aerosol containing 0.797, 1.091, 2.02, and 3.44 μm PSL particles.

The resolution of an instrument can be described by the geometric standard deviation of monodisperse aerosols as measured by the instrument. Figure 9 shows a typical size distribution of a PSL aerosol shown on log probability paper. Table 2 shows the geometric standard deviation of various PSL and DOP aerosols measured by the APS. Column 3 of Table 2 shows the standard deviations provided by the manufacturer.

Since the measured geometric standard deviation also includes the standard deviation of the aerosol itself, it is not an indication of the absolute resolution of the instrument. However, since both PSL and DOP calibration aerosols are normally used for instrument calibration and these aerosols are highly reproducible, these overall geometric standard deviations can be used for the intercomparison of various instruments.

APPLICATION OF APS TO CYCLONE EFFICIENCY TESTING

One application of the APS is in evaluating size classifying devices such as cyclones. We have performed some preliminary experiments to work out a procedure for such tests. The experimental set-up is shown in Figure 10. A fluidized bed aerosol generator (TSI Model 3400) was used to generate an aluminum oxide aerosol. The generator produced a steady aerosol into a plastic bag. The aerosol from the bag was sampled through the cyclone into the APS. Since the total flow of the APS was 5 LPM, make-up dilution air was added between the cyclone and the APS and monitored by a thermal flowmeter (TSI Model 2011). The flow through the cyclone could be varied by adjusting the dilution air added near the APS inlet. The size distribution of the aerosol passing through the cyclone is measured by the APS. For the measurement of true aerosol concentration in the plastic bag, the cyclone was removed and the

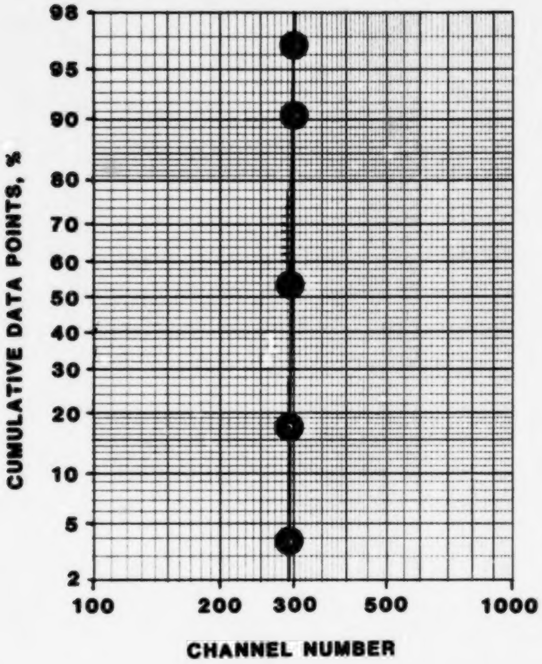

Figure 9. Distribution of PSL aerosol.

TABLE 2. MEASURED GEOMETRIC STANDARD DEVIATION

Diameter (μm)	Particle Composition	Geometric Standard Deviation Manufacturer's Specification	Geometric Standard Deviation Measured
.797	PSL	1.005	1.025
1.091	PSL	1.0075	1.020
2.02	PSL	1.007	1.011
6.792	DOP	<1.06	1.0058

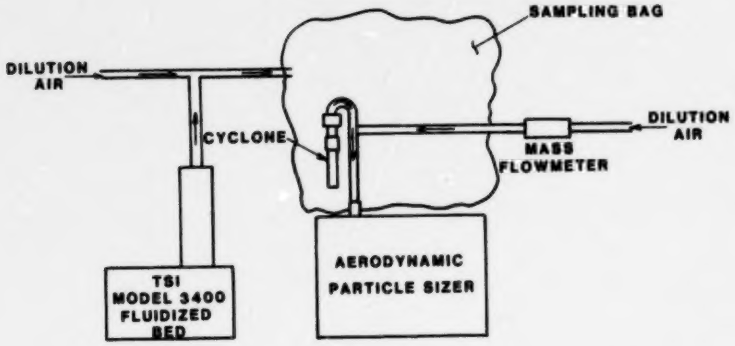

Figure 10. Experimental set-up for cyclone efficiency tests.

APS sampled the aerosol from the bag with the same amount of dilution air added. Since the aerosol passed through the same sampling system, the losses in the line are identical and can be ignored. The efficiency of the cyclone is calculated by comparing the number of particles in each channel.

Figures 11(a) and 11(b) show the particle size distribution measured by the APS with and without the cyclone, respectively. Figure 11(c) shows the ratio of the size distribution shown in 11(a) and 11(b). Figure 11(c) represents the sampling efficiency curve of the cyclone.

Figure 12 shows the sampling efficiency curve of the cyclone at various flow rates. These preliminary tests show that the APS can be used to test cyclones. It should be mentioned that the curves shown in Figure 12 are not intended to be representative penetration curves. In the present experimental set-up, the flow through the cyclone could be substantially inaccurate, as much as 20 percent. The primary intention of these experiments was to illustrate the application of the APS, not to test the cyclone.

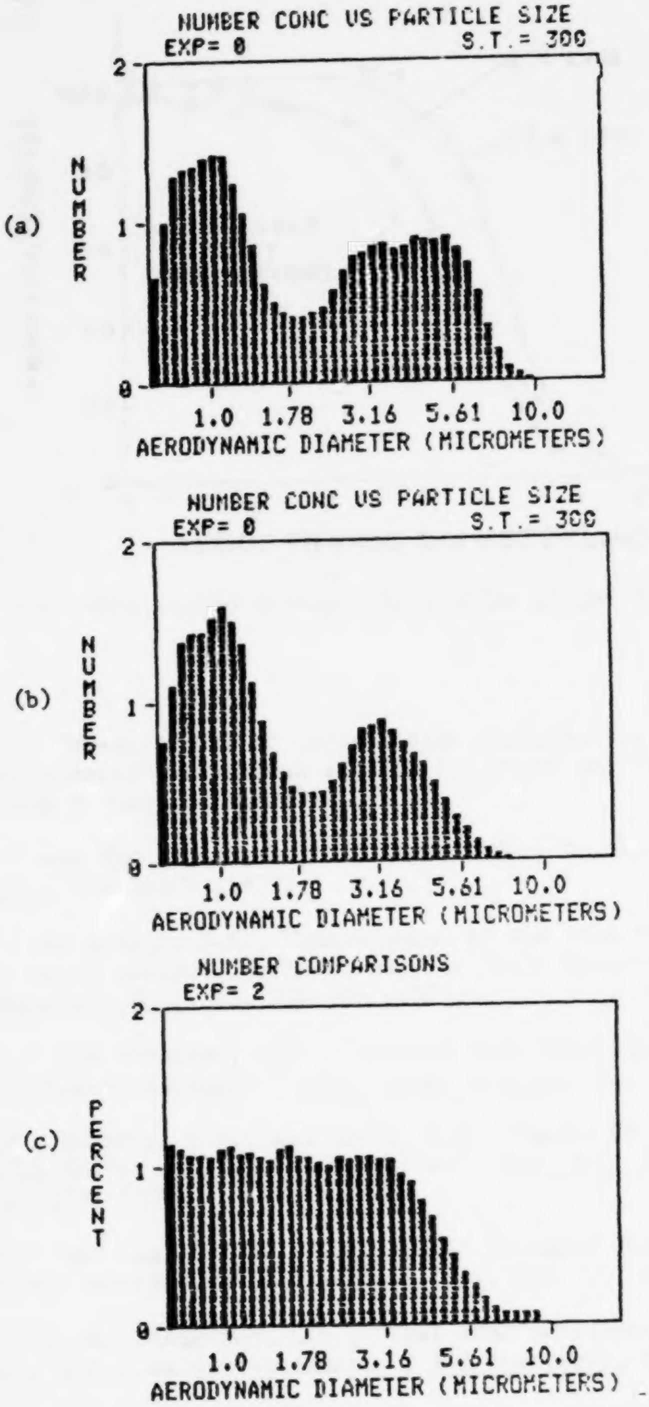

Figure 11. Particle size distribution before and after the cyclone and the percent penetration through the cyclone.

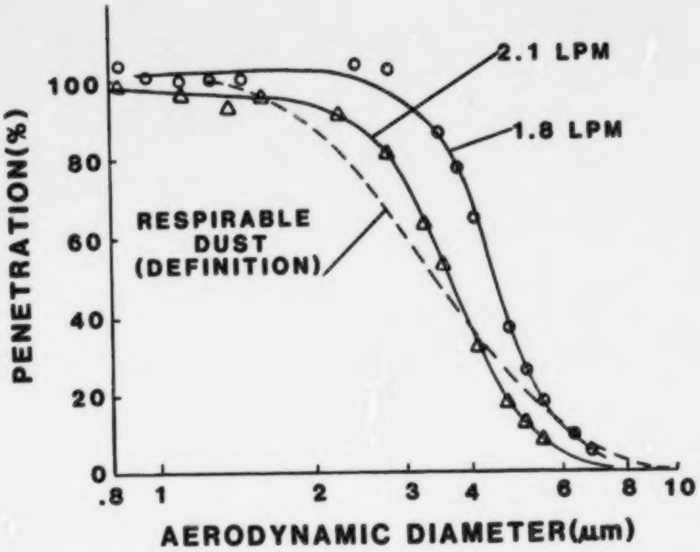

Figure 12. Penetration through the cyclone at two flow rates.

REFERENCES

1. Yanta, W.J., "Measurements of Aerosol Size Distribution with a Laser Doppler Velocimeter", Presented at AIAA 6th Fluid and Plasma Dynamics Meeting, Palm Springs, CA (1973).

2. Dahneke, G. and Flachsbart, H., "An Aerosol Beam Spectrometer", J. Aerosol Sci., 3:345-349 (1972).

3. Chabay, I. and Bright, D.S., "Measurement of the Size Distribution of Liquid and Solid Aerosols by Laser Doppler Shift Spectroscopy", J. Colloid Interface Sci., 63, 204-309 (1977).

4. Kirsch, K.J. and Mazumder, M.K., "Aerosol Size Spectrum Analysis Using Relaxation Time Measurement", Appl. Phys. Letters, 26, 193-195 (1975).

5. Russo, A.J., Hackett, C.E., and Croll, R.H., "Laser Velocimeter Method for the Inertial Sizing of Airborne Particles", Rev. Sci. Instrum., Vol. 50, No. 11, pp. 1391-1395.

6. Wilson, J.C. and Liu, B.Y.H., "Aerodynamic Particle Size Measurement by Laser-Doppler Velocimetry", J. Aerosol Sci., Vol. 11, pp. 139-150 (1980).

7. Agarwal, J.K. and Fingerson, L.M., "Real-Time Aerodynamic Particle Size Measurement with a Laser Velocimeter", TSI Quarterly, Vol. V, Issue 1 (1979).

The work described in this paper was not funded by the U.S. Environmental Protection Agency. The contents do not necessarily reflect the views of the Agency and no official endorsement should be inferred.

The work described in this paper was not funded by the U.S. Environmental Protection Agency. The contents do not necessarily reflect the views of the Agency and no official endorsement should be inferred.

Paper 24

A HIGH FLOW RATE, HIGH SENSITIVITY OPTICAL PARTICLE COUNTER: DESIGN AND PERFORMANCE

A. Lieberman
HIAC/ROYCO Instruments Division
Pacific Scientific

ABSTRACT

Design and operation of a new laser illuminated optical particle counter are described. Use of an elliptical mirror and a rectangular sample stream cross section permit measurement of particles 0.3 μm and larger at a sample flow rate of 28 LPM with good resolution and acceptably low coincidence errors at 35 particles per ml. An 8-channel comparator system covers the size range from 0.3 μm to 15 μm. Data pulse sorting, display, alarm, printing, operation sequencing and self-testing are under control of a dedicated microprocessor. Programming is based on past experience in industrial particle counting and sizing requirements.

INTRODUCTION

Design and operation of a new laser illuminated optical particle counter are described. The optical/air handling systems relationships required to permit defining particles of 0.3 μm and larger in a sample stream of 28 LPM are discussed. Electronic system control, data processing and self test capabilities are described.

Design considerations were based upon anticipated use in a variety of applications. It was realized that the major use would be in relatively clean assembly areas with operation by personnel whose training ranged from near zero to highly skilled operators. At the same time applications in atmospheric research and in environmental monitoring was considered. With such a wide range of applications in mind, the need for handling a maximum sample flow rate, detecting the smallest possible particle with minimum coincidence error at that flow rate, along with the capability for data processing that ranged from a simple go-no-go indication to multi-size range recording resulted in developing the general specifications for the system. These are shown in Table 1.

TABLE 1. PARTICLE COUNTER SPECIFICATIONS

Particle Size Sensitivity	0.3 µm
Concentration Limit (10% coincidence)	35/ml
Sample Flow Rate	28 LPM
Dynamic Range	0.3 - 15 µm
Illumination	He Ne Laser
Scattering Angles	30° - 170°
Particle Size Ranges Displayed	2
Particle Size Ranges Printed	2 - 8
Alarm, Audible/Visual	Pre-set Rate Base
Sample Time Selection	0.1 - 10 min
Print Format	Alpha Numeric
Self-check	Optics, RAM, Clock
Auxiliary Output	RS232, 20 ma loop

SYSTEM DESCRIPTION

The overall particle counter system is shown in Fig 1. The Model 1000 sensor package contains the optics assembly, an 8-channel comparator/digitizer and signal output controls. The vacuum pump is packaged separately. The Model 4000 controller receives particle count data and sensor status information from the sensor. It then records and processes the particle count data in either cumulative or differential format, verifies sensor calibration, sets data recording intervals and interval delays, establishes alarm level actuation, printing information as desired, and displays system status as required. Auxiliary outputs provide data to a computer or printer and permit remote device (blower, valve, etc.) operation by relay closure.

The optics layout is shown in Fig 2. Illumination is provided by a low wattage He Ne laser. A rectangular aerosol stream is passed through the laser beam at one focus of an ellipsoidal mirror with the axis of the beam, the mirror and the aerosol stream mutually orthogonal. The direct beam is then set to a Brewster's angle reflective light trap for dissipation with a portion of the beam collected on a laser monitor photodetector whose output is used for gain control. Gain control is also set by a pulsed calibration signal (initiated on command, on system turn-on and at 10 min. intervals) that is received by the photomultiplier located at the other focus of the ellipsoid. With this system light is collected over scattering angles from 30° to 170°. By discarding small angle scattering, the tendency for a polytonic response curve from transparent particles is eliminated, but adequate response is obtained for 0.3 µm particle detection.

Since the specifications for the system required a viewed sample flow rate of 28.3 LPM and weight was a problem, a fully sheathed air flow system was not possible. A rotary vane vacuum pump, rated at 1.3 SCFM free air was

Reproduced from
best available copy.

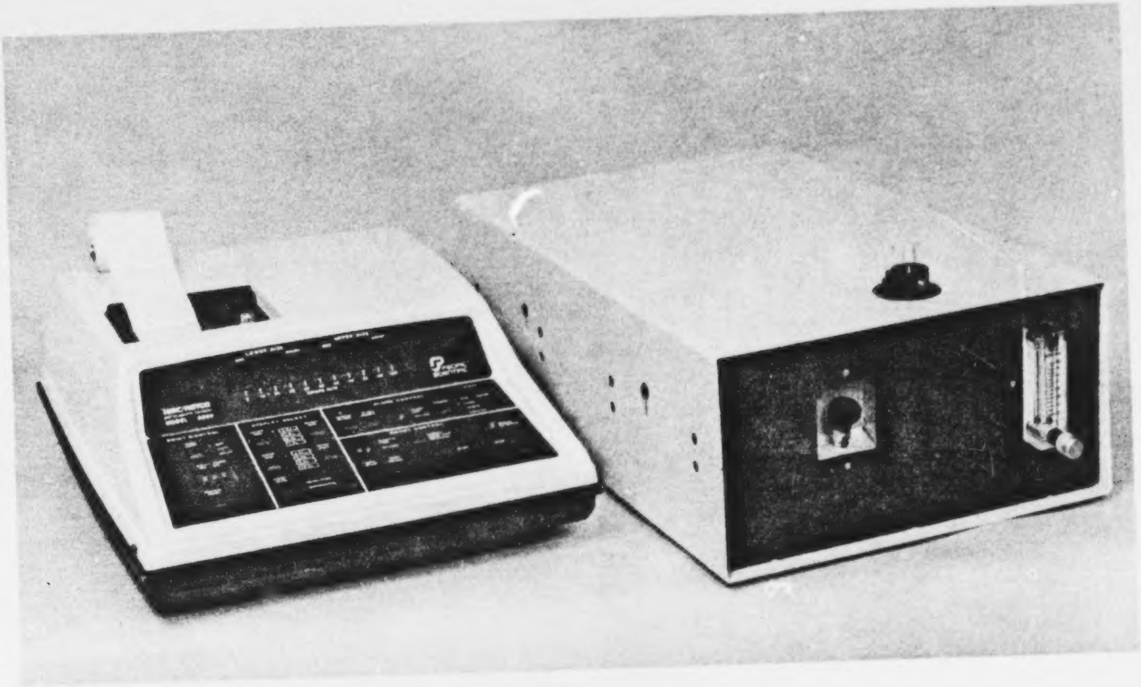

Figure 1. Sensor system

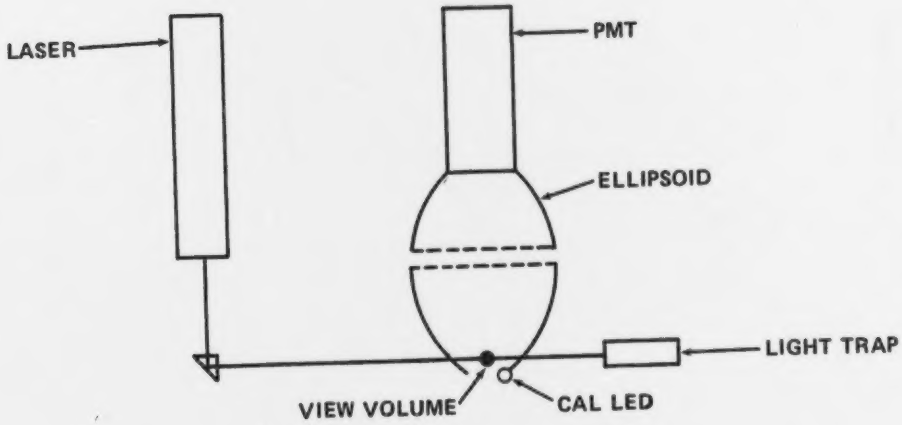
LASER
PMT
ELLIPSOID
LIGHT TRAP
VIEW VOLUME
CAL LED

Figure 2. Optics layout, model 1000.

used to draw sample air at a metered flow rate of 1.0 SCFM. Filtered pump exhaust air is passed through a HEPA-type cartridge filter with approximately 0.15 SCFM returned to flush the optical assembly and 1.0 SCFM vented. The aerosol inlet tube is shaped to provide a rectangular sample jet of 0.5 mm x 6.6 mm passing through the laser beam. The rectangular jet is formed by smooth transition from a cylindrical inlet tube so as to minimize pressure drop at 28.3 LPM flow rate.

The electronic system within the sensor assembly handles pulses from the photomultiplier pre-amplifier. The pulses are fed to an 8-channel comparator, thresholds set to differentiate pulse amplitudes based on calibration levels derived from latex sphere measurements. The pulses are digitized for parallel transmission to the controller assembly. The sensor electronic system includes the auto gain control based on laser output level and calibrator LED pulse level measurements. In addition, status reporting components define in digital format to the controller the laser status, the signal level between pulses to verify optical component alignment, the calibrator operation.

The controller is a microprocessor assembly that receives and processes information from the sensor, returns operation commands to the sensor and provides data and control information to external devices. A Rockwell AIM 65 microcomputer is the control base. The on board 20 character alphanumeric display and printer are used. In addition, an interface assembly containing input/output and digital processing circuitry for communication to and from the sensor assembly is used. The interface assembly also provides a serial output to external printers and computers, along with hardware for alarm and audible pulse rate indicator. Battery back-up and charging components are also included. A keyboard interfaces to the microprocessor to allow the operator to input system operating commands for counting control, display selection, print/record control and alarm control.

SENSOR PERFORMANCE

The optical system performance was defined by using monosized latex particles and recording pulse height distribution with Tracor-Northern TN 1705 pulse height analyzer. Fig 3 shows the response curve for particles ranging from 0.312 μm to 15 μm. The sensitivity at the smallest size range and the response curve monotonicity are adequate. Fig 4 shows pulse height distribution for several monosized particles within the system dynamic range. Data for Figs 3 and 4 were obtained with a sample flow rate of 28.3 LPM and with the particle concentration recorded at approximately 25 per ml. In this way the coincidence error was maintained below 10% and the pulse width was maintained at 10 μsec.

CONTROLLER OPERATION

Although the sensor performance is quite good at the high flow rate and the relatively large sensing volume required to handle this flow rate without

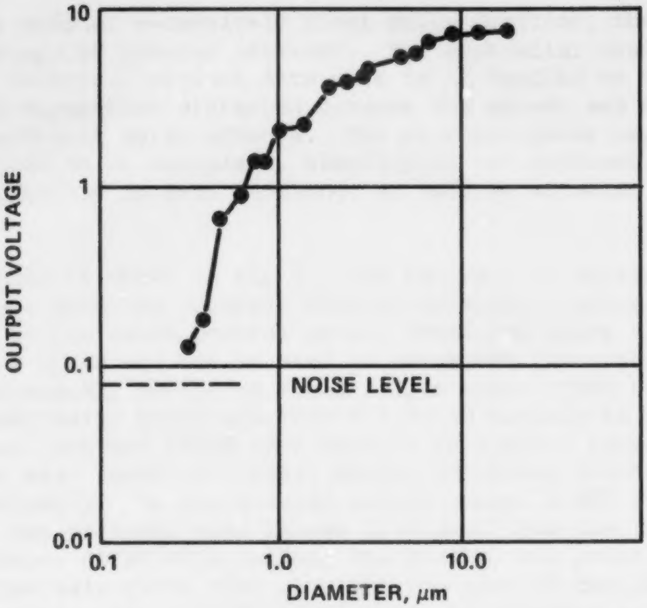

Figure 3. Response curve.

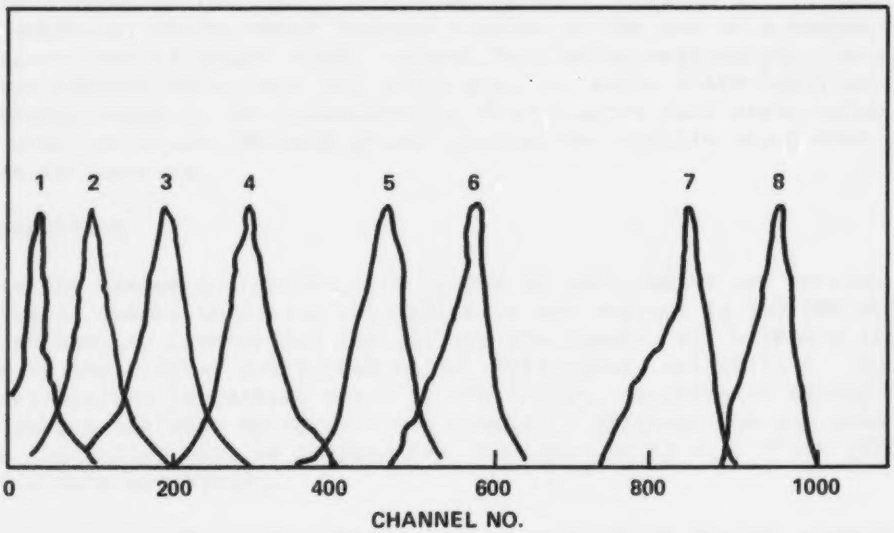

Figure 4. Pulse height distributions - PSL.

1 - 0.312 μm
2 - 0.500 μm
3 - 0.95 μm
4 - 1.32 μm
5 - 2.02 μm
6 - 2.82 μm
7 - 10.1 μm
8 - 20.1 μm

extreme pressure drop or excessively short pulse duration, the controller operation is perhaps of greater interest. The controller design base considered several factors. Digital data were to be handled so as to permit relatively large separation distances between the sensor and the controller with minimum electrical noise effects. The microprocessor capability for pre-programming was to be maximized, simplifying the keyboard operation while maintaining versatility in data handling, as well as allowing self-checking functions.

The controller is shown in Fig 5. The keyboard is divided into four functional groups: counting control, display selection, printing control and alarm control. In the count control group, START initiates counting cycle; STOP terminates a cycle and can be used to interrupt data printing; AUTO START enables the continuously restarted timed sample mode; TIMER ENABLE enables the timed sample mode, using intervals from 0.1 to 10 minutes as set by the SAMPLE TIME thumbwheels; AUDIBLE PULSE RATE enables an audible pulse output for the selected smaller size range particles; MANUAL CALIBRATE initiates a calibration cycle manually. In the display select group, LOWER SIZE AND UPPER SIZE select the two particle size ranges displayed from the four each available for each range; COUNT MODE selects the display and print mode as cumulative or differential; CLOCK TIME displays the time of day and is used for the clock setting procedure; COUNT RATE causes the display to show a bar graph equivalent to the counting rate for the selected lower size range. In the print control group, PRINT MODE selects the printer operation from the choices shown between AUTO after each count cycle and DELAY after the count cycle following a delay period from 1.0 minutes to 10.0 hours as set by the DELAY TIMER thumbwheel; MANUAL PRINT enables a print at the end of a sample period. In the alarm control group, RANGE selects full scale setting for alarm initiation and the count rate bar graph display, while ALARM LIMIT sets the alarm trigger value in 10% increments of the selected full scale value; ALARM ENABLE arms the alarm; AUDIBLE ENABLE enables the audible alarm when the preset limit is exceeded.

SYSTEM OPERATION

When the system is turned on, a series of self checks are carried out. These include checks to ensure that all bits are correct in the RAM and EPROM as well as battery back-up for the RAM and the clock. All keyboard LED's and segments in the display are turned on to verify their reliability. An initial sensor calibration is carried out. If the initial calibration cannot be made, three attempts are made to correct the problem. If these are not effective, then the controller will be inoperative and the display will flash SENSOR FAIL. Audible outputs are tested.

During operation, a calibration cycle occurs at 10 minute intervals, along with continuous monitoring of the sensor alignment by baseline level observation. If any of these levels move out of acceptable range, up to three calibration attempts occur and if not achieved, the sensor failure signal is received. In addition, particle concentration is monitored to ensure that over concentration or over rate conditions do not occur. If the data indicate over concentration or over rate then the printer reports the condition along with the data collected so that the operator can decide on disposition of the data. When the system is to be used to supply data to an

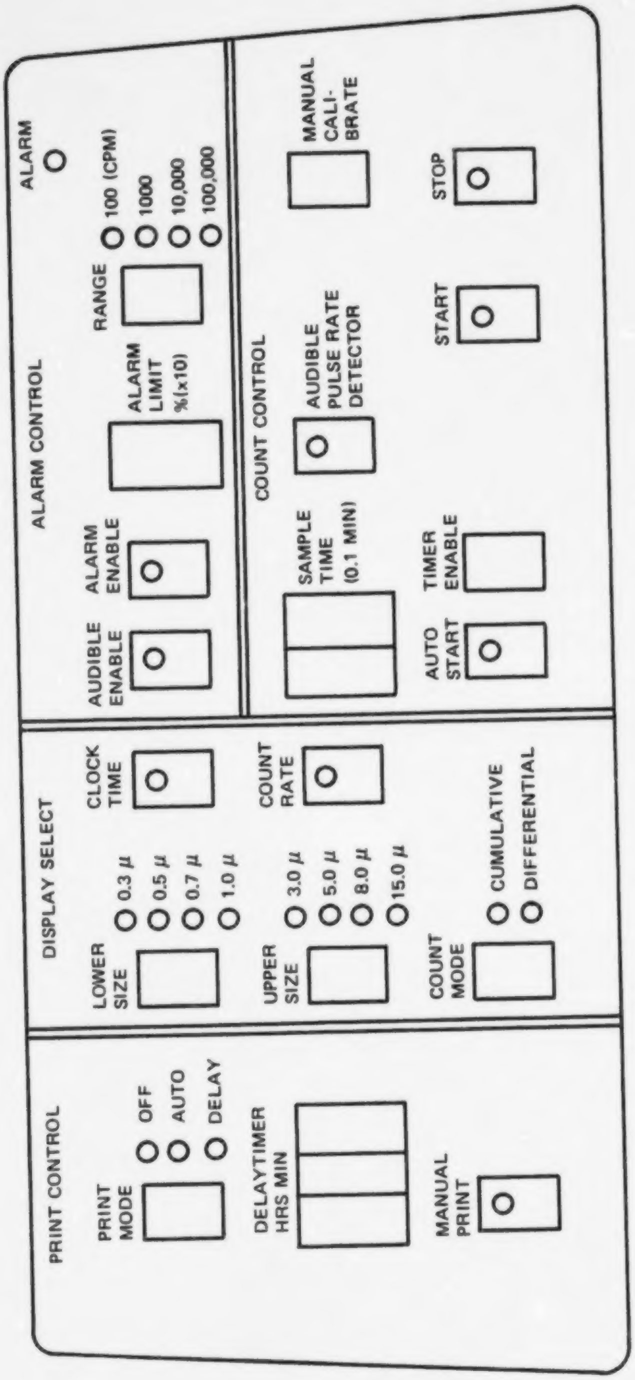
PRINT CONTROL
PRINT MODE
OFF
AUTO
DELAY
DELAYTIMER HRS MIN
MANUAL PRINT
DISPLAY SELECT
LOWER SIZE
0.3 μ
0.5 μ
0.7 μ
1.0 μ
CLOCK TIME
UPPER SIZE
3.0 μ
5.0 μ
8.0 μ
15.0 μ
COUNT RATE
COUNT MODE
CUMULATIVE
DIFFERENTIAL
ALARM CONTROL
AUDIBLE ENABLE
ALARM ENABLE
ALARM LIMIT %(x10)
RANGE
100 (CPM)
1000
10,000
100,000
ALARM
COUNT CONTROL
SAMPLE TIME (0.1 MIN)
AUDIBLE PULSE RATE DETECTOR
MANUAL CALI-BRATE
AUTO START
TIMER ENABLE
START
STOP

Figure 5. Controller keyboard.

external computer, either RS232C or 20 ma current loop output can be used. If the receiving computer does not support the handshaking capability of the controller, then the printer will operate indicating SERIAL TIME OUT, but preserving the data.

DATA EXAMPLES

Some examples of the printed data are shown to illustrate operation of the system. Table 2 shows the print-outs obtained at turn-on when the system has passed or failed the several test criteria for sensor and controller. If the sensor has passed the test criteria then no print-out occurs. Table 3 shows a print of a timed sample in the differential mode. Table 4 shows a print when only two channels of data are desired and an alarm condition has occurred. Table 5 shows the data printed when the computer/receiver has not supplied the clear-to-send signal. Table 6 shows manual and timed data in the cumulative mode with 8 channels of print-out and an alarm condition.

TABLE 2. PASS/FAIL PRINTS

PRINTOUT	EXPLANATION
PASS TESTS	
HIAC/ROYCO MODEL 430	Heading
07/29/81 11:45:10	Time
SELF TEST RESULTS	Self Test Headling
RAM TEST OK	Regular RAM Test
CHECK SUM OK	EPROM Test
BATTERY TEST OK	Battery Test
BATTERY RAM OK	Battery RAM Test
CLOCK RUNNING	Clock Test
FAIL TESTS	
HIAC/ROYCO MODEL 430	Heading
07/29/81 11:45:10	Time
SELF TEST RESULTS	Self Test Heading
* RAM TEST FAILED	Regular RAM Test
* CHECK SUM FAILED	EPROM Test
* BATTERY TEST FAIL	Battery Test
* BATTERY RAM FAIL	Battery RAM Test
* CLOCK NOT RUNNING	Clock Test
HIAC/ROYCO MODEL 430	Heading
07/29/81 11:45:10	Time
SENSOR FAILS	Sensor Failure Heading
3RD ATTEMPT	Calibrate Fail Number
* SELF CAL FAIL	Calibrate Level Failure
* LASER OFF	Laser is blocked or not ON
* ALIGNMENT FAIL	Alignment is bad
* CAL STATUS FAIL	Calibrate Hardware Fail
* LASER SOLENOID FAIL	Laser Blockage Solenoid Failure

TABLE 3. EIGHT-CHANNEL DATA

PRINTOUT	EXPLANATION
EIGHT CHANNEL DIFFERENTIAL DATA	
HIAC/ROYCO MODEL 430	Heading
07/29/81 11:45:10	Time
** DATA PARAMETERS *	Sample Parameters Heading
DIFFERENTIAL MODE	Count Mode
100K CPM at 10%	Alarm Range and Setting
0.1 MIN SAMPLE TIME	Timed Sample Time
** ALARM STATUS **	Alarm Status Heading
NO OVERRATE	Status of Alarm
** PARTICLE COUNTS *	Particle Count Data Heading
DISPLAYED DIFF	Displayed Channels Data
SIZE COUNTS	
1.0-3.0 000000	
3.0-INF 000000	
8 CHANNEL DIFF	Eight Channel Data
SIZE COUNTS	
0.3-0.5 000000	
0.5-0.7 000000	
0.7-1.0 000000	
1.0-3.0 000000	
3.0-5.0 000000	
5.0-8.0 000000	
8.0-15. 000000	
15.-INF 000000	

TABLE 4. TWO-CHANNEL PRINT

PRINTOUT	EXPLANATION
TWO CHANNEL DIFFERENTIAL DATA USING OPTION SWITCH 5	
HIAC/ROYCO MODEL 430	Heading
07/29/81 11:45:10	Time
** DATA PARAMETERS *	Sample Parameters Heading
DIFFERENTIAL MODE	Count Mode
100K CPM AT 10%	Alarm Range and Setting
0.1 MIN SAMPLE TIME	Timed Sample Time
** ALARM STATUS **	Alarm Status Heading
NO OVERRATE	Status of Alarm
** PARTICLE COUNTS *	Particle Count Data Heading
DISPLAYED DIFF	Displayed Channels Data
SIZE COUNTS	
1.0-3.0 000000	
3.0-INF 000000	

TABLE 5. HANDSHAKE NOT SATISFIED

DATA REPORT AFTER THE SERIAL TIMEOUT
CTS NOT RECEIVED WITHIN 30 SECONDS

********************	
SERIAL TIMEOUT FAIL	Identification of Serial Timeout
********************	
HIAC/ROYCO MODEL 430	Heading
07/29/81 11:45:10	Time
** DATA PARAMETERS *	Sample Parameters Heading
CUMULATIVE MODE	Count Mode
100K CPM AT 10%	Alarm Range and Setting
0.1 MIN SAMPLE TIME	Timed Sample Time
** ALARM STATUS **	Alarm Status Heading
NO OVERRATE	Status of Alarm
** PARTICLE COUNTS *	Particle Count Data Heading
DISPLAYED CUM	Displayed Channels Data
SIZE COUNTS	
1.0-INF 000000	
3.0-INF 000000	

TABLE 6. DATA WITH ALARM

```
HIAC/ROYCO MODEL 430                      HIAC/ROYCO MODEL 430
 08/17/81  14:42:54                        08/17/81  14:43:19

** DATA PARAMETERS *                      ** DATA PARAMETERS *
  CUMULATIVE MODE                           CUMULATIVE MODE
 1000 CPM at 100%                          1000 CPM AT 100%
00:01:54 SAMPLE TIME                      0 1 MIN SAMPLE TIME

**  ALARM STATUS  **                      **  ALARM STATUS  **
OVERRATE AT 14:42:39                      OVERRATE AT 14:43:13
 1000 CPM AT 100%                          1000 CPM AT 100%

** PARTICLE COUNTS *                      ** PARTICLE COUNTS *
   DISPLAYED CUM                             DISPLAYED CUM
   SIZE     COUNTS                           SIZE     COUNTS
  0.3-INF   001529                          0.3-INF   000078
  3.0-INF   000000                          3.0-INF   000000

   8 CHANNEL CUM                             8 CHANNEL CUM
   SIZE     COUNTS                           SIZE     COUNTS
  0.3-INF   001529                          0.3-INF   000078
  0.5-INF   000511                          0.5-INF   000029
  0.7-INF   000149                          0.7-INF   000013
  1.0-INF   000008                          1.0-INF   000000
  3.0-INF   000000                          3.0-INF   000000
  5.0-INF   000000                          5.0-INF   000000
  8.0-INF   000000                          8.0-INF   000000
  15.-INF   000000                          15.-INF   000000
```

The work described in this paper was not funded by the U.S. Environmental Protection Agency. The contents do not necessarily reflect the views of the Agency and no official endorsement should be inferred.

Paper 25

A COMPARISON OF SOOT SIZE AND NUMBER DENSITY MEASURED SIMULTANEOUSLY IN A SWIRL-STABILIZED COMBUSTOR BY EXTRACTIVE AND NON-INTRUSIVE OPTICAL PROBES

G. S. Samuelsen, R. L. Hack
Mechanical Engineering
University of California, Irvine

C. C. Poon, W. D. Bachalo
Spectron Development Laboratories

H. J. Clewell
Air Force Engineering and Services Center

ABSTRACT

Measurements of soot size, number density, morphology, weight concentration, and chemical composition were made on samples from a swirl-stabilized combustor. The integrity of the sample was tested using non-intrusive optical measurement of soot size and number density at the entrance of the extractive probe, at various locations in the combustor. The optical measurements showed sample perturbation by the extractive probe; e.g., the soot number density varied from no change to a 200-fold increase to a 70-fold decrease compared to the soot number density measured in the absence of the extractive probe. The extent of perturbation depended on the combustor operating conditions, the location of the optical probe in the flow, and the position of the extractive probe relative to the optical probe.

INTRODUCTION

An increase in soot production is closely tied to changes in the types of fuels contemplated for use in a variety of power plants. Prime examples of principal concern include gas turbine engines, boilers, and furnaces. Coal and shale derived jet fuels considered for gas turbine applications are rich in aromatics and inevitably have a high propensity to form soot. The net result is an increased radiative thermal loading to the combustor wall, increased erosion to turbine blades, and increased emission of particulate. Fuels available for boilers and furnaces are increasing not only in aromaticity, but in fuel nitrogen as well as the supply moves to heavy oils and syncrudes. To suppress the formation of fuel NO, the primary zone of boilers must be operated fuel rich with an associated potential for increased particulate formation and emission.

As the interest focuses on the mechanics of soot formation, so does the need to measure local properties of soot such as number density, weight concentration, and particulate size distribution. Extractive probes have been and continue to be used for these measurements. The use of such techniques is dictated by state-of-the-art and cost. The only viable alternatives are non-intrusive, optical methods which are in their infancy in development.

Two major questions are associated with the use of extractive probes -

- Representativeness of sample. Is the extracted sample representative of particulate at the probe entrance or do the processes of extraction, transport, and subsequent deposition of the particulate on a filter transform the morphology and number density of the soot?
- Flow perturbation. Does the presence of the probe in the flow perturb the local conditions (e.g., temperature, aerodynamics, chemistry) and thereby produce a condition at the probe entrance that is different from that which occurs in the absence of the probe?

These questions are especially important in flows, such as those that occur in gas turbine combustors, boilers, and furnaces, where the aerodynamics includes swirl and flow reversal.

This paper presents data on probe perturbation in a swirl-stabilized combustor using nonintrusive optical techniques focused at the entrance of an extractive probe. The optical techniques are on the forefront of technology for point measurements in flows dominated by strong aerodynamics. The net result is that the present results are exploratory, and not exhaustive. However, the results reveal the type of problems introduced by extractive probes, specific questions that must be raised in the interpretation of data from extractive and optical probes, and the type of experiments necessary to develop and test soot measurement methods in order to ensure that the data obtained are representative of the events that occur within swirl-stabilized combustors. A detailed description of this work along with analyses of extracted soot morphology is available.[1]

EXPERIMENT

Combustor Configuration

The combustor configuration is presented in Figure 1. The combustor housing is 51mm (2-inch) O.D. quartz tubing. Swirl vanes located 57mm (2 1/2-inches) upstream of an internal centerbody face impart a 60° swirl to the annular air jet and thereby produce a stabilized recirculating flow concentrated in the center of the combustor. The fuel is introduced through a central aperture 1.3mm (0.052-inch) in diameter. The principal criteria for the selection of this combustor design were the inclusion of complex (i.e., turbulent, reverse flow) aerodynamics and optical accessibility.

Test Conditions

The test conditions are itemized in Table 1. The range of reference velocities was selected to (1) be representative of those produced in practical gas turbine combustors, (2) span a range of operating conditions, and (3) bracket effects observed in the probe perturbation studies. The mixture ratios were selected to (1) be representative of those in practical gas turbine combustors, and (2) in the case of $\phi = 0.37$, produce conditions suitable for good optical measurements. Finally, the sampling locations were selected such that sampling points were located in the wake of the zone of recirculation (6d) and within the zone of recirculation (3 1/2d).

The fuel utilized in this study was gaseous ethylene.

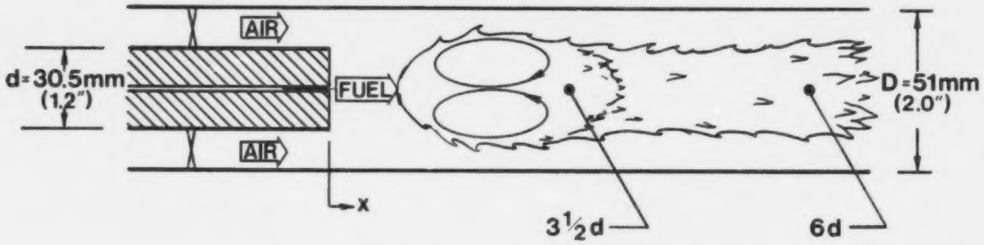

Figure 1. Combustor configuration

TABLE 1. TEST CONDITIONS

Reference Velocity,[a] U_{ref} (m/s)	Overall Equivalence Ratio,[b] ϕ	Sampling Location,[c] (x/d)
0.65	0.2	6
5.5	0.2, 0.37	6, 3 1/2
7.5	0.2, 0.37	6
15.0	0.2	6

a. cold flow velocity referenced to duct diameter, 51mm (2-inches)
b. actual overall fuel-to-air ratio divided by stoichiometric ratio
c. x,d: Refer to Figure 1

Extractive Probe

The probe and sample systems are shown in Figure 2. The probe is constructed of stainless steel with a 9.5mm (3/8-inch) O.D. and a 3.0mm (1/8-inch) I.D. sampling tube. The overall length of the probe is 914mm (36 inches) including a large radius bend in order to clear the combustor exhaust stream. The probe is hot water cooled at approximately 80°C and has isokinetic pressure ports, a gas sampling port for gas analysis, and an inert gas injection port. The purpose of the latter is to dilute the mixture, quench reactions, and prevent deposition along the walls.

The 9.5mm (3/8-inch) probe diameter is the smallest reasonable size to incorporate the necessary ports and provide clearance for sample transport. As a result, the probe to combustor duct diameter is large (3/8-inch to 2 inches). However, this proved beneficial in the present study by enabling the demonstration of blockage. In particular, combustor operating conditions were established for which blockage by the extractive probe dominated the results, and conditions were identified for which blockage did not influence the results.

Optical Probe

The integrated particle sizing optical probe (Figure 3) is capable of characterizing particles from about 0.02 microns to several microns in size. Because of the vast dynamic range incurred in this particle size range, four techniques are used as shown in Table 2.

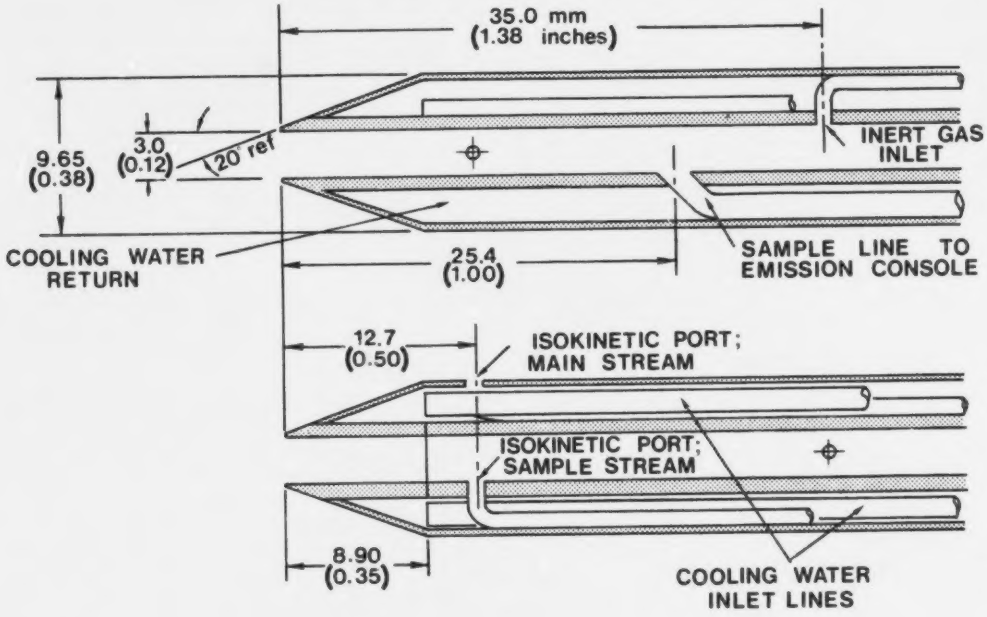
35.0 mm (1.38 inches)
9.65 (0.38)
3.0 (0.12)
20 ref
INERT GAS INLET
COOLING WATER RETURN
25.4 (1.00)
SAMPLE LINE TO EMISSION CONSOLE
12.7 (0.50)
ISOKINETIC PORT; MAIN STREAM
ISOKINETIC PORT; SAMPLE STREAM
8.90 (0.35)
COOLING WATER INLET LINES

Figure 2. Extractive probe

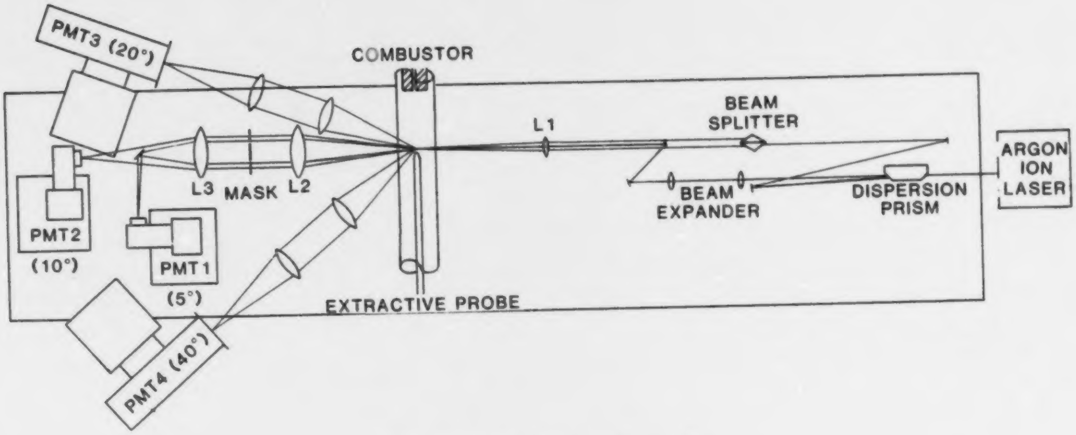

Figure 3. Optical probe

TABLE 2. OPTICAL PROBE SYSTEM

	Technique	Size Range (Microns)	Single/Multiple Particle Sizing	Reference
(1)	Particle Sizing Interferometery	2 to 7 or larger if necessary	Single	2
(2)	Intensity Ratioing	0.4 to 2.3	Single	3
(3)	Large Angle Ratioing	0.08 to 0.4	Single	4
(4)	Polarization Ratio	All	Multiple	5

The entire system is constructed on a horizontal platform. Most of the optics centers within a horizontal plane with the laser (5W argon ion) mounted above it. The laser beam is brought to this plane and is dispersed by the dispersion prism such that the dominant green (514.5 nm) and blue (488.0 nm) lines are isolated for diagnostic usage. The green line is split into two beams of equal intensity at the beam splitter for interferometric measurements. The blue line is suitably expanded at the beam expander for the ratioing techniques.

The three beams are combined and focused by the transmitting lens (L1) so that the green beams are crossed and the blue beam is reduced into a tightly focused beam at the sample volume within the combustor. The scattered light is observed by the five detectors PMT1 to PMT5. A portion of the scattered blue light is focused by lenses L2 and L3 and allowed to pass through three quadrants of a circular annular mask. The scattered light at 5° and 10° is then extracted and focused onto the detectors PMT1 (5°) and PMT2 (10°). These two detectors provide size information between 0.4 and 2.3 μm. Part of the scattered green light passes through the fourth quadrant of the mask which is open and is observed by the detector PMT5 (not shown in figure), located above the platform, for interferometric analysis. Another portion of the scattered blue light is observed by the detectors PMT3 (20°) and PMT4 (40°-60° adjustable) for large angle ratioing (0.08 to 0.4 μm). These two detectors (RCA 8575) have both high gain and high quantum efficiency and are useful for small signal detection.

For the polarization ratio technique, a half wave plate is inserted in one of the two green beams to rotate polarization by 90°. A motorized chopper (not shown) will alternately allow only one of the two beams to cross the sample volume. The 60° detector is then used for observation. Data can be recorded using a chart recorder corresponding to the polarization orientations and background radiation.

The performance of the optical probe was satisfactorily demonstrated using specified-size particles under cold flow conditions. Nine specified-size spherical polystyrene particles were used: 3.3 μm (0.12 μm S.D.), 2.26 μm (0.07 μm S.D.), 1.74 μm (0.076 μm S.D.), 1.32 μm (0.053 μm S.D.), 0.481 μm (0.0018 μm S.D.), 0.357 μm (0.0056 μm S.D.), 0.330 μm (0.0040 μm S.D.), 0.198 μm (0.0036 μm S.D.), and 0.085 μm (0.0055 μm S.D.).

The principal optical data reported in the present paper are for the intensity ratioing technique. Data were also collected for the interferometric technique. The observed interferometric data rate was esentially zero indicating that no particles larger than 2 μm were present. One noteable exception occurred, however. After prolonged periods of combustor operation, soot deposits could build up on the centerbody surface. Once a sufficient amount of particulate build up had occurred, the interferometric data rate became non zero, suggesting that large particles (ca. 5 μm), attrited from the surface, were being ingested by the probe. This size range, which can rapidly increase the weight concentration measured by the extractive probe, would have escaped detection in the absence of the simultaneous optical measurement. Although the large angle ratioing and polarization ratio techniques have been proven under cold flow conditions, they have yet to be fully tested for reacting flow. This was not limiting in the present case, however, as the intensity ratioing technique provides valuable insights into the potential of optical diagnostics for the measurement of soot in complex flows as well as demonstrating (1) conditions under which extractive probe perturbation can occur and (2) the extent of such perturbations.

RESULTS

The position of the extractive probe was changed relative to the optical probe to assess the perturbation produced by the extractive probe. Beginning at the nominal sampling (i.e., with the extractive probe at centerline of axial location and optical probe positioned at extractive probe entrance), the probe was removed axially in incremental steps while the optical probe remained at the original centerline location. The impact of the probe location on the optical probe measurements was recorded in terms of intensity ratioing data rate ($\dot{n}$) and particle size distribution. In addition, radial profiles of data rate and particle size distribution were obtained optically with and without the extractive probe in the flame.

Nonreacting Flow with Seeding

The study was initiated by seeding the nonreacting flow of the annular jet with 0.48 μm polystyrene particles, and comparing the measured optical data rate to that calculated from scanning electron micrographs of the filtered seed. The calculated data rate verified that the measured data rate was correct within acceptable experimental limits. Next, the optically measured data rate was recorded as the extractive probe was removed axially from the optical probe volume.

The cold flow study was conducted at 7.5mps and at an axial sampling station of $x/d = 6$. As shown in Figure 4a, the intensity ratioing data rate (n) decreased as the extractive probe was withdrawn, with an overall decrease of more than 200-fold between the "with-extractive-probe" and "without-extractive-probe" conditions. The relatively low data rate in the absence of the extractive probe is due to the strong centrifugal force on

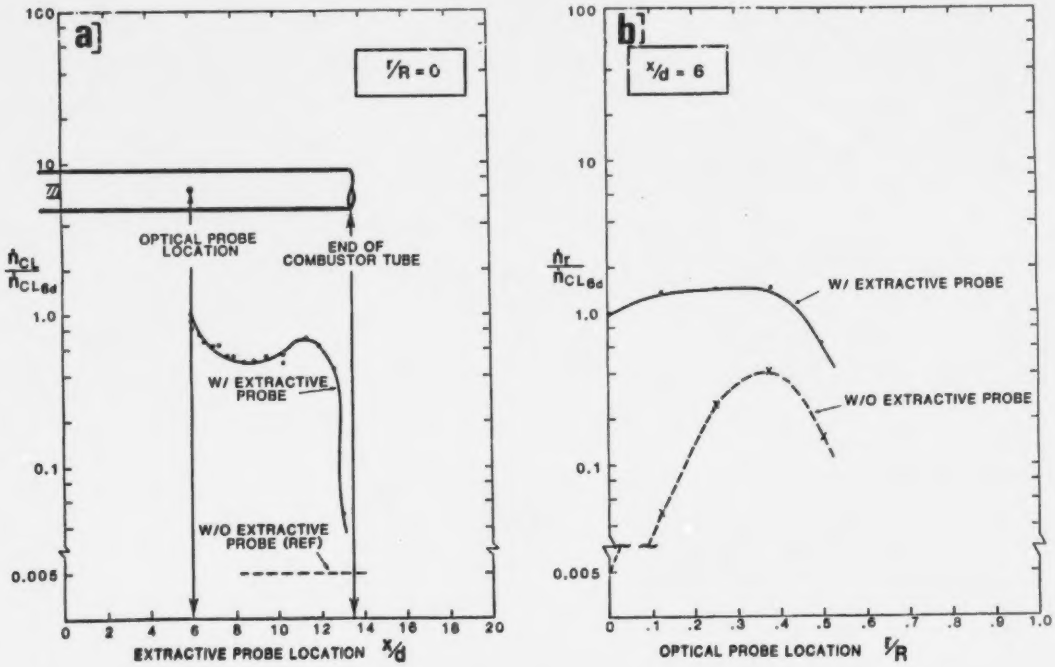

Figure 4. Extractive probe perturbation -- nonreacting flow with seeding (U_{ref} = 7.5mps, 0.48μm particles)
(a) Removal of extractive probe
(b) Optical probe radial traverse

the particles caused by the swirl. When the probe is present, this force is reduced and particles can more freely diffuse radially toward the centerline. The radial diffusion of the particles becomes evident by examining Figure 4b. Two observations are noteworthy from this figure. First, the without-probe profile exhibits a very small data rate in the center which increases radially. This shows that diffusion is quite small and that very few particles are able to reach the central core of the combustor. However, in the presence of the probe, radial diffusion is enhanced. This is supported by the flat data profile in the figure. Secondly, because of experimental difficulties, radial measurements were not obtained beyond $r/R = 0.5$, thus a particle rate balance could not be performed.

Reacting flow

The presence of the extractive probe produced an impact on the optically measured data rate that ranged from a small to a substantial effect depending on the operating conditions. For example, at 5.5mps, $\phi = 0.37$, and at the sampling station $x/d = 6$, the data rate remained relatively constant (Figure 5a) as the extractive probe was separated from the optical probe. The radial profiles (Figure 5b) also remain similar for both the with-probe and without-probe condition. The factor of two difference (Figure 5b) in data rate at $r/R = 0$ is not significant and within the re-

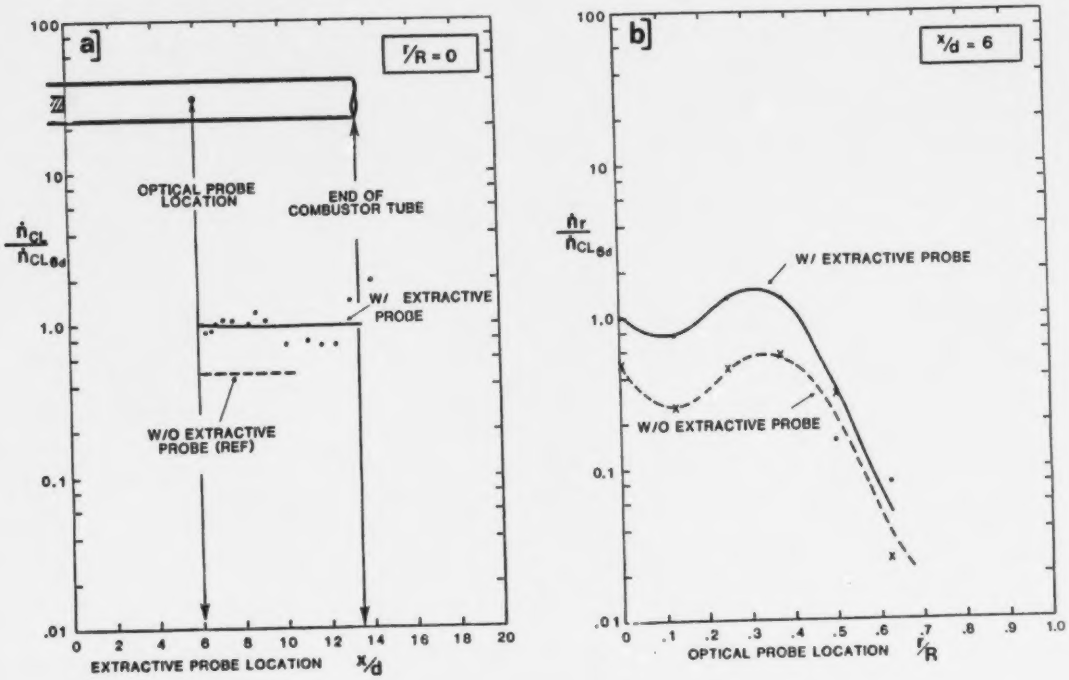

Figure 5. Extractive probe perturbation -- reacting flow (U_{ref} = 5.5mps, $\phi = 0.37$)

(a) Removal of extractive probe

(b) Optical probe radial traverse

producibility at $\phi = 0.37$. For example, a two-fold change in data rate was observed for small changes (e.g., $\Delta\phi = 0.01$) in mixture ratio. The lack of change in these measurements is attributed to the relatively small axial and radial gradients in flow properties at this sampling location as a result of the upstream recirculation and mixing.

No observable change in the optically measured particle size was recorded as the extractive probe was removed from the optical probe. For verification, optically measured particle size distribution was compared to scanning electron micrographs of the filtered sample with no unexplained discrepancy.[1]

Closer to the centerbody (x/d = 3 1/2), the results are dramatically different (Figure 6a). Here, the sampling station is located within the recirculation zone (refer to Figure 1). The data rate increases more than 70-fold as the probe was withdrawn from the optical sampling volume, with the steepest gradient in data rate occurring within 2 centerbody diameters of the sampling station. The change then is likely a result of a substantial perturbation of the local flow field with a concomitant change in mixing, chemistry, and temperature due to the intrusion of a solid, cold body into a zone of reverse flow. It is noteworthy that the effect on data rate levels off to the without-probe condition at approximately 6 centerbody diameters downstream of the recirculation zone.

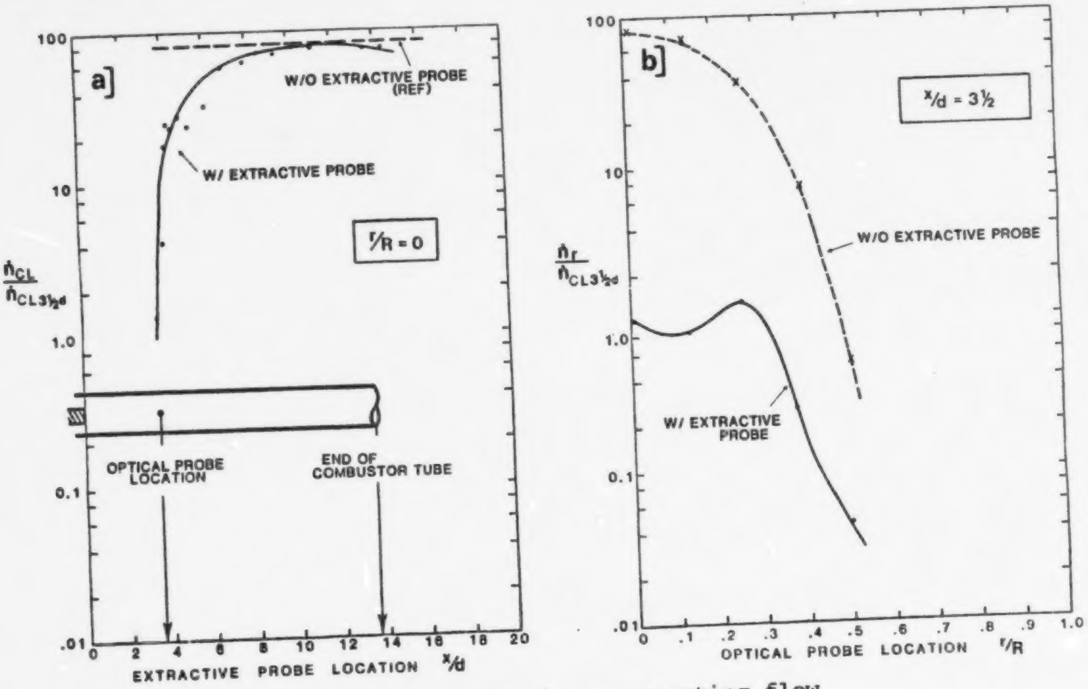

Figure 6. Extractive probe perturbation -- reacting flow (U_{ref} = 5.5mps, $\phi = 0.37$)
(a) Removal of extractive probe
(b) Optical probe radial traverse

The substantial probe perturbation is further evidenced in the radial profiles (Figure 6b). Here, the with-extractive-probe profile resembles the previous case (Figure 5b). However, the without-extractive-probe profile is markedly different, having a distinct maximum data rate on the centerline and decreasing monotonically radially outward.

Increasing the reference velocity from 5.5 to 7.5mps produces an even more dramatic impact even though the sampling volume was located in the wake of the recirculation zone ($x/d = 6$). Again, the data rate increases about 40-fold as the probe is removed from the sampling volume (Figure 7a). However, for this case there is an appreciable scatter in the measurements. This is attributed to a small but perceptible change in flame structure, probably due to blockage, as the extractive probe is moved from one location to another. In particular, the flame compressed, and the wake region moved upstream as the extractive probe was moved toward the centerbody. The extractive probe perturbation was therefore not limited just to local changes (as in the previous two cases), but extended to dominate flame behavior throughout the combustor. This gross impact on data rate notwithstanding, the change in particle size in the range measured optically was not appreciable. The radial profiles (Figure 7b) resemble the last case (5.5mps, $\phi = 0.37$, $x/d = 3\ 1/2$), showing both the large increase in data rate and large change in the presence of the probe.

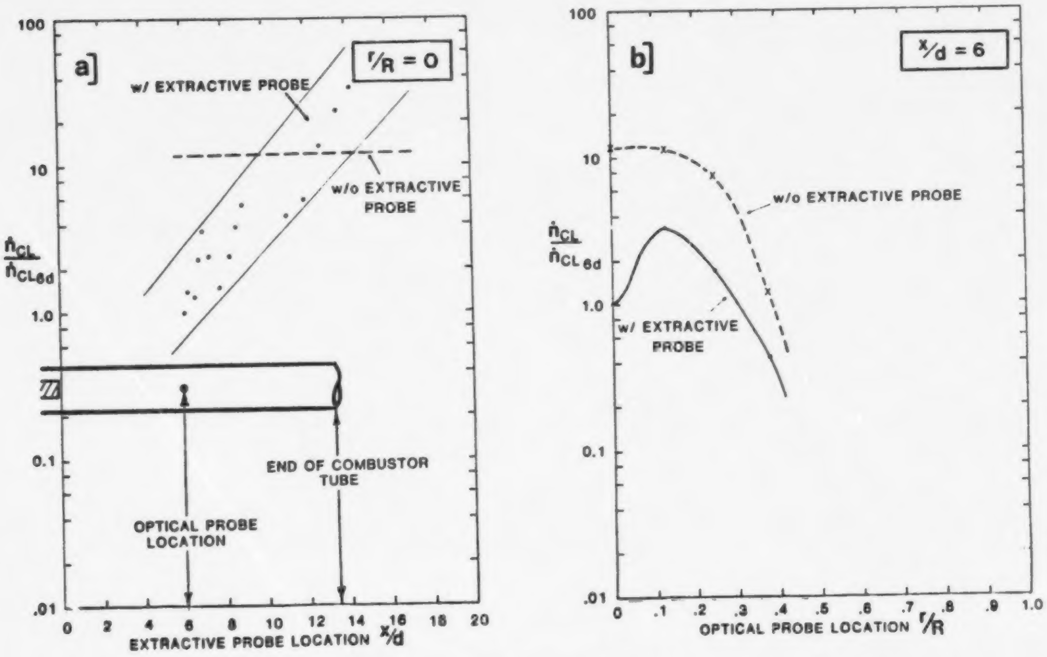

Figure 7. Extractive probe perturbation -- reacting flow ($U_{ref} = 7.5$, $\phi = 0.37$)

(a) Removal of extractive probe

(b) Optical probe radial traverse

Extractive Probe Flowrate

In a final test, the effect of variation in the extractive probe flowrate on data rate was optically assessed. Tests were first conducted for the case of nonreacting flow by seeding with 0.48 μm polystyrene spheres and the effect of sample flowrate on the opticlly measured data rate at the extractive probe entrance was recorded. For a 7.5mps reference velocity, the data rate increased 40% at the maximum flowrate (Figure 8), consistent with theories relating to nonisokinetic efects; namely, the higher flowrate promotes the radial convection of small particles into the sampling volume.

For reacting flows, the effect of extractive probe flowrate on the optically measured data rate was shown to depend on the operating condition and sample volume location. The extractive probe perturbation results provide some explanation of these trends. At 5.5mps, $\phi = 0.37$, and $x/d = 6$, the perturbation of the extractive probe is minimal and the effect of an increase in sample flowrate is to increase the data rate to the same degree observed in the nonreacting flow tests. At 3 1/2d, the sampling volume is in the recirculation zone. An increase in sample flowrate has no effect on data rate, which indicates that the flow aerodynamics fully control the

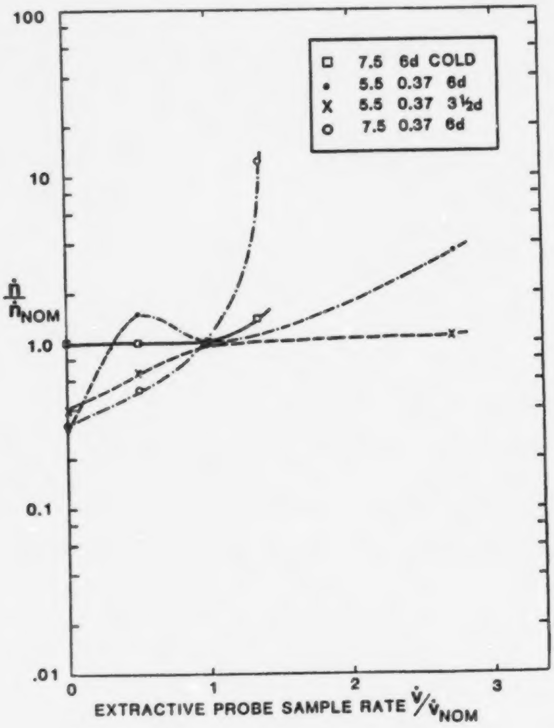

Figure 8. Extractive probe conditions -- effect of sampling flowrate on optically measured data rate

local flow properties. Finally, at 7.5mps, $\phi = 0.37$, and $x/d = 6$, the blockage of the probe dominates and, because the blockage is influenced by sample flowrate, an increase in flowrate was observed to produce a perceptible change in flame structure and, as a result, a substantial change in data rate.

SUMMARY

The present study represents an exploratory investigation into the sample perturbation associated with extractive probe sampling for soot. The use of nonintrusive optical measurement techniques focused at the entrance of an extractive probe provides a unique and independent measurement of number density (i.e., data rate) and particle size.

The results pertaining to extractive probe sampling conditions provided new insights as well as reinforcing the traditionally perceived "isokinetic" effect. For example, number density increases with an increase in extractive probe flowrate. In addition, the optical measurements allowed the identification of non-flame source of particulate--in this case, the attrition of particles off the centerbody.

The effect of the physical presence of the extractive probe varied from no significant impact on data rate and particle size (in the particle size range measured) to a dramatic effect on data rate. The dramatic perturbation occurred when the sampling volume was located in the recirculation zone, or when the reference velocity was increased beyond the value (5.5mps in the present case) above which the blockage produced by the extractive probe became significant.

The results reported here are undoubtedly specific to the combustor configuration employed, and the size and design of the extractive probe used. In addition, the results are limited by the small particle size cutoff for the optical technique. As a result, the effect of extractive probe conditions and perturbation on soot particle formation, and on formed soot particles in the size range considered to be heavily populated ($\cong 0.02\mu m \leq d_p \leq 0.3\mu m$) requires the expanded optical capability provided by the full four-range instrument.

This notwithstanding, the present results reveal:

- The type of problems associated with extractive probes
- Questions that must be raised in the interpretation of data from extractive and optical probes
- The type of experiments necessary to develop and test methods employed to measure soot in gas turbines, boilers, and furnaces.

ACKNOWLEDGMENT

The results presented were obtained in a soot formation/alternative fuels study in progress at the UCI Combustion Laboratory and supported by the Air Force Engineering and Services Center, Research and Development Directorate, Environics Divison (Air Force Contract #FO-8635-79-C-0158).

REFERENCES

1. Hack, R.L., G.S. Samuelsen, C.C. Poon, and W.D. Bachalo. An Exploratory Study of Soot Sample Integrity and Probe Perturbation in a Swirl-Stabilized Combustor. ASME Paper 81-GT-27, presented at the International Gas Turbine Conference, Houston, March, 1981. To be published, ASME Journal of Engineering for Power.

2. Bachalo, W.D., C.F. Hess, and C.A. Hartwell. An Instrument for Spray Droplet Size and Velocity Measurements. ASME Journal of Engineering for Power. Vol. 102, No. 4, Oct. 1980.

3. Hirleman, E.D. Optical Technique for Particular Characterization in Combustion Environments: The Multiple Ratio Single Particle Counter. Ph.D. Thesis. Purdue University. Aug. 1977.

4. Poon, C.C. and W.D. Bachalo. To be published.

5. D'Alessio, A., A. DiLorenzo, F. Beretta, and C. Venitozzi. Optical and Chemical Investigations on Fuel-Rich Methane-Oxygen Premixed Flames at Atmospheric Pressure. Fourteenth Symposium (International) on Combustion. The Combustion Institute. 1973.

The work described in this paper was not funded by the U.S. Environmental Protection Agency. The contents do not necessarily reflect the views of the Agency and no official endorsement should be inferred.

Paper 26

A SENSITIVE PARTICULATE MONITOR FOR MEASURING THE APPROXIMATE OPACITY FOR FABRIC FILTER SYSTEMS

William J. Steele
Wallace B. Smith
William E. Farthing
Southern Research Institute

Robert C. Carr
Electric Power Research Institute

ABSTRACT

This paper describes a sensitive opacity measuring device for use in monitoring fabric filter systems. The usual technique for measuring opacity is to measure the incident (I_0) and transmitted (I) light intensities. Opacity (OP) is calculated as (Io-I)/Io. In the device described here, opacity is obtained by measuring the scattered light rather than the transmitted component. This is accomplished by using a commercially available electro-optical particle analyzer with a specially designed dilution system and electronic circuits. This device has been used at the EPRI Advanced Emissions Facility in Denver, Colorado to monitor four individual compartments in a 30,000 ACFM pilot scale fabric filter plant. Typical field results are presented to illustrate the performance of the device.

INTRODUCTION

This paper describes a sensitive particulate measuring device that was developed to measure the approximate opacity at the outlet of a fabric filtering system. This system is being used at the EPRI Advanced Emissions Control Facility in Denver, Colorado to monitor each of the four compartments of the 30,000 ACFM pilot scale fabric filter plant.

The usual technique employed by a transmissometer to measure the opacity of a given path through an aerosol is to measure the incident, (I_0), and the transmitted, (I), light intensities. The opacity, (OP), is then defined as the difference of the two divided by the incident light intensity. This is expressed mathematically as:

$$OP = \frac{I_0 - I}{I_0} .$$

This technique, illustrated in Figure 1A, offers good practical results for medium to high values of opacity. However, as opacity becomes small, i.e. I approaches I_0 or $OP<0.1$, this approach becomes increasingly inaccurate since even moderately small errors in the measurements of I and I_0 result in large errors in the small difference. Therefore, this scheme is not appropriate to measure the small values of opacity at the outlets of a high efficiency baghouse.

In order to circumvent these difficulties, the described device attempts to measure opacity by measuring the total scattered light in a single particle detecting device such as a Climet particle analyzer, Model 225, manufactured by Climet Instrument Co. This is illustrated in Figure 1B. A statistical value of opacity is obtained by integrating the Climet's output over a suitable length of time, i.e., 0.5 sec. The rationale for this approach is covered in detail in the section entitled Background.

A. SIMPLIFIED SCHEMATIC OF A TRANSMISSOMETER FOR MEASURING MED-HIGH OPACITY

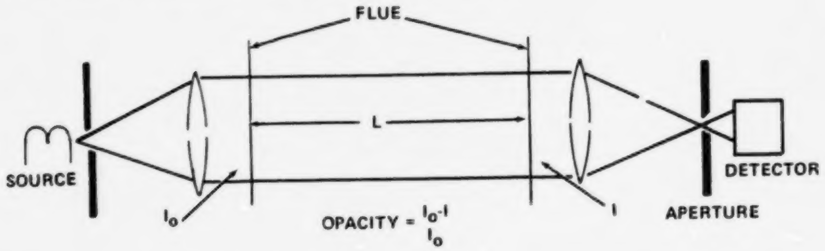
FLUE
L
SOURCE
I_o
OPACITY = $\frac{I_o - I}{I_o}$
I
DETECTOR
APERTURE

B. SENSITIVE MONITOR FOR MEASURING VALUES OF LOW OPACITY

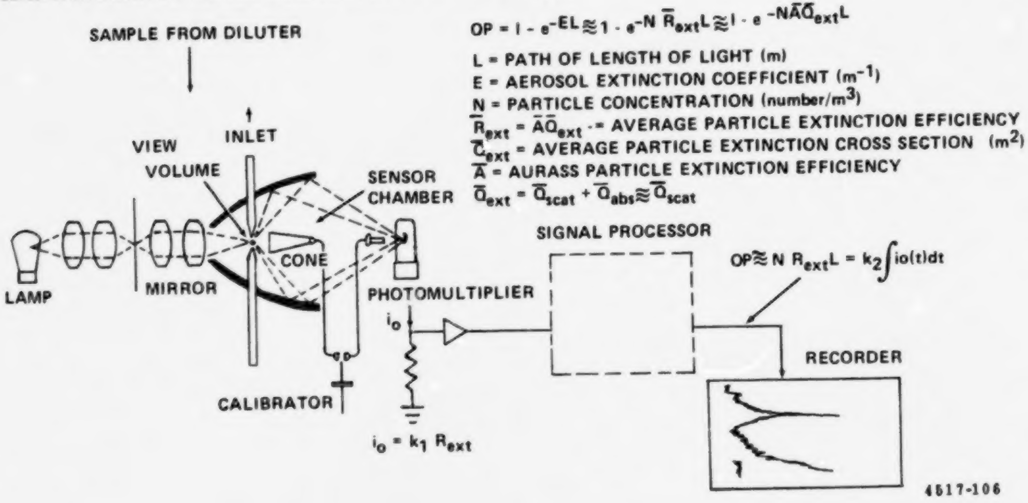
SAMPLE FROM DILUTER
$OP = 1 - e^{-EL} \approxeq 1 - e^{-N \overline{R}_{ext} L} \approxeq 1 - e^{-N \overline{A} \overline{Q}_{ext} L}$
L = PATH OF LENGTH OF LIGHT (m)
E = AEROSOL EXTINCTION COEFFICIENT (m^{-1})
N = PARTICLE CONCENTRATION (number/m^3)
$\overline{R}_{ext} = \overline{A}\overline{Q}_{ext}$ = AVERAGE PARTICLE EXTINCTION EFFICIENCY
$\overline{C}_{ext}$ = AVERAGE PARTICLE EXTINCTION CROSS SECTION (m^2)
$\overline{A}$ = AURASS PARTICLE EXTINCTION EFFICIENCY
$\overline{Q}_{ext} = \overline{Q}_{scat} + \overline{Q}_{abs} \approxeq \overline{Q}_{scat}$
VIEW VOLUME
INLET
SENSOR CHAMBER
SIGNAL PROCESSOR
$OP \approxeq N R_{ext} L = k_2 \int io(t)dt$
LAMP
MIRROR
CONE
PHOTOMULTIPLIER
i_o
CALIBRATOR
$i_o = k_1 R_{ext}$
RECORDER
4517-106

Figure 1. Opacity measuring devices

BACKGROUND

As defined previously, opacity is the fractional decrease in energy or intensity of a light beam penetrating an aerosol. In terms of the properties of the aerosol:

$$O_p = 1 - e^{-EL} \equiv 1 - e^{-N\bar{R}_{ext}L} \equiv 1 - e^{-N\bar{A}\bar{Q}_{ext}L}$$

where: L = path length of the light (m)
E = aerosol extinction coefficient (m^{-1})
N = particle concentration (number/m^3)
$\bar{R}_{ext} = \bar{A}\bar{Q}_{ext}$ = average particle extinction cross section (m^2)
$\bar{A}$ = average particle projected area (m^2)
$\bar{Q}_{ext}$ = average particle extinction efficiency

The particle extinction efficiency, Q_{ext}, is a function of the particle diameter and composition; the latter is expressed by its complex refraction index (n - in'). Q_{ext} varies about a value of approximately two for particle diameters above 0.5 µm. At smaller diameters, Q_{ext} normally decreases rapidly with diameter.

The conventional determination of opacity, with a transmissometer, measures the light energy not removed from the beam. When opacity is small this approach is inherently inaccurate. For small values of opacity, the measurement of $N\bar{A}\bar{Q}_{ext}$, or the extinction coefficient, provides more accurate results. Although in general the extinction of light is caused by scattering and absorption (i.e., $Q_{ext} = Q_{scat} + Q_{abs}$), the absorbed component is frequently much less than the scattered component.[1] Therefore, an economical device which measures only the scattered component can be useful for opacity determinations. There are several optical particle counters, commercially available, which can be modified to perform that function.

The instrument presently utilized is the Climet Model 225 with the optical system shown in Figure 1B. The photomultiplier signal is scaled and integrated to sum the photocurrent produced by particles passing through the beam; the output signal is related to the extinction coefficient, E. The theoretical values, calculated from Lorentz - Mie theory,[2,3] of the extinction cross section, R_{ext}, for two types of spherical particles are tabulated in Table 1. The Climet calibration curve, normalized to the R_{ext} data at a particle diameter of 2 µm, is shown in Figure 2.

The correlation is very good for particle sizes above one micron. The differences in the Climet response function and R_{ext} are due to the fact that the Climet optical system does not collect all of the scattered light. This deficiency becomes important if a major portion of the opacity is due to particles with diameters less than 0.5 µm.

TABLE 1

EXTINCTION CROSS SECTION VS PARTICLE DIAMETER OF SPHERICAL PARTICLES CALCULATED FROM MIE THEORY

	Extinction Cross Section R_{ext} (μm^2)	
Particle Diameter (μm)	Refractive Index= 1.59 - 0.00i	Refractive Index= 1.50 - 0.00i
0.112	0.516E-03	0.382E-03
0.126	0.103E-20	0.757E-03
0.141	0.204E-02	0.149E-02
0.158	0.398E-02	0.289E-02
0.178	0.761E-02	0.551E-02
0.200	0.141E-01	0.102E-01
0.224	0.256E-01	0.183E-01
0.251	0.459E-01	0.323E-01
0.282	0.841E-01	0.575E-01
0.316	0.150	0.103
0.355	0.236	0.174
0.398	0.348	0.267
0.447	0.537	0.411
0.501	0.763	0.627
0.562	1.03	0.890
0.631	1.34	1.24
0.708	1.62	1.63
0.794	1.82	2.03
0.891	1.86	2.35
1.00	1.79	2.50
1.12	1.86	2.49
1.26	2.47	2.51
1.41	4.01	3.07
1.58	5.54	4.46
1.78	6.67	6.81
2.00	6.74	8.60
2.24	8.26	9.09
2.51	12.0	10.6
2.82	15.0	14.7
3.16	17.4	19.1
3.55	23.5	21.8
3.98	28.0	27.9
4.47	35.3	35.1
5.01	43.8	43.9
5.62	55.5	54.3
6.31	68.2	68.8
7.08	85.5	86.2

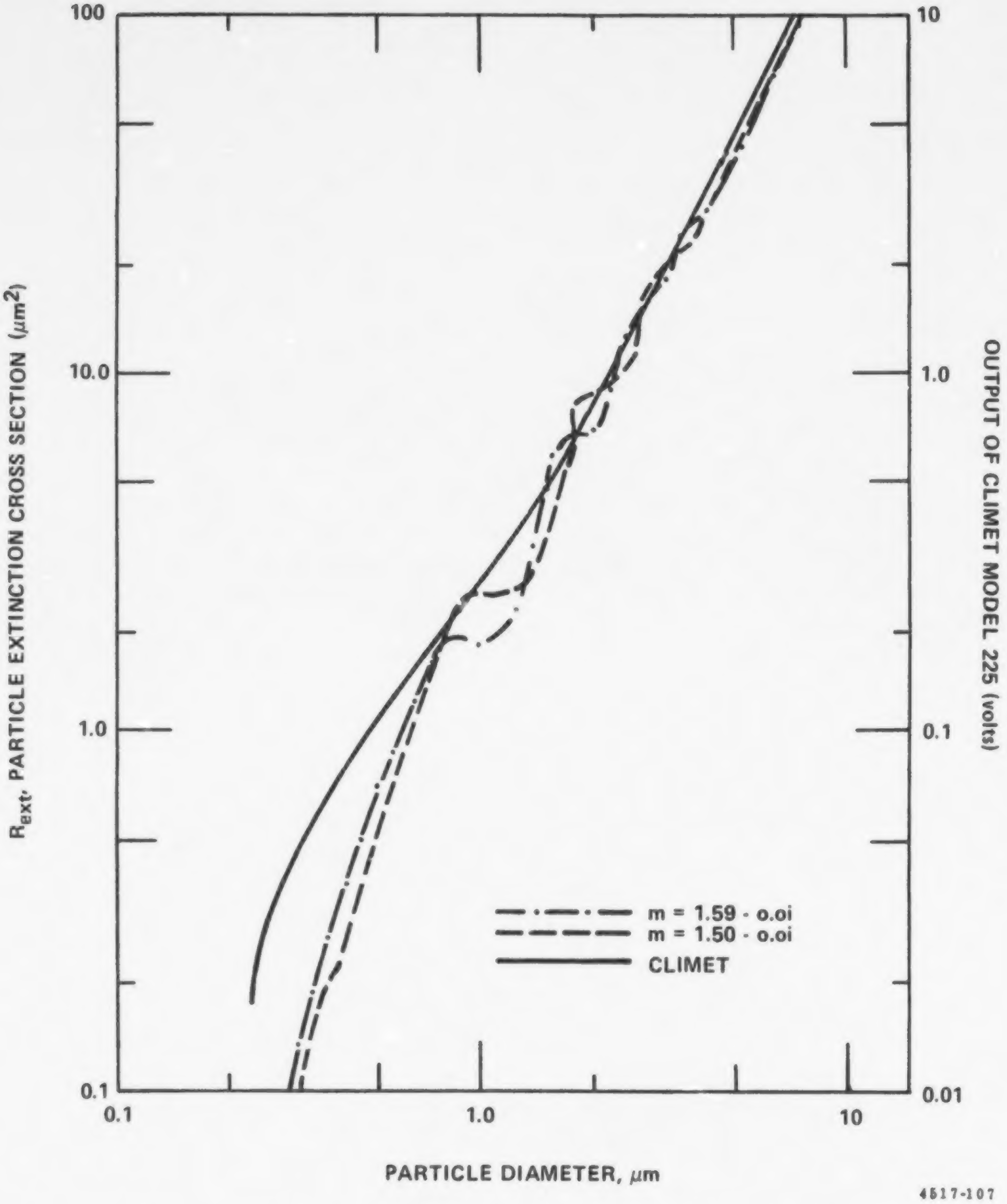

Figure 2. Calculated extinction coefficient curves and Climet calibration curve.

A quantitative study of the response of the Climet to particles of other refractive indices has not been performed; however, the results for similar optical systems are available.[4] The factor of greatest concern is the possibility that absorption (present when the imaginary portion n' of the refractive index is finite) may be present. Then the Climet response would be smaller than predicted. However, in most circumstances the resulting error would still be less than the uncertainties of transmissometer measurements for opacities less than 0.01.

DESCRIPTION OF THE OPACITY MONITORING SYSTEM

The opacity measuring system at the EPRI Advanced Emissions Control Facility consists of four separate systems to monitor each of the four compartments of the pilot scale fabric filter plant. Each monitoring system consists of a dilution assembly, a Climet Model 225 particle detector, and signal processing and control circuits. The signal processing circuits are located in a local assembly; the controls for these circuits are located in the local assembly as well as in a remote assembly. Figure 3 is a pictorial representation of one of the local systems at a stack. It consists of a dilution assembly in the stack, a Climet particle detector, and a local control

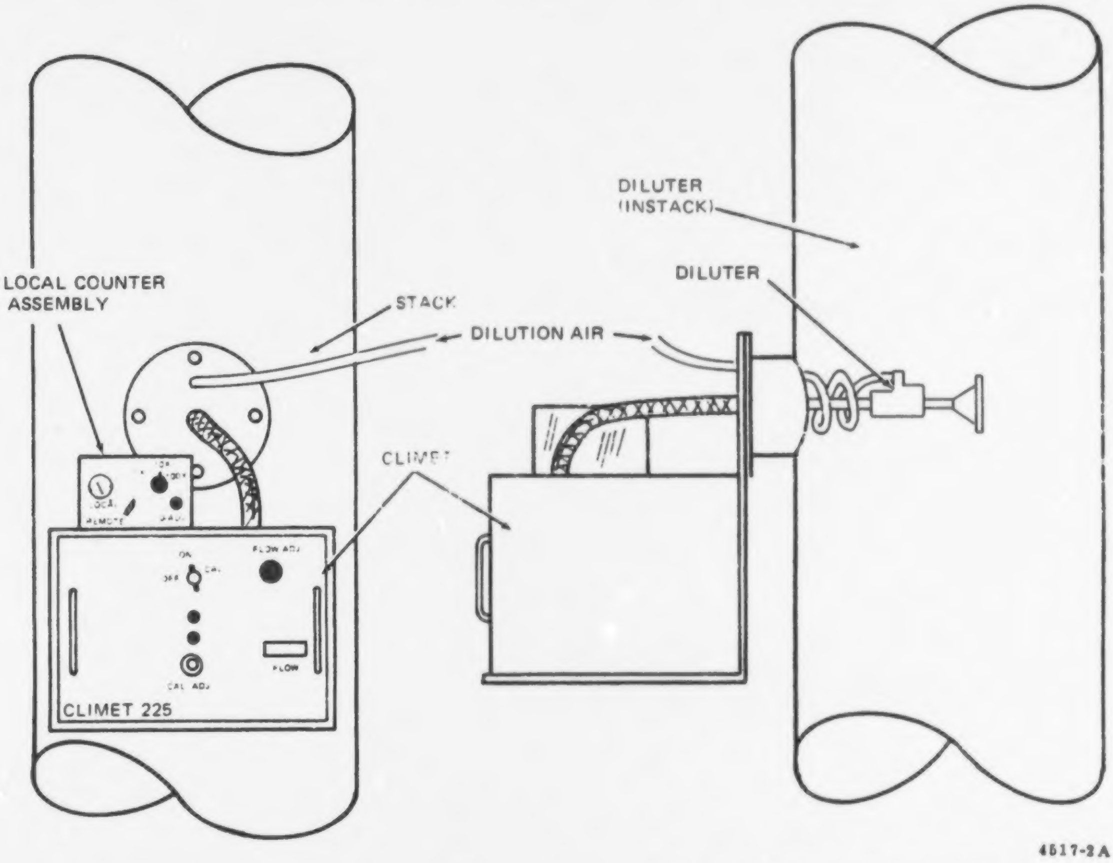

Figure 3. Sketch of the local station of the outlet opacity monitor.

and signal processing assembly. Filtered air to the diluter is provided by the remote station. The signal from the Climet detector is applied to the local processing circuits that provide an output related to the extinction coefficient. The output signal from the local signal processing circuits are displayed locally and are provided to the remote station for display and recording purposes. A pictorial representation of the remote station is illustrated in Figure 4. It consists of dilution controls, electronic controls and displays along with two dual channel chart recorders for recording the measured extinction coefficients of the four compartments.

The major components of the opacity measuring system are discussed below.

Dilution Assembly

The signal processor in the Climet is designed for pulse mode operation. This circuit converts photomultiplier current to voltage and dynamically corrects the signal baseline to zero volts. Therefore, a dilution assembly, illustrated in Figure 5, is provided to ensure the proper operation of the signal processing circuits. In addition the use of dilution reduces deposition of dust on the optical surfaces, increases the dynamic range of the system, and minimizes condensation in the Climet. The dilution ratio is adjustable from zero to greater than 10:1.

Particle Detector

A Climet, Model 225, is employed as the detector for the opacity measuring system. This unit is modified to allow the sampling of hot gases (~350°F) from the outlet of the baghouse. Other features of the Climet include (1) detectable concentrations to 1×10^7 particles/ft^3, (2) detection of particles down to 0.3 µm, (3) uniform particle response due to the controlled flow of sampled air in the view volume, a quartz-halogen lamp and superior optics, (4) a sample rate of 0.25 CFM, and (5) a calibration mode that allows field calibration of the device. The signal from each detected particle is of uniform pulse width and the pulse amplitude is proportional to the particle area. The output signal from the detector of the Climet provides the dynamic input to the special processing circuits described below.

Signal Processing and Control Circuits

The signal processing circuits are located in the local station assembly. This assembly also has external controls that allow for local or remote gain selection mode, local selection of gain, zeroing adjustments for each of the three decades of the measured extinction coefficient, and a meter for displaying the measured extinction coefficient. The extinction coefficient is output on a co-axial connector to the remote station for recording purposes.

The remote station has controls and displays for each of the four measuring stations. Each module has a meter to display the extinction coefficient, controls to select gain (in the remote mode), and zeroing adjustments for the three decades of gain. Two dual pen recorders at the remote station provide a record of the measured extinction coefficients of the four compartments.

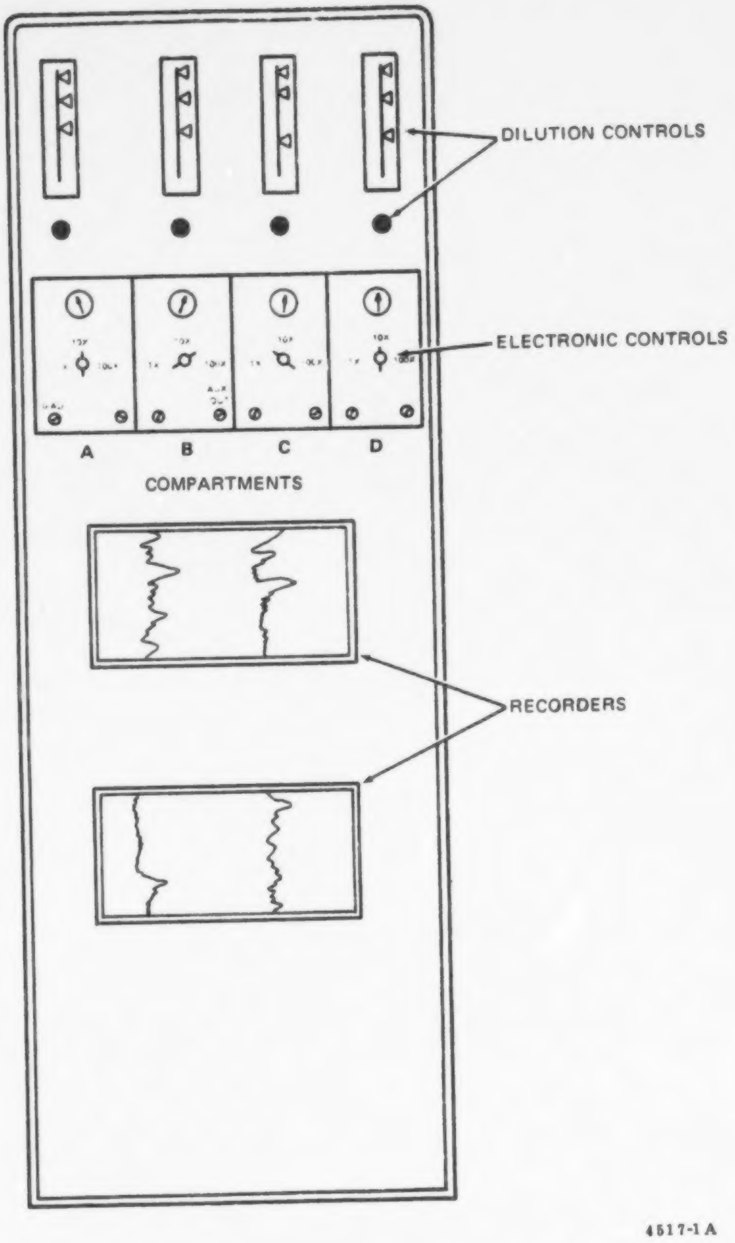
DILUTION CONTROLS
ELECTRONIC CONTROLS
A
B
C
D
COMPARTMENTS
RECORDERS
4517-1A

Figure 4. Sketch of the remote station of the outlet opacity monitors.

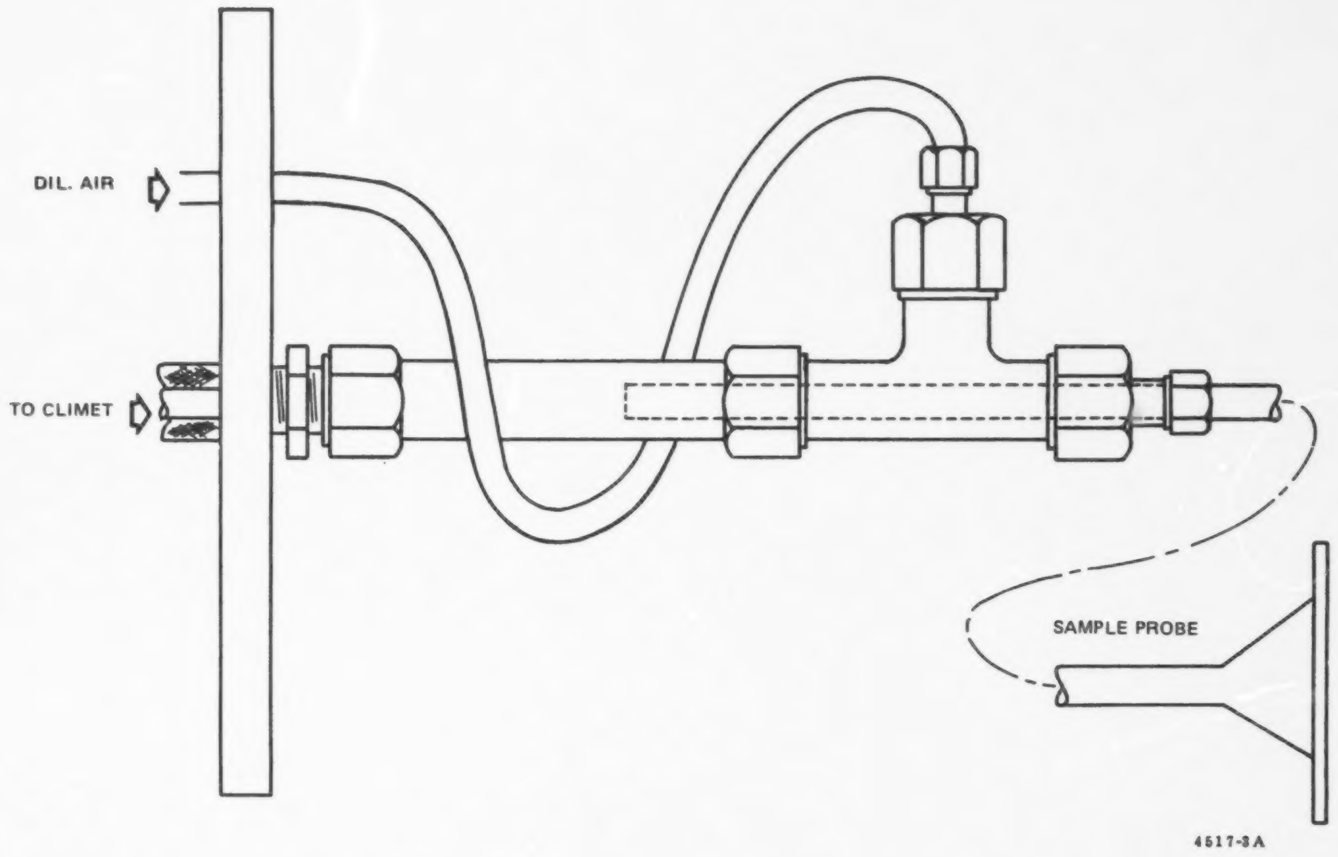
DIL. AIR
TO CLIMET
SAMPLE PROBE
4517-3A

Figure 5. Diluter assembly and sampling probe for the outlet opacity monitors.

The signal processing circuits are shown schematically in Figure 6. The output of the Climet is applied to three amplifiers, A_1, A_2 and A_3 that have gains of 1, 0.1 and 0.01, respectively. The signal from the appropriate amplifier is selected either locally or remotely, and the signal is integrated by amplifier A_4. A timer control allows the signal to be integrated for 0.5 second. The integrated value is then stored on capacitor C1 by momentarily closing switch 1. The timer control then resets the integrator by closing switch 2 momentarily. The output of the processing circuits provides an updated value of the extinction coefficient every 0.5 second.

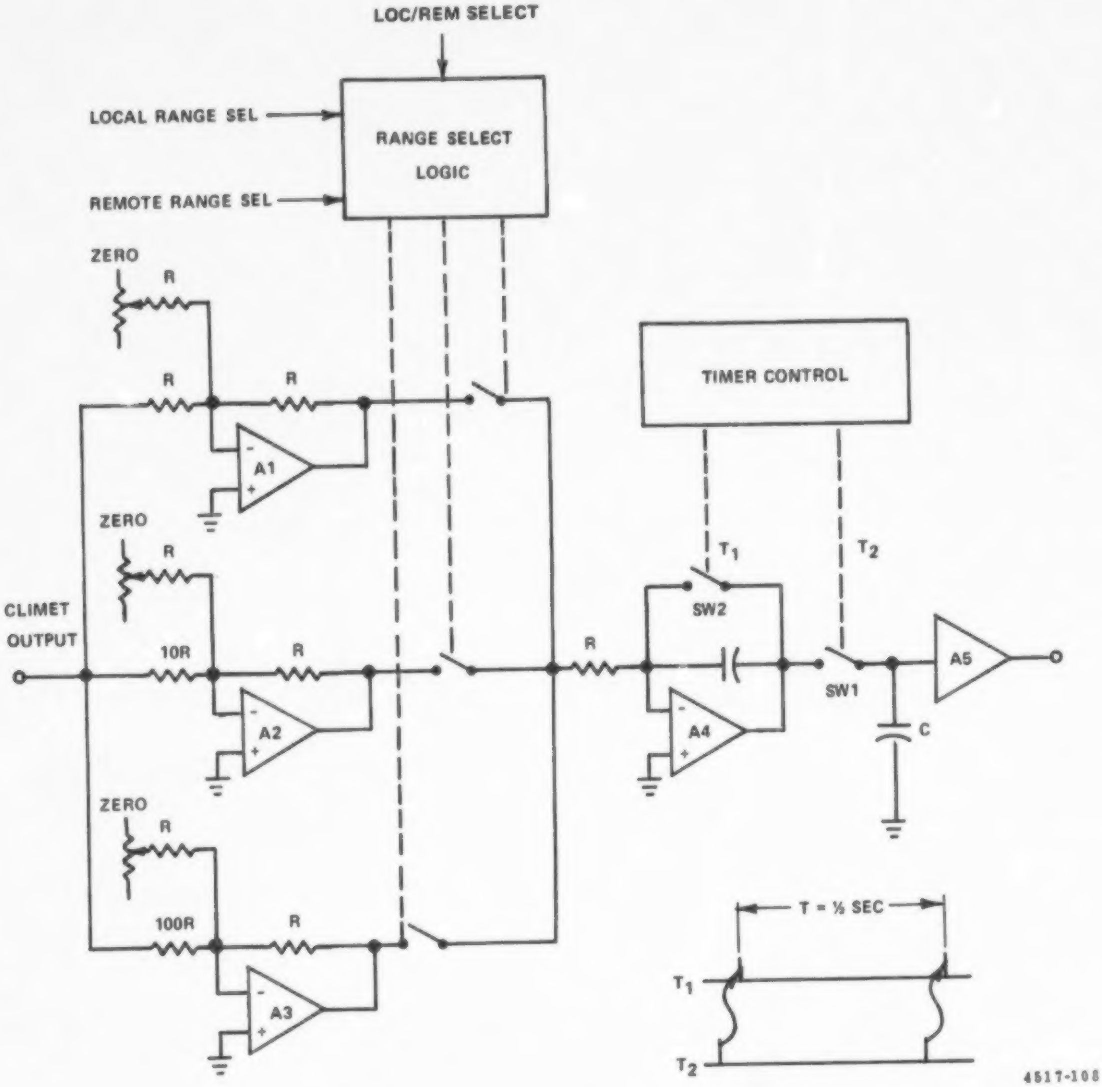
LOC/REM SELECT
LOCAL RANGE SEL
RANGE SELECT LOGIC
REMOTE RANGE SEL
ZERO
R
R
R
A1
ZERO
R
CLIMET OUTPUT
10R
R
A2
ZERO
R
100R
R
A3
TIMER CONTROL
T_1
T_2
SW2
R
SW1
A4
A5
C
T = ½ SEC
T_1
T_2
4517-108

Figure 6. Signal processing circuits.

One unique feature of these circuits is the sensitivity of the circuits to small particles since no threshold or "dead band" is encountered. The zero control compensates for input signal offset and noise in the input signal. In the laboratory, the zero for each range is set for zero output with the associated Climet sampling air passed through an absolute filter. In the field, the zero is adjusted by backflushing the diluter such that only the filtered dilution air is introduced into the Climet. The zeroing is repeated fairly frequently to compensate for voltage drifts (i.e., photomultiplier, amplifier, etc.) within the measuring system.

SYSTEM CALIBRATION

The opacity monitoring system is normally calibrated in the laboratory using monodisperse polystyrene latex (PSL) spheres, manufactured by the Dow Chemical Co., as the sampled aerosol. A multichannel analyzer, such as a Tracor Northern, Model TN-1705, or Nuclear Data, Model 60, is used in the calibration procedure to verify the size and to determine the number of particles sampled. The relationship of the various PSL particle sizes to the factor ($A\ Q_{ext}$) is illustrated in Table 1. The extinction coefficient is found by multiplying the effective number of particles sampled by ($A\ Q_{ext}$). The gain of the signal processing circuits is then adjusted to output a voltage proportional to the extinction coefficient. For example, an output of 0-10 volts could represent an extinction coefficient of $0\text{-}10^{-3}\ m^{-1}$. For a 10 m effective path length, this would relate directly to an opacity of 0-1%.

Once the signal processing circuits have been calibrated, the Climet is placed in the calibrate mode and the output of the signal processing circuits is noted. This provides a means of "calibrating" the system in the field by adjusting the gain of the Climet's photomultiplier to maintain a constant system sensitivity. Since the Climet's elliptical optics are not used in the calibrate mode, the system sensitivity can deteriorate with dust or dirt on these surfaces. Therefore, the optical system is cleaned periodically, followed by a complete calibration procedure.

Part of the calibration procedure for the Arapahoe installation is to ensure that all four of the opacity measuring systems have equal responses to the same aerosol. This is accomplished by having all four units sample an aerosol from a large mixing chamber such as a 50-gal. drum. Such an apparatus was designed and built for the system; it is used in the laboratory as well as in the field to ensure comparability between the separate units.

TEST RESULTS

The opacity measuring system has been in operation at the Arapahoe Facility in Denver, Colorado for over one year. During that time, the only significant problem encountered was a failure in one of the Climet particle monitors. The system has been valuable to the testing program by providing a temporal history of each of the four baghouse compartments as they are cycled through filtering and cleaning operations. At this facility, each compartment can be cleaned either by shaking or by means of reverse air. The cleaning operations can be initiated through programmable time periods or programmable pressure thresholds across the filtration medium. The opacity monitors have been valuable in assessing the combination of cleaning techniques that provide optimum baghouse performance. Although it might be argued that the opacity monitors do not provide an absolute measure of opacity, they provide a good relative performance of the four baghouse compartments.

A typical temporal history of the output of compartment B over several cleaning cycles is illustrated in Figure 7. The rapid rise in opacity occurs after the cleaning cycle (reverse air in this case) is completed. The cleaning cycle lasts approximately 2.5 min and consists of a 90 sec null period (i.e., no air is introduced into the compartment) and a 30 sec reverse air period, followed by a 30 sec null period. During this time the opacity monitor is isolated from the baghouse compartment. The spike in opacity occurs when the cleaned bag is brought back on line. Note that the filtration efficiency increases as the filtration cycle progresses. This is attributed to the dust cake that forms over the filtration material, providing added filtering to the baghouse. In the case illustrated, the cleaning cycle was initiated based on a maximum threshold pressure drop across the compartment. This accounts for the non-periodic nature of the cleaning cycles.

SUMMARY

The opacity measuring system consists of a simple dilution system, a standard particle detector that has been proven reliable in field testing, and special signal processing circuits to output a signal related to the aerosol opacity. Some of the salient features of this system are:

(1) use of a reliable commercially available particle detector

(2) high sensitivity to low opacities due to the sensitivity of the particle detector and no processing "dead band"

(3) good comparative measured opacities from the four measured baghouse compartments

(4) adaptability to a large range of aerosols through a dilution system with a range of zero to >10:1 dilution

(5) easily calibrated in the field

(6) packaged for field use

(7) range and zero adjusted locally or remotely

Some of the shortcomings of this system are:

(1) sensitivity to photomultiplier drift

(2) autoranging not provided in the three decades of sensitivity

(3) short temporal variations masked by systems sampling rate of 0.5 sec.

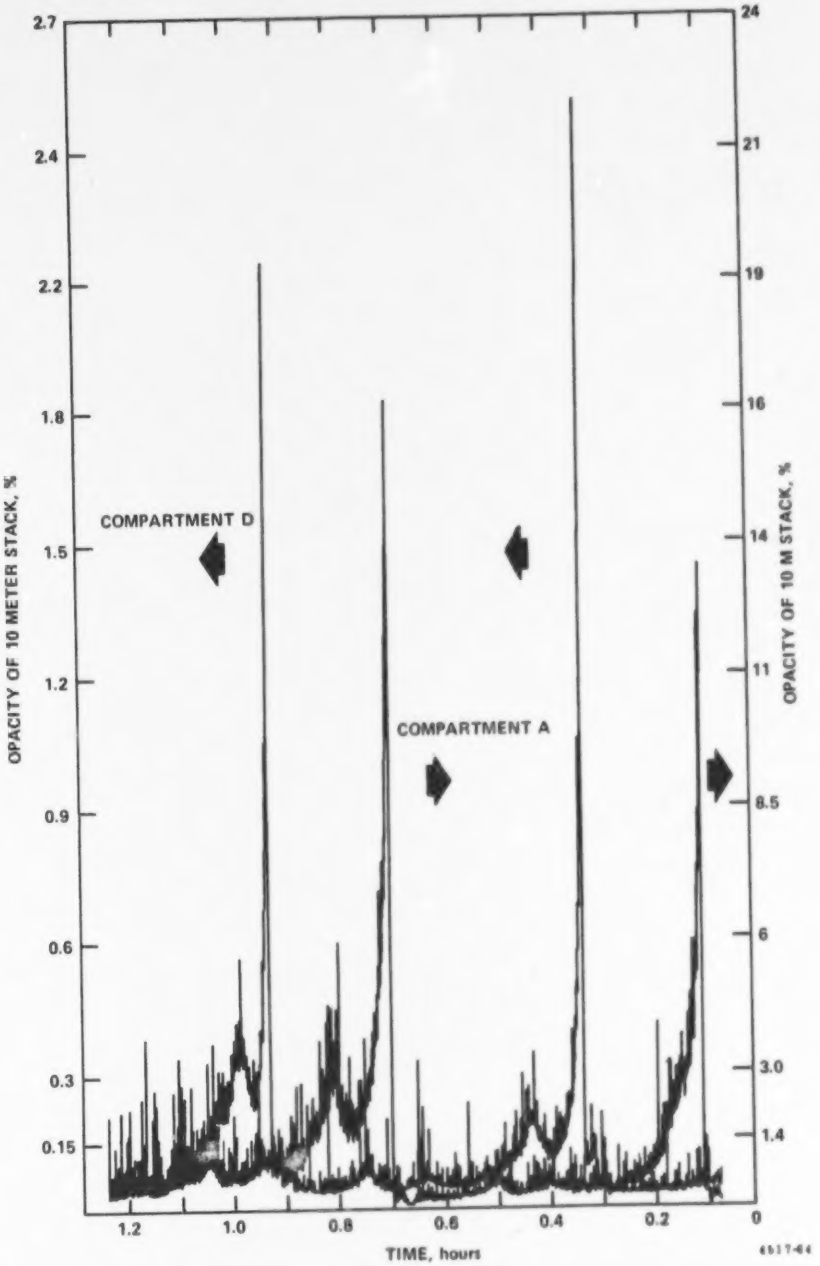

Figure 7. Typical responses of the opacity monitors on compartments A and B.

ACKNOWLEDGEMENTS

We wish to acknowledge the assistance of Raymond N. Coker and Donald E. Ashworth in the assembly of the various devices for the opacity monitoring system. We also appreciate the able assistance of Myron McCallum in the operation of the system at the Arapahoe facility. This project is supported under EPRI Contract No. 1129-8.

REFERENCES

1. Cowen, Stanton J., David S. Ensor, and Les E. Sparks. The Relationship of Fly Ash Light Absorption to Smoke Plume Opacity. In: Proceedings of the Third EPA Symposium for the Transfer and Utilization of Particulate Control Technology, sponsored by the Particulate Technology Branch, Industrial Environmental Research Laboratory, USEPA, Research Triangle Park, NC, 1981.

2. Van de Hulst, H. C. Light Scattering by Small Particles. John Wiley & Sons, Inc., New York, 1957. 470 pp.

3. Kerker, Milton. The Scattering of Light and Other Electromagnetic Radiation . Academic Press, New York, 1979. 435 pp.

4. Quenzel, H. Influence of Refractive Index on the Accuracy of Size Determination of Aerosol Particles with Light-Scattering Aerosol Counters. Appl. Opt. 8(1): 165-169, 1969.

This paper has been reviewed in accordance with the U.S. Environmental Protection Agency's peer and administrative review policies and approved for presentation and publication.

Paper 27

A COMPARISON OF SEVERAL PARTICLE-SIZING TECHNIQUES

Kenneth M. Cushing, R. Ray Wilson, and William E. Farthing
Southern Research Institute

and

D. Bruce Harris
Industrial Environmental Research Laboratory
U.S. Environmental Protection Agency

and

Robert C. Carr
Electric Power Research Institute

ABSTRACT

Particle size measurements have been performed on the inlet and outlet flue gases from a fabric filter pilot plant operating downstream from a utility boiler burning low sulfur coal. Particle size distributions at the inlet of the fabric filter have been measured with four different commercial cascade impactors, a novel five stage in-line cyclone system, and an electrical aerosol size analyzer. The cascade impactors and the five stage cyclone size particles gravimetrically in the range of 0.5 to 20.0 micrometers aerodynamic diameter. The electrical aerosol size analyzer uses the particles' electrical mobility to size particles in the range from 0.05 to 1.0 micrometer aerodynamic diameter. At the outlet of the pilot scale fabric filter, three methods have been used to measure particle size. These methods include gravimetric measurements using cascade impactors, optical particle counters in conjunction with a multichannel analyzer, and a unique laser light scattering fine particle sizing system. The optical and laser light scattering devices size in the 0.5 to 11.0 micrometer aerodynamic diameter range. Particle size distributions obtained with each of the instruments are presented.

INTRODUCTION

Particle size measurements have been performed on the inlet and outlet flue gases from a fabric filter pilot plant (FFPP) operating downstream from a utility boiler burning low sulfur western coal. The purpose of this paper is to give a brief overview of the particle size data acquired with a number of different types of instruments. Particle sizing methods have included gravimetric, light scattering, and electrical mobility techniques. Comparisons of particle size distributions obtained by these different methods are shown whenever possible. Following are brief descriptions of the particle sizing devices, together with graphs comparing the particle size distributions obtained with the various instruments.

PARTICLE SIZING INSTRUMENTS

Gravimetric Technique

Cascade Impactors--

Five models of commercial cascade impactors were used at the inlet and outlet of the fabric filter pilot plant. These were: The seven-stage University of Washington Mark V Cascade Impactor (UW); the six-stage Modified Brink Cascade Impactor (Brink); the seven-stage Meteorology Research Institute Model 1502 Cascade Impactor (MRI); the eight-stage Andersen Mark III Cascade Impactor (Andersen); and the seven-stage Flow Sensor In-Stack Sampler (Flow Sensor). All of these cascade impactors measure particle size in the range from 10 to 0.5 μm aerodynamic diameter.[1]

Series Cyclone System--

In order to collect large quantities of sized particles at the inlet to the fabric filter pilot plant, a five-stage series cyclone system was used. Figure 1 shows a sketch of this instrument.[2] Since no theory has been developed which can adequately predict the behavior of cyclones over a range of temperatures and flowrates, empirical performance equations have been developed for the five cyclones from high temperature calibration data. Particles are sized by this system from about 8 to 0.5 μm aerodynamic diameter.

Light Scattering Technique

Climet Optical Particle Analyzer--

The Climet Model 225HT Particle Analyzer is an optical light scattering instrument incorporating forward scattering of white light over an angular range from 15° to 105° into a photomultiplier detector. As used in the fabric filter pilot plant, the Climet is part of a sensitive extractive outlet opacity monitor. Each of the four FFPP compartments has a Climet system on its outlet duct. This system is described elsewhere in these proceedings under the title "A Sensitive Particulate Monitor For Measuring The Approximate Opacity For Fabric Filter Systems." The Climet 225HT does not in itself discriminate particles by size; however in conjunction with a multichannel analyzer particle size information between 0.5 and 5 μm aerodynamic diameter can be obtained. For the present study a Canberra Series 30 Multichannel Analyzer was used to separate Climet signals (photocurrent pulses) into seven size fractions within the bounds mentioned above.

Fine Particle Stack Spectrometer System--

The FPSSS is a single particle laser light scattering instrument developed and manufactured by Particle Measuring Systems, Inc. In contrast to the Climet system, the FPSSS measures particles in situ. The active components are mounted inside and on a water-cooled probe assembly. A photomultiplier senses

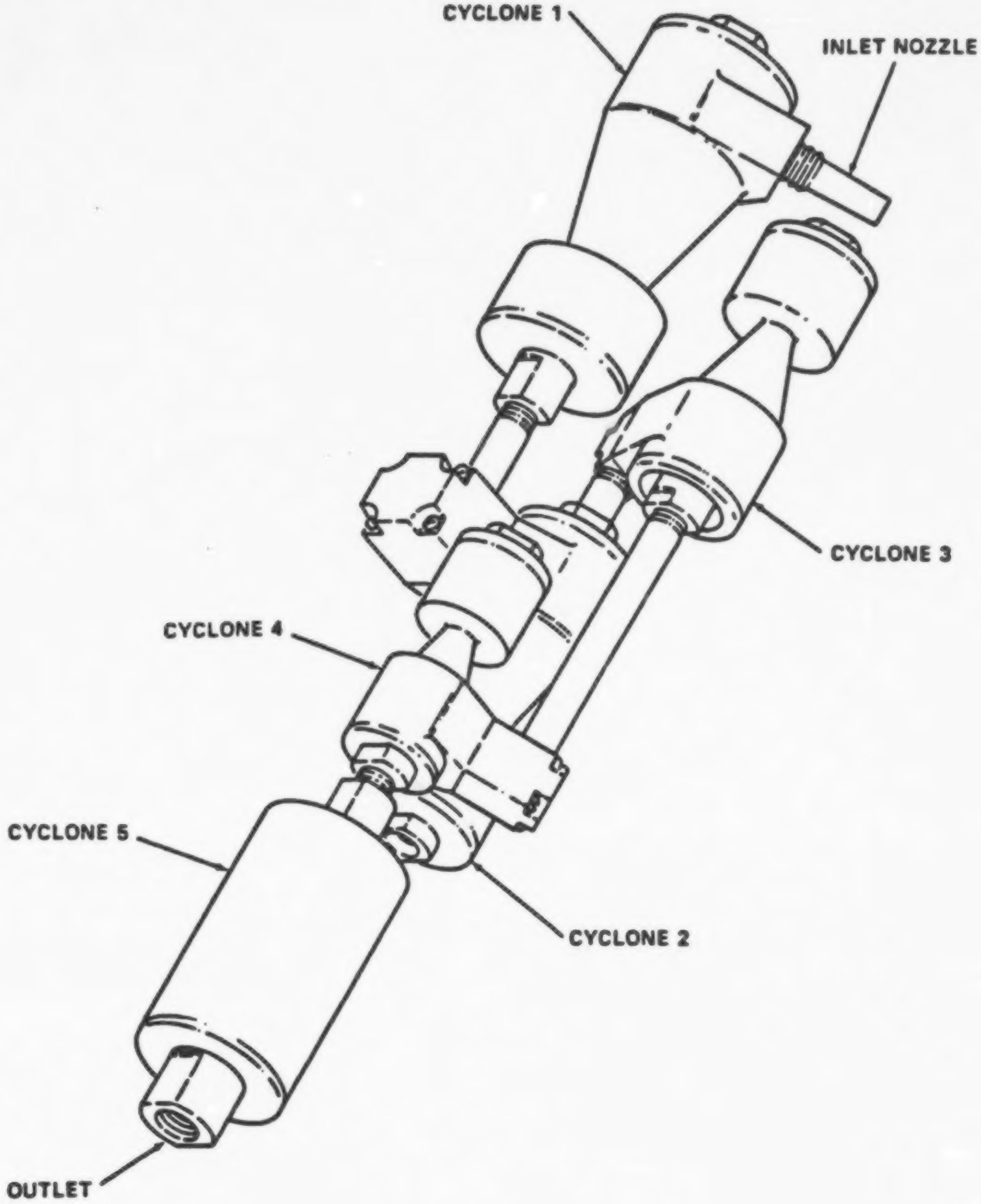
CYCLONE 1
INLET NOZZLE
CYCLONE 3
CYCLONE 4
CYCLONE 5
CYCLONE 2
OUTLET

4181-04

Figure 1. The Five-Stage Series Cyclone System.

the light scattered by particles passing through the view volume of a helium-neon laser beam. Particles can be classified in one of four particle size ranges, 0.4-1.15, 0.5-2.0, 1.15-5.65, and 2.0-11.0 μm aerodynamic diameter. Only one counting range is active at any given time. A sophisticated microprocessor/minicomputer allows for a wide variety of particle sampling time periods on a non-attended basis as well as several mass and number concentration output modes.

Electrical Mobility Technique

Electrical Aerosol Size Analyzer--

A TSI, Incorporated, Model 3030 Electrical Aerosol Analyzer was used to size particles in the range from 0.01 to 1 μm aerodynamic diameter. Counting and sizing with the EASA is based on a process of charging the particles with a unipolar charge and then measuring the mobility distribution of the charged particles. This instrument was used at the inlet to the fabric filter pilot plant; the particle concentrations were diluted by a Sample Extraction Dilution System in order to reduce the particle concentration to a level which can be measured by the EASA[3]. A TSI Model 3900-30 Data Analysis Package which included an Apple II microcomputer, printer, interface, and data handling software, provided tables and graphs of aerosol number, surface area, and volume concentration.

PARTICLE SIZE DISTRIBUTION GRAPHS

Figures 2 and 3 present the inlet particle size distribution for the fabric filter pilot plant as measured with the University of Washington Mark V cascade impactor. Data from fifteen tests during July and August 1981, are shown on dM/dlogD and dN/dlogD bases in Figures 2 and 3, respectively. The primary point of interest of these graphs is the consistency in the inlet particle size distribution both on a number and a mass basis. This stability is of importance in reliably comparing data taken with the other types of particle sizing instruments as will be demonstrated in Figures 4-9.

These six figures present particle size distributions as measured with several different cascade impactors, the University of Washington Mark V cascade impactor, the MRI Model 1502 cascade impactor, the modified Brink cascade impactor, the Andersen Mark III Stack Sampler, and the Flow Sensor Stack Sampler. Figures 4 and 5 present inlet particle size distributions as measured on May 4, 1981, with the U of W, Brink, and MRI impactors. Data are shown on dM/dlogD and dN/dlogD bases, respectively. The Brink and U of W impactor data show a distinct bimodal distribution with a minimum at about 4 μm, while the MRI data do not indicate such a minimum. It is not clear at this time why this disparity occurred. Below one micrometer, the U of W catch is higher than either the Brink or MRI value. This could be due to particle bounce and reentrainment from higher stages or to an error in estimating stage cut points.

Figures 6 and 7 present inlet particle size distributions measured on August 14, 1981, with four cascade impactors. In addition to the Brink, MRI, and U of W impactors, the Andersen Mark III impactor was tested on this date.

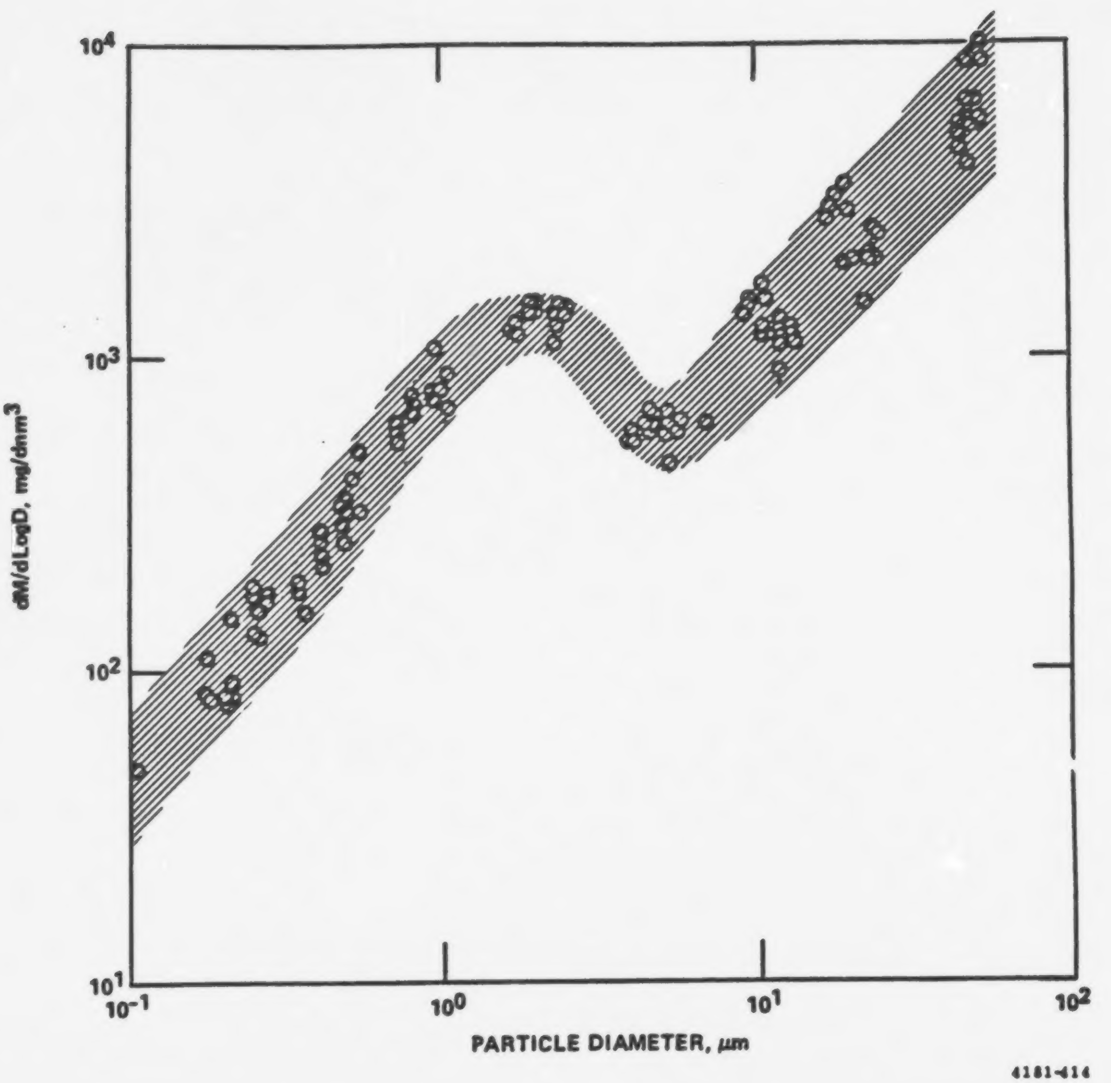

Figure 2. Fabric filter pilot plant inlet particle size distributions (dM/dLogD). Composite of 15 tests, July - August 1981, University of Washington Mark V Cascade Impactor.

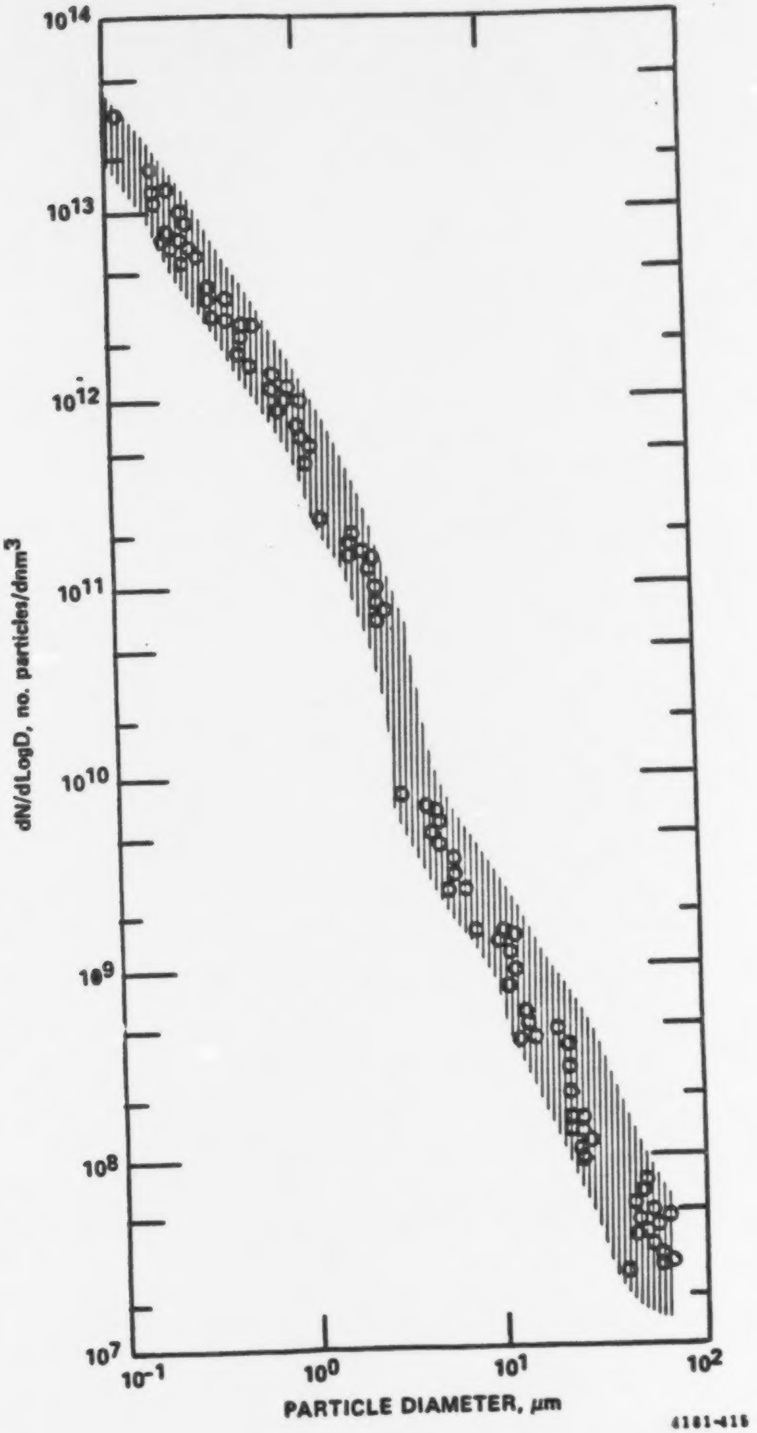

Figure 3. Fabric filter pilot plant inlet particle size distributions (dN/dLogD). Composite of 15 tests, July - August 1981, University of Washington Mark V Cascade Impactor.

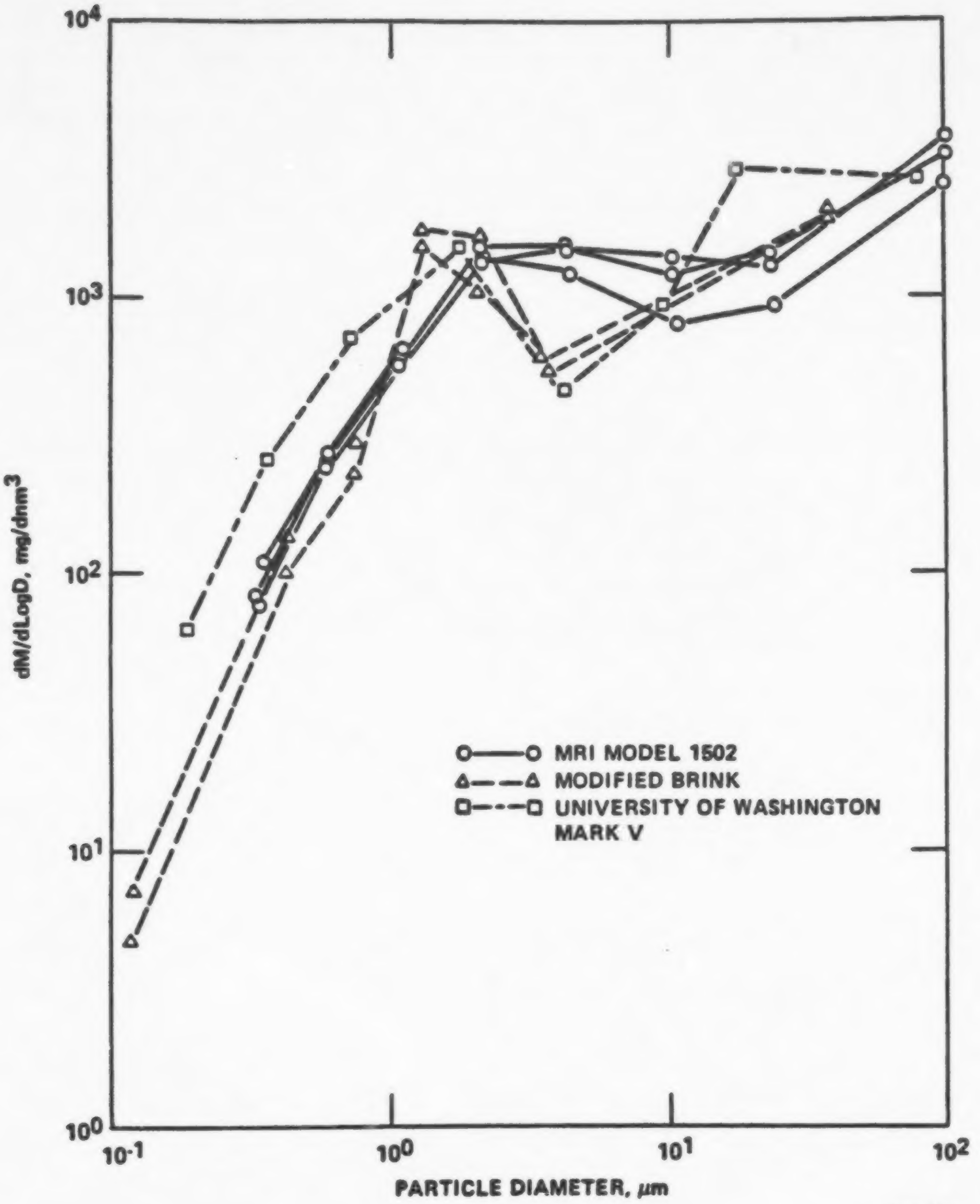

Figure 4. Fabric filter pilot plant inlet particle size distributions (dM/dLogD), May 4, 1981. Three different cascade impactors.

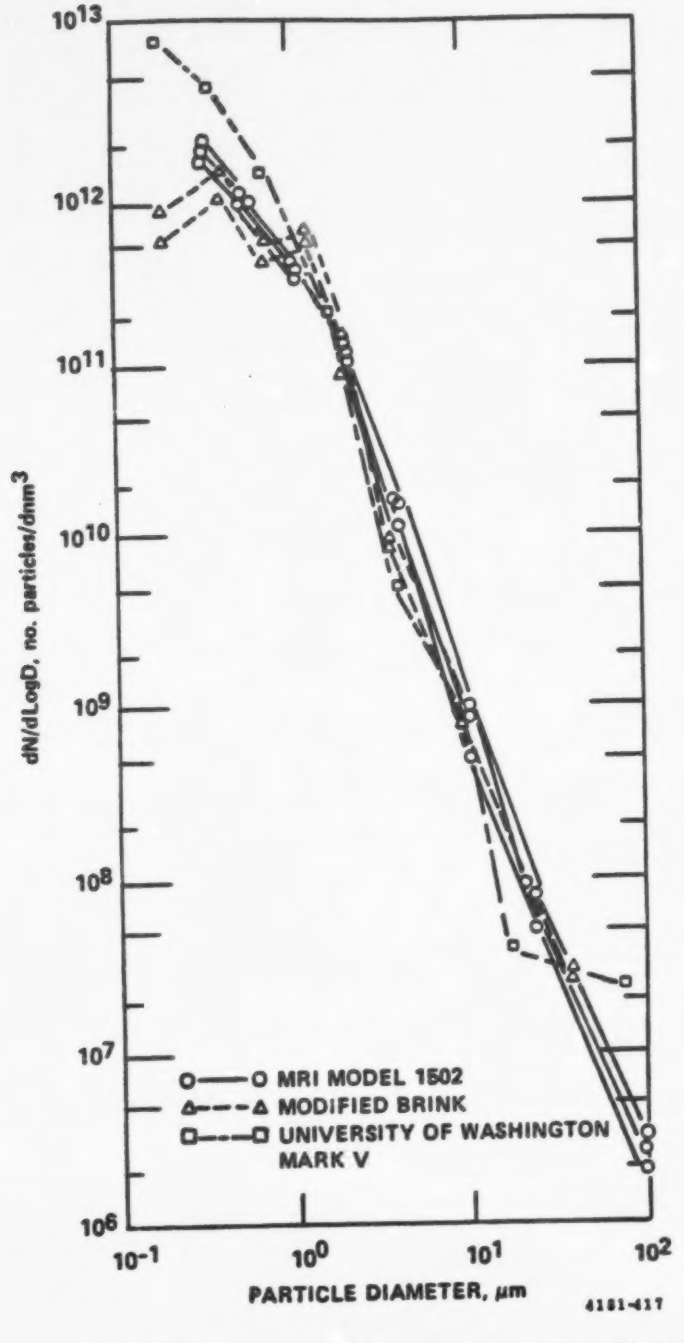

Figure 5. Fabric filter pilot plant inlet particle size distributions (dN/dLogD), May 4, 1981. Three different cascade impactors.

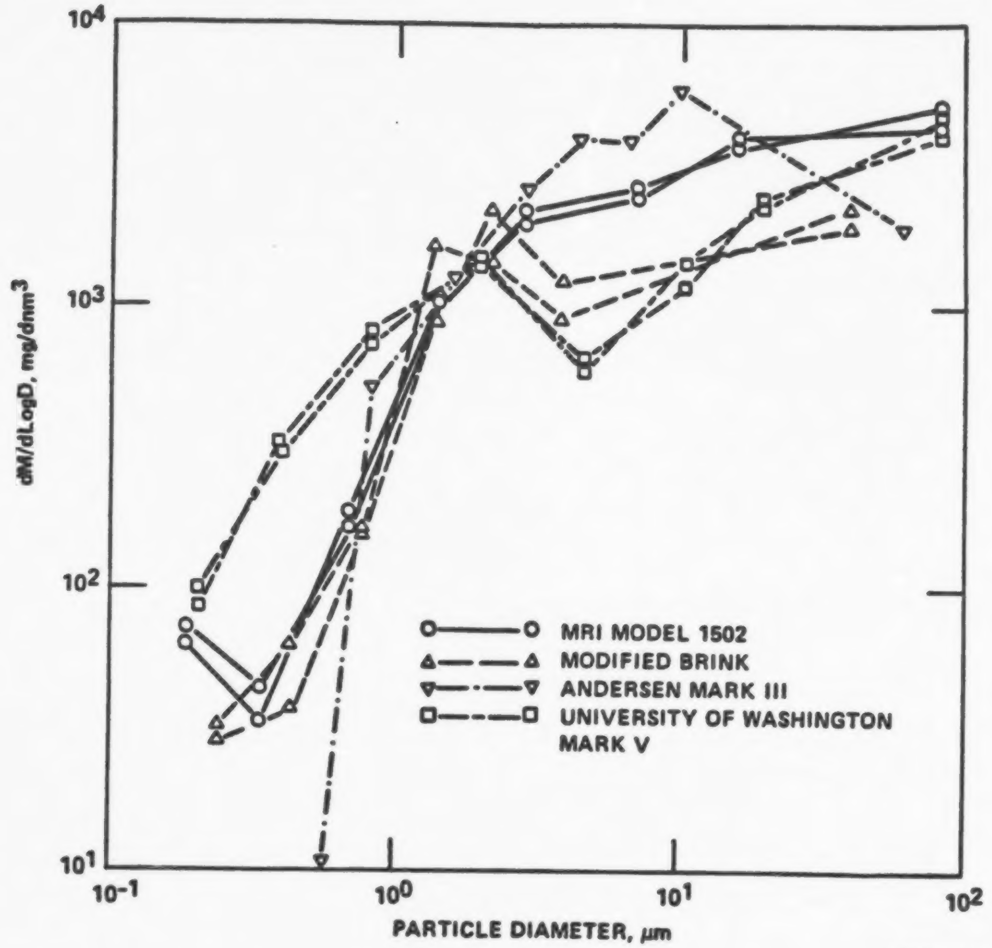

4181-418

Figure 6. Fabric filter pilot plant inlet particle size distributions (dM/dLogD), August 14, 1981. Four different cascade impactors.

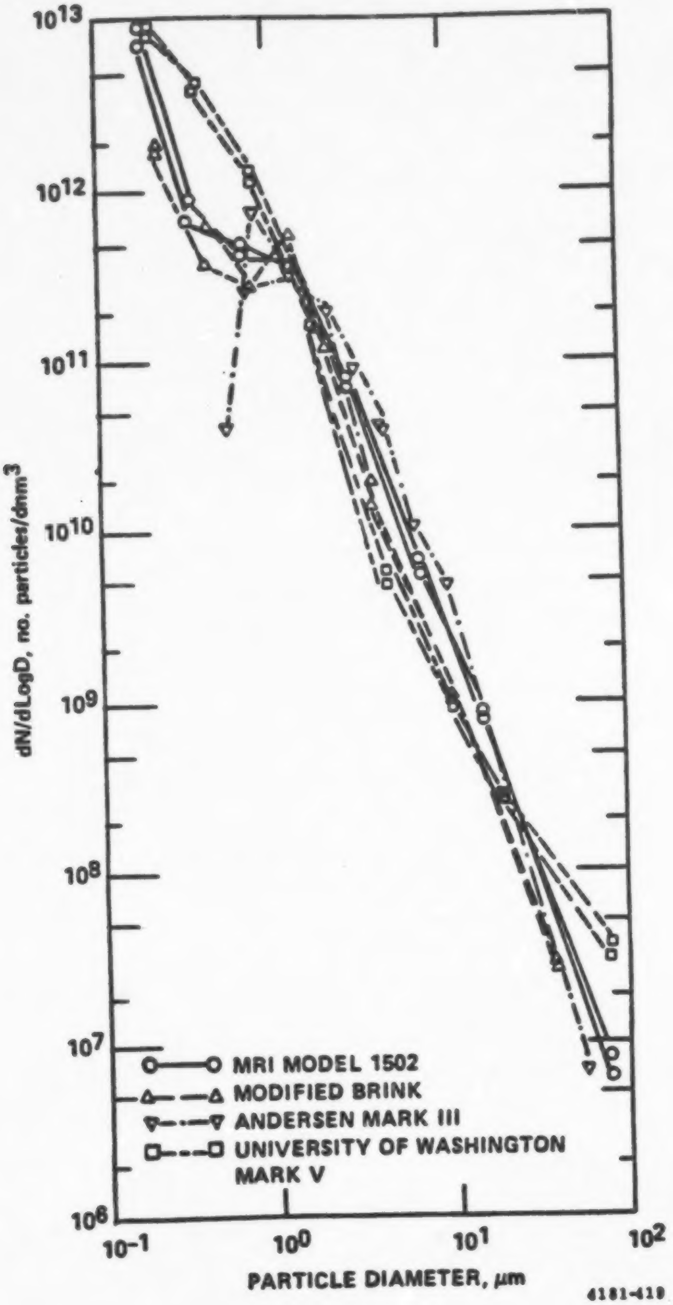

Figure 7. Fabric filter pilot plant inlet particle size distributions (dN/dLogD), August 14, 1981. Four different cascade impactors.

In these tests, the U of W and Brink data again indicate the bimodal distribution at about 4 µm, while the Andersen and MRL data do not. The U of W impactor data are again significantly higher in concentration below one micrometer.

Particle size distribution data taken at the outlet of the baghouse are presented in Figures 8 and 9. These data were obtained with four different cascade impactors, the MRI, Andersen, U of W, and Flow Sensor. Data are presented in Figures 8 and 9 on dM/dlogD and dN/dlogD bases, respectively. Since each outlet test required about 18 hours in order to obtain sufficient particle mass, these tests were performed on consecutive nights. The shapes of the outlet particle size distributions from all five cascade impactors can be seen to be quite similar, independent of the boiler load.

Figures 10 and 11 show data obtained with the Electrical Aerosol Size Analyzer for seven test periods during August 1981 on DM/dlogD and dN/dlogD bases, respectively. As with the data presented in Figures 2 and 3, the FFPP inlet particle size distributions in the ultrafine particle range are quite stable. Because of the large inlet particle stream concentrations, the sample stream is diluted about 350 to 1 prior to being sampled by the EASA. The data points in each graph are average values for the indicated 12-30 samples. The figures also show the 90% confidence levels.

Figures 12 and 13 show FFPP inlet particle size distributions obtained with the five-stage series cyclone system on dM/dlogD and dN/dlogD bases, respectively. These data are from five tests between March and August 1981. As with the cascade impactor data, these tests show a consistent inlet size distribution behavior. Cyclones are not subject to particle bounce and reentrainment problems; the size data below one micrometer are probably quite accurate.

Figures 14 and 15 show comparisons of the FFPP inlet particle size distributions as measured with cascade impactors, the series cyclone, and EASA on dM/dlogD bases only. Figure 14 presents the five-stage series cyclone data and the August 14, 1981, impactor data. The significant item to notice in this graph is that the cyclone data below one micrometer agree quite well with the MRI, Brink, and Andersen data, but not at all well with the U of W data. This indicates that there is an error either in the performance of the impactor or in the equations and values used for the data analysis. The disagreement between the devices at 4 µm will also require further study. Some of the cyclone tests showed the minimum while others did not.

The inlet size distributions in Figure 14 were combined with the EASA data to form Figure 15. To simplify matters, the pairs of different impactor tests have been averaged. The cyclone and the MRI, Brink, and Andersen impactor data fall in with the EASA data better than the U of W data. From the consistency of the EASA over many different days, it is concluded that the minimum in particle concentration at about 0.6 µm is probably a real phenomenon.

Figures 16 and 17 show FFPP outlet particle size distribution data taken at the baghouse outlet with the Fine Particle Stack Spectrometer System and the Climet/Canberra system on dM/dlogD and dN/dlogD bases, respectively. Also

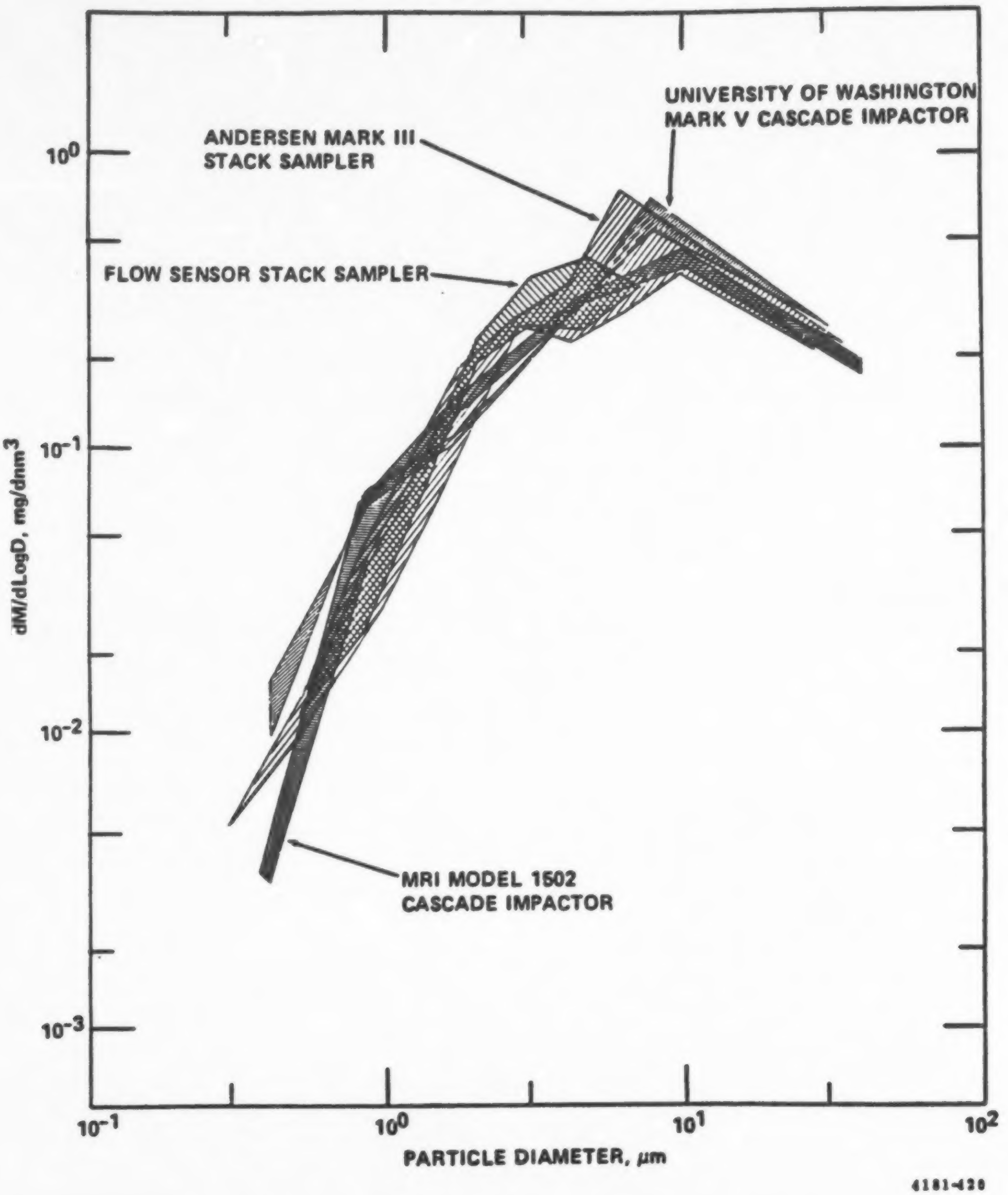

Figure 8. Fabric filter pilot plant outlet particle size distributions (dM/dLogD), November 1981. Four different cascade impactors.

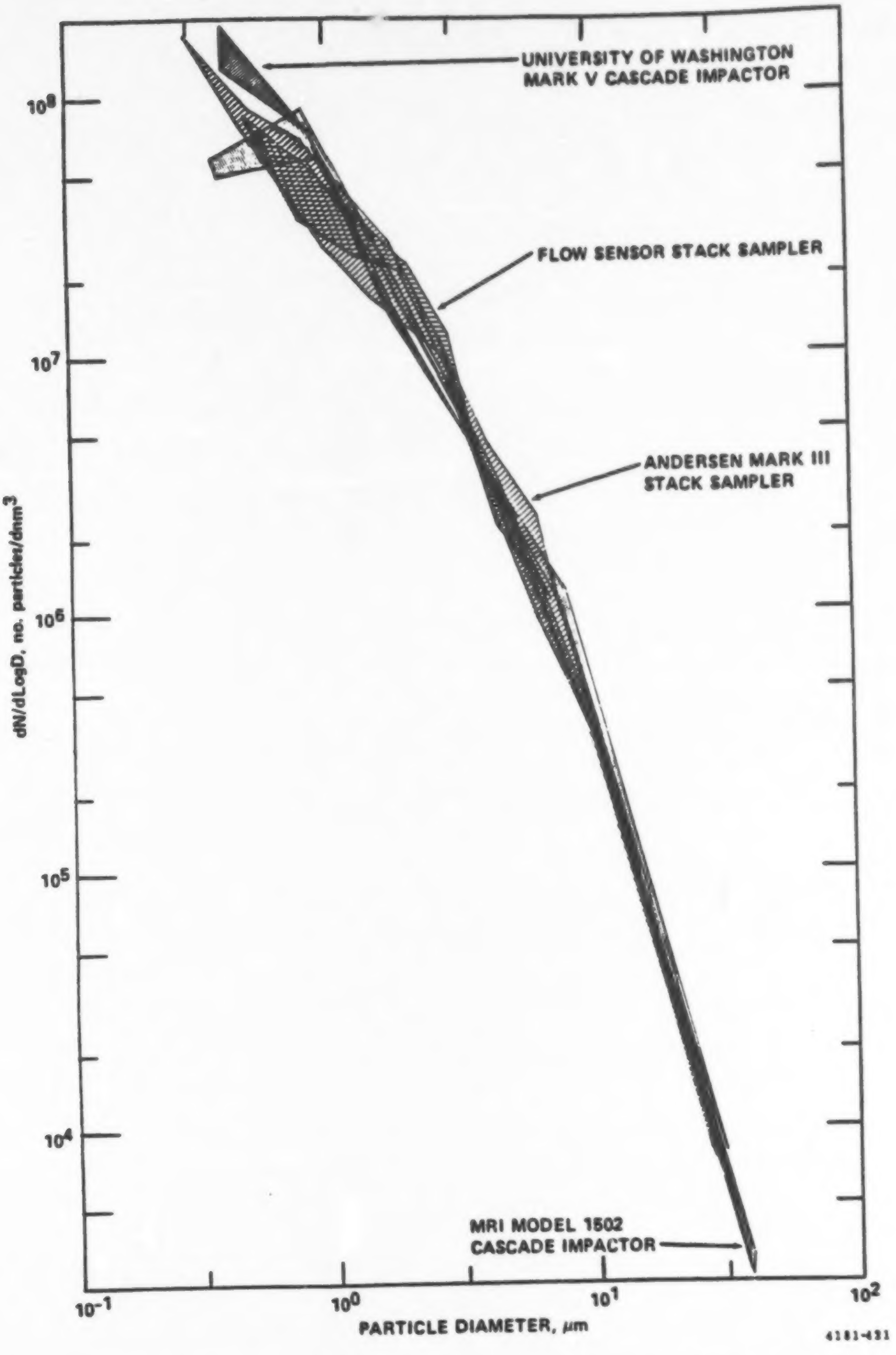

Figure 9. Fabric filter pilot plant outlet particle size distributions (dN/dLogD), November 1981. Four different cascade impactors.

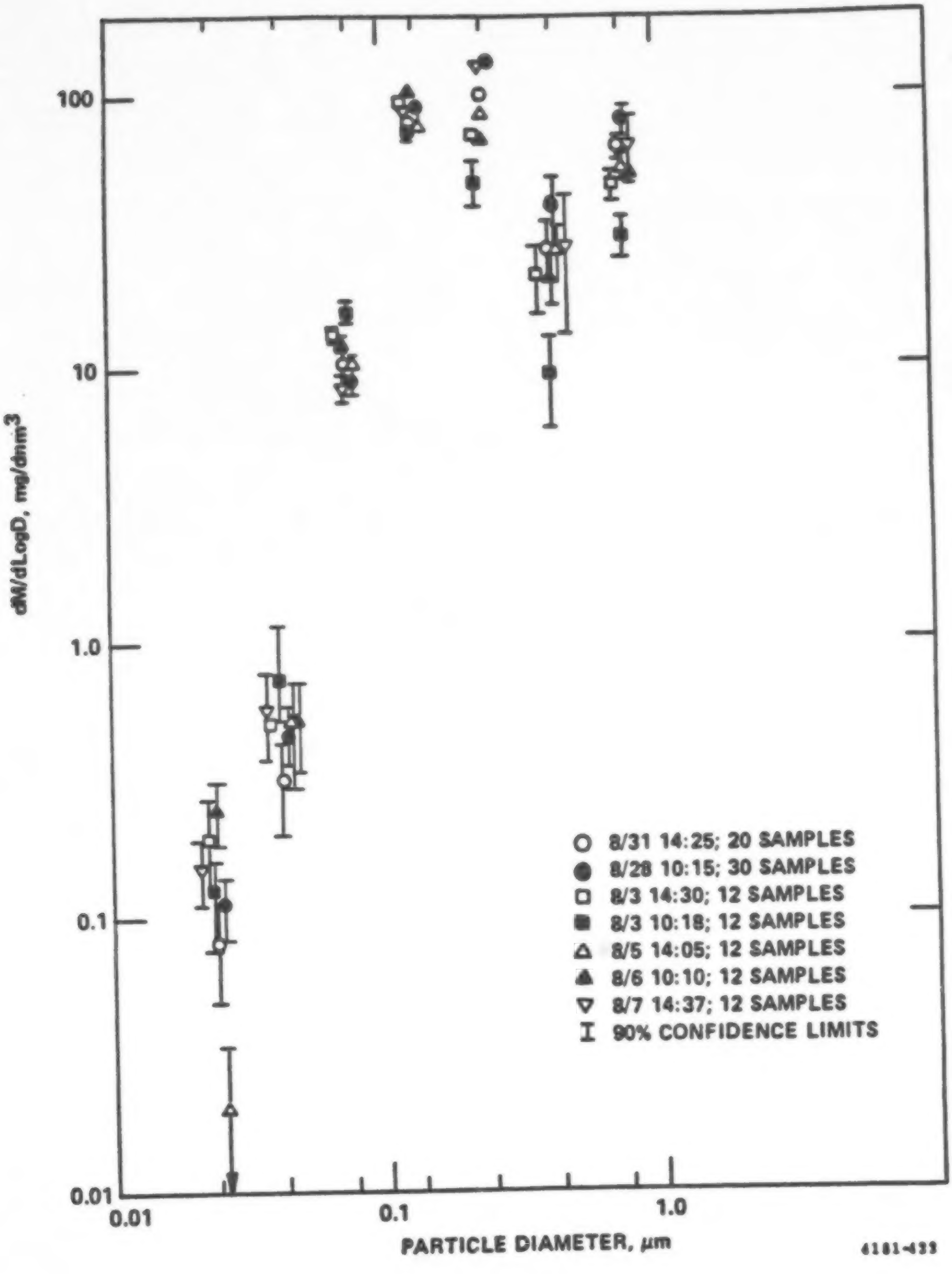

Figure 10. Fabric filter pilot plant inlet particle size distributions (dM/dLogD), August 1981. Electrical aerosol size analyzer.

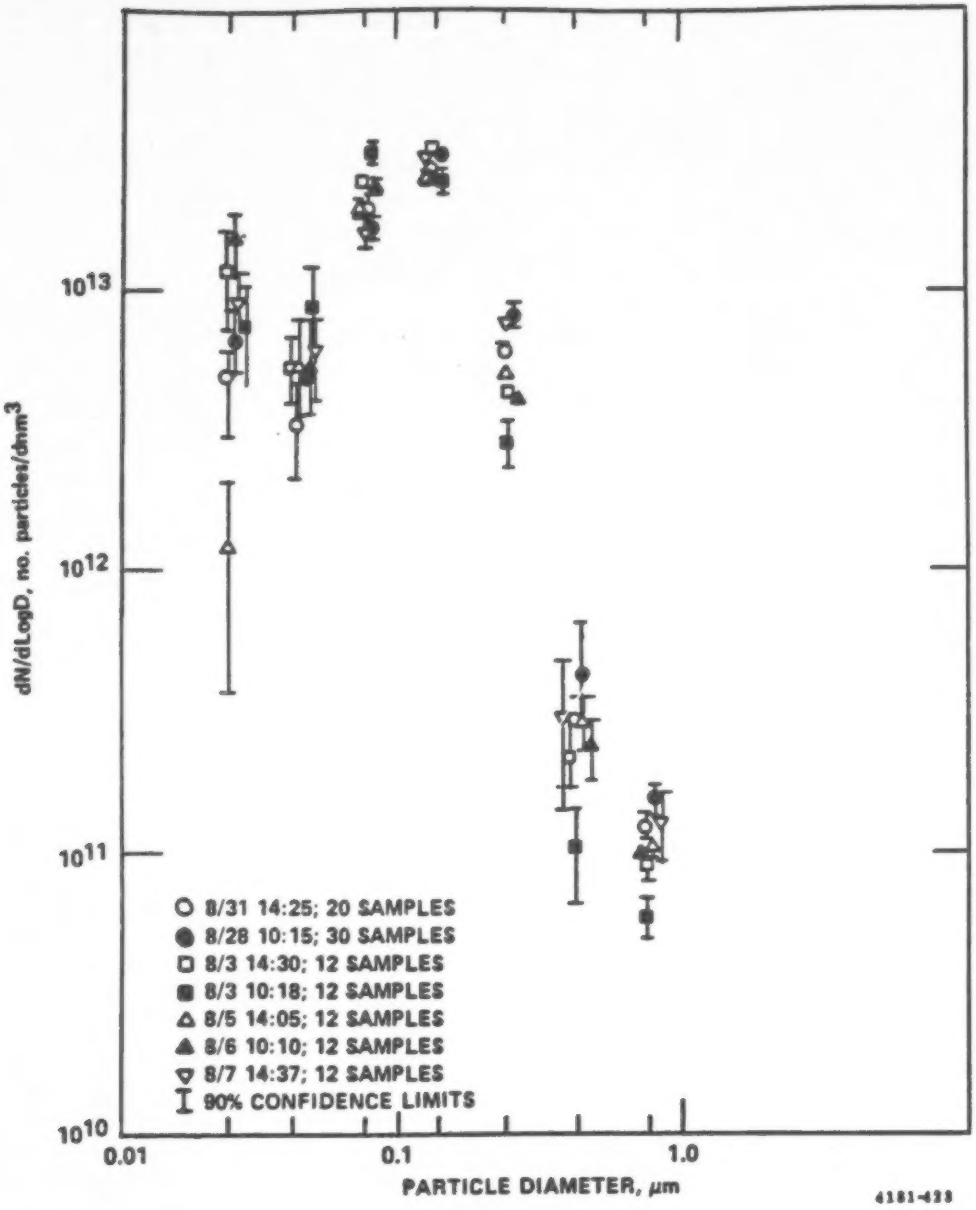

Figure 11. Fabric filter pilot plant inlet particle size distributions (dN/dLogD), August 1981. Electrical aerosol size analyzer.

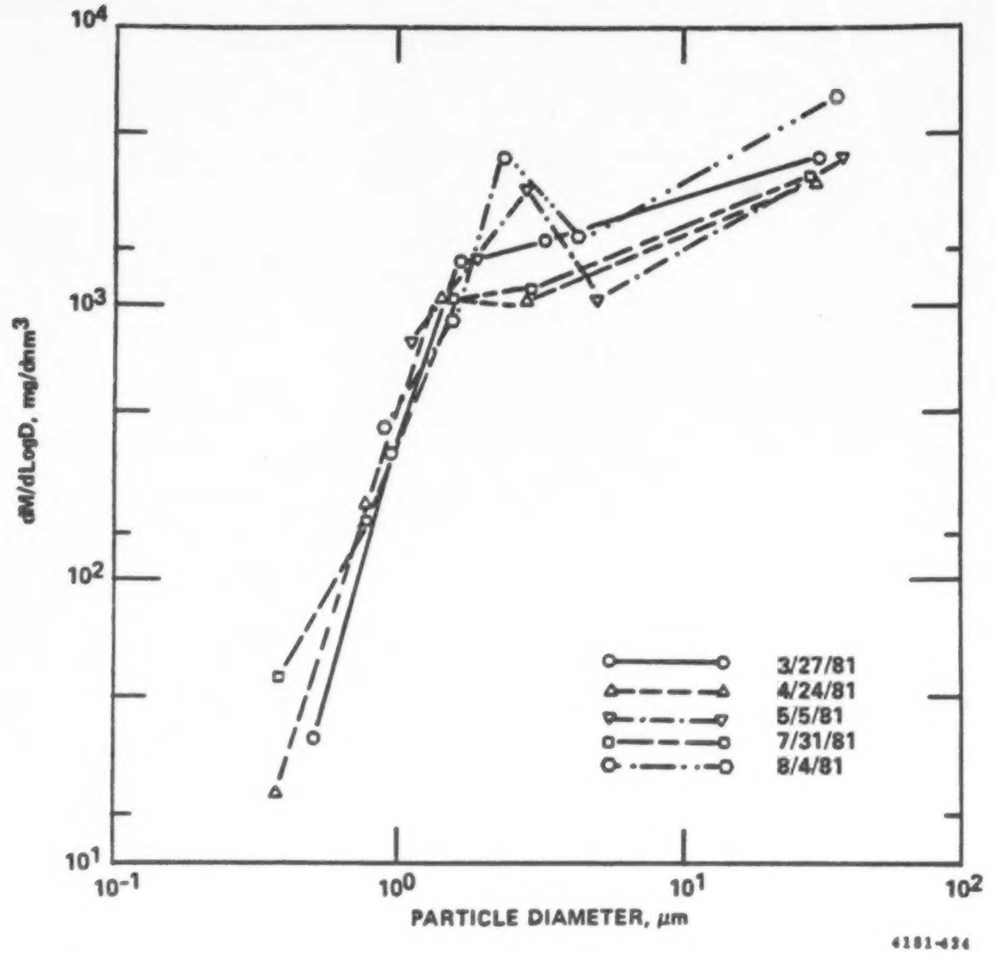

Figure 12. Fabric filter pilot plant inlet particle size distributions (dM/dLogD). Five stage series cyclone system.

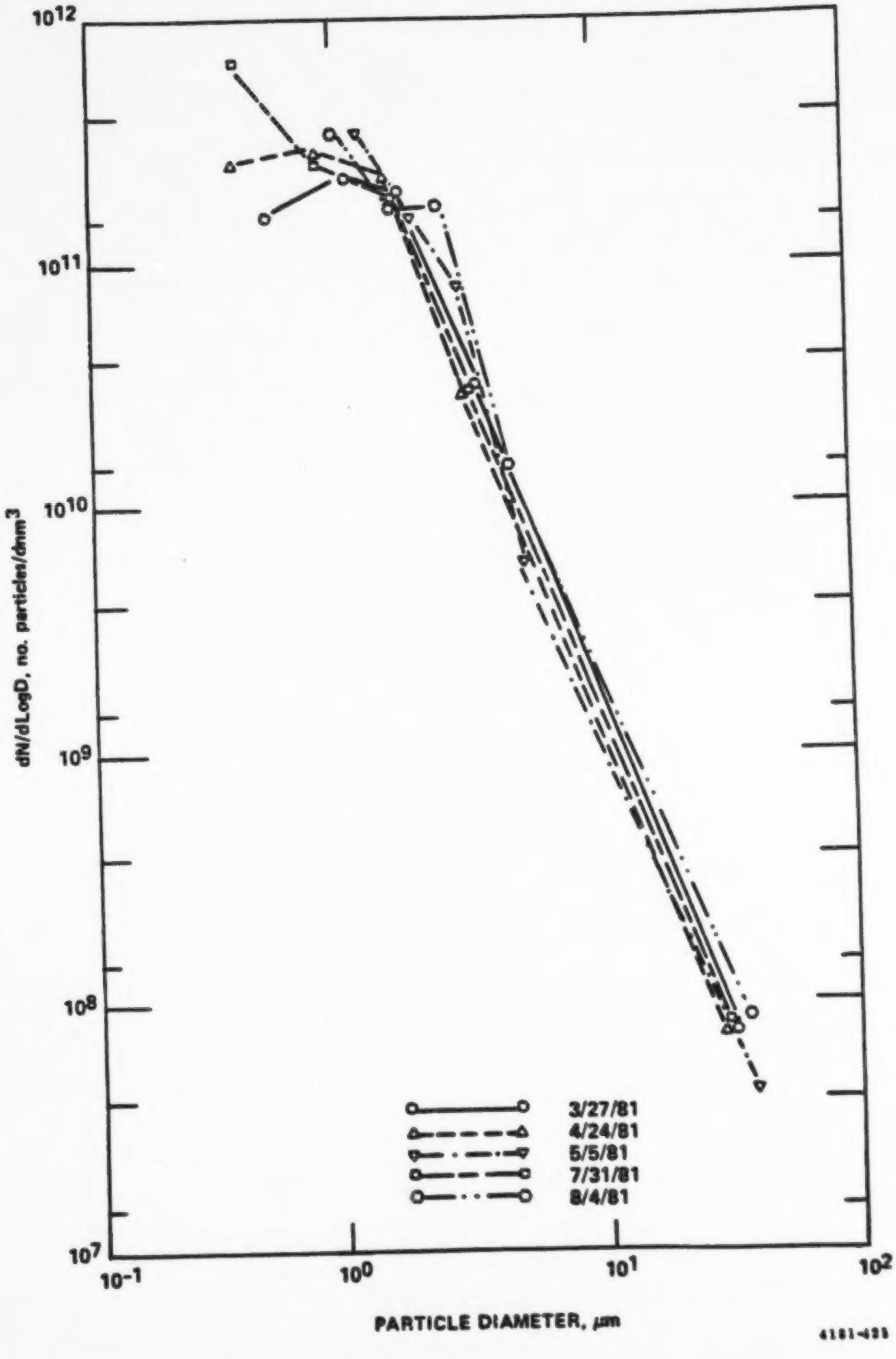

Figure 13. Fabric filter pilot plant inlet particle size distributions (dN/dLogD). Five stage series cyclone system.

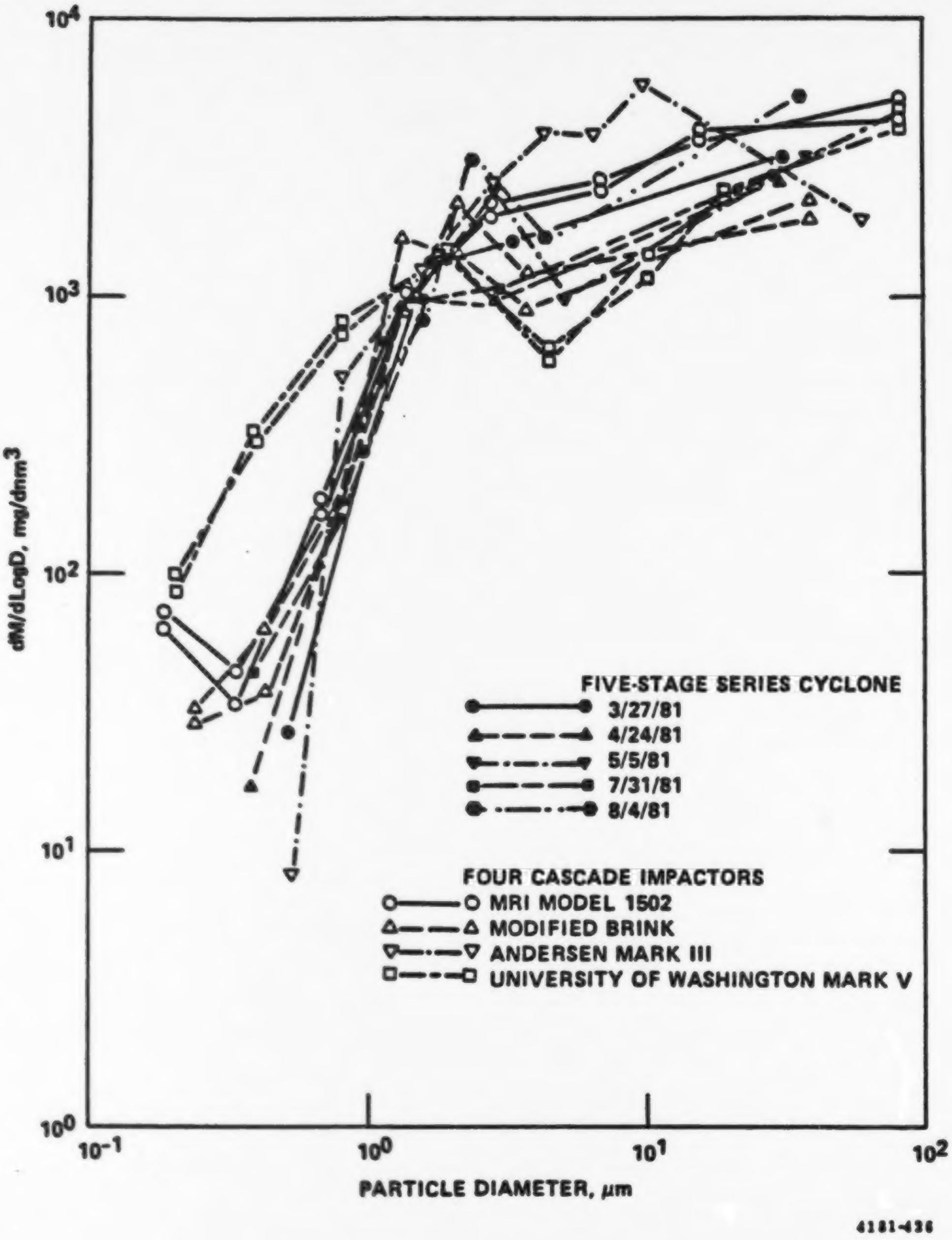

Figure 14. Fabric filter pilot plant inlet particle size distributions. Four cascade impactors and series cyclone system.

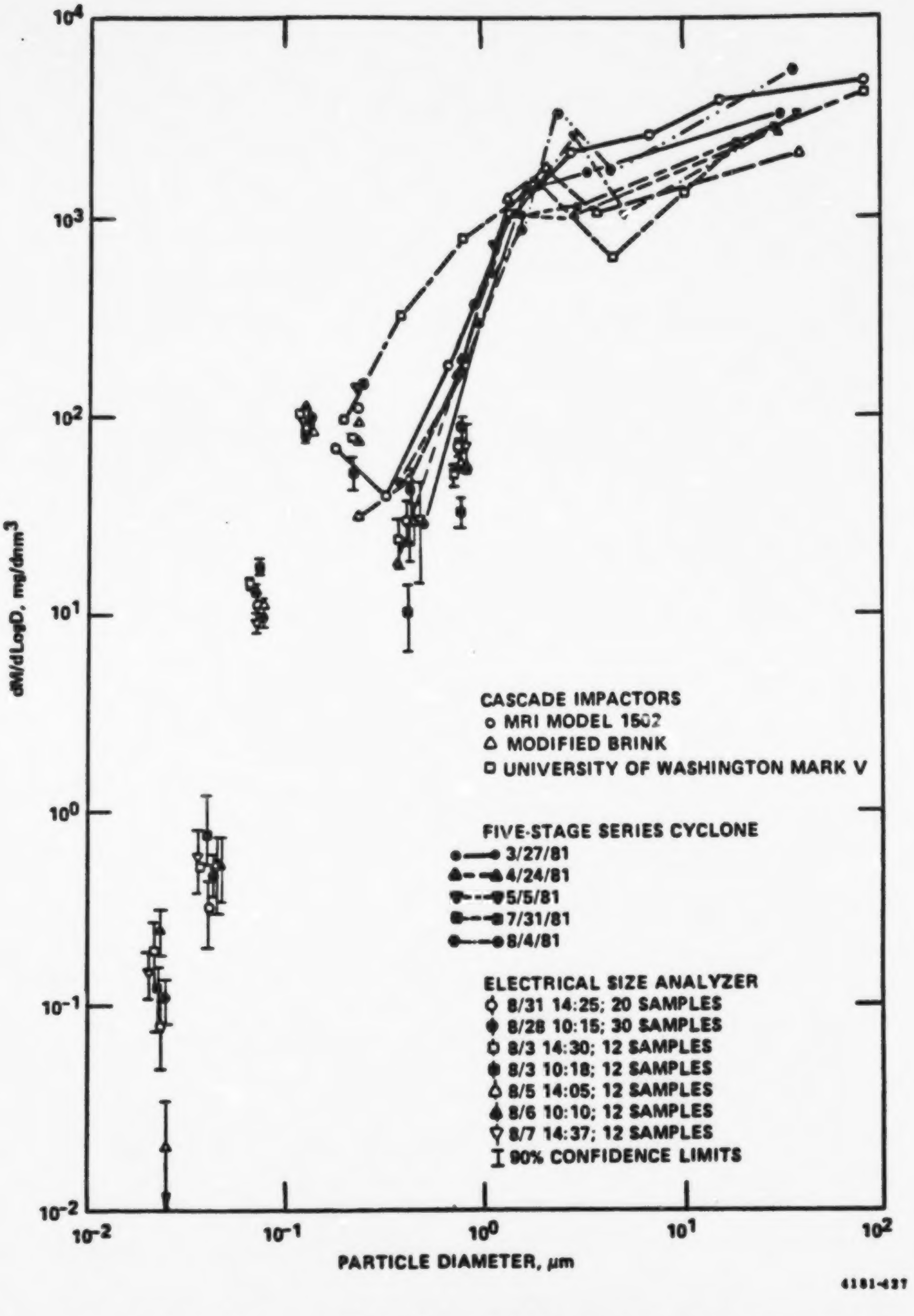

Figure 15. Fabric filter pilot plant inlet particle size distributions, August 14, 1981. Four cascade impactors and series cyclone system.

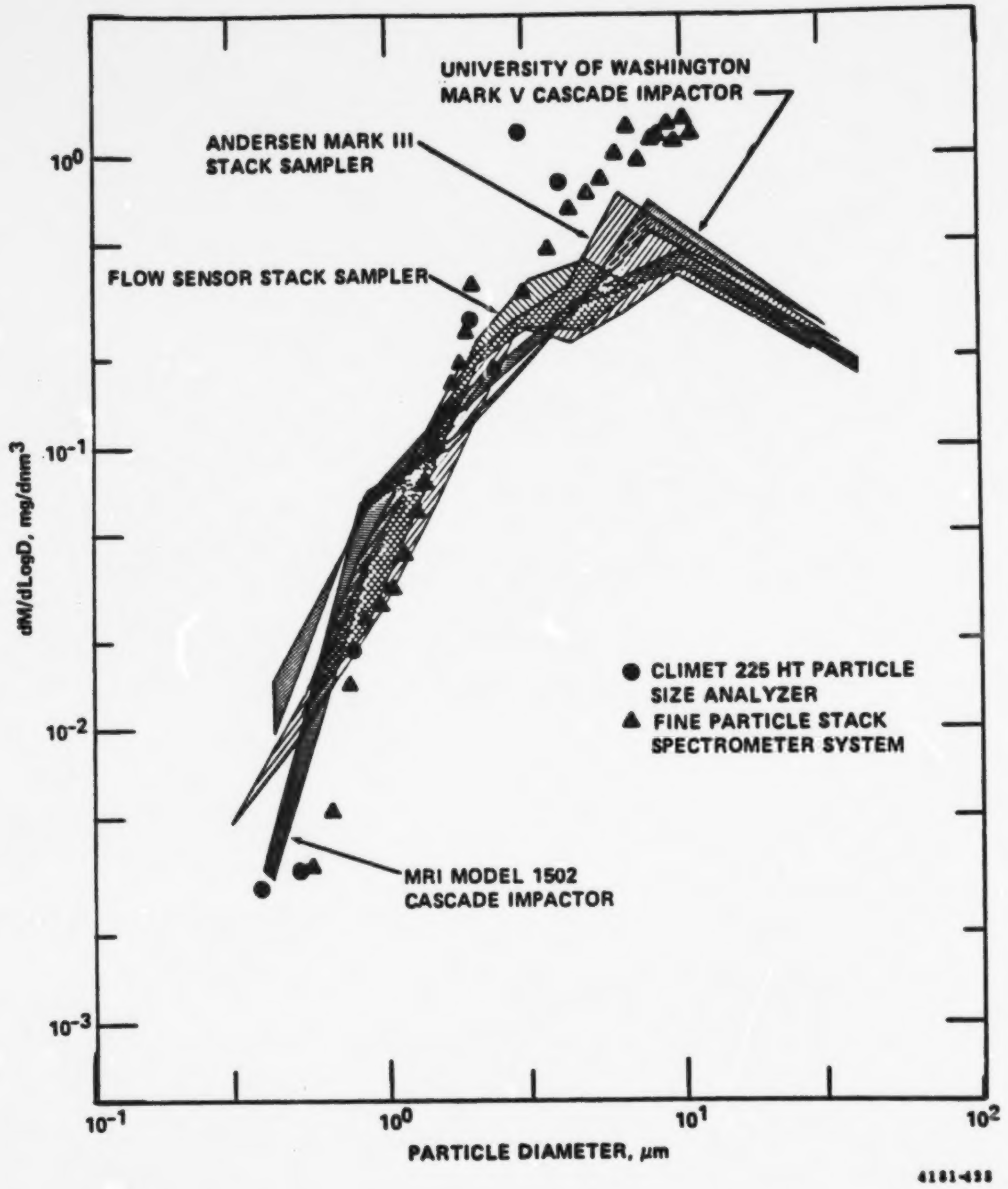

Figure 16. Fabric filter pilot plant outlet particle size distributions (dM/dLogD), November 1981. Climet particle analyzer, fine particle stack spectrometer system, and four cascade impactors.

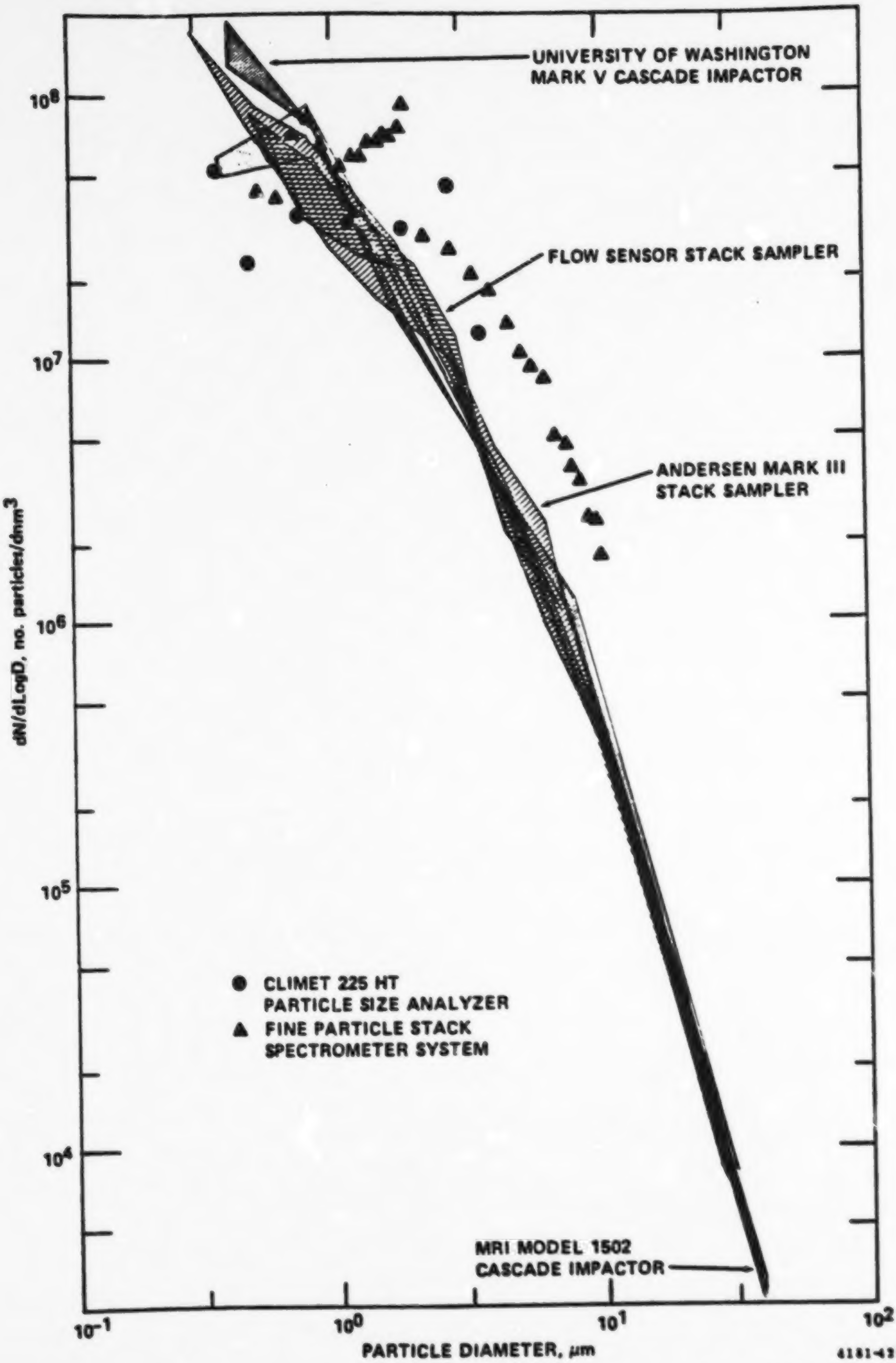

Figure 17. Fabric filter pilot plant outlet particle size distribution (dN/dLogD). Climet particle analyzer, fine particle stack spectrometer system, and four cascade impactors.

shown on these graphs for comparison are the impactor data from Figures 8 and 9. Although the agreement is quite good, the FPSSS and Climet indicate fewer particles in the lower sizes. This could be a result of the data having been taken on different days. The basic shape is similar, however.

CONCLUSIONS

In general, all of the particle sampling methods presented here give comparable results, considering the different types of sizing techniques which are used. Not surprisingly, the ability to obtain comparable data with cascade impactors at inlet concentrations is difficult. The main reasons for this are short sampling times, small nozzles, non-traversing, particle bounce and reentrainment, impactor geometry, and substrate interferences. With care, these problems can be reduced and in some cases eliminated. These difficulties also make the series cyclone system a welcome addition to the available particle sizing inventory. The Fine Particle Stack Spectrometer System and Electrical Aerosol Size Analyzer both proved to be reliable instruments for obtaining real-time particle size distribution data.

REFERENCES

1. Cushing, Kenneth M., and Wallace B. Smith. Procedures Manual for Fabric Filter Evaluation. U.S. Environmental Protection Agency Report, EPA-600/7-78-113 (NTIS-PB283289), Southern Research Institute, Birmingham, AL, June 1978. 451 pp.

2. Smith, Wallace B., Rufus R. Wilson, Jr., and D. Bruce Harris. A Five-Stage Cyclone System for In-Situ Sampling. Environmental Science and Technology 13 (11): 1387-1392, 1979.

3. Felix, Larry G., Randy L. Merritt, Joseph D. McCain, and James W. Ragland. Sampling and Dilution System Design for Measurement of Submicron Particle Size and Concentration in Stack Emissions Aerosols. TSI Quarterly 7 (4): 3-12, 1981.

This paper has been reviewed in accordance with the U.S. Environmental Protection Agency's peer and administrative review policies and approved for presentation and publication.

Paper 28

INTERACTIVE PARTICLE DATA REDUCTION FOR FINE PARTICLES TESTING

C. E. Tatsch
W. M. Yeager
Research Triangle Institute

G. L. Johnson
U. S. Environmental Protection Agency

ABSTRACT

Increasing awareness of the limited resources available for making environmental measurements has focussed attention on the quality and utility of data collected for the use of EPA. The quality of the data is being addressed by the Agency-wide Quality Assurance program; its utility and quality are being increased by use of computerized data bases being developed by EPA. The Environmental Assessment Data System (EADS) is one such data base.

The Fine Particle Emissions Information System (FPEIS) forms a subset of EADS. This system has the capability of storing fine particle (primarily cascade impactor) test results, in both raw and reduced form, and of providing data entry and analysis services, in both interactive and "batch" modes. Its purpose is to assist users in data interpretation, as well as collection.

The feature of primary interest for cascade impactor testing is the recently completed Particle Data Reduction (PADRE) system, which interactively accepts observed data using a portable computer terminal and provides reduced results within a few seconds. Test- and run-related data are entered interactively, and stored for reduction and analysis on the user's request. Calculated impactor stage D_{50}'s and mass concentration are printed, as well as interpolated results at standard particle diameters, to assist test-related decision making and test report preparation. The focus of this paper is on the capabilities of PADRE to accept, edit, and reduce test data in a manner which can assist test crews in making informed decisions regarding cascade impactor tests and produce report-ready reduced data.

BACKGROUND

Funds available for obtaining environmentally related data are scarce, and the situation is not likely to improve. For this reason, the data which are collected must be of known quality and must be available for as wide use as possible. The Environmental Assessment Data System (EADS) is designed to assist EPA meet this need. As shown in Figure 1, the complete system includes environmental data from all types of waste streams and includes

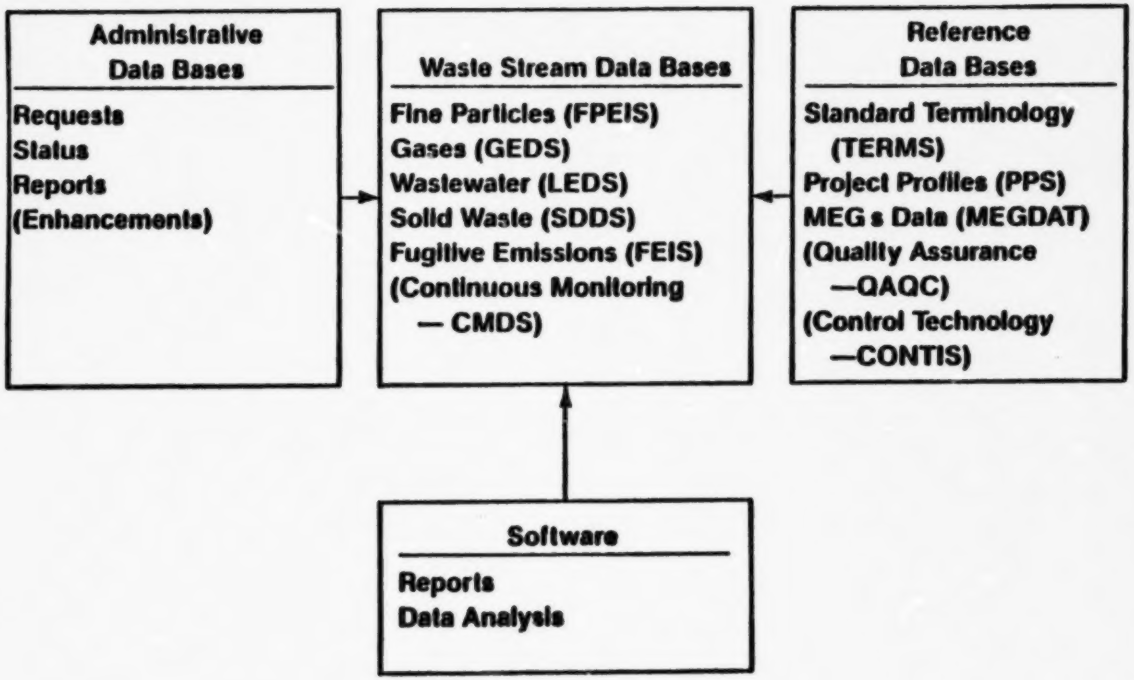
Administrative
Data Bases
Requests
Status
Reports
(Enhancements)
Waste Stream Data Bases
Fine Particles (FPEIS)
Gases (GEDS)
Wastewater (LEDS)
Solid Waste (SDDS)
Fugitive Emissions (FEIS)
(Continuous Monitoring
— CMDS)
Reference
Data Bases
Standard Terminology
(TERMS)
Project Profiles (PPS)
MEG s Data (MEGDAT)
(Quality Assurance
—QAQC)
(Control Technology
—CONTIS)
Software
Reports
Data Analysis

Figure 1. Environmental assessment data systems - overview

reference data bases which may be used to assist with the interpretation of the environmental data. The Fine Particle Emissions Information System (FPEIS) is the data base of interest at this symposium. It contains fine particles data in observed and reduced form. The necessary aspect of data base design is now complete, and increased attention is being given to issues of easing data entry and developing suitable data processing capabilities. This latter effort focuses on converting the massive amount of EADS data into information which is relevant to the needs of a diverse community of users. The type of information which is routinely available through EADS—and, therefore, FPEIS--is comprehensive, as shown in Figure 2. It includes emission source description, waste stream description, test-specific information (e.g. plant load), and detailed sample information. The desired information is accessed through selection criteria common to any data base in EADS, with exclusive or inclusive capabilities on virtually any parameter.

SYSTEM OVERVIEW

The Particle Data Reduction and Entry (PADRE) system, which is the subject of this paper, is designed to accept and store cascade impactor raw data in field-observable form. It can be used to produce on-site decision-making information for a test, as well as the report-ready reduced data. It is an interactive system, running on the Univac at the EPA National Computer Center at Research Triangle Park, North Carolina, and is available to users via the TYMNET communications system using a local telephone in most U. S. cities. Data items may be entered as they are observed, and modified as necessary.

PADRE USER DIALOG

The system is designed to perform the requested operations immediately, and the prompts from PADRE are structured to match the user's needs. Weights, test conditions, and specific run information may be entered and modified. Once all the necessary raw data have been entered and checked, the reduced data may be calculated. The usually available values such as stage D_{50}s, cumulative mass, and geometric mean diameter are produced. Additionally, the interpolated cumulative mass at eight standard diameters is provided. The algorithms which form the basis for PADRE were developed for batch use at Southern Research Institute and are known as the Cascade Impactor Data Reduction System (CIDRS); comparability with CIDRS results has been maintained in PADRE.

Raw data are entered and stored at the user's discretion. For example, the preweights for all the substrates to be used in a test may be entered before the test is begun; the conditions for various impactor runs for a day may be entered at the close of each day's testing; and the substrate postweights may be entered after the substrates have been cooled and desiccated to constant weight. Any data point may be modified by the user, when it is recognized to be incorrect, either during the session when it is entered, or at a later date.

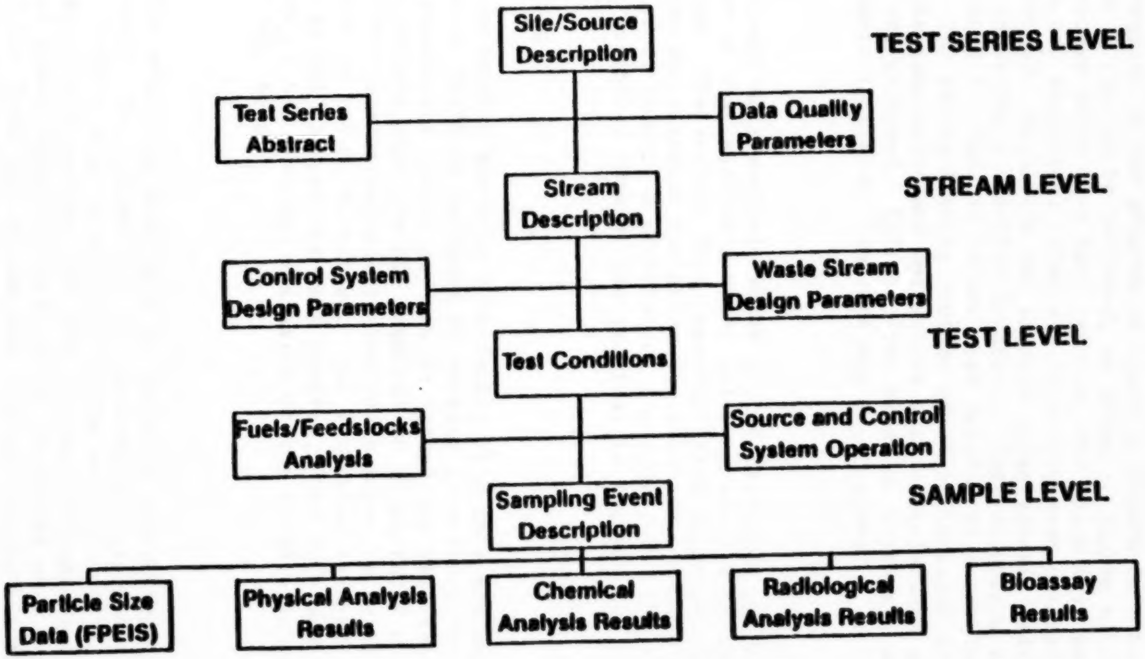
Site/Source Description
TEST SERIES LEVEL
Test Series Abstract
Data Quality Parameters
Stream Description
STREAM LEVEL
Control System Design Parameters
Waste Stream Design Parameters
Test Conditions
TEST LEVEL
Fuels/Feedstocks Analysis
Source and Control System Operation
Sampling Event Description
SAMPLE LEVEL
Particle Size Data (FPEIS)
Physical Analysis Results
Chemical Analysis Results
Radiological Analysis Results
Bioassay Results

Figure 2. EADS waste stream data base structure/hierarchy

User interaction with PADRE is in response to a series of prompts. The major logic flow through the program is selected by a 'yes-no' response: values are requested at the appropriate places. In order to ensure interaction between users and programmers, a bulletin board with current information is always printed. User comments are solicited, and may be entered at the terminal, if desired. A PADRE system summary is also available on request to the program as shown in Figure 3. The complete set of raw data for a run may be reviewed, as shown in Figure 4. All the observed parameters which have been entered, and which will be available for data reduction, are displayed. When all data have been entered and edited, they may be reduced. Reduction can be done using generic calibration constants, or those for a specific impactor. Typical output at the terminal is shown in Figure 5. Reduced values most helpful in a testing situation are provided. The spline-fitting routine has been included as a standard feature, and the cumulative and derivative mass calculations at a standard set of points are provided. Calculations based on physical, aerodynamic, and/or aerodynamic impaction diameters may be obtained.

DATA ANALYSIS

The additional data analysis which may be performed on PADRE-reduced data is similar to that available under the programs STATIS and PENTRA of the CIDRS system. The results from user-specified impactor runs may be used to obtain a mean and standard deviation distribution. Similarly, specified runs may be used to compute a penetration distribution. These are presented in tabular and graphical form at the terminal to assist with optimizing test planning.

USER REQUIREMENTS

The user investment has been consciously held to a minimum. The terminal for which PADRE is designed to operate is a Texas Instruments Silent 700 or equivalent, which may now be leased for less than $100 per month. Communications with the NCC computer on which PADRE operates are via the 300 baud TYMNET communications system which supports local telephone numbers available in all U. S. cities. The financial cost of operating PADRE is borne by EPA through the EADS program. The only additional user cost is to agree to the eventual inclusion of the finally accepted data into the FPEIS/EADS data base.

BENEFITS

The benefits which are available by use of a centrally maintained PADRE system are several. The system will be expanded in response to user needs. Algorithms for various aspects of calculations will be updated (and documented) regularly to reflect the best current methods--and users will be kept informed of these changes. Data can be evaluated as a test progresses by personnel in the field and at the home office, by the EPA Project Officer, or any other person who knows the four keys which access the data. Data quality aids are an integral aspect of the PADRE system. The current parameter range checks will be extended to relational checks: these are generally geared to assisting the user in making professional judgements. Some, such as missing data, simply prevent data reduction on inadequate data.

```
 INTRODUCTION TO THE PARTICULATE DATA REDUCTION AND ENTRY (*PADRE*) SYSTEM
-
-
AN OUTLINE FOR LOGICAL FLOW OF THE PROGRAM FOLLOWS:
YOUR COMMENTS AND SUGGESTIONS WILL BE SOLICITED AT THE END OF THE PROGRAM.
-
     "@ADD" *PADRE*
            !
  --->ENTER/MODIFY           REFERS ONLY TO SUBSTRATE WEIGHTS.
 ^      WEIGHTS?                    (PRE- & POST-SAMPLING VALUES)
 ^          !
 ^    ENTER/MODIFY           A TEST OCCURS DURING ONE DAY, WITH COMMON ID,
 ^  TEST CONDITIONS?             PARTICLE DENSITY, ETC.
 ^          !
 ^       ENTER               A RUN INCLUDES FLOW RATES, TEMPERATURES, ETC.
 ^      NEW RUN              COMMON TO ONE IMPACTOR RUN.
 ^    CONDITIONS?
 ^          !
 ^  REVIEW/MODIFY/REDUCE
 ^      RUN DATA?               .... FOR PREVIOUSLY ENTERED DATA.
 ^          !
 ^          !
 ^          +---)--------(YES)-------->.
 ^          !                          !
 ^          !                   .->----+
 ^       ENTER                  ^      !
 ^     MORE DATA?               ^      !
 ^          !                   ^  REVIEW RUN
 ^-<-(YES)+                     ^  CONDITIONS?
 ^          !                   ^      !
 ^       ENTER                  ^  MODIFY RUN
 ^     COMMENTS?                ^  CONDITIONS?
 ^          !                   ^      !
 ^     TERMINATE                ^  REDUCE DATA?
 ^      SESSION                 ^      !
 ^                              ^  PRINT FPEIS
 ^                              ^  INPUT CARDS?
 ^                              ^      !
 ^                              ^  REVIEW/MODIFY/REDUCE
 ^                              ^  MORE OLD DATA?
 ^                              ^      !
 ^                            --(YES)--+
 ^                                     !
 ^                              ENTER NEW DATA?
 ^                                     !
 ^----------------------------<-(YES)--+
                                       !
                                  ENTER COMMENTS?
                                       !
                                 TERMINATE SESSION
```

Figure 3. PADRE logical structure

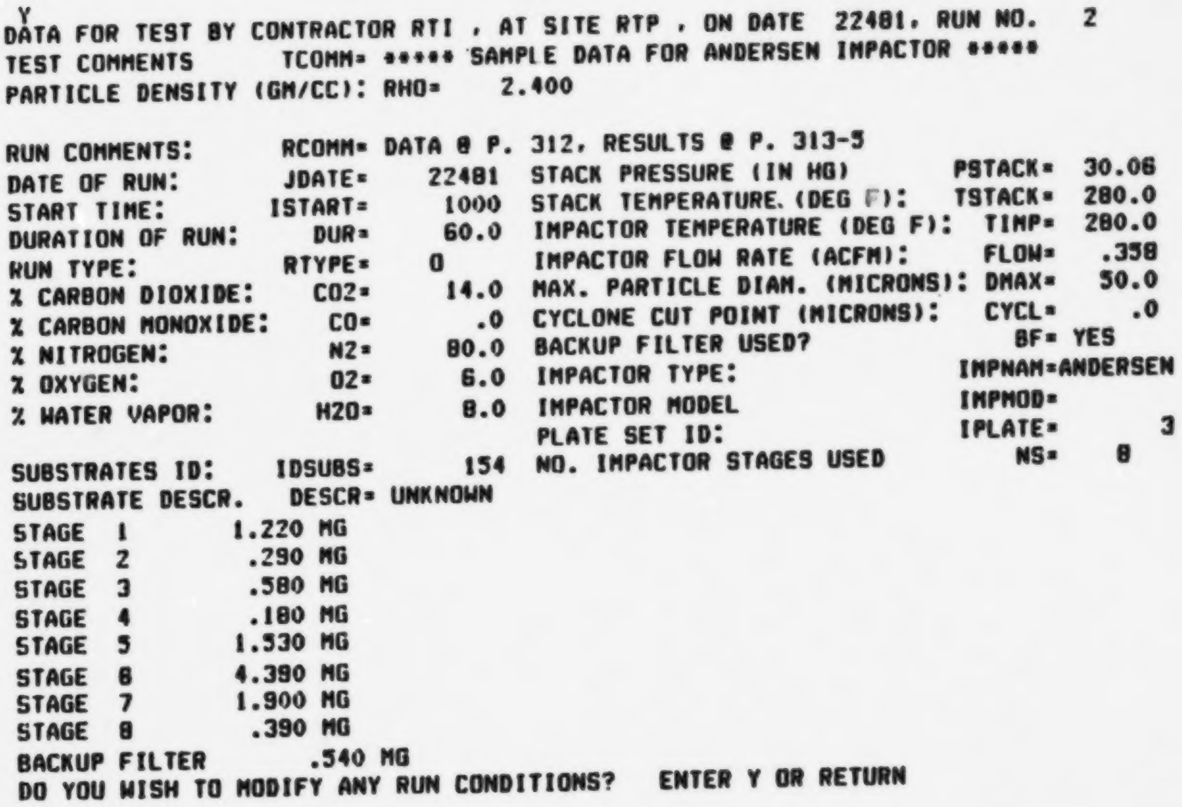

```
 Y
DATA FOR TEST BY CONTRACTOR RTI , AT SITE RTP , ON DATE  22481, RUN NO.   2
TEST COMMENTS      TCOMM= ***** SAMPLE DATA FOR ANDERSEN IMPACTOR *****
PARTICLE DENSITY (GM/CC): RHO=    2.400

RUN COMMENTS:       RCOMM= DATA @ P. 312, RESULTS @ P. 313-5
DATE OF RUN:        JDATE=    22481 STACK PRESSURE (IN HG)          PSTACK=  30.06
START TIME:        ISTART=     1000 STACK TEMPERATURE (DEG F):      TSTACK=  280.0
DURATION OF RUN:      DUR=     60.0 IMPACTOR TEMPERATURE (DEG F):     TIMP=  280.0
RUN TYPE:           RTYPE=   0      IMPACTOR FLOW RATE (ACFM):        FLOW=   .358
% CARBON DIOXIDE:     CO2=     14.0 MAX. PARTICLE DIAM. (MICRONS): DMAX=   50.0
% CARBON MONOXIDE:     CO=       .0 CYCLONE CUT POINT (MICRONS):      CYCL=     .0
% NITROGEN:            N2=     80.0 BACKUP FILTER USED?                  BF= YES
% OXYGEN:              O2=      6.0 IMPACTOR TYPE:                 IMPNAM=ANDERSEN
% WATER VAPOR:        H2O=      8.0 IMPACTOR MODEL                 IMPMOD=
                                    PLATE SET ID:                  IPLATE=       3
SUBSTRATES ID:     IDSUBS=      154 NO. IMPACTOR STAGES USED           NS=    8
SUBSTRATE DESCR.    DESCR= UNKNOWN
STAGE  1       1.220 MG
STAGE  2        .290 MG
STAGE  3        .580 MG
STAGE  4        .180 MG
STAGE  5       1.530 MG
STAGE  6       4.390 MG
STAGE  7       1.900 MG
STAGE  8        .390 MG
BACKUP FILTER       .540 MG
DO YOU WISH TO MODIFY ANY RUN CONDITIONS?   ENTER Y OR RETURN
```

Figure 4. Typical PADRE data review

```
DO YOU WISH TO TO REDUCE THE DATA?  ENTER Y OR RETURN
>Y
WANT TO SEE RESULTS USING CLASSICAL  (STOKES) DEF. OF DIAM.?  ENTER Y OR RETURN
>Y

DATA @ P. 312, RESULTS @ P. 313-5
TOTAL MASS  7.9174-003  1.1968-002  1.8118+001  2.7387+001
               GR/ACF      GR/DCNF     MG/ACM      MG/DNCM

                                                                 DN/DLOGD
 STAGE     MASS      MASS     CUM. MASS     D50    GEO. MEAN DM/DLOGD   (NO/DNCM)
           (MG)  (MG/DNCM) (MG/DNCM)  (MICRONS) (MICRONS) (MG/DNCM)  3.34+005
                                                  21.41   4.12+000
   1       1.22      3.03     24.36       9.17                       3.34+007
   2        .29       .72     23.63       8.67     8.91   2.97+001   1.72+007
   3        .58      1.44     22.19       5.26     6.75   6.65+000   2.64+007
   4        .18       .45     21.75       3.63     4.37   2.77+000   5.96+008
   5       1.53      3.80     17.94       1.84     2.58   1.29+001   1.33+010
   6       4.39     10.91      7.03        .86     1.26   3.34+001   5.81+010
   7       1.90      4.72      2.31        .55      .69   2.37+001   4.43+010
   8        .39       .97      1.34        .28      .39   3.26+000   4.78+011
 FILTER     .54      1.34                           .20   4.46+000
  INTERPOLATED TO STD. INTERVALS:
                              27.39      20.00            9.49+000
                              26.23      15.00            9.07+000
                              24.68      10.00            8.74+000
                              22.10       5.00            4.73+000
                              20.25       2.50            1.31+001
                              12.38       1.25            3.49+001
                               9.03       1.00            3.38+001
                               3.30        .63            1.77+001
WANT TO SEE RESULTS USING THE TGLD  DEF. OF AERO. DIAM.?  ENTER Y OR RETURN
>
WANT TO SEE RESULTS USING MERCERS  DEF. OF AERO. DIAM.?  ENTER Y OR RETURN
```

Figure 5. Typical PADRE data reduction output

SUMMARY

In summary, the PADRE system is designed to provide easy, reliable, rapid, and inexpensive data storage and processing capabilities to cascade impactor users. It also provides EPA with an increased quantity and quality of particle sizing data which can serve to increase the Agency's capabilities for making informed decisions.

This paper has been reviewed in accordance with the U.S. Environmental Protection Agency's peer and administrative review policies and approved for presentation and publication.

Paper 29

ISOKINETIC SAMPLING WITH FIXED FLOW RATE DEVICES USING EXHAUST GAS RECIRCULATION

D. B. Harris and L. Beddingfield
U.S. Environmental Protection Agency
Industrial Environmental Research Laboratory
Research Triangle Park, North Carolina

ABSTRACT

In the measurement of suspended particle concentrations in a gas duct with a conventional sampling train, the gas velocity through the inlet nozzle of the inertial sampling device is adjusted to be equal to the velocity of the surrounding gas stream, so that sampling takes place under isokinetic conditions and a representative sample is obtained. However, for measurement of particle-size distributions, the gas should be sampled at a fixed flow rate through the sampler, to avoid changes in cut points that will occur if the flow rate changes. In an attempt to meet both of these requirements, a sampling train has been developed which uses the concept of exhaust gas recirculation. The sampling train is constructed by a simple modification of an EPA Method 5 meter box. The sample taken from the gas stream isokinetically is augmented to a predetermined fixed flow rate by introduction of recirculated gas in the sampling nozzle. The results of tests comparing performance of the modified train and an unmodified one in a laboratory wind tunnel showed good reproducibility and good agreement in the concentrations measured by the sampling trains.

INTRODUCTION

Accurate determination of the concentration of particles suspended in a gas stream requires isokinetic sampling; that is, the gas velocity in the sampling nozzle must equal the velocity of the surrounding gas stream, if a representative sample is to be obtained. When the gas being sampled is in a duct, test protocols such as EPA Reference Methods 5 and 17 specify that samples are to be taken at a grid of locations in a cross-section of the duct, with adjustment of the sampling flow rate at each location to maintain isokinetic conditions.

When the particle-size distribution is to be measured, however, sampling must be performed at a constant flow rate, since the cut point of an inertial sizing device varies with the flow rate through the device. This procedure avoids errors in determining the boundaries of size fractions. However, anisokinetic sampling leads to size-dependent biases in the particulate mass collected in each size fraction. The bias in the smaller size fractions may be minimal; for larger particles and for reconstruction of total particulate mass, the errors may be substantial. It is currently the practice to traverse the duct maintaining a sample flow rate such that the nozzle velocity is equal to the mean duct velocity. For many purposes, such as design and evaluation of particulate control devices, the accuracy of particle-size distributions obtained by nonisokinetic, constant flow operation is adequate. However, this mode of operation is probably not suitable for size-specific emission measurements which would be used for regulatory purposes such as emission inventory development, attainment strategy formulation, or enforcement of any source particulate regulations which may be defined on a size-specific basis.

In an attempt to eliminate anisokinetic error in size-specific particulate sampling, a sampling train has been developed which uses the concept of exhaust gas recirculation. In order to maintain continuity with current sampling techniques, the EGR train is constructed by modifications to an existing isokinetic sampler (Method 5) meter box. Since the same control valves and flow monitoring orifice are used, operation of the train is similar to the Method 5 procedure and can easily be learned by an experienced sampling technician.

DESIGN OF SAMPLING TRAIN

Figure 1 is a conceptual drawing of an exhaust gas recirculation nozzle, showing annular introduction of the recirculated gas. The gas being sampled is extracted at a flow rate Q_{nozzle} dictated by the requirement for isokinetic conditions. At the same time, the total flow rate Q_{total} is maintained through the sizing device. The difference, $Q_{recycle}$, is provided by recirculation of part of the exhaust gas to the impactor inlet.

Figure 2 is a block diagram of the EGR train with details of the gas flow paths. The gas being sampled is extracted from the duct isokinetically and is augmented to a predetermined constant flow rate using recirculated gas introduced in the sampling nozzle as shown in Figure 1. The mixed gas flow passes through the inertial sampler, probe, filter, and impinger, and into the modified control box. The gas flow rate is controlled using the existing pump and flow control valves (V_1 and V_2) in the commercial meter box. Downstream of the pump a branch in the flow path has been added to the modified train. One part of the gas flow passes through the dry gas meter and sample flow monitoring orifice of the original meter box. The other portion of the total gas flow is recirculated through a new gas flow line to the makeup air of the mixing nozzle. The flow split between the two gas streams is determined by a new valve V_3 added in the recycle flow line. As can be seen in Figure 2, the recycle line forms a closed flow loop with entry and exit branch points at the nozzle and in the control box upstream of the dry gas meter. By mass balance, then, the nozzle mass flow rate Q_n, expressed in dry standard volume flow units, must equal the sample flow rate Q_s passing through the dry gas meter. Thus, the flow rate required for isokinetic sampling can be monitored using the in-stack pitot tube and sample orifice exactly as in EPA Method 5 and analogous sampling protocols.

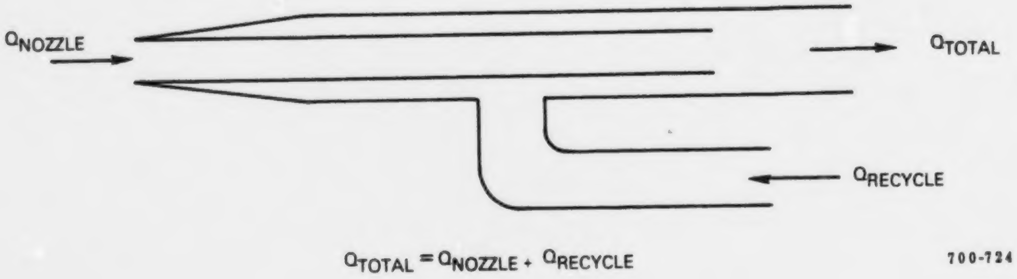
Q_{NOZZLE}
Q_{TOTAL}
$Q_{RECYCLE}$
$Q_{TOTAL} = Q_{NOZZLE} + Q_{RECYCLE}$
700-724

Figure 1. Conceptual drawing of exhaust gas recirculation nozzle showing annular introduction of recycle gas.

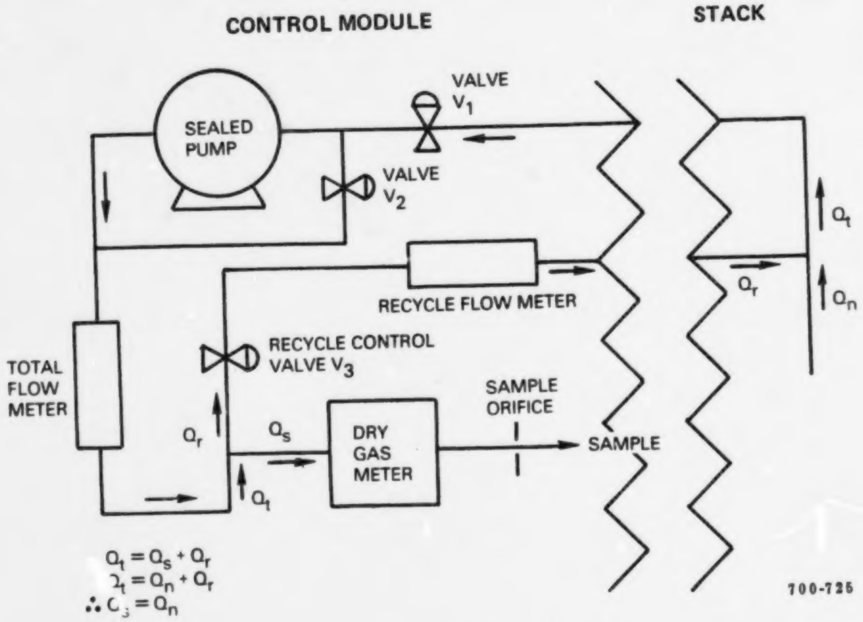
CONTROL MODULE
STACK
SEALED PUMP
VALVE V_1
VALVE V_2
RECYCLE FLOW METER
Q_t
Q_r
Q_n
RECYCLE CONTROL VALVE V_3
TOTAL FLOW METER
Q_r
Q_s
Q_t
DRY GAS METER
SAMPLE ORIFICE
SAMPLE
$Q_t = Q_s + Q_r$
$Q_t = Q_n + Q_r$
$\therefore Q_s = Q_n$
700-725

Figure 2. Block diagram of exhaust gas recirculation sampling train showing gas flow balance.

Other new components of the EGR flow control module include gas flow metering stages for the total and recycle gas lines. In the original breadboard EGR train, orifice flow monitors were used. In the current device these have been replaced by calibrated laminar flow elements to increase the dynamic range and flow stability of the gas metering system. The total flow metering element is used to set and monitor the gas flow rate required for proper operation of the inertial sampling device. The recirculated gas flow rate can also be monitored as a quality control check, to confirm that the proper mass flow rate balance exists or to indicate operating problems in either of the other two flow meters.

Operation of the EGR system involves only a few simple modifications of Method 5 operating procedures. First, an additional calculation step is required to determine the flow rate required for proper operation of the inertial sampler. Since Q_{total} must exceed Q_{nozzle} for the process to operate, the sampling nozzle must be small enough that this relationship can be retained for the range of gas velocities encountered. Thus, nozzle selection must consider the required sampler flow rate as well as duct gas conditions. Since the total gas flow rate is primarily controlled by valves V_1 and V_2, these valves will not be changed greatly after their initial adjustments. The sample flow rate is primarily affected by the recycle valve V_3, so that while the operator does not have to read a new indicator for sample flow, he does have to adjust a new valve. The only other addition to the traversing procedure of the EGR train is the addition of new pressure drops and perhaps temperatures to the run sheet.

PERFORMANCE TESTS

Performance tests were made in a laboratory wind tunnel on a sampling train modified for exhaust gas recirculation and an unmodified Method 17 train, simultaneously sampling air containing resuspended fly ash from coal combustion. Each sampler was located at a fixed position in the tunnel and was operated for 10 minutes each for tunnel air velocities of 20, 30, and 40 ft/sec to simulate sampling across a duct with changing gas velocity. Isokinetic conditions were maintained by controlling the total gas flow in the Method 17 train and by varying the recirculation gas flow in the modified train.

Good reproducibility was obtained in the results, and good agreement between the values of particle concentration measured by the two sampling trains, 0.099 mg/m^3 for the EGR train and 0.103 mg/m^3 for the Method 17 train. The results indicated that the operation of the modified train was not affected by recirculation of the gas.

The results of these tests indicate that exhaust gas recirculation is feasible. Planned future research includes adapting EGR sampling technique to inertial sizing devices, and field demonstration of the system.

METRIC CONVERSION FACTORS

To convert from:	To:	Multiply by:
pounds, avoirdupois (lb)	kilograms (kg)	0.454
grains (gr)	grams (g)	0.0648
grains/cubic foot (gr/ft^3)	grams/cubic meter (g/m^3)	2.29
inches (in.)	centimeters (cm)	2.54
feet (ft)	meters (m)	0.305
feet/minute (ft/min)	meters/second (m/s)	0.00508
cubic feet/minute (ft^3/min or cfm)	cubic meters/second (m^3/s)	0.000472
gallons (U.S.) (gal.)	liters (ℓ)	3.79
inches water gauge (in. WG or H_2O)	millimeters of mercury (mm Hg)	1.87
temperature °F	temperature °C	(°F-32) x 5/9